2011

Gravitational Waves
and
Experimental Gravity

Sponsored by

. CNRS (Centre National de la Recherche Scientifique)
. CEA (Commissariat à l'Énergie Atomique)
. IN2P3 (Institut National de Physique Nucléaire et de Physique des Particules)
. CNES (Centre National d'Etudes Spatiales)
. ESA (European Space Agency)
. Observatoire de Paris
. GPhyS (Gravitation et Physique Fondamentale dans l'Espace)

XLVIth Rencontres de Moriond and GPhyS Colloquium
La Thuile, Aosta Valley, Italy – March 20-27, 2011

2011 Gravitational Waves and Experimental Gravity

Printed in Vietnam
GPXB: 1119-2011/CXB/12-149/ThG (10.10.2011)
VN-TG-12149-1

Proceedings of the XLVIth RENCONTRES DE MORIOND
And GPhyS Colloquium

Gravitational Waves and Experimental Gravity

La Thuile, Aosta Valley Italy *March 20-27, 2011*

2011

Gravitational Waves and Experimental Gravity

edited by

Etienne Augé,
Jacques Dumarchez
and
Jean Trân Thanh Vân

THẾ GIỚI
PUBLISHERS

The XLVIth Rencontres de Moriond and GPhyS Colloquium

2011 Gravitational Waves and Experimental Gravity

was organized by :

Etienne Augé (IN2P3, Paris)
Jacques Dumarchez (LPNHE, Paris)

with the active collaboration of :

M.-Ch. Angonin (Observatoire de Paris)
R. Ansari (LAL, Orsay)
M.-A. Bizouard (LAL, Orsay)
L. Blanchet (IAP, Paris)
M. Cruise (Univ of Birmingham)
Y. Giraud-Héraud (APC, Paris)
S. Hoedl (University of Washington, Seattle)
Ch. Magneville (IRFU/SPP, Saclay)
E. Rasel (Hannover Institute of Quantum Optics)
S. Reynaud (LKB, Paris)
F. Ricci (Univ Roma I)
R. Schnabel (AEI, Hannover)
J.-Y. Vinet (OCA, Nice)
P. Wolf (Observatoire de Paris)

2011 RENCONTRES DE MORIOND

The XLVIth Rencontres de Moriond were held in La Thuile, Valle d'Aosta, Italy.

The first meeting took place at Moriond in the French Alps in 1966. There, experimental as well as theoretical physicists not only shared their scientific preoccupations, but also the household chores. The participants in the first meeting were mainly french physicists interested in electromagnetic interactions. In subsequent years, a session on high energy strong interactions was added.

The main purpose of these meetings is to discuss recent developments in contemporary physics and also to promote effective collaboration between experimentalists and theorists in the field of elementary particle physics. By bringing together a relatively small number of participants, the meeting helps develop better human relations as well as more thorough and detailed discussion of the contributions.

Our wish to develop and to experiment with new channels of communication and dialogue, which was the driving force behind the original Moriond meetings, led us to organize a parallel meeting of biologists on Cell Differentiation (1980) and to create the Moriond Astrophysics Meeting (1981). In the same spirit, we started a new series on Condensed Matter physics in January 1994. Meetings between biologists, astrophysicists, condensed matter physicists and high energy physicists are organized to study how the progress in one field can lead to new developments in the others. We trust that these conferences and lively discussions will lead to new analytical methods and new mathematical languages.

The XLVIth Rencontres de Moriond in 2011 comprised four physics sessions:

- March 13 - 20: "Electroweak Interactions and Unified Theories"
- March 13 - 20: "Quantum Mesoscopic Physics"
- March 20 - 27: "QCD and High Energy Hadronic Interactions"
- March 20 - 27: "Gravitational Waves and Experimental Gravity"

We thank the organizers of the XLVIth Rencontres de Moriond:

- A. Abada, J. Conrad, S. Davidson, P. Fayet, J.-M. Frère, P. Hernandez, L. Iconomidou Fayard, P. Janot, M. Knecht, J. P. Lees, S. Loucatos, F. Montanet, L. Okun, J. Orloff, A. Pich, S. Pokorski, D. Wood for the "Electroweak Interactions and Unified Theories" session,
- D. Averin, C. Beenakker, Y. Blanter, K. Ennslin, Jie Gao, L. Glazman, C. Glattli, Y. Imry, Young Kuk, T. Martin, G. Montambaux, V. Pellegrini, M. Sanquer, S. Tarucha for the "Quantum Mesoscopic Physics" session,
- E. Augé, E. Berger, S. Bethke, A. Capella, A. Czarnecki, D. Denegri, N. Glover, B. Klima, M. Krawczyk, L. McLerran, B. Pietrzyk, L. Schoeffel, Chung-I Tan, J. Trân Thanh Vân, U. Wiedemann for the "QCD and High Energy Hadronic Interactions" session,
- M.-Ch. Angonin, R. Ansari, M.-A. Bizouard, L. Blanchet, M. Cruise, J. Dumarchez, Y. Giraud-Héraud, S. Hoedl, Ch. Magneville, E. Rasel, S. Reynaud, F. Ricci, R. Schnabel, J.-Y. Vinet, P. Wolf for the "Gravitational Waves and Experimental Gravity" session, joint with the GPhyS Colloquium

and the conference secretariat and technical staff:

V. de Sá-Varanda and C. Bareille, I. Cossin, G. Dreneau, D. Fligiel, S. Hurtado, N. Ribet, S. Vydelingum.

We are also grateful to Andrea Righetto, Gioacchino Romani, Erik Agostini, Patrizia Rago, Matteo Tuzzi and the Planibel Hotel staff who contributed through their hospitality and cooperation to the well-being of the participants, enabling them to work in a relaxed atmosphere.

The Rencontres were sponsored by the Centre National de la Recherche Scientifique, the Institut National de Physique Nucléaire et de Physique des Particules (IN2P3-CNRS), the Fondation NanoSciences, the Commissariat à l'Energie Atomique (DSM and IRFU), the Centre National d'Etudes Spatiales, the European Space Agency, the Fonds de la Recherche Scientifique (FRS-FNRS), the Belgium Science Policy and the National Science Foundation. We would like to express our thanks for their encouraging support.

It is our sincere hope that a fruitful exchange and an efficient collaboration between the physicists and the astrophysicists will arise from these Rencontres as from previous ones.

E. Augé, J. Dumarchez and J. Trân Thanh Vân

Contents

reword

Gravitational Waves

First generation detectors

st-generation interferometric gravitational-wave detectors	H. Grote	5

Data analysis: Searches

ırches for gravitational wave transients in the LIGO and VIRGO data	F. Robinet	19
ırches for continuous gravitational wave signals and stochastic backgrounds in ȝO and VIRGO data	C. Palomba	27
ıltimessenger astronomy	N.L. Christensen	35
ırching for electromagnetic counterparts of gravitational wave transients	M. Branchesi	43
ırching for gravitational waves associated with gamma-ray bursts using the ȝO/Virgo network	M. Was	47
ward an optimal strategy for detecting coincident optical and gravitational wave nals from neutron star mergers	D.M. Coward	51

Sources of Gravitational Waves

ward Computing the Gravitational Wave Signatures of Core Collapse Supernovae	A. Mezzacappa	57
utron Stars as Gravitational Wave Sources	L. Gualtieri	65
neral Relativistic Magnetohydrodynamic Simulations of Binary Neutron Star ergers	L. Rezzolla	69
.e coalescence rates of double black holes	K. Belczynski	77
rturbative, post-newtonian, and general relativistic dynamics of black hole binaries	A. Le Tiec	81
ı the eccentricity OF NS-NS binaries	I. Kowalska	85
mpact objects with spin parameter $a_* > 1$	C. Bambi	89

Space Detectors

ȝA Pathfinder and the LTP	P. W. McNamara	95
ȝA Pathfinder: In-orbit experiments and characterisation	M. Hewitson	103
ȝA Pathfinder: an experimental analysis of the LPF free-fall performance	W. J. Weber	109
arch for GWs from white dwarf binaries in Mock LISA Data Challenge data	A. Królak	113

Advanced Detectors

lvanced Virgo	R. L. Ward	119
ientific potential of Einstein Telescope	B. Sathyaprakash	127
:perimental approaches for the Einstein Telescope	R. Nawrodt	137
ry high frequency gravitational wave science	A.M. Cruise	145
ımparison of LISA and atom interferometry for gravitational wave astronomy in ace	P. L. Bender	149
alisation of the ALIGO fused silica suspension	A. Bell	155
stematic study of newtonian gravitational constant measurement in MAGIA experiment	Y.-H. Lien	159
tra-stable, high-power laser systems	P. Kwee	165
gh power input optics for advanced VIRGO	J. Marque	169
ıermal effects and their compensation in the erferometric gravitational wave detector Advanced Virgo	A. Rocchi	173
easuring the Virgo area tilt noise with a laser gyroscope	J. Belfi	179
avitational wave detectors are driven away from thermodynamic equilibrium. why ould we care	P. De Gregorio	183

II. Experimental Gravity

6. Short Range Gravity

Gravitation at short distances : theory — I. Antoniadis
Casimir and short-range gravity tests — S. Reynaud
Testing the inverse square law of gravitation at short range with a superconducting torsion balance — E.C. Chalkley
Short range tests with neutrons at ILL — V. Nesvizhevsky
Gravity Spectroscopy — T. Jenke
Forca-G: A trapped atom interferometer for the measurement of short range forces — B. Pelle

7. Tests of relativity in the solar system

Planetary ephemerides and gravity tests in the solar system — A. Fienga
Tests of gravity at the solar system scale — M.-T. Jaekel
OSS (Outer Solar System) Mission — B. Christophe
On the anomalous increase of the lunar eccentricity — L. Iorio
Radioscience simulations in General Relativity and in alternative theories of gravity — A. Hees
GAME - Gravitation Astrometric Measurement Experiment — M. Gai
A relativistic and autonomous navigation satellite system — P. Delva
Optical clock and drag-free requirements for a Shapiro time-delay mission — P. Bender

8. Long range gravity

Probing the dark energy nature with type Ia supernovae : cosmological constraints from the Supernova Legacy Survey first 3-years — D. Hardin
Is Dark Energy needed? — A. Blanchard
Testing MOND in the Solar System — L. Blanchet
Testing dark matter with GAIA — O. Bienaymé
Beyond Einstein: cosmological tests of model independent modified gravity — D.B. Thomas

9. Weak equivalence principle

Equivalence Principle Torsion Pendulum Experiments — T. A. Wagner
Among space fundamental physics missions, MICROSCOPE, a simple challenging free fall test — P. Touboul
Atom interferometry and the Einstein equivalence principle — P. Wolf
Significance of the Compton frequency in atom interferometry — M. A. Hohensee
Observability of short-range gravitation with the experiment FORCA-G — S. Pelisson
Major challenges of a high precision test of the equivalence principle in space — A.M. Nobili

10. Lorentz invariance and CPT

Lorentz symmetry, the SME, and gravitational experiments — J. D. Tasson
Electromagnetic cavity tests of lorentz invariance on earth and in space — A. Peters

11. Clocks

The ACES mission: fundamental physics tests with cold atom clocks in space — L. Cacciapuoti

12. Pulsars

Gravitational wave detection through pulsar timing arrays — D. J. Champion

13. Other Topics

Measuring g with a beam of antihydrogen (AEgIS) — C.Canali
GBAR - Gravitational Behavior of Antihydrogen at Rest — P. Dupré
Evidence for time-varying nuclear decay dates: experimental results and their implications for new physics — E. Fischbach
Analysis of experiments exhibiting time-varying nuclear decay rates: systematic effects or new physics? — J.H. Jenkins

l. Posters

ıstein Equivalence Principle and Bose–Einstein condensates	A. Camacho	411
CROSCOPE instrument servo-loops and digitization	A. Lévy	413
ectrostatic accelerometer with bias rejection for deep space gravitation tests	B. Lenoir	415
rentz invariant phenomenology of quantum gravity: Main ideas behind the model	Y. Bonder	417
wards an ultra-stable optical sapphire cavity system for testing Lorentz invariance	M. Nagel	419
e search for primordial gravitational waves with SPIDER: a balloon-borne cmb larimeter	C. Clark	421
rong lensing system and dark energy models	B. Malec	423
nstraints on a model with extra dimensions for the black hole at the galactic center	A.F. Zakharov	425
smological and solar-system constraints on tensor-scalar theory with chameleon ect	A. Hees	427
ie STAR Mission: SpaceTime Asymmetry Research	T. Schuldt	439
ı the maximum mass of differentially rotating neutron stars	A. Snopek	431
easurement of slow gravitational perturbations with gravitational wave interferom-ers	V.N.Rudenko	433
ikes in Gravitational Wave Radiation from Quickly Rotating Galactic Centers	A. A. Sadoyan	437
ck Processes in the Merger of Two Black Holes	I. Damião Soares	439
smology models and graviton counting in a detector	A. Beckwith	441
ansverse, traceless, plane fronted, monochromatic plane waves in conformal gravity ıve zero-energy	M. Paranjape	443
ravitational wave recoil in nonsymmetric Robinson-Trautman spacetimes	A. Saa	445
odification of atomic states in a vertical optical trap near a surface	R. Messina	447
ərsion pendulum with 2 DoF for the study of residual couplings between the TM ıd the GRS: approaching thermal noise limited sensitivity	L. Marconi	451
ist of participants		453

I.
Gravitational Waves

1.
First generation detectors

FIRST-GENERATION INTERFEROMETRIC GRAVITATIONAL-WAVE DETECTORS

H. GROTE*, D. H. REITZE+

*MPI for Grav. Physics (AEI), and Leibniz University Hannover, 38 Callinstr., 30167 Hannover, Germany
E-mail: hartmut.grote@aei.mpg.de

+Physics Department, University of Florida, Gainesville, FL 32611, USA
E-mail: reitze@phys.ufl.edu

In this proceeding, we review some of the basic working principles and building blocks of laser-interferometric gravitational-wave detectors on the ground. We look at similarities and differences between the instruments called GEO, LIGO, TAMA, and Virgo, which are currently (or have been) operating over roughly one decade, and we highlight some astrophysical results to date.

1 Introduction

The first searches for gravitational waves began in earnest 50 years ago with the experiments of Joseph Weber using resonant mass detectors ('Weber Bars').[1] Weber's pioneering efforts were ultimately judged as unsuccessful regarding the detection of gravitational waves, but from those beginnings interest in gravitational wave detection has grown enormously. For some decades after, a number of resonant mass detectors were built and operated around the globe with sensitivities far greater than those at Weber's time. Some resonant bars are still in operation, but even their enhanced sensitivities today are lower and restricted to a much smaller bandwidth than those of the current laser interferometers.

Over the past decade, km-class ground-based interferometers have been operating in the United States, Italy and Germany, as well as a 300 m arm length interferometer in Japan. Upgrades are underway to second generation configurations with far greater sensitivities. With further astrophysics 'reach', these detectors will usher in the era of gravitational wave astronomy with the expectation of tens or possibly hundreds of events per year based on current rate estimates.[2] (See also the contributions about *Advanced* detectors in this volume.)

Section 2 of this paper presents a brief introduction to ground-based gravitational wave interferometry, detector architecture, and methods used to minimize the influence of external perturbations. Section 3 surveys the currently operational (or operational until late 2010) interferometers, with a particular view on some unique features of the individual instruments. Finally we give a brief review of the most significant observational results to date in Section 4. Parts of this paper have been published as proceeding of the 12th Marcel Grossmann meeting.[3]

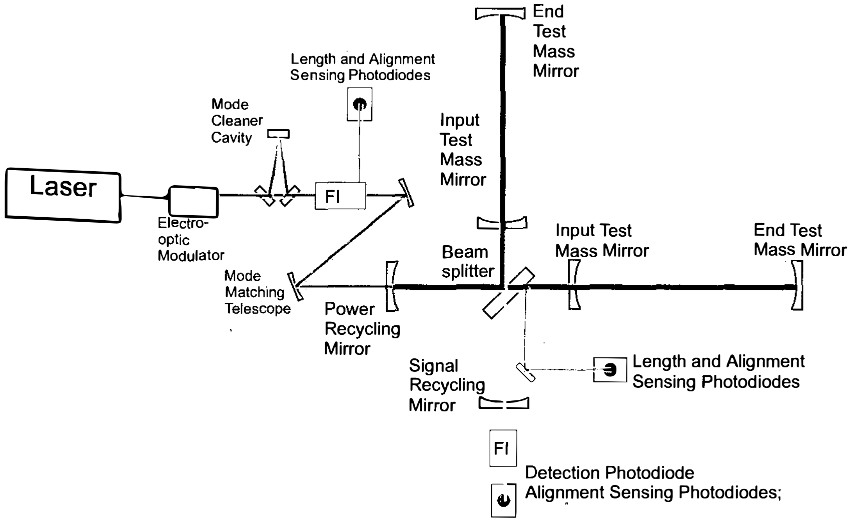

Figure 1: Generic layout example of a ground-based laser-interferometric gravitational-wave detector. The basic building blocks are a laser, input optics (mode cleaner cavity, Faraday Isolator FI, mode matching telescope), and a Michelson interferometer consisting of a beam splitter and two end test mass mirrors. Additional optics are: Power recycling mirror, to resonantly enhance the circulating light power, Input test mass mirrors, to increase the light storage time in the long arms, a signal recycling mirror to increase and optimize gravitational-wave signal storage time. First-generation interferometers around the globe only use subsets of these optics, as detailed in the text. Length- and alignment sensing photodiodes are shown, together with the detection photodiode at the output port of the Michelson interferometer (or the signal recycling cavity, respectively).

2 Principles of ground-based Gravitational Wave Interferometers

Gravitational waves are strains, or changes in length per unit length, $\Delta L/L$, which come about due to the time dependence of the quadrupole mass moment, $I_{\mu\nu}(t)$, of massive objects. From a practical standpoint, astrophysical objects moving at relativistic speeds are needed to generate gravitational waves of sufficient amplitude to enable detection by earth-based interferometers. Several excellent references exist which describe gravitational waves and their intimate connection with astrophysics (see, for example, Ref.[4] and Ref.[5] and references therein). In this section, we briefly describe the generic workings of laser-interferometric gravitational wave detectors.

Figure 1 displays the most general layout of a ground-based interferometer. A frequency- and amplitude-stabilized laser is phase-modulated via electro-optic modulation and injected into a mode-cleaner triangular optical cavity to provide an additional level of frequency and amplitude stabilization as well as to suppress pointing fluctuations of the input laser beam. The mirrors in the mode cleaner cavity and all subsequent mirrors comprising the interferometer are isolated from low-frequency ground motion by seismic isolation platforms and mirror suspensions (see section 2.1). From the mode-cleaner, the beam passes through a Faraday isolator (FI) which functions somewhat analogously to an optical 'diode', diverting back-reflections from the interferometer to length and alignment sensing photodiodes and preventing the light from entering the mode-cleaner. The FI is followed by a beam-expanding telescope which mode-matches the input laser mode into the interferometer cavity mode.

The basis for the interferometer architecture is a Michelson interferometer, consisting of a beam splitter and the two end test mass mirrors, and a detection photodiode. A second FI can be used to prevent light scattering from the photodiode back into the interferometer. To minimize noise associated with amplitude fluctuations of the laser, the interferometer differential path length is set to interfere carrier light destructively at the detection photodiode such that the quiescent state is nearly dark. A passing gravitational wave differentially modulates the round-trip travel time of the light in the arms at the gravitational wave frequency which in turn modulates the light intensity at the detection photodiode. In effect, the interferometer transduces the dynamic metric perturbation imposed by the passing gravitational wave to photocurrent in the detection photodiode. The magnitude of photocurrent depends not only on the amplitude, but also on the direction and polarization of the passing gravitational wave.

Beyond the simple Michelson configuration, the sensitivity of the interferometer can be further increased in three ways. By adding input test mass mirrors into each arm, Fabry-Perot cavities are formed, effectively increasing the light storage time in the arms (or, in an alternative view, amplifying the phase shift for a given amount of displacement). Second, since the recombined laser light at the beam splitter interferes constructively toward the laser, it can be coherently recirculated back into the interferometer by a 'power-recycling' mirror located in between the mode-matching telescope and the beam splitter. Finally, the gravitational signal itself can be recycled by placing a 'signal-recycling' mirror between the beam splitter and the detection photodiode to recirculate the light modulated by the gravitational wave into the interferometer, further increasing the light storage time and thus the depth of modulation by the gravitational wave. The signal-recycling mirror also allows for tuning of the response curve of the interferometer. By shifting the signal-recycling mirror a fraction of a wavelength from resonant recirculation ('tuned' operation), specific frequencies of the light are resonantly recycled at the expense of others ('detuned' operation), allowing for enhanced sensitivities over specific frequency ranges of interest.

Current interferometers are designed to be sensitive in the frequency range from approximately 10-50 Hz out to a few kHz. Fundamental noises limiting interferometer sensitivity depend on the specifics of the interferometer design, and different interferometers have approached the task of minimizing interferometer noise in different ways. However, the limiting sensitivity envelope for all ground-based detectors roughly breaks down as follows: seismic ground motion at low frequencies, thermal noise due to the Brownian motion of the mirror suspension wires and mirror coatings in the mid-frequency bands, and shot noise at high frequencies. In addition, technical noise sources from length and alignment sensing and control systems can also limit interferometer performance, in particular at the low-frequency end. To minimize phase noise from light scattering off molecules, the components of the interferometer and the input optics (mode-cleaner, FI, and telescope) are located in an ultrahigh vacuum system. Light scattering off mirrors however, which can be reflected by seismically 'noisy' components and then being re-directed to interfere with the main interferometer beams, can also contribute to excess noise.

2.1 Seismic isolation and suspensions

A typical ambient horizontal ground motion on the surface of the earth is about $10^{-10}\,\mathrm{m}/\sqrt{\mathrm{Hz}}$ at 50 Hz. Depending on the choice of sensitive frequency band, the test mass mirrors of gravitational-wave interferometers have to be quieter by roughly 10 orders of magnitude at these frequencies, motivating sophisticated seismic isolation systems.

The principle used to isolate optical components such as mirrors from ground motion is to suspend the components as pendulums, making use of the attenuation provided by the pendulums displacement transfer function above the fundamental pendulum resonance frequency. Most of the projects to date use cascaded multiple-pendulum chains, in order to increase the amount of attenuation. Figure 2 shows two examples of cascaded pendulums as in use in Virgo and GEO 600 (see section 3 below, for the individual projects), namely a), the Virgo 'super attenuator', and b), the GEO 600 suspension.

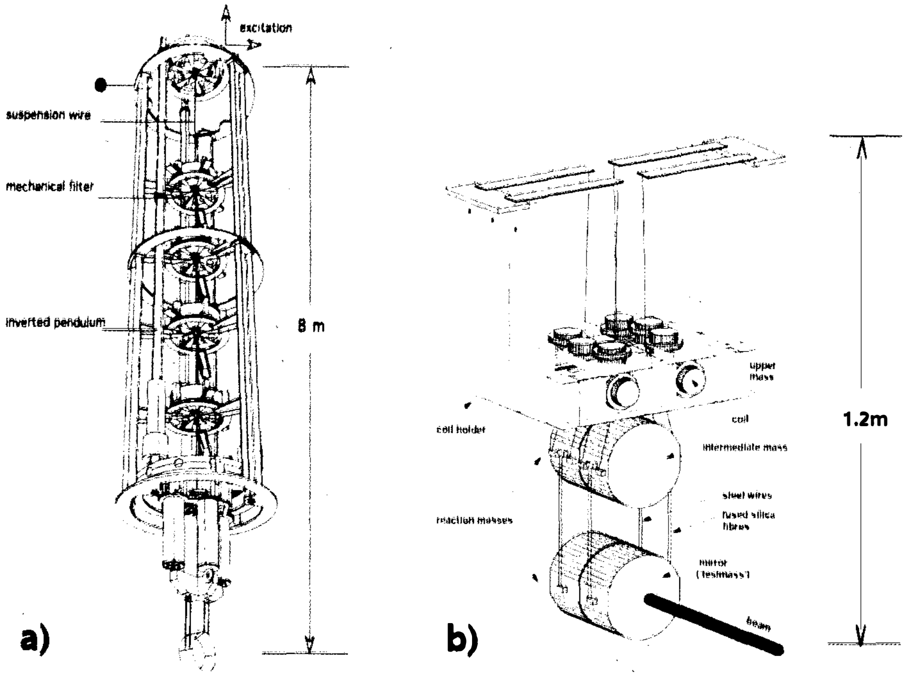

Figure 2: a) The Virgo 'super attenuator' consists of multiple pendulum stages connected by single suspension wires. Vertical isolation is provided by the 'mechanical filter' stages, which act as pendulum masses, but also hold the subsequent suspension wire by blade-springs. b) The GEO 600 suspension consists of 3 pendulum stages (including the test-mass mirror). The upper two stages provide vertical isolation by steel springs holding the suspension wires. Both suspension types a) and b) use fused silica fibres to suspend the test mass mirror from the penultimate, or intermediate mass.

A Virgo super-attenuator [6] consists of multiple pendulum stages, which are connected to each other by single suspension wires. In addition to the inherent horizontal isolation of the pendulums, the intermediate pendulum masses, denoted as *mechanical filters,* provide vertical isolation by a *magnetic anti-spring* mechanism. The penultimate mass holds the test-mass mirror on 4 suspension slings, such that angular control can be applied to the mirror from the penultimate mass. In addition to this, angular and longitudinal control forces can be applied to the mirror by a reaction mass (not shown in Figure 2), suspended around the test mass. Coils are attached to the reaction mass, applying forces to magnets glued onto the test mass. The mechanical filter at the top of the suspension chain is supported by an inverted pendulum, completing the supreme low-frequency passive isolation of the super-attenuator. Active feedback control using position- and inertia sensors is required to keep the inverted pendulum at its operating point. The GEO suspension is much more compact in total dimensions, and makes use of three cascaded pendulum stages. Vertical isolation is provided by blade springs, holding the suspension wires of the first and second pendulum stage. For two of the main test masses GEO uses two similar pendulum chains closely located to each other, as shown in Figure 2. The second pendulum chain serves as a reaction 'platform' from which forces can be applied to the test-mass chain without using force actuators referenced to the much larger ground motion.

2.2 Control

While suspended optics are supremely quiet in the measurement band of interest (i.e. above 10-50 Hz) the motion of the suspended optics is resonantly enhanced on the eigenmodes of the suspensions, typically around 0.5 to a few Hz. Therefore, different techniques are employed to reduce motion amplitudes of these modes. In many cases, actual mirror motion is measured locally by shadow-sensors, CCD images, or optical lever configurations. Feedback is then applied by coil/magnet actuators to damp the motion of pendulum components. This type of damping can be applied at different levels of the suspension chain, preferably on one of the upper masses to reduce re-introduced displacement noise in the measurement band.

To achieve the sensitivities required for gravitational wave detection, all of the interferometer mirrors must be held to absolute positions of a picometer or less in the presence of several sources of displacement noise. Global length sensing and control systems keep the cavities locked on resonance, using sophisticated variants of the Pound-Drever-Hall cavity locking technique. Phase modulation by the electro-optic modulator (see Figure 1) produces radio-frequency (RF) sidebands on the laser light which serve as references (local oscillators) for sensing length changes in the various length degrees of freedom. In addition, the alignment of the mirrors must be maintained to a few nanoradians using a sensing and control system based on a spatial analog of Pound-Drever-Hall locking.

Hundreds of control loops are thus necessary to keep the interferometer at its nominal operating point. The procedure of bringing the interferometer to this highly-controlled state is non-trivial, and all of the projects have spent many months to years to arrive at reliably reproducible locking sequences, which have become highly automated in most cases.

3 First generation Detectors around the Globe

At the present time, there are five gravitational wave observatories — two LIGO sites in the US, the Virgo and GEO 600 sites in Europe, and the TAMA 300 observatory in Japan (see Figure 3). These observatories have been in operation for the past decade, and constitute the first generation of large-scale interferometers. In this sense the term 'first generation' refers to the time at which these instruments have been built and are operating. However, as we will see below, some of the instruments employ techniques which are technically more advanced than others. These techniques are commonly described as 'second generation' or 'advanced' techniques, with the anticipation that they will be widely implemented in the detector generations planned to replace the existing ones. On these planned upgrades (see other papers in this volume) the infrastructures including buildings, vacuum systems etc. will be re-used, but substantial parts of the interferometer will be replaced with new systems.

3.1 LIGO

LIGO consists of two separately located facilities in the United States, one in Hanford, Washington and one in Livingston, Louisiana. The LIGO Hanford Observatory used to house two interferometers, a 4-km arm length interferometer and a 2-km arm length interferometer. The LIGO Livingston Observatory houses a single 4-km long interferometer. The 2-km interferometer in Hanford was taken out of operation in summer 2009, and the two 4-km interferometers were taken out of operation in October 2010, to make way for the *Advanced LIGO* project (see article on Advanced LIGO in this volume). Here we report on the LIGO interferometers up to October 2010, referred to as *Initial* and *Enhanced* LIGO.

The three initial LIGO interferometers were identical in configuration, employing Fabry-Perot arm cavities and power-recycling (but not signal recycling). The seismic isolation system of initial LIGO consisted of passive pre-isolation stacks, using alternating layers of metal and

Figure 3: Global map showing the locations of the first-generation laser-interferometric gravitational wave detectors: The LIGO interferometers in the US, the GEO 600 interferometer in Germany, the Virgo interferometer in Italy, and the TAMA 300 interferometer in Japan.

constrained-layer damped metal coil springs in fluoro-elastomer seats. The test masses were suspended as single-stage pendulums with the suspension point of the pendulums being pre-isolated by the passive spring/metal stacks. At the Livingston site, the higher environmental (mainly anthropogenic) seismic noise made it necessary to install an additional active seismic pre-isolation stage, making use of hydraulic actuators which move the bases of the spring/metal stacks, to counteract seismic motion.[7]

While conservative in the suspension design, the two LIGO 4–km interferometers have been leading in peak sensitivity, as well as over most of the frequency spectrum, with peak strain sensitivities of approximately 2 x $10^{-23}/\sqrt{Hz}$ in the 150–200 Hz region. (See Figure 4 for the strain sensitivities of the three LIGO interferometers during the S5 science run.) An alternative way of characterizing interferometer sensitivity comes from considering how far a specific astrophysical source can be detected. A typical measure of this kind is the range as the distance to which an interferometer can detect the last few moments of orbital decay (inspiral) and merger of a 1.4–1.4 M_{sun} (solar mass) binary neutron star system (for non-spinning neutron stars) with a signal-to-noise ratio of 8. If an optimal orientation of the orbital plane of the neutron stars with respect to the interferometer is assumed, the LIGO interferometers were capable of detecting 1.4–1.4 M_{sun} binary neutron star coalescences out to approximately 35 Mpc during the S5 science run.

In the years from 2007 to 2009, the two 4–km instruments were partially upgraded (within the *enhanced* LIGO project) to moderately increase their sensitivity and to test techniques, to be used in the advanced LIGO project. The most important of these upgrades comprised:

- installation of a more powerful main laser, increasing the available power at the input modecleaner from approx. 10 to 30 W, and the replacement of electro-optic modulators and Faraday isolators to handle the increased power with out distorting the laser beam.

- upgrade of the thermal compensation system, required to compensate for optical distor-

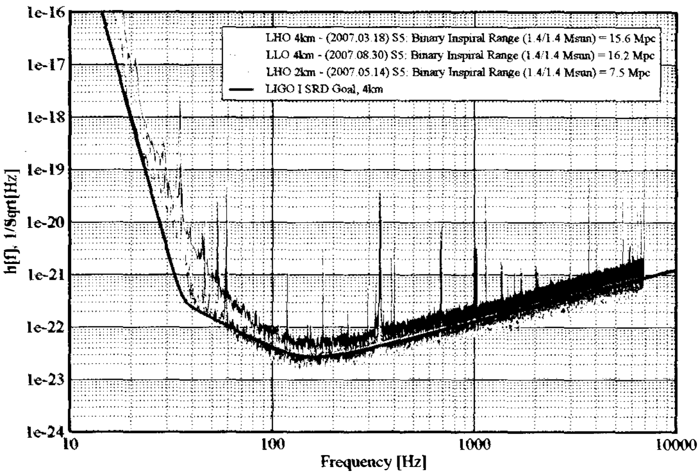

Figure 4: Representative strain sensitivities of the three LIGO interferometers during LIGO's S5 science run. The binary inspiral ranges are here given for an average orientation of the source with respect to the detector.

tions of the laser beams, caused by the high utilized laser power.

- the transition from heterodyne to homodyne readout of the gravitational-wave signal, and the installation of an output-mode cleaner (an additional optical resonator in the output beam) compatible with homodyne readout.

The achieved sensitivities of the two 4–km LIGO instruments up to their end of operation were factors of about 1.4-1.6 better in the high-frequency region above several 100 Hz, compared to the sensitivities shown in Figure 4. The range to detect binary neutron star coalescences was increased from 35 Mpc to about 50 Mpc for an optimal orientation of the source.

A much more detailed overview of the LIGO interferometers can be found in Ref. [8].

3.2 Virgo

The Virgo interferometer located in Cascina, Italy (near Pisa), is operated by a joint consortium of Italian, French, Dutch, Polish, and Hungarian scientists.[9,10] The Virgo interferometer topology is identical to that of the LIGO interferometers, consisting of power-recycling and employing Fabry-Perot arm cavities. The Virgo arms are 3 km in length. A very distinct difference to LIGO is the use of the 'super-attenuator' as seismic isolation system, as described in section 2.1.

As a result of the sophisticated low-frequency isolation, the Virgo interferometer possesses the best strain sensitivity in the low 10–40 Hz band. Virgo was designed to be slightly less sensitive than the LIGO 4 km interferometers in the 40–1000 Hz band, and comparably sensitive above 1 kHz. The Virgo interferometer also enjoys a higher duty cycle than LIGO due to its enhanced seismic isolation, which allows allocation of required actuation forces along different points in the suspension chain. Virgo strain sensitivity curves are shown in Figure 5.

Virgo conducted its first long-duration science run (designated VSR1) during the period May - October 2007. Virgo and LIGO entered into a data sharing agreement prior to the VSR1 run, joining the LIGO and GEO 600 interferometers; since May 2007, Virgo, LIGO, and GEO 600 have been conducting joint science runs and coordinated run planning. Upon

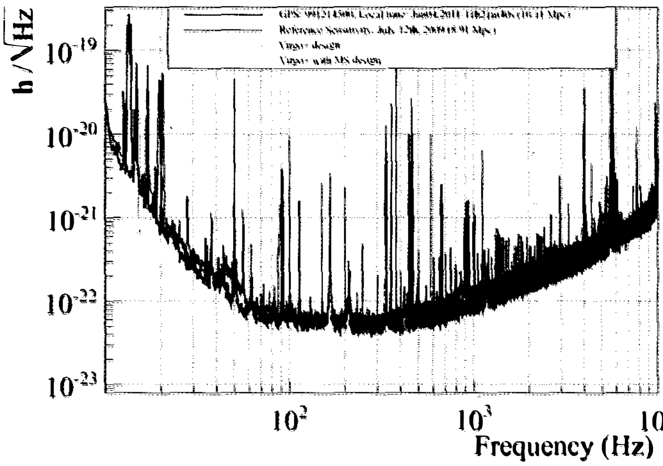

Figure 5: Representative strain sensitivities of Virgo, as of July 2009 and June 2011 (VSR4). In the period after 2009, monolithic suspensions were implemented and the finesse of the arm cavities was increased. The sensitivity to binary neutron star inspirals is about 10 Mpsec for average source orientation. Due to its unique low-frequency sensitivity Virgo achieves a range of more than 70 Mpc for 100–100 M_{sun} black-hole binary systems with an average source orientation.

completion of VSR1, Virgo entered into a period of upgrades to improve detector sensitivity and test advanced techniques. In 2009/2010 Virgo has implemented monolithic fibre suspensions [11] directly bonded to the mirrors, to lower thermal noise. Further, the finesse of the Fabry-Perot arms was increased and thermal compensation systems for radius-of-curvature adjustment were implemented, in order to optimally match the radii-of curvature of the test masses. A science run together with the GEO 600 detector has started on 3rd June 2011 (VSR4/S6e), and is scheduled to last 3 months. After this period, Virgo is starting the advanced Virgo project (see contribution about advanced Virgo in this volume).

3.3 GEO 600

GEO 600[12] is a British-German project located 20 km south of Hannover, Germany. The detector has arm lengths of 600 m and consists of a Michelson interferometer with power- and signal recycling. GEO 600 has no Fabry-Perot cavities in the arms, but once folded arms, resulting in an effective arm length of 1.2 km. GEO uses triple suspensions as described in section 2.1, and the final stage uses fused silica fibres [13] since 2001. GEO is the only project to use electro-static drives to actuate on the main test masses. Other actuation points using coil/magnet actuators are located at the intermediate mass level and at the upper mass level (see Figure 2 b) for the suspension stages). Like for the super-attenuator, this arrangement allows for actuation at different points in the suspension chain, and is a key element for a robust locking of the interferometer. The GEO detector is highly automated and achieved a high duty cycle in the 24/7 run mode of S5 of more than 90 %.

The initial GEO detector was operational until summer 2009, when an upgrade program called *GEO-HF* started. The GEO-HF upgrade focuses on techniques to increase the shot-noise limited sensitivity of GEO. Yet, noise reduction at frequencies below 500 Hz will be done to potentially reach the thermal noise limit of dielectric test-mass coatings. The main points of the

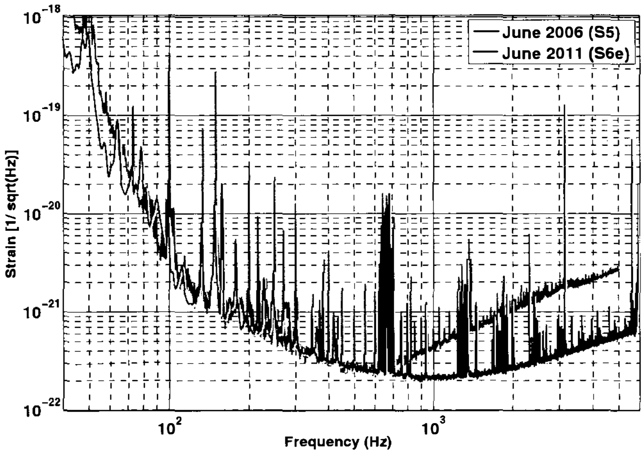

Figure 6: Representative strain sensitivities of the GEO 600 detector. During the fifth science run of the LSC (S5), GEO has been operating with a peak sensitivity around 500Hz, where the signal recycling cavity was tuned to have maximal signal enhancement. Since 2009, GEO operates signal recycling with maximal sensitivity at 'DC' and since 2010 with a higher signal-recycling bandwidth. Together with other improvements, this resulted in a higher sensitivity in the shot-noise limited region above approx. 500 Hz, as shown by the trace from June 2011 (S6e).

GEO-HF upgrade comprise (see also [14]):

- the transition from heterodyne readout to homodyne readout for the gravitational-wave signal, and the installation of an output-mode cleaner compatible with homodyne readout.
- transition from the *detuned* signal recycling, having the peak sensitivity around 500 Hz to *tuned* signal recycling with the peak (shot-noise limited) sensitivity at 'DC'. This goes together with an increase of bandwidth of the signal recycling cavity from about 200Hz to 1 kHz.
- installation of a more powerful main laser, and change of some input optics to accommodate an increased laser power of up to 25 W incident onto the main interferometer.
- injection of squeezed vacuum into the output port of GEO 600, to lower the shot noise.[15,16]

Figure 6 shows strain sensitivities of GEO 600 from 2006 (during the S5 science run) and from 2011, after the GEO-HF upgrade had been under way since about 2 years. GEO now reaches a strain sensitivity of $2 * 10^{-22}/\sqrt{\mathrm{Hz}}$ around 1 kHz, and is comparable sensitive to the Virgo detector at higher frequencies.

3.4 Tama 300

TAMA 300 is a 300 m arm length interferometer located near Tokyo, Japan and is operated by a consortium of Japanese scientists. TAMA 300 employs a Fabry-Perot arm cavity power-recycled Michelson architecture similar to LIGO and Virgo. Although not as sensitive as other large-scale interferometers in operation today, TAMA 300 was the first interferometer to conduct a science

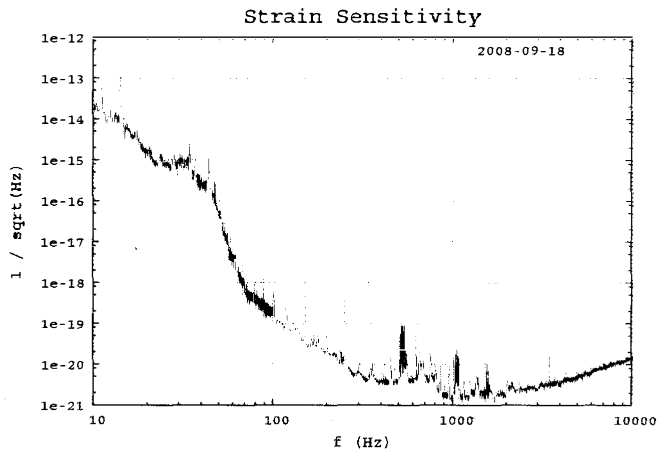

Figure 7: Strain sensitivity of TAMA 300 as of September 2008.

run (August 1999) and has completed eight science runs in the 1999–2004 time frame, with over 1000 hours of accumulated data.

In recent years, TAMA has undergone an extended period of upgrades. TAMA 300's location within a major metropolitan area subjects the interferometer to large amounts of seismic noise. Thus, a two-stage active seismic attenuator system has been developed to mitigate ground noise coupling to the interferometer. [17] Because of its short arm length and high level of seismic disturbance, TAMA 300 is most sensitive in the 1–1.5 kHz band, achieving a strain sensitivity approaching $10^{-21}/\sqrt{Hz}$. The TAMA 300 strain sensitivity curve as of September 2008 is shown in Figure 7. Experience from operating TAMA is utilized in the design of the Large Cryogenic Gravitational-Wave Observatory LCGT in Japan (see contribution in this volume).

4 Astrophysics with the Global Network

Ground-based interferometers have been actively searching for gravitational wave emission from different astrophysical sources for almost a decade. Searches are classified broadly along four types of sources: i) compact binary systems (inspiral, merger, and ring-down), ii) continuously emitting systems (rapidly spinning neutron stars), iii) stochastic sources (noise, eg, the primordial gravitational wave background), and iv) 'burst' sources whose waveforms are unknown or poorly modeled. Analysis methods and algorithms are specifically tailored to each source class. The first observational results on searches for inspiraling compact binaries were published by the TAMA collaboration. [18] A thorough review of recent gravitational wave observational results can be found in Ref. [8]. Here, we simply present a few highlights from recent papers.

4.1 GRB 070201

Gamma ray bursts (GRBs) are intensely bright emissions of γ-rays arising from compact objects, primarily observed at cosmological distances. Most of the observed short hard GRBs are thought to have binary black hole-black hole (BH-BH), black hole-neutron star (BH-NS), or neutron star-neutron star (NS-NS) mergers as their progenitors, although no definitive experimental evidence exists to associate short hard GRBs with binary mergers. The simultaneous observation of a GRB and gravitational wave signal would provide confirmation that binary mergers are a source f GRBs.

GRB 070201 was an exceptionally short hard GRB observed in the x-ray spectrum by satel-tes in the Interplanetary Network (IPN). The error box had significant overlap with the M31 Andromeda) galaxy (located 730 kpc from the Milky Way galaxy), thus making it a prime can-idate for gravitational wave searches. Data from the LIGO Hanford detectors were analyzed in . 180 s time window around GRB 070201 using both template-based searches for binary mergers .nd burst search algorithms.[19] No signal was found, and LIGO was able to exclude a compact inary BH-NS, NS-NS merger progenitor of GRB 070201 located in M31 at $> 99\%$ and 90% onfidence levels, respectively. The analysis did not rule out a soft gamma repeater (SGR) in M31, but was able to place a limit on energy conversion to gravitational wave of less than 4×10^{-4} M_{sun}.

1.2 *Beating the Spindown Limit on the Crab Pulsar*

Spinning neutron stars can emit gravitational waves if they possess ellipticities arising from crustal deformations, internal hydrodynamic modes, or free precession ('wobble'). Ground-based gravitational wave detectors are potentially sensitive to gravitational wave emissions from neutron stars in our galaxy. The Crab pulsar (PSRB0531+21, PSRJ0534+2200), located 2 kpc distant, is a particularly appealing candidate for gravitational wave emission because it s relatively young and rapidly slowing in rotation ('spinning down'). While the predominant energy dissipation mechanisms are magnetic dipole radiation or charged particle emission in the pulsar's magnetosphere, the measured braking index of the Crab pulsar suggests that neither dipole radiation or particle ejection can account for the rotational braking.

Using a subset of data from LIGO's S5 science run, the LIGO Scientific Collaboration searched for gravitational wave emission from the Crab pulsar during a nine month duration during which no pulsar timing jumps occurred.[20] No gravitational waves were observed, and the data was used to set upper limits on the strain $h = 3.35 \times 10^{-25}$ and ellipticity $\epsilon = 1.79 \times 10^{-4}$. The limit on strain is significant in that it implies no more than 5.5% of the energy emitted by the Crab pulsar is in the form of gravitational waves. An updated analysis by the LIGO and Virgo collaborations using a more extensive data set have reduce the upper limit on radiated gravitational wave energy to approximately 2%.[21]

4.3 *The Primordial Gravitational Wave Background*

A stochastic gravitational wave background could arise from an incoherent superposition of point source emitters or from the remnant gravitational wave emission from the Big Bang. Electro-magnetic observations of the cosmic microwave background have provided the best knowledge so far of the early universe, however they are limited to probe the universe after the recombination era when the universe became transparent to electromagnetic radiation. Searches for primordial gravitational waves are thus particularly significant from a cosmological standpoint since they directly probe the universe at its earliest epoch.

Recent results by the LIGO Scientific and Virgo Collaborations have placed the most strin-gent direct observational limit on a stochastic gravitational wave background from the primordial universe. By cross-correlating data from the LIGO Livingston and Hanford 4-km interferome-ters during the S5 science run, an upper limit of $\Omega_{0,GW} < 6.9 \times 10^{-6}$ on the energy density of stochastic gravitational waves (normalized to the closure energy density of the universe) assum-ing the gravitational wave background is confined within the 50–150 Hz frequency band.[22] This limit is the best experimental limit in the LIGO frequency band, beating the limit inferred from the Big Bang Nucleosynthesis by almost a factor of 2.

Acknowledgments

The authors gratefully acknowledge support from the Science and Technology Facilities Council (STFC), the University of Glasgow in the UK, the Bundesministerium für Bildung und Forschung (BMBF) and the state of Lower Saxony in Germany. We further gratefully acknowledge the support of the US National Science Foundation through grants PHY-0855313 and PHY-0757968. We also thank Francesco Fidecaro, David Shoemaker, Giovanni Losurdo, and Daisuke Tatsumi for very useful discussions and for supplying material for this article.

References

1. J. Weber, *Phys. Rev.* **117**, 306 (1960).
2. J. Abadie, et al., arXiv:1003.2480 (submitted).
3. D. Reitze, WSPC proceedings MG12, (2010)
4. P. Saulson, *Fundamentals of Interferometric Gravitational Wave Detectors*, 1st edn. (World Scientific Publishing, Hackensack, NJ, 1994).
5. M. Maggiore, *Gravitational Waves: Volume 1: Theory and Experiments*, 1st edn. (Oxford University Press, Oxford, UK, 2007).
6. G. Ballardin, et al., *Rev. Sci. Instrum.* **72**, 3643 (2001).
7. http://etd.lsu.edu/docs/available/etd-01212009-101352/unrestricted/Wen_diss.pdf
8. B. Abbott, et al. (LIGO Science Collaboration), Rep. Prog. Phys. **72**, 076901 (2009).
9. T Accadia and B L Swinkels (for the Virgo Collaboration), Class. Quantum Grav. **27**, 084002 (2010).
10. Information about Virgo can be found at www.virgo.infn.it.
11. M Lorenzini (on behalf of the Virgo Collaboration), Class. Quantum Grav. **27**, 084021 (2010).
12. H Grote (for the LIGO Scientific Collaboration), Class. Quantum Grav. **27**, 084003 (2010).
13. M. V. Plissi, C. I. Torrie, M. E. Husman, N. A. Robertson, K. A. Strain, H. Ward, H. Lück, and J. Hough, *Rev. Sci. Instrum.* **71**, 2539 (2000).
14. H Lück, et al., J. Phys.: Conf. Ser. 228, 012012 (2010).
15. H Vahlbruch, Alexander Khalaidovski, Nico Lastzka, Christian Gräf, Karsten Danzmann, and Roman Schnabel, Class. Quantum Grav. **27**, 084027 (2010).
16. R Schnabel, N Mavalvala, D E McClelland, P K Lam, Nat. Commun. 1:121 doi: 10.1038/ncomms1122 (2010).
17. R Takahashi, K Arai, D Tatsumi, M Fukushima, T Yamazaki, M-K Fujimoto, K Agatsuma, Y Arase, N Nakagawa, A Takamori, K Tsubono, R DeSalvo, A Bertolini, S Marka, and V Sannibale (TAMA Collaboration), *Class. Quantum Grav.* **25**, 114036 (2008).
18. H. Tagoshi, et al., (TAMA Collaboration) *Phys. Rev. D* **63**, 062001 (2001).
19. B. Abbott, et al. (LIGO Science Collaboration), *Astrophys. J.* **681**, 1419 (2008).
20. B. Abbott, et al. (LIGO Science Collaboration), *Astrophys. J. Lett.* **683**, L45 (2008).
21. B. Abbott, et al. (LIGO Science Collaboration), *Astrophys. J.* **713**, 671-685 (2010).
22. B. Abbott, et al. (LIGO Science Collaboration), *Nature* **460**, 990 (2009).

2.
Data analysis: Searches

SEARCHES FOR GRAVITATIONAL WAVE TRANSIENTS IN THE LIGO AND VIRGO DATA

F. ROBINET, for the LIGO Scientific Collaboration and the Virgo Collaboration
LAL, Univ. Paris-Sud, CNRS/IN2P3, Orsay, France.

In 2011, the Virgo gravitational wave (GW) detector will definitively end its science program following the shut-down of the LIGO detectors the year before. The years to come will be devoted to the development and installation of second generation detectors. It is the opportune time to review what has been learned from the GW searches in the kilometric interferometers data. Since 2007, data have been collected by the LIGO and Virgo detectors. Analyses have been developed and performed jointly by the two collaborations. Though no detection has been made so far, meaningful upper limits have been set on the astrophysics of the sources and on the rate of GW events. This paper will focus on the transient GW searches performed over the last 3 years. This includes the GW produced by compact binary systems, supernovae core collapse, pulsar glitches or cosmic string cusps. The analyses which have been specifically developed for that purpose will be presented along with the most recent results.

1 Introduction

Gravitational waves (GW) were predicted by Albert Einstein [1] with his theory of general relativity. It shows that an asymmetric, compact and relativistic object will radiate gravitationally. The waves propagate with a celerity c and their amplitude is given by the dimensionless strain h which can be projected over two polarizations h_+ and $h_\times$. The existence of GW was indirectly confirmed through observations on the binary pulsar PSR 1913+16 discovered in 1974. This binary system has been followed-up over more than 30 years and the orbit decay can be fully explained by the energy loss due to the gravitational wave emission [2]. The great challenge of this century is to be able to detect gravitational waves directly by measuring the space-time deformation induced by the wave. The Virgo[3] and the two LIGO [4] interferometric detectors are designed to achieve this goal. Thanks to kilometric arms, Fabry-Perot cavities, sophisticated seismic isolation, a high laser power and the use of power-recycling techniques, the LIGO and Virgo detectors were able to reach their design sensitivity which is to measure h below 10^{-21} over a wide frequency band, from tens to thousands of Hz (and below 10^{-22} at a few hundreds Hz). Such sensitivity over a large range of frequencies offers the possibility to detect gravitational waves originating from various astrophysical sources which will be described in Section 2.

The searches for GW in LIGO-Virgo were historically divided into four analysis groups. The physics of these groups does not really match the type of GW sources but rather the expected signals. This has the advantage to develop efficient searches adapted to the signal seen in the detector. The CBC group is specifically searching for signals resulting from the last instants of the coalescence and the merging of compact binary systems of two neutron stars, two black holes or one of each. The expected signal is well-modeled, especially the inspiral part, so that the searches are designed to be very selective. On the contrary, the burst group performs more generic searches for any type of sub-second signals. This unmodeled approach offers a robustness to the analyses and remains open to the unexpected. Doing so, the burst group covers a large variety of GW sources for which the expected signals are poorly known. This includes the asymmetric core bounce of supernovae, the merging of compact objects, the starquakes of neutron stars or the oscillating loops of cosmic strings. This paper will focus on the work performed within the CBC and the burst group and present the searches for short-duration GW signals. C. Palomba will describe the searches for continuous signals and for a stochastic background of GW [5]. Section 3 will detail the different aspects of a multi-detector GW transient search while Section 4 will highlight some of the latest results of the analyses.

Very early on, the Virgo and LIGO collaborations chose to share their data and to perform analyses in common in order to maximize the chance of detection. Indeed, having several detectors in operation presents many advantages such as performing coincidences, reconstructing the source location, having a better sky coverage or estimating the background for analyses. This close collaboration started in 2007 with the Virgo first science run VSR1 (2007) and LIGO S5 (2005-2007) run and continued until recently with the following science runs VSR2 (2009), VSR3 (2010) and S6 (2009-2010). In October 2010, the LIGO detectors shut-down to install the second generation of detectors which should resume science in 2015. Virgo will perform one more science run, VSR4, during the summer jointly with the GEO 600 [6] detector in Germany. After that, Virgo will start the preparation for the next phase with Advanced Virgo.

As the first generation of interferometers is about to take an end, the analyses performed so far were not able to claim a detection. However it was possible to set astrophysically relevant upper limits and this paper will present some of them. Moreover the pioneering work performed to build efficient analyses pipelines will be a great strength for the Advanced detector era and the first steps of gravitational wave astronomy.

2 Sources, signals and searches

2.1 The coalescence of binary objects

The coalescence of stellar compact binary systems is often seen as the most promising candidate for a first detection. Indeed, such objects have been extensively studied and the expected waveform is rather well-modeled. The inspiral phase, up to the last stable circular orbit, can be reliably described with a post-Newtonian approximation [7]. The signal is expected to sweep upwards in frequency and to cross the detector bandwidth for a short period of time (from a few ms to tens of s). This is followed by the merger of the two bodies whose waveform can be derived from numerical relativity [8] even though this part of the waveform is the least known of the evolution of the binary. Finally, the resulting black hole is excited and loses part of its energy by radiating gravitationally. Black hole pertubation theory is well able to predict the ringdown waveform [9] and the signal is expected to be in the detector sensitive band for masses larger than 100 $M_\odot$.

The search for coalescence signals, led by the CBC group, takes two free parameters into account: the masses of the two binary components. The low-mass search covers a total mass range between 2 and 35 $M_\odot$ where most of the energy is contained in the inspiral phase. As a complement, the high-mass search probes the 25-100 $M_\odot$ total mass region where the signal-to-noise ratio is significant mostly during the merger and ringdown phase. A ringdown-only search is also performed for very high-mass systems (75-750 $M_\odot$) in which case it is possible to use the spin as an additional parameter. The merger and the ringdown signals are also included in the burst searches. The robust nature of the burst analyses offers a nice complement to the CBC searches, especially for the merger phase for which the waveform is less reliable.

Astrophysical rates for compact binary coalescence are still uncertain since they are based on a few assumptions like the population of observed double pulsars in our galaxy. A plausible rate for the coalescence of two neutron stars could be somewhere between 0.01 to 10 Myr^{-1} Mpc^{-3}. These numbers offers a chance for a detection which could span between 2×10^{-4} and 0.2 events per year [10] with the initial detector sensitivities.

2.2 Supernovae core collapse

The core bounce of supernovae could also be an interesting source of GW bursts. In this case, the GW production is a complex interplay of general relativity, nuclear and particle physics. Recent studies [11] show that various emission mechanisms could come into play. The coherent motion of the collapsing and bouncing core during the proto-neutron star formation could be asymmetric enough to produce GW. Then the prompt convective motion behind the hydrodynamic shock in the central part of the star due to non-axisymmetric rotational instabilities could also trigger some GW radiation. Recent 2- or 3-dimensional simulations [11] are able to extract complex waveforms but they are extremely parameter-dependent and not robust enough to be used directly in a GW search. In this case again, the burst's unmodeled searches are well-suited. Some studies are in progress to decompose the supernova signatures over a basis of main components which could be then searched in the data [12].

2.3 Isolated neutron stars

Instabilities of isolated neutron stars can also produce GW bursts which could be detected by earth-based interferometers. The invoked mechanism corresponds to the excitation of quasi-normal mode oscillations which couple to GW emission. This excitation could occur as a consequence of flaring activity in soft-gamma repeaters (SGR) resulting from intense magnetic fields [13]. Another possibility comes from the merging of a binary system of two neutron stars. In that case a massive neutron star can be formed. Often excited, it could radiate gravitational waves. Fractures or star-quakes of the neutrons star crust are other possible scenarios for the quasi-normal mode oscillations of the star. F-modes oscillations are the preferred mechanism to produce GW in case of neutron stars. Hence, ringdown waveforms are often used in the searches with a high frequency (from 500 Hz to 3 kHz) and a short damping time (from 50 ms to 500 ms).

2.4 Cosmic strings

The hypothetic existence of cosmic strings [14] could be proven by looking for a signature in the GW spectrum. Indeed, gravitational radiation is the main mechanism for the cosmic string network to lose its energy. When intersecting with each other, strings can form loops which oscillate and produce some cuspy features with a strong Lorentz boost. Cosmic string cusps are therefore a powerful source of GW. Gravitational waveforms are very well predicted [15] and this motivates a dedicated search in the LIGO/Virgo data. In case of no detection, it is possible to set constraints on the string tension which is the main parameter to describe the cosmic string network.

2.5 External triggers

GW emission often results from violent events in the universe. Therefore, these events could also be seen through other channels like electro-magnetism or neutrino emission. The coincidence of a GW event with another type of trigger could critically increase the confidence into the veracity of the event. Moreover the knowledge of the position and/or the time of the event can considerably enhance the sensitivity of the searches. For instance, a gamma-ray burst (GRB) trigger could be an indication that either a binary system merged or a hyper-massive star collapsed. Dedicated analyses over GRB triggers are performed and are presented by M. Was in these proceedings [16].

3 How to extract a GW signal

3.1 Trigger production

As discussed above, many LIGO/Virgo GW searches benefit from the knowledge of the expected waveform. In this case, match-filtering techniques can be used to produce the GW triggers. One first needs to define a template bank where the reference waveforms are covering the parameter space (the component masses for the CBC searches, for example). The distance from one template to the next must be small enough to insure a negligible loss of efficiency but large enough to limit the total number of templates and the computational cost. Then each template is slid over the detector gravitational wave strain $h_{det}(t)$ and the match between the two is computed as a function of time. If this match exceeds a given threshold then a trigger is produced and a signal-to-noise ratio (SNR) is defined.

Most of the burst searches cannot rely on a modeled waveform. The main procedure is to perform a time-frequency analysis. It consists in tiling the time-frequency plane and in looking for an excess of energy in clusters of pixels. Again, a threshold on the energy is set to define triggers.

With an ideal detector, if no GW event is present in the detection strain, the distribution of the SNR should follow a Gaussian statistic. Then a GW event could be detected if its SNR is much larger than the noise SNR distribution. In reality the noise of the detector displays a non Gaussian behavior and the tail of the distribution is composed by many detector artefacts called glitches. Therefore, using only a single detector output, a genuine GW event cannot be disentangled from the noise. When performing a multi-detector analysis, it is possible to set in coincidence different parameters of the search like the time of the trigger or any discriminative variables describing the event. This significantly reduces the tail of the background. However the remaining distribution of events is still not Gaussian and the accidental background distribution needs to be evaluated to quantify confidence of a given event.

3.2 Background estimation

There is a reliable way to evaluate the accidental background distribution when performing a multi-detector analysis. It consists in time-sliding the data of one detector with respect to the other and looking at the time-coincident triggers which cannot contain any real signal. This gives a fair estimation for the background provided that the time shift is larger than the duration of the expected signals and that the noise is locally stationary. With the resulting distribution one can set a detection threshold corresponding to a fixed false alarm rate.

3.3 Data quality

After having performed coincidences between detectors, the background tail is still the main limiting factor for the searches. It is crucial to understand the origin of the glitches to remove them safely and to be able to lower the detection threshold as much as possible. The data quality groups in Virgo [17] and LIGO [18] play a major role in the analysis. They study the couplings between the detection channel and the auxiliary channels to define efficient vetoes to reduce the number of glitches in the tails. Interferometers are sensitive instruments to the environment so it is imperative to monitor disturbances of different natures: acoustic, magnetic, mechanical etc. Then selective vetoes based on environmental channels are produced to increase the sensitivity of the searches.

3.4 Upper limits

Until now, no GW detection has been made. However upper limits can be obtained provided that the efficiency of the search is known. To achieve this, analyses pipelines are run on the detector data streams where fake signals have been injected. The number of recovered injections provides the efficiency of the search. In case of template searches, the modeled waveforms are injected to cover the parameter space. Then upper limits can be given as a function of the physical parameters. For unmodeled searches generic waveforms are injected with varying parameters. For instance, for the burst all-sky analyses, sine-Gaussian, Gaussian, ringdowns and cosmic string cusps signals are injected. Because of the unmodeled nature of the search, the upper limits are given on the rate as a function of the GW amplitude for a specific set of waveforms.

4 Selection of results

4.1 Limits on the rate of binary coalescence

The first search for gravitational waves from compact binary coalescence with the coincidence of the LIGO and Virgo data was performed on S5 and VSR1 data[19]. It covers the low-mass region (from 2 to 35 $M_\odot$). No detection resulted from this search and upper limits on the rate of compact binary coalescence were estimated. If the spin is neglected and assuming a mass of 1.35 ± 0.04 $M_\odot$ for the neutron star and 5.0 ± 1.0 $M_\odot$ for the black hole, the upper limits at 90% confidence level are:

$$\mathcal{R}^{BNS}_{90\%} = 8.7 \times 10^{-3} \mathrm{yr}^{-1} \mathrm{L}_{10}^{-1}, \tag{1}$$
$$\mathcal{R}^{BHNS}_{90\%} = 2.2 \times 10^{-3} \mathrm{yr}^{-1} \mathrm{L}_{10}^{-1}, \tag{2}$$
$$\mathcal{R}^{BBH}_{90\%} = 4.4 \times 10^{-4} \mathrm{yr}^{-1} \mathrm{L}_{10}^{-1}, \tag{3}$$

where BNS stands for binary neutron stars, BHNS for black hole neutron star binary and BBH for binary black holes. L_{10} corresponds to 10^{10} times the blue solar luminosity (typical for a galaxy) which is expected to be proportional to the binary coalescence rate (blue luminosity density[20]: (1.98×10^{-2}) L_{10} Mpc^{-3}). Upper limits can also be produced in mass bins and are presented on Figure 1.

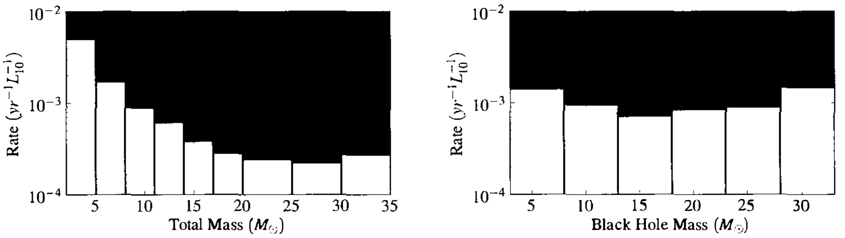

Figure 1: The 90% rate upper limits as a function of mass. The first figure gives the upper-limit on the rate of coalescence from BBH system as a function of the total mass of the system. The second figure gives the BHNS upper-limit as a function of black hole mass, assuming a fixed neutron star mass of 1.35 $M_\odot$.

Recently, the high-mass search (from 25 to 100 $M_\odot$) has also been completed and full coalescence waveforms have been used[21]. The analysis has been performed only on LIGO data since the Virgo sensitivity was not sufficient for these high mass systems during VSR1. Upper limits have been placed on the merger rate of binary black holes as a function of the component masses. For example, for two black holes with a component mass between 19 and 28 $M_\odot$ the merger rate should not exceed 2.0 Myr^{-1} Mpc^{-3} at 90 % confidence.

4.2 *All-sky burst search*

The all-sky search for unmodeled gravitational-wave bursts has been performed on the LIGO and Virgo data for S5 and VSR1 science runs[22]. This is a null result for a detection and upper limits have been estimated in terms of an event rate versus strength for several types of plausible burst waveforms as presented on Figure 2. The signal strength is measured with $h_{\rm rss}$ defined as:

$$h_{\rm rss} = \sqrt{\int_{-\infty}^{+\infty} dt\ (|h_+(t)|^2 + |h_\times(t)|^2)}. \tag{4}$$

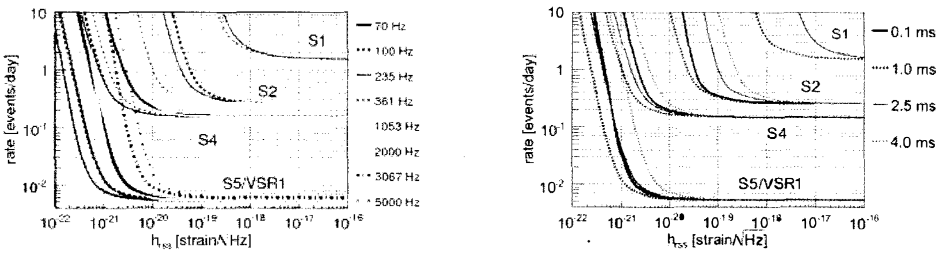

Figure 2: Selected exclusion diagrams showing the 90% confidence rate limit as a function of signal amplitude for sine-Gaussian with a quality factor of 9 and various frequencies (left) and Gaussian of different widths (right) waveforms for the results of the entire S5 and VSR1 runs compared to the results reported with the previous runs (S1, S2, and S4).

4.3 *GW associated to neutron stars*

There are several new LIGO/Virgo results dealing with the physics of neutron stars. The search for GW associated with the timing glitch of the Vela pulsar (PSR B083345) has recently been published [23]. Upper limits have been placed on the peak intrinsic strain amplitude of gravitational wave ring-down signals, depending on which spherical harmonic mode is excited as shown in Table 1.

Spherical Harmonic Indices	$h^{90\%}_{2m}$	$E^{90\%}_{2m}$ (erg)
$l = 2, m = 0$	1.4×10^{-20}	5.0×10^{44}
$l = 2, m = \pm 1$	1.2×10^{-20}	1.3×10^{45}
$l = 2, m = \pm 2$	6.3×10^{-21}	6.3×10^{44}

Table 1: The Bayesian 90% confidence upper limits on the intrinsic strain amplitude and energy associated with each spherical harmonic mode of oscillation assuming only a single harmonic (i.e. value of $|m|$) is excited.

An external triggered search has been conducted on electromagnetic triggers from six magnetars which are neutron stars powered by extreme magnetic fields [24]. These rare objects are characterized by repeated and sometimes spectacular gamma-ray bursts which could also be a source of GW. The upper limits for band- and time-limited white noise bursts in the detector sensitive band, and for f-mode ringdowns (at 1090 Hz), are $3.0 \times 10^{44} d_1^2$ erg and $1.4 \times 10^{47} d_1^2$ erg respectively, where $d_1 = d_{0501}/1\text{kpc}$ and d_{0501} is the distance to SGR 0501+4516 which is likely to be ~ 1 kpc from Earth. These limits on GW emission from f-modes are an order of magnitude lower than any previous results, and approach the range of electromagnetic energies seen in SGR giant flares for the first time.

4.4 *Cosmic string upper limits*

The burst group tries to constrain the cosmic string parameter space by looking for GW emitted by cuspy features of oscillating loops [25]. The first analyses of the S4 LIGO data reports upper limits on the $G\mu$-ε plane where $G\mu$ is the string tension and ε is a parameter for the loop size. Figure 3 shows the region of the parameter space which can be rejected for a cosmic string reconnection probability of 10^{-3}. The up-coming analysis of S5/S6-VSR1/VSR2/VSR3 should be able to place the most stringent limits on the cosmic string models.

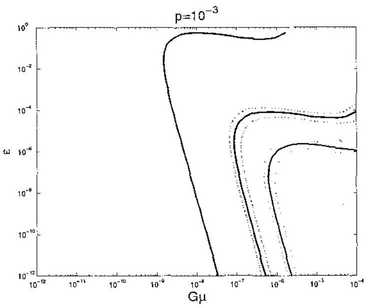

Figure 3: Plot of the upper-limit results of the S4 cosmic string analysis for a reconnection probability of 10^{-3}. Areas to the right of the red curves show the regions excluded at the 90% level. The dotted curves indicate the uncertainty. The black and blue curves limit the regions of parameter space unlikely to result in a cosmic string cusp event detected in S4: a cosmic string network with model parameters in these regions would result in less than one event (on average) surviving the search. The black curve was computed using the efficiency for all recovered injections. The blue curve shows regions of parameter space unlikely to result in a cosmic string cusp being detected in a year long search with the initial LIGO sensitivity estimate.

5 Conclusion

Searches for GW transient signals in Virgo and LIGO data have reached maturity. No GW detection can be claimed yet but significant astrophysical upper limits can be extracted from the data covering a large variety of sources. The data-taking campaigns are now over for the first generation of GW detectors but some more analysis results are expected to be released in the next months. The most recent data of S6/VSR2-3 are being analyzed and new results are about to be published.

The second generation of detectors is now in preparation and the GW science should resume in 2015. With an increased sensitivity of about a factor 10, we should expect to extend the visible volume of sources by a factor 1000. This offers a great opportunity for a detection. Even with the most pessimistic scenarios, advanced detectors should be able to detect GW. For instance, it is reasonable to expect a rate for binary neutron star coalescences of about 40 events per year.

Acknowledgments

The authors gratefully acknowledge the support of the United States National Science Foundation for the construction and operation of the LIGO Laboratory, the Science and Technology Facilities Council of the United Kingdom, the Max-Planck-Society, and the State of Niedersachsen/Germany for support of the construction and operation of the GEO600 detector, and the Italian Istituto Nazionale di Fisica Nucleare and the French Centre National de la Recherche

Scientifique for the construction and operation of the Virgo detector. The authors also gratefully acknowledge the support of the research by these agencies and by the Australian Research Council, the International Science Linkages program of the Commonwealth of Australia, the Council of Scientific and Industrial Research of India, the Istituto Nazionale di Fisica Nucleare of Italy, the Spanish Ministerio de Educación y Ciencia, the Conselleria d'Economia Hisenda i Innovació of the Govern de les Illes Balears, the Foundation for Fundamental Research on Matter supported by the Netherlands Organisation for Scientific Research, the Polish Ministry of Science and Higher Education, the FOCUS Programme of Foundation for Polish Science, the Royal Society, the Scottish Funding Council, the Scottish Universities Physics Alliance, The National Aeronautics and Space Administration, the Carnegie Trust, the Leverhulme Trust, the David and Lucile Packard Foundation, the Research Corporation, and the Alfred P. Sloan Foundation.

References

1. A. Einstein, Preuss. Akad. Wiss. Berlin, Sitzungsberichte der physikalisch-mathematischen Klasse, 688 (1916).
2. J. Taylor and J. Weisberg., *Astrophys. J.* **345**, 434 (1989).
3. F. Acernese *et al* (Virgo Collaboration), *Class. Quant. Grav.* **25**, 114045 (2008).
4. B. P. Abbott *et al* (LIGO Scientific Collaboration), *Rep. Prog. Phys.* **72**, 076901 (2009).
5. C. Palomba (LIGO Scientific Collaboration and the Virgo Collaboration), submit. to these proceedings.
6. H. Grote (the LIGO Scientific Collaboration), *Class. Quant. Grav.* **25**, 114043 (2008).
7. L. Blanchet, *Living Rev. Rel.* **9**, 3 (2006).
8. Frans Pretorius, *Phys. Rev. Lett.* **95**, 121101 (2005).
9. E. Berti *et al*, *Phys. Rev.* D **73**, 064030 (2006).
10. J. Abadie *et al* (LIGO Scientific Collaboration and the Virgo Collaboration), *Class. Quant. Grav.* **27**, 173001 (2010).
11. C. D. Ott, *Class. Quant. Grav.* **26**, 063001 (2009).
12. C. Röver *et al*, *Phys. Rev.* D **80**, 102004 (2009).
13. R. C. Duncan and C. Thompson, *Astrophys. J.* **392**, L9 (1992).
14. A. Vilenkin and E. Shellard, Cambridge University Press (2000).
15. T. Damour and A. Vilenkin, *Phys. Rev. Lett.* **85**, 3761 (2000).
16. M. Was (LIGO Scientific Collaboration and the Virgo Collaboration), submit. to these proceedings.
17. F. Robinet (LIGO Scientific Collaboration and the Virgo Collaboration), *Class. Quant. Grav.* **27**, 194012 (2010)
18. N. Christensen (LIGO Scientific Collaboration and the Virgo Collaboration), *Class. Quant. Grav.* **27**, 194010 (2010)
19. J. Abadie *et al* (LIGO Scientific Collaboration and the Virgo Collaboration), *Phys. Rev.* D **82**, 102001 (2010)
20. R. K. Kopparapu *et al*, *Astrophys. J.* **675**, 1459 (2008)
21. J. Abadie *et al* (LIGO Scientific Collaboration and the Virgo Collaboration), to appear in *Phys. Rev.* D, arXiv:1102.3781.
22. J. Abadie *et al* (LIGO Scientific Collaboration and the Virgo Collaboration), *Phys. Rev.* D **81**, 102001 (2010).
23. J. Abadie *et al* (the LIGO Scientific Collaboration), *Phys. Rev.* D **83**, 042001 (2011).
24. J. Abadie *et al* (LIGO Scientific Collaboration and the Virgo Collaboration), to appear in *ApJ Lett*, arXiv:1011.4079.
25. B. Abbott *et al* (the LIGO Scientific Collaboration), *Phys. Rev.* D **80**, 062002 (2009).

SEARCHES FOR CONTINUOUS GRAVITATIONAL WAVE SIGNALS AND STOCHASTIC BACKGROUNDS IN LIGO AND VIRGO DATA

C. PALOMBA for the LIGO Scientific Collaboration and the Virgo Collaboration
Istituto Nazionale di Fisica Nucleare, sezione di Roma, I-00185 Roma, Italy

Abstract

We present results from searches of recent LIGO and Virgo data for continuous gravitational wave signals (CW) from spinning neutron stars and for a stochastic gravitational wave background (SGWB).

The first part of the talk is devoted to CW analysis with a focus on two types of searches. In the targeted search of known neutron stars a precise knowledge of the star parameters is used to apply optimal filtering methods. In the absence of a signal detection, in a few cases, an upper limit on strain amplitude can be set that beats the spindown limit derived from attributing spin-down energy loss to the emission of gravitational waves. In contrast, blind all-sky searches are not directed at specific sources, but rather explore as large a portion of the parameter space as possible. Fully coherent methods cannot be used for these kind of searches which pose a non trivial computational challenge.

The second part of the talk is focused on SGWB searches. A stochastic background of gravitational waves is expected to be produced by the superposition of many incoherent sources of cosmological or astrophysical origin. Given the random nature of this kind of signal, it is not possible to distinguish it from noise using a single detector. A typical data analysis strategy relies on cross-correlating the data from a pair or several pairs of detectors, which allows discriminating the searched signal from instrumental noise.

Expected sensitivities and prospects for detection from the next generation of interferometers are also discussed for both kind of sources.

1 Introduction

The most recent results obtained in the search of CW and SGWB have used data from LIGO S5 [1] and Virgo VSR2 [2] runs. S5 run involved all three LIGO detectors, Hanford 4km (H1), Hanford 2km (H2) and Livingston 4km (L1), and took place from November 2005 to September 2007 with an average single-interferometer duty cycle of 73.6%, an average two-site coincident duty cycle of 59.4% and an average triple-interferometer duty cycle of 52.5%. Virgo (V1) VSR2 run took place from July 2009 to January 2010 with a duty cycle of 80.4%. At low frequency, say below 70 Hz, VSR2 sensitivity was better than S5. At intermediate frequency, between 70 Hz and 500 Hz, S5 sensitivity was better than VSR2. At frequency above about 500 Hz the sensitivity of the two runs were very similar.

In 2010 two more scientific runs, LIGO S6 and Virgo VSR3, took place. The data are being analyzed and some interesting results have already been obtained, but are still under internal review, so we will not discuss them here.

A generic gravitational wave (GW) signal is described by a tensor metric perturbation $\mathbf{h}(t) = h_+(t)\,\mathbf{e}_+ + h_\times(t)\,\mathbf{e}_\times$, where $\mathbf{e}_+$ and $\mathbf{e}_\times$ are the two basis polarization tensors. The form of the two amplitudes depends on the specific kind of signal.

Rapidly spinning neutron stars, isolated or in binary systems. are a potential source of CW. To emit GW some degree of non-axisymmetry is required. It can be due to several mechanisms including elastic stress or magnetic field which induce a deformation of the neutron star shape, free-precession around the rotation axis or accretion of matter from a companion star. The size of the distortion, typically measured by the *ellipticity* $\epsilon = \frac{I_{xx}-I_{yy}}{I_{zz}}$, which is defined in terms of the star principal moments of inertia, can provide important information on the neutron star equation of state.

The signal emitted by a tri-axial neutron star rotating around a principal axis of inertia is characterized by amplitudes

$$h_+(t) = h_0 \left(\frac{1+\cos^2\iota}{2}\right) \cos\Phi(t); \qquad h_\times(t) = h_0 \cos\iota \sin\Phi(t), \tag{1}$$

The angle ι is the inclination of the star's rotation axis with respect to the line of sight and $\Phi(t)$ is the signal phase function, where t is the detector time, while the amplitude h_0 is given by

$$h_0 = \frac{4\pi^2 G}{c^4}\frac{I_{zz}\epsilon f^2}{d}, \tag{2}$$

being d the star distance and f the signal frequency (twice the star rotation frequency). While we expect $f < 2$ kHz and $d < 10$ kpc. the typical value of the ellipticity is largely unknown. Standard equations of state (EOS) of neutron star matter foresee maximum value of the ellipticity [3] of the order of $\epsilon_{max} \approx 5\cdot 10^{-6}$. For some 'exotic' EOS a maximum value $\epsilon_{max} \approx 10^{-2} - 10^{-4}$ is foreseen [4, 5, 6].

The signal frequency gradually decreases due to the intrinsic source spin-down, caused by elecromagnetic and hopefully gravitational energy losses. The received signal phase is affected by the Doppler modulation due to the detector-source relative motion and by some relativistic effects. Moreover, the signal is also affected by the amplitude and phase modulation due to the detector beam-pattern functions $F_+(t;\psi)$, $F_\times(t;\psi)$, which depend on the polarization angle ψ, on the source position in the sky and on the detector position and orientation on the Earth.

Assuming that the observed spin-down $\dot{f}$ of a given neutron star is totally due to the emission of GW, an absolute upper limit to the amplitude of the GW signal, called *spin-down limit*, can be derived[7]:

$$h_0^{sd} = 8.06\cdot 10^{-19}\, I_{38}\, d_{\rm kpc}^{-1}\sqrt{\frac{|(\dot{f}/{\rm Hz\,s^{-1}})|}{(f/{\rm Hz})}}, \tag{3}$$

where I_{38} is the star's moment of inertia in units of $10^{38}\,{\rm kg\,m^2}$ and $d_{\rm kpc}$ is the star's distance from the Sun in kiloparsecs. Going below the *spin-down limit* means we are putting a constraint on the fraction of spin-down energy due to the emission of GW.

Two types of CW searches have received the most effort up to now: *targeted* searches and *wide parameter* searches.

In the targeted searches the source parameters $(\alpha, \delta, f, \dot{f}, ...)$ are assumed to be known with high accuracy. The search for known pulsars belongs to this category. This kind of search is computationally cheap and a fully coherent analysis, based on matched filtering, over long observation time is feasible. Various methods of implementing matched filtering have been developed [8, 9, 10]. In order to make a coherent analysis over long times Doppler, Einstein and possibly Shapiro effects must be accurately compensated. Radio-astronomic observations can be used to accurately track the GW signal phase evolution (assuming the GW signal is phase locked to the EM pulses). Moreover, they are also important to know if a *glitch*, i.e. a sudden jump in frequency and frequency derivative, occurred during the period of data to be analyzed.

The sensitivity of a coherent search, i.e. the minimum signal amplitude detectable over an observation time T_{obs}, with a false alarm probability of 1 % and a false dismissal probability of 10 % and taking also an average over source and detector parameters, is given by

$$h_{0,min} \approx 11\sqrt{\frac{S_n(f)}{T_{obs}}} \tag{4}$$

where $S_n(f)$ is the detector noise spectrum. The exact value of the coefficient depends on the specific analysis method employed.

A coherent search for CW using LIGO-S5 data has been recently done for more than 100 pulsars [11] but the resulting upper limits have beaten the spin-down limit for only the Crab pulsar and have grazed it for PSRJ0537-6910 (less than a factor of 2 above). For the Crab the analysis was carried out both assuming the polarization parameters ι, ψ are unknown (uniform priors) and that they are known with values estimated from x-ray observations [12] (restricted priors). Updated ephemeris from Jodrell Bank were used. The 95% degree-of-belief upper limits are $h_0^{95\%} = 2.4 \cdot 10^{-25}$ (uniform prior) and $h_0^{95\%} = 1.9 \cdot 10^{-25}$ (restricted prior) corresponding to a star ellipticity of $\sim 10^{-4}$. These results are below the spin-down limit by a factor of about 7, and constrain the fraction of spin-down energy due to the emission of GW to about 2% (assuming the canonical value for the star moment of inertia, $10^{38}\ kg \cdot m^2$). We expect to improve the upper limit on the Crab pulsar by jointly analysing data from LIGO S5, S6 runs and Virgo VSR2, VSR3, VSR4 runs (this last tentatively scheduled for summer 2011).

Virgo VSR2 data have been used for a coherent search of CW from the Vela pulsar. Updated ephemeris have been computed using TEMPO2 software from the time-of-arrivals of EM pulses observed by Hobart and Hartebeesthoek radio-telescopes. The excellent seismic isolation of Virgo detector allows for a very good sensitivity at low frequencies thus making the spin-down limit potentially beatable. Results of this analysis are described in [13].

In the wide parameter searches the analysis is done over a portion of the source parameter space as large as possible. In particular, we would like to search for unknown sources located everywhere in the sky, with signal frequency as high as 2 kHz and with values of spin-down as large as possible. This kind of analysis is computationally bound. Fully coherent methods which would allow to reach the 'best' search sensitivity, like the ones used for targeted searches, are unfeasible due to the computing power limitation. Various incoherent methods have been developed in which the data are divided in small Fourier transformed segments which are then properly combined to compensate for Doppler and spin-down for a particular source location [14–19]. In the so-called *hierarchical methods* coherent (over relatively short periods) and incoherent steps are alternated in order to increase sensitivity [23, 24]. The output of an analysis is given by a set of *candidates*, i.e. points in the source parameter space with high values of a given statistic and which need a deeper study. Typically *coincidences* are done among the candidates obtained by the analysis over different data sets in order to reduce the false alarm probability [25, 26]. The surviving candidates can be then analyzed coherently over longer times in order to discard them or confirm detection. The basic sensitivity of a wide parameter search is given by

$$h_{0,min} \approx \frac{25}{N^{1/4}}\sqrt{\frac{S_n(f)}{T_{coh}}} \tag{5}$$

where N is the number of segments in which the data are divided, each of length T_{coh}. The exact value of the numerical factor depends again on the specific incoherent method used and weakly also on the parameter space that is being considered.

Early LIGO S5-data have been analyzed with two different methods. No GW signal has been detected but interesting upper limits have been placed. A search using the first 8 months of S5 has been described in [27]. It covered the whole sky, the frequency band $50 - 1100\ Hz$ and a range of spin-down values between $-5 \cdot 10^{-9}\ Hz/s$ and 0. At the highest frequency the search would have been sensitive to the GW emitted by a neutron star placed at 500 *pc* with equatorial ellipticity larger than 10^{-6}. In Fig. 1 the upper limits as a function of frequency are shown. Another search, using the Einstein@Home infrastructure - a volunteer distributed computing project [28], was done over the first 2 months of S5 [26]. The analysis consisted in matched filtering over 30-hours data segments followed by incoherent combination of results via a concidence strategy. The explored parameter space consisted in the full sky, frequency range $50 - 1500\ Hz$, spin-down range between $-2 \cdot 10^{-9}\ Hz/s$ and 0. This search would have been sensitive to 90 % of signals in the frequency band $125 - 225\ Hz$ with amplitude greater than $3 \cdot 10^{-24}$. The search sensitivity, estimated through the injection of software simulated signals, is shown in Fig. 2.

Various improvements to the wide parameter search pipelines are being implemented in order to have a better sensitivity at fixed computing power [20, 21, 22].

Other kinds of searches have been or are being developed and applied to detector data: *directed* searches, searches for accreting neutron stars, searches for neutron stars in binary systems, transient searches for short-lived signals. In particular, *directed* searches are somewhat intermediate between targeted and all-sky. To this category belong, e.g., the search for sources with known

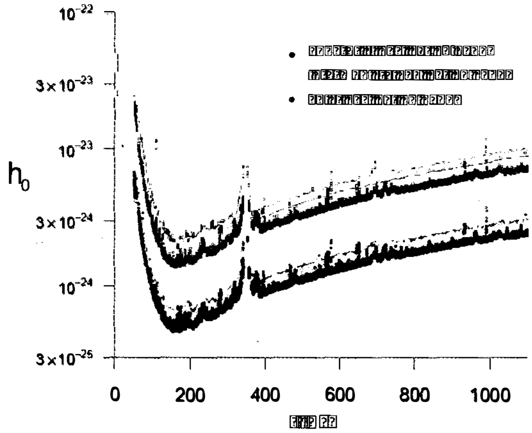

Figure 1: Minimum (H1 or L1) 95% confidence level upper limits on signal amplitude for equatorial, intermediate a polar declination bands. Lower curves corresponds to best neutron star orientation, upper curves to worst neutron s orientation. Figure adapted from PRL [27].

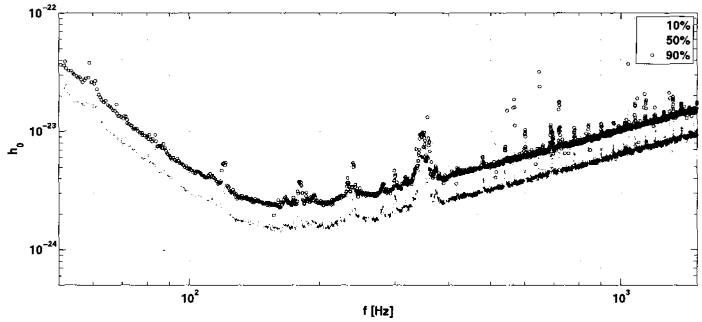

Figure 2: Estimated sensitivity of the Einstein@Home search for early LIGO S5 data. The three curves show the sour amplitude h_0 at which 10% (bottom), 50% (middle), 90% (top) of the simulated sources would be confidently detecte Figure adapted from PRD [26].

position but unknown frequency (like the compact objects in supernova remnants) and the search over relatively small sky area (like the galactic center or globular clusters). An interesting upper limit has been obtained in the analysis of ~ 12 days of S5 data searching for GW signals from the supernova remnant Cassiopeia A [29]. The source position is known and a coherent search over the frequency range $100 - 300$ Hz and a wide range of spin-down values has been done establishing a 95% confidence upper limit below the indirect limit based on energy conservation and age of the remnant. This search established also the first upper limit on r-modes amplitude.

With Advanced LIGO and Virgo detectors the spin-down limit on GW emission from known pulsars will be beatable for tens of objects and in few cases the minimum detectable ellipticity will be below 10^{-5} and down to 10^{-8}, a range of values which is sustainable also by standard neutron star EOS. Concerning all-sky searches, nearby *gravitars* (say, a few hundreds of parsecs away) would be detectable for ellipticity larger than a few units in 10^{-8}. Objects with ellipticity of the order of 10^{-6} would be detectable up to the Galactic center (see, e.g., Fig. 41 of [19] after up-scaling by a factor of about 10 the distance associated to red curves).

3 The search for stochastic gravitational wave backgrounds

Typically, two kinds of stochastic gravitational wave backgrounds (SGWB) are considered. Cosmological backgrounds, due to processes taking place in the very early stages of Universe evolution, like amplification of vacuum fluctuations, phase transition, cosmic string cusps. These kinds of backgrounds are expected to be stationary, gaussian, unpolarized and, in a first approximation, isotropic. Astrophysical backgrounds, due to the superposition of many unresolved sources, since the beginning of stellar activity, like core collapse to supernovae or the final stages of compact binary mergers. The assumption of isotropy would not hold, if of galactic origin, and an astrophysical background could also be not gaussian, if the number of contributing sources is not very large. Detection of a background of cosmological origin may allow us to probe time scales and energy not accessible with conventional astronomy or accelerators. Even in case of non-detection important constraints to model parameters can be established. An astrophysical background, interesting in its own right, could in fact be a foreground obscuring the cosmological background in some frequency band. See references in the review papers by Maggiore [30] and Regimbau [31] for a more detailed description of various possible sources of SGWB.

A SGWB is usually characterized by the dimensionless parameter

$$\Omega_{GW}(f) = \frac{1}{\rho_c}\frac{d\rho_{gw}}{dlnf} \tag{6}$$

where ρ_{gw} is the gravitational wave densitiy, f is the frequency in the observer frame and $\rho_c = \frac{3H_0^2}{8\pi G}$ is the critical energy density to close the Universe (H_0 is the Hubble constant). It is also useful, in particular to make easier the comparison with detector sensitivity, to express the background in terms of the signal energy spectral density

$$S_h(f) = \frac{3H_0^2}{4\pi^2}\Omega_{GW}(f) \tag{7}$$

In Fig.3 theoretical predictions (for given model parameters, see figure caption) of various SGWB of cosmological origin and observational bounds are shown.

The signal would appear as excess noise in a single detector. In principle, to conclude that a SGWB is really present one should exclude that the excess noise is not due to some source of noise not taken into account. The difficulty in doing this is also increased by the fact that the signal-to-noise ratio does not increase with the observation time, differently from what happens in the search for continuous signals. On the other hand, the signal would show up as a coherent stochastic process between two or more detectors. Then, a typical analysis strategy consists in cross-correlating the data from multiple detectors. By indicating with $s_1(t)$, $s_2(t)$ the data streams from two detectors, the cross-correlation is

$$Y = \int_{-T_{obs}/2}^{+T_{obs}/2} dt \int_{-T_{obs}/2}^{+T_{obs}/2} dt' \; s_1(t)s_2(t')Q(t-t') \tag{8}$$

where $Q(t-t')$ is a filter function chosen to maximize the signal-to-noise ratio. In the frequency domain the optimal filter function takes the form

$$\tilde{Q}(f) \propto \frac{\Gamma(f)\Omega_{gw}(f)}{f^3 S_1(f) S_2(f)} \tag{9}$$

where S_1, S_2 are the power spectral noise density of the two detectors and $\Gamma(f)$ is the overlap reduction function which takes into account the fact that the two detectors can see a different signal because they are at a different location or because they have a different angular sensitivity. In particular, if the separation between the two detectors is much larger than the signal reduced wavelength, the correlation is strongly suppressed. On the other hand, if the distance among two detectors is very small, or if they are co-located, the identification of coherent disturbances is not a trivial task. The sensitivity of a pair of detectors is usually given in terms of the minimum detectable amplitude for a flat spectrum [32]:

$$\Omega_{min} \approx \frac{34}{H_0^2\sqrt{T_{obs}}}\left[\int_0^\infty \frac{\Gamma^2(f)}{f^6 S_1(f) S_2(f)} df\right]^{-1/2} \tag{10}$$

where a false alarm rate of 1% and a false dismissal rate of 10% have been considered.

The full-S5 data set from LIGO detectors has been analyzed to search for a SGWB cross-correlating data from the detector pairs H1-L1 and H2-L1 [33]. The effective observation time was $\sim$ 293 days. The analysis was focused on the frequency band 41 – 170 Hz, which includes about 99% of the instrumental sensitivity. A bayesian 95% degree of belief upper limit has been set, taking the S4 posterior as a prior:

$$\Omega_{gw}(f) < 6.9 \cdot 10^{-6} \tag{11}$$

Models to explain the element abundance observation constrain total energy at the time of the Big-Bang nucleosynthesis to $\int \Omega_{gw}(f) d(ln\ f) < 1.5 \cdot 10^{-5}$. Allocating all the energy to the analyzed frequency band implies an upper bound of $1.1 \cdot 10^{-5}$. Then the limit of Eq. 11 beats the indirect limits provided by Big-bang nucleosynthesis and cosmic microwave background, see Fig.3. This result constrains also models of cosmic super-strings, in which the gravitational background is due to the superposition of many cusp burst signals [34], excluding regions in the $G\mu - \epsilon$ plane, as shown in Fig.4.

The analysis of data from the pair H1-H2 is also underway. From one hand having two co-located detectors would give a sensitivity improvement of about one order of magnitude. On the other, the presence of correlations between the two data streams reduces the gain. A big effort is being done in order to identify all the environmental contributions to the H1-H2 cross-correlation. Also the search for non-isotropic backgrounds is being considered, and an analysis method optimized for this kind of signal, called *radiometer* analysis [35], has already produced results for S4 and is being applied to S5 data.

Advanced detectors should push the upper limit a couple of orders of magnitude below the current limit thus further constraining the parameter space of various models of cosmological SGWB, see Fig.3. In particular, for cosmic super-string models they could exclude regions of $G\mu > 10^{-11}$ and $\epsilon > 10^{-10}$. They should be also able to put constraints on Pre-Big-Bang models by excluding regions in the $f_1 - \mu$ plane.

4 Conclusions

The search for continuous gravitational wave signals and stochastic gravitational wave backgrounds in LIGO and Virgo data has already produced several upper limits of astrophysical interest, altough no detection. New results will come soon by analyzing most recent data and using improved analysis pipelines. The development of more sensitive and robust methods will follow in the next years in order to be ready for the advanced detectors era.

Acknowledgments

The authors gratefully acknowledge the support of the United States National Science Foundation for the construction and operation of the LIGO Laboratory, the Science and Technology Facilities Council of the United Kingdom, the Max-Planck-Society, and the State of Niedersachsen/Germany for support of the construction and operation of the GEO600 detector, and the Italian Istituto

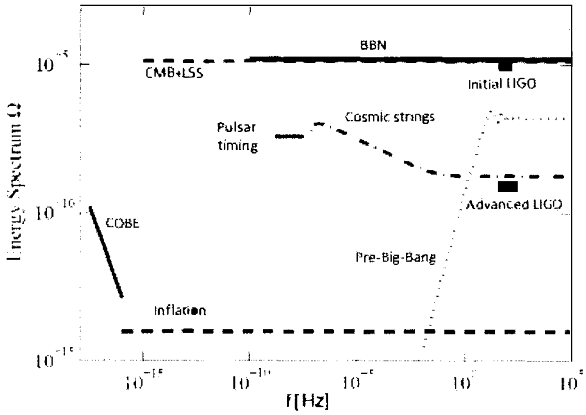

gure 3: Theoretical predictions of various cosmological SGWB and observational bounds. The cosmic super-string rve corresponds to parameters $p = 0.1$ (probability that two strings would undergo reconnection to form a loop), $= 7 \cdot 10^{-5}$ (loop size), $G\mu = 10^{-8}$ (dimensionless string tension). The Pre-Big-Bang curve corresponds to parameters $= 1.5$ (measure of the growth of the dilaton field during the stringy phase), $f_1 = 4.3 \cdot 10^{10}$ Hz (redshifted frequency GWs beginning at the end of the stringy phase and lasting to the present day), $f_s = 100$ Hz (redshifted frequency of Ws beginning at the advent of the stringy phase, and lasting to the present day). The bound due to Advanced LIGO is ised on its planned sensitivity curve. Figure prepared using the tool at http://homepages.spa.umn.edu/%7Egwplotter/.

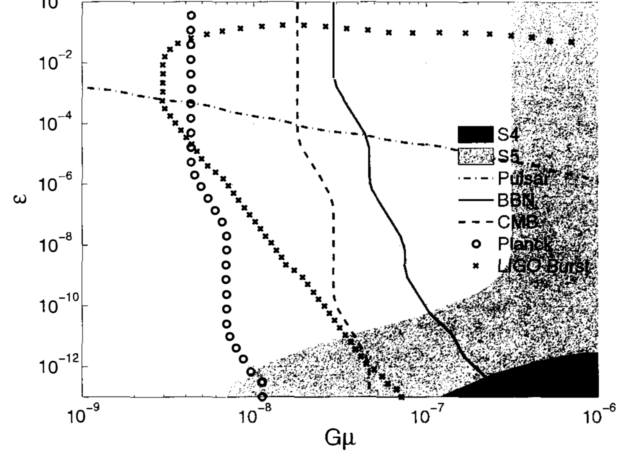

igure 4: Exclusion regions in the $\epsilon - G\mu$ plane. LIGO-S5 results exclude region of low ϵ and low $G\mu$ (Reprinted from Nature[33]).

Nazionale di Fisica Nucleare and the French Centre National de la Recherche Scientifique for the construction and operation of the Virgo detector. The authors also gratefully acknowledge the support of the research by these agencies and by the Australian Research Council, the International Science Linkages program of the Commonwealth of Australia, the Council of Scientific and Industrial Research of India, the Istituto Nazionale di Fisica Nucleare of Italy, the Spanish Ministerio de Educación y Ciencia, the Conselleria d'Economia Hisenda i Innovació of the Govern de les Illes Balears, the Foundation for Fundamental Research on Matter supported by the Netherlands Organisation for Scientific Research, the Polish Ministry of Science and Higher Education, the FOCUS Programme of Foundation for Polish Science, the Royal Society, the Scottish Funding Council, the Scottish Universities Physics Alliance, The National Aeronautics and Space Administration, the Carnegie Trust, the Leverhulme Trust, the David and Lucile Packard Foundation, the Research Corporation, and the Alfred P. Sloan Foundation.

References

1. B. P. Abbott *et al*, Reports on Progress in Physics720769012009
2. T. Accadia *et al*, *Class. Quant. Grav.* **28**, 025005 (2011)
3. C. J. Horowitz and K. Kadau, *Phys. Rev. Lett.* **102**, 191102 (2009)
4. B. Owen, *Phys. Rev. Lett.* **95**, 211101 (2005)
5. L. M. Lin, *Phys. Rev.* D **76**, 081502 (2007)
6. B. Haskell *et al*, *Phys. Rev. Lett.* **99**, 231101 (2007)
7. B. Abbott *et al*, *Phys. Rev.* D **76**, 042001 (2001)
8. R. J. Dupuis and G. Woan, *Phys. Rev.* D **72**, 102002 (2005)
9. P. Jaranowski, A. Krolak, B. F. Schutz, *Phys. Rev.* D **58**, 063001 (1998)
10. P. Astone, S. D'Antonio, S. Frasca and C. Palomba *Class. Quant. Grav.* **27**, 194016 (2010)
11. B. Abbott *et al*, *The Astrophysical Journal* **713**, 671 (2010)
12. C.-Y. Ng and W. Romani, *The Astrophysical Journal* **673**, 411 (2008)
13. J. Abadie *et al*, submitted to *The Astrophysical Journal* , (2011)
14. V. Dergachev, LIGO technical document *LIGO-T050186*, 2005
15. P. Brady, T. Creighton, C. Cutler and B. F. Schutz, *Phys. Rev.* D **57**, 2101 (1998)
16. B. Krisnan, A. Sintes, M. A. Papa, B. F. Schutz, S. Frasca and C. Palomba, *Phys. Rev.* D **70**, 082001 (2004)
17. C. Palomba, S. Frasca and P. Astone, *Class. Quant. Grav.* **22**, S1255 (2005)
18. B. Abbott *et al Phys. Rev.* D **72**, 102004 (2005)
19. B. Abbott *et al Phys. Rev.* D **77**, 022001 (2008)
20. H. J. Pletsch and B. Allen, *Phys. Rev. Lett.* **103**, 181102 (2009)
21. V. Dergachev, *Class. Quant. Grav.* **27**, 205017 (2010)
22. F. Antonucci, P. Astone, S. D'Antonio, S. Frasca and C. Palomba, *Class. Quant. Grav.* **25**, 184015 (2008)
23. P. Brady and T. Creighton, *Phys. Rev.* D **61**, 082001 (2000)
24. S. Frasca, P. Astone and C. Palomba, *Class. Quant. Grav.* **22**, S1013 (2005)
25. F. Acernese *et al*, *Class. Quant. Grav.* **24**, S491 (2007)
26. B. P. Abbott *et al*, *Phys. Rev.* D **80**, 042003 (2009)
27. B. P. Abbott *et al*, *Phys. Rev. Lett.* **102**, 11102 (2009)
28. http://einstein.phys.uwm.edu
29. B. P. Abbott *et al*, *The Astrophysical Journal* **722**, 1504 (2010)
30. M. Maggiore, Phys. Rep.3312832000
31. T. Regimbau, Research in Astronomy and Astrophysics **11**, 369 (2011)
32. B. Allen and J. D. Romano, *Phys. Rev.* D **59**, 102001 (1999)
33. B. P. Abbott *et al*, Nature **460**, 990 (2009)
34. X. Siemens, V. Mandic and J. Creighton, *Phys. Rev. Lett.* **98**, 111101 (2007)
35. B. Abbott *et al.*, *Phys. Rev.* D **76**, 082003 (2007)

MULTIMESSENGER ASTRONOMY

N.L. CHRISTENSEN[a]
for the LIGO Scientific Collaboration and the Virgo Collaboration
Physics and Astronomy, Carleton College,
Northfield, Minnesota 55057, USA

Multimessenger astronomy incorporating gravitational radiation is a new and exciting field that will potentially provide significant results and exciting challenges in the near future. With advanced interferometric gravitational wave detectors (LCGT, LIGO, Virgo) we will have the opportunity to investigate sources of gravitational waves that are also expected to be observable through other messengers, such as electromagnetic (γ-rays, x-rays, optical, radio) and/or neutrino emission. The LIGO-Virgo interferometer network has already been used for multimessenger searches for gravitational radiation that have produced insights on cosmic events. The simultaneous observation of electromagnetic and/or neutrino emission could be important evidence in the first direct detection of gravitational radiation. Knowledge of event time, source sky location, and the expected frequency range of the signal enhances our ability to search for the gravitational radiation signatures with an amplitude closer to the noise floor of the detector. Presented here is a summary of the status of LIGO-Virgo multimessenger detection efforts, along with a discussion of questions that might be resolved using the data from advanced or third generation gravitational wave detector networks.

1 Introduction

The era of gravitational wave (GW) astronomy has begun. The LIGO [1] and Virgo [2] GW interferometric detectors have demonstrated their ability to operate at or near their initial design sensitivities. LIGO's sixth scientific run, S6, and Virgo's third scientific run, VSR3, were recently completed; GEO 600 [3] also acquired data during this period. The LIGO Scientific Collaboration (LSC) and the Virgo Collaboration have been working together in their effort to detect binary inspiral [4, 5], burst [6,7], continuous wave [8,9], and stochastic background [10] signals, as well as GWs associated with electromagnetic (EM) events (such as a γ-ray burst, GRB) [11,12]. In 2014, a new generation of detectors, with an even better ability to observe the universe,

[a]nelson.christensen@ligo.org

will come on-line; advanced LIGO (aLIGO) [16] and advanced Virgo (AdV) [17] will work toward achieving a factor of 10 better sensitivity than the initial detectors. The Large-scale Cryogenic Gravitational wave Telescope (LCGT) is expected to also come on-line around 2015 [18]. A truly global network of advanced detectors will be simultaneously operating in the second half of this decade. The initial ground based laser interferometers were sensitive to GWs in the frequency band from 20 Hz (for Virgo, 40 Hz for LIGO) up to 8 kHz, while the lower frequency for the advanced detectors should drop to 10 Hz.

The existence of GWs was predicted by Einstein [13], and confirmed through observations on the binary pulsar PSR 1913+16. This binary system was discovered in 1974 by Taylor and Hulse[14], and subsequent observations by Taylor and Weisberg[15] have shown that the decay of the orbit matches perfectly with what is predicted via energy loss by GW emission. GW detectors, like LIGO and Virgo, hope to observe GWs produced by astrophysical sources. The observation of these GWs will provide information about the astrophysical event. LIGO, Virgo, and other detectors will not be just GW detectors, they will also be the new generation of astronomical observatories. It is possible that some sources of GWs may not emit EM radiation; for example, imagine the oscillations of a newly formed black hole. Other sources, like a supernova, will likely emit both EM radiation and GWs, and the observation of the GWs in coincidence with EM observations could give new insight about the source. EM observations of the universe are done with radiation having frequencies above 10 MHz. On the other hand, GW observations will be from frequencies below 10 kHz; this should provide very different information about the universe. Since GWs are weakly interacting, any waves produced will traverse the universe without being scattered or absorbed; this gives another unique opportunity for scientists to *see* new phenomena in our universe. In this article we discuss how LIGO and Virgo are searching for GW signals in coincidence with EM events. This is an example of multimessenger astronomy. Searches are conducted for GWs at times of observed EM events (the external trigger strategy) [11,12]. Since GW data from LIGO and Virgo is non-stationary [19,20], finding a GW signal candidate in coincidence with an EM transient will increase confidence that the signal is astrophysically produced, and not a spurious noise event.

LIGO and Virgo have developed another strategy for finding GW events in association with EM transients. During a period of joint data collection directional information was sent to EM observatories soon after outlier events were observed in the LIGO-Virgo data; these initial tests took place from Dec 17 2009 to Jan 8 2010, and Sep 4 to Oct 20 2010. When interesting GW triggers were generated, numerous EM observatories have been notified within 30 minutes as part of an EM follow-up effort [21].

There are a number of possible sources for an EM signal accompanying a GW. Long GRBs are likely associated with massive star collapse [22], producing γ-rays then subsequent x-ray and optical afterglows. A double neutron star (NS) or NS/blackhole merger could be the source of short GRBs [23] (with prompt γ-rays and maybe weak, isotropic afterglows). Other interesting phenomena include soft gamma repeater (SGR) flares; these are highly magnetized ($10^{15}G$) neutron stars that emit γ-ray flares sporadically [29].

In addition, many astrophysical events will produce detectable high and low energy neutrinos; neutrino events will be another important multimessenger area. LIGO and Virgo are currently working with IceCube [24,25] and ANTARES [26,27] in the search for GW signals at the time these neutrino observatories register events. It is suspected that high energy neutrinos could be emitted from long GRBs [22], short GRBs [23], low-luminosity GRBs [28], or even *choked* GRBs [30]. Core collapse supernovae have prompt low energy neutrino emission (along with delayed optical signals). In the future, with the advanced detectors, it will be fruitful to search for GWs in coincidence with low energy neutrinos from supernovae [31].

Multimessenger observations could help to address and perhaps resolve a number of open questions in astrophysics [32]. For example:

* What is the speed of GWs? (subluminal or superluminal?)
* Can GW detectors provide an early warning to EM observers? (to allow the detection of early light curves.)
* What is the precise origin of SGR flares? (what is the mechanism for GW and EM emission and how are they correlated?)
* What happens in a core collapse supernova before the light and neutrinos escape?
* Are there electromagnetically hidden populations of GRBs?
* What GRB progenitor models can we confirm or reject?
* Is it possible to construct a competitive Hubble diagram based on GW standard sirens? [33,34]

These are just a few of the astrophysical problems that LIGO and Virgo hope to address with their multimessenger studies. The remainder of this paper is organized as follows. In Sec. 2 there is a summary of the multimessenger results to date by LIGO and Virgo. Sec. 3 summarizes methods for searching for GW events in coincidence with EM transients, while Sec. 4 does the same for neutrino events. A conclusion is given in Sec. 5.

2 LIGO - Virgo Multimessenger Results

LIGO and Virgo have already published astrophysically important multimessenger papers; while no GWs were observed, the upper limits that have been set do provide significant constraints on the systems in question [11,12,35,36,37]. Virgo and LIGO have developed methods whereby searches are conducted for GWs at times of GRBs. By constraining the GW search to a relatively short period (typically tens to hundreds of seconds) the background rejection is improved, and the sensitivity for GW detection is increased. Long GRB events are assumed to be produced by massive star collapse, and GW searches by LIGO and Virgo use their unmodeled *burst* search pipelines [12,35,36,37]. The coalescence of a neutron star - neutron star, or neutron star - black hole binary system is suspected to be the source of the short GRBs; the LIGO-Virgo *compact binary coalescence* and burst pipelines are both used to search for GWs from short GRBs [11].

Even by not seeing a GW signal in association with a GRB, important astrophysical statements can be made. For example, LIGO and Virgo were able to set lower limits on source distances for 22 short GRBs during LIGO's fifth and Virgo's first scientific runs (S5, VSR1) based on the assumption that these were neutron star - neutron star, or neutron star - black hole binary coalescences [11]. For the same S5/VSR1 period, LIGO and Virgo were able to set upper limits on the amplitude of GWs associated with 137 GRBs, and also place lower bounds on the distance to each GRB under the assumption of a fixed energy emission in GWs; the search was conducted for burst waveforms ($< 1s$) with emission at frequencies around 150 Hz, where the LIGO - Virgo detector network had its best sensitivity [37]. The average exclusion distance for the set of GRBs was about 15 Mpc.

The short-duration, hard-spectrum GRB 070201 had an EM determined sky position coincident with the spiral arms of the Andromeda galaxy (M31). For a short, hard GRB as this was, possible progenitors would be the merger of two neutron stars, a neutron star and a black hole, or a SGR flare. No GW candidates were found in LIGO data within a 180 s long window around the time of this GRB [38]. The results imply that a compact binary progenitor of GRB 070201 was not located in M31.

SGRs intermittently emit brief ($\approx 0.1s$) intense bursts of soft γ-rays, often with peak luminosities up to $10^{42} erg/s$; intermediate bursts with greater peak luminosities can last for seconds. Rare *giant flare* events can even be 1000 times brighter than common bursts [39]. SGRs could be good sources of GWs. These *magnetars* are likely neutron stars with exceptionally strong magnetic fields (up to $10^{15} G$). The SGR bursts may be from the interaction of the stars magnetic field with its solid crust, with crustal deformations, catastrophic cracking, excitation of the stars nonradial modes, and then emission of GWs [40]. The sources are also potentially close by.

LIGO has conducted searches for short-duration GWs associated with SGR bursts. There was no evidence of GWs associated with any SGR burst in a sample consisting of the 27 Dec 2004 giant flare from SGR 1806-20[36], and 190 lesser events from SGR 1806-20 and SGR 1900+14[41]. An innovative technique was also used to look for repeated GW bursts from the storm of flares from SGR 1900+14; the GW signal power around each EM flare was *stacked*, and this yielded per burst energy limits an order of magnitude lower than the individual flare analysis for the storm events[42].

3 Electromagnetic Transients

There are numerous scenarios where one could expect a GW signal to appear at the same time as an EM event. LIGO and Virgo have recently pursued two strategies to try and find coincident GW and EM events. One is to look for GWs in LIGO and Virgo data at times when EM observatories have registered a transient signal. In the other, LIGO and Virgo have sent times and sky locations to numerous EM observatories with a 30 minute latency; these correspond to LIGO and Virgo *triggers* that have been determined to be statistically significant.

3.1 External Trigger Strategy

Presently there is a search of recent data from LIGO's sixth scientific run (S6) and Virgo's second and third scientific runs (VSR2 and VSR3) for GWs in association with GRBs; LIGO and Virgo are examining events recorded by Swift[43] and Fermi[44]. Because the time and sky position of the GRB are known, this has the effect of reducing the background noise, and improving the sensitivity of the GW search. LIGO and Virgo have also commenced with an effort to find GWs in association with GRBs where the GW signal extends for a time scale of many seconds, to weeks[46]; the search for these intermediate duration signals has not been previously attempted.

For long GRBs[22] LIGO and Virgo use their unmodeled burst pipeline[6,7] to search for GW signals (since the assumption is that the source is a massive star collapse). while for short GRBs[23] they use both the coalescing compact binary search[4,5] and unmodeled burst pipelines. The GRBs provide information on the sky position and event time; this simplifies the analysis of the GW data since the time delay between the different GW detectors is known. This also significantly diminishes the data set to be analyzed, reduces the noise background, and therefore increases the sensitivity of the search by about a factor of two[45]. For short GRBs a time window for the GW search about the GRB is several seconds; for long GRBs the time window is dictated by GRB astrophysics, and for the LIGO - Virgo search is $-600s$ to $+60s$. LIGO and Virgo results for GRB events during S6-VSR2/3 will for forthcoming soon.

3.2 EM Followups

During two recent periods (17 Dec 2009 to 8 Jan 2010, and 4 Sep 2010 to 20 Oct 2010, within S6-VSR2/3) LIGO and Virgo worked with a number of EM observatories, testing a new method whereby GW data was rapidly analyzed[21]. The time and sky location of statistically significant GW triggers were sent to EM observatories within 30 minutes. Wide EM field of view observations are important to have, but sky location information that is as accurate as possible is also necessary. For this effort the start of the pipeline consisted of triple coincident (from the two LIGO detectors and Virgo) unmodeled burst, or compact binary coalescence triggers. Within a period of 10 minutes it was determined whether the events were statistically significant or not, and whether the quality of the data from the GW observatories was good. The significance above threshold for an event was determined via comparisons with background events. The target false alarm rates were 1 event per day for the initial test period, then reduced to 0.25 event per day for the second test period (excluding Swift[43] and the Palomar Transient

Factory [47], where the rate was 0.1 event per day). Information on known globular cluster and galaxy locations were then used to further restrict the likely sky position of the potential source; only sources out to a distance of 50 Mpc were considered to be possible. Within 30 minutes of the initial registration of the potential GW event, the significant triggers were manually vetted by on-call scientific experts, and scientific monitors in the the observatory control rooms. If a potential GW trigger passed all of the tests the direction information was then sent to various EM observatories, including a number of optical observatories: The Liverpool telescope [48], the Palomar Transient Factory [47], Pi of the Sky [53], QUEST [59], ROTSE III [54], SkyMapper [55], TAROT [56], and the Zadko Telescope [57]. Trigger information was also sent to the Swift X-ray observatory [43,58], and the radio network LOFAR [49]. Part of the research work from LIGO and Virgo has also involved the development of image analysis procedures able to identify the EM counterparts. In the initial S6-VSR2/3 test period there were 8 potential GW events where the information was passed onto the EM observatories, and observations were attempted for 4 of them; for the second test period there were 6 potential GW events, and 4 of them had EM observations attempted. The full results from this EM follow-up effort will be published in the near future. This EM follow-up effort during S6-VSR2/3 was a successful milestone, and a positive step toward the advanced detector era where the chances of GW detections will be very enhanced, and these rapid EM observations, when coupled with the GW data, could provide important astrophysical information on the sources.

Long and short GRB afterglows peak a few minutes after the prompt EM/GW emission [50,51], and it is critical to have EM observations as soon as possible after the GW trigger validation. *Kilo-ñovae* model afterglows peak about a day after the GW emission [52], so EM observations a day after the GW trigger would be an important validation for these type of events. In order to discriminate between the possible EM counterpart (to the GW source) from contaminating transients repeated observations over several nights are necessary to study the light curve.

4 Neutrinos

Many of the energetic astrophysical events that could produce GWs are also expected to emit neutrinos. LIGO and Virgo are currently investigating methods to use observations of high and low energy neutrinos to aid in the effort to observe GWs.

4.1 High Energy Neutrinos

High energy neutrinos (HENs) are predicted to be emitted in astrophysical events that also produce significant amounts of GWs, and by using the time and sky location of observed HENs the ability to confidently identify GWs will be improved. HENs should be emitted in long GRBs; in the prompt and afterglow phases, HENs ($10^5 - 10^{10}$ GeV) are expected to be produced by accelerated protons in relativistic shocks [22]. HENs can also be emitted during binary mergers involving neutron stars [23]. HENs and GWs could both come from low luminosity GRBs; these would be associated with an energetic population of core-collapse supernovae [28]. There is a class of events where GWs and HENs might be observed in the absence of a GRB observation, namely with choked GRBs; these could plausibly come from baryon-rich jets. Because the environment could be optically thick, the choked GRB events may be hidden from conventional EM astronomy, and HENs and GWs will be the only messengers to reveal their properties [30].

LIGO and Virgo are presently working with IceCube[24,25] and ANTARES [26,27] to see if there are HEN events in coincidence with GW signals in LIGO (S5 and S6) and Virgo (VSR1, VSR2 and VSR3) data. The HEN event time, sky position, and reconstructed energy information enhance the sensitivity of the GW search. During S5 and VSR1 IceCube had 22 of its strings in operation, while ANTARES had 5 strings. IceCube reached its full complement of 86 strings near the time of the end of S6 and VSR3, while ANTARES reached 12 strings. IceCube can provide a neutrino trigger sky location to about 1 degree squared accuracy; then by using catalogs of galaxy positions, including distance, the trigger information from the LIGO and Virgo data can provide a joint test statistic, and reduced false alarm rate. For example, there would be a false alarm rate of about 1 in 435 years for a one-second coincidence time window and spatial coincidence p-value threshold of 1% [60,61]. The size of the time window to be used about the neutrino trigger is a critical parameter in the search, and will need to be larger than 1 s; taking into account the physical processes that could result in neutrino, γ-ray, and GW emission, it was determined that a conservative $\pm 500s$ time window would be appropriate [62]. The results of this research effort be published soon.

A potential problem for a neutrino - GW search occurs with long GRBs, where HENs from relativistic shocks might be emitted between a few hours (internal shocks [28]) to a few days (external shocks [22]) after the GW emission caused by core bounce [60]. For these events a larger time window will be necessary (days) which will increase the false alarm rate. Better sky position accuracy, either through an improved neutrino detector or an expanded GW detector network (for example with the coming network of advanced detectors), would help to address this issue.

4.2 Low Energy Neutrinos

Low energy neutrinos (LENs) will be an important multimessenger partner to GWs for core collapse supernovae (CCSN). LIGO and Virgo are developing search methods involving LENs, especially for the advanced detector era. A range of 3 to 5 Mpc is admittedly at the edge of detectability for aLIGO and Super-K [63]; at this distance the supernovae rate becomes about 1/year [64]. A weak coincident signal in both GWs and LENs may be convincing, especially if there were also an optical signal. For a galactic supernova, the neutrino signal will be large, and LIGO and Virgo would do a standard external trigger search (GRB search) with a tight coincidence window. A CCSN produces 10-20 MeV neutrinos (all flavors) over a few 10s of seconds. It is expected that all three neutrino flavors would be created; GWs and neutrinos would be emitted promptly in the CCSN, while EM radiation could be delayed. The neutrino and GW information would truly provide a probe of the physics of the core collapse [65]. The onset of the signal could probably be determined to better than 1 s. Detectors, such as Super-K [63], would detect of order 10^4 neutrinos for a CCSN at the galactic center. The optical (EM) signature of a CCSN could be obscured; for example, SN 2008iz in M82 was missed via optical observations [66]. With just EM information the exact time of the core collapse bounce could be uncertain to many hours. A tight coincidence window provided by neutrino observations could be used to establish a correlation with GWs. In the advanced GW detector era the sensitivity range of GW and neutrino detectors will be similar, and it is a research goal of LIGO and Virgo that LEN information will be used in association with data from the advanced GW detectors.

5 Conclusions

There is an active effort by LIGO and Virgo to find GWs in coincidence with EM or neutrino counterparts. Numerous studies have already been conducted using LIGO and Virgo data from the initial generation of detectors, and more results will be forthcoming soon. AdV [17], aLIGO [16], and GEO-HF (an upgraded GEO, with improved high frequency response) [3,67] should be on-line in 2014 and start trying to achieve their enhanced sensitivities. LCGT [18] could be operating in 2015. A global network of advanced detectors will be simultaneously observing in the second half of this decade, and multimessenger techniques using EM and neutrino event information will improve the probability for detecting GWs. By using GW, EM and neutrino observations all together there will be a tremendous opportunity to decipher the astrophysics pertaining to many different types of cataclysmic events in the universe.

Acknowledgments

This document has been assigned LIGO Document Number P-1100053. The work was funded by NSF Grant PHY-0854790. The authors gratefully acknowledge the support of the United States National Science Foundation for the construction and operation of the LIGO Laboratory, the Science and Technology Facilities Council of the United Kingdom, the Max-Planck-Society, and the State of Niedersachsen/Germany for support of the construction and operation of the GEO600 detector, and the Italian Istituto Nazionale di Fisica Nucleare and the French Centre National de la Recherche Scientifique for the construction and operation of the Virgo detector. The authors also gratefully acknowledge the support of the research by these agencies and by the Australian Research Council, the Council of Scientific and Industrial Research of India, the Istituto Nazionale di Fisica Nucleare of Italy, the Spanish Ministerio de Educación y Ciencia, the Conselleria d'Economia Hisenda i Innovació of the Govern de les Illes Balears, the Foundation for Fundamental Research on Matter supported by the Netherlands Organisation for Scientific Research, the Polish Ministry of Science and Higher Education, the FOCUS Programme of Foundation for Polish Science, the Royal Society, the Scottish Funding Council, the Scottish Universities Physics Alliance, The National Aeronautics and Space Administration, the Carnegie Trust, the Leverhulme Trust, the David and Lucile Packard Foundation, the Research Corporation, and the Alfred P. Sloan Foundation.

References

1. B. Abbott *et al* (LIGO Scientific Collaboration), *Rep. Prog. Phys.* **72**, 076901 (2009).
2. F. Acernese *et al* (Virgo Collaboration), *Class. Quantum Grav.* **25**, 114045 (2009).
3. H. Grote (LIGO Scientific Collaboration). *Class. Quantum Grav.* **25**, 114043 (2008).
4. B. Abbott *et al* (LIGO Scientific Collaboration), *Phys. Rev.* D **80**, 047101 (2009).
5. F. Acernese *et al* (Virgo Collaboration) *Class. Quantum Grav.* **24**, 5767 (2007).
6. B. Abbott *et al* (LIGO Scientific Collaboration), *Phys. Rev.* D **80**, 102001 (2009).
7. F. Acernese *et al* (Virgo Collaboration), *Class. Quantum Grav.* **26**, 085009 (2009).
8. B. Abbott *et al* (LIGO Scientific Collaboration and the Virgo Collaboration), *ApJ* **713**, 671 (2010).
9. F. Acernese *et al* (Virgo Collaboration), *Class. Quantum Grav.* **26**, 204002 (2009).
10. B. Abbott *et al* (LIGO Scientific Collaboration and the Virgo Collaboration), *Nature* **460**, 990 (2009).
11. J. Abadie *et al* (LIGO Scientific Collaboration and the Virgo Collaboration), *ApJ* **715**, 1453 (2010).
12. F. Acernese *et al* (Virgo Collaboration), *Class. Quantum Grav.* **25**, 225001 (2008).
13. A. Einstein, 'Preuss. *Akad. Wiss. Berlin*, Sitzungsberichte der physikalisch-mathematischen Klasse, 688 (1916).
14. R. Hulse and J. Taylor, *ApJ* **195**, L51 (1975).
15. J. Taylor and J. Weisberg, *ApJ* **345**, 434 (1989).
16. G.M. Harry (LIGO Scientific Collaboration), *Class. Quantum Grav.* **27**, 084006 (2010).
17. https://wwwcascina.virgo.infn.it/advirgo/docs.html
18. K. Kuroda and the LCGT Collaboration, *Class. Quantum Grav.* **27**, 084004 (2010).
19. N. Christensen (LIGO Scientific Collaboration and the Virgo Collaboration), *Class. Quantum Grav.* **27**, 194010 (2010).
20. F. Robinet (LIGO Scientific Collaboration and the Virgo Collaboration), *Class. Quantum Grav.* **27**, 194012 (2010).

21. J. Kanner *et al*, *Class. Quantum Grav.* **25**, 184034 (2008).
22. E. Waxman and J.N. Bahcall, *ApJ* **541**, 707 (2000).
23. E. Nakar, *Phys. Rep.* **442**, 166 (2007).
24. R. Abbasi *et al* (IceCube Collaboration), *Phys. Rev.* D **83**, 012001 (2011).
25. F. Halzen and J.P. Rodrigues, *Class. Quantum Grav.* **27**, 194003 (2010).
26. J.A. Aguilar *et al*, *Phys. Lett.* B **696**, 16 (2011).
27. T. Pradier (Antares Collaboration), *Class. Quantum Grav.* **27**, 194004 (2010).
28. N. Guptaa and B. Zhang, *Astropart. Phys.* **27**, 386 (2007).
29. K. Ioka, *MNRAS* **327**, 639 (2001).
30. S. Horiuchi and Shin'ichiro Ando, *Phys. Rev.* D **77**, 063007 (2008).
31. C.D. Ott, Adam Burrows, Luc Dessart and Eli Livne, *ApJ* **685**, 1069 (2008).
32. S. Marka (LIGO Scientific Collaboration and the Virgo Collaboration), *J. Phys. Conf. Ser.* **243**, 012001 (2010).
33. B.S. Sathyaprakash *et al*, *Class. Quantum Grav.* **27**, 215006 (2010).
34. S. Nissanke *et al*, *ApJ* **725**, 496 (2010).
35. B. Abbott *et al* (LIGO Scientific Collaboration), *Phys. Rev.* D **72**, 042002 (2005).
36. B. Abbott *et al* (LIGO Scientific Collaboration), *Phys. Rev.* D **77**, 062004 (2008).
37. B. Abbott *et al* (LIGO Scientific Collaboration and the Virgo Collaboration), *ApJ* **715**, 1438 (2010).
38. B. Abbott *et al* (LIGO Scientific Collaboration), *ApJ* **681**, 1419 (2008).
39. D.M. Palmer *et al*, *Nature* **434**, 1107 (2005).
40. J.E. Horvath, *Mod. Phys. Lett.* A **20**, 2799 (2005).
41. B. Abbott *et al* (LIGO Scientific Collaboration), *Phys. Rev. Lett.* **101**, 211102 (2008).
42. B. Abbott *et al* (LIGO Scientific Collaboration), *ApJ* **701**, L68 (2009).
43. http://swift.gsfc.nasa.gov/docs/swift/swiftsc.html
44. http://fermi.gsfc.nasa.gov/
45. M. Was, PhD thesis, Université Paris Sud, Document LAL-11-119 (2011).
46. E. Thrane *et al*, *Phys. Rev.* D **83**, 083004 (2011).
47. A. Rau *et al*, *Publ. Astron. Soc. Pac.* **121**, 1334 (2009).
48. I.A. Steele *et al*, *Proceedings of the SPIE* **5489**, 679 (2004).
49. H.D. Falcke *et al*, *Proceedings of the International Astronomical Union* **2**, 386 (2007).
50. D.A. Kann *et al*, arXiv:0804.1959v2 (2008).
51. D.A. Kann *et al*, *ApJ* **720**, 1513 (2010).
52. B. D. Metzger *et al* *MNRAS* **406**, 2650 (2010).
53. K. Malek *et al*, *Proceedings of the SPIE* **7502**, 75020D (2009).
54. C.W. Akerlof *et al*, *Publ. Astron. Soc. Pac.* **115**, 132 (2003).
55. S. C. Keller *et al*, *Publ. Astron. Soc. of Australia* **24**, 1 (2007).
56. A. Klotz *et al*, *AJ* **137**, 4100 (2009).
57. D.M. Coward *et al*, *Publ. Astron. Soc. of Australia* **27**, 331 (2010).
58. N. Gehrels *et al*, *New Journal of Physics* **9**, 37 (2007).
59. C. Baltay *et al*, *Publ. Astron. Soc. Pac.* **119**, 1278 (2007).
60. Y. Aso *et al*, *Class. Quantum Grav.* **25**, 114039 (2008).
61. E. Chassande-Mottin (LIGO Scientific Collaboration and the Virgo Collaboration) *J. Phys. Conf. Ser.* **243**, 012002 (2010).
62. B. Baret *et al*, *Astropart. Phys.* **35**, 1 (2011).
63. M. Ikeda *et al*, *ApJ* **669**, 519 (2007).
64. S. Ando *et al*, *Phys. Rev. Lett.* **95**, 171101 (2005).
65. C.D. Ott *et al*, *ApJ* **685**, 1069 (2008).
66. A. Brunthaler *et al*, *Astronomy and Astrophysics* **499**, L17 (2009).
67. B. Willke *et al*, *Class. Quantum Grav.* **23**, S207 (2006).

SEARCHING FOR ELECTROMAGNETIC COUNTERPARTS OF GRAVITATIONAL WAVE TRANSIENTS

M. BRANCHESI
on behalf of the LIGO Scientific Collaboration and the Virgo Collaboration
DiSBeF, Università degli Studi di Urbino "Carlo Bo", 61029 Urbino, Italy
INFN, Sezione di Firenze, 50019 Sesto Fiorentino, Italy

A. KLOTZ
Université de Toulouse, Institut de Recherche en Astrophysique et Planétologie
9 Avenue Colonel Roche, 31028 Toulouse Cedex 4 France

M. LAAS-BOUREZ
ICRAR / School of Physics, University of Western Australia,
Crawley WA 6009, Australia

A pioneering electromagnetic (EM) observation follow-up program of candidate gravitational wave (GW) triggers has been performed, Dec 17 2009 to Jan 8 2010 and Sep 4 to Oct 20 2010, during the recent LIGO/Virgo run. The follow-up program involved ground-based and space EM facilities observing the sky at optical, X-ray and radio wavelengths. The joint GW/EM observation study requires the development of specific image analysis procedures able to discriminate the possible EM counterpart of GW trigger from background events. The paper shows an overview of the EM follow-up program and the developing image analysis procedures as they are applied to data collected with TAROT and Zadko.

1 Introduction

The LIGO[1] and Virgo[2] detectors aim at the first direct detection of gravitational waves from very energetic astrophysical events. The most promising sources are mergers of neutron stars (NS) and/or stellar mass black holes (BH) and the core collapse of massive stars. More exotic sources include cosmic string cusps. It is likely that a fraction of the large energy reservoir associated to those sources be converted into electromagnetic radiation. This possibility is a feature of several astrophysical scenarios. For instance, Gamma-Ray Bursts (GRBs) are thought to be associated with the coalescence of NS-NS or NS-BH binaries or the collapse of very massive stars (see[3] and references therein). Another scenario associated with compact object mergers is the prediction[4] of an isotropic EM emission from supernova-like transients powered by the radioactive decay of heavy elements produced in merger ejecta (this is referred to as the *kilonova* model). There are models that predict that cusps produce electromagnetic radiation[5].

In this respect, multi-messenger GW and EM astronomy is a very promising field of research. An electromagnetic counterpart discovered through a follow-up of a gravitational wave candidate event would considerably increase the confidence in the astrophysical origin of the event. The detection of an EM counterpart would give the precise localization and possibly lead to the identification of the host galaxy and redshift. Furthermore, EM and GW observations provide complementary insights into the progenitor and environment physics. In the long term combined measurements of the luminosity distance through GW radiation and redshifts through EM observations may allow a new way of estimating some cosmological parameters.

2 Enabling EM Follow-up of Candidate GW Events

2.1 Selection of Candidate GW Events

A first program of EM follow-up to GW candidates took place (Dec 17 2009 to Jan 8 2010 and Sep 4 to Oct 20 2010) during the last LIGO/Virgo observation periods, thanks to the development of a low-latency GW data analysis pipeline that uses real time gravitational wave triggers to obtain prompt EM observations to search for the EM counterparts.

One of the challenges of successfully obtaining "target of opportunity" EM observations is to identify the GW candidates quickly: the data from the three operating detectors (the two LIGOs and Virgo) must be transferred and analyzed in near-real time. As soon as the data become available, three search algorithms (Omega Pipeline, coherent Wave Burst both described in [6,7] and Multi Band Template Analysis [8]) run over the data. For each generated trigger, the direction of arrival of the wave (and hence potential sky position of the source) is estimated using a method based on differences in arrival time at each detector. The event candidates are collected in the Gravitational-wave candidate event database (GraCEDb). Two software packages LUMIN and GEM select statistically significant triggers and determine the telescope pointing positions. This process typically takes $\sim$10 minutes. It is followed by a manual event validation. A team of trained experts is on duty and their role is to rapidly coordinate with scientists at the GW detectors to evaluate the detector performances. If no problem is found the alert is sent to telescopes. The entire process is typically completed within 30 minutes. The triggers selected as GW candidates for EM follow-up are the ones detected in triple coincidences and with a power above a threshold estimated from the distribution of background events. A full description of the GW trigger selection and the entire EM follow-up process will be detailed in [9].

2.2 Sky Pointing strategy

The uncertainty in the source direction reconstruction scales inversely with the signal-to-noise ratio [10]. GW events near the detection threshold are localized into regions of tens of square degrees. Generally, the error regions have a non-trivial geometrical shape, often formed of several disconnected patches. Follow-up EM-telescopes with a wide Field Of View (FOV) are thus required. However, the majority of those telescopes have a FOV which is much smaller than the GW angular error box. Additional priors are necessary to improve the location accuracy and increase the chance that the actual source be in the selected FOV. The observable Universe is limited to an horizon of 50 Mpc, taking into account the detector sensitivity to the signals coming from NS binaries [11]. The observation of the whole GW error box is not required [12], but it can be restricted to the regions occupied by Globular Clusters and Galaxies within 50 Mpc, listed in the Gravitational Wave Galaxy Catalog [13]. Tens of thousands of galaxies are included within this horizon and the GW observable sources are more likely to be extragalactic.

To determine the telescope pointing position, the probability sky map based on GW data is "weighted" taking into account the mass and the distance of nearby galaxies [14] and globular clusters. It is assumed that the probability of a given galaxy being the host of the actual source i) is directly proportional to the galaxy's mass (the blue luminosity is used as proxy for the mass and thus for the number of stars) and, ii) is inversely proportional to the distance.

2.3 *Follow-up EM Observatories and Observation Strategy*

The follow-up program involved ground-based and space EM facilities: the *Liverpool Telescope*, the *Palomar Transient Factory* (PTF), *Pi of the Sky*, *QUEST*, *ROTSE III*, *SkyMapper*, *TAROT* and the *Zadko Telescope* observing the sky in the optical band, the *Swift* satellite with X-ray and UV/Optical telescopes and the radio interferometer *LOFAR*. The observing strategy employed by each telescope will be described in [9].

The cadence of EM observations is guided by the expected EM counterpart. The optical afterglow of an on-axis GRB peaks few minutes after the EM/GW prompt emission. The kilonova model predicts an optical ligth curve that peaks a day after the GW event, due to the time that the out flowing material takes to become optically thin. The agreement with the EM facilities allowed observations as soon as possible, the day after the GW event and, repeated observations over longer time-lag to follow the transient light curve dimming.

During the recent winter and summer LIGO/Virgo runs a total of 14 alerts have been sent out to the telescopes and 8 of them led to images being taken.

3 Optical Transient Search in the Wide-Field Telescope Observations

Once the follow-up observations are completed, the collected set of images needs to be analyzed to decide the presence or not of an optical transient of interest. The analysis method is conceptually similar to one used to study a GRB afterglow with a main difference: the arc minute localization of the current generation gamma-ray observatories allows a significant reduction of the search area with respect to the GW observations.

Searching for optical transients in a large sky area requires the development and use of specific image analysis procedures able to discriminate the EM counterpart from background/contaminant events. Several analysis pipelines are being developed and tested by groups within the LIGO Scientific Collaboration and the Virgo Collaboration in partnership with astronomers.

This section describes one of the considered approaches based on the cross-correlation of object catalogs obtained from each image. The resulting pipeline has been designed and tested with the images collected by the two *TAROT* and the *Zadko* telescopes.

TAROT [15] are two robotic 25 cm telescopes with a FOV of 3.5 square degrees located in Calern (France) and in La Silla (Chile). In case of a GW alert, *TAROT* followed a nominal observation schedule including six consecutive images with 180 second exposures during the first night and same for the three following nights. An exposure of 180 seconds corresponds to a red limiting magnitude of 17.5 under ideal conditions. *Zadko* [16] is a 1 meter telescope with a FOV of 0.17 square degrees located in Gingin (Western Australia). For each GW trigger, *Zadko* followed a nominal observation schedule including a mosaic of five fields with six consecutive images during the first night and same for the three following nights. A 120 sec exposure corresponds to a red limiting magnitude of 20.5 under ideal conditions.

The main steps of the fully automated analysis pipeline are as follows:
1) extraction of the catalog of objects visible in the images using `SExtractor` [17];
2) removal of "known objects" listed in USNO-A2.0 or USNO-B star catalogs that are complete down to a fainter magnitude than the collected images by using a positional cross-correlation tool `match` [18];
3) trace objects in common to several image catalogs by using a cross-positional check. This results in a light curve for each traced object;
4) rejection of "rapid contaminating transients" (like cosmic rays, asteroids or noise): the presence is required in at least four consecutive images;
5) rejection of "background transients": the objects are selected in the image regions associated with the galaxies within 50 Mpc. A circular region with a diameter equal to 4 times the major

axis galaxy size is used. This is to take into account the possible offset between the host galaxy center and the optical transients (observed up to tens of kpc for GRBs);
6) rejection of "contaminating events" like galaxies, variable stars or false transients by analyzing the light curves. The code selects the objects that show a luminosity dimming with time. Assuming that the dimming is described by a single power-law $\mathcal{L} \propto t^{-\beta}$, corresponding to a linear variation in terms of magnitude equal to $\boldsymbol{m} = 2.5\beta \log_{10}(t) + C$, a "slope index" 2.5β is defined and evaluated for each objects. The expected "slope index" for GRB afterglows and kilonova-like light curves is around 2.5-3. In practice, a conservative cut is applied by selecting as the possible EM counterparts the objects with the "slope index" larger than 0.5. This value has been checked using Monte Carlo simulations.

The preliminary results on the pipeline sensitivity indicate for a survey red limiting magnitude of 15.5 that the majority of GRB afterglows can be detected further away the GW horizon distance of 50 Mpc, while the kilonova objects can be detected up to a distance of 15 Mpc. These results are obtained by repeatedly running the pipeline over sets of *TAROT* and *Zadko* images where fake on-axis GRB and kilonova optical transients were injected.

Estimates of the rate of false detections may be deduced from the occurence of detected optical transients that would be unrelated to the GW event and observed by chance in the field. The contaminant transients that are able to pass the light-curve cut include some rapid variable Cepheid stars and Active Galactic Nuclei.

4 Concluding remarks

The present paper reports on the first EM follow-up program to GW candidates performed by the LIGO/Virgo collaborations together with partner observatories. This follow-up program is a milestone toward the advanced detector era. With a ten-fold improvement of sensitivity[19], the number of detectable sources increases by a factor of 10^3. It is likely that advanced detectors will make the first direct detection of GWs. The observation of an EM counterpart may be a crucial ingredient in deciding the astrophysical nature of the first event.

References

1. B. P. Abbott *et al.*, *Reports on Progress in Physics* **72**, 076901 (2009)
2. F. Acernese *et al.*, *Classical and Quantum Gravity* **25**, 184001 (2008)
3. J. Abadie *et al.*, *Astrophys. J* **715**, 1438 (2010)
4. B. D. Metzger *et al.*, *MNRAS* **406**, 2650 (2010)
5. T. Vachaspati, *Phys. Rev. Lett.* **101**, 141301 (2008)
6. J. Abadie *et al.*, *Phys. Rev.* D **81**, 102001 (2010)
7. A. C. Searle *et al*, *Classical and Quantum Gravity* **26**, 155017 (2009)
8. D. Buskulic for the LVC, *Classical and Quantum Gravity* **27**, 194013 (2010)
9. The LSC and Virgo Collaboration, "Implementation and testing of the first prompt search for electromagnetic counterparts to gravitational wave transients" (in preparation).
10. S. Fairhurst, *Classical and Quantum Gravity* **28**, 105021 (2011)
11. J. Abadie *et al.*, arxiv:1003.2481
12. J. Kanner *et al.*, *Classical and Quantum Gravity* **25**, 184034 (2008)
13. D. J. White, E. J. Daw & V. S. Dhillon, *Classical and Quantum Gravity* **28**, 085016 (2011)
14. L. K. Nuttall & P. J. Sutton, *Phys. Rev.* D **82**, 102002 (2010)
15. A. Klotz *et al.*, *PASP* **120**, 1298 (2008)
16. D. M. Coward *et al.*,*PASA* **27**, 331 (2010)
17. E. Bertin & S. Arnouts, *Astronomy & Astrophysics Supplement* **117**, 393 (1996)
18. M. Richmond `http://spiff.rit.edu/match`
19. J. Abadie *et al.*, *Classical and Quantum Gravity* **27**, 173001 (2010)

Searching for gravitational waves associated with gamma-ray bursts using the LIGO/Virgo network

M. Was, for the LIGO Scientific Collaboration and the Virgo Collaboration
LAL, Univ Paris-Sud, CNRS/IN2P3, Orsay, France.

Gamma-ray bursts are among the most violent events observed in the universe; their progenitors could also emit copious amounts of gravitational waves. We discuss the astrophysical motivations and prospects of searching for gravitational waves associated with gamma ray bursts in data collected in 2009-2010 by the LIGO and Virgo network of gravitational wave detectors.

Gamma-ray bursts (GRBs) are among the most violent events observed in the universe. The energy released by the progenitors into γ-rays is estimated to be of the order of $10^{-3}\,\mathrm{M}_{\odot}\mathrm{c}^2$, and this energy is released in a matter of seconds. The duration of the γ-ray emission is characterized by T_{90}, the time length over which the 5^{th} to 95^{th} percentile of the total photon count in the $\sim 15 - 300\,\mathrm{keV}$ energy range is collected by a γ-ray satellite. The distribution of the duration has a bimodal structure, and GRBs are observationally classified by their duration into short GRBs ($T_{90} < 2\,\mathrm{s}$) and long GRBs ($T_{90} > 2\,\mathrm{s}$). However, one should note that there is no clear cut separation between the two families at the 2 s duration threshold [1].

The most popular model for explaining GRBs is the beamed emission by a relativistic jet. For long GRBs the progenitor is thought to be the core collapse of a massive rapidly spinning star, which in extreme cases might form a black hole or a magnetar and launch the relativistic jet along the rotation axis. For short GRBs the central engine which launches the jet is thought to be the coalescence of a neutron star with either another neutron star or a black hole. In both cases the central engine could emit copious amounts of gravitational waves.

When analyzing data from gravitational wave detectors such as LIGO [2] and Virgo [3] a crucial question for improving the search is what are the expectations on the sought signal. In particular for the case of searching for gravitational waves emitted by GRB progenitors, the questions to answer are what are the expected signal time of arrival with regard to the GRB, and what waveform and polarization of the potential gravitational wave is expected. We look at these two questions in the next sections.

1 Gravitational wave emission and polarization

In this section we discuss the expectations one should have for the gravitational waves potentially associated with a GRB observation. We separate the discussion for the case of the compact binary coalescence model (short GRBs) and the extreme stellar collapse model (long GRBs).

1.1 Compact binary coalescence

The gravitational waves emitted by the inspiral of a neutron star and another compact object is well understood, and precise waveforms can be derived using the post-newtonian expansion formalism [4]. The gravitational wave emission at the time of the merger and afterwards is not well known, among others due to the uncertainty in the neutron star equation of state. However for current gravitational wave detectors only the inspiral part is of importance, as the merger and post-merger GW emission is at higher frequencies resulting in a much smaller signal to noise ratio. The inspiral gravitational wave signal enters the sensitive band of current detectors at most 50 s before the merger.

A GRB observation means that the opening angle θ_j of the relativistic jet includes the observer, hence the rotation axis of the binary has an inclination angle that is smaller than θ_j. The opening angle for short GRBs is estimated to be typically [5,6] $\theta_j \sim 10° - 50°$. For orbital inclination angles smaller than 60° the emitted gravitational waves are approximately circularly polarized, with an amplitude discrepancy between the "plus" and "cross" polarizations of at most 20%.

1.2 Extreme stellar collapse

The collapse of a star is notoriously difficult to model or simulate, moreover the GRB progenitors models corresponds to extreme cases of stellar collapse with very rapid rotation, which requires full 3D modelling. Hence the gravitational wave emission for long GRBs is poorly known.

Many possible emission channels have been proposed. A first family comes from numerical simulations of the stellar collapse, which are by necessity simplified in some aspects (micro-physics, number of dimensions, ...). These numerical simulation predict gravitational emission [7] of at most $\sim 10^{-8}\,M_\odot c^2$, which if compared to the most sensitive point in the current detectors spectrum correspond to a detection range [8] of $\sim$ 10 kpc. Hence these models are not relevant for the detection of gravitational waves from extra-galactic progenitors.

A second class of models come from analytical estimation of extreme scenarios. These models predict an energy radiated in gravitational waves of up to $10^{-2}\,M_\odot c^2$ and correspond to various rotational instability scenarios. For (proto)-neutron star central engines these could be bar mode instabilities [9], or fragmentation of the neutron star [10]. For central engines consisting of a black hole with dense accretion disk the instabilities could involve disk fragmentation [11] or disk precession [12]. A common aspect of these extreme models is that emission is coming from a rotating quadrupole mass moment. Given that for long GRBs the typical jet opening angles are estimated [6,13] to be $\theta_j \sim 5° - 10°$, the gravitational emission associated with long GRBs in these models is expected to be circularly polarized.

2 Gravitational wave - GRB coincidence

The expected time of arrival between gravitational waves and GRBs is also crucial. Obtaining a small coincidence window while keeping all the plausible emission scenarios allows to reduce the background without losing any sensitivity, when searching for gravitational waves associated with a GRB.

2.1 Compact binary coalescence

For the compact binary coalescence a central engine composed of a black hole surrounded by a dense disk should be formed on a viscous time scale and launch a jet in less than 1 s after the merger [14]. In the standard fireball internal shock model [1] the expected delay between the jet launch and the γ-ray emission is of the order of the GRB variability time scale, which is shorter than the duration ≤ 2 s of the short GRB. Hence the merger time should be within $[-3 - T_{90}, 0]$ s of the GRB trigger time, and the inspiral gravitational wave emission spread within $[-53 - T_{90}, 0]$ s of the GRB trigger time.

2.2 Extreme stellar collapse

For the stellar collapse scenario several models have been proposed for the central engine and have not been ruled out by observations [15]: type I and type II collapsars [16] and the millisecond magnetar model [17]. Each of these models has difficulties with explaining some of the observed GRB properties and the actual picture of GRB progenitors remains unclear. In particular the predictions on the timing of the different parts of the GRB progenitor emissions are not precise, we will mention here only the most extreme contribution that would cause a large time delay between the time of arrival of GWs and γ-rays.

The type II collapsar model has the largest time span with a two step central engine [16]. The star collapses first to a proto neutron star, which forms a black hole through fall back accretion up to 100 s later. Gravitational wave and γ-ray emission might be produced at either of these two stages. The propagation of the jet through the stellar envelope at sub-relativistic speed may take as long as 100 s. After break-out the jet accelerates to relativistic speed. In the standard fireball model with internal shocks the γ-ray emission is delayed by the GRB variability time scale compared to the jet break-out, that is at most 100 s later. In the Poynting flux dominated jet of the electromagnetic model [18], the GRB is emitted with a similar delay. In total, in the most extreme cases the gravitational wave emission may happen up to several hundred seconds before the GRB trigger, and at the latest throughout the γ-ray emission.

3 Analysis

This astrophysical models discussion has consequences on how gravitational wave data analysis is performed. For the compact binary coalescence model of short GRBs the waveform is well known, hence a template based search is performed for binary systems of total mass between 2 and 40 $M_{\odot}$. For gravitational wave candidates the recovered merger time should coincide with a short GRB trigger time within a $[-5, 1]$ s window to account for the astrophysical delay and detection timing uncertainty. Such a search has been performed previously using LIGO-Virgo data from 2005-2007 [19], and is currently being finalized for the 2009-2010 data set. On the 2005-2007 data set a typical exclusion distance of ~ 7 Mpc for neutron star - black hole system was obtained [19]. This exclusion was performed without assuming any orientation for the binary system, but that assumption will be used for the 2009-2010 data set. Overall an improvement of a factor ~ 2 in the exclusion distance is expected for this new data set.

For the extreme stellar collapse models, the only reliable astrophysical input is that a detectable gravitational wave should be circularly polarized. This polarization constraint is now used with a coincidence window of $[-600, \max(60, T_{90})]$ s to search for gravitational waves associated with both long and short GRBs. The results of the analysis of the 2009-2010 data set are currently being finalized. For the previous data set, the circular polarization assumption was not used and a shorter coincidence window was used [20]. Expanding the coincidence window allows to fully include all possible gravitational wave emission models, whereas using the circular polarization assumption one can constructs powerful noise rejection tests. For circularly polarized signals at the optimal frequency the lack of detection in the 2005-2007 data put a typical exclusion distance of ~ 12 Mpc assuming that an energy of $10^{-2}\,M_{\odot}c^2$ is carried by the gravitational wave [20]. For the latest data set a slight improvement in these exclusion distances is expected, unless a gravitational wave is found.

The two approaches (template vs. unmodelled) are complementary as one is tailored for one particular well understood model for which it is more sensitive, whereas the second is broad scope and includes most available models of joint gravitational wave and GRB emission.

Acknowledgments

The authors gratefully acknowledge the support of the United States National Science Foundation for the construction and operation of the LIGO Laboratory, the Science and Technology Facilities Council of the United Kingdom, the Max-Planck-Society, and the State of Niedersachsen/Germany for support of the construction and operation of the GEO600 detector, and the Italian Istituto Nazionale di Fisica Nucleare and the French Centre National de la Recherche Scientifique for the construction and operation of the Virgo detector. The authors also gratefully acknowledge the support of the research by these agencies and by the Australian Research Council, the International Science Linkages program of the Commonwealth of Australia, the Council of Scientific and Industrial Research of India, the Istituto Nazionale di Fisica Nucleare of Italy, the Spanish Ministerio de Educación y Ciencia, the Conselleria d'Economia Hisenda i Innovació of the Govern de les Illes Balears, the Foundation for Fundamental Research on Matter supported by the Netherlands Organisation for Scientific Research, the Polish Ministry of Science and Higher Education, the FOCUS Programme of Foundation for Polish Science, the Royal Society, the Scottish Funding Council, the Scottish Universities Physics Alliance, The National Aeronautics and Space Administration, the Carnegie Trust, the Leverhulme Trust, the David and Lucile Packard Foundation, the Research Corporation, and the Alfred P. Sloan Foundation.

References

1. G. Vedrenne and J.-L. Atteia. *Gamma-Ray Bursts.* Springer (2009).
2. B. P. Abbott *et al. Rep. Prog. Phys.* **72**, 076901 (2009).
3. F. Acernese *et al. Class. Quantum Grav.* **25**, 184001 (2008).
4. L. Blanchet. *Living Rev. Relativity* **9**, 4 (2006).
5. Gao. Y. and Dai. Z. *Res. Astron. Astrophys.* **10**, 142 (2010).
6. A. Goldstein *et al.* arxiv:1101.2458 (2011).
7. C. D. Ott. *Class. Quantum Grav.* **26**(6), 063001 (2009).
8. J. Abadie *et al. Phys. Rev. D* **81**, 102001 (2010).
9. M. Shibata, K. Shigeyuki, and E. Yoshiharu. *Mon. Not. R. Astron. Soc.* **343**, 619 (2003).
10. M. B. Davies, A. King, S. Rosswog, and G. Wynn. *Astrophys. J. Lett.* **579**, L63 (2002).
11. A. L. Prio and E. Pfahl. *Astrophys. J.* **658**, 1173 (2007).
12. G. E. Romero, M. M. Reynoso, and H. R. Christiansen. *Astron. Astrophys.* **524**, A4 (2010).
13. J. L. Racusin *et al. Astrophys. J.* **698**, 43 (2009).
14. E. Rantsiou, S. Kobayashi, P. Laguna, and F. A. Rasio. *Astrophys. J.* **680**, 1326 (2008).
15. S. E. Woosley and J. S. Bloom. *Annu. Rev. Astron. Astrophys.* **44**, 507 (2006).
16. A. I. MacFadyen, S. E. Woosley, and A. Heger. *Astrophys. J.* **550**, 410 (2001).
17. B. D. Metzger *et al. Mon. Not. R. Astron. Soc.* **413**, 2031 (2011).
18. M. Lyutikov. *New J. Phys.* **8**, 119 (2006).
19. B. P. Abbott *et al. Astrophys. J* **715**, 1453 (2010).
20. B. P. Abbott *et al. Astrophys. J.* **715**, 1438 (2010).

Toward an optimal strategy for detecting coincident optical and gravitational wave signals from neutron star mergers

D.M. Coward and E.J. Howell
School of Physics, University of Western Australia.
Crawley WA 6009, Australia

A pan-spectral approach to gravitational wave detection is one of the most prioritized goals in the gravitational wave community. Observations of an optical source coincident with gravitational wave emission detected from a binary neutron star merger will improve the confidence of detection, provide host galaxy localisation, and test models for the progenitors of short gamma ray bursts. We employ optical observations of three short gamma ray bursts, GRB050724, GRB050709, GRB051221, to estimate the detection rate of a coordinated optical and gravitational wave search for neutron star mergers. We use the sensitivity limits of two robotic telescopes, TAROT (m=18) and Zadko (m=21) that have participated in the optical follow-up of LIGO/Virgo triggers in 2010. For a broad distribution of short gamma ray burst beaming angles the optimal strategy for identifying the optical emissions is a combination of rapid response triggered searches followed by deep imaging at late times if an afterglow is not detected within several days of the trigger.

1 Introduction

The search for gravitational waves is entering a new era. Combining an optical search with coincident gravitational wave (GW) observatory data is one of the most prioritized search techniques in the gravitational wave community. It allows gravitational wave candidates that are too weak to claim detection based on gravitational wave data alone to be associated with an optical signal that could provide strong confirmation. In principle a joint electromagnetic-gravitational wave search for binary neutron star mergers (NS-NS) reduces the gravitational wave amplitude detection threshold by a factor of about 1.5.

One expected EM counterpart of a NS-NS merger is a short gamma ray burst (SGRB). The favoured model for SGRBs is a compact object merger triggering an a burst of collimated γ-rays [2] powered by accretion onto the newly formed compact object. The outflow is eventually decelerated by interaction with interstellar matter to produce a fading x-ray and optical afterglow. After Γ decreases to $\Gamma \sim \theta_j^{-1}$, where θ_j is the jet opening half angle, the radiation beam is wider than the outflow, so the afterglow becomes observable from angles greater than θ_j.

Because the coalescing binary NSs are expected to radiate GWs in the sensitivity band of Advanced LIGO/Virgo, coincident GW-EM observations of SGRBs will determine if the engine is a NS-NS or NS-BH binary merger. Furthermore, the rates of EM and coincident GW detections could constrain the distribution of jet collimation angles of SGRBs, crucial for understanding energetics. This is possible because the binary inclination angle to the line of sight is a GW observable[a]. A direct consequence of collimation is that the rate of (both long and short) GRB afterglows should be higher than those observed as prompt bursts (see Coward et al. (2011)[1] for a more detailed description of this effect on coincidence detection rates).

1.1 *SGRB observations*

In order to constrain the detection rate, we require localisation (including redshift), beaming angles and the optical flux values for our sample of bursts. We use three SGRBs that have estimates for these parameters: namely GRB 050709, GRB 050724, and GRB 051221A.

GRB 050709: From comparison of X-ray and optical data, a jet break is present in the optical at about 10 days after the burst[3]. On the other hand,[4] claimed that the light curves were not displaying such a break. We note however that they excluded one optical data point within their fit, arguing it was coincident with a late X-ray flare. However, the data point they excluded was 9.8 days after the burst, compared to 16 days for the X-ray flare. We assume the explanation of Fox et al. (2005), noting that the detection of the jet-break is supported by only one data point.
GRB 050724: From radio and near infrared data,[5,6] claimed evidence of a jet break about 1 day after the burst. The X-ray light curve is consistent with no jet break up to 22 days after the event.
GRB 051221A: The detection of the jet break was observed in X-ray only[7]. A jet-break is clearly visible in the light curve at about 5 days post-burst.

2 Coincident detection rates

To estimate the optical flux of a SGRB as the EM counterpart of a NS-NS coalescence, we use the plausible estimates of[8] for the Advanced LIGO/Virgo sensitivity distances and detection rates of NS-NS coalescences. Taking a rate density of NS-NS coalescences $\sim 10^{-6}\,\mathrm{Mpc}^{-3}\mathrm{yr}^{-1}$ and $D_{\mathrm{H}} = 445\,\mathrm{Mpc}$, they find $D_s \approx 200$ Mpc and a detection rate $R_{\mathrm{det}} \sim 40\ \mathrm{yr}^{-1}$. This rate could potentially be increased by considering the improved signal to noise ratio for a coincident GW and optical search. The estimated increase in signal to noise ratio is about 1.5, assuming a narrow coincidence window, but the optical afterglows may not be imaged until hours after the GW trigger. Nonetheless, the afterglows should be relatively bright at the distances we are considering so it is possible that light curves could be extracted and extrapolated to earlier times. Hence, we assume the sensitivity distance increases by a factor of 1.5, to 300 Mpc, so that $R_{\mathrm{det}} \sim 135\ \mathrm{yr}^{-1}$.

Table 1 shows the derived parameters, including $\theta_{\mathrm{j}}^{\circ}$ using the observed jet break times andextrapolated R-band magnitudes at 1 hr post burst at 300 Mpc. We point out that the optical data used in the references to derive the beaming angle and break times is uncertain, and we do not account for optical bumps and flares that can be significant, especially at early times. Nonetheless, it is clear from Table 1 that if one of the well localised SGRBs occurred

[a]In practice, for sources not associated with host galaxies, the inclination angle has a strong degeneracy with distance, particularly for angles less than 45°.

Table 1: The main observed and derived parameters of GRB 050724, GRB 050709 and GRB 051221. Magnitudes are converted from flux (Jy) to the AB magnitude system using m_{AB} = -2.5 log(F) + 8.9 at a source distance of 300 Mpc.

GRB	log E_{iso}	z	R-mag (1 hr)	t_j (d)	θ_j^o
050724	50.21	0.26	12.7	< 22	25
050709	49.06	0.16	17.2	10	14
051221	50.95	0.55	13.7	5	7

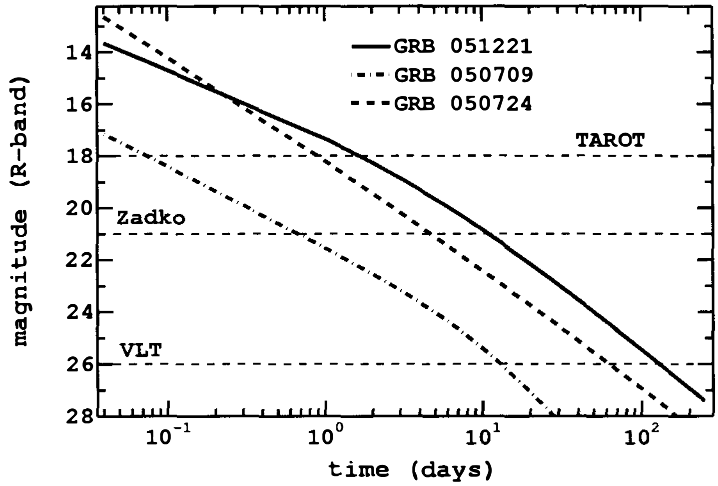

Figure 1: Three model light curves for GRB 050724, GRB 050709 and GRB 051221 extrapolated to a source distance of 300 Mpc, the horizon limit for the Advanced LIGO/Virgo detector network. The beaming angles and break times for the model bursts are (25°. 22d), (14°, 10d), (7°, 5d) respectively. Power law indices before and after the breaks are $(-1.5, -2)$, $(-1.25. -2.83)$ and $(-1, -2)$ respectively. The horizontal dashed lines from bottom to top are the approximate sensitivities for an (8-10)m class telescope, Zadko Telescope (1m) and TAROT (0.25m) respectively.

within D_s, and was on-axis, it would be bright at early times and easily detected by modest aperture telescopes.

3 Results and discussion

Using the light curve characteristics for GRB 050724, GRB 050709 and GRB 051221, we extrapolate the light curves beyond the jet-break times to constrain detection limits, rates and cadence times using the sensitivities of TAROT, Zadko and an $(8-10)$m class telescope. Figure 1 shows the temporal evolution of the three $R-band$ light curves at a source distance of 300 Mpc, and published values for the decay indices. The three curves are quite different, GRB 050724 and GRB 051221, are relatively bright at early times, and can be seen from days to some tens of days by meter class telescopes.

The figure also shows the maximum time, $t_{\max}$, that the telescopes could detect the SGRB afterglows. This sets the limit on the cadence times for imaging. GRB 051221 has the brightest afterglow and is potentially detectable the longest time; $t_{\max} \sim$ 11d for Zadko. Given that the GW error ellipse is of order degrees in size, identification of a transient is more feasible for this afterglow type. Unfortunately, they occur at a rate of 1 yr^{-1}, and given optical selection effects may be missed altogether. GRB 050724 like events, occurring at an optimistic rate of 13 yr^{-1}, would be detectable up to 5d by Zadko. This would allow time for surveying degree size fields and multiple telescopes at different longitudes to perform follow-up imaging. Coward et al. (2011)[1], extends this work to show that SGRB afterglows could be observed off-axis at late times by telescopes sensitive to $m = 21 - 26$.

The first attempts for a triggered search of the optical counterparts of NS-NS coalescences using GW detectors are just commencing. There are many uncertainties and issues that will need careful consideration for these types of searches. Firstly, our results show that the coincident detection rate depends critically on the beaming angle distribution. For nearly isotropic optical emission, similar to GRB 050724, the coincident rates are very promising and will improve the confidence of the GW detection and provide much needed localisation.

Another important issue for the joint searches is the large errors in the GW source localisation, which can extend to some tens of degrees. To address this, the GW triggered search strategy may use the estimated horizon distance of the detector network to reduce the number of potential host galaxies, as opposed to a 'blind' error box that extends to cosmological distances. Another problem that manifests with large coincidence error boxes is the increasing chance of detecting false coincident optical transients. False coincident sources may include supernovae, flare stars, variable active galactic nuclei and even Earth orbiting space debris. Fortunately, some of these sources can be excluded in the analysis because of the sensitivity distance of GW searches and the expectation that the strongest GW sources will be associated with catalogued host galaxies.

The science pay-off for joint optical and GW observations is enormous and provides motivation to address the issues discussed here in more detail. Now is the time to determine the optimal strategies for optical follow-up in readiness for the more sensitive GW searches in the following years. To accomplish this will require a more comprehensive understanding of optical selection effects, the false alarm rate expected from SGRBs within the error ellipses of GW networks, and techniques to improve the localisation of the host galaxy.

Acknowledgments

D. M. Coward is supported by an Australian Research Council Future Fellowship. He thanks the organisers of the 2011 Rencontres de Moriond for providing a rich and stimulating environment.

References

1. D.M. Coward *et al*, *MNRAS* , Accepted 2011 April 22 (arXiv:1104.5552)
2. D. Eichler *et al*, *Nature* **340**, 126 (1989)
3. Fox *et al*, *Nature* **437**, 845 (2005)
4. Watson *et al*, *Astronomy and Astrophysics* **454**, L123 (2006)
5. A. Panaitescu, *MNRAS* **367**, L42 (2006)
6. E. Berger *et al.Nature* **438**, 988 (2005)
7. A.M., Soderberg *et al*, ApJ **650**, 261 (2006)
8. J. Abadie *et al*, *Classical and Quantum Gravity* **27**, 173001 (2010)

3.
Sources of Gravitational Waves

Toward Computing the Gravitational Wave Signatures of Core Collapse Supernovae

Anthony Mezzacappa[1,2], Konstantin N Yakunin[3], Pedro Marronetti[3], Stephen W Bruenn[3], Ching-Tsai Lee[2], M Austin Chertkow[2], W Raphael Hix[1,2], John M Blondin[4], Eric J Lentz[1,2], O E Bronson Messer[5]

[1] *Physics Division, Oak Ridge National Laboratory, Oak Ridge, TN 37831-6354*

[2] *Department of Physics and Astronomy, University of Tennessee, Knoxville, TN 37996-1200*

[3] *Physics Department, Florida Atlantic University, Boca Raton, FL 33431-0991*

[4] *Department of Physics, North Carolina State University, Raleigh, NC 27695-8202*

[5] *National Center for Computational Sciences, Oak Ridge National Laboratory, Oak Ridge, TN 37831-6161*

We present the gravitational wave signatures of three non-parameterized core collapse supernova explosion models for 12, 15, and 25 $M_\odot$ non-rotating progenitors. The signatures exhibit four distinct stages. The third stage, induced by mass accretion onto the proto-neutron star owing to neutrino-driven convection and the SASI, dominates. The total gravitational wave energy emitted rises quickly as the SASI develops at $\sim$ 200 ms after bounce in all three models and levels off as explosion develops and the convection- and SASI-induced mass accretion powering the explosions and gravitational wave emission decreases. We decompose the gravitational wave signatures spectrally and show that the signal is within AdvLIGO's bandpass for a Galactic event. The fundamental limitation of the current models and their associated predictions is the restriction to axisymmetry. Counterpart three-dimensional models are forthcoming.

1 Introduction

Recent advances in multidimensional core collapse supernova modeling and the promise of a gravitational wave detection by AdvLIGO [1] for a Galactic event engender an optimism that core collapse supernovae will be much better understood in the near future, that more detailed predictions of their gravitational wave emission will therefore be possible in that time frame, and that, consequently, a Galactic core collapse supernova event will both be identifiable in gravitational waves and used to probe the extreme environments present at the center of such explosions.

Colgate and White [2] were the first to propose that core collapse supernovae could be neutrino driven and performed the first numerical simulations of these events. More recently, the discovery by Wilson [3] of the delayed revival of the core collapse supernova shock wave by neutrino heating provided the framework for contemporary core collapse supernova theory—the majority of models performed in the last two decades are centered around this phenomenon (for a review, see Mezzacappa [4] and Janka et al. [5]).

Core collapse supernovae are spatially three-dimensional events involving turbulent magnetohydrodynamics in interaction with an intense flux of neutrinos and antineutrinos emanating from the proto-neutron star, of all three flavors. The neutrinos behave in a fluid-like manner only in the deepest regions of the core. A multidimensional kinetic description in phase space, which encompasses the three dimensions of space and the three dimensions of momentum space required to uniquely specify a neutrino's location, direction of propagation, and energy, is required more generally. In addition, the thermodynamic state on which the magnetohydrodynamics rests is described by a complex nuclear, leptonic, and photonic equation of state (EOS), and the neutrino–matter interactions are commensurately complex and difficult to model with realism. Thus, core collapse supernova models have evolved in sophistication and dimensionality painstakingly. However, the rate of progress has certainly increased, particularly with the introduction of two- and three-dimensional models.

The first target of core collapse supernova theory is arguably the explosion mechanism. Without first-principles predictions of explosion, it is certainly difficult to discuss core collapse supernova gravitational wave emissions quantitatively. Fortunately, a consensus is emerging based on the results of ongoing two-dimensional models that neutrinos aided by the recently discovered core collapse supernova standing accretion shock instability (SASI)[6] can power such explosions (see Bruenn et al. [7], Marek and Janka[8], and Suwa et al. [9]). Components of the gravitational wave signatures of core collapse supernovae are associated with various explosion epochs: (1) stellar core collapse and bounce, (2) the prompt convection epoch, (3) the development of other proto-neutron star instabilities and neutrino-driven convection, (4) SASI development and the development of the large-scale flows the SASI induces, and (5) explosion.

The underlying theory of gravitational wave emission by core collapse supernovae has been developed over the past two decades by various groups (see the references cited here; for a comprehensive review, see Ott [10]). Based on this foundation, recent work by Yakunin et al. [11] provided the first view of the gravitational wave signatures for all epochs of gravitational wave emission mentioned above, based on first-principles non-parameterized models, albeit in the context of two dimensional models. Their results are discussed here.

2 Underlying Formalism

The transverse-tracefree part (TT) of the gravitational strain can be written as

$$h_{ij}^{TT} = \frac{1}{r} \sum_{m=-2}^{m=2} \left(\frac{d}{dt}\right)^2 I_{2m} \left(t - \frac{r}{c}\right) f_{ij}^{2m}, \tag{1}$$

where the mass quadrupole (as a function of retarded time) is computed by

$$I_{2m} = \frac{16\pi G}{5c^4} \sqrt{3} \int \tau_{00} Y_{2m}^{*} r^2 dV. \tag{2}$$

τ_{00} is the corresponding component of the linearized stress-energy tensor, and $f^{2m}(\theta, \phi)$ are the spherical harmonics. In the weak-field case, we approximate $\tau_{00} \simeq \rho$, where ρ is the rest-mass density. Following Finn and Evans[12] to reduce the second time derivative $A_{2m} \equiv \frac{d^2}{dt^2} I_{2m} = \frac{d}{dt} N_{2m}$ and using the continuity equation as in Blanchet et al. [13], we calculate N_{2m} as in Equation (34) in Finn and Evans[12]. In axisymmetric cases, N_{20} is the only non-null component, and we evaluate its time derivative numerically. The wave amplitude is related to the dimensionless gravitational strain, h_+, by

$$h_+ = \frac{1}{8} \sqrt{\frac{15}{\pi}} \sin^2 \theta \frac{A_{20}}{r}, \tag{3}$$

where r is the distance to the source and θ is the angle between the symmetry axis and the observer's line of sight. (We will assume $\sin^2 \theta = 1$.) To compute the gravitational waves produced by anisotropic axisymmetric neutrino emission, we use the formalism of Epstein[14] and Müller & Janka[15]:

$$h_\nu^{TT} = \frac{4G}{c^4 r} \int_0^t dt' \int_0^\pi d\theta' \ \Psi(\theta') \frac{dL(\theta', t')}{d\Omega'}, \tag{4}$$

with $\Psi(\theta)$ given in Kotake et al. [16]. The direction-dependent differential neutrino luminosity, $dL/d\Omega$, is calculated at the outermost radial grid zone. In order to determine the detectability of the gravitational waves, we calculate the characteristic gravitational wave strain for a given frequency f using [17]

$$h_c\left(f\right) = \frac{1}{r}\sqrt{\frac{2}{\pi^2}\,\frac{G}{c^3}\,\frac{dE_{GW}\left(f\right)}{df}}\frac{dE_{GW}\left(f\right)}{df} = \frac{c^3}{G}\,\frac{\left(2\pi f\right)^2}{16\pi}\left|\tilde{A}_{20}\left(f\right)\right|^2, \tag{5}$$

with

$$\frac{dE_{GW}\left(f\right)}{df} = \frac{c^3}{G}\,\frac{\left(2\pi f\right)^2}{16\pi}\left|\tilde{A}_{20}\left(f\right)\right|^2, \tag{6}$$

where $dE_{GW}\left(f\right)/df$ is the gravitational-wave energy spectrum and $\tilde{A}_{20}\left(f\right)$ is the Fourier transform of $A_{20}\left(t\right)$.

3 Our Code

CHIMERA contains five primary modules: hydrodynamics, neutrino transport, self-gravity, a nuclear equation of state, and a nuclear reaction network (see Bruenn et al. [7] for details). The hydrodynamics is evolved via a Godunov finite-volume scheme—specifically, a Lagrangian remap implementation of the piecewise parabolic method [18]. Neutrino transport along our radial rays is computed by means of multigroup flux-limited diffusion (in the "ray-by-ray-plus" approximation [19]), with a flux limiter that has been tuned to reproduce Boltzmann transport results to within a few percent [20]. A spectral Poisson solver is used to determine the gravitational field [21], with general relativistic corrections to the spherical component [22]. The Lattimer–Swesty (LS) EOS [23] is used for matter in NSE above 1.7×10^8 g/cm^3. (The runs documented here assumed a bulk compressibility of 180 MeV.) Below this density, matter in NSE is described by 4 species (neutrons, protons, helium, and a representative heavy nucleus) in a corrected and improved version of the Cooperstein EOS [24], extended to regions where the composition is determined externally by a reaction network. Continuity with the LS-EOS is achieved by use of a common electron–positron EOS (a revised and extended version of that in Cooperstein [24]) and establishment of a common zero for the mass energy. For regions not in NSE, an EOS with a nuclear component consisting of 14 α-particle nuclei from ^{4}He to ^{60}Zn, protons, neutrons, and an iron-like nucleus is used. An electron–positron EOS with arbitrary degeneracy and degree of relativity spans the entire density–temperature regime of interest. The nuclear composition in the non-NSE regions of these models is evolved by the thermonuclear reaction network of Hix and Thielemann [25]. Finally, a complete weak interaction set is used in the neutrino transport evolution, including neutrino–antineutrino pair emission from nucleon–nucleon bremsstrahlung and angle and energy exchange from scattering on electrons and nucleons (see Bruenn et al. [7] for a complete list).

The history of field variables for a given parcel of material, crucial for nucleosynthesis, is lost for Eulerian hydrodynamics schemes, such as the one deployed in CHIMERA. To compensate for this, and to allow post-processed nuclear network computations, the tracer (or test) particle method [26] has been implemented. The tracer particles are equally distributed on the spherical grid (40 particles/row x 125 rows) at the pre-collapse phase and follow the flow in the course of the Eulerian simulation, recording their temperature and density history by interpolating the corresponding quantities from the underlying Eulerian grid [26]. Each particle is assigned a constant mass (1/5000 of the progenitor mass) and the gravitational wave signal it produces is calculated taking the quadrupole integral. Comparing the gravitational wave signal corresponding to a given group of tracers with the signal produced by the bulk matter motion allows us to identify what part of the fluid generates a specific gravitational wave feature.

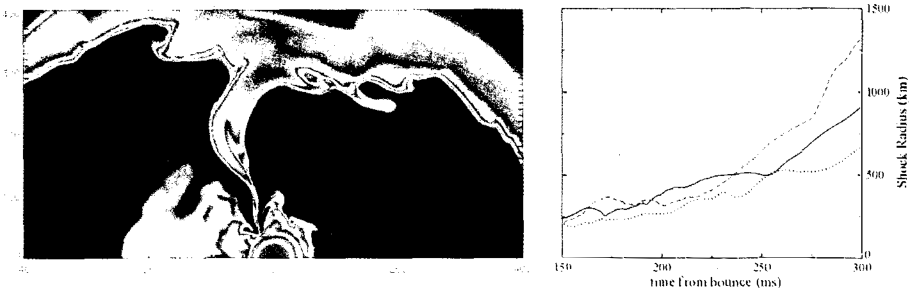

Figure 1: *Left:* Entropy distribution at 244 ms after bounce in our 15 $M_\odot$ model. A large, low-entropy (blue-green) accretion funnel at an angle quasi-orthognal to the symmetry axis and high-entropy (yellow-orange-red) outflows below the shock, along the symmetry axis, are evident. *Right:* Shock radius as a function of time for three regions: the north pole (solid blue), the equatorial plane (dotted black), and the south pole (dashed red).

4 Gravitational Wave Predictions

We performed three axisymmetric two-dimensional core collapse supernova simulations, beginning with 12, 15, and 25 $M_\odot$ non-rotating progenitors [27]. Successful explosions were obtained in all three cases. (Details are provided in Bruenn et al. [7].)

A clear gravitational wave signature, in four parts (left column of Figure 2), emerges: (1) A prompt signal, which is an initial and relatively weak signal that starts at bounce and ends at between 50 and 75 ms post-bounce. (2) A quiescent stage that immediately follows the prompt signal and ends somewhere between 125 ms and 175 ms after bounce. (3) A strong signal, which follows the quiescent stage and is the most energetic part of the gravitational wave signal. This stage ends somewhere between 350 ms and 450 ms after bounce. (4) A tail, which starts before the end of the strong signal at about 300 ms after bounce and consists of a slow increase in rh_+.

Computations of the gravitational waveforms covering the first three of four phases (prior to explosion) based on non-parameterized models have also been reported by Marek et al. [28], and waveforms covering all four phases and based on parameterized explosions were reported by Murphy et al. [29].

The prompt signal arises from two phenomena: Prompt convection inside the proto-neutron star generates a high-frequency signal that is superimposed on a lower-frequency component. The low-frequency signal from 20 ms to 60 ms after bounce originates at the shock radius, which is at $\sim$100 km at this time and well outside the proto-neutron star. The separation of these two components is clearly seen in the inset of Figure 3.

The quiescent stage corresponds to the period after prompt convection has ceased and before neutrino-driven convection and the SASI have developed. It is followed by a strong signal. The strong signal arises from neutrino-driven-convection- and SASI-induced funnels impinging on the proto-neutron star surface (see Figure 1) and has two components (also described in Marek et al. [28]): The low-frequency component arises from the modulations in the shock radius as the SASI develops and evolves. The high-frequency component is generated when the neutrino-driven-convection- and SASI-induced accretion flows strike the proto-neutron star. The shock modulations affect the kinetic energy of the accretion flows and, consequently, the amplitude of the gravitational waves generated when these flows hit the surface. Hence the high-frequency modulations are beneath a low-frequency envelope.

All of our gravitational wave signals end with a slowly increasing tail, which reflects the gravitational memory associated with accelerations at the prolate outgoing shock (see also Murphy et al. [29]).

Looking at h_{char} (Figure 2 right), the peak at $\sim 700-800$ Hz is associated with the high-frequency component of rh_+, which in turn is associated with the accretion downflows hitting

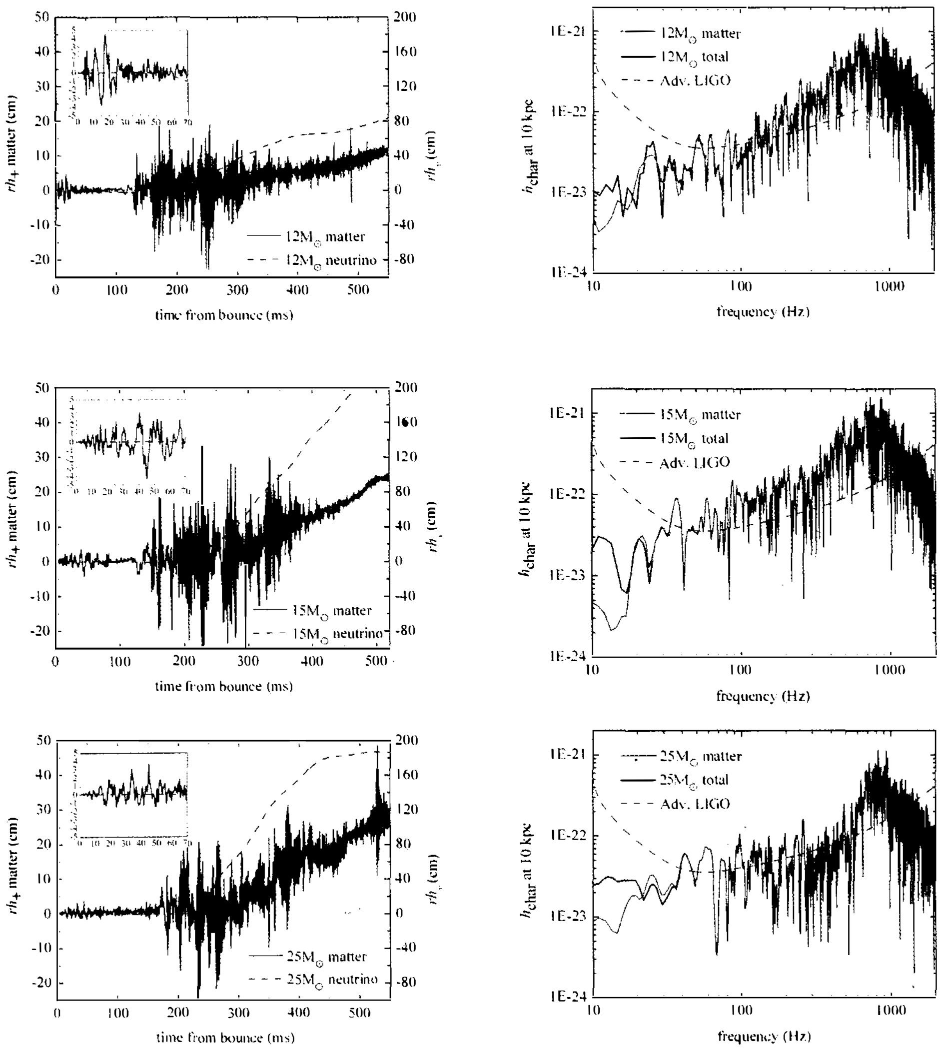

Figure 2: The left column shows the gravitational wave strain times the distance to the observer versus post-bounce time for non-rotating progenitors of 12, 15, and 25 $M_{\odot}$. The signal is split into matter- (red-solid) and neutrino-generated (blue-dashed) signals. Note that the scales are different for these two signals. The insets show the first 70 ms after bounce. The right column shows the corresponding characteristic strain for both the matter (red) and the total (black) signals, compared to the AdvLIGO sensitivity curve.

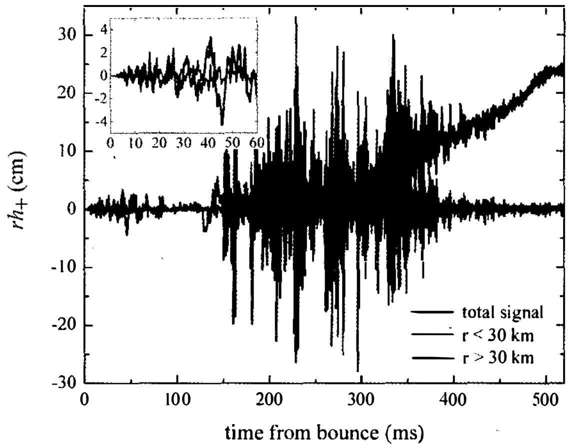

Figure 3: Contributions to the matter-generated gravitational wave signal from two different regions in our 15 $M_\odot$ model: the proto-neutron star ($r < 30$ km) and the region above the proto-neutron star ($r > 30$km). The latter includes the region of neutrino-driven convection, the SASI, and the shock.

the proto-neutron star surface, as discussed above. A precise association of the signal at lower frequencies with phenomena in the post-bounce dynamics will require a detailed analysis using tracer particles and will be left to a subsequent paper. The lower-frequency modulations (the envelope) in rh_+, which in turn are associated with the SASI-induced shock modulations, will certainly be an important component of this lower frequency signal (see Marek et al. [28]).

The amplitudes of the gravitational waves from neutrino emission are negative from bounce to $\sim 180 - 220$ ms after bounce and then increase dramatically, becoming positive throughout the end of the simulation. The positive sign is consistent with a relative dominance of neutrino emission along the poles [16]. The change in sign from negative to positive correlates with the formation of the funnel-like downflows of dense matter, which increase neutrino opacities in the equatorial plane (orthogonal to the symmetry axis; see Figure 1). Note that the amplitude of the neutrino-generated gravitational wave signal is much larger than the matter-generated gravitational wave signal. However, these gravitational waves have relatively low frequencies, and their contribution to the total characteristic strain is only significant at frequencies below 20 Hz (see also [15,16,30,31]).

The total emitted gravitational wave energy in our models is shown in Figure 4. In all three cases, the energy rises quickly at $\sim$ 200 ms after bounce, consistent with the development of the SASI and the initial SASI-induced increase in shock radius (see Figure 1). The rate of increase of emitted energy decreases considerably as explosion develops and the accretion powering the explosions and gravitational wave emission in our models decreases.

5 Shortcomings and Next Steps

While approximations have been made in important components of our models (e.g., the use of ray-by-ray versus multidimensional neutrino transport), the imposition of axisymmetry is the most significant shortcoming. The simulations delineated here, and their associated gravitational wave predictions, must be reconsidered in three spatial dimensions. A hint as to how

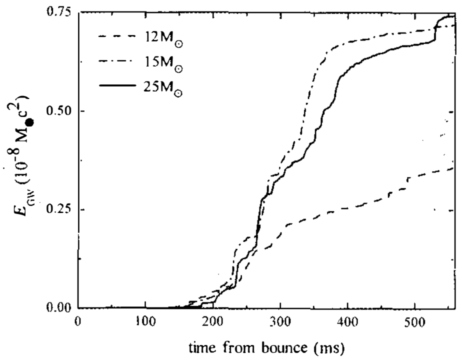

Figure 4: Energy emitted by gravitational waves during the first 500 ms after bounce for all three models.

the extension to three dimensions may impact the results shown here can be obtained by considering, comparatively, the two- and three-dimensional SASI simulations of Blondin et al. [6,32] In two dimensions, with axisymmetry imposed, the dominant SASI mode is the $l = 1$ mode and explosions occur preferentially along the symmetry axis, leading to prolate explosions. The linearly increasing and positive memory exhibited in all of the gravitational wave signatures discussed here, a consequence of the prolate nature of our explosions, is a consequence of the axisymmetry imposed in our models. In three spatial dimensions, the SASI is more complex, with both $l = 1$ and $m = 1$ modes present, leading in turn to less prolate explosions. Thus, at the very least, we should expect the DC offset reported here to be grossly affected as we move to three spatial dimensions. The gravitational wave phase prior to the DC offset would also likely be affected in a significant way given this phase is strongly correlated with the development of neutrino-driven convection and the SASI, with a higher-frequency component resulting from convection- and SASI-induced accretion funnels impinging on the proto-neutron star and a lower-frequency component associated with the SASI modulation of the shock wave itself. The difference between the development of convection and the SASI in two and three spatial dimensions will likely affect both the low- and high-frequency components quantitatively. This has been studied recently by Kotake et al. [31].

In addition to the imposition of axisymmetry, we also have not yet considered nonrotating progenitors and, consequently, our predictions for stellar core bounce gravitational wave signatures are surely underestimated, although we do not expect these signatures to dominate the signatures highlighted here. Moreover, current stellar evolution theory does not predict rapid rotation for massive stars [33].

Nonetheless, the simulations outlined here mark a distinct step forward toward the goal of making detailed predictions of the gravitational wave emission of core collapse supernovae. Three-dimensional simulations using CHIMERA are ongoing, and the gravitational wave predictions of these runs await report in a future publication.

Acknowledgments

The authors would like to acknowledge computational resources provided by the Oak Ridge Leadership Computing Facility in ORNL's National Center for Computational Sciences, made available through the Department of Energy (DOE) Office of Advanced Scientific Computing Research's (OASCR) INCITE Program, and computational resources made available at the Texas Advanced Computing Center and the National Institute for Computational Sciences, through the NSF TeraGrid (TG-MCA08X010). AM and WRH acknowledge support from the DOE Office of Nuclear Physics, and AM and OEBM acknowledge support from DOE OASCR.

AM, OEBM, PM, SWB, and WRH acknowledge support from NASA ATFP (07-ATFP07-0011). PM acknowledges support from NSF-PHYS-0855315, and PM and SWB acknowledge support from NSF-OCI-0749204.

References

1. http://www.ligo.caltech.edu/advLIGO
2. Colgate, S A and White, R H 1966 *Astrophys. J.* **143** 626
3. Wilson J R 1985, in *Numerical Astrophysics*, eds. Centrella, J M, LeBlanc, J M, and Bowers, R L, Jones and Bartlett, Boston, 422
4. Mezzacappa A 2005 *Ann. Rev. Nucl. Part. Sci.* **55** 467
5. Janka H-T, Langanke, K, Marek, A, Martinez-Pinedo G, and Müller B 2007 *Phys. Rep.* **442** 38
6. Blondin J M, Mezzacappa A, and DeMarino C 2003 *Astrophys. J.* **584** 971
7. Bruenn S W, Mezzacappa A, Hix W R, Blondin J M, Marronetti P, Messer O E B, Dirk C and Yoshida S 2009 *Journ. Phys. Conf. Ser.* **180** 012018
8. Marek A and Janka, H-T 2009 *Astrophys. J.* **694** 664
9. Suwa Y, Kotake, K, Takiwaki, T, Whitehouse, S C, Liebendörfer, M, and Sato K 2010 *PASJ* **62** L49
10. Ott C 2009 *Class. Quant. Grav.* **26** 063001
11. Yakunin K N, Marronetti P, Mezzacappa A, Bruenn S W, Lee C-T, Chertkow M A, Hix W R, Blondin J M, Lentz E J, Messer O E B, and Yoshida S 2010 *Class. Quant. Grav.* **27** 194005
12. Finn L S and Evans C R 1990 *Astrophys. J.* **351** 588
13. Blanchet L, Damour T, and Schaefer G 1990 *MNRAS* **242** 289
14. Epstein R 1978 *Astrophys. J.* **223** 1037
15. Müller E and Janka H-T 1997 *Astron. Astrophys.* **317** 140
16. Kotake K, Ohnishi N, and Yamada S 2007 *Astrophys. J.* **655** 406
17. Flanagan E and E Hughes S A 1998 *Phys. Rev.* D **57** 4566
18. Colella P and Woodward P R 1984 *Journ. Comp. Phys.* **54** 174
19. Buras R, Rampp M, Janka H T, and Kifonidis K 2006 *Astron. Astrophys.* **447** 1049
20. Liebendörfer M, Messer O E B, Mezzacappa A, Bruenn S W, Cardall C, and Thielemann F-K 2004 *Astrophys. J. Suppl. Ser.* **150** 263
21. Müller E and Steinmetz M 1995 *Comp. Phys. Comm.* **89** 45
22. Marek A, Dimmelmeier H, Janka H-T, Müller E, and Buras R 2006 *Astron. Astrophys.* **445** 273
23. Lattimer J M and Swesty F D 1991 *Nucl. Phys.* A **535** 331
24. Cooperstein J 1985 *Nucl. Phys.* A **438** 722
25. Hix W R and Thielemann F-K 1999 *Astrophys. J.* **511** 862
26. Lee C-T 2008 The Applications of the Tracer Particle Method to Multi-Dimensional Supernova Simulations *PhD Thesis* The University of Tennessee Knoxville TN USA
27. Woosley S E and Heger A 2007 *Phys. Rep.* **442** 269
28. Marek A, Janka H-T, and E. Müller 2009 *Astron. Astrophys.* **496** 475
29. Murphy J, Ott C, and Burrows A 2009 *Astrophys. J.* **707** 1173
30. Burrows A and Hayes J 1996 *Phys. Rev. Lett.* **76** 352
31. Kotake K, Iwakami W, Ohnishi N, and Yamada S 2009 *Astrophys. J.* **697** 133
32. Blondin J and Mezzacappa A 2007 *Nature* **445** 58
33. Heger A, Fryer C L, Woosley S E, Langer N, and Hartmann D H 2003 *Astrophys. J.* **591** 288

Neutron Stars as Gravitational Wave Sources

Leonardo Gualtieri
Dipartimento di Fisica, "Sapienza" Università di Roma
& Sezione INFN Roma1, P.A. Moro 5, 00185 Roma, Italy

Neutron stars, among the most extreme objects in the universe, are very promising sources for the gravitational wave detectors of the present and next generation. On the other hand, gravitational waves can give us unvaluable information on neutron stars, since we do not know the behaviour of matter in their inner core. Detection of the gravitational emission from neutron stars could teach us something about the nature of hadronic interactions. I discuss some neutron star processes associated to gravitational wave emission, looking at both aspects: whether the neutron star can produce detectable gravitational waves, and whether a gravitational wave detection could tell us something about the neutron star equation of state.

1 Introduction

Neutron stars (NSs) can be considered as the "ground state" of matter: they are the most compact self-graviting stellar objects in nature. Several quantities reach extreme values in NSs:

- The density can reach, at the center, $\rho \sim 10^{15}$ g/cm^3, larger than nuclear density.
- The surface gravitational potential, of the order of $GM/R \sim (0.1 - 0.3)c^2$; therefore, general relativity has to be included to model a NS.
- The rotation rate reaches (in the fastest spinning NSs) $\nu \sim 700$ Hz.
- The magnetic field strength reaches (in "magnetars", i.e. strongly magnetized NSs) $B \sim 10^{15}$ G on the surface, and probably even larger values in the interior.
- The electromagnetic luminosity can reach, in violent events like giant flares, peaks as large as $L_\gamma \sim 10^{47}$ erg/s.

All these features make NSs very promising sources of gravitational waves (GWs). Since most processes involving NSs have characteristic frequencies ranging from some tens of Hz to some kHz, they are relevant sources for ground based interferometers (LIGO, VIRGO)[a], which are sensitive in this range of frequency, in their advanced configurations.

On the other hand, GWs can give us unvaluable information on NSs. We probably know how matter is organized in the crust of a NS (and maybe in the outer core, too), but our understanding of their inner core, where matter reaches supranuclear densities, is very poor. Indeed, in these conditions hadron interactions play a crucial role; neglecting such interactions and considering neutron Fermi pressure only, one would find a NS maximum mass of $\sim 0.7\,M_\odot$,

[a] http://www.virgo.infn.it ; http://www.ligo.caltech.edu

in contrast with the observations of $M \sim (1.2 - 2.0)\, M_{\odot}$. Our lack of knowledge on the NS equation of state (EOS) in the inner core reflects our ignorance on the non-perturbative regime of quantum cromo-dynamics. We do not even know the particle content of the core: Hadrons? Hyperons? Meson condensates? Deconfined quark matter?

Unfortnuately, supranuclear densities cannot be reproduced in the laboratory, and electromagnetic signals do not carry direct information about the physics of NS inner cores; our only hope to have observative data on this extreme regime relies on GWs, which are mainly generated where the star is most dense, and are nearly unaffected by interaction with interstellar matter and energy. For instance, knowing the radius of NSs we would learn a lot about its EOS, but it is very difficult to get a "clean" observation of a NS radius in the electromagnetic spectrum; detection of gravitational waves from NS oscillations, instead, would allow us to estimate the radius, and then to set constraints on the NS EOS (see Sec. 2).

I will discuss some processees involving NS as GWs sources, trying to answer to the following questions: Can detectable GWs be produced? Would a GW detection tell us something about the EOS of NSs? The answer to both questions is potentially affirmative for NS oscillations (discussed in Sec. 2) and coalescences of NS binary systems (discussed in Sec. 3). I will not discuss, instead, NS deformations: even though they are a promising source of GWs, it would be very difficult to infer information on the NS EOS from the gravitational signal they produce.

2 Gravitational wave asteroseismology

When a neutron star is perturbed, it oscillates and (if the oscillations are non-radial and non-dipolar) it emits gravitational waves. The perturbation can be due to a variety of different processes, like glitches, accreting matter or, when the NS is born, the shock originating from the gravitational collapse. These oscillations occur with characteristic frequencies and damping times, which do not depend on the nature of the exciting perturbation, but only on the structure of the NS; they are called quasi-normal modes (QNMs).

Similarly to normal modes of Newtonian stars, QNMs are classified in terms of the main restoring force which brings a displaced element of matter back to equilibrium: we have g-modes if the main restoring force is buoyancy, p-modes if it is pressure; the fundamental mode (f-mode) has an intermediate character between g-modes and p-modes. Typically, NS g-modes have frequencies of some hundreds of Hz; the f-mode of $1 - 2$ kHz; and p-modes of a few kHz. Furthermore, there are pure space-time modes, the w-modes, with higher frequencies; r-modes, associated with the stellar rotation; and other classes of modes associated to the magnetic field and to the elastic properties of the crust.

The detection of the GWs emitted by an oscillating star will allow us to measure the frequencies and damping times of the QNMs, which carry the imprint of the NS EOS. The study of the structure of NSs through the observation of their proper oscillations by gravitational wave detectors, is named *gravitational wave asteroseismology*.

The case of cold, old NSs has been studied in a series of articles in the last decade [1], which have been focussing onto the g, f, p modes of spherically symmetric stars. It was found that a GW detection from a pulsating star would allow to: (i) infer the value of the NS radius, which would strongly constrain the EOS; (ii) discriminate between different possible EOS; (iii) establish whether the emitting source is a NS or a quark star, constraining, in the latter case, the quark star EOS. More recently different kinds of oscillations have been modeled, including more and more physics in the game: the star rotation [2], magnetic fields and elastic properties of the crust [3], superfluidity [4].

Oscillations of hot, young proto-neutron stars (PNSs) are a very interesting source of GWs. Indeed, they are likely to be strongly excited by the processes associated to the gravitational collapse, and they can give information not only on the PNS EOS, but also on the thermodynamical properties, and on the neutrino dynamics, of the PNS. They have been studied in [5,6]. In these works, the first minute after the core bounce is considered, and the evolution is treated as a sequence of quasi-stationary configurations. In [5] the thermodynamical variables and the lepton fraction are determined by solving Boltzmann's equation, and the EOS is obtained within the mean field approximation [7]. In [6], instead, a microscopic EOS is employed, obtained within the Brueckner-Hartree-Fock nuclear many-body approach [8]; Boltzmann's equation is not solved: different entropy and lepton fraction profiles are considered, in order to understand how the QNMs depend on the thermodynamical and composition variables.

By comparing the QNMs of old, cold NS [1] with that of hot, young PNS [5,6], one finds that:

- In cold, old NSs the f-mode has the shortest damping time ($\nu_f \sim 1$ s); thus, it is expected to be the best candidate for QNM detection by gravitational interferometers. Since $\nu_f \sim 1-2$ kHz, it falls in the detector bandwidth ($\sim 100- \sim 1000$ Hz) only marginally. The p- and g-modes are unnlikely to be detected, since p-modes have higher frequencies, and g-modes, when present, have very large gravitational damping times, and are then damped by other dissipative mechanisms, like viscosity and heat transport.

- The frequency of the g-mode in a hot, young PNS carries information on the entropy profile of the star: higher frequencies correspond to larger entropy gradients.

- In hot, young PNSs the f-mode has lower frequency (which is better for GW detection) than in older and colder NSs, but its damping time is larger (which is worst for GW detection). It is not clear which of the two effects prevails.

- In the first seconds of the PNS life, g-mode excitation is a promising source of GWs. Indeed, its damping time is comparable with the damping time of the f-mode. These damping times, of the order of seconds, are smaller than the dissipation timescale associated to non-gravitational processes (like viscosity, heat transport, neutrino diffusion, etc.). More generally, when the PNS is very hot the lowest order g- f- and p-modes cluster, acquiring similar frequencies and damping times.

In order to make solid statements about the QNMs of PNS, further studies are required, to include in the model the cooling of the star and its rotation. We remark that including rotation should yield lower values of the frequencies and the damping times of the QNMs [2], i.e. a more likely detection of the GW signal.

3 Gravitational waves from neutron stars in binaries

The coalescence of binary systems with neutron stars (NS-NS and black hole (BH)-NS binaries) is one of the most promising GW sources for advanced LIGO/VIRGO. Recent studies have shown that the gravitational signal from these processes can carry the imprint of the NS EOS.

In the latest stage of a BH-NS coalescence, the neutron star is disrupted by the BH tidal field. If this occurs when the NS has not yet reached the innermost circular orbit about the BH, it forms an accretion torus; otherwise, it directly plunges in the BH horizon. In the former case, the gravitational signal is characterized by a cut-off frequency ν_c, corresponding to the stellar disruption [9,10]. The presence of this cut-off, and its value, strongly depends on the NS EOS; its observation would give us valuable information about the behaviour of matter in the NS core.

This problem has been studied both in the framework of numerical relativity (numerical integration of Einstein's equations coupled with hydrodynamical equations) [11] and using semi-analytical approaches [10,12]. As shown in [10], if we know the mass and angular momentum of the black hole, and measure the cut-off frequency ν_c, it would be possible to estimate the NS radius with an error of few percent, thus discriminating between different possible equations of state.

In NS-NS binaries, the signature of the EOS is expected to be even stronger. As shown in [13]. even in the early inspiral phase the stars are significantly affected by tidal deformation. The post-Newtonian analysis of [13] shows that it is possible to extract from the GW signal the tidal deformability λ, which measures the stellar quadrupole deformation in response to the perturbing tidal field of the companion. This parameter strongly depends on the features of the NS EOS. The dependence of the merger phase on the EOS has been studied in [14], using the techniques of numerical relativity; the outcome of the merger (a black hole, or a hypermassive neutron star) crucially depends on the equation of state of the coalescing NSs.

The detection of GWs from NSs will then be of utmost importance, not only to understand the behaviour of astronomical objects, but also to have a deeper insight on the behaviour of matter at supranuclear densities, shedding light on the nature of hadronic interactions.

Acknowledgements

I thank V. Ferrari for useful suggestions. This work was supported by CompStar, a Research Networking Programme of the European Science Foundation.

References

1. N. Andersson, K.D. Kokkotas, *Mon. Not. Roy. Astron. Soc.* **299**, 1059 (1998); K.D. Kokkotas, T.A. Apostolatos, N. Andersson, *Mon. Not. Roy. Astron. Soc.* **320**, 307 (2001); O. Benhar, V. Ferrari, L. Gualtieri, *Phys. Rev.* D **70**, 124015 (2004); O. Benhar, V. Ferrari, L. Gualtieri, S. Marassi, *Gen. Rel. Grav.* **39**, 1323 (2007).
2. H. Dimmelmeier, N. Stergioulas, J.A. Font, *Mon. Not. Roy. Astron. Soc.* **368**, 1609 (2006); A. Passamonti, A. Stavridis, K.D. Kokkotas, *Phys. Rev.* D **77**, 024029 (2008); E. Gaertig, K.D. Kokkotas, *Phys. Rev.* D **78**, 064003 (2008); *ibid.* **80**, 064026 (2009); *ibid.* **83**, 064031 (2011); A. Passamonti, B. Haskell, N. Andersson, D.I. Jones, I. Hawke, *Mon. Not. Roy. Astron. Soc.* **394**, 730 (2009); B. Zink, O. Korobkin, E. Schnetter, N. Stergioulas, *Phys. Rev.* D **81**, 084055 (2010).
3. H. Sotani, K.D. Kokkotas, N. Stergoiulas, *Mon. Not. Roy. Astron. Soc.* **385**, L5 (2008); A. Colaiuda, H. Beyer, K.D. Kokkotas, *Mon. Not. Roy. Astron. Soc.* **396**, 1441 (2009); A. Colaiuda, K.D. Kokkotas, *Mon. Not. Roy. Astron. Soc.* (2011), DOI: 10.1111/j.1365-2966.2011.18602.x; M. Gabler, P. Cerda Duran, J.A. Font, E. Müller, N. Stergioulas *Mon. Not. Roy. Astron. Soc.* **410**, L37 (2011).
4. N. Andersson, K. Glampedakis, L. Samuelsson, *Mon. Not. Roy. Astron. Soc.* **396**, 894 (2009); N. Andersson, B. Haskell, N. Andersson, *Mon. Not. Roy. Astron. Soc.* **396**, 951 (2009); A. Passamonti, N. Andersson, *Mon. Not. Roy. Astron. Soc.* **413**, 47 (2011).
5. V. Ferrari, G. Miniutti, J.A. Pons, *Mon. Not. Roy. Astron. Soc.* **342**, 629 (2003).
6. G.F. Burgio, V. Ferrari, L. Gualtieri, H.-J. Schultze, *in preparation.*
7. J.A. Pons, S. Reddy, M. Prakash, J.M. Lattimer, J.A. Miralles, *Astrophys. J.* **513**, 780 (1999).
8. G.F. Burgio, H.-J. Schultze, *Astron. & Astrophys.* **518**, A17 (2010).
9. M. Vallisneri, *Phys. Rev. Lett.* **84**, 3519 (2000).
10. V. Ferrari, L. Gualtieri, F. Pannarale, *Phys. Rev.* D **81**, 064026 (2010).
11. M. Shibata, K. Kyutoku, T. Yamamoto, K. Taniguchi, *Phys. Rev.* D **79**, 044030 (2009); Z.B. Etienne, Y.T. Liu, S.L. Shapiro, T.W. Baumgarte, *Phys. Rev.* D **79**, 044024 (2009).
12. F. Pannarale, A. Tonita, L. Rezzolla, *Astrophys. J.* **727**, 1 (2011); V. Ferrari, L. Gualtieri, A. Maselli, *in preparation.*
13. T. Hinderer, B.D. Lackey, R.N. Lang, J.S. Read *Phys. Rev.* D **81**, 123016 (2010).
14. K. Hotokezaka, K. Kyutoku, H. Okawa, M. Shibata, K. Kiuki, arXiv:1105.4370.

General Relativistic Magnetohydrodynamic Simulations of Binary Neutron Star Mergers

Bruno Giacomazzo

Department of Astronomy, University of Maryland, College Park, Maryland, USA
Gravitational Astrophysics Laboratory, NASA Goddard Space Flight Center, Greenbelt, Maryland, USA

Luciano Rezzolla

Max-Planck-Institut für Gravitationsphysik, Albert-Einstein-Institut, Potsdam Germany
Department of Physics and Astronomy, Louisiana State University, Baton Rouge, Louisiana, USA

Luca Baiotti

Institute of Laser Engineering, Osaka University, Osaka, Japan

We report on our recent general-relativistic simulations of magnetized, equal-mass neutron-star binaries and on the role that realistic magnetic fields may have in the evolution of these systems. In particular, we study the evolution of the magnetic fields and show that they can influence the survival of the hypermassive neutron star produced at the merger by accelerating its collapse to a black hole. We also show how the magnetic field can be amplified and that this can lead to the production of the relativistic jets observed in short gamma-ray bursts.

1 Introduction

The numerical investigation in full general relativity (GR) of the merger of binary neutron stars (BNSs) has produced a series of new and interesting results in the last years.[1] Thanks to several numerical improvements, it has been indeed possible to start to investigate the full dynamics of these systems including the formation of tori around rapidly rotating black holes (BHs)[2,3,4,5] which could not be modeled via Newtonian simulations. This progress has allowed the beginning of an accurate investigation of whether BNS mergers could indeed be behind the central engine of short γ-ray bursts (GRBs).[6,7,8] Fully GR simulations have shown that the end result of BNS mergers is the formation of a rapidly spinning BH surrounded by a hot torus. Driven by neutrino processes and magnetic fields, such a compact system may be capable of launching a relativistic fireball with an energy of $\sim 10^{48}$ erg on a timescale of $0.1 - 1$ s.[9] Moreover, BNSs are also one of the most powerful sources of gravitational waves (GWs) that will be detected in the next few years by advanced LIGO and advanced Virgo.[10] GR simulations of BNSs have then started to provide accurate templates that can be used to infer properties of the NSs composing the binaries, such as the equation of state (EOS) of NSs, once their GWs will be detected.[11] Here we review some of the main results we published recently[5,8] and that describe the merger of magnetized equal-mass BNSs. We will show how magnetic fields can affect the dynamics of these systems and their role in powering short GRBs.

Table 1: Properties of the eight equal-mass binaries considered: baryon mass M_b of each star; total ADM mass $M_{\rm ADM}$; initial orbital angular velocity Ω_0; mean coordinate radius r_e along the line connecting the two stars; maximum initial magnetic field B_0, where $*$ is 8, 10 or 12.

Binary	M_b ($M_\odot$)	$M_{\rm ADM}$ ($M_\odot$)	Ω_0 (rad/ms)	r_e (km)	B_0 (G)
`M1.45-B*`	1.445	2.680	1.78	15.0 ± 0.3	0 or $1.97 \times 10^*$
`M1.62-B*`	1.625	2.981	1.85	13.6 ± 0.3	0 or $1.97 \times 10^*$

2 Numerical and Physical Setup

All the details of the mathematical and numerical setup used for producing the results presented here are discussed in depth in our previous publications [5,8] and here we limit ourselves to a brief overview.

We have used the general relativistic magnetohydrodynamic (GRMHD) `Whisky` code [12,13,14], which solves the equations of GRMHD on dynamical curved backgrounds. In particular `Whisky` makes use of the `Cactus` framework which provides the evolution of the Einstein equations for the metric expressed in the BSSN formulation. [15] The GRMHD equations are solved using high resolution shock capturing schemes and in particular by using the Piecewise Parabolic Method (PPM), [16] and the Harten-Lax-van Leer-Einfeldt (HLLE) approximate Riemann solver [17] to compute the fluxes. In order to guarantee the divergence-free character of the MHD equations we have employed the flux-CD approach, [18] but with one substantial difference, namely, that we use as an evolution variable the vector potential instead of the magnetic field. [5] The system of GRMHD equations is closed by an EOS and we have employed the commonly used "ideal-fluid" EOS, in which the pressure p is expressed as $p = \rho\epsilon(\Gamma - 1)$, where ρ is the rest-mass density, ϵ is the specific internal energy and Γ is the adiabatic exponent.

Both the Einstein and the GRMHD equations are solved using the vertex-centered AMR approach provided by the `Carpet` driver. [19] The results presented below refer to simulations performed using 6 levels of mesh refinement with the finest level having a resolution of $h = 0.1500\,M_\odot \simeq 221\,\mathrm{m}$ and covering each of the two NSs, while the coarsest grid extends up to $r = 254.4\,M_\odot \simeq 375.7\,\mathrm{km}$ and has a resolution of $h = 4.8\,M_\odot \simeq 7.1\,\mathrm{km}$. For all the simulations reported here we have used a reflection-symmetry condition across the $z = 0$ plane and a π-symmetry condition across the $x = 0$ plane.[a]

Finally, the initial data [2,20] were produced by Taniguchi and Gourgoulhon [21] with the multi-domain spectral-method code `LORENE`. [b] Since no self-consistent solution is available for magnetized binaries yet, a poloidal magnetic field is added a-posteriori and it is initially confined inside each of the NSs. [20,5] The main properties of the initial data are listed in Table 1 and we have considered two classes of binaries differing in the initial masses, *i.e.*, binaries `M1.45-B*`, and binaries `M1.62-B*`. For each of these classes we have considered four different magnetizations (indicated by the asterisk) so that, for instance, `M1.62-B12` is a high-mass binary with a maximum initial magnetic field $B_0 = 1.97 \times 10^{12}$ G.

3 Results

In order to highlight some of the most salient aspects of the binary dynamics we will focus on the high-mass models `M1.62-B*` since they describe all the aspects of a typical BNS merger. The main difference with the low-mass models `1.45-B*` is that the latter will collapse to a BH on a

[a]Stated differently, we evolve only the region $\{x \geq 0,\ z \geq 0\}$ applying a 180°-rotational-symmetry boundary condition across the plane at $x = 0$.

[b]http://www.lorene.obspm.fr

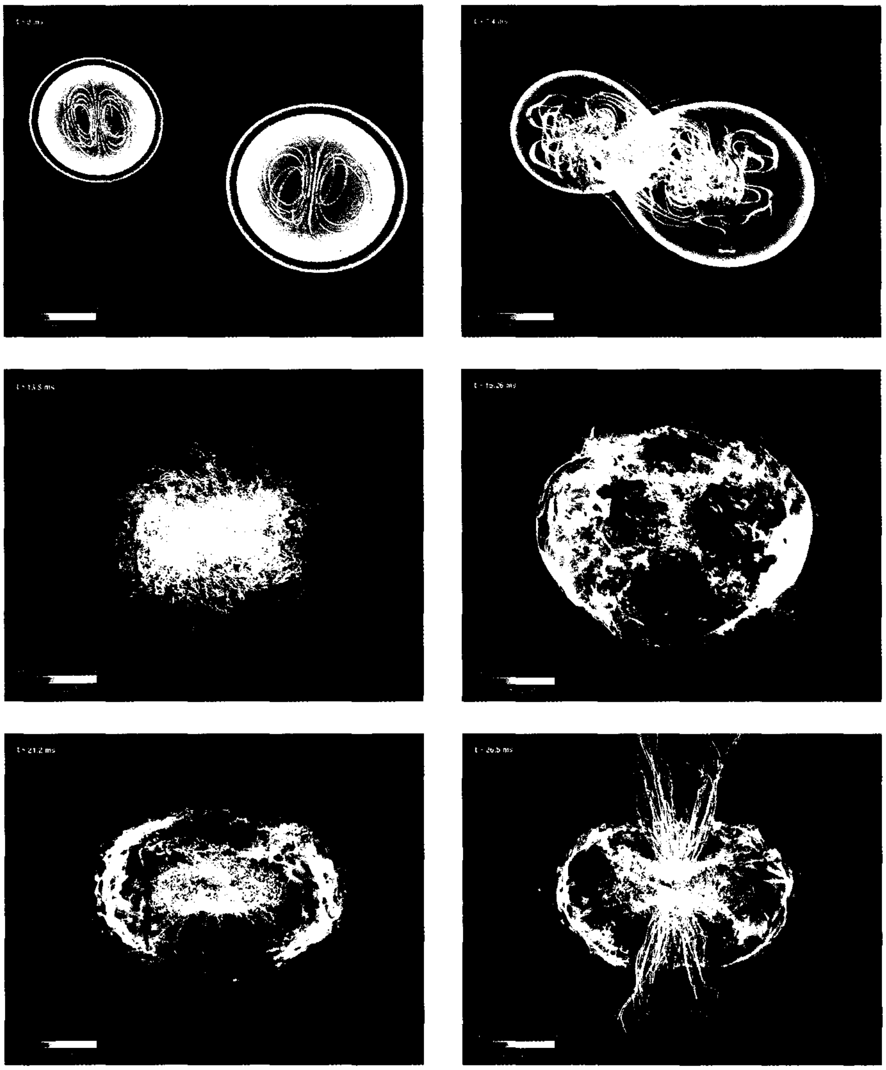

Figure 1: Snapshots at representative times of the evolution of the high-mass binary with initial maximum magnetic field of 10^{12} G, *i.e.*, M1.62-B12. The first panel shows the initial condition, the second one the moment of the merger and the third one the HMNS formed after it. The rest-mass density is visualized using volume rendering (colors from red to yellow) while the white lines are the magnetic field lines inside the stars. The last three panels show instead the evolution of the torus after the collapse of the HMNS to BH (white sphere at the center). In these last three panels the white lines are the magnetic field lines in the region close to the spin axis of the BH and the green lines are the magnetic field lines in the torus. Figure published in Rezzolla et al 2011.

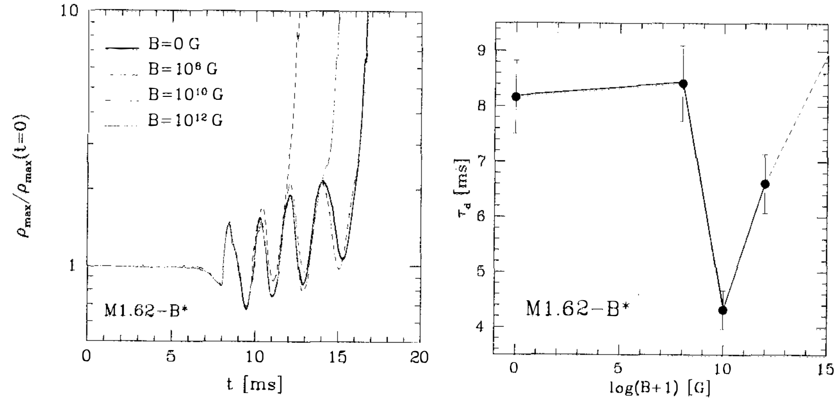

Figure 2: *Left Panel*: Evolution of the maximum of the rest-mass density ρ normalized to its initial value for the high-mass models. *Right panel*: Lifetime of the HMNS formed after the merger in the high-mass case as a function of the initial magnetic field. The error bar has been estimated from a set of simulations of unmagnetized binary NS mergers at three different resolutions; in particular, we have assumed that the magnetized runs have the same relative error on the delay time of the corresponding unmagnetized model. Indicated with a dashed line is the continuation of the delay times to ultra-high magnetic fields of 10^{17} G. Figure published in Giacomazzo et al 2011.

much longer timescale [4] and, because of the much higher computational cost, we have followed those models only for $\approx$ 10ms after the merger and hence before their collapse to BH.

A synthetic overview of the dynamics is summarized in Fig. 1, which shows snapshots at representative times of the evolution of the high-mass binary with an initial maximum magnetic field of 10^{12} G, *i.e.*, M1.62-B12. The rest-mass density ρ is visualized using volume rendering with colors from red to yellow, while the white lines represent the magnetic field lines. The first panel shows the initial conditions with the two NSs having a purely poloidal field contained inside each star. The second panel shows the time when the two NSs enter into contact ($t \approx 7$ms) and when the Kelvin-Helmholtz instability starts to curl the magnetic field lines producing a strong toroidal component. [20,5] The third panel shows the HMNS formed after the merger, while the three last panels show the evolution of the formed BH and of the torus surrounding it. In the last three panel the green lines refer to the magnetic field in the torus and the white ones to the field lines near the spin axis of the BH. We will comment on these three last panels later in this section.

All the high-mass models studied here form tori with masses between $\approx 0.03 M_\odot$ (model M1.62-B10) and $\approx 0.09 M_\odot$ (model M1.62-B8) which are sufficiently massive to be able to power a short GRB. The mass and spin of the BH formed from the merger of all the high-mass models are respectively $M_{BH} \approx 2.9 M_\odot$ and $J_{BH}/M_{BH}^2 \approx 0.8$. As mentioned before, we did not evolve the low-mass models until collapse to BH, but our previous studies [4] have shown that such models can form tori of similar or even larger masses.

An important effect of the magnetic field is that by redistributing the angular momentum inside the HMNS it can accelerate its collapse to BH. [5] While magnetic fields as low as $\sim 10^8$ G are too low to affect the dynamics, magnetic fields $\sim 10^{10}$ G or larger can instead shorten the life of the HMNS. This is shown in Fig. 2 where in the left panel we show the evolution of the maximum of the rest-mass density ρ normalized to its initial value for all the high-mass models. The first minimum in the evolution of the maximum of ρ corresponds to the time of the merger of the two NS cores. The HMNS that is subsequently formed oscillates for few ms before collapsing

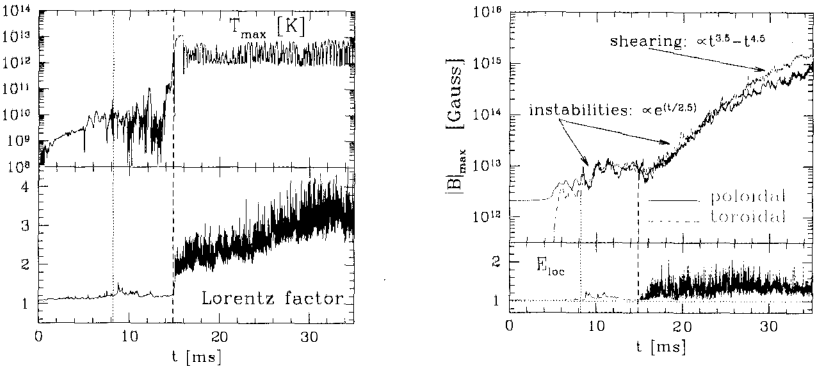

Figure 3: *Left panel:* Evolution of the maximum of the temperature T (top) and of the maximum of the Lorentz factor (bottom). The two vertical dotted and dashed lines represent respectively the time of the merger and of the collapse to BH. *Right panel:* Evolution of the maximum of the magnetic field in its poloidal (red solid line) and toroidal (blue dashed line) components. The bottom panel shows the maximum local fluid energy indicating that an unbound outflow (*i.e.*, $E_{loc} > 1$) develops and is sustained after BH formation. All the panels refer to the high-mass model `M1.62-B12`. Figure published in Rezzolla et al 2011.

to a BH which happens when the maximum of ρ grows exponentially. As one can see from this figure the evolution of ρ in the case with a magnetic field $\sim 10^8$ G (blue dot-dashed line) is almost identical to the unmagnetized case (solid black line). The models with higher values of the magnetic field instead collapse much earlier (magenta long-dashed line, model `M1.62-B12` and red short-dashed line, model `M1.62-B10`). In the right panel of Fig. 2 we plot instead the lifetime of the HMNS formed after the merger of the high-mass models as a function of the initial magnetic field. The fact that this curve exhibits a minimum should not come as a surprise. As said before low magnetic fields do not change the lifetime τ_d and so the curve is expected to be flat for low magnetic fields, *i.e.*, smaller than $\sim 10^8$ G. Stronger magnetic fields, *i.e.*, larger than $\sim 10^{16}$ G, will instead increase the total pressure in the HMNS and extend its lifetime.[20] Intermediate field values instead do not sufficiently contribute to the the total pressure in the HMNS, but are still sufficient to redistribute its angular momentum and accelerate its collapse to BH. From this figure it is also clear that if we were able to determine the lifetime of the HMNS (by measuring for example the delay between the merger and the collapse to BH in the GW signal), we would then be able to infer approximatively the strength of the magnetic field.

3.1 Jet formation

By continuing the evolution of the high-mass model `M1.62-B12` far beyond BH formation we were also able to show for the first time that BNS mergers can generate the jet-like structures that are behind the emission of short GRBs.[8] In particular the last three panels of Fig. 1 show the evolution of the rest-mass density and magnetic field lines in the torus and around the BH formed after the collapse of the HMNS. In these panels the white lines are the magnetic field lines in the region close to the spin axis of the BH and the green lines are the magnetic field lines in the torus. It is evident that after the formation of the BH, the magnetic field lines change from the "chaotic" structure they had in the HMNS (third panel in Fig. 1) to a more ordered structure with a mainly toroidal field in the torus (green lines) and a mainly poloidal field along the spin-axis of the BH (white lines). It has been already shown in the past that such a configuration can launch the relativistic jets that are thought to be behind the short GRBs,[22] but it is the first time that it has been shown that such configuration is the natural result of the

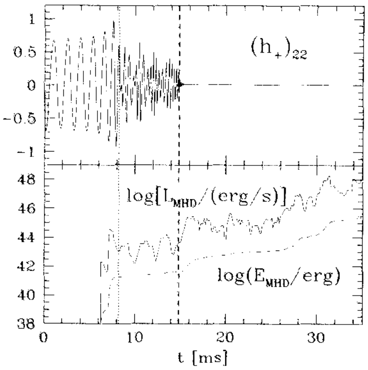

Figure 4: the GW signal shown through the $\ell = 2, m = 2$ mode of the + polarization, $(h_+)_{22}$, (top part) and the MHD luminosity, $L_{\rm MHD}$, (bottom part) as computed from the integrated Poynting flux and shown with a solid line for the high-mass model M1.62-B12. The corresponding energy, $E_{\rm MHD}$, is shown with a dashed line. The dotted and dashed vertical lines show the times of merger (as deduced from the first peak in the evolution of the GW amplitude) and BH formation, respectively. Figure published in Rezzolla et al 2011.

merger of magnetized BNSs.

The left panel of Fig. 3 shows on the top the evolution of the maximum of the temperature and on the bottom the maximum Lorentz factor. Soon after the merger and because of the shocks produced the temperature grows to $\sim 10^{10}$ K and remains almost constant during the lifetime of the HMNS. During the collapse the temperature increases further and reaches maximum values of $\sim 10^{12}$ K in the torus. Such an high temperature could potentially lead to a strong emission of neutrinos. The maximum Lorentz factor after the collapse to BH is associated to matter outflow along the boundaries of the funnel created by the magnetic field lines. In the bottom-right panel of Fig. 3 we also show the maximum local fluid energy and it highlights that this outflow is unbound (*i.e.*, $E_{\rm loc} > 1$) and persists for the whole duration of the simulation. Even if the Lorentz factor of this outflow is still low compared to the typical values observed in short GRBs, much larger values could be obtained by including the emission of neutrinos or via the activation of mechanism, such as the Blandford-Znajek mechanism [23], which could produce relativistic jets. [22]

A quantitative view of the magnetic-field growth is shown instead in the top-right panel of Fig. 3. which shows the evolution of the maximum values in the poloidal and toroidal components. Note that the latter is negligible small before the merger, reaches equipartition with the poloidal field as a result of a Kelvin-Helmholtz instability triggered by the shearing of the stellar surfaces at merger [20], and finally grows to $\simeq 10^{15}$ G by the end of the simulation. At later times ($t >\sim 22\,$ms), when the instability is suppressed, the further growth of the field is due to the shearing of the field lines and it increases only as a power-law with exponent 3.5 (4.5) for the poloidal (toroidal) component. Although the magnetic-field growth essentially stalls after $t \simeq 35$ ms, further slower growths are possible[24], yielding correspondingly larger Poynting fluxes. Indeed, when the ratio between the magnetic flux across the horizon and the mass accretion rate becomes sufficiently large, a Blandford-Znajek mechanism [23] may be ignited; [22] such conditions are not met over the timescale of our simulations, but could develop over longer timescales.

We have also computed the GW signal emitted by this model as well as an estimate of the electro-magnetic emission. In the top panel of Fig. 4 we show indeed the GW signal, while in the bottom part we plot the evolution of the MHD luminosity, $L_{\rm MHD}$, as computed from the integrated Poynting flux (solid line) and of the corresponding energy, $E_{\rm MHD}$, (dashed line).

Clearly, the MHD emission starts only at the time of merger, it is almost constant and equal to $\approx 10^{44}$ erg/s during the life of the HMNS, and increases exponentially after BH formation, when the GW signal essentially shuts off. Assuming that the quasi-stationary MHD luminosity is $\sim 4\times10^{48}$ erg/s, the total MHD energy released during the lifetime of the torus is $\sim 1.2\times10^{48}$ erg, which, if considering that our jet structure has an opening half-angle of $\sim 30°$, suggests a lower limit to the isotropic equivalent energy in the outflow of $\sim 9 \times 10^{48}$ erg. While this is at the low end of the observed distribution of gamma-ray energies for short GRBs, larger MHD luminosities are expected either through the additional growth of the magnetic field via the on-going winding of the field lines in the disk (the simulation covers only one tenth of $t_{\rm accr}$), or when magnetic reconnection (which cannot take place within our ideal-MHD approach), is also accounted for. Even if we did not follow the entire evolution of the torus, by measuring its accretion rates we estimated that its lifetime would be ≈ 0.3 seconds and consequently in good agreement with the duration of short GRBs.

4 Conclusions

We have reported on some of the main results obtained from the first general relativistic simulations of magnetized BNSs with astrophysically realistic magnetic fields.[5,8] We have shown for the first time how the magnetic fields can impact the evolution of the HMNS formed after the merger and that fields equal or larger than $\sim 10^{10}$ G accelerate its collapse to BH. We have shown that all the systems that collapse to BH form tori sufficiently massive to power short GRBs and that the magnetic field structure around the BH has those characteristics that are necessary in order to launch relativistic jets. A detailed analysis of our results has also shown a good agreement with observations, even if the introduction of more physical ingredients (*e.g.,* neutrino emission and more realistic EOS) will be required in order to increase the accuracy of this model.

Acknowledgments

We thank the developers of `Lorene` for providing us with initial data and those of `Cactus` and `Carpet` for the numerical infrastructures used by `Whisky`. Useful input from M. A. Aloy, J. Granot, I. Hinder, C. Kouveliotou, J. Read, C. Reisswig, E. Schnetter, A. Tonita, A. Vicerè, and S. Yoshida is also acknowledged. We also thank M. Koppitz for assisting us in the production of Fig. 1. The computations were performed on the Damiana Cluster at the AEI, on QueenBee through LONI (`www.loni.org`), and at the Texas Advanced Computing Center through TERAGRID Allocation No. TG-MCA02N014. This work was supported in part by the DFG Grant SFB/Transregio 7, by "CompStar", a Research Networking Programme of the European Science Foundation, by the JSPS Grant-in-Aid for Scientific Research (19-07803), by the MEXT Grant-in-Aid for Young Scientists (22740163) and by NASA Grant No. NNX09AI75G.

References

1. Matthew D. Duez. Numerical relativity confronts compact neutron star binaries: a review and status report. *Class. Quantum Grav.*, 27:114002, 2010.
2. L. Baiotti, B. Giacomazzo, and L. Rezzolla. Accurate evolutions of inspiralling neutron-star binaries: Prompt and delayed collapse to a black hole. *Phys. Rev. D*, 78:084033, 2008.
3. K. Kiuchi, Y. Sekiguchi, M. Shibata, and K. Taniguchi. Exploring Binary-Neutron-Star-Merger Scenario of Short-Gamma-Ray Bursts by Gravitational-Wave Observation. *Phys. Rev. Lett.*, 104:141101, 2010.

4. L. Rezzolla, L. Baiotti, B. Giacomazzo, D. Link, and J. A. Font. Accurate evolutions of unequal-mass neutron-star binaries: properties of the torus and short GRB engines. *Class. Quantum Grav.*, 27:114105, 2010.
5. Bruno Giacomazzo, Luciano Rezzolla, and Luca Baiotti. Accurate evolutions of inspiralling and magnetized neutron stars: Equal-mass binaries. *Phys. Rev. D*, 83:044014, 2011.
6. R. Narayan, B. Paczynski, and Tsvi Piran. Gamma-ray bursts as the death throes of massive binary stars. *Astrophys. J.*, 395:L83, 1992.
7. B. Zhang and P. Meszaros. *Int. J. Mod. Phys. A*, 19:2385, 2004.
8. L. Rezzolla, B. Giacomazzo, L. Baiotti, J. Granot, C. Kouveliotou, and M. A. Aloy. The missing link: Merging neutron stars naturally produce jet-like structures and can power short Gamma-Ray Bursts. *Astrophys. Journ. Lett.*, 732:L6, 2011.
9. Tsvi Piran. The physics of gamma-ray bursts. *Rev. Mod. Phys.*, 76:1143–1210. 2004.
10. K. Belczynski, R. E. Taam, V. Kalogera, F. Rasio, and T. Bulik. On the Rarity of Double Black Hole Binaries: Consequences for Gravitational Wave Detection. *Astrophys. J.*, 662:504, 2007.
11. J. S. Read, C. Markakis, M. Shibata, K. Uryu, J. D. E. Creighton, and J. L. Friedman. Measuring the neutron star equation of state with gravitational wave observations. *Phys. Rev. D*, 79:124033, 2009.
12. Luca Baiotti, Ian Hawke, Pedro Montero, and Luciano Rezzolla. A new three-dimensional general-relativistic hydrodynamics code. In R. Capuzzo-Dolcetta, editor, *Computational Astrophysics in Italy: Methods and Tools*, volume 1, page 210, Trieste, 2003. MSAIt.
13. Luca Baiotti, Ian Hawke, Pedro J. Montero, Frank Löffler, Luciano Rezzolla, Nikolaos Stergioulas, José A. Font, and Ed Seidel. Three-dimensional relativistic simulations of rotating neutron star collapse to a Kerr black hole. *Phys. Rev. D*, 71:024035, 2005.
14. Bruno Giacomazzo and Luciano Rezzolla. WhiskyMHD: a new numerical code for general relativistic magnetohydrodynamics. *Class. Quantum Grav.*, 24:S235, 2007.
15. Denis Pollney, Christian Reisswig, Luciano Rezzolla, Béla Szilágyi, Marcus Ansorg, Barret Deris, Peter Diener, Ernst Nils Dorband, Michael Koppitz, Alessandro Nagar, and Erik Schnetter. Recoil velocities from equal-mass binary black-hole mergers: a systematic investigation of spin-orbit aligned configurations. *Phys. Rev. D*, 76:124002, 2007.
16. P. Colella and P. R. Woodward. *J. Comput. Phys.*, 54:174, 1984.
17. A. Harten, P. D. Lax, and B. van Leer. *SIAM Rev.*, 25:35, 1983.
18. G. Toth. The div b=0 constraint in shock-capturing magnetohydrodynamics codes. *J. Comput. Phys.*, 161:605–652, 2000.
19. Erik Schnetter, Scott H. Hawley, and Ian Hawke. Evolutions in 3D numerical relativity using fixed mesh refinement. *Class. Quantum Grav.*, 21:1465–1488, 2004.
20. B. Giacomazzo, L. Rezzolla, and L. Baiotti. Can magnetic fields be detected during the inspiral of binary neutron stars? *Mon. Not. R. Astron. Soc.*, 399:L164–L168, 2009.
21. K. Taniguchi and E. Gourgoulhon. *Phys. Rev. D*, 66:104019, 2002.
22. S. S. Komissarov and M. V. Barkov. Activation of the Blandford-Znajek mechanism in collapsing stars. *Mon. Not. R. Astron. Soc.*, 397:1153–1168, 2009.
23. R. D. Blandford and R. L. Znajek. Electromagnetic extraction of energy from Kerr black holes. *Mon. Not. R. Astron. Soc.*, 179:433–456, 1977.
24. M. Obergaulinger, P. Cerdá-Durán, E. Müller, and M. A. Aloy. Semi-global simulations of the magneto-rotational instability in core collapse supernovae. *Astronomy and Astrophysics*. 498:241–271, 2009.

THE COALESCENCE RATES OF DOUBLE BLACK HOLES

BELCZYNSKI K.[1,2], BULIK. T.[1], DOMINIK., M.[1], PRESTWICH. A.[3]
[1] *Astronomical Observatory, University of Warsaw, Al. Ujazdowskie 4, 00-478 Warsaw, Poland*
[2] *Center for Gravitational Wave Astronomy, University of Texas at Brownsville, Brownsville, TX 78520, USA*
[3] *Harvard-Smithsonian Center for Astrophysics, Cambridge, MA 02138, USA*

We present the summary of the recent investigations of double black hole binaries in context of their formation and merger rates. In particular we discuss the spectrum of black hole masses. the formation scenarios in the local Universe and the estimates of detection rates for gravitational radiation detectors like LIGO and VIRGO. Our study is based on observed properties of known Galactic and extra-galactic stellar mass black holes and evolutionary predictions. We argue that the binary black holes are the most promising source of gravitational radiation.

1 Population Synthesis Coalescence Rates

We employ the `StarTrack` population synthesis code (Belczynski et al. 2002, 2008) to perform several Monte Carlo simulations of binary evolution with a range of metallicity. We base the calculations on recent results from the Sloan Digital Sky Survey observations (Panter et al. 2008) indicating ($\sim 300,000$ galaxies) that recent star formation (within the last 1 billion years) is bimodal: half the stars form from gas with high amounts of metals (solar metallicity), and the other half form with small contribution of elements heavier than Helium ($\sim 10-30\%$ solar). Additionally, we use the recent estimates of mass loss rates producing much heavier stellar black holes than previously expected ($\sim 30-80$ $M_\odot$; Belczynski et al. 2010a). The results of these calculations were presented for the first time by Belczynski et al. (2010b). We have evolved a population of 2 million massive binary stars, and investigated the formation of close double compact objects: double neutron stars (NS-NS), double black hole binaries (BH-BH), and mixed systems (BH-NS). Our modeling utilizes updated stellar and binary physics, including results from supernova simulations (Fryer & Kalogera 2001) and compact object formation (Timmes et al. 1996), incorporating elaborate mechanisms for treating stellar interactions like mass transfer episodes and tidal synchronization and circularization. We put special emphasis on the common envelope evolution phase, which is crucial for close double compact object formation as the attendant mass transfer allows for efficient hardening of the binary. This orbital contraction can be sufficiently efficient to cause the individual stars in the binary to coalesce and form a single highly rotating object, thereby aborting further binary evolution and preventing the formation of a double compact object. Due to significant radial expansion, stars crossing the Hertzsprung gap (HG) very frequently initiate a common envelope phase. HG stars do not have a clear entropy jump at the core-envelope transition (Ivanova & Taam 2004); if such a star overflows its Roche lobe and initiates a common envelope phase, the inspiral is expected to lead to a coalescence (Taam & Sandquist 2000). In particular, it has been estimated that for a solar

Table 1: Galactic Merger Rates [Myr^{-1}]

Type	$Z_\odot$ (100%)	0.1 $Z_\odot$ (100%)	$Z_\odot$ + 0.1 $Z_\odot$ (50% + 50%)
NS-NS	40.8 (14.4)	41.3 (3.3)	41.1 (8.9)
BH-NS	3.2 (0.01)	12.1 (7.0)	7.7 (3.5)
BH-BH	1.5 (0.002)	84.2 (6.1)	42.9 (3.1)
TOTAL	45.5 (14.4)	138 (16.4)	91.7 (15.4)

Table 2: LIGO/VIRGO Detection Rates [yr^{-1}]

Sensitivity ($d_{0,\mathrm{nsns}}-$)	Type	$Z_\odot$ (100%)	0.1 $Z_\odot$ (100%)	$Z_\odot$ + 0.1 $Z_\odot$ (50% + 50%)
	NS-NS	0.01 (0.003)	0.01 (0.001)	0.01 (0.002)
18 Mpc	BH-NS	0.007 (0.00002)	0.04 (0.02)	0.02 (0.01)
	BH-BH	0.02 (0.00005)	9.9 (0.1)	4.9 (0.05)
	TOTAL	0.03 (0.003)	10.0 (0.1)	5.0 (0.06)

metallicity environment (e.g., our Galaxy), properly accounting for the HG gap may lead to a reduction in the merger rates of BH-BH binaries by $\sim 2-3$ orders of magnitude (Belczynski et al. 2007). The details of the common envelope phase are not yet fully understood, and thus in what follows we consider two models, one which does not take into account the suppression (optimistic model: A), and one that assumes the maximum suppression (pessimistic model: B).

The results are presented in Table 1 (Galactic merger rates) and 2 (LIGO/VIRGO detection rates). In Table 1 the rates are calculated for a Milky Way type galaxy (10 Gyr of continuous star formation at a rate of 3.5 $M_\odot$ yr^{-1}), with the assumption that all stars have either solar metallicity or 10% solar, or a 50-50 mixture of both types of stars. The rates are presented for the optimistic model (A) where progenitor binaries survive through the common envelope phase, while the results in parentheses represent the pessimistic model (B), where the binaries do not survive if the phase is initiated by a Hertzsprung gap star. In table 2 the detection rates are given for model A (B) for a given sensitivity of LIGO/VIRGO instrument. Sensitivity is defined as the sky and angle averaged distance horizon for detection of a NS-NS inspiral. The rates are given for a local Universe consisting of only solar composition stars (unrealistically high), 0.1 $Z_\odot$ stars (unrealistically low) and for a 50-50 mixture of the above (realistic local Universe; Panter et al. 2008). The sensitivity of $d_{0,\mathrm{nsns}} = 18$ Mpc corresponds to the expected initial LIGO/VIRGO detector.

The results show two clear trends. First, the rates are generally larger for model A than B. This is the direct consequence of our assumptions on common envelope outcome in both models as mentioned earlier and discussed in detail by Belczynski et al. (2007). Since black hole progenitors are the most massive stars and thus experience the most dramatic expansion (CE mergers in model B) the BH-BH rates are affected in the largest extent. Second, we note that the rates are higher for the low metallicity model ($Z = 0.1$ $Z_\odot$) as compared with high metallicity model ($Z = Z_\odot$). The major reason behind this trend is the smaller radii of stars at low metallicity. This directly leads back to CE evolution: the smaller the radius of a given star the later in evolution the star overflows its Roche lobe. Thus for low metallicity, massive stars tend to initiate CE phase after HG, and so they have a chance of surviving this phase and forming a double compact object independent of assumed model of CE evolution. The increase of rates with decreasing metallicity is additionally connected with the fact that low metallicity stars experience low wind mass loss and thus form more massive compact objects. This leads to a shorter merger times and higher merger rates.

Had the initial configuration of LIGO/VIRGO instruments reached its design sensitivity of $d_{0,\mathrm{nsns}}18$ Mpc for its entire lifetime (averaged horizon for NS-NS merger) we would be able to exclude model A from our considerations. This model generates about 5 BH-BH inspirals per year within this horizon (of course the actual horizon for BH-BH detection was accordingly extended with the increased mass of each BH-BH merger). So far there was no report of detection in LIGO/VIRGO data so one would be tempted to exclude this model from further considerations. However, the time averged sensitivity of the last LIGO/VIRGO run (S5, the most recently relesed) has reached only about $d_{0,\mathrm{nsns}} \approx 9$ Mpc. Therefore, the rates should be decreased by factor $(18/9)^3 = 8$ and the expected detection rate for BH-BH binaries would drop below 1 yr^{-1} and consequently model A cannot be yet excluded.

2 Empirical Coalescence Rates

The optical followup of X-ray sources revealed the nature of several X-ray binaries in the galaxies in the Local Group. Two objects: IC10 X-1 and NGC300 X-1 are of particular interest. The identification of optical counterparts and their spectroscopy allowed to estimate the properties of these two binaries. Both host massive black holes on a tight orbit with WR stars. Both reside in low metallicity environments (Crowther et al. 2007, Crowther et al. 2010, Prestwich et al. 2007, Silverman and Filipenko 2008). In the future the accretion in these binaries will continue and the WR stars will loose mass through stellar winds. The typical lifetime of the WR stars in such systems is from 100 to 300 kyrs. After that time the WR stars will explode as supernovae leading to formation of a BH, or a NS in the case of extremely large mass loss. The systems will most likely survive the explosions and remain bound since the current orbital velocities are above 500km s^{-1}. Both systems will end up as binary black holes in a few hundred thousand years.

Given the estimate of the future evolution of the two binaries: IC10 X-1 and NGC300 X-1, we estimate the formation rate of such binaries.The estimated merger time is smaller than the Hubble time. Therefore assuming that the star formation rate was constant the merger rate of the binary black holes formed from such systems will be the same as their formation rate. For each system we estimate the volume in which it is detectable. This is determined by the possibility of measuring the radial velocity curve, which can be done up to the distance of $r \approx 2$Mpc, thus $V_{obs} = 4\pi r^3/3$. Each binary was detected only because of its X-ray radiation, thus the observability is proportional to the X-ray active phase. The formation rate of each binary can be approximated as: $R = (V_{obs} t_{obs})^{-1}$. A detailed statistical analysis is presented in Bulik, Belczynski and Prestwich (2010). We present the probability distributions of the formation and merger rates of the binary black holes corresponding to each binary IC10 X-1 and NGC300 X-1 in Figure 1. The thick line in Figure 1 represents the probability density of the sum of the two rates. This calculation implies a merger rate density of $\mathcal{R} = 0.36^{+0.50}_{-0.26}\mathrm{Mpc}^{-3}\mathrm{Myr}^{-1}$. For the time averaged the sensitivity range of LIGO and VIRGO to binary black holes coalescence of ≈ 100Mpc, this implies the expected detection rate around one per year. This is in a striking agreement with the population synthesis results.

3 Conclusions

Both theoretical simulations and empirical estimate indicate that detection rates of BH-BH binaries are significantly higher than other double compact objects (NS-NS and BH-NS). The population synthesis predictions for our realistic model of local Universe with a mixture of high

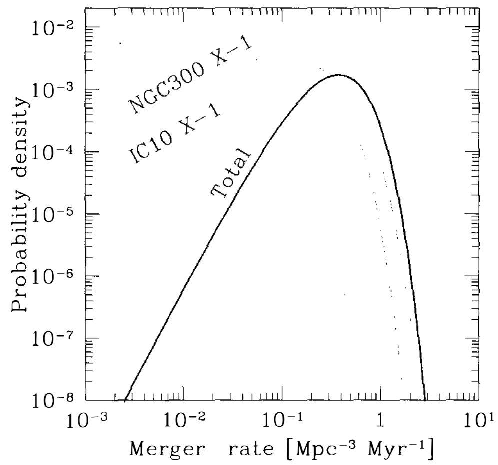

Figure 1: The probability density of the binary black hole merger rate density. We present separately the contributions of IC10 X-1 and NGC300 X-1 and the total rate.

and low metallicity stars results in about 100 BH-BH detections per 1 NS-NS detection by LIGO/VIRGO. The empirical estimate presented here for BH-BH detection rate based on the observed extra-galactic BH binaries is $\approx 1\ \mathrm{yr}^{-1}$, again much higher than the corresponding empirical detection rate for NS-NS inspiral ($\approx 0.06\ \mathrm{yr}^{-1}$, Kim, Kalogera & Lorimer 2006). Thus it is likely that the existing LIGO/VIRGO data contains a coalescence signal that may be discovered with a more elaborate reanalysis.

Acknowledgments

Authors acknowledge support from MSHE grants N N203 302835 and N N203 404939.

References

1. Bauer, F. E., & Brandt, W. N. 2004, ApJ, 601, L67
2. Belczynski, K., Kalogera, V., & Bulik, T. 2002, ApJ, 572, 407
3. Belczynski, K., et al. 2007, ApJ, 662, 504
4. Belczynski, K., et al. 2008, ApJ Sup., 174, 223
5. Belczynski K., et al. 2010a, ApJ, 714, 1217
6. Belczynski, K., et al. 2010b, ApJ, 715, L138
7. Bulik, T., Belczynski, K., Pretwich, A., 2011, ApJ, 730, 140
8. Crowther, P. A., et al. 2010, MNRAS, 403, L41
9. Crowther, P. A., Carpano, S., Hadfield, L. J., & Pollock, A. M. T. 2007, A&A, 469, L31
10. Fryer, C., & Kalogera, V. 2001, ApJ, 554, 548
11. Ivanova, N., & Taam, R. E. 2004, ApJ, 601, 1058
12. Kim, C., Kalogera, V., & Lorimer, D. 2006, New Astronomy Rev. 54, 148
13. Panter B., et al. 2008, MNRAS, 391, 1117
14. Prestwich, A. H., et al. 2007, ApJ, 669, L21
15. Silverman, J. M., & Filippenko, A. V. 2008, ApJ, 678, L17
16. Taam, R. E., & Sandquist, E. L. 2000, ARA&A, 38, 113
17. Timmes, F., Woosley, S., & Weaver, T. 1996, ApJ, 457, 834

PERTURBATIVE, POST-NEWTONIAN, AND GENERAL RELATIVISTIC DYNAMICS OF BLACK HOLE BINARIES

A. LE TIEC
Maryland Center for Fundamental Physics & Joint Space-Science Institute, Department of Physics, University of Maryland, College Park, MD 20742, USA

The orbital motion of inspiralling and coalescing black hole binaries can be investigated using a variety of approximation schemes and numerical methods within general relativity: post-Newtonian expansions, black hole perturbation theory, numerical relativity, and the effective-one-body formalism. We review two recent comparisons of the predictions from these various techniques. Both comparisons rely on the calculation of a coordinate invariant relation, in the case of non-spinning binary black holes on quasi-circular orbits. All methods are shown to agree very well in their common domain of validity.

1 Introduction

The detection and analysis of the gravitational radiation from black hole binaries by the ground-based LIGO/Virgo observatories, and future space-based antennas, requires very accurate theoretical predictions for use as gravitational wave templates. The orbital motion of such compact binary systems can be analyzed using multiple approximation schemes and numerical methods in general relativity: post-Newtonian (PN) expansions, black hole perturbation theory, the effective-one-body (EOB) formalism, and numerical relativity (NR). It is crucial to compare the predictions from these various techniques for several reasons: such comparisons (i) provide independent consistency checks of the validity of the various calculations, (ii) they help to delineate the respective domains of validity of each method, and (iii) they can inform the development of a universal semi-analytical model of the binary dynamics and gravitational wave emission. In this paper, we shall summarize the main results of two such recent comparisons, both related to the *local* orbital dynamics of non-spinning black hole binaries on quasi-circular orbits.

2 Redshift Observable

Our first comparison is concerned with the relativistic motion of compact binary systems within black hole perturbation theory and the PN approximation. Consider two non-spinning black holes with masses m_1 and m_2, moving on an exactly circular orbit with angular frequency Ω_φ. The dissipative effects associated with the emission of gravitational radiation are neglected, which is formalized by assuming the existence of a helical Killing vector (HKV) field k^α. The 4-velocity u_1^α of the "particle" m_1 is necessarily tangent to the HKV evaluated at that location; hence $u_1^\alpha = U\, k_1^\alpha$. The scalar U is a constant of the motion associated with the helical symmetry. It also measures the gravitational redshift of light rays emitted from m_1, and received at large distance, along the helical symmetry axis perpendicular to the orbital plane;[1] we shall henceforth refer to U as the "redshift observable". Being coordinate invariant, the relation $U(\Omega_\varphi)$ provides a handy testbed to compare the predictions from the two approximation schemes.

For an extreme mass ratio black hole binary, such that $m_1 \ll m_2$, the redshift observable $U(\Omega_\varphi; m_1, m_2)$ is conveniently expanded in powers of the mass ratio $q \equiv m_1/m_2$, according to

$$U = U_{\text{Schw}} + q\, U_{\text{GSF}} + \mathcal{O}(q^2)\,. \tag{1}$$

All coefficients in the expansion (1) are functions of the dimensionless coordinate invariant PN parameter $y \equiv (m_2\Omega_\varphi)^{2/3}$. The result for a test mass in circular orbit around a Schwarzschild black hole of mass m_2 is known in closed form as $U_{\text{Schw}} = (1-3y)^{-1/2}$. The invariant relation $U_{\text{GSF}}(y)$ encoding the first order mass ratio correction has been computed numerically, with high precision.[1,2] This gravitational self-force (GSF) effect has also been computed analytically up to high PN orders.[2,3] The post-Newtonian expansion of U_{GSF} is of the form

$$U_{\text{GSF}} = \sum_{k\geqslant 0} \alpha_k\, y^{k+1} + \ln y \sum_{k\geqslant 4} \beta_k\, y^{k+1} + \cdots\,, \tag{2}$$

where the coefficients α_k and β_k are pure numbers, and the dots stand for terms involving powers of logarithms $(\ln y)^p$, with $p \geqslant 2$, which are expected not to occur before the very high 7PN order.[3] The Newtonian, 1PN, 2PN and 3PN polynomial coefficients $\{\alpha_0, \alpha_1, \alpha_2, \alpha_3\}$ were determined analytically,[1,2] as well as the leading-order 4PN and next-to-leading order 5PN logarithmic coefficients $\{\beta_4, \beta_5\}$.[3] Their values are reported in the left panel of Table 1.

Table 1: The analytically determined post-Newtonian coefficients α_k and β_k (left panel), and the numerically determined values of higher-order PN coefficients, based on a fit to the GSF data (right panel). The uncertainty in the last digit is indicated in parenthesis.

Coeff.	Value
α_0	-1
α_1	-2
α_2	-5
α_3	$-\frac{121}{3} + \frac{41}{32}\pi^2$
β_4	$-\frac{64}{5}$
β_5	$+\frac{956}{105}$

Coeff.	Value
α_4	$-114.34747(5)$
α_5	$-245.53(1)$
α_6	$-695(2)$
β_6	$+339.3(5)$

Making use of the known results for the coefficients $\{\alpha_0, \alpha_1, \alpha_2, \beta_4, \beta_5\}$, a fit to the GSF data for $U_{\text{GSF}}(\Omega_\varphi)$ gave the numerical estimate $\alpha_3^{\text{fit}} = -27.6879035(4)$ for the 3PN coefficient,[4] to be compared with the exact value $\alpha_3 = -27.6879026\cdots$.[2] The results are in agreement with *nine* significant digits, at the 2σ level. This provides a strong and independent test of the validity of both calculations, which rely on very different regularization schemes to subtract the divergent self-fields of point particles (mode-sum regularization in the self-force, and dimensional regularization in PN theory). By fitting the accurate GSF data to a PN model of the form (2), now taking into account all known PN coefficients, including the exact value of the 3PN coefficient α_3, the values of previously unknown PN coefficients α_k and β_k were measured, up to the very high 6PN order.[3] These are reported in the right panel of Table 1. Notice in particular how the 4PN and 5PN coefficients α_4 and α_5 could be determined with high precision.

Figure 1 shows the exact results for $U_{\text{GSF}}(\Omega_\varphi)$, as computed within the self-force, as well as the successive truncated PN series up to 6PN order, based on the analytically and numerically determined PN coefficients summarized in Table 1. This comparison illustrates the complementarity of the two approximation schemes: previous knowledge of analytically determined "low" order PN coefficients allows to extract from the accurate GSF data information about higher order PN effects, which otherwise would likely remain inaccessible to standard PN calculations.

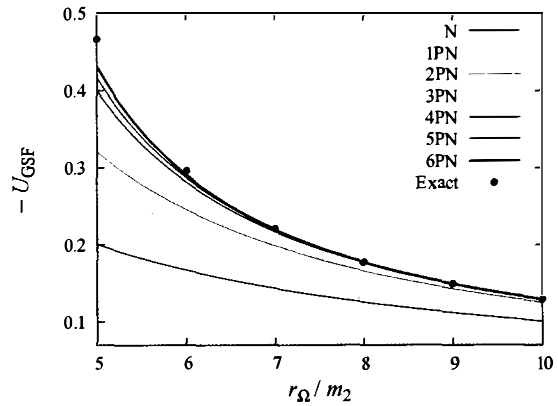

Figure 1: The gravitational self-force contribution U_{GSF} to the redshift observable U, as a function of $r_\Omega \equiv m_2/y$, a coordinate invariant measure of the orbital separation. Notice that $r_\Omega = 6m_2$ corresponds to the very relativistic innermost stable circular orbit (ISCO) of a test-mass orbiting a Schwarzschild black hole of mass m_2.

3 Periastron Advance

As long as the radiation-reaction time scale is much longer than the typical orbital time scale, the motion of two non-spinning black holes on a generic eccentric orbit depends on two independent frequencies: the radial frequency (or mean motion) $\Omega_r = 2\pi/P$, where P is the radial period, i.e. the time interval between two successive periastron passages, and the periastron precession frequency $\Delta\Phi/P$, where $\Delta\Phi/(2\pi) \equiv K - 1$ is the fractional advance of the periastron per radial period. In the zero eccentricity limit, the relation between the circular orbit frequency Ω_φ and $K = \Omega_\varphi/\Omega_r$ is coordinate invariant; it can thus be used as a convenient reference for comparison.

The invariant relation $K(\Omega_\varphi)$ has been computed at the 3PN accuracy in PN theory,[5] at first order in perturbation theory,[6] and in the EOB formalism.[7] This genuine general relativistic effect has also recently been measured for the first time in fully non-linear NR simulations.[8] Le Tiec *et al.*[9] considerably improved upon the accuracy of this initial measurement. Making use of new and longer simulations of the late stage of the inspiral of non-spinning black hole binaries with mass ratios $q = 1, 2/3, 1/3, 1/5, 1/6$, and $1/8$,[10] they measured K with a relative uncertainty $\sim 0.1 - 1\%$. This accuracy made possible an extensive comparison which, for the first time, (i) encompassed all the analytical and numerical methods currently available, and (ii) focused on the orbital dynamics of the binary, rather than the asymptotic waveform.

Figure 2 shows the invariant relation $K(\Omega_\varphi)$ for binary black holes with mass ratios $q = 1$ (left panel), and $q = 1/8$ (right panel), as computed in NR (in cyan), PN theory (red), and the EOB formalism (yellow). For comparable masses (e.g. $q = 1$ or $2/3$), the 3PN prediction is in good agreement with the exact result from NR (to better than 1%). However, as expected, it performs less well when $q \to 0$.[11] The EOB (3PN) prediction, on the other hand, is in very good agreement with the NR data over the entire range of frequencies and mass-ratios considered.

Also shown in Fig. 2 are the predictions for a test mass in circular orbit around a Schwarzschild black hole (green), and the inclusion of the GSF (magenta and blue). While perturbative self-force calculations are commonly formulated as expansions in powers of the usual mass ratio q [see e.g. Eq. (1)], PN expansions naturally involve the *symmetric* mass ratio $\nu \equiv m_1 m_2/m^2$, where $m = m_1 + m_2$ is the total mass of the binary. Since at first order $q = \nu + \mathcal{O}(\nu^2)$, the GSF result for the periastron advance may as well be written in the "resummed" form

$$K = K_{\text{Schw}} + \nu\, K_{\text{GSF}} + \mathcal{O}(\nu^2)\,, \tag{3}$$

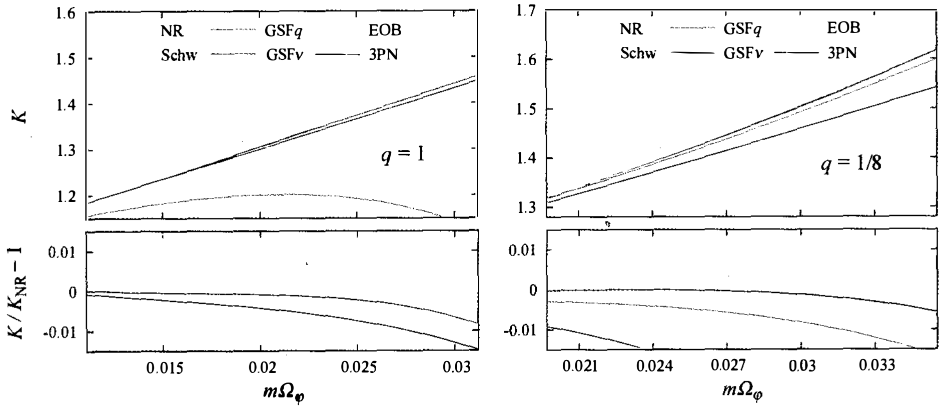

Figure 2: The periastron advance $K = 1 + \Delta\Phi/(2\pi)$, as a function of the circular orbit frequency Ω_φ, for black hole binaries with mass ratios 1 : 1 (left panel) and 1 : 8 (right panel). Notice that in the later case, $\Delta\Phi$ reaches half an orbit per radial period for $m\Omega_\varphi \sim 0.03$, corresponding to an orbital separation $r \sim 10m$.

where all coefficients are functions of the dimensionless invariant PN parameter $x \equiv (m\Omega_\varphi)^{2/3}$. The GSF correction K_{GSF} to the test-particle result $K_{\mathrm{Schw}} = (1 - 6x)^{-1/2}$ has recently been computed numerically.[6] Although the GSFq prediction [obtained by replacing $\nu \to q$ in Eq. (3)] agrees with the exact result within a relative difference of magnitude $\sim q^2$, as expected, the GSFν prediction (3) agrees remarkably well with the NR data for *all* mass ratios. This surprising result suggests that GSF calculations may very well find application in a broader range of physical problems than originally envisaged, including the modelling of intermediate mass ratio inspirals, a plausible source of gravitational waves for Advanced LIGO/Virgo.

Acknowledgments

The results summarized in this paper were obtained in collaboration with L. Barack, L. Blanchet, A. Buonanno, S. Detweiler, A.H. Mroué, H.P. Pfeiffer, N. Sago, A. Taracchini, and B.F. Whiting. The author acknowledges support from NSF Grant PHY-0903631, and from the Maryland Center for Fundamental Physics. He is grateful to the organizing committee of the *46th Rencontres de Moriond & GPhyS Colloquium* for their kind invitation, and for providing financial support.

References

1. S. Detweiler, *Phys. Rev.* D **77**, 124026 (2008).
2. L. Blanchet, S. Detweiler, A. Le Tiec, and B.F. Whiting, *Phys. Rev.* D **81**, 064004 (2010).
3. L. Blanchet, S. Detweiler, A. Le Tiec, and B.F. Whiting, *Phys. Rev.* D **81**, 084033 (2010).
4. L. Blanchet, S. Detweiler, A. Le Tiec, and B.F. Whiting, in *Mass and Motion in General Relativity*, eds. L. Blanchet, A. Spallicci, B. Whiting (Springer, 2011).
5. T. Damour, P. Jaranowski, and G. Schäfer, *Phys. Rev.* D **62**, 044024 (2000).
6. L. Barack, T. Damour, and N. Sago, *Phys. Rev.* D **82**, 084036 (2010).
7. T. Damour, *Phys. Rev.* D **81**, 024017 (2010).
8. A.H. Mroué, H.P. Pfeiffer, L.E. Kidder, S.A. Teukolsky, *Phys. Rev.* D **82**, 124016 (2010).
9. A. Le Tiec *et al.*, submitted for publication (2011), arXiv:1106:3278 [gr-qc].
10. A.H. Mroué *et al.*, in preparation.
11. L. Blanchet, *Phys. Rev.* D **65**, 124009 (2002).

ON THE ECCENTRICITY OF NS-NS BINARIES.

I. KOWALSKA[1], T. BULIK[1], K. BELCZYNSKI[1,2], M. DOMINIK [1], D. GONDEK-ROSINSKA [3]
[1]*Astronomical Observatory, University of Warsaw, Al Ujazdowskie 4, 00-478 Warsaw, Poland*
[2]*Dept. of Physics and Astronomy, University of Texas, Brownsville, TX 78520, USA*
[3]*Institute of Astronomy, University of Zielona Góra, ul. Lubuska 2, 65-265 Zielona Góra, Poland*

The current gravitational wave detectors have reached their operational sensitivity and are nearing detection of compact object binaries. In the coming years, we expect that the Advanced LIGO/VIRGO will start taking data. We discuss the eccentricity distribution of double neutron stars during they inspiral phase. We analyze the expected distributions of eccentricities at the frequency that is characteristic for Advanced Virgo and LIGO detectors. We use the `StarTrack` binary population code to investigate the properties of the population of compact binaries in formation. We evolve their orbits until the point that they enter a detector sensitivity window and analyze the eccentricity distribution at that time. Within the range of considered models, we found that a fraction of between 0.2% and 2% NS-NS binaries will have an eccentricity above 0.01 for the Advanced LIGO/VIRGO detectors.

1 Motivation

Binary neutron stars are among the most promising candidates for gravitational wave sources. During the inspiral phase bounding energy is carried away from the system by gravitational waves. Separation between components and eccentricity of the orbit are decreasing very rapidly. The evolution of the orbit of compact object binary under the influence of gravitational radiation had been calculated by Peters [1,2]. Last stable orbits are very well circularized. In current detectors such as Virgo[3] and LIGO[4], only those last orbits before coalescence are within sensitivity band. Therefore, eccentricity is negligible and there is no need to include it during data analysis. Situation will change when the second generation detectors will appear. Sensitivity window for Advanced Virgo and LIGO detectors will be expanded towards lower frequencies. Observing earlier stages of inspiral evolution will be possible. In that regime, eccentricity could play important role. Brown et al. [5] shown, that searching for eccentric binary using circular template may lead to serious lost of efficiency. It is very important to check how many eccentric binaries is expected within advanced detectors sensitivity band.

2 Initial parameters

So far we have very few observations of binary compact objects. All of them are double neutron stars observed in radio band (at least one of the components is seen as a pulsar). That sample is not representative, because of selection effects. Therefore, we created synthetic sample of double compact objects using `StarTrack` code[6]. It perform a suite of Monte Carlo simulations of the stellar evolution of stars in environments of two typical metallicities: $Z = Z_{\odot} = 0.02$ and $Z = 10\% Z_{\odot} = 0.002$ [7] (denoted by Z and z, respectivley). We place special emphasis on the common envelope evolution phase [8], which is crucial for close double compact object formation because the attendant mass transfer permits an efficient hardening of the binary. Because of significant radial expansion, stars crossing the Hertzsprung gap (HG) very frequently initiate a common envelope phase. If such a star overflows its Roche lobe and initiates a common envelope phase, the inspiral is expected to lead to a coalescence [9]. In particular, it has been estimated that for a solar metallicity environment (e.g., our Galaxy), properly accounting for the HG gap may lead to a reduction in the merger rates of BH-BH binaries by $\sim 2-3$ orders of magnitude [10]. In contrast, in a low metallicity environment this suppression is much less severe (~ 1 order of magnitude; [7]). The details of the common envelope phase are not yet fully understood, thus in what follows we consider two set of models, one that does not take into account the suppression (optimistic models: marked with A), and another that assumes the maximum suppression (pessimistic models: marked with B). In the case of NSs, we adopt natal kick distributions from observations of single Galactic pulsars [11] with $\sigma = 265$ km/s (marked with K) and lower by a factor of 2, to $\sigma = 132.5$ km/s (marked with k), as some observations and empirically based arguments seem to indicate that natal kicks in close binaries are lower than for single stars [12,13]. The detailed list of models considered is presented in Table 1. Model AZK is a standard set of parameters described in detail by Belczynski et al. [14].

Table 1: The list of models of stellar evolution used in simulation.

Model	Metallicity	σ $[kms^{-1}]$	HG
AZK	$Z_\odot$	265.0	+
BZK	$Z_\odot$	265.0	-
AZk	$Z_\odot$	132.5	+
BZk	$Z_\odot$	132.5	-
AzK	10% $Z_\odot$	265.0	+
BzK	10% $Z_\odot$	265.0	-
Azk	10% $Z_\odot$	132.5	+
Bzk	10% $Z_\odot$	132.5	-

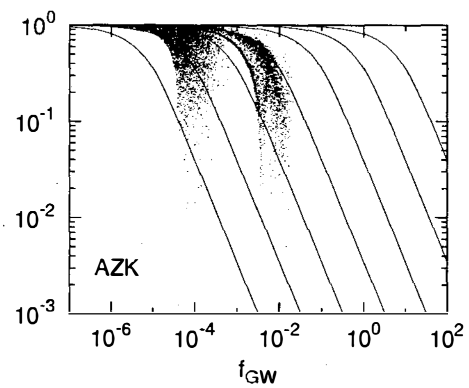

Figure 1: Initial parameters of NS-NS systems.

Initial parameters of the standard model (AZK) are presented in Figure 1. The boundary of the region populated by the systems on the left-hand side corresponds to the requirement that we only consider binaries that merge within a Hubble time. The bulk of the binaries on the 'able 2: Fraction of the compact binaries 'ith eccentricity greater than 10^{-2}.

Model	%	(#)
AZK	0.60%	(51)
BZK	1.27%	(36)
AZk	0.16%	(27)
BZk	0.30%	(15)
AzK	0.29%	(25)
BzK	1.87%	(13)
Azk	0.26%	(37)
Bzk	1.74%	(21)

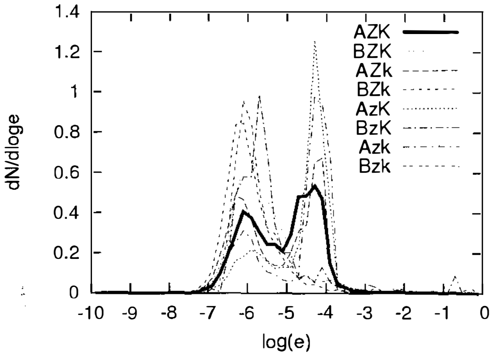

Figure 2: Eccentricity distribution of NS-NS at 30 Hz.

ow-frequency site correspond to those that have undergone one CE phase in their evolution. In he higher frequency branch we allow the binaries to cross through the common envelope with he donor on the Hertzsprung gap, denoted by " † " in Table 1. These binaries may undergo ı second common envelope phase with a helium star companion. At the second CE stage, the ırbit is tightened even more leading to formation of the stripe in the diagram stretching from $f_{GW} \approx 10^{-2}$ Hz at $e \approx 10^{-2}$. Solid lines correspond to evolutionary tracks for initial gravitational vaves frequencies from $f_0 = 10^{-8}$ Hz (first line from the left-hand side) to $f_0 = 10^{2}$ Hz (first ine from the right-hand side).

3 Results

In order to find eccentricity distribution within Advanced Virgo/LIGO detectors, we evolved nitial population of double neutron stars until they reached gravitational wave frequency $f_{GW} =$ 30 Hz. Normalized histogram of eccentricity at that time is shown in Figure 2. The solid line corresponds to the standard model (AZK). Other models are also presented. All models marked by "A" in Table 1 are bimodal. Second peak (higher eccentricities) corresponds to the ultra-compact binaries, which undergone second common envelope phase. In Table 2, we present the fraction of binaries with eccentricities above 0.01 at the time of entering the detector band, to help quantify the extent of the large eccentricity tails of the distributions presented in Figure 2. This fraction does not reflect the detectability of eccentricity [15].

4 Summary

We have presented the eccentricity distributions of double neutron stars at the frequency where advanced detectors (Advanced Virgo and LIGO) will be sensitive. The properties of the compact object binaries have been calculated using the `StarTrack` population synthesis code. We have found that the eccentricity distributions of the compact object binaries do not depend strongly on the assumed model of binary evolution. Any dependence has been found to be the strongest for binary neutron stars, whose distributions may be either single or double peaked. The extra peak corresponds to ultra-compact NS-NS binaries that have undergone an additional CE phase immediately before forming the second NS. Even for models with ultra-compact binaries, eccentricity is negligible within sensitivity band of Advanced Virgo/LIGO detectors. The eccentricity of BH-BH and BH-NS binaries are very small, for detailed discussion see Kowalska et al. [16].

Acknowledgments

This work was supported by the FOCUS 4/2007 Program of Foundation for Polish Science, the Polish grants N N203 511238, N N203 387237, DPN/N176/VIRGO/2009, N N203 302835, N N203 404939 and by CompStar a Research Networking Programme of the European Science Foundation.

References

1. P. C. Peters and J. Mathews, *Phys. Rev.* **131**, 435 (1963).
2. P. C. Peters, *Phys. Rev.* **136**, 1224 (1964).
3. A. D. A. M. Spallicci *et al*, *Class. Quantum Grav* **22**, 461 (2005).
4. J. R. Smith and LIGO Scientific Collaboration, *Class. Quantum Grav* **26**, 114013 (2009).
5. D. A. Brown and P. J. Zimmerman , *Phys. Rev.* D **81**, 024007 (2010).
6. K. Belczynski *et al*, *ApJ* **174**, 223 (2008).
7. K. Belczynski *et al*, *ApJ* **715**, L138 (2010).
8. R. F. Webbink, *ApJ* **277**, 355 (1984).
9. R. E. Taam and E. L. Sandquist *Ann. Rev. A&A* **38**, 113 (2000).
10. K. Belczynski *et al*, *ApJ* **662**, 504 (2007).
11. G. Hobbs *et al*, *MNRAS* **360**, 974 (2005).
12. L. Dessart *et al*, *ApJ* **644**, 1063 (2006).
13. F. S. Kitaura *et al*, *A&A* **450**, 345 (2006).
14. K. Belczynski *et al*, *ApJ* **572**, 407 (2002).
15. K. J. Shapiro and N. J. Cornish, ArXiv e-prints, 2010.
16. I. Kowalska *et al*, *A&A* **527**, A70 (2011).

COMPACT OBJECTS WITH SPIN PARAMETER $a_* > 1$

COSIMO BAMBI

Institute for the Physics and Mathematics of the Universe, The University of Tokyo Kashiwa, Chiba 277-8583, Japan

In 4-dimensional General Relativity, black holes are described by the Kerr solution and are completely specified by their mass M and by their spin angular momentum J. A fundamental limit for a black hole in General Relativity is the Kerr bound $|a_*| \leq 1$, where $a_* = J/M^2$ is the spin parameter. Future experiments will be able to probe the geometry around these objects and test the Kerr black hole hypothesis. Interestingly, if these objects are not black holes, the accretion process may spin them up to $a_* > 1$.

1 Introduction

Today we believe that the final product of the gravitational collapse is a black hole (BH). In 4-dimensional General Relativity, BHs are described by the Kerr solution and are completely specified by two parameters: the mass, M, and the spin angular momentum, J. A fundamental limit for a BH in General Relativity is the Kerr bound $|a_*| \leq 1$, where $a_* = J/M^2$ is the spin parameter. For $|a_*| > 1$, the Kerr solution does not describe a BH, but a naked singularity, which is forbidden by the weak cosmic censorship conjecture [1].

From the observational side, we have at least two classes of astrophysical BH candidates [2]: stellar-mass bodies in X-ray binary systems ($M \sim 5 - 20$ Solar masses) and super-massive bodies in galactic nuclei ($M \sim 10^5 - 10^{10}$ Solar masses). The existence of a third class of objects, intermediate-mass BH candidates ($M \sim 10^2 - 10^4$ Solar masses), is still controversial, because there are not yet reliable dynamical measurements of their masses. All these objects are commonly interpreted as BHs because they cannot be explained otherwise without introducing new physics. The stellar-mass objects in X-ray binary systems are too heavy to be neutron or quark stars. At least some of the super-massive objects in galactic nuclei are too massive, compact, and old to be clusters of non-luminous bodies.

2 Testing the Kerr Black Hole Hypothesis

In Newtonian gravity, the potential of the gravitational field, Φ, is determined by the mass density of the matter, ρ, according to the Poisson's equation, $\nabla^2\Phi = 4\pi G_N \rho$. In the exterior region, Φ can be written as

$$\Phi(r, \theta, \phi) = -G_N \sum_{lm} \frac{\mathcal{M}_{lm} Y_{lm}(\theta, \phi)}{r^{l+1}}, \tag{1}$$

where the coefficients $\mathcal{M}_{lm}$ are the multipole moments of the gravitational field and Y_{ml} are the Laplace's spherical harmonics.

Because of the non-linear nature of the Einstein's equations, in General Relativity it is not easy to define the counterpart of Eq. (1). However, in the special case of a stationary, axisymmetric, and asymptotically flat space-time, one can introduce something similar to Eq. (1) and define the mass-moments $\mathcal{M}_n$ and the current-moments $\mathcal{S}_n$ [3]. For a generic source, $\mathcal{M}_n$ and $\mathcal{S}_n$ are unconstrained. In the case of reflection symmetry, all the odd mass-moments and the even current-moments are identically zero. In the case of a Kerr BH, all the moments depend on M and J in a very specific way:

$$\mathcal{M}_n + i\mathcal{S}_n = M\left(\frac{iJ}{M}\right)^n , \tag{2}$$

where i is the imaginary unit; that is, $i^2 = -1$. By measuring the mass, the spin, and at least one more non-trivial moment of the gravitational field of a BH candidate (e.g the mass-quadrupole moment $Q \equiv \mathcal{M}_2 = -J^2/M$), one can test the Kerr BH hypothesis [4].

By considering the mean radiative efficiency of AGN, one can constrain possible deviations from the Kerr geometry [5]. In term of the anomalous quadrupole moment q, defined by $Q = Q_{\rm Kerr} - qM^3$, the bound is

$$-2.00 < q < 0.14 . \tag{3}$$

Let us notice that this bound is already quite interesting. Indeed, for a self-gravitating fluid made of ordinary matter, one would expect $q \sim 1 - 10$. In the case of stellar-mass BH candidates in X-ray binaries, q can be potentially constrained by studying the soft X-ray component [6]. The future detection of gravitational waves from the inspiral of a stellar-mass compact body into a super-massive object, the so-called extreme mass ratio inspiral (EMRI), will allow for putting much stronger constraints. LISA will be able to observe about $10^4 - 10^6$ gravitational wave cycles emitted by an EMRI while the stellar-mass body is in the strong field region of the super-massive object and the mass quadrupole moment of the latter will be measured with a precision at the level of $10^{-2} - 10^{-4}$ [7].

3 Formation of Compact Objects with $a_* > 1$

If the current BH candidates are not the BHs predicted by General Relativity, the Kerr bound $|a_*| \le 1$ does not hold and the maximum value of the spin parameter may be either larger or smaller than 1, depending on the metric around the compact object and on its internal structure and composition. In Ref. [8,9,10,11], I studied some features of the accretion process onto objects with $|a_*| > 1$. However, an important question to address is if objects with $|a_*| > 1$ can form.

For a BH, the accretion process can spin the object up and the final spin parameter can be very close to the Kerr bound. In the case of a geometrically thin disk, the evolution of the spin parameter can be computed as follows. One assumes that the disk is on the equatorial plane [a] and that the disk's gas moves on nearly geodesic circular orbits. The gas particles in an accretion disk fall to the BH by loosing energy and angular momentum. After reaching the innermost stable circular orbit (ISCO), they are quickly swallowed by the BH, which changes its mass by $\delta M = \epsilon_{\rm ISCO}\delta m$ and its spin by $\delta J = \lambda_{\rm ISCO}\delta m$, where $\epsilon_{\rm ISCO}$ and $\lambda_{\rm ISCO}$ are respectively the specific energy and the specific angular momentum of a test-particle at the ISCO, while δm is the gas rest-mass. The equation governing the evolution of the spin parameter is

$$\frac{da_*}{d\ln M} = \frac{1}{M}\frac{\lambda_{\rm ISCO}}{\epsilon_{\rm ISCO}} - 2a_* . \tag{4}$$

[a] For prolonged disk accretion, the timescale of the alignment of the spin of the object with the disk is much shorter than the time for the mass to increase significantly and it is correct to assume that the disk is on the equatorial plane.

An initially non-rotating BH reaches the equilibrium $a_*^{eq} = 1$ after increasing its mass by a factor $\sqrt{6} \approx 2.4$ [12]. Including the effect of the radiation emitted by the disk and captured by the BH, one finds $a_*^{eq} \approx 0.998$ [13], because radiation with angular momentum opposite to the BH spin has larger capture cross section.

As ϵ_{ISCO} and λ_{ISCO} depend on the metric of the space-time, if the compact object is not a BH, the value of the equilibrium spin parameter a_*^{eq} may be different. The evolution of the spin parameter of a compact object with mass M, spin angular momentum J, and non-Kerr quadrupole moment Q was studied in [14,15]. In [15], I considered an extension of the Manko-Novikov-Sanabria Goméz (MMS) solution [16,17], which is a stationary, axisymmetric, and asymptotically flat exact solution of the Einstein-Maxwell's equations. In Fig. 1, I show the evolution of the spin parameter a_* for different values of the anomalous quadrupole moment $\tilde{q}$, defined by $Q = -(1 + \tilde{q})J^2/M$. For $\tilde{q} > 0$, the compact object is more oblate than a BH; for $\tilde{q} < 0$, the object is more prolate; for $\tilde{q} = 0$, one recovers exactly the Kerr metric. In Fig. 1 there are two curves for every value of $\tilde{q}$ because, for a given quadrupole moment Q, the MMS metric may have no solutions or more than one solution. In other words, two curves with the same $\tilde{q}$ represent the evolution of the spin parameter of two compact objects with the same mass, spin, and mass-quadrupole moment, but different values of the higher order moments.

As shown in Fig. 1, objects more oblate than a BH ($\tilde{q} > 0$) have an equilibrium spin parameter larger than 1. For objects more prolate than a BH ($\tilde{q} < 0$), the situation is more complicated, and a_*^{eq} may be either larger or smaller than 1. The origin of this fact is that for $\tilde{q} < 0$ the radius of the ISCO may be determined by the vertical instability of the orbits, while for $\tilde{q} \geq 0$ (which includes Kerr BHs) it is always determined by the radial instability.

Lastly, let us notice that Fig. 1 shows how, "in principle", the accreting gas can spin a compact object with non-Kerr quadrupole moment up. It may happen that the compact object becomes unstable before reaching its natural equilibrium spin parameter. This depends on the internal structure and composition of the object. For example, neutron stars cannot rotate faster than about ~ 1 kHz, or $a_* \sim 0.7$. If the accretion process spins a neutron star up above its critical value, the latter becomes unstable and spins down by emitting gravitational waves. If the same thing happens to the super-massive BH candidates in galactic nuclei, they may be an unexpected source of gravitational waves for experiments like LISA.

4 Conclusions

The future gravitational wave detector LISA will be able to check if the super-massive objects at the center of most galaxies are the BHs predicted by General Relativity. A fundamental limit for a BH in General Relativity is the Kerr bound $|a_*| \leq 1$, which is the condition for the existence of the event horizon. If the current BH candidates are not the BHs predicted by General Relativity, the Kerr bound does not hold and the maximum value of the spin parameter may be either larger or smaller than 1. Here I showed that compact objects with $|a_*| > 1$ may form if they have a thin disk of accretion.

Acknowledgments

This work was supported by World Premier International Research Center Initiative (WPI Initiative), MEXT, Japan, and by the JSPS Grant-in-Aid for Young Scientists (B) No. 22740147.

References

1. R. Penrose, Riv. Nuovo Cim. Numero Speciale 1, 252 (1969).
2. R. Narayan, New J. Phys. **7**, 199 (2005).

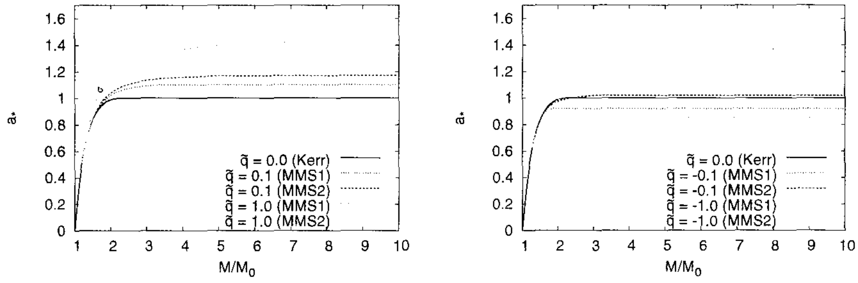

Figure 1: Evolution of the spin parameter a_* for an initially non-rotating object as a function of M/M_0, where M_0 is the mass at $a_* = 0$.

3. R. Hansen, J. Math. Phys. **15**, 46 (1974).
4. F. D. Ryan, Phys. Rev. D **52**, 5707 (1995).
5. C. Bambi, arXiv:1102.0616 [gr-qc].
6. C. Bambi and E. Barausse, Astrophys. J. **731**, 121 (2011).
7. L. Barack and C. Cutler, Phys. Rev. D **75**, 042003 (2007).
8. C. Bambi *et al.*, Phys. Rev. D **80**, 104023 (2009).
9. C. Bambi, T. Harada, R. Takahashi and N. Yoshida, Phys. Rev. D **81**, 104004 (2010).
10. C. Bambi and N. Yoshida, Phys. Rev. D **82**, 064002 (2010).
11. C. Bambi and N. Yoshida, Phys. Rev. D **82**, 124037 (2010).
12. J. M. Bardeen, Nature **226**, 64 (1970).
13. K. S. Thorne, Astrophys. J. **191**, 507 (1974).
14. C. Bambi, arXiv:1101.1364 [gr-qc].
15. C. Bambi, arXiv:1103.5135 [gr-qc].
16. V. S. Manko, E. W. Mielke and J. D. Sanabria-Gomez, Phys. Rev. D **61**, 081501 (2000).
17. V. S. Manko, J. D. Sanabria-Gomez and O. V. Manko, Phys. Rev. D **62**, 044048 (2000).

4.
Space Detectors

LISA Pathfinder and the LTP

Paul W. McNamara on behalf of LISA Pathfinder Collaboration*

European Space Technology Centre, European Space Agency, Keplerlaan 1, 2200AG, Noordwijk, The Netherlands

LISA Pathfinder (formerly known as SMART-2) is an ESA mission designed to pave the way for the joint ESA/NASA *Laser Interferometer Space Antenna* (LISA) mission by validating in flight the critical technologies required for space-borne gravitational wave detection: it will put two test masses in a near-perfect gravitational free-fall and control and measure their motion with unprecedented accuracy. This is achieved through technology comprising inertial sensors. high precision laser metrology, drag-free control. and an ultra precise micro-Newton propulsion system.

This paper gives an overview of the mission. focusing on the scientific and technical goals.

1 Introduction

LISA Pathfinder (LPF), the second of the European Space Agency's Small Missions for Advanced Research in Technology (SMART), is a dedicated technology validation mission for the joint ESA/NASA Laser Interferometer Space Antenna (LISA) mission [1].

LISA, a mission to observe low frequency gravitational waves. has continually been ranked as one of the most scientifically important missions under study [2]. However the very concept of low frequency gravitational wave detection, *i.e.* that a particle falling under the influence of gravity alone follows a geodesic in spacetime, has never been demonstrated to the required precision. This is the most basic assumption of Einstein's General Relativity: LISA Pathfinder has been designed to test this hypothesis with unprecedented accuracy.

The LISA Pathfinder mission essentially mimics one arm of the LISA constellation by shrinking the 5 million kilometre armlength down to a few tens of centimetres. The distance between the two test masses is measured using a laser interferometric technique similar to one aspect of LISA interferometry system.

LISA Pathfinder is due to be launched in 2014 on-board a dedicated launch vehicle. The spacecraft and expendable propulsion module are injected into a low earth orbit (200 km x 1600 km). from which, after a series of apogee raising manoeuvres, will enter a transfer orbit towards the first Sun-Earth Lagrange point (L1). After separation from the propulsion module. the LPF spacecraft will be stabilised using micro-Newton thrusters, entering a Lissajous orbit around L1 (500,000 km by 800,000 km orbit). Following the initial on-orbit check-out and instrument calibration. the in-flight validation of the LISA technology will take place.

*http://www.rssd.esa.int/index.php?project=LISAPATHFINDER&page=Author_List

2 LISA Pathfinder Mission Concept

LISA Pathfinder will test in a space experiment that free falling bodies do follow geodesics in spacetime by more than two orders of magnitude better than any past, present, or planned mission (with the exception of LISA itself). The concept that a particle falling under the influence of gravity alone follows a geodesic in space-time is at the very foundation of General Relativity (GR).

In GR, gravity is not considered as an external force: instead gravity is the source of spacetime curvature. Therefore, in a universe devolved of mass (a flat spacetime) free-falling test masses will move in straight lines with uniform velocity (Newton's 1st Law). In the real (as described by General Relativity) Universe, the presence of mass, hence gravity/curvature, modifies Newton's 1st Law to state that in the absence of any external force, test masses move along geodesics.

All experiments aimed at directly measuring curvature caused by celestial bodies, or to test subtle effects of GR, *e.g.*, frame-dragging, detection of gravitational waves, or to probe its very foundation - the Equivalence Principle, invariably search for violation of geodesic motion.

The difficulty of achieving ***high purity geodesic motion*** is that any parasitic forces compete with spacetime geometry to set masses into motion, perturbing them away from their geodesic lines. As gravity is by far the weakest of all fundamental interactions, achieving the required extremely low level of non-gravitational acceleration requires the understanding, reduction and control of the disturbances produced by a wide range of physical phenomena.

LISA Pathfinder's experiment concept is to improve the uncertainty in the proof of geodesic motion. This is achieved by tracking, using pico-meter resolution laser interferometry, two test-masses nominally in free-fall, and by showing that their relative parasitic acceleration, at frequencies around 1 mHz, is at least two orders of magnitude smaller than anything demonstrated or planned so far. The LISA Pathfinder spacecraft as an inertial platform, free of spurious accelerations, will be the best laboratory ever created for Fundamental Physics experiments, where the conditions hypothesised by Einstein will be realised in the real world.

LISA Pathfinder is both a mission in General Relativity and in Precision Metrology, pushing these disciplines several orders of magnitude beyond their current state of the art. In doing so it opens new ground for an entire class of new missions in General Relativity, in Fundamental Physics at large, and in Earth Observation. The high resolution optical readout of test-mass motion allows test-mass to test-mass tracking even when they are located in different spacecraft, at large distance and in interplanetary space, *e.g.* LISA, or at short distance in low Earth orbit, like in future geodesy missions.

It must be stated that the true objective of LISA Pathfinder is not to develop hardware, but to confirm the overall physical model of the forces that act on a test mass in interplanetary space. To fulfill this program, the mission is not going to just make a measurement of acceleration but will implement a full menu of measurements: at the end of this set of measurements, the residual acceleration noise model will be verified down to painstaking detail.

3 Mission Goals

The mission goals of LISA Pathfinder can be split into three categories, covering the performance of the inertial sensor, the performance of the laser interferometer, and the demonstration of the flight readiness of the technologies critical for a successful LISA mission. The mission goals can be summarised as follows (for a full description of the mission goals, the reader is directed to[3]):

- demonstrate that a test mass can be put in a pure gravitational free-fall within approximately one order of magnitude of the LISA requirement. The one order of magnitude applies also to the measurement bandwidth. Therefore, the differential acceleration noise requirement of LISA Pathfinder is stated quantitively as:

$$\Delta a \leq 3 \times 10^{-14} \left[1 + \left(\frac{f}{3\,\mathrm{mHz}}\right)^2\right] \mathrm{ms}^{-2}/\sqrt{\mathrm{Hz}} \tag{1}$$

over the frequency bandwidth, f, of 1 - 30 mHz. *This is the top-level science requirement of the mission.*

- demonstrate laser interferometry with free-falling mirrors (test masses of the LISA Technology Package) with a displacement sensitivity equal to the LISA requirements. Therefore, the flight test is considered successful if the laser metrology resolution is demonstrated to within:

$$\Delta x \leq 9 \times 10^{-12} \left[1 + \left(\frac{3\,\mathrm{mHz}}{f}\right)^2\right] \mathrm{m}/\sqrt{\mathrm{Hz}} \tag{2}$$

  over a frequency bandwidth of 1 - 30 mHz with a dynamic range on the order of one millimetre.

- assess the lifetime and reliability of the micro-Newton thrusters, lasers and optics in a space environment.

4 The LISA Technology Package

Unlike traditional observatory or planetary missions, the payload in LISA Pathfinder cannot be considered as a discrete piece of hardware carried by the spacecraft. Instead, during science operations, the payload and the spacecraft act as a single unit: the attitude control of the spacecraft is driven by the payload. LISA Pathfinder will carry two payloads; the LISA Technology Package (LTP), and the Disturbance Reduction System (DRS). The LISA Technology Package is provided by a consortium of European national space agencies (France, Germany, Italy, Spain, Switzerland, The Netherlands, and the United Kingdom) and ESA, while the DRS is provided by NASA. Only the LTP will be described here.

The LTP consists of two major subsystems; the Inertial Sensor Subsystem, and the Optical Metrology Subsystem. Both subsystems are described in further detail in the following sections.

4.1 Inertial Sensor Subsystem

The Inertial Sensor Subsystem (ISS) is at the heart of the LISA Pathfinder mission; the development and on-orbit testing of this subsystem are the main reasons for ESA implementing the mission. *The ISS of LISA Pathfinder is the ISS of LISA* - the relaxation in the requirements of LPF comes from the relaxation in the environmental conditions of the LPF spacecraft as compared to LISA.

The inertial sensor subsystem comprises the test masses and all systems interacting directly with the test masses, *i.e.* the electrode housing, front-end electronics, vacuum system, charge management, and caging mechanism. This section will describe each of these subsystems in turn.

The test masses consist of a 1.96 kg cube of Gold:Platinum mono-phasic alloy of dimension 46 mm on a side. The alloy is formed from 73% gold and 27% platinum, chosen as this alloy has an extremely low magnetic susceptibility ($\chi_m \approx 10^{-5}$) and high density $\approx 2 \times 10^4$ kgm^{-3}. The combination of both greatly reduces the effect of external forces on the test mass.

The test masses' position is readout by two means: high resolution laser interferometry, and electrostatic (capacitive) sensing. The former only senses the test mass position along the

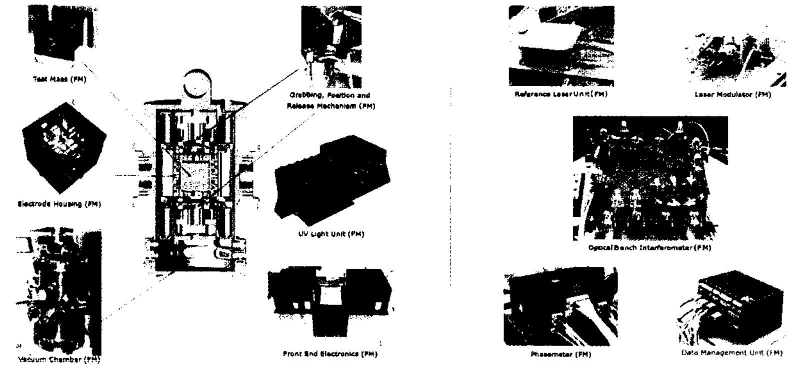

Figure 1: *Left*: Photographs of the Inertial Sensor Subsystem flight models (FM). From bottom left: Vacuum Chamber (Carlo Gavazzi Space), Electrode Housing (Thales Alenia Space), (uncoated) Test Mass (Thales Alenia Space), Caging Mechanism (RUAG), UV Lamp Unit (Imperial College London), Front-End Electronics (ETH, Zurich). *Right*: Photographs of the Optical Metrology System Flight Hardware. From top left: Reference Laser Unit (Tesat), Laser Modulator (APC/Contraves), Data Management Unit (ICE, Barcelona), Phasemeter (Uni Birmingham). Centre: Optical Bench Interferometer (Uni Glasgow)

sensitive axis (the line joining the two test masses) and the angles of rotation around the axes perpendicular to the sensitive axis, whereas the capacitive sensor measures the position of the test mass in all six degrees of freedom. The capacitive sensor comprises a hollow cubic molybdenum housing with gold coated sapphire electrodes mounted in the faces (see Figure 1). The housing is sized to allow for a $\approx$4 mm gap between the electrode faces and the test mass. The size of the gap is a trade off between reducing the effects of noise sources, *e.g.* from uncontrolled potentials on the electrodes, and being able to meet the capacitive sensing requirement of $1.8\,\mathrm{nm}/\sqrt{\mathrm{Hz}}$ over the measurement bandwidth.

The capacitive readout system, known as the *Inertial Sensor Subsystem Front End Electronics* (ISS FEE), is arranged such that electrodes facing opposing faces of the test mass are combined via a capacitive bridge. A change in the position of the test mass gives a differential, bi-polar, signal at the output of the bridge, which is used as an input to the drag-free control system. As well as sensing the position of the test masses, the ISS FEE can also be used to actuate (force) the test mass.

The test mass and electrode housing are mounted inside a dedicated vacuum enclosure. To meet the mission requirements, the vacuum around the test mass must be maintained, throughout the mission lifetime, to less than 10^{-5} Pa. In order to limit the pressure increase due to outgassing or virtual leaks within the vacuum enclosure, the enclosure will be vented to space once the spacecraft reaches its operational science orbit. As with all equipment used in LISA Pathfinder (with the exception of a few components mounted on the outer wall of the spacecraft as far as possible from the test masses) only non-magnetic materials are permitted to be used in the system, forcing the vacuum chamber to be manufactured from titanium as opposed to the standard stainless steel construction techniques.

As there is no physical contact between the test mass and the surrounding environment, one issue that must be dealt with is charging of the test mass due to cosmic ray and solar energetic particle impacts. A build up of charge on the test mass, coupled with the potentials on the electrodes, creates a force, resulting in additional noise in the test mass position. The charge is controlled using a non-contact discharge system based on the photo-electric effect. UV light from Mercury vapour lamps is channelled to the electrode housing via fibre optic cables. Depending on the sign of the charge on the test mass, the light is either shone onto the test mass or the electrode housing, thereby extracting electrons from either surface, providing bi-polar charge management.

A further challenge which is unique to space flight hardware is the need for a launch-lock device to prevent hardware being damaged during the extreme vibration conditions experienced during launch. In LISA Pathfinder, this is especially true for the test masses - the most sensitive part of the experiment must survive a random load of $\approx 50\,g_{rms}$, requiring a holding force of $\approx$1200 N, while not damaging the gold coated surface of the cube. In addition to the launch load requirement, when on-orbit, the device must release the test mass within an error box of 200 μm, with a velocity of less than $5\mu ms^{-1}$. These requirements are met by the *Caging Mechanism Assembly*. This device consists of three actuators: a first stage launch lock mechanism providing the 1200 N preload; a second stage positioning actuator, which is used to break the adhesion of the launch lock and position the test mass to the desired location; and finally, the release actuator, a small diameter pin which is used to break the adhesion of the positioning plunger and release the mass with the required accuracy.

Several other challenges must also be solved in order to meet the requirements of the LTP. These include: balancing of the differential gravitational force and gradient at the test mass positions - achieved by mounting compensation masses inside, and external to, the vacuum enclosure; creating a thermally quiet environment around the test mass - a temperature stability of $10^{-5}\,\mathrm{K}/\sqrt{\mathrm{Hz}}$ over the measurement bandwidth; associated with the thermal stability requirement is the need to have thermometers with a resolution better than $10^{-5}\,\mathrm{K}/\sqrt{\mathrm{Hz}}$; and as mentioned earlier, no magnetic materials can be used - this makes the design of several of the subsystem units especially difficult (*e.g.* vacuum chamber, mounting brackets, bolts, *etc*).

4.2 Optical Metrology Subsystem

The Optical Metrology Subsystem (OMS) is the high resolution laser interferometric readout of the test masses' positions. The OMS comprises several subsystems, namely; the reference laser unit, the laser modulator, the optical bench interferometer, the phasemeter, and the data management unit (Figure 1).

The *Reference Laser Unit* (RLU) comprises a 40 mW Nd:YAG non-planar ring oscillator[4] of the same design commonly used in metrology labs around the world. This laser design is ideal for space applications due to its small size, high electrical to optical efficiency and inherent low noise operation. The challenges for space applications come from the need for a robust design which can survive both the launch loads and thermal environment, as well as having a sufficient lifetime to guarantee the life of the mission. All of these challenges have been overcome and similar lasers are now flying in space on optical communication satellites[5]. The RLU is baselined as the master oscillator in the LISA laser system.

The RLU output is fibre coupled using single-mode, polarisation-maintaining (sm/pm) fibre. The fibre couples the light to the subsequent component in the optical chain, the *Laser Modulator* (LM). The LM consists of a beam splitter, two acousto-optic modulators, and optical pathlength actuators. The light from the laser is split into two paths, each path is passed through an acousto-optic modulator. One modulator is driven at 80 MHz, while the other is driven at 80 MHz + 1.2 kHz, thereby creating two beams with a frequency difference of 1.2 kHz. The beams are then passed through the optical pathlength difference (OPD) actuator which consists of a fibre optic cable wrapped around a cylindrical piezo-electric transducer. The OPD is used to stabilise the optical pathlength of the fibre optic cables leading to the optical bench. After the OPD, the beams are transmitted, again via sm/pm fibre, to the *Optical Bench Interferometer* (OBI).

The main function of the OBI is to direct the beams to the relevant positions in 3-dimensional space, without adding any significant noise to the measurement path. The primary optical bench requirement is that the pathlength noise induced by the components on the optical bench should not exceed 1 pm/$\sqrt{\text{Hz}}$ over the measurement bandwidth. The optical bench is constructed from a block of Zerodur ceramic glass with fused silica mirrors and beamsplitters bonded to the bench using hydroxy catalysis bonding [6] . The mirrors and beamsplitters are used to direct the two beams to form four interferometers: the $x_2 - x_1$ interferometer which measures the differential motion of the two test masses - this is the primary science measurement of the mission: x_1 interferometer which measures the position and angles of test mass 1 with respect to the optical bench (and therefore, the spacecraft) - equivalent to the LISA local test mass interferometer; the *Frequency* interferometer which is an unequal arm Mach-Zehnder interferometer, the output of which is sensitive to laser frequency fluctuations, and therefore can be used to stabilise the laser frequency; and the *Reference* interferometer which is a rigid equal arm interferometer which provides the system noise floor, and is used to stabilise the optical pathlengths via the OPD. The light from each fibre is also sent directly to a photodiode which is used to monitor the laser intensity noise. The signal from these photodiodes is used to stabilise the intensity of both beams by feeding back to the acousto-optic modulator drive signal.

The signals from the (quadrant) photodiodes of each interferometer (each interferometer has two quadrant photodiodes for redundancy) are sent to the *Phasemeter Assembly.* The phasemeter samples the data at 50 kHz and performs a Single Bin Discrete Fourier Transform [7] to measure the phase of the signal at the heterodyne frequency. This technique is used due to the efficiency of the algorithm. The phasemeter not only outputs the longitudinal phase from the respective interferometers, but also outputs the angles between the wavefronts interfering on the photodetectors - commonly known as *differential wavefront sensing* (DWS) - at 100 Hz. The DWS signals from the x_1 and $x_2 - x_1$ interferometers are used to align the test mass to the interferometer. The longitudinal signals from the interferometers are used to stabilise the laser frequency, the optical pathlength, and (with the DWS signals) as inputs for the Drag-Free and Attitude Control System (DFACS) [8].

As mentioned above, the phasemeter outputs the data at 100 Hz. However, the 100 Hz samples are not required for routine operation, and so the data is downsampled to 10 Hz prior to transmission to the on-board computer (and hence the DFACS). The downsampling is performed inside the *Data Management Unit* (DMU) - a 12 MHz ERC32 processor. The DMU is also responsible for the interface to the LTP subsystems, routing telecommands and timing information to the units, and collecting and transmitting telemetry to the on-board computer.

4.3 Micropropulsion

The LISA Pathfinder Micro-Propulsion Subsystem (MPS) is based on Field Emission Electric Propulsion (FEEP) technology. An extensive account can be found in [9] and [10]. In field emission electrical propulsion, positive ions are directly extracted from liquid metals (for LISA Pathfinder, Caesium has been chosen as the liquid metal source) and accelerated by means of electrostatic force in high vacuum. This function is carried out by applying a high voltage to a suitable electrode configuration, which is able to create and enhance very high electrical fields (up to 10^9 V/m). An additional external source of electrons, the neutraliser, needs to be included to maintain the balance of the overall electrical charge of the system (ions$^+$ = e$^-$).

The LISA Pathfinder MPS is composed of three main parts: a FEEP Cluster Assembly; a Power Control Unit (PCU); and a Neutraliser Assembly (NA). The FEEP Cluster Assembly consists of a self-contained unit of 4 FEEP Thruster Assemblies, which include propellant reservoir, mounted on a support structure. The four thrusters are devoted to provide thrust to the required vector directions and are commanded individually and work in hot redundancy.

The Neutralizer Assembly consists of a self-contained unit of two neutraliser units necessary to null the spacecraft charge imbalance due to ion thruster operations. The neutralisation func-

Figure 2: The LISA Pathfinder launch composite being in the vacuum chamber in preparation for the Transfer Orbit Thermal Balance test. The test was performed at the IABG, Germany.

tion is implemented by means of cold redundant hardware. The Power Control Unit consists of an electronic unit interfacing to the spacecraft for power supply and telecommand and telemetry tasks and provides power and control to both the FEEP Cluster and Neutraliser assemblies.

5 Spacecraft

The spacecraft platform structure provides the mechanical support for the hardware of the other spacecraft subsystems. The spacecraft has a shape of an octagonal prism, with outer diameter of 231 cm and height of 96 cm. One of the two bases is covered by a sunshield panel supporting an array of triple-junction GaAs solar cells of $2.8\,\mathrm{m}^2$, providing at end-of-life 650 W of power, while the other base interfaces with the propulsion module (Figure 2). A large central cylinder accommodates the LTP core assembly, while the rest of the payload equipment and the spacecraft units are mounted as far away as possible on shear walls connecting the central cylinder to the outer panel forming the octagonal structure. The cylinder and all structural panels are constructed from sandwich panels or shells with carbon fibre laminate skins bonded to aluminium honeycomb core. Aluminium items are limited to structural rings, cleats, inserts and minor brackets.

The Thermal Control Subsystem must guarantee the very stable thermal environment required by the science measurements. Together with the stringent thermal stability required at LTP level, a stable thermal environment of $10^{-3}\,\mathrm{K}/\sqrt{\mathrm{Hz}}$ is also required at the LTP interface, in order to minimise the thermo-elastic distortions. Passive means are used to control the upper temperatures of sensitive equipments, with electrical heaters to control the lower temperatures. The entire module is wrapped in Multi-Layer Insulation (MLI) except for designated radiator areas designed to reject to space the excessive heat. The minimum necessary heater power is applied in the cold cases so that the lower temperature of each unit is maintained towards the bottom of their allowable range. By using the full design temperature range of each unit in this way, the heater power requirement is minimised. Heater switching is not permitted during the science operations as the transient variations in temperature that happen as heaters switch can interfere with the payload measurements. On the sensitive equipment, different combinations of trimming heaters are used to obtained the required temperatures.

6 Conclusions

Throughout the history of the LISA mission, the science return has never been in doubt - LISA will observe the Universe in a way which has never been possible before. This has captured the imagination of the science community, but at the same time has cast doubt on the probability that such a mission can be realised. Together, this prompted the European Space Agency to adopt the LISA Pathfinder mission - the science return of LISA easily justifies the technology development mission.

The final return of LISA Pathfinder is not only related to the development of the critical technologies for LISA - in the process of implementing the mission, the industrial experience required to build a mission like LPF (and LISA) has also been acquired, as has the knowledge of the ground segment required by a LISA-like mission.

In conclusion, LISA Pathfinder is on track to demonstrate the first in-flight test of low frequency gravitational wave detection metrology. Launch is scheduled for 2014, with first results available to the science community approximately three months thereafter.

Acknowledgments

The authors would like to thank the entire LISA Pathfinder team for their continued work in making the mission possible. The LISA Pathfinder mission is funded through the European Space Agency, while the LTP is funded by ESA, France, Germany, Italy, The Netherlands, Spain, Switzerland, and the United Kingdom.

References

1. Jennrich, O., *et al.*, *LISA - Unveiling a hidden Universe*, ESA/SRE(2011)3 unpublished (2011)
2. National Academy of Sciences, *New Worlds, New Horizons in Astronomy and Astrophysics*, Report of the National Research Council's Decadal survey of Astronomy and Astrophysics (2010)
3. Vitale, S., *et al.*, *Science Requirements and Top-Level Architecture Definition for the LISA Technology Package (LTP) on board LISA Pathfinder (SMART-2)*, ESA Ref: LTPA-UTN-ScRD-Iss3-Rev1 (2005)
4. Kane, T.J., and Byer, R.L., *Monolithic, unidirectional single-mode Nd:YAG ring laser*, Optics Letters, **10**, 2, 65-67 (1985)
5. Lange, R, *et al.*, *BPSK Laser communication terminals to be verified in space*, MILCOM 2004 - IEEE Military Communications Conference (2004)
6. Middleton, K., *et al.*,*Prototype optical bench instrument in the interferometer for the LISA-Pathfinder space mission*, Optical Engineering, **45** (2006)
7. Heinzel, G, *et al.*, *Interferometry for the LISA Technology Package, LTP: an update*, Journal of Physics Conference Series, **32**, 132 (2006)
8. Fichter, W., *et al.*, *Drag-Free Control Design with Cubic Test Masses*, In "Lasers, Clocks, and Drag-Free Control", Astrophysics and Space Science Library, Vol. 349, Dittus, H.J.; Lammerzahl, C.;Turyshev, S. (Eds.), December 2007, Springer, ISBN: 978-3-540-34376-9
9. Nicolini, D., *LISA Pathfinder Field Emission Thruster System Development Program*, 30th International Electric Propulsion Conference, IEPC-2007-363, Florence, (2007)
10. Ceruti, L., and Nicolini, D., *Power Processing Control Units for FEEP Micro-Propulsion Subsystems*, International Astronautic Congress, Glasgow, (2008)

LISA Pathfinder: In-orbit experiments and characterisation

M. Hewitson for the LISA Pathfinder Collaboration[a]
Albert-Einstein-Institut, Max-Planck-Institut für Gravitationsphysik und Universität Hannover, Callinstr. 38, 30167 Hannover, Germany

The LISA Pathfinder (LPF) mission aims to demonstrate and characterise some of the key technologies needed for the space-borne gravitational wave observatory, LISA. On the one hand, we aim to show that a test-mass can be placed in free-fall at a level of $3 \times 10^{-14}\,\mathrm{m\,s^{-2}}/\sqrt{\mathrm{Hz}}$ at 1 mHz. On the other hand, in order to extrapolate the performance of the key technologies from LPF to LISA, we must develop a detailed and accurate model of the system. By characterising the instrument through a series of experiments, the noise in the system should be reduced to achieve the desired level of free-fall and a detailed physical model of the system can be developed. In this paper we describe the scope of the experiments that are planned for the mission operations phase.

1 Introduction

In order to do gravitational wave astronomy at frequencies below 1 Hz, it is desirable to go to space. To this end, the LISA mission[1] will put a large-scale gravitational wave observatory in a heliocentric orbit trailing the Earth. Such an ambitious mission will depend on a host of technologies including micro-Newton thrusters, gravitational reference sensors, precision interferometery, and drag-free control.

These technologies will be tested and characterised in the demonstrator mission LISA Pathfinder (LPF). The LISA Pathfinder satellite will carry two payloads. The first is a European system, the LISA Technology Package (LTP), which comprises a full optical and capacitive readout of the differential motion of two free-falling test-masses using micro-Newton thrusters to maintain a drag-free control of the SC with respect to one of the test-masses. The second is a NASA payload which utilises parts of the LTP together with alternative micro-Newton thrusters and an alternative drag-free control system. This paper will focus on the former, the LTP.

Further details of LPF and LTP are given in [2] and [3]. In short, LISA Pathfinder comprises two test masses and one spacecraft (SC). The first test mass (TM1) is placed in free-fall along the x-axis of the spacecraft. This means that no forces are applied between the SC and TM1 and as such the level of free-fall achieved will depend on the existence of any spurious forces in the system. The position of the SC with respect to TM1 is read-out using an interferometer. The measurement is used to drive micro-Newton thrusters so that the SC follows the motion of TM1. Since the thrusters are noisy, in order to estimate the residual forces acting on TM1 we need a quiet reference from which to measure. This is where the second test mass comes in. Using a second interferometer, the differential position of the two test masses is read-out and used to control the position of TM2 with respect to TM1 by applying forces to TM2 via

[a] http://www.rssd.esa.int/index.php?project=LISAPATHFINDER&page=Author_List

an electrostatic actuator. The bandwidth of this so-called suspension control is 1 mHz and the drag-free control has a band-width of around 100 mHz. A schematic of this control system is shown in Figure 1.

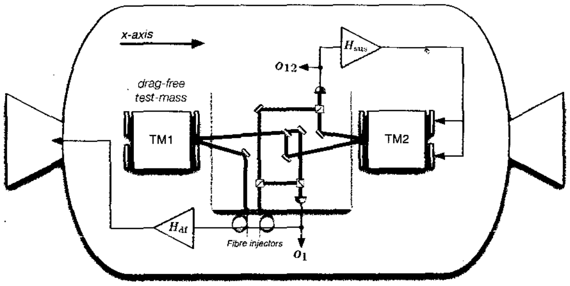

Figure 1: A schematic of the two x-axis control loops on LPF. The SC surrounds two test masses. The first test mass is in free fall and the SC is made to follow it by using the interferometric readout shown to control the force applied to SC by the thrusters. The second test mass is electrostatically suspended and made to follow TM1 using the differential interferometer measurement.

2 Characterisation of LPF

Characterisation of LPF has two aims. The first is to optimise the system so that the quietest possible free-fall of TM1 can be achieved. The second is to develop a detailed physical model of the system so that the performance of the different subsystems can be extrapolated to give an expected performance for LISA. Both of these aims require various physical parameters of the system to be estimated. For example, the precise behaviour of x-axis control loops described above will depend critically on any residual couplings in the system, such as the spring-like stiffness couplings between the TMs and the SC arising from the voltages applied in the electrostatic actuation scheme and imperfections in the gravitational balancing of the spacecraft as a whole. Such couplings, as well as actuator gains and system delays will need to be measured through a series of experiments. The typical way to identify such system parameters is to stimulate the system in such a way that the observed response depends on the parameter(s) of interest.

Measuring physical parameters of the system is only the first step in building a noise model of the entire system. Two other components are needed to complete the picture: estimates or models of any noise sources which may couple to the sensitive differential position measurement, and models or measurements of the transfer functions that describe the coupling of these noise sources to the observations. For some sources of noise we have various environmental and system monitors which will provide a wealth of data. For other noise sources, we will need to rely on ground measurements and/or models. The various couplings of the system will need to be modelled. Typically these models will be parametric and the determination of the parameter values will be done through dedicated experiments. In this way we aim to build up a full noise model of the system which should, when complete, explain the observed level of differential acceleration of the two TMs.

Clearly, the process of optimising the system to achieve the purest free-fall and of developing the physical model are fully entwined. The system model can be used to develop a noise budget for the differential measurement which in turn will identify the limiting noise sources which are disturbing the free-fall. Once identified, these noise sources have to be mitigated, either by suppressing the noise source (through optimisation of the responsible subsystem), or by reducing the coupling to the differential test mass motion. The design of the various experiments that will be carried out during the mission operations phase is critical to the success of this plan. As each experiment is performed, the data must be retrieved and analysed so that subsequent experiments can be optimised and performed in the optimal order.

3 Data flow and data analysis

As mentioned above, data from each experiment will be analysed as soon as it becomes available. It is expected that we will have contact with the SC for a few hours each day. As such, the experiments will be carried out in an automated fashion and the data for the experiments carried out on day N will be retrieved on day $N + 1$. The analysis of the data for day N must be completed before the end of day $N + 1$ so that the turn-around time for reconfiguring the mission time-line (and as such, the up-coming experiments) can be minimised.

In order to allow the mission scientists to analyse the data coming from the experiments, a robust and flexible data analysis infrastructure (The LISA Technology Package Data Analysis Toolbox) has been developed[4]. As well as providing a wealth of standard data analysis tools expected to be required for instrument characterisation, the toolbox will also contain LTP-specific high-level routines and algorithms to allow routine data analysis tasks common to multiple experiments to be performed in an efficient way. In addition, the data analysis procedures for all planned experiments will be developed and tested in advance under the LTPDA framework. One of the main features of this data analysis toolbox is the ability to inspect analysis results and to determine precisely what processing has been done to the original data. This is achieved using an object-oriented system where the result of any particular analysis is an object which comprises, not only the numerical results, but also a full history tree of the steps taken to arrive at that result. The reason for implementing such a scheme is to ensure that the results obtained during LPF can still be understood and reconstructed during the time of LISA, which will take place perhaps 1 decade after LPF.

4 System Identification and Modelling

Many of the experiments that will be carried out on LPF will be system identification experiments. Typically, by means of stimulating the system and observing the response, parameters of a system model can be determined. If the models are sufficiently detailed, these parameters will usually be closely, if not directly, related to actual physical parameters of the system. Figure 2 shows a schematic of a model of the x-axis dynamics of the system. Here we see the two control loops described earlier in this paper. The parameters of the system are shown in red. They are:

S_{21} The cross-talk of the interferometer due to the imperfect common-mode rejection arising from the geometry of the system. This parameter forms a coupling which allows the noise of the drag-free loop (essentially the thruster noise) to leak in to the sensitive differential measurement. This coupling is flat in frequency and its effect can be subtracted in data processing due to the fact that we have a very precise (pm resolution) measurement of the thruster noise via the first interferometer channel (o_1). In order to subtract the contribution, however, we need to determine/measure the coupling coefficient.

D_1 and D_2 The delay on the execution of commanded guidance signals on the drag-free and suspension loops respectively. These arise from the finite processing power available on-board the satellite. Depending on what else the main computer is doing, the command to start a signal injection may not be executed at exactly the requested time. As such we have some uncertainty as to when any stimulus is applied, and this needs to be identified for each experiment.

A_1 and A_2 An overall gain factor for the drag-free and suspension loops respectively. In practice, this will be dominated by uncertainty in the calibration of the actuators. Nonetheless, they need to be identified if we are to be able to correctly determine the acceleration of the SC and the differential acceleration of the two test-masses.

ω_1^2 and ω_2^2 The stiffness coefficients for the coupling of SC motion to the motions of TM1 and TM2 respectively. These parameters are particularly important in determining the characteristics of the loops at lower frequencies (1 mHz and below).

ω_{12}^2 The difference of the stiffness coefficients for the coupling of SC motion to the motions of TM1 and TM2. Although this is directly related to the two stiffness coefficients described above, it represents a different cross-coupling path which allows thruster noise to leak in to the sensitive differential measurement. This is a frequency dependent ($1/f^2$) coupling which produces a differential motion due to the fact that motion of the SC will result in different motions of the two test masses. It can be modelled (as shown here) as the motion of the SC relative to TM1 producing a spurious force on TM2 through this coupling constant.

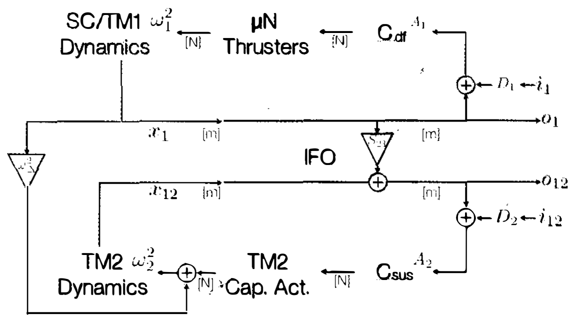

Figure 2: A model of the two x-axis control loops on LPF. The parameters of the model are shown in red. The physical units of the signals as they propagate around the loops are shown in blue. The observations are o_1 and o_{12} whereas the inputs to the system are labelled i_1 and i_{12}. The upper loop is the drag-free loop which uses the micro-Newton thrusters to force the SC to follow the motion of TM1. The lower loop, the suspension loop, uses the electrostatic actuators to control the distance between TM1 and TM2 at frequencies below 1 mHz.

Two experiments have been devised to allow the parameters above to be identified from measured data. These two experiments involve injecting a sequence of sinusoidal signals of increasing frequency firstly in to the guidance input of the drag-free loop (i_1) and then in to the guidance input of the suspension loop (i_{12}). Due to the cross-couplings in the system, these signals can also be observed in the output of the differential interferometer. A parametric model of the system is then fit to the data. We have explored a number of methods to to perform this fitting: linear least-squares, non-linear least-squares and Markov Chain Monte Carlo. Further details of these parameter estimation techniques can be found in [5,6,4].

Once the fit is performed, we can evaluate the goodness of the fit by forming the residuals. The fitted parameter values are used in the model to generate the predicted output signals in response to the injected signals. These predicted outputs can then be subtracted from the observed data. If the parameter estimation is perfect and the model is an accurate match to the true system, then the residuals will contain only noise. Assuming the system to be stationary, this noise can be compared to noise taken at a time when no signals were being injected. Figure 4 shows spectra of the residuals from one example experiment. The time-series data were produced

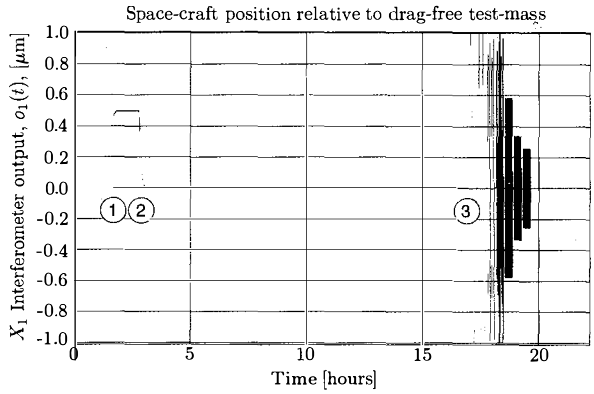

Figure 3: A time-series plot of the output of the interferometer which measures the position of the SC relative to TM1. The data is produced using the mission simulator. The plot shows three distinct phases: at 1) the interferometer is activated and starts to measure the relative position of the SC and TM1. At position 2) the control is switched from accelerometer mode (in which both test masses are electrostatically suspended) to the main science control mode in which the interferometric readout is fed back to the thrusters to make the SC follow TM1; at this point no control forces are applied to TM1 along the x-axis. At position 3) a sequence of sinusoidal injections starts.

using the mission simulator and fit using the three methods described above. The injections are the same as those shown in Figure 3. The injections are many orders of magnitude above the noise but we can see that only a small trace remains in the residuals at one of the injection frequencies. Since the residuals from each fitting method show similar results, the remaining trace amounts of signal are likely due to the model being not sufficiently accurate.

References

1. *Laser Interferometer Space Antenna: a cornerstone mission for the observation of gravitational waves*, P Bender *et al*, ESA-SCI(2000)11, 2000.
2. *LISA Pathfinder: mission and status*, P McNamara *et al*, 2011, Classical and Quantum Gravity, **28**, 094001.
3. *From laboratory experiments to LISA Pathfinder: achieving LISA geodesic motion*, S Vitale *et al*, 2011, Classical and Quantum Gravity, **28**, 094002.
4. *LISA Pathfinder data analysis*, M Hewitson *et al*, 2011, Classical and Quantum Gravity, **28**, 094006.
5. *Non-linear parameter estimation for the LTP experiment*, G Congedo *et al*, 2010, Journal of Physics: Conference Series, Proceedings of the 8th International LISA Symposium.
6. *Bayesian parameter estimation in the second LISA Pathfinder Mock Data Challenge*, M Nofrarias *et al*, 2010, Phys. Rev. D, **82**, 122002.

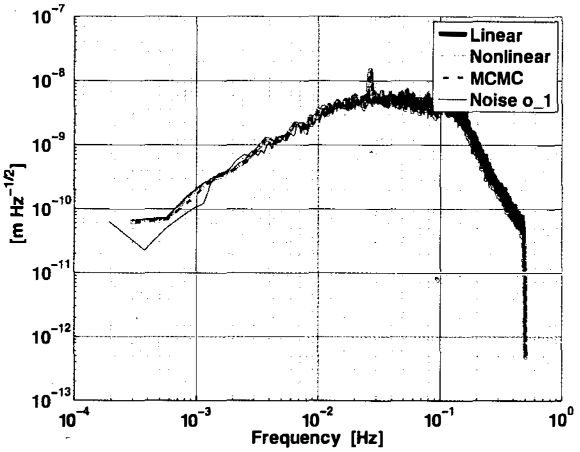

Figure 4: Spectra of the residuals formed by subtracting the predicted system outputs which are calculated by the model with the fitted parameters from the data from the mission simulator. Results are shown for three parameter estimation methods. Also shown is a noise spectrum taken from data at a time where no signals were being injected.

LISA Pathfinder: an experimental analysis of the LPF free-fall performance

William J. Weber on behalf of the LISA Pathfinder Collaboration[a]
Dipartimento di Fisica and INFN, Università di Trento,
Via Sommarive 14, 38123 Povo, Trento, Italy

The LISA gravitational wave observatory requires free-falling test masses that serve as references of geodesic motion to within a residual stray acceleration of 3 $\mathrm{fm/s^2}\ /\sqrt{\mathrm{Hz}}$ at frequencies above 0.1 mHz. The LISA Pathfinder (LPF) mission is dedicated to demonstrating the technology of free-falling test masses at a level close to the LISA goal. This article addresses the experimentally-based performance analysis for the LPF measurement of differential test mass acceleration noise, including a discussion of the applicability of the LPF results to the LISA mission.

1 Introduction

The primary science objective of the LISA Pathfinder (LPF) mission is demonstrating by direct measurement that two geodesic reference test masses (TM) can be placed in perfect free-fall to within a residual differential acceleration noise of 30 $\mathrm{fm/s^2}\ /\sqrt{\mathrm{Hz}}$ at frequencies down to 1 mHz[1]. Using the same TM, gravitational sensor (GRS), and local interferometer metrology hardware as for the proposed gravitational wave mission LISA, LPF is a testbed for most of the needed performance aboard LISA, where the target sensitivity requires free-falling test masses at the level of 3 $\mathrm{fm/s^2}\ /\sqrt{\mathrm{Hz}}$ acceleration relative to an inertial system at 0.1 mHz.

In the main LPF acceleration noise measurement[2], an optical interferometer measures the relative acceleration of two free-falling TM. One TM is used as a "drag-free" reference to control the translation and attitude of the satellite, and the other (TM2) is electrostatically forced to maintain constant separation from the first TM. The measurement and subsequent analysis are designed to measure the stray forces acting on the TM in conditions as close as possible to those relevant to the LISA TM. The TM2 electrostatic suspension introduces additional force noise. This suspension is not needed for LISA – it is necessitated here by the LPF single spacecraft configuration – and as such the mission also foresees a dedicated free-fall "drift mode" test [3] where the electrostatic suspension is turned off for the sensitive X axis, to allow measurement of TM acceleration noise in the absence of electrostatic actuation, as is most relevant for LISA.

Preparation for LPF hinges on an analysis of all sources of TM acceleration noise and metrology noise, but also on an aggressive laboratory campaign for directly measuring the performance with prototype flight hardware. This short paper summarizes the noise budget for the LPF measurement of stray TM acceleration, and its application to the performance for LISA. A detailed analysis of the LISA Pathfinder noise performance and the experimental background for the predictions for the various noise sources can be found in Ref. [4].

[a] Full author list available at http://www.rssd.esa.int/index.php?project=LISAPATHFINDER&page=Author_List

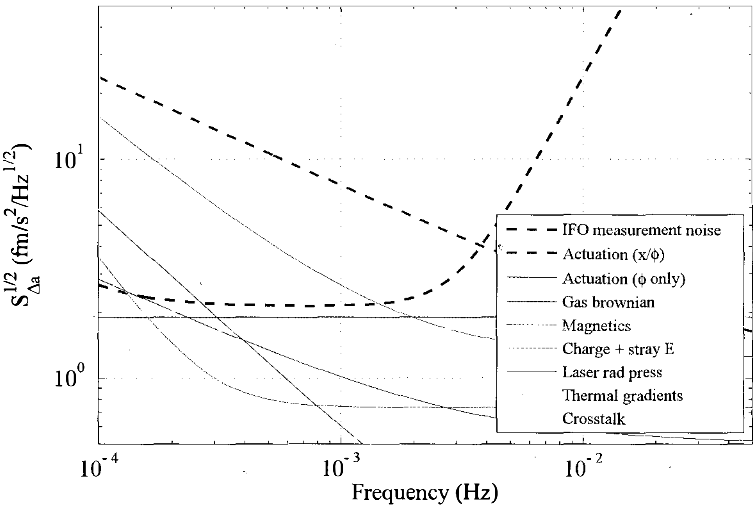

Figure 1: Estimate of differential acceleration noise sources for LISA Pathfinder. The thicker dashed lines correspond to instrumental noise from the interferometry readout and X axis actuation, while the remaining lines are sources of stray TM acceleration that are relevant to the LISA acceleration noise budget.

2 LPF performance analysis

Viewing LPF as a differential accelerometer for measuring stray TM acceleration for LISA, the various stray force contributions are the LPF "science sources," measured against a background of instrumental noise. The leading acceleration noise sources are shown in Figure 1 as thin lines, with the two dominant instrumental contributions, from the interferometer metrology and from fluctuating actuation forces, as thicker dashed lines.

The interferometry (IFO) limit, shown as a black dashed line, corresponds to the design specification of 6 pm $/\sqrt{\mathrm{Hz}}$, relaxed as f^{-2} in linear spectral density below 3 mHz, converted into acceleration. This performance has been demonstrated with prototype flight optical bench, laser, and phasemeter hardware at all frequencies above 1 mHz [5], with current lower frequency data reflecting harsh laboratory environmental conditions and, even so, with a possible impact on the LPF performance only below 0.2 mHz.

Noise from the TM2 X axis actuation (blue dashed line) should exceed the IFO noise at frequencies below 5 mHz. This is estimated by direct measurements of fluctuations in the flight electronics actuation circuitry and analysis of the spacecraft gravitational balancing, which sets the required force levels. This noise source, however, is not relevant to LISA and can be removed in the dedicated free-fall test, leaving a much lower noise contribution from the need to electrostatically control the TM rotation, as envisioned for LISA.

For the remaining acceleration noise sources, the Brownian gas damping, electrostatic forces from charge and stray field fluctuations, laser radiation pressure fluctuations, and thermal gradient related forces are all directly estimated from laboratory measurements with GRS and laser prototype hardware. The magnetic contribution, which is the dominant low frequency contribution in this analysis, is related to a number of parameters, with this calculation based on conservative estimates of the spacecraft AC magnetic environment and shielding, and to unexpectedly large measured values for the magnetic gradient (traced to a temperature sensor near the TM) and for the Au-Pt TM magnetic susceptibility. As such, the magnetic noise represents

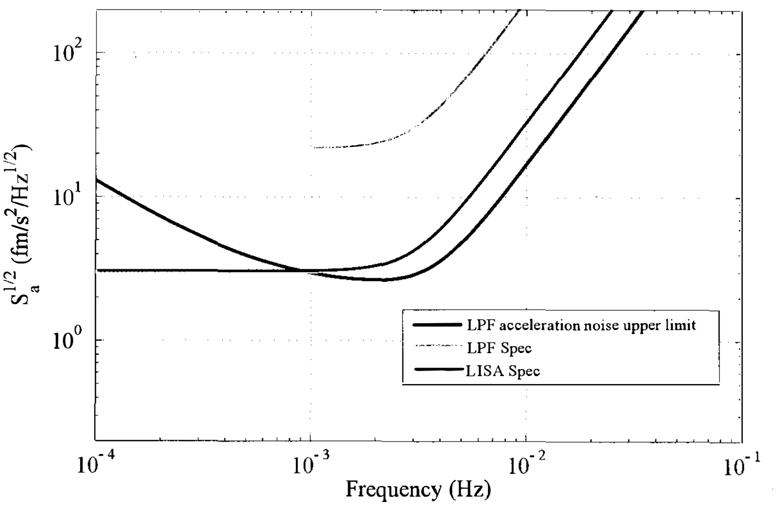

Figure 2: Prediction for the LISA single test mass acceleration noise limit that will be provided by LISA Pathfinder in the dedicated free-fall test without X actuation, compared with the LPF and LISA design goals.

an upper limit that can be significantly and relatively easily improved for LISA.

We note that the gas damping noise estimate has been lowered relative to that in Ref. [4] in accord with recent planned improvements in the vacuum system, which will now be vented directly to space, with a conservatively estimated maximum gas pressure of 2 μPa. This makes a noticeable improvement in the predicted overall LPF noise performance at frequencies around 1 mHz, where gas damping noise was expected to dominate.

3 Applicability for LISA

The LPF result can be taken as a global acceleration noise upper limit for LISA. A prediction for this upper limit is performed in Fig. 2. We have considered the sum of the noise power from the LPF acceleration noise sources in Fig. 1, including the interferometer and excluding the X axis actuation (ie, the projection for the dedicated free-fall "drift mode" experiment). We have also divided the LPF differential noise power by two, to compare with the single TM requirement for LISA.

Taken as an overall upper limit to TM acceleration noise – a model-independent limit that also includes possible noise sources that have not yet been identified – achieving this acceleration noise curve would verify the LISA performance goal down to 1 mHz, with an excess of only a factor 4 in linear spectral density at 0.1 mHz. This is more than sufficient to guarantee a rich observational astrophysics return from the LISA gravitational wave observatory.

A final consideration on the scientific return of LISA Pathfinder and its applicability to LISA regards the possibility to solidify the physical model of acceleration noise for various known noise sources, to levels even below the LISA goals. A number of dedicated measurements will target known sources of disturbance, measuring key parameters that can only be accessed in orbit. In closing, we note several noise sources for which the LPF flight test will provide a unique test bed for establishing free-fall for gravitational wave astronomy:

- *Gravitational self balancing* LPF will provide a test of the sub-nm/s^2 and 10 nrad/s^2 analysis and compensation of the translational and rotational spacecraft-generated gravitational accelerations that is required, to limit actuation-related noise, for both LPF and LISA. This information will be obtained from the DC levels of actuation needed in flight, for three translational and six rotational degrees of freedom, and will be the first verification of the detailed design and analysis of the LPF spacecraft self-gravity.

- *Test mass charging and charge fluctuations* LPF will measure TM charging from cosmic ray and solar particles, both the deterministic charging and, in dedicated long term high precision measurements, the low frequency stochastic fluctuations relevant for producing low frequency force noise in the presence of a steady stray electrostatic field. Also, LPF will test both the TM discharge system and techniques for measuring and compensating stray fields.

- *Spacecraft thermal environment* With an array of thermometers, LPF will monitor the thermal environment around the TM at the 10 μK resolution[6]. In addition to use in possible correlations with force noise – through the thermal gradient coupling with the radiometric, radiation pressure and outgassing effects – the measurements will allow a real verification of the thermal model for a LISA-like satellite across the LISA band. A similar characterization should be possible for the magnetic environment and fluctuations onboard the satellite[7].

References

1. M Armani *et al*, *Class. Quantum Grav.* **26**, 094001 (2009).
2. D Bortoluzzi *et al*, *Class. Quantum Grav.* **21**, S573 (2004).
3. A Grynagier *et al*, *Class. Quantum Grav.* **26**, 094007 (2009).
4. F Antonucci *et al*, *Class. Quantum Grav.* **28**, 094002 (2011).
5. F Antonucci *et al*, *Class. Quantum Grav.* **28**, 094003 (2011).
6. P Canizares *et al*, *Class. Quantum Grav.* **28**, 094004 (2011).
7. M Diaz-Aguiló, E García-Berro and A Lobo, *Class. Quantum Grav.* **27**, 035005 (2010).

Search for GWs from white dwarf binaries in Mock LISA Data Challenge data

S. Babak
Albert Einstein Institute, Golm, Am Muchlenberg 1, D-14476 Golm bei Potsdam, Germany

A. Błaut
Institute of Theoretical Physics, University of Wrocław, Pl.Maxa Borna 9, Pl-50-204 Wrocław, Poland

A. Królak
Institute of Mathematics, Polish Academy of Sciences, Warsaw, Poland

Methods and results of the analysis of the simulated data of the proposed gravitational wave detector LISA for the case of white dwarf binaries are presented. The simulated data are produced by the Mock LISA Data Challenge project. Our method is based on maximum likelihood method and uses the popular $\mathcal{F}$-statistic that is applied in the analysis of ground gravitational wave detector data. We show that the LISA detector has the potential do identify over ten thousand of white dwarf binary systems in our Galaxy.

1 Introduction

LISA is a laser interferometric detector of gravitational waves in the orbit around the Sun trailing the Earth by 20 degrees. LISA was planned to be launched in the next decade as a joint ESA and NASA project. The bandwidth of the LISA detector is from 0.1 mHz to 100 mHz. In this band LISA could observe gravitational radiation originating from compact white dwarf binaries, coalescence of massive black hole binaries, inspirals of stelar mass compact stars into massive black holes and gravitational wave stochastic background from the early Universe.

The Mock LISA Data Challenges (MLDC) were initiated by the LISA International Science Team (LIST) at the end of 2005. A taskforce exists which decides on the severity of the challenge, the types and number of sources etc. and also conducts the analysis of entries at the end of each challenge. A challenge data set is regularly issued with a deadline ranging from six to twelve months. These challenges are open to everyone within the GW community, and allow the community to simulate a realistic data analysis effort where the number of input sources and parameters are relatively unknown.

We shall present data analysis methods to detect signals and estimate parameters for white dwarf binaries in MLDC data sets. This is a particularly challenging task because the number of such signals so large that the signals interfere and the problem of signal resolution arises.

2 Gravitational waves from compact white dwarf binaries

In the LISA frequency band we expect around 6×10^7 compact white dwarf binaries. The expected number of binaries below 3 mHz is so large that they are not individually resolvable (except for the brightest ones) and form a stochastic background which dominates over the instrumental noise above 0.1 mHz. It is expected that above 3mHz all the statistically significant white dwarf binary signals are resolvable.

There are two major types of white dwarf binaries:

(i) Detached, separated white-dwarf/white-dwarf binaries whose evolution is driven by radiation reaction. They are the end points of many binary evolution scenarios. The gravitational wave carry information about the mass of the binary and the distance.

(ii) Interacting binaries. Those are close systems with a significant tidal interaction and/or with the Roche lobe overflow. In those systems the gravitational radiation reaction competes against mass transfer and the orbital period can either increase or decrease.

3 Detection gravitational waves signals from compact binaries and estimation of their parameters

The response of the LISA detector to a gravitational wave (GW) signal from a binary system is given by a linear combination of the four time-dependent functions $h^{(k)}(t)$.

$$s(t) = \sum_{k=1}^{4} a^{(k)} h^{(k)}(t), \tag{1}$$

where $a^{(k)}$ are 4 constant amplitudes. The functions $h^{(k)}(t)$ are periodic functions of gravitational wave frequency ω with complicated amplitude and phase modulations[3,5]. The phase modulation function $\phi(t)$ is given by

$$\phi(t) = \omega t + \frac{1}{2}\dot{\omega}t^2 + (\omega + \dot{\omega}t)\, R\cos\beta\cos(\Omega t + \eta_o - \lambda), \tag{2}$$

where β is the ecliptic latitude of the source, λ is the ecliptic longitude of the source, $\Omega = 2\pi/1\text{year}$, η_o is the position of the constellation on the orbit around the Sun at time $t = 0$, and R is 1 astronomical unit. The parameter $\dot{\omega}$ is the frequency drift which may occur either due to the gravitational radiation reaction or as a result of the tidal interaction between the components of the binary system. In the case of a detached binary system evolving only due to the gravitational radiation reaction the frequency drift $\dot{\omega}$ is approximately given by[3]

$$\dot{\omega} = \frac{48}{5}\left(\frac{\mathcal{M}_c}{2}\right)^{5/3} \omega^{11/3}, \tag{3}$$

where $\mathcal{M}_c = m_1^{3/5} m_2^{3/5}/(m_1 + m_2)^{1/5}$ is the chirp mass (m_1 and m_2 are the individual masses of the components of the binary).

In order to detect the signal $s(t)$ above in LISA data x we apply the maximum likelihood method in the form of $\mathcal{F}$-statistic[1,3,2]. The $\mathcal{F}$-statistic is the reduced form of maximum likelihood function where amplitude parameters $a^{(k)}$ are eliminated:

$$\mathcal{F} = \frac{T_o}{S_o} \sum_{l=1}^{4} \sum_{k=1}^{4} (M^{-1})^{(l)(k)} N^{(l)} N^{(k)}, \tag{4}$$

where

$$M^{(l)(k)} = \langle h^{(k)}\, h^{(l)} \rangle, \tag{5}$$
$$N^{(l)} = \langle x\, h^{(l)} \rangle. \tag{6}$$

T_o is the observation time and S_o is the spectral density of noise at frequency ω. The time-averaging operator $\langle\cdot\rangle$ is defined by

$$\langle g \rangle := \frac{1}{T_o}\int_0^{T_o} g(t)\, dt. \tag{7}$$

In our entries for MLDC we have used the following procedure to extract GW signals from white-dwarf/white-dwarf binaries. We search the band from frequency $f = 0.1$ mHz to frequency 12 mHz where $f = \omega/2\pi$. We divide the data into bands of 0.1 mHz each. We include in our search the frequency drift parameter $\dot{\omega}$ above 3mHz. In each band we search for the signals calculating the $\mathcal{F}$-statistic over an optimal constrained grid [5]. The constraint in the grid is such that its nodes coincide with Fourier frequencies what enables application of the FFT algorithm in $\mathcal{F}$-statistic computation. We select the signal having the largest value of the $\mathcal{F}$-statistic over the grid and we apply the fine search based on the Nelder-Mead algorithm with the initial values provided by that signal's parameters. We reconstruct the signal in the time domain and remove it from the data. We then search for the next strongest signal and so on until the signal-to-noise ratio (SNR) of the detected signal falls below a certain threshold.

4 Mock LISA data challenge results

We have applied the method presented in Section 3 to MLDC round 3 challenge data [4,5]. As a result we have detected and estimated accurately parameters of 12805 signals out of total of 40628 signals present in the band from $f = 0.1$ mHz to 12 mHz that we have searched. Here we present results of the analysis of MLDC3 data set after a number of improvements that we have introduced after our first analysis. One important improvement involved increase of the overlap between the narrow bands that we search. As a result of these improvements the number of resolved signals increased to 15824. In Figure 1 we present the number of signals resolved as a function of frequency for our original and improved analysis. In Figure 2 we show how

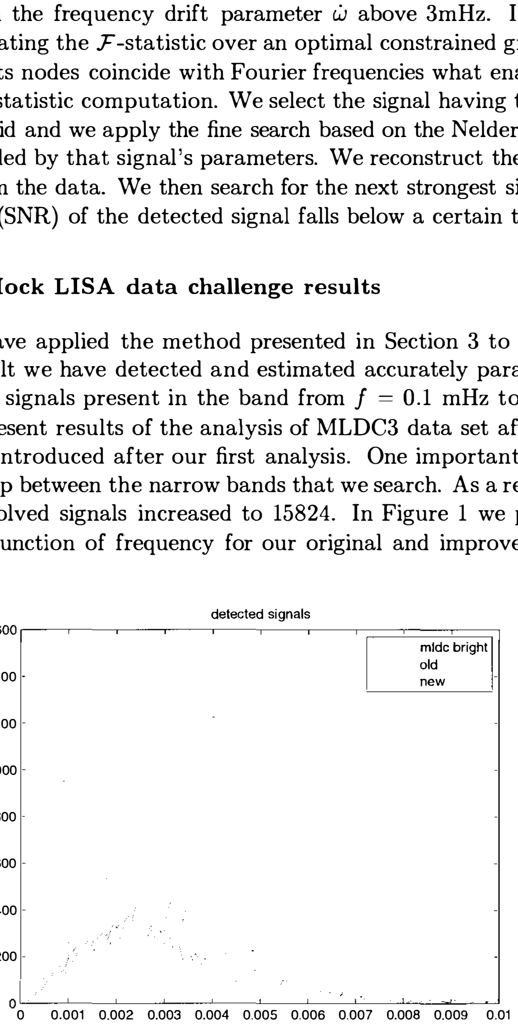

Figure 1: Number of signals detected by our search method as a function of frequency: *mldc bright* denotes the distribution of the signal present, *old* signals recovered originally, *mldc new* signals recovered by the improved method.

accurately we estimate parameters of the resolved signals. We present again comparison of the original and improved analysis. We see that on the average we estimate the frequency within a fraction of a bin, where one bin is 1 over the observation time T_o ($T_o = 2$ years for MLDC3 data) and we estimate position angles of the source within a fraction of a degree.

Our results compare well with other methods that were used to analyse white dwarf binaries signals. The best method so far - Block Annealed Metropolis-Hastings (BAM) algorithm [6] yielded 19324 resolved signal.

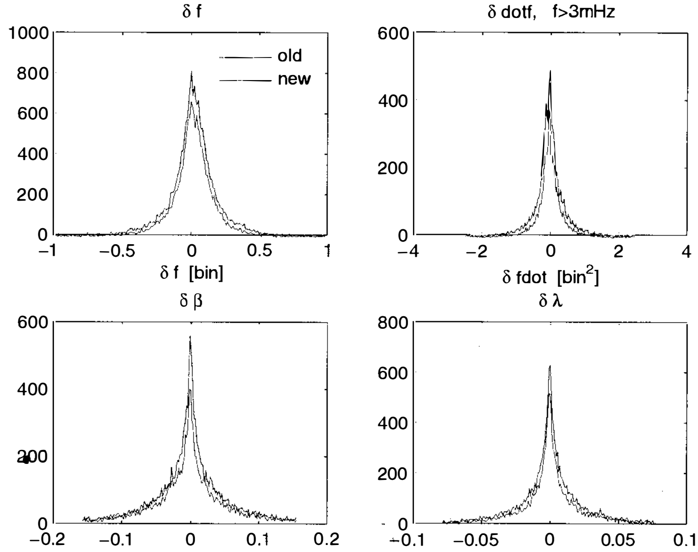

Figure 2: Accuracy of parameter estimation. The top two panels are errors in estimation of frequency and frequency derivative and the bottom two are errors in ecliptic latitude β and ecliptic longitude λ.

Acknowledgments

The work of A.B. and A.K. was supported in part by MNiSW grant no. N N203 387237. S.B was supported in part by DFG grant SFB/TR 7 "Gravitational Wave Astronomy" and by DLR (Deutsches Zentrum für Luft- und Raumfahrt).

References

1. P. Jaranowski, A. Królak, and B. F. Schutz, *Phys. Rev.* D **58**, 063001 (1998).
2. P. Jaranowski and A. Królak, *Analysis of Gravitational-Wave Data* (Cambridge University Press, Cambridge, 2009).
3. A. Królak, M. Tinto, and M. Vallisneri, *Phys. Rev.* D **70**, 022003 (2004); *Phys. Rev.* D **76**, 069901(E) (2007).
4. S. Babak et al, Class.Quant.Grav. **27**, 84009 (2010).
5. A. Błaut, S. Babak, A. Królak, *Phys. Rev.* D **82**, 022005 (2010).
6. J. Crowder, Class.Quant.Grav. **24**, S575 (2007).

5.
Advanced Detectors

Advanced Virgo

T. Accadia[1], F. Acernese[2ac], P. Astone[3a], G. Ballardin[4], F. Barone[2ac], M. Barsuglia[5], A. Basti[6ab], Th. S. Bauer[7a], M. Bebronne[1], M. Bejger[8c], M.G. Beker[7a], A. Belletoile[1], M. Bitossi[6a], M. A. Bizouard[9a], M. Blom[7a], F. Bondu[10b], L. Bonelli[6ab], R. Bonnand[11], V. Boschi[6a], L. Bosi[12a], B. Bouhou[5], S. Braccini[6a], C. Bradaschia[6a], M. Branchesi[13ab], T. Briant[14], A. Brillet[10a], V. Brisson[9a], T. Bulik[8b], H. J. Bulten[7ab], D. Buskulic[1], C. Buy[5], G. Cagnoli[13a], E. Calloni[2ab], B. Canuel[4], F. Carbognani[4], F. Cavalier[9a], R. Cavalieri[4], G. Cella[6a], E. Cesarini[13b], O. Chaibi[10a], E. Chassande-Mottin[5], A. Chincarini[15], A. Chiummo[4], F. Cleva[10a], E. Coccia[16ab], P.-F. Cohadon[14], C. N. Colacino[6ab], J. Colas[4], A. Colla[3ab], M. Colombini[3b], A. Conte[3ab], J.-P. Coulon[10a], E. Cuoco[4], S. D'Antonio[16a], V. Dattilo[4], M. Davier[9a], R. Day[4], R. De Rosa[2ab], G. Debreczeni[17], W. Del Pozzo[7a], M. del Prete[18b], L. Di Fiore[2a], A. Di Lieto[6ab], M. Di Paolo Emilio[16ac], A. Di Virgilio[6a], A. Dietz[1], M. Drago[18ab], G. Endrőczi[17], V. Fafone[16ab], I. Ferrante[6ab], F. Fidecaro[6ab], I. Fiori[4], R. Flaminio[11], L. A. Forte[2a], J.-D. Fournier[10a], J. Franc[11], S. Frasca[3ab], F. Frasconi[6a], M. Galimberti[11], L. Gammaitoni[12ab], F. Garufi[2ab], M. E. Gáspár[17], G. Gemme[15], E. Genin[4], A. Gennai[6a], A. Giazotto[6a], R. Gouaty[1], M. Granata[5], C. Greverie[10a], G. M. Guidi[13ab], J.-F. Hayau[10b], A. Heidmann[14], H. Heitmann[10], P. Hello[9a], P. Jaranowski[8d], I. Kowalska[8b], A. Królak[8ae], N. Leroy[9a], N. Letendre[1], T. G. F. Li[7a], N. Liguori[18ab], M. Lorenzini[13a], V. Loriette[9b], G. Losurdo[13a], E. Majorana[3a], I. Maksimovic[9b], N. Man[10a], M. Mantovani[6ac], F. Marchesoni[12a], F. Marion[1], J. Marque[4], F. Martelli[13ab], A. Masserot[1], C. Michel[11], L. Milano[2ab], Y. Minenkov[16a], M. Mohan[4], N. Morgado[11], A. Morgia[16ab], B. Mours[1], L. Naticchioni[3ab], F. Nocera[4], G. Pagliaroli[16ac], L. Palladino[16ac], C. Palomba[3a], F. Paoletti[6a,4], M. Parisi[2ab], A. Pasqualetti[4], R. Passaquieti[6ab], D. Passuello[6a], G. Persichetti[2ab], F. Piergiovanni[13ab], M. Pietka[8d], L. Pinard[11], R. Poggiani[6ab], M. Prato[15], G. A. Prodi[18ab], M. Punturo[12a], P. Puppo[3a], D. S. Rabeling[7ab], I. Rácz[17], P. Rapagnani[3ab], V. Re[16ab], T. Regimbau[10a], F. Ricci[3ab], F. Robinet[9a], A. Rocchi[16a], L. Rolland[1], R. Romano[2ac], D. Rosińska[8cf], P. Ruggi[4], B. Sassolas[11], D. Sentenac[4], L. Sperandio[16ab], R. Sturani[13ab], B. Swinkels[4], M. Tacca[4], L. Taffarello[18c], A. Toncelli[6ab], M. Tonelli[6ab], O. Torre[6ac], E. Tournefier[1], F. Travasso[12ab], G. Vajente[6ab], J. F. J. van den Brand[7ab], C. Van Den Broeck[7a], S. van der Putten[7a], M. Vasuth[17], M. Vavoulidis[9a], G. Vedovato[18c], D. Verkindt[1], F. Vetrano[13ab], A. Viceré[13ab], J.-Y. Vinet[10a], S. Vitale[7a], H. Vocca[12a], R. L. Ward[5], M. Was[9a], K. Yamamoto[18bd], M. Yvert[1], A. Zadrożny[8e], J.-P. Zendri[18c]

[1]*Laboratoire d'Annecy-le-Vieux de Physique des Particules (LAPP), Université de Savoie, CNRS/IN2P3, F-74941 Annecy-Le-Vieux, France*

[2]*INFN, Sezione di Napoli [a]; Università di Napoli 'Federico II [b] Complesso Universitario di Monte S.Angelo, I-80126 Napoli; Università di Salerno, Fisciano, I-84084 Salerno[c], Italy*

[3]*INFN, Sezione di Roma[a]; Università 'La Sapienza [b], I-00185 Roma, Italy*

[4]*European Gravitational Observatory (EGO), I-56021 Cascina (PI), Italy*

[5]*Laboratoire AstroParticule et Cosmologie (APC) Université Paris Diderot, CNRS: IN2P3, CEA: DSM/IRFU, Observatoire de Paris, 10 rue A.Domon et L.Duquet, 75013 Paris - France*

[6]*INFN, Sezione di Pisa[a]; Università di Pisa[b]; I-56127 Pisa; Università di Siena, I-53100 Siena[c], Italy*

[7]Nikhef, Science Park, Amsterdam, the Netherlands[a]; VU University Amsterdam, De Boelelaan 1081, 1081 HV Amsterdam, the Netherlands[b]

[8]IM-PAN 00-956 Warsaw[a]; Astronomical Observatory Warsaw University 00-478 Warsaw[b]; CAMK-PAN 00-716 Warsaw[c]; Bialystok University 15-424 Bialystok[d]; IPJ 05-400 Świerk-Otwock[e]; Institute of Astronomy 65-265 Zielona Góra[f], Poland

[9]LAL, Université Paris-Sud, IN2P3/CNRS, F-91898 Orsay[a]; ESPCI, CNRS, F-75005 Paris[b], France

[10]Université Nice-Sophia-Antipolis, CNRS, Observatoire de la Côte d'Azur, F-06304 Nice[a]; Institut de Physique de Rennes, CNRS, Université de Rennes 1, 35042 Rennes[b], France

[11]Laboratoire des Matériaux Avancés (LMA), IN2P3/CNRS, F-69622 Villeurbanne, Lyon, France

[12]INFN, Sezione di Perugia[a]; Università di Perugia[b], I-06123 Perugia, Italy

[13]INFN, Sezione di Firenze, I-50019 Sesto Fiorentino[a]; Università degli Studi di Urbino 'Carlo Bo', I-61029 Urbino[b], Italy

[14]Laboratoire Kastler Brossel, ENS, CNRS, UPMC, Université Pierre et Marie Curie, 4 Place Jussieu, F-75005 Paris, France

[15]INFN, Sezione di Genova; I-16146 Genova, Italy

[16]INFN, Sezione di Roma Tor Vergata[a]; Università di Roma Tor Vergata, I-00133 Roma[b]; Università dell'Aquila, I-67100 L'Aquila[c], Italy

[17]RMKI, H-1121 Budapest, Konkoly Thege Miklós út 29-33, Hungary

[18]INFN, Gruppo Collegato di Trento[a] and Università di Trento[b], I-38050 Povo, Trento, Italy; INFN, Sezione di Padova[c] and Università di Padova[d], I-35131 Padova, Italy

The Virgo interferometer, a detector for gravitational waves located near Pisa in Italy, will soon be upgraded to become the next-generation detector Advanced Virgo. Advanced Virgo will be approximately ten times more sensitive than Virgo, with a design strain sensitivity better than $10^{-23}/\sqrt{\text{Hz}}$ near 100 Hz. This is expected to enable regular detections of gravitational waves and to yield significant astrophysical results. Many of the components of the detector will be changed for this upgrade. These changes include new core optics, a more powerful laser system, the signal-recycling technique, the use of homodyne detection at the output port, and an improvement of the vacuum system. The existing seismic isolation system in Virgo will be re-used. Advanced Virgo will form part of a global network of advanced gravitational wave detectors along with Advanced LIGO, GEO HF, and LCGT.

1 Introduction

Interferometric gravitational wave (GW) detectors of the first generation (Virgo[1], LIGO[2], GEO600[3]) have successfully completed their first long-duration data taking runs and are installing significant upgrades. Advanced Virgo is the project to upgrade the Virgo detector to a second generation instrument. Even though it will be hosted in the same infrastructures as Virgo, the Advanced Virgo sensitivity will be better by one order of magnitude over most of the detection band, and thus will increase by a factor of 1000 the accessible volume of the Universe when compared to initial Virgo. This paper provides a brief overview of the challenges that must be overcome to achieve this sensitivity increase, and the solutions designed to meet those challenges.

The Advanced Virgo detector will be based on the same basic principles of the Virgo detector, an electromagnetically coupled broadband gravitational wave antenna based on a Michelson interferometer with Fabry-Pérot cavities in the arms (cf. figure 1). The seismic isolation system

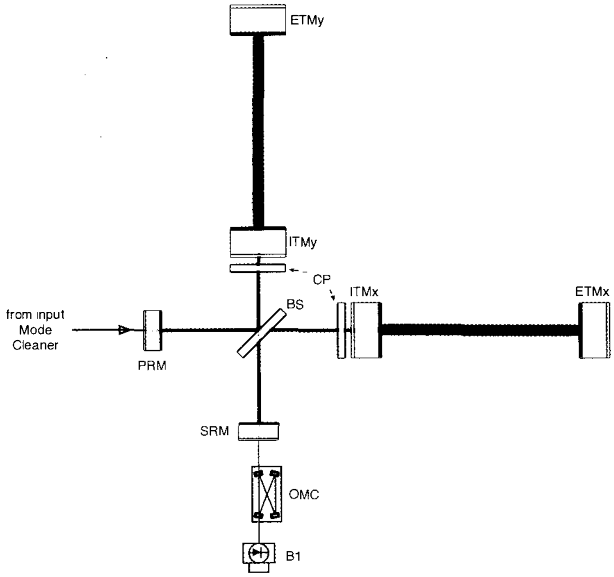

Figure 1: Optical layout of the Advanced Virgo interferometer. The input (ITM) and end (ETM) test mass mirrors are 42 kg and 35 cm in diameter. The beamsplitter (BS) is 55 cm in diameter. The interferometer has both power (PRM) and signal (SRM) recycling mirrors, the 3 km arm cavities are bi-concave, and thermal compensation plates (CP) are located between the ITMs and the BS.

(the superattenuator, cf. figure 2), will remain the same, as it already meets the requirements for Advanced Virgo[4].

Advanced Virgo will form part of a worldwide network of interferometric gravitational wave detectors, along with Advanced LIGO[5], LCGT[6], and GEO600[7], with all the detectors operating in coincidence, having comparable sensitivities, and co-operating on analysis of data. The expected event rate for the network for neutron star-neutron star inspiral and mergers will be around 40 events per year[8].

2 The path to Advanced Virgo

Figure 3 shows the expected (design) sensitivity curves of Virgo and Advanced Virgo, with contributions from several important noise sources. Each of the noise sources in Virgo that are larger than the designed Advanced Virgo sensitivity must be lowered, and we will briefly describe the technologies used to achieve this for each noise source.

3 Suspension thermal noise

At low frequencies (below 40 Hz) the Virgo sensitivity was limited by suspension thermal noise (shown in violet traces in figure 3), which arises from mechanical losses in the suspension wires[10]; the relationship between the mechanical losses and the thermal noise is given by the fluctuation-dissipation theorem. This noise will be reduced in Advanced Virgo by using so-called monolithic suspensions[11], where the optics are suspended by fused silica fibers rather than the steel wires used in Virgo. Much of the technology for these monolithic suspensions, including the pulling and bonding of the fused silica fibers, has already been demonstrated in Virgo+MS (Virgo+ with monolithic suspensions), an intermediate upgrade of the Virgo detector that is currently

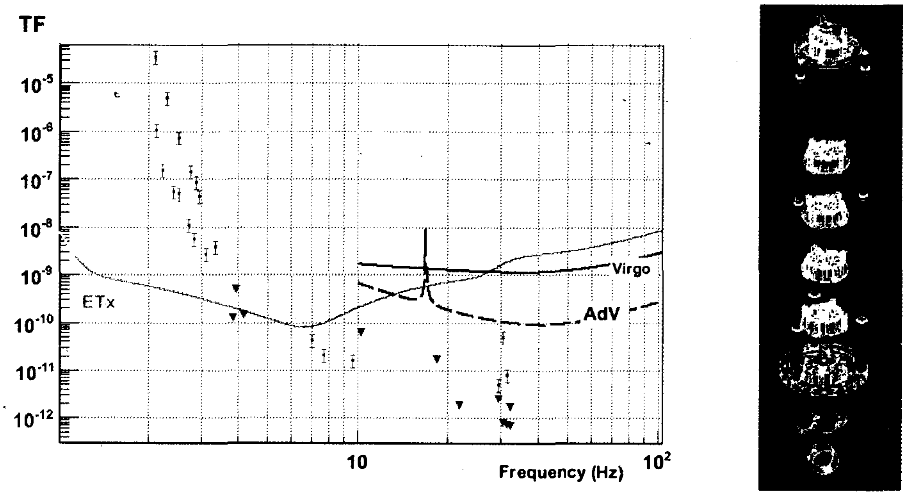

Figure 2: The superattenuator system employed in Virgo already meets the seismic isolation requirements for Advanced Virgo. On the left are measured upper limits on the seismic isolation transfer function of a superattenuator, shown with Virgo, Advanced Virgo, and Einstein Telescope[9] requirements. On the right is a rendering of a superattenuator.

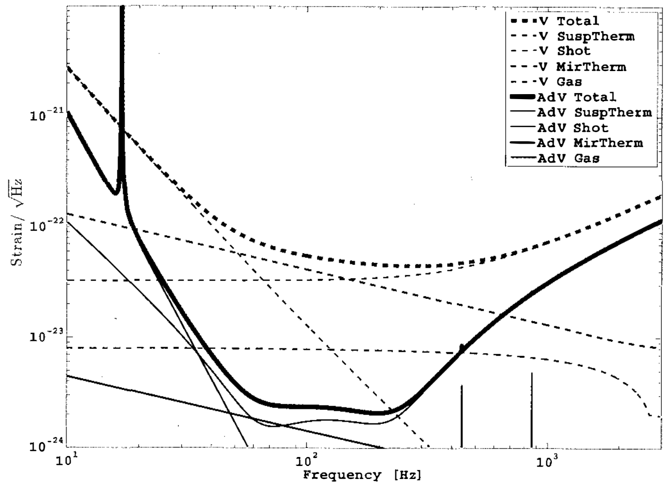

Figure 3: A comparison of the expected Virgo (dashed lines) and Advanced Virgo (solid lines) design sensitivities (in blue), shown as a strain-equivalent amplitude noise spectral density; contributions to the total noise from various specific noise sources are also shown . The noise contributions to the Virgo sensitivity which lie above the Advanced Virgo sensitivity are the principal targets of the upgrade technologies.

taking data with a modestly increased sensitivity compared to Virgo. The fibers themselves have an optimized geometry, with thick end points and a thinner middle section (approximately 300 μm in diameter), to minimize the thermal noise for a given maximum tensile load. Figure 4 shows a side view of a monolithic suspension from Virgo+MS, where the fiber thickness profile can be seen.

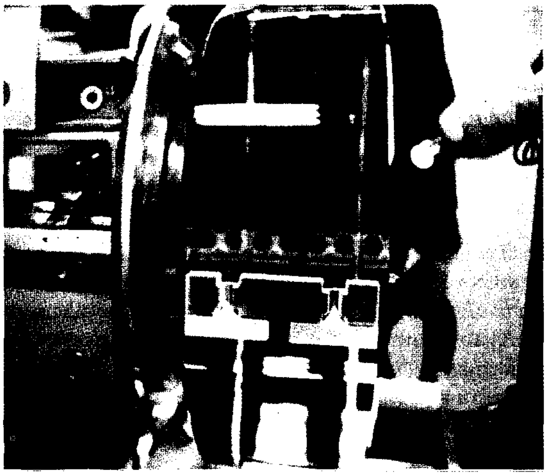

Figure 4: Side view of a monolithic suspension used in Virgo+MS. The pair of fused silica fibers used to suspend this mirror can be seen, along with the mechanism to attach the fibers to the test mass. In Advanced Virgo the test masses will be the same diameter (35 cm) but twice as thick: 20 cm instead of 10 cm.

The suspension thermal noise is also reduced by having heavier test masses, which for Advanced Virgo are 42 kg, twice as much as in Virgo and Virgo+MS. Further significant increases in this mass are limited by the weight carrying capacity of the superattenuator, which will remain unchanged.

For Advanced Virgo, the complete suspension design must be further upgraded to accommodate the thermal compensation plates (cf. figure 1 and section 5.1) which will be suspended from the same superattenuators as the input mirrors, while maintaining the superior thermal noise performance.

4 Mirror thermal noise

In the middle of the detection band, both Virgo and Advanced Virgo are limited by the mirror thermal noise (shown in black traces in figure 3) which arises due to thermal fluctuations of either the substrate or the multi-layer dielectric coating. Mirror thermal noise can be combatted with a combination of higher quality, lower loss materials for the mirror components, which directly reduces the thermal noise in the detection band, and with larger beam sizes, which average more of the fluctuating mirror surface and thus reduce their impact on the detector sensitivity. Both of these techniques will be used in Advanced Virgo, which will use lower loss materials and have larger beams than Virgo.

4.1 Beam size

In Advanced Virgo the beam size on the arm cavity end mirrors (ETM) will be approximately 6 cm (radius to $1/e^2$ in intensity) and on the arm cavity input mirrors (and thus also the beamsplitter) it will be approximately 5 cm. The beam waist size is less than 1 cm, located near the midpoint of the arm cavities. This is in contrast to Virgo, where the beam size on the end mirror was 5 cm and on the input mirror it was 2 cm, with the waist at the input mirror.

4.2 Substrate thermal noise

Mechanical losses in the substrate material determine the quality factor of mechanical resonances, and this determines the level of broadband thermal noise arising from the substrate. Virgo was limited by thermal noise in the mirror substrates. For Advanced Virgo, a higher quality of fused silica with lower mechanical losses will be used for the test mass substrates, and thermal noise from the substrates should no longer be a limiting noise source.

4.3 Coating thermal noise

The mechanical losses in the dielectric coating (alternating layers of silica and tantala) determine the quality factor of the mirror and as a consequence the displacement of the mirror surface due to its thermal vibration[12]. A research program has been undertaken at the *Laboratoire des Matériaux Avancés* (LMA) to improve the mechanical performances of these coatings without degrading the optical performances, by studying the properties of dielectric coatings composed of differing materials and constructed with varying recipes. Titanium doped SiO_2/Ta_2O_5 coatings developed at LMA are the best solution known so far[13], and are currently the baseline solution for Advanced Virgo.

5 Quantum noise

In laser interferometric gravitational wave detectors, only the quantum noise of the light (shot noise and radiation pressure noise, both of which arise from the particle nature of the laser light) is important, while the quantum noise of the masses is not significant. In Virgo, the only important quantum noise was the shot noise, which dominates above 200 Hz. In Advanced Virgo, which will operate with a signal recycling mirror, the distinction between shot noise and radiation pressure noise is not as clear, and so both are considered together as *quantum noise* (shown as red traces in figure 3).

5.1 Higher laser power

At the higher frequencies of the detection band, where photon shot noise dominates, the shot noise limited signal to noise ratio scales inversely with the square root of the input laser power. To reduce this noise source, a higher power laser will be used (with 125 W of 1064 nm laser light expected at the interferometer input, after the suspended input mode cleaning cavity). The reference solution to achieve such a high power is a master-oscillator power amplifier configuration, with a fiber-coupled NPRO as the master oscillator followed by two stages of fiber amplification from a commercial system.

The higher circulating laser power brings two complications: larger thermal effects from optical absorption, and the effects of optical rigidity.

Compensation of thermal effects

The foreseen level of injected power will increase the total circulating power to 700 kW in the arm cavities and about 5 kW in the power recycling cavity. Such high circulating powers mean that even with very low absorption optics, the heat absorbed by the mirrors and substrates will cause sufficient thermoelastic and thermorefractive changes to severely degrade the optical performance of the interferometer. For this reason a thermal compensation system is necessary; this system illuminates the compensation plates (cf. figure 1) with a 10 μm laser projector with a pattern complementary to that of the heat deposited by the main laser beam. As 10 μm light is strongly absorbed by fused silica, much less power (about 15 W) is needed in this system than for the main laser light. In addition to this projector + compensation plate system, which compensates for thermorefractive effects in the mirror substrates, annular heating elements will surround the test masses to adjust the radii of curvature of these mirrors to counteract thermoelastic deformation of the mirror surfaces caused by absorption in the mirror coatings.

Optical rigidity

The high circulating power means that the dynamics of the interferometer mirrors, particularly in the arm cavities, are modified by the light fields due to radiation pressure. This results in opto-mechanical resonances (i.e., optical springs) in the differential length degree of freedom [14], which is the one sensitive to gravitational waves, and in the angular degrees of freedom[15]. Such opto-mechanical resonances are in general dynamically unstable, but appropriately designed control systems can quench these instabilities.

5.2 Signal recycling

The use of the signal recycling technique permits a certain amount of flexibility in shaping the spectrum of quantum noise; this allows optimization of the sensitivity in the presence of other noise sources [14]. The sensitivity plotted in figure 3 has been optimized for neutron star binary inspirals, in the presence of suspension and mirror thermal noise. Small changes in the parameters of the signal recycling cavity (such as a small change in the reflectivity of the signal recycling mirror or even a microscopic, sub-wavelength adjustment of the signal recycling mirror position) can modify the quantum noise, to maximize the sensitivity to another source (e.g., a particular millisecond pulsar, or stellar mass black hole binaries).

5.3 DC readout

In place of the optical heterodyne technique used in Virgo, Advanced Virgo will use optical homodyne detection in the form of the technique known as DC readout. This technique involves a slight detuning of the differential arm degree of freedom (the one which is also sensitive to gravitational waves) slightly from destructive interference to allow a small amount of light to leak out the detection port to serve as a local oscillator. Because this light has been stored in the interferometer, it has been passively filtered by the so-called coupled-cavity pole[16]. This passive optical filtering, combined with the laser pre-stabilization system, means this light is a very low noise optical local oscillator in the detection band. Furthermore, optical homodyne detection has a lower level of shot noise than optical heterodyne detection[17]. To implement DC readout an output mode cleaner (OMC in figure 1) is placed after the interferometer and before the photodetector (B1 in figure 1).

5.4 Optical losses

The surface quality of the test mass substrates is an important factor in the optical performance (i.e., the optical losses) of the interferometer, which can impact the quantum noise limited sensitivity. To achieve an appropriately low level of surface figure error, a corrective coating process has been developed at LMA. This process is expected to suppress surface figure errors with spatial scale larger than $50\,\mathrm{m}^{-1}$, which have a large effect on the optical performance of km-scale cavities with large beam sizes. The apparatus for this corrective coating has been constructed, and the first tests of this process on large scale mirrors (i.e., the 35 cm diameter of the Advanced Virgo substrates) will take place soon.

6 Residual gas noise

Residual gas in the 3 km beam tubes can induce phase fluctuations in the laser light circulating in the Fabry-Pérot arm cavities, resulting in noise in the interferometer output (the green traces in figure 3). The current Virgo vacuum system operates at a residual pressure of about 10^{-7} mbar; this level must be reduced to about 10^{-9} mbar to meet the Advanced Virgo requirements. This will be done by performing a vacuum bake-out of the beam tubes and installing cryotraps at each end of each beam tube. The cryotraps will allow regular intervention into the vacuum system at the mirror locations without spoiling the level of vacuum in the beam tubes through water migration.

7 Conclusions

Achieving a factor of 10 sensitivity improvement over Virgo requires pushing the limits of technology on several frontiers. The maturing Advanced Virgo design will meet these limits. Expected to be online in 2015, Advanced Virgo will be a crucial part of the network of next generation gravitational wave detectors that will usher in the era of gravitational wave astronomy.

Acknowledgments

Advanced Virgo is a joint project of the *Centre National de la Recherche Scientifique* (CNRS) and the *Istituto Nazionale di Fisica Nucleare* (INFN).

References

1. F. Acernese et al., *Class. Quant. Grav.* **25**, 184001 (2008)
2. B. Abbott, et al., *Rep. Prog. Phys.* **72**, 076901 (2009)
3. H Grote and the LIGO Scientific Collaboration, *Class. Quant. Grav.* **27**, 084003 (2010)
4. F. Acernese et al., *Astropart. Phys.*, **33**, 182 (2010)
5. G. Harry and the LIGO Scientific Collaboration *Class. Quant. Grav.* **27**, 084007 (2010)
6. K. Kuroda (on behalf of the LCGT Collaboration), *Class. Quant. Grav.* **27**, 084004 (2010)
7. B. Willke et al., *Class. Quant. Grav.* **23**, S207 (2006)
8. J. Abadie et al., *Class. Quant. Grav.* **27**, 173001 (2010)
9. M. Punturo et al., *Class. Quant. Grav.* **27**, 194002 (2010)
10. P.R. Saulson. *Phys. Rev.* D **42**, 2437 (1990)
11. M. Lorenzini and the Virgo Collaboration, *Class. Quant. Grav.* **27**, 084021 (2010)
12. G.M. Harry, *et al.*, *Appl. Opt.*, **45**, 1569 (2006)
13. C.Comtet *et al.*, *Proceedings of the 42nd Rencontres de Moriond*, (2007)
14. A. Buonanno and Y. Chen, *Phys. Rev.* D **64**, 042006 (2001)
15. J.A. Sidles and D.Sigg. *Physics Letters A*, **354**, 167 172, (2006).
16. J.B. Camp, *et al.*, *J. Opt. Soc. Am. A*, **17** 12 (2000)
17. A.Buonanno, Y.Chen, and N.Mavalvala. *Phys. Rev.* D **67**, 122005 (2003)

SCIENTIFIC POTENTIAL OF EINSTEIN TELESCOPE

B Sathyaprakash[18], M Abernathy[3], F Acernese[4,5], P Amaro-Seoane[33,46], N Andersson[7], K Arun[8], F Barone[4,5], B Barr[3], M Barsuglia[9], M Beker[45], N Beveridge[3], S Birindelli[11], S Bose[12], L Bosi[1], S Braccini[13], C Bradaschia[13], T Bulik[14], E Calloni[4,15], G Cella[13], E Chassande Mottin[9], S Chelkowski[16], A Chincarini[17], J Clark[18], E Coccia[19,20], C Colacino[13], J Colas[2], A Cumming[3], L Cunningham[3], E Cuoco[2], S Danilishin[21], K Danzmann[6], R De Salvo[23], T Dent[18], R De Rosa[4,15], L Di Fiore[4,15], A Di Virgilio[13], M Doets[10], V Fafone[19,20], P Falferi[24], R Flaminio[25], J Franc[25], F Frasconi[13], A Freise[16], D Friedrich[6], P Fulda[16], J Gair[26], G Gemme[17], E Genin[2], A Gennai[16], A Giazotto[2,13], K Glampedakis[27], C Gräf[6] M Granata[9], H Grote[6], G Guidi[28,29], A Gurkovsky[21], G Hammond[3], M Hannam[18], J Harms[23], D Heinert[32], M Hendry[3], I Heng[3], E Hennes[45], S Hild[3], J Hough[4], S Husa[44], S Huttner[3], G Jones[18], F Khalili[21], K Kokeyama[16], K Kokkotas[27], B Krishnan[6], T.G.F. Li[45], M Lorenzini[28], H Lück[6], E Majorana[34], I Mandel[16,35], V Mandic[31], M Mantovani[13], I Martin[3], C Michel[25], Y Minenkov[19,20], N Morgado[25], S Mosca[4,15], B Mours[37], H Müller–Ebhardt[6], P Murray[3], R Nawrodt[3,32], J Nelson[3], R Oshaughnessy[38], C D Ott[39], C Palomba[34], A Paoli[2], G Parguez[2], A Pasqualetti[2], R Passaquieti[13,40], D Passuello[13], L Pinard[25], W Plastino[42], R Poggiani[13,40], P Popolizio[2], M Prato[17], M Punturo[1,2], P Puppo[34], D Rabeling[10,45], I Racz[47], P Rapagnani[34,41], J Read[36], T Regimbau[11], H Rehbein[6], S Reid[3], L Rezzolla[33], F Ricci[34,41], F Richard[2], A Rocchi[19], S Rowan[3], A Rüdiger[6], L Santamaría[23], B Sassolas[25], R Schnabel[6], C Schwarz[32], P Seidel[32], A Sintes[44], K Somiya[39], F Speirits[3], K Strain[3], S Strigin[21], P Sutton[18], S Tarabrin[6], A Thüring[6], J van den Brand[10,45], M van Veggel[3], C van den Broeck[45], A Vecchio[16], J Veitch[18], F Vetrano[28,29], A Vicere[28,29], S Vyatchanin[21], B Willke[6], G Woan[3], K Yamamoto[30]

[1] *INFN, Sezione di Perugia, I-6123 Perugia, Italy*

[2] *European Gravitational Observatory (EGO), I-56021 Cascina (Pi), Italy*

[3] *SUPA, School of Physics and Astronomy, The University of Glasgow, Glasgow, G12 8QQ, UK*

[4] *INFN, Sezione di Napoli, Italy*

[5] *Università di Salerno, Fisciano, I-84084 Salerno, Italy*

[6] *Max–Planck–Institut für Gravitationsphysik and Leibniz Universität Hannover, D-30167 Hannover, Germany*

[7] *University of Southampton, Southampton SO17 1BJ, UK*

[8] *LAL, Université Paris-Sud, IN2P3/CNRS, F-91898 Orsay, France*

[9] *AstroParticule et Cosmologie (APC), CNRS; Observatoire de Paris, Université Denis Diderot, Paris VII, France*

[10] *VU University Amsterdam, De Boelelaan 1081, 1081 HV, Amsterdam, The Netherlands*

[11] *Université Nice 'Sophia–Antipolis', CNRS, Observatoire de la Côte d'Azur, F-06304 Nice, France*

[12] *Washington State University, Pullman, WA 99164, USA*

[13] *INFN, Sezione di Pisa, Italy*

[14] *Astronomical Observatory, University of warsaw, Al Ujazdowskie 4, 00-478 Warsaw, Poland*

[15] *Università di Napoli 'Federico II', Complesso Universitario di Monte S. Angelo, I-80126 Napoli, Italy*

[16] *University of Birmingham, Birmingham, B15 2TT, UK*

[17] *INFN, Sezione di Genova, I-16146 Genova, Italy*

[18] *Cardiff University, Cardiff, CF24 3AA, UK*

[19] *INFN, Sezione di Roma Tor Vergata I-00133 Roma, Italy*

[20] *Università di Roma Tor Vergata, I-00133, Roma, Italy*

[21] *Moscow State University, Moscow, 119992, Russia*

[22] *INFN, Laboratori Nazionali del Gran Sasso, Assergi l'Aquila, Italy*

[23] *LIGO, California Institute of Technology, Pasadena, CA 91125, USA*

[24] *INFN, Gruppo Collegato di Trento, Sezione di Padova; Istituto di Fotonica e Nanotecnologie, CNR-Fondazione Bruno Kessler, I-38123 Povo, Trento, Italy*

[25] *Laboratoire des Matériaux Avancés (LMA), IN2P3/CNRS, F-69622 Villeurbanne, Lyon, France*

[26] *Institute of Astronomy, University of Cambridge, Madingley Road, Cambridge, CB3 0HA, UK*

[27] *Theoretical Astrophysics (TAT) Eberhard-Karls-Universität Tübingen, Auf der Morgenstelle 10, D-72076 Tübingen, Germany*

[28] *INFN, Sezione di Firenze, I-50019 Sesto Fiorentino, Italy*

[29] *Università degli Studi di Urbino 'Carlo Bo', I-61029 Urbino, Italy*

[30] *INFN, sezione di Padova, via Marzolo 8, 35131 Padova, Italy*

[31] *University of Minnesota, Minneapolis, MN 55455, USA*

[32] *Friedrich-Schiller-Universität Jena PF, D-07737 Jena, Germany*

[33] *Max Planck Institute for Gravitational Physics (Albert Einstein Institute) Am Mühlenberg 1, D-14476 Potsdam, Germany*

[34] *INFN, Sezione di Roma 1, I-00185 Roma, Italy*

[35] *NSF Astronomy and Astrophysics Postdoctoral Fellow, MIT Kavli Institute, Cambridge, MA 02139*

[36] *University of Mississippi, University, MS 38677, USA*

[37] *LAPP-IN2P3/CNRS, Université de Savoie, F-74941 Annecy-le-Vieux, France*

[38] *The Pennsylvania State University, University Park, PA 16802, USA*

[39] *Caltech–CaRT, Pasadena, CA 91125, USA*

[40] *Università di Pisa, I-56127 Pisa, Italy*

[41] *Università 'La Sapienza', I-00185 Roma, Italy*

[42] *INFN, Sezione di Roma Tre and Università di Roma Tre, Dipartimento di Fisica, I-00146 Roma, Italy*

[43] *Università degli Studi di Firenze, I-50121, Firenze, Italy*

[44] *Departament de Fisica, Universitat de les Illes Balears, Cra. Valldemossa Km. 7.5, E-07122 Palma de Mallorca, Spain*

[45] *Nikhef, Science Park 105, 1098 XG Amsterdam, The Netherlands*

[46] *Institut de Ciències de l'Espai (CSIC-IEEC), Campus UAB, Torre C-5, parells, 2[na] planta, ES-08193, Bellaterra, Barcelona, Spain*

[46] *KFKI Research Institute for Particle and Nuclear Physics, Budapest, Hungary*

Abstract

Einstein gravitational-wave Telescope (ET) is a design study funded by the European Commission to explore the technological challenges of and scientific benefits from building a third generation gravitational wave detector. The three-year study, which concluded earlier this year, has formulated the conceptual design of an observatory that can support the implementation of new technology for the next two to three decades. The goal of this talk is to introduce the audience to the overall aims and objectives of the project and to enumerate ET's potential to influence our understanding of fundamental physics, astrophysics and cosmology.

1 Introduction

Interferometric gravitational wave (GW) detectors, Laser Interferometer Gravitational-Wave Observatory (LIGO) in the US, Virgo, GEO600 and TAMA, have successfully operated at design sensitivities for a year or more [1,2]. They have demonstrated that it is possible to build and run these highly sensitive instruments with a large duty cycle [3]. While no signal has so far been observed in any of these detectors, their data have been used to break new ground on several astronomical sources [4,5,6,7].

The network of advanced detectors, which includes advanced LIGO [8], advanced Virgo [9], Large Cryogenic Gravitational Telescope [10] (to be built in Kamioka mines in Japan) and GEO-HF [11] (GEO High Frequency), is expected to make the first direct detection of GW sometime during this decade. This will be a new milestone for observational astronomy that will facilitate the study of formations and interactions of neutron stars (NSs) and black holes (BHs) in the Universe.

Direct detection of GW will allow the study of phenomena associated with strong gravitational fields and relativistic gravity that are otherwise not accessible to us. They will allow new tests of general theory of relativity in regimes where one might expect to see departure from standard predictions. The study of GW sources will by itself establish as a new field of observational astronomy. However, there is much more to be benefitted beyond the mere study of phenomena associated with GW sources. Just as stars, GW sources are markers in space, sometimes with precisely known distances. They could, therefore, serve to study the structure and dynamics of the Universe and hence a new tool for cosmology.

Advanced detectors will study NSNS, NSBH and BHBH binaries at distances of 200 Mpc, 600 Mpc and 3 Gpc, respectively, within which the nominal event rates are about 40 per year for NSNS binaries and similar, but much more uncertain, rates for NSBH and BHBH binaries [12]. The signal-to-noise ratio (SNR) for most of the sources detected by advanced detectors will be around 10. This should already make it possible to carry out a number of accurate measurements that will impact fundamental physics and astrophysics [13]. For instance, it should be possible to measure the Hubble constant to within 1% if NSNS and NSBH binaries are progenitors of short-hard gamma ray bursts (GRBs) and confirm the presence of tails of gravitational waves by observing BHBH mergers [14].

Third generation detectors, such as the Einstein Telescope (ET), will have ten times greater SNR for the same events and their reach will increase to $z \simeq 2$, for NSNS binaries, $z \simeq 6$ for NSBH binaries and $z \simeq 17$ for BHBH binaries (cf. Fig. 3). They will help address a variety of issues associated with phenomena that have remained as enigmas for several years to decades after their initial discovery. More than anything else, ET might well unveil new physics beyond the standard models of particle physics and cosmology.

The purpose of this talk is to discuss the science potential of ET and how it will be a powerful new tool for observing phenomena associated with strong field, relativistic gravity. The design study has already provided useful insight on what really will be the benefit of building a third generation GW detector [15]. However, the *full* science potential of ET and the challenges posed by science exploitation, remain unexplored. Yet what has been investigated is already very exciting and should provide the impetus for further studies. The talk will begin with a brief description of the technical aspects of the design and different sensitivity options, followed by a discussion of ET's science potential.

2 ET Sensitivity

The ET design study was commissioned by the European Commission to scope out the technological feasibility of building a 3rd generation detector and to explore its science potential. The study team set itself the goal of designing a detector that is better than advanced detectors ten times in strain sensitivity and reaches down to 1 Hz rather than the 10-20 Hz low frequency limit of advanced detectors. It was soon realized that the infrastructure, in which advanced detectors will have been housed for more than 20 years since their inception, will be highly inadequate in realizing the sensitivity of a 3rd generation detector. ET will be more than just a detector; it will be a facility that will house a 3rd generation observatory but with infrastructure that can support new designs and improvements for several decades.

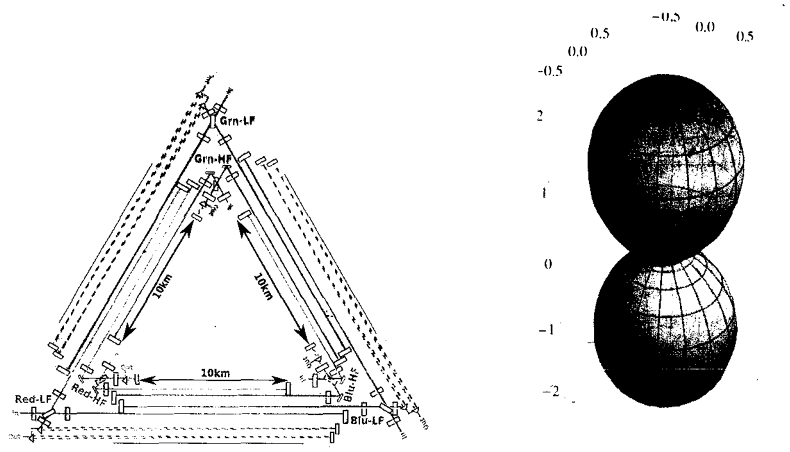

Figure 1: *Left*: Schematic full view of the optical layout of the ET Observatory. It consists of 3 pairs of km-scale interferometers positioned such that they form a triangular shape. Each interferometer pair represents one wide-band detector, in which one interferometer is optimized for gravitational waves at low frequencies (i.e., < 100Hz) and the other for high frequencies (i.e., > 100 Hz). *Right:* The joint antenna pattern of the three interferometers to sources from around the sky. ET has virtually full sky coverage.

A factor ten in strain sensitivity is achieved by a combination of increased arm lengths (10 km arms as opposed to 3-4 km arms afforded by the current infrastructures), seismically quieter underground environments to mitigate seismic noise, higher arm cavity laser powers to confront photon shot noise and cryogenic mirrors cooled down to 10 K to reduce thermal noise.

2.1 Arm lengths and topology

In the long-wavelength approximation, the strain sensitivity of an interferometer increases in direct proportion to the length of its arms. The arm lengths of current (large) detectors is either 3 or 4 km. The strain sensitivity of an interferometer with 10 km arms will be 2.5 to 3 greater. Current ground-based detectors are L-shaped interferometers since an opening angle of 90 degrees maximizes their sensitivity. However, careful considerations taking into account continuous operation, ability to resolve the two independent wave polarizations and minimizing the infrastructure costs, favours the construction of a triangular configuration.

The advantage of a triangular topology is that each side of the triangle can be deployed twice to build, in effect, three V-shaped interferometers with an opening angle of 60 degrees and rotated relative to each other by 120 degrees (see the panel on the left in Fig. 1). An opening angle of 60 degrees means that the sensitivity reduces to $\sqrt{3}/2$ that of an L-shaped detector; the three detectors in the triangle enhance the sensitivity by a factor of $\sqrt{3}$ and so an overall gain in sensitivity of 3/2. The panel on the right in Fig. 1 shows the antenna pattern of the triangular network. The triangular ET has virtually complete sky coverage and it has no blind spots. Its reach to sources lying in the plane of the triangle will be a third of its reach to sources lying overhead!

The three V-shaped interferometers are, of course, equivalent in sensitivity to two L-shaped interferometers with arms that are only three-quarters in size of the triangular arms and rotated relative to each other by 45 degrees. However, the responses of the three detectors in a triangle can be used to construct a *null stream* that is *not* possible with the two L-shaped interferometers. It turns out that the sum of the responses of the three detectors in a triangle (for that matter any closed topology) is completely devoid of any gravitational wave. This is the closest that one can get to measuring the "dark current" in interferometers. The null stream will be an invaluable tool to characterize the background.

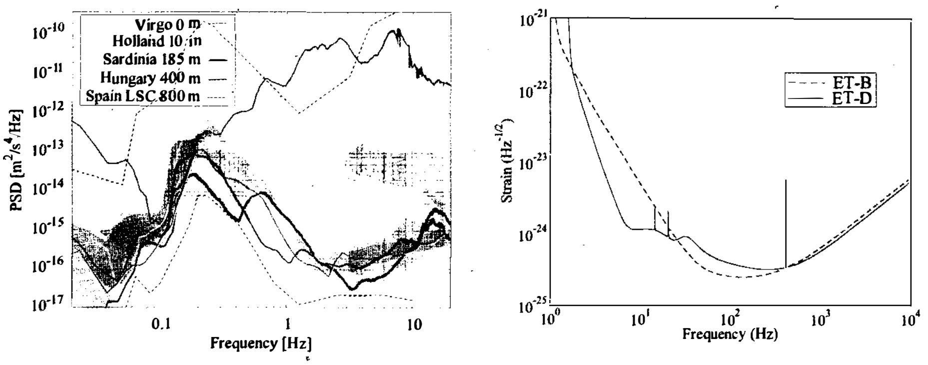

Figure 2: *Left:* The spectrum of horizontal motion over one-week period at Cascina, where Virgo is located, is compared to those measured at several underground locations in Europe. The solid lines correspond to the mode, while the upper and lower limits of the transparent regions are the PSD levels that weren't exceeded for 90% and 10% of the time respectively. *Right:* The sensitivity of ET for the xylophone configuration, ET-D, is compared with that of a conventional configuration that achieves broadband sensitivity with a single interferometer, ET-B.

2.2 Going underground

Achieving good low frequency sensitivity requires mitigation of gravity gradients that are far too high on ground. They can be circumvented either by getting into space (the option pursued by the Laser Interferometer Space Antenna) or by going underground. To be useful, any underground site must be seismically quiet. Figure 2 shows the seismic noise in several European underground sites compared to the seismic noise at Cascina, where Virgo is located. Clearly, underground environments could be several orders of magnitude quieter than ground-based ones.

Achieving a good sensitivity over a broad frequency range from 1 Hz to 10 kHz with the same technology is impractical. The technology required for better high frequency (i.e. $> 100\,\mathrm{Hz}$) sensitivity – higher laser powers – is in direct conflict with that required for improving the low frequency (i.e. $< 100\,\mathrm{Hz}$) sensitivity, namely low thermal and radiation pressure noises. Thus it is not prudent to build a single detector that meets the design goal in the entire frequency band. Instead, the design study concluded that it is best to build separate interferometers for the low and high frequency regions.

2.3 Megawatt lasers, squeezed light and cryogenic mirrors

The key to high frequency sensitivity is high laser power. Above $\sim$ 100 Hz, the main source of noise is the photon shot noise, which can be reduced by simply using as high a power in the cavity as possible. ET aims to achieve the required 3 MW of power by using inherently more powerful input lasers (500 W as opposed to the 180 W in advanced interferometers). Furthermore, the use of non-classical light, squeezed light, leads to further improvement in sensitivity[16]. Indeed, ET design assumes a squeezing factor of 10 dB, which is equivalent to shot noise reduction resulting from an increase in laser power of a factor of 10.

Although, higher laser power works well at frequencies above 100 Hz, it has the adverse effect of worsening the sensitivity in the 10-100 Hz. This is due to enhanced thermal noise in mirror substrates and coating. Thus, it is not sensible to achieve the sensitivity goal over the entire band with a single interferometer. The current thinking is to build a pair of interferometers in each V of the triangle, one using high laser powers and the other with lower laser powers and cryogenic mirrors to mitigate thermal noise.

Figure 2, right panel, plots the strain sensitivity (per $\sqrt{\mathrm{Hz}}$) for the xylophone configuration ET-D[17][a]. The xylophone configuration deploys a pair of interferometers to achieve good

[a] The data for the sensitivity curves can be found at `http://www.et-gw.eu/etsensitivities`.

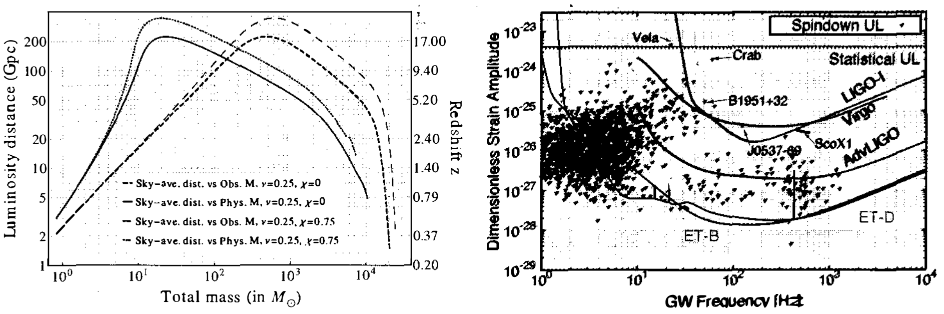

Figure 3: Plots show the distance reach of ET for compact binary mergers as a function of the total mass (left) and its sensitivity to GWs from known pulsars (right). See the text for details.

broadband sensitivity. Also shown is the sensitivity of a conventional configuration ET-B[18], that has only one interferometer in each V of the triangle. Apart from the frequency range from 20 to 200 Hz where ET-B is slightly better than ET-D, the xylophone configuration quite significantly wins over ET-B in the low frequency range.

3 ET's science objectives

ET's distance reach for inspiralling and merging black holes for ET-B sensitivity is shown in the left panel of Fig. 3. The long- and short-dashed curves correspond to the observed total mass $M_{\rm obs}$ and the solid and dotted curves correspond to the intrinsic total mass $M_{\rm int}$; the two are related by $M_{\rm int} = M_{\rm obs}/(1+z)$. The solid and short-dashed curves are for non-spinning binaries consisting of two equal masses, while the dotted and long-dashed curves are the same except that the component black holes are both assumed to have a dimensionless spin magnitude of 0.75.

It is immediately apparent that ET will be sensitivity to BHBH binaries of intrinsic total mass 10-20$M_\odot$ at a redshift of $z \sim 10$ and beyond. NSNS binaries could be seen when the star formation in the Universe is at its peak at $z \sim 2$. NSBH binaries comprising of a 1.4 $M_\odot$ NS and a 10 $M_\odot$ BH can be detected from redshifts of at least $z \sim 6.5$. Together with the fact that the inspiral phase of compact binaries are standard sirens[19] means that ET will be able to explore not only the properties of the sources themselves but can also act as a tool to probe the properties of the Universe. Intermediate mass black holes of intrinsic total mass in the range 10^2-$10^4 M_\odot$ can be seen in the redshift range of 1 to 10, thus offering a unique probe to uncover a host of questions related to their existence and their role in the formation and evolution of galaxies.

Also shown in Fig. 3, right panel, are the sensitivities of initial LIGO, Virgo, advanced LIGO and ET (two versions, ET-B and ET-D), to continuous waves from rotating, asymmetric neutron stars, for an integration period of five years. Inverted black triangles give the upper limit on the amplitude of GW of known pulsars derived by assuming that their observed spin-down rate is entirely due to the emission of GW - Vela, Crab, B1951+32 and J0537-69 being specific examples. The horizontal line shows the limit on the amplitude of GW from pulsars obtained from statistical arguments. ET-D (red curve) will be sensitive to intrinsic GW amplitudes greater than $h \sim 10^{-27}$ in the frequency range 6 Hz to 3 kHz, and a factor 3 better in the range 20 Hz to 1 kHz. It is particularly important that ET is able to reach sensitivity levels that are two to four orders of magnitude lower than the spin-down limits, where one might have a real chance of detecting a signal.

The rest of this paper enumerates ET's science goals in fundamental physics, astrophysics and cosmology.

Probing fundamental physics with ET

3.1 Is the nature of gravitational radiation as predicted by Einstein's theory?

ET will allow a test of the wave generation formula beyond the quadrupole approximation [20]. It could accurately measure the GW propagation speed by coincident observation of GW and EM radiation from NSNS binary coalescences at $z \sim 2$ and constrain the graviton mass [21].

3.2 Are black hole spacetimes uniquely given by the Kerr geometry?

By measuring different quasi-normal modes, ET will test if the spacetime geometry of a BH is uniquely described by its mass and spin [22]. Additionally, ET can measure the multipole moments of a source from the radiation emitted as a stellar-mass BH spirals into an intermediate-mass BH and confirm if the different moments depend only on the massive BH's mass and spin [23,24].

3.3 What is the physics of gravitational collapse?

ET can study supernovae and explore if they leave behind a massive object that is trapped inside an event horizon or lead to a naked singularity, or some other exotic object. ET could well reveal a new class of objects and phenomena, for instance *silent supernovae* [25] and other gravitationally unstable transients.

3.4 What is the equation of state of matter at supra-nuclear densities as might be found in NS cores?

The equation of state (EoS) of NSs affects the late-time evolution of NSNS and NSBH binaries. By matching the observed radiation from the coalescence of such sources to theoretical predictions ET will deduce the EoS of NS cores [26,27].

3.5 What is the maximum mass of a neutron star?

The maximum mass of a white dwarf is $\simeq 1.4 M_\odot$ as determined by the electron degeneracy pressure. The maximum mass of a NS is an additional test of the nature of matter at extremely high densities; it is currently unknown and should be determined by ET by accurately constructing their mass function from millions of NSNS binaries [28].

ET's impact on astrophysics and multimessenger astronomy

3.6 What is the mass function of BHs and NSs and their redshift distribution?

ET will measure masses and spins of millions of NSs and BHs in binary systems and will thereby obtain a census of these objects as a function of redshift. This will be a very valuable tool for understanding a host of questions in astronomy related to redshift evolution of compact objects [29].

3.7 What are the progenitors of gamma-ray bursts?

GRBs are the most luminous electromagnetic sources in the Universe. While advanced detectors might provide some clues as to their origin, ET will provide a large statistical sample of events that could be used to understand GRB progenitors and to test their astrophysical models [28].

3.8 How do compact binaries form and evolve?

The process by which main sequence binary stars evolve into compact binaries (that is, NSNS, NSBH and BHBH) could be understood by ET's observation of millions of coalescing binaries with different masses, mass ratios and spins and mapping the observed population to astrophysical models [30].

3.9 What is the physical mechanism behind supernovae and how asymmetric is the gravitational collapse that ensues?

Supernovae are complex processes whose modelling requires many different inputs, including relativistic magneto-hydrodynamics, general relativity and nuclear and particle physics [31]. ET's observation of supernovae in coincidence with the detection of neutrinos could provide the data necessary to constrain models and help understand the process by which stars collapse to form NSs and BHs.

3.10 Do relativistic instabilities occur in young NSs and if so what is their role in the evolution of NSs?

Non-linearities of general relativity could cause instabilities in NSs that lead to parametric amplification of GWs. ET's observations of the formation of NSs can explore if such instabilities occur in young NSs and how that might affect their spin frequencies [27].

3.11 Why are spin frequencies of NSs in low-mass X-ray binaries bounded?

ET will verify if gravitational radiation back-reaction torque is responsible for the observed upper limit on NS spin frequencies in low-mass X-ray binaries [32].

3.12 What is the nature of the NS crust and its interaction with the core?

ET should detect NS ellipticities that are few $\times\ 10^{-10}$ (for sources within a distance of 1 kpc) or larger depending on their spin frequency and their distance from earth. Such observations can be used to deduce the property of NS crusts. ET might also detect GWs that are expected to be emitted when pulsars glitch and magnetars flare and thereby help understand crust-core interaction that is believed to transfer angular momentum from the core to crust [33].

3.13 What is the population of GW sources at high redshifts?

A large population of point sources would produce a confusion background that would be detectable by ET if the energy density of the background is large enough. Detection of confusion backgrounds can be used to understand the nature and population of GW sources in the Universe.

ET as a new cosmological tool

3.14 What are the luminosity distances of cosmological sources?

Compact binaries are an astronomer's ideal *standard candles* or, more appropriately, *sirens.* Gravitational wave observations can alone determine both the apparent and absolute luminosity of a source and hence deduce their luminosity distance. With ET, these self-calibrating standard sirens can be used to calibrate the cosmic distance ladder [34].

3.15 What is the EoS of dark energy and how does it vary with redshift?

ET could observe thousands of coalescing NSNS and NSBH systems in coincidence with optical or gamma-ray observations and hence measure both the luminosity distance and redshift. ET will, therefore, facilitate precision measurement of the dark energy EoS and its variation with redshift [35].

3.16 How did the black holes at galactic nuclei form and evolve?

ET can verify if seeds of galaxy formation were intermediate BHs of hundreds to thousands of solar masses and map their merger history up to redshifts of $z \sim 5$–15 depending on the total mass and mass ratio of progenitor binaries [36,24,37].

3.17 What were the physical conditions in the primeval Universe and what phase transitions occurred in its early history?

Stochastic GW backgrounds could be produced by quantum processes in the primordial Universe or during phase transitions in its early history. ET will be sensitive to background densities $\rho_{\rm GW} \sim 10^{-12}\,\rho_c$, where ρ_c is the critical density of the Universe[38].

4 Conclusions

This decade will see the construction and operation of second generation interferometric detectors, pulsar timing arrays and results from the Planck space mission. There is little doubt that we are at the verge of a new era in astronomy that will witness the opening of the gravitational window for observing the Universe. I hope this talk has convinced you that the field promises to have a huge potential and that ET can not only help solve some of the enigmas in astronomy and cosmology but push the frontiers of science into new avenues.

References

1. B. Abbott et al. (LIGO Scientific Collaboration). LIGO: the Laser Interferometer Gravitational-Wave Observatory. *Reports on Progress in Physics*, 72(7):076901, 2009.
2. T. Accadia et al. Commissioning status of the Virgo interferometer. *Class. Quantum Grav.*, 27, 2010.
3. H. Grote for the LIGO Scientific Collaboration. The status of GEO 600. *Classical and Quantum Gravity*, 25(11):114043 (9pp), 2008.
4. B. Abbott et al. Beating the spin-down limit on gravitational wave emission from the crab pulsar. *The Astrophysical Journal Letters*, 683(1):L45. 2008.
5. B.P. Abbott et al. An Upper Limit on the Stochastic Gravitational-Wave Background of Cosmological Origin. *Nature*, 460:990, 2009.
6. B. Abbott et al. (LIGO Scientific Collaboration) and K. Hurley. Implications for the Origin of GRB 070201 from LIGO Observations. *Astrophys. J.*, 681:1419–1430, 2008.
7. J. Abadie et al. Search for gravitational-wave inspiral signals associated with short gamma-ray bursts during ligo's fifth and virgo's first science run. *The Astrophysical Journal*, 715(2):1453, 2010.
8. David Shoemaker for the Advanced LIGO Team. Advanced ligo reference design. 2009.
9. The VIRGO Collaboration. Advanced Virgo baseline design. Virgo Technical Report VIR-0027A-09, 2009.
10. Large-scale cryogenic gravitational-wave telescope project.
11. B. Willke et al. The GEO-HF project. *Class. Quantum Grav.*, 23:S207–S214, 2006.
12. J. Abadie, B. P. Abbott, R. Abbott, M. Abernathy, T. Accadia, F. Acernese, C. Adams, R. Adhikari, P. Ajith, B. Allen, and et al. TOPICAL REVIEW: Predictions for the rates of compact binary coalescences observable by ground-based gravitational-wave detectors. *Classical and Quantum Gravity*, 27(17):173001–+, September 2010.
13. B.S. Sathyaprakash and Bernard F. Schutz. Physics, astrophysics and cosmology with gravitational waves. *Living Reviews in Relativity*, 12(2), 2009.
14. L. Blanchet and B.S. Sathyaprakash. Detecting the tail effect in gravitational wave experiments. *Phys. Rev. Lett.*, 74:1067–1070, 1995.
15. M Abernathy et al. *Einstein gravitational wave Telescope: Conceptual Design Study.* available from *European Gravitational Observatory,* document number ET-0106A-10, 2011.
16. K. McKenzie et al. Squeezing in the audio gravitational-wave detection band. *Phys. Rev. Lett.*, 93(16):161105, Oct 2004.
17. S. Hild, M. Abernathy, F. Acernese, P. Amaro-Seoane, N. Andersson, et al. Sensitivity Studies for Third-Generation Gravitational Wave Observatories. *Class. Quant. Grav.*, 28:094013, 2011.
18. Stefan Hild, Simon Chelkowski, and Andreas Freise. Pushing towards the ET sensitivity using 'conventional' technology. *arXiv:0810.0604v2 [gr-qc]*, 2008.

19. B F Schutz. Determining the Hubble constant from gravitational wave observations. *Nature (London)*, 323:310, 1986.
20. C.K. Mishra, K.G. Arun, B.R. Iyer, and B.S. Sathyaprakash. Parameterized tests of post-newtonian theory using advanced ligo and einstein telescope. *Phys. Rev. D*, 82:064010, 2010.
21. K. G. Arun and Clifford M. Will. Bounding the mass of the graviton with gravitational waves: Effect of higher harmonics in gravitational waveform templates. *Class. Quant. Grav.*, 26:155002, 2009.
22. I. Kamaretsos, M. Hannam, S. Husa, and B.S. Sathyaprakash. Black-hole hair loss: learning about binary progenitors from ringdown signal. 2011.
23. E.A. Huerta and J.R. Gair. *Phys. Rev. D*, 83:044020, 2011.
24. Pau Amaro-Seoane and Lucia Santamaria. Detection of IMBHs with ground-based gravitational wave observatories: A biography of a binary of black holes, from birth to death. *Astrophys. J.*, 722:1197–1206, 2010.
25. S. E. Woosley and E. Baron. The collapse of white dwarfs to neutron stars. *Astrophys. J.*, 391:228–235, May 1992.
26. Jocelyn S. Read et al. Measuring the neutron star equation of state with gravitational wave observations. *Phys. Rev.*, D79:124033, 2009.
27. N. Andersson, V. Ferrari, D. I. Jones, K. D. Kokkotas, B. Krishnan, J. S. Read, L. Rezzolla, and B. Zink. Gravitational waves from neutron stars: promises and challenges. *General Relativity and Gravitation*, 43:409–436, February 2011.
28. B.S. Sathyaprakash and C. Van Den Broeck. Astrophysics with einstein telescope. 2011.
29. C. Van Den Broeck and A.S. Sengupta. Binary black hole spectroscopy. *Class. Quantum Grav.*, 24:1089–1114, 2007.
30. K. Belczynski, V. Kalogera, and T. Bulik. A comprehensive study of binary compact objects as gravitational wave sources: Evolutionary channels, rates, and physical properties. *Astrophys. J.*, 572:407–431, 2002.
31. Christian D. Ott. Probing the Core-Collapse Supernova Mechanism with Gravitational Waves. *Class.Quant.Grav.*, 26:204015, 2009.
32. L. Bildsten. Gravitational radiation and rotation of accreting neutron stars. *Astrophys. J. Lett.*, 501:L89, 1998.
33. M. Ruderman. Crust-breaking by neutron superfluids and the vela pulsar glitches. *Astrophys. J.*, 203:213–222, 1976.
34. B.S. Sathyaprakash, B.F. Schutz, and C. Van Den Broeck. Cosmography with the Einstein Telescope. *Class.Quant.Grav.*, 27:215006, 2010.
35. W. Zhao, C. Van Den Broeck, D. Baskaran, and T.G.F. Li. Determination of Dark Energy by the Einstein Telescope: Comparing with CMB, BAO and SNIa Observations. *Phys.Rev.*, D83:023005, 2011.
36. A. Sesana, J. Gair, I. Mandel, and A. Vecchio. Observing Gravitational Waves from the First Generation of Black Holes. *Astrophys. J. Lett.*, 698:L129–L132, 2009.
37. Jonathan R. Gair, Ilya Mandel, M.Coleman Miller, and Marta Volonteri. Exploring intermediate and massive black-hole binaries with the Einstein Telescope. *Gen.Rel.Grav.*, 43:485–518, 2011.
38. T. Regimbau, C. Robinson, B. Sathyaprakash, C. Van Den Broeck, D. Meacher, C. Rodriguez, T. Dent, S. Giampanis, T.G.F. Li, and W.Del Pozzo. A Mock Data Challenge for the Proposed Einstein GW Telescope. 2011.

EXPERIMENTAL APPROACHES FOR THE EINSTEIN TELESCOPE

R Nawrodt[32,3], M Abernathy[3], F Acernese[4,5], P Amaro-Seoane[33,46], N Andersson[7], K Arun[8], F Barone[4,5], B Barr[3], M Barsuglia[9], M Beker[45], N Beveridge[3], S Birindelli[11], S Bose[12], L Bosi[1], S Braccini[13], C Bradaschia[13], T Bulik[14], E Calloni[4,15], G Cella[13], E Chassande Mottin[9], S Chelkowski[16], A Chincarini[17], J Clark[18], E Coccia[19,20], C Colacino[13], J Colas[2], A Cumming[3], L Cunningham[3], E Cuoco[2], S Danilishin[21], K Danzmann[6], R De Salvo[23], T Dent[18], R De Rosa[4,15], L Di Fiore[4,15], A Di Virgilio[13], M Doets[10], V Fafone[19,20], P Falferi[24], R Flaminio[25], J Franc[25], F Frasconi[13], A Freise[16], D Friedrich[6], P Fulda[16], J Gair[26], G Gemme[17], E Genin[2], A Gennai[16], A Giazotto[2,13], K Glampedakis[27], C Gräf[6] M Granata[9], H Grote[6], G Guidi[28,29], A Gurkovsky[21], G Hammond[3], M Hannam[18], J Harms[23], D Heinert[32], M Hendry[3], I Heng[3], E Hennes[45], S Hild[3], J Hough[4], S Husa[44], S Huttner[3], G Jones[18], F Khalili[21], K Kokeyama[16], K Kokkotas[27], B Krishnan[6], T G F Li[45], M Lorenzini[28], H Lück[6], E Majorana[34], I Mandel[16,35], V Mandic[31], M Mantovani[13], I Martin[3], C Michel[25], Y Minenkov[19,20], N Morgado[25], S Mosca[4,15], B Mours[37], H Müller–Ebhardt[6], P Murray[3], J Nelson[3], R Oshaughnessy[38], C D Ott[39], C Palomba[34], A Paoli[2], G Parguez[2], A Pasqualetti[2], R Passaquieti[13,40], D Passuello[13], L Pinard[25], W Plastino[42], R Poggiani[13,40], P Popolizio[2], M Prato[17], M Punturo[1,2], P Puppo[34], D Rabeling[10,45], I Racz[47], P Rapagnani[34,41], J Read[36], T Regimbau[11], H Rehbein[6], S Reid[3], L Rezzolla[33], F Ricci[34,41], F Richard[2], A Rocchi[19], S Rowan[3], A Rüdiger[6], L Santamaría[23], B Sassolas[25], B Sathyaprakash[18], R Schnabel[6], C Schwarz[32], P Seidel[32], A Sintes[44], K Somiya[39], F Speirits[3], K Strain[3], S Strigin[21], P Sutton[18], S Tarabrin[6], A Thüring[6], J van den Brand[10,45], M van Veggel[3], C van den Broeck[45], A Vecchio[16], J Veitch[18], F Vetrano[28,29], A Vicere[28,29], S Vyatchanin[21], B Willke[6], G Woan[3], K Yamamoto[30]

[1] *INFN, Sezione di Perugia, I-6123 Perugia, Italy*

[2] *European Gravitational Observatory (EGO), I-56021 Cascina (Pi), Italy*

[3] *SUPA, School of Physics and Astronomy, The University of Glasgow, Glasgow, G12 8QQ, UK*

[4] *INFN, Sezione di Napoli, Italy*

[5] *Università di Salerno, Fisciano, I-84084 Salerno, Italy*

[6] *Max-Planck-Institut für Gravitationsphysik and Leibniz Universität Hannover, D-30167 Hannover, Germany*

[7] *University of Southampton, Southampton SO17 1BJ, UK*

[8] *LAL, Université Paris-Sud, IN2P3/CNRS, F-91898 Orsay, France*

[9] *AstroParticule et Cosmologie (APC), CNRS; Observatoire de Paris, Université Denis Diderot, Paris VII, France*

[10] *VU University Amsterdam, De Boelelaan 1081, 1081 HV, Amsterdam, The Netherlands*

[11] *Université Nice 'Sophia-Antipolis', CNRS, Observatoire de la Côte d'Azur, F-06304 Nice, France*

[12] *Washington State University, Pullman, WA 99164, USA*

[13] *INFN, Sezione di Pisa, Italy*

[14] *Astronomical Observatory, University of warsaw, Al Ujazdowskie 4, 00-478 Warsaw, Poland*

[15] *Università di Napoli 'Federico II', Complesso Universitario di Monte S. Angelo, I-80126 Napoli, Italy*

[16] *University of Birmingham, Birmingham, B15 2TT, UK*

[17] *INFN, Sezione di Genova, I-16146 Genova, Italy*

[18] *Cardiff University, Cardiff, CF24 3AA, UK*
[19] *INFN, Sezione di Roma Tor Vergata I-00133 Roma, Italy*
[20] *Università di Roma Tor Vergata, I-00133, Roma, Italy*
[21] *Moscow State University, Moscow, 119992, Russia*
[22] *INFN, Laboratori Nazionali del Gran Sasso, Assergi l'Aquila, Italy*
[23] *LIGO, California Institute of Technology, Pasadena, CA 91125, USA*
[24] *INFN, Gruppo Collegato di Trento, Sezione di Padova; Istituto di Fotonica e Nanotecnologie, CNR-Fondazione Bruno Kessler, I-38123 Povo, Trento, Italy*
[25] *Laboratoire des Matériaux Avancés (LMA), IN2P3/CNRS, F-69622 Villeurbanne, Lyon, France*
[26] *Institute of Astronomy, University of Cambridge, Madingley Road, Cambridge, CB3 0HA, UK*
[27] *Theoretical Astrophysics (TAT) Eberhard-Karls-Universität Tübingen, Auf der Morgenstelle 10, D-72076 Tübingen, Germany*
[28] *INFN, Sezione di Firenze, I-50019 Sesto Fiorentino, Italy*
[29] *Università degli Studi di Urbino 'Carlo Bo', I-61029 Urbino, Italy*
[30] *INFN, sezione di Padova, via Marzolo 8, 35131 Padova, Italy*
[31] *University of Minnesota, Minneapolis, MN 55455, USA*
[32] *Friedrich-Schiller-Universität Jena PF, D-07737 Jena, Germany*
[33] *Max Planck Institute for Gravitational Physics (Albert Einstein Institute) Am Mühlenberg 1, D-14476 Potsdam, Germany*
[34] *INFN, Sezione di Roma 1, I-00185 Roma, Italy*
[35] *NSF Astronomy and Astrophysics Postdoctoral Fellow, MIT Kavli Institute, Cambridge, MA 02139*
[36] *University of Mississippi, University, MS 38677, USA*
[37] *LAPP-IN2P3/CNRS, Université de Savoie, F-74941 Annecy-le-Vieux, France*
[38] *The Pennsylvania State University, University Park, PA 16802, USA*
[39] *Caltech-CaRT, Pasadena, CA 91125, USA*
[40] *Università di Pisa, I-56127 Pisa. Italy*
[41] *Università 'La Sapienza', I-00185 Roma, Italy*
[42] *INFN, Sezione di Roma Tre and Università di Roma Tre, Dipartimento di Fisica, I-00146 Roma, Italy*
[43] *Università degli Studi di Firenze, I-50121, Firenze, Italy*
[44] *Departament de Fisica, Universitat de les Illes Balears, Cra. Valldemossa Km. 7.5, E-07122 Palma de Mallorca, Spain*
[45] *Nikhef, Science Park 105, 1098 XG Amsterdam, The Netherlands*
[46] *Institut de Ciències de l'Espai (CSIC-IEEC), Campus UAB, Torre C-5, parells, 2$^{\text{na}}$ planta, ES-08193, Bellaterra, Barcelona, Spain*
[46] *KFKI Research Institute for Particle and Nuclear Physics, Budapest, Hungary*

Interferometric gravitational wave detectors currently under operation have reached their design sensitivities and will by upgraded to their second generation having ten times more sensitivity. It is expected that these instruments will detect gravitational waves directly for the first time and thus opening the era of gravitational wave astronomy. The Einstein Telescope design study - funded by the European Commission - investigates the technical and scientific challenges for a third generation of gravitational wave detectors that will have a 100 times better sensitivity compared to the first generation. This contribution summarises selected experimental approaches for the Einstein Telescope and will discuss challenges for the future research within this vital field of precision measurements.

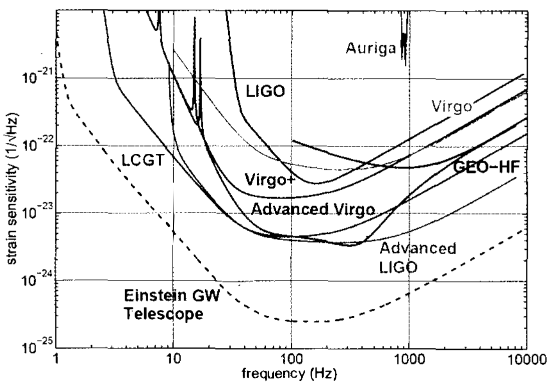

Figure 1: Overview of the sensitivities of the fist (LIGO, Virgo, Virgo+) and second generation (Adv. LIGO, Adv. Virgo, GEO-HF, LCGT) GW detectors compared with the Einstein Telescope. Additionally, the typical sensitivity for a bar detector (Auriga) is given as well.

1 Introduction

The interferometric gravitational wave detectors - LIGO [1], Virgo [2], GEO600 [3] and TAMA [4] - currently under operation have reached their design sensitivity within a wide frequency range from about several 10's of Hz up to a few kHz. They have demonstrated an operational regime in a world wide network having a large duty cycle. While during their operational time no gravitational wave signal was detected the experimental data has been used to study several astronomical sources allowing the determination of unknown properties [5,6].

Currently, these detectors - which are called the first generation - are upgraded to a second generation. These detectors will have a ten times larger sensitivity for gravitational waves. This network of second generation detectors including Advanced LIGO [7], Advanced Virgo [8], GEO-HF [9] and LCGT [10] is expected to detect gravitational directly when coming up online in 2014/15. The direct observation of gravitational waves will open a new window to the universe exploring new physics of astronomical objects and the universe itself. Novel experimental and technical approaches have been developed in order to increase the detectors sensitivity. Their potential has been demonstrated in the first generation detection and were included in the design of the second generation detectors. Amongst them are important technologies for the Advanced Detectors as for example the monolithic fused silica suspension that have has pioneered in GEO600 [11,12,13] or the Squeezing Technique [14,15] that allows to overcome quantum limitations.

Beyond the Advanced Detector generation there are already efforts that focus on a further enhancement of the detectors. The Einstein Telescope (ET) design study [16,17] is a European Commission funded project to investigate a conceptual design for a future GW observatory that included novel technologies needed for a long time operation for two to three decades.

A summary of the scientific potential of the Einstein Telescope can be found e.g. in [18,19].

2 Sensitivity considerations

The focus of the ET Design Study was the demonstration of a conceptual design of a GW observatory that has ten times better sensitivity compared to the Advanced Detectors within a wide range of frequencies (see Fig. 1).

The main sensitivity limitations of a GW detector are:

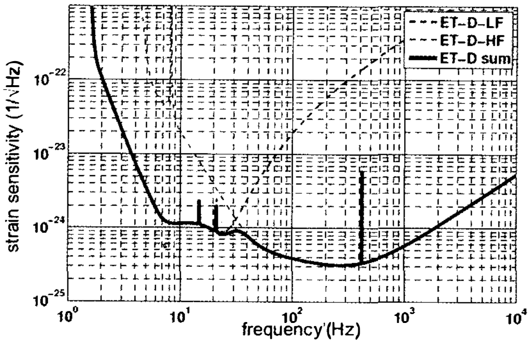

Figure 2: Xylophone design of the Einstein Telescope. The low frequency part (LF) of the sensitivity curve is realised with a low laser power interferometer operating at cryogenic temperatures while the high frequency (HF) part is covered by a room temperature interferometer with a circulating laser power of up to 3 MW.

- at low frequencies: seismic noise, thermal noise of the suspension elements, radiation-pressure noise,
- in the mid-frequency range: thermal noise of the optical components,
- at high frequencies: photon shot noise of the laser light.

All these noise contributions have been carefully studied and influenced the design of the second generation detectors. This design is based on the available infrastructure from the first generation (e.g. detector site, vacuum tubes, etc.). In contrast, for the ET design study the site selection and the design of the infrastructure was included into the conceptual design allowing more flexibility and a further reduction of these noise contributions by novel techniques.

In order to overcome the different noise limitations different techniques are required. While for the high frequency part high laser powers of up to 3 MW are preferable the low and mid frequency part of the sensitivity curve requires the use of cryogenic techniques to reduce thermal noise from the suspension elements as well as the optical components [20]. These two approaches are contradictory. Initial estimates have shown that a cryogenic operation of the optical components at around 20 K is not feasible with circulating laser powers in the MW range.

The solution was the suggestion of a design that uses two different interferometers - the so-called Xylophone design [21,22]. The low frequency part of the sensitivity curve is realised with a low laser power interferometer with optics operating at around 10-20 K. The high frequency part is covered with a high power interferometer with up to 3 MW laser power operating at room temperature and is based on the sophisticated techniques that have been developed for the Advanced Detectors.

3 Material Issues and Thermal Noise

3.1 Optical Materials

The reduction of thermal noise of the optical components and the suspension elements is realised by means of utilising cryogenic temperatures of about 10 K for the low frequency detector. Brownian thermal noise [23,24] of a component is dependent on its temperature and its mechanical loss. Both values should be as low as possible in order to get a low Brownian thermal noise level. The first and second generation of GW detectors use fused silica as the test mass materials as well as (in parts) for suspension elements. This material provides a low mechanical loss as well

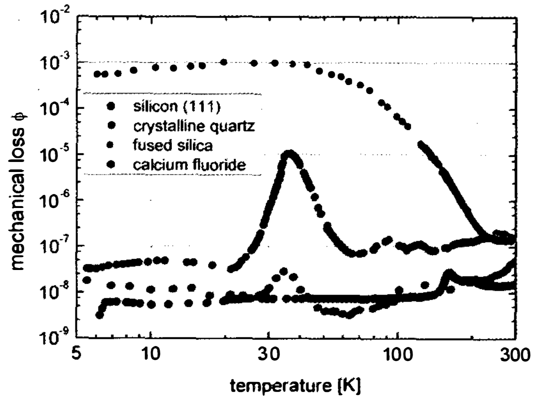

Figure 3: Comparisson of the mechanical loss of different materials at low temperatures.

as excellent optical properties. It is known that amorphous materials like fused silica have a high level of mechanical loss at cryogenic temperatures (see e.g. [25,26]). Thus, different materials have to be used for a low thermal noisc operation. Different materials have been discussed in the past for cryogenic applications. Among them sapphire, calcium fluoride and silicon have been studied in detail. Sapphire is the material of choice for the LCGT detector [10]. Calcium fluoride showed low mechanical losses [27,28,29] - however, the expected dimensions of the ET main optics of about dia. 50 cm and a thickness of 45 cm rule this material out. It is currently not available in such large dimensions and it cannot be foreseen that this will change within the next years. In contrast silicon also shows very low mechanical losses at cryogenic tcmperatures [30]. Currently, the semiconductor industry is pushing for large single crystals due to their demand for large wafers. Thus, silicon has been proposed as an optical material for GW detectors for a long time [31,32,33].

The total thermal noise budget of an end mirror of the Einstein Telescope is shown in Fig. 4. The main contribution of the total thermal noise is the Brownian thermal noise of the coating

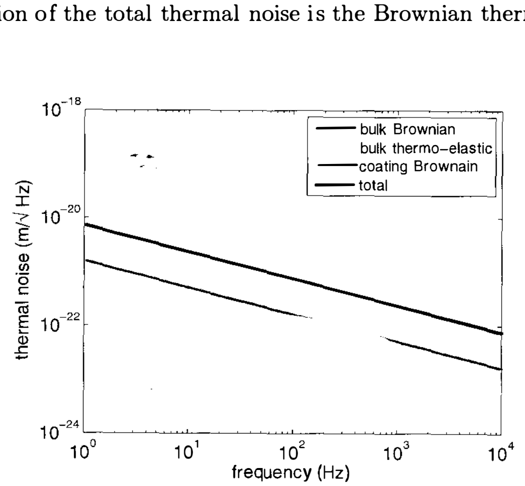

Figure 4: Summary of the thermal noise of a silicon end mirror coated with a standard tantala:silica HR multilayer.

material. A detailed study of the mechanical loss of different coating materials is currently ongoing[34,35,36,37] in order to minimise the coating contribution.

3.2 Suspension Materials

A monolithic suspension technique based on fused silica as the material and hydroxide-catalysis bonding for jointing materials has been adapted for the Advanced Detectors [7,38,39,40]. As discussed previously fused silica cannot be used in cryogenic applications due to its large mechanical loss. Additionally to the low thermal noise design the suspension elements of the cryogenic optics needs to fulfill a second duty: It has to extract the residual heat from the mirror that is caused by optical absorption of the optics. Thus, a material with high thermal conductivity is preferable. Silicon and sapphire are both materials that show low thermal noise at cryogenic temperatures and a high thermal conductivity. Sapphire is currently investigated as the suspension material for the LCGT detector. Silicon has been studied as a suspension material for the Einstein Telescope. Low mechanical loss as well as the possibility to fabricate strong and reliable bonds based on the hydroxide-catalysis technique have been shown for silicon[41,42].

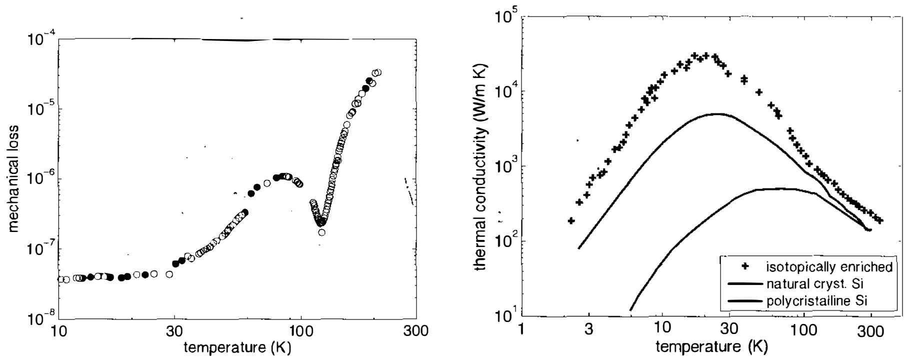

(a) (b)

Figure 5: Mechanical loss (a) and thermal conductivity (b) of silicon as a suspension material.

These material properties allow a similar monolithic design to the Advanced Detectors. The last stage of the suspension is proposed to be fabricated in monolithic way allowing low thermal noise and high thermal conductivity at cryogenic temperatures (see Fig. 5). Details of the suspension design and the cryogenic aspects can be found in[18,43].

4 Optical Layout, Infrastructure and Site Selection

A Michelson-based detector with a triangular shape[44] was identified to give the optimum solution regarding scientific output, future flexibility and construction efforts. Each corner station will be equipped with one detector (which consists of two interferometers - LF and HF, see Fig. 6). The observatory will be placed underground in order to reduce seismic disturbances as much as possible. The arm length of the interferometers was fixed to a length of 10 km. The length is based on a trade-off study between scientific benefits and the construction costs. This trade-off was a central point of the Einstein Telescope Design Study[18]. The conceptual design study contains detailed analyses of the scientific benefits and the costs of the instrument and its potential configuration.

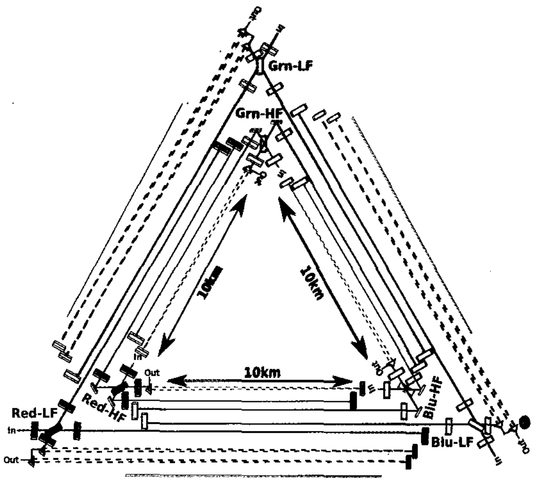

Figure 6: Triangular shape of the proposed Einstein Telescope design. Each corner station contains two interferometers - one cryogenic interferometer for the low frequency part and one high laser power interferometer for the high frequency part of the spectrum.

Several potential candidate sites have been studied in detail regarding their local seismic noise, their compositions of the soil and the possibility to construct the infrastructure for the proposed observatory.

Different optical techniques are within current investigations for implementation in third generation GW detectors. One example are Laguerre Gauss (LG) modes as a replacement for the Gaussian laser beams[45]. Due to the different averaging of the mirror surface fluctuations the LG modes provide a low level of thermal noise. Compared to other non-Gaussian beam profiles - like Mexican hat or flat-top profiles - the LG beams are compliant with spherical optics as currently in use.

5 Summary

A selection of experimental approaches for a European third generation gravitational wave detector has been presented. The full design study document can be found online at www.et-gw.eu describing the experimental approaches as well as scientific benefits of such a detector more in detail.

Acknowledgments

The authors would like to thank the European Commission for the financial support under the Framework Programme 7 (FP7) 'Capacities' - project *Einstein Telescope* (ET) design study (Grant Agreement 211743). RN acknowledges the support of the German Science Foundation under contract SFB TR7.

References

1. A. Abramovici et al., *Science* **256**, 325 (1992).
2. B. Caron et al., *Class. Quantum Grav.* **14**, 1461 (1997).

3. H. Lück and the GEO600 Team, *Class. Quantum Grav.* **14**, 1471 (1997).
4. K. Kawabe and the TAMA collaboration, *Class. Quantum Grav.* **14**, 1477 (1997).
5. B. Abbott et al., *The Astrophysical Journal Letters* **683**, L45 (2008).
6. B. Abbott et al., *Nature* **460**, 990 (2009).
7. G. M. Harry and the LIGO Scientific Collaboration, *Class. Quantum Grav.* **27**, 084006 (2010).
8. F. Acernese et al., *Class. Quantum Grav.* **25**, 114045 (2008).
9. B. Willke et al., *Class. Quantum Grav.* **23**, S207 (2006).
10. K. Kuroda et al., *Class. Quantum Grav.* **27**, 084004 (2010).
11. S. Traeger, B. Willke, K. Danzmann, *Phys. Lett. A* **225**, 39 (1997).
12. B. W. Barr et al., *Class. Quantum Grav.* **19**, 1655 (2002).
13. J. R. Smith et al., *Class. Quantum Grav.* **21**, S1091 (2004).
14. C. M. Caves, *Phys. Rev. D* **23**, 1693 (1981).
15. R. Schnabel, *Nature Physics* **4**, 440 (2008).
16. M. Punturo et al., *Class. Quantum Grav.* **27**, 084007 (2010).
17. M. Punturo et al., *Class. Quantum Grav.* **27**, 194002 (2010).
18. Einstein Telescope Design Study, available at www.et-gw.eu.
19. B. Sathyaprakash et al., *Moriond Proceedings 2011.*
20. S. Hild, S. Chelkowski, A. Freise, *arXiv:0810.0604v2* (2008).
21. S. Hild, S. Chelkowski, A. Freise, J. Franc, N. Morgado, R. Flaminio, R. DeSalvo, *Class. Quantum Grav.* **27**, 015003 (2010).
22. S. Hild et al., *Class. Quantum Grav.* **28**, 094013 (2011).
23. P. R. Saulson, *Phys. Rev. D* **42**, 2437 (1990).
24. R. Nawrodt, S. Rowan, J. Hough, M. Punturo, F. Ricci, J.-Y. Vinet, *General Relativity and Gravitation* **43**, 593 (2010).
25. R. E. Strakna, *Phys. Rev.* **123**, 2020 (1961).
26. H. J. McSkimin, *J. Appl. Phys.* **24**, 988 (1953).
27. P. Amico et al., *Class. Quantum Grav.* **19**, 1663 (2002).
28. R. Nawrodt et al., *Eur. Phys. J. Appl. Phys.* **38**, 53 (2007).
29. C. Schwarz et al., *physica status solidi a* DOI: 10.1002/pssa.201127331.
30. D. F. McGuigan, C. C. Lam, R. Q. Gram, A. W. Hoffman, D. H. Douglass, H. W. Gutche, *J. Low. Temp. Phys.* **30**, 621 (1978).
31. W. Winkler, K. Danzmann, A. Rüdinger, R. Schilling, *Phys. Rev. A* **44**, 7022 (1991).
32. S. Rowan et al., *Proc. SPIE* **4856**, (2003).
33. S. Rowan, J. Hough, D. R. M. Crooks, *Phys. Lett. A* **347**, 25 (2005).
34. I. W. Martin et al., *Class. Quantum Grav.* **26**, 155012 (2009).
35. I. W. Martin et al., *Class. Qauntum Grav.* **27**, 225020 (2010).
36. R. Flaminio, J. Franc, C. Michel, N. Morgado, L. Pinard, B. Sassolas, *Class. Quantum Grav.* **27**, 084030 (2010).
37. R. Bassiri, K. B. Borisenko, D. J. H. Cockayne, J. Hough, I. MacLaren, S. Rowan, *Appl. Phys. Lett.* **98**, 031904 (2011).
38. S. Rowan, S. M. Twyford, J. Hough, D.-H. Gwo, *Phys. Lett. A* **246**, 471 (1998).
39. A. Cumming et al., *Class. Quantum Grav.* **26**, 215012 (2009).
40. M. Lorenzini et al., *Class. Quantum Grav.* **27**, 084021 (2010).
41. A. A. van Veggel et al., *Class. Quantum Grav.* **26**, 175007 (2009).
42. N. L. Beveridge et al., *Class. Quantum Grav.* **28**, 085014 (2011).
43. P. Puppo, F. Ricci, *General Relativity and Gravitation* **43**, 657 (2011).
44. A. Freise, S. Chelkowski, S. Hild, W. Del Pozzo, A. Perreca, A. Vecchio, *Class. Quantum Grav.* **26**, 085012 (2009).
45. P. Fulda, K. Kokeyama, S. Chelkowski, A. Freise, *Phys. Rev. D* **82**, 012002 (2010).

VERY HIGH FREQUENCY GRAVITATIONAL WAVE SCIENCE

A.M.CRUISE
School of Physics and Astronomy, University of Birmingham, Edgbaston, Birmingham B15 2TT, England

While the obvious candidates for gravitational wave emission fall in the frequency bands of LIGO, VIRGO, Pulsar Timing Arrays and LISA, the technology to make observations at much higher frequencies is now being explored. Perhaps surprisingly there are already predictions of signals in the MHz to GHz range and even at higher fequencies into the optical regime. This paper explores the possible sources of such emission and the means of detecting them.

1 Introduction

The history of astronomy is one of surprises - even in the 21st century new observational data has led to a succession of new phenomena being revealed in the absence of theoretical prediction. Most of these discoveries have followed directly from new observational techniques becoming available. For this reason alone we should take the opportunity to explore any new parameter space available as a result of technological advances. Given the fact that the whole spectrum of gravitational wave emission is unexplored it is rational to focus initial efforts on frequency ranges which have the best predictions for detectable sources and these are obviously the frequencies expected of stellar mass systems such as neutron stars (tens of hertz to kilohertz- the LIGO range) and the frequency range expected of supermassive black holes (micro hertz to millihertz- the LISA range). These are the frequencies at which the first detections are to be expected. Well motivated predictions are becoming available for gravitational waves at much higher frequencies- at MHz, GHz, THz and above. Since objects radiate efficiently at wavelengths comparable to their size such radiation would require energy concentrations sufficient to cause significant spacetime curvature on the scale of metres, centimetres or microns. On the face of it this is an unlikely proposition but there are three plausible possibilities: the very early universe, oscillations in curved higher dimensions and coherent conversion of metre, centimeter or micron scale electromagnetic waves to gravitational waves in plasmas.

2 Possible Sources

2.1 Cosmological Waves

The scale of the universe at the time of inflation corresponded to the wavelength range of relevance to very high frequency gravitational waves. A succession of authors [1-9] have modelled these early phases of the universe and found that very high frequency gravitational waves will be produced as a result of inflation, string decay or phase transitions. In some sense all these predictions involve new or unexplored physics but even so they are limited by the observational constraint provided by the excellent match of the abundances of light elements to the predictions of nucleosynthesis based on a modelled expansion rate. If the energy density of gravitational waves exceeded a certain level (about 10^{-5} of the closure density) then the change in the expansion rate would cause a detectable change in the abundances. This limit- the nucleosynthesis limit- constrains any ubiquitous gravitational wave flux at frequency ν to have a characteristic dimensionless amplitude, h, averaged over a frequency range of order ν, to be less than

$$h = 3.0 \cdot 10^{-20} \frac{100}{\nu} \sqrt{\Omega} \qquad (1)$$

For frequencies in the range 1 GHz to 10^{15} Hz, this gives an upper limit on dimensionless amplitudes of between 10^{-30} and 10^{-35} - extremely challenging signals to detect.

2.2 *Higher Dimensional Gravity*

The well known problem of incorporating gravity into a quantum field theory has led to serious investigation of the properties of higher dimensional spaces, prompted in part by the Kaluza-Klein calculations linking electromagnetism and gravitation. Considering the observable four dimensional manifold as a brane embedded in a higher dimensional space, models of black holes on the brane have been developed requiring two branes for reasons of stability. Stellar mass sized compact objects falling into such a black hole generate the expected gravitational waves in the brane at the (low) frequencies related to the orbital motion as in four dimensional gravity. An additional feature found by Seahra and Clarkson [10-11] is the stimulation of gravitational modes in the fifth dimension, the dimension separating the two branes. The amplitudes predicted from such an interaction at our galactic centre are large- dimensionless amplitudes of 10^{-18} , again averaged over a bandwidth of order the observed frequency. Such amplitudes are within the range of possible detectors currently being commissioned at GHz and optical frequencies. While there is no doubt that such a source mechanism is highly speculative in the absence of firm evidence that we do inhabit a five dimensional universe, the ability to probe the existence of possible extra dimensions is a rare experimetal opportunity worth exploring.

2.3 *Plasma conversion of intense electromagnetic waves to gravitation modes*

Servin and Brodin [12] have shown that the presence of a magnetised plasma can improve the coupling between electromagnetic and gravitational wave modes. For plasmas magnetised by a static field parallel to an intense incoming electromagnetic wave an instability developes in which the generation of gravitational waves is theoretically limited by the available free energy of the plasma. In extreme astrophysical situations-AGN jets, SS433, GRB's, for example, this could represent a substantial source of gravitational wave energy at the frequency of the electromagnetic wave. Higher frequencies are more effective, well above the plasma and hybrid frequency, because the phase velocity of the electromagnetic wave will be closer to that of the gravitational wave allowing phase coherence over larger pathlengths. Observations at radio or optical frequencies can already identify sources with suitable geometry and electromagnetic stimulus.

Perhaps surprisingly then, there are possible mechanisms for generating gravitational waves at very high frequencies despite the most obvious sources being at very much longer wavelengths. The important issue is whether there are detectors at these high frequencies of sufficient sensitivity. An interesting parallel may be noticed with the 1960's when the only X-Ray source detected in the universe was thermal X-Ray emission from the Sun, an emission process which, if placed at the distance of the nearest local stars, would have been undetectable. However, simple space instruments easily detected the unpredicted X-Rays from local neutron stars (Sco-X1) and black holes (Cyg-X1) because they were radiating via a different mechanism.

3 Possible Detectors

The sophistication and sensitivity of laser interferometers is remarkable and these instruments , on the ground or in space, seem likely to achieve the first detections. Such instruments can be configured to work at very high frequency as Akutsu and Kawamura [13-14] have shown, with sensitivities in averaged dimensionless amplitude of order 10^{-17} being achieved at 100 MHz. However, the minimum detectable signal of an interferometer increases as $\nu^{1/2}$ with the operating frequency ν and this may preclude such instruments from being competitive at the higher frequencies, essentially due to the photon statistics from current lasers being inadequate at such high frequencies. A more direct method of detecting very high frequency gravitational waves is to use a static electromagnetic field to convert the gravitational wave to an electromagnetic wave at the same frequency and travelling in the same direction, a process described by Gershenstein [15-18] and many others. Provided the generated electromagnetic wave has the same phase velocity as the incoming gravitational wave over a path length of N wavelengths, the power converted to an electromagnetic wave is given by

$$P = \frac{\pi^2 B^2 N^2 h^2 c}{2\mu_0} \tag{2}$$

where B is the perpendicular, static magnetic field, h is the dimensionless amplitude of the gravitational wave, μ_0 is the permeability of free space and c is the velocity of light. Once converted to an electromagnetic wave, the signal can be detected by the normal range of electromagnetic detectors, depending on the frequency. One interesting feature of such a detector is the fact that the full range of electromagnetic technology becomes available to improve sensitivity, wavelength resolution or angular response and techniques such as aperture synthesis are now being explored by a collaboration between groups at the University of Birmingham and Jodrell Bank.

4 Current Status

The prototype detector at the University of Birmingham operates at two frequency ranges, 14 GHz and $3.10^{14} - 10^{15}$ Hz using the same magnetic field volume which is approximately one metre long and a few square centimetres cross section. The sensitivity is very strongly constrained to the long axis of the magnetic field volume and therefore the detector is constructed on an equatorial mount which permits continuous pointing at selected astronomical objects. A second prototype is being constructed with a similar geometry to carry out an all-sky scan over a period of six months. The graph below shows the current and future expected sensitivity of such detectors at microwave and optical frequencies in comparison to predicted gravitational wave signals. As equation 2 indicates the converted signal power is proportional to the square of the magnetic field and current facilities can provide fields between 0.2T and 40T. Higher sensitivity would come from higher magnetic fields but there is no immediate prospect of very substantial increases in this parameter. Sensitivity improvements are likely with the use of cryogenic front end amplifiers to reduce thermal noise, correlating co-located detectors which experience the same signal but uncorrelated thermal noise and building detectors with a larger collecting area. These steps are planned in the form of a two element interferometer to be based at Jodrell Bank.

Acknowledgments

The author is grateful for support from the Science and Technology Facilities Council in the UK.

Statement

The work presented here has no connection with publications by the HFGW group in the US and China.

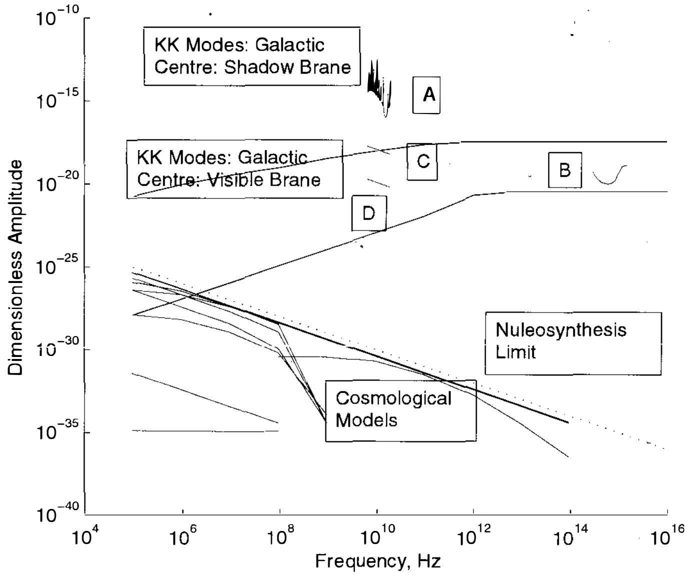

Figure 1: Possible source dimensionless amplitudes, averaged over bandwidths of the same order as the observing frequency. Detector sensitivities: A: Current 14 GHz system, B: Current optical system, C: Planned cryogenic detector at 5GHz, D: Planned two element interferometer based on C

References

1. Grischuk L P *JETP Letts* **23** 293, 1976
2. Giovannini M *Phys Rev D* **60** 123511, 1999
3. Gasperini M and Veneziano G *CERN-TH* 2002-104, 2002
4. Garcia-Bellido and Feguira *Class Quantum Grav* **22** s155, 2000
5. Easther R, Giblin J T and Lim E A, *Phys Rev Letts* **99** 221301, 2007
6. Caprini C, Durrer R, Konstandin T and Servant G *Phys Rev D* **79**, 083519, 2009
7. Copeland E J, Mulryne D J ,Nunes N J and Shaeri, M *Phys Rev D* **79**, 023508, 2009
8. Caldwell R R, Battye R A and Shellard E P S *Phys Rev D* **54** 7146, 1996
9. Leblond l,Shlaer B and Siemens X *Phys Rev D* **79**,123519, 2009
10. Seahra S S, Clarkson C and Maartens R *Phys Rev Letts* **94** 121302, 2005
11. Clarkson C and Seahra S S *Class Quantum Grav* **24** F33, 2007
12. Servin M and Brodin G *Phys Rev D* **68**, 044017, 2003
13. Akutsu T, Kawamura S, Nishizawa A, Arai K, Yamamoto K, Tatsumi D, Nagano S, Nishida E, Chiba T, Takahashi N, Sugiyama N, Fukushima M, Yamazaki T and Fujimoto M-K *Phys Rev Letts* **101**, 101101, 2008
14. Nishizawa A, Kawamura S, Akutsu T, Arai K, Yamamoto K, Tatsumi D, Nishida E, Sakagami M-a, Chiba T, Takahashi R, and Sugiyama N *Phys Rev D* **77**, 022002, 2008
15. Gertsenshtein M E *Sov Phys JETP* **14** No 1, 84, 1962
16. Lupanov G A *Sov Phys JETP* **25** No 1 76, 1967
17. Boccaletti D, De Sabbata V, Fortini P and Gualdi *Nuovo Cimento* **70 B** No 2, 129, 1970
18. De Logi W K and Mickelson A R *Phys Rev D* **16** No 10, 2915, 1977

COMPARISON OF LISA AND ATOM INTERFEROMETRY FOR GRAVITATIONAL WAVE ASTRONOMY IN SPACE

PETER L. BENDER
JILA, University of Colorado and National Institute of Standards and Technology, Boulder, CO

One of the atom interferometer gravitational wave missions proposed by Dimopoulos *et al.*[1] in 2008 was called AGIS-Sat. 2. It had a suggested gravitational wave sensitivity set by the atom state detection shot noise level that started at 1 mHz, was comparable to LISA sensitivity from 1 to about 20 mHz, and had better sensitivity from 20 to 500 mHz. The separation between the spacecraft was 1,000 km, with atom interferometers 200 m long and shades from sunlight used at each end. A careful analysis of many error sources was included, but requirements on the time-stability of both the laser wavefront aberrations and the atom temperatures in the atom clouds were not investigated. After including these considerations, the laser wavefront aberration stability requirement to meet the quoted sensitivity level is about 1×10^{-8} wavelengths, and is far tighter than for LISA. Also, the temperature fluctuations between atom clouds have to be less than 1 pK. An alternate atom interferometer GW mission in Earth orbit called AGIS-LEO with 30 km satellite separation has been suggested recently. The reduction of wavefront aberration noise by sending the laser beam through a high-finesse mode-scrubbing optical cavity is discussed briefly, but the requirements on such a cavity are not given. Unfortunately, such an Earth-orbiting mission seems to be considerably more difficult to design than a non-geocentric mission and does not appear to have comparably attractive scientific goals.

1 Introduction

The purpose of this paper is to discuss some proposals that have been made to use atom interferometry in space missions to observe gravitational waves. Three specific space mission candidates were proposed by Dimopoulos *et al.* in 2008.[1] The missions were called Atom Gravitational wave Interferometric Sensor (AGIS), Satellite 1, 2, and 3 (*i.e.*, AGIS-Sat. 1, etc.). It appears useful to compare these missions with the Laser Interferometer Space Antenna (LISA) gravitational wave mission[2,3] that has been studied extensively as a proposed joint mission of the European Space Agency and NASA. The AGIS-Sat. 2 mission has a nominal sensitivity curve closest to that of LISA, and it will be the main mission discussed here.

After reading ref. 1 and attempting to obtain more information about the proposed missions, it became clear that there were quite severe additional requirements needed in order to meet the given nominal sensitivities. Thus a Comment on the paper by Dimopoulos et al. was prepared and submitted to Physical Review D in August, 2010. A somewhat modified version of this Comment[4] has now been accepted for publication.

In September, 2010, a paper by Hogan *et al.*[5] describing a proposed AGIS mission in low Earth orbit called AGIS-LEO was placed on arXiv. For this mission, the optimum part of the nominal sensitivity curve is moved up in frequency to 0.03 to 10 Hz, compared with 0.003 to 0.5

Hz for AGIS-Sat. 2, and the sensitivity is about a factor 20 worse. The main orbit geometry considered was a leader-follower configuration on a circular orbit at nearly constant altitude.

The proposed AGIS-Sat. 2 mission and the requirements to meet its sensitivity goals will be described in Section 2. This will be followed by a discussion of the proposed AGIS-LEO mission in Section 3. Then, a brief comparison with the requirements of LISA will be given in Section 4.

2 AGIS-Sat. 2 Mission

In ref. 1, each of the three space missions proposed was assumed to make use of short sequences of laser pulses at three different times separated by times T to carry out the atom interferometry. Satellites at each end of a path of length L would prepare atom clouds with temperatures of 100 pK and send them out at a rate of one per second, along the path. Pulsed laser beams from one end would provide the light pulses for the atom interferometry, and a continuous laser beam from the other end would provide the phase reference needed to permit correlation of the results obtained by the atom interferometers at the two ends.

The proposals for AGIS-Sat. 2 and AGIS-Sat. 3 assumed times T between the three pulse sequences of 100 s, atom interferometer path lengths of 100 to 200 m at each end, and a difference of 200 to 400 photon momenta between momenta transferred to the two split parts of the atom wavefunctions by the first of the short laser pulse sequences. However, a factor 10 larger value for the distance L between satellites was assumed for AGIS-Sat. 3, and a factor 10 better phase sensitivity for detecting differences in the atom populations in two ground-state sublevels at the end of each atom interferometer, leading to about a factor 50 better nominal gravitational wave sensitivity than for AGIS-Sat. 2.

In ref. 4, the proposal for AGIS-Sat. 3 was considered. However, ref. 1 says that AGIS-Sat. 3 "is an aggressive possibility that might be realizable in the future." Since the sensitivity for AGIS-Sat. 2 is comparable with that for LISA from about 1 to 20 mHz, and since AGIS-Sat. 3 appears to be much more difficult to implement, attention will be focused on the AGIS-Sat. 2 proposal in this paper. For AGIS-Sat. 1, the nominal gravitational wave sensitivity is a factor of roughly 20 worse than for AGIS-Sat. 2 down to about 0.03 Hz, and much worse at lower frequencies. Whether there is a science justification for such a mission appears to be uncertain.

It is stated clearly in ref. 1 that the nominal gravitational wave sensitivities given are only those due to the statistical uncertainties in atom sublevel populations determined at the ends of the atom interferometers. A large number of other error sources are considered, but none are estimated to exceed the statistical uncertainties. However, two additional error sources that were not considered are the subject of ref. 4. The first of these is laser wavefront aberration variations over periods of 1 to 200 s. For a number of error sources considered in ref. 1, there is a strong cancellation of the errors because they are closely the same for the atoms in the two atom interferometers. For example, the effect of laser phase noise at fairly low frequencies is reduced because the travel time between the two interferometers separated by 1000 km is only 0.003 s. However, this is not true for laser wavefront aberrations.

The expected size of the atom clouds is considerably less than the suggested telescope diameter of roughly 1 m for AGIS-Sat. 2. And there will be a substantial reduction in the amplitude of the wavefront aberrations over the 1000 km path length. An estimate similar to that made in ref. 4 based on primary spherical aberrations indicates that such aberration variations would need to be kept down to 1x10-8 wavelengths in order to keep the gravitational wave noise from this source down to that from the statistical atom state sensing noise.

The second additional error source is fluctuations from cloud to cloud in the atom cloud temperatures. For 0.001 wavelength of dc primary spherical aberration in the initially transmitted laser beam, fluctuations of only 1 pK in the atom cloud temperature from cloud to cloud would substantially increase the gravitational wave noise level.

3 AGIS-LEO proposal

The proposal in ref. 5 for a mission called AGIS-LEO was quite different. To reduce some of the effects of being in Earth orbit, the baseline length between the satellites was reduced to 30 km and the time interval T between the different short sets of laser pulses applied to the atoms was reduced to 4 s. In addition, the use of five short sets of pulses instead of three and operation at 1,000 km altitude are assumed. The disturbing effects are mainly gradients in the Earth's gravity field and the Coriolis force.

Although the suggested gravitational wave sensitivity for AGIS-LEO is about a factor 20 worse than for AGIS-Sat. 2, the requirement on the laser wavelength aberration fluctuations is slightly tighter because of the satellite separation being only 30 km. The use of a high-finesse mode-scrubbing cavity is discussed, but no estimate of the possible level of wavefront aberration noise from a suitable laser is given, and corresponding requirements on the filter cavity performance are not considered. The conceptual design shown for a single AGIS-LEO telescope is a 30 cm diameter off-axis Gregorian system, and 1 W of laser power is assumed.

The possible use of a pinhole spatial filter at the real intermediate focus of the telescope to eliminate wavefront errors from all optics and lasers before the primary mirror is mentioned. However, in view of the suggested laser beam waist size of 10 cm and the 30 cm telescope diameter, careful apodization of the beam from the telescope appears to be needed in order to reduce the amplitude of near-field diffraction ripples, which would affect the atom clouds in the near interferometer differently than those in the far interferometer.

For the laser wavefront aberration noise, some information is available on the fluctuations in wavefront tilt[6] from a set of 8 lasers similar to those that might be used in the Advanced LIGO program. These lasers had roughly 2 W of output power, and similar ones may be used as the master lasers in the laser amplifier or injection-lock configurations needed to get the required high input power for Advanced LIGO. The relative pointing fluctuations for the lasers were measured at frequencies down to 1 Hz, and were much higher at that frequency than at 3 Hz.

In the AGIS-LEO proposal, a possible alternative interferometer laser beam geometry is discussed. In this approach, the atom optics laser beams can be made to first propagate between two satellite stations along a path that is displaced from the atoms before being redirected to interact with the atoms. As a consequence, the first propagation segment would serve as a spatial filter, allowing high frequency wavefront noise to diffract out of the beam. It is suggested that "If needed, this alternative beam geometry could be used in conjunction with a mode-scrubbing cavity." However, for the longer wavelength wavefront aberrations such as variations in wavefront curvature, it appears that a substantial reduction in aberration amplitude would also lead to a significant reduction in the laser power.

Because of the reduction in the time T between short sequences of laser pulses for AGIS-LEO, the tight requirement on the temperature differences between the atom clouds in the two atom interferometers is removed. However, this requirement is replaced by a very tight requirement on the fluctuations in mean radial velocity for the clouds of 10 nm/s. This requirement comes from item 12 in Table IV of ref. 5, and involves the Earth's gravity gradient and the satellite orbital frequency, plus a factor T^4. It is stated that such requirements could be relaxed by a moderate reduction in T, but there would be some reduction in the measurement bandwidth also.

In Fig. 4 of ref. 5, signal strength curves are shown for four types of gravitational wave sources. One of these is white dwarf binaries at 10 kpc distance. However, such binaries would only be detectable by AGIS-LEO at frequencies above about 0.03 Hz, and it is not clear that there are likely to be any white dwarf binaries currently in the galaxy at frequencies higher than this. The other types of sources shown are inspirals of one solar mass black holes into 10^3 or 10^5 solar mass black holes at distances of up to 10 Mpc, but the expected rates for such events is very low. Thus it does not appear that there is a substantial scientific case for such a mission based on gravitational wave detection.

A secondary objective for AGIS-LEO that is mentioned in ref. 5 is the determination of time variations in the Earth's gravity field. The GRACE satellite mission currently is monitoring such variations, but is near the end of its life. The next mission after GRACE probably will still fly at roughly 500 km altitude, but later missions with fairly simple drag-free systems are expected to fly at about 300 km altitude. This is because of the importance of monitoring time variations in the higher harmonics of the Earth's field, and thus of obtaining higher spatial resolution. The 1,000 km altitude for AGIS-LEO would be a substantial limitation, since for degree 100 harmonics the attenuation of the signal at that altitude would be a factor 20,000 higher than at 300 km altitude.

4 Comparison of the LISA and AGIS-Sat. 2 Missions

A major difference between the LISA and AGIS-Sat. 2 missions is in the degree of complexity. For LISA, one of the two main mechanical requirements is to be able to clamp the test masses during launch, and then release them reliably later. The other, because of LISA needing to have at least two interferometer arms, is to be able to change the angle between the two optical assemblies sending beams along the arms smoothly over about a degree range during the year. These are quite standard engineering design requirements. For laser interferometry, the requirement of about 2×10^{-5} wavelength/$\sqrt{\mathrm{Hz}}$ accuracy in measuring distance changes down to about 1 mHz does not come close to the state of the art at all, and the only challenge is to accomplish this reliably over the whole mission lifetime with fairly simple hardware.

For AGIS-Sat. 2, even without the additional requirements discussed earlier, there are many more and more challenging requirements. For example, 10^8 atom clouds have to be prepared and cooled to 100 pK temperature at a rate of one cloud per second. The clouds then have to be moved 30 m or more from the satellite, placed along the axis of the laser beams, and sent off accurately along the desired path. The velocities have to be different for the different clouds in order to permit them to be interrogated separately. And the population ratios of the atom ground-state sublevels have to be determined to 1×10^{-4} accuracy up to more than 100 m from the spacecraft. No sketch of what a satellite capable of accomplishing this might look like appears to have been presented so far in descriptions of the proposed mission.

There also appears to be a problem with the 200 atom clouds assumed to be simultaneously in each interferometer. If sequences of Bragg and/or Raman pulses are used to apply 100 units of photon momentum to each part of the atom wavefunction, with 1 W of laser power and 1 m diameter telescopes, and the stimulated Rabi frequency is 100 Hz, the spontaneous emission rate for the atoms appears to be too high. The possibility of operating about 10 concurrent interferometers is stated in Section V A 3 of ref. 5, but it isn't clear that 200 clouds can be handled simultaneously for the set of parameters assumed for AGIS-Sat. 2, unless there has been an error in understanding the calculations.

For the additional requirement on reducing laser wavefront aberration noise, it is not clear if the impact on the design of the satellites would be substantial. In principle, a fairly small filter cavity could do what is needed if the aberration noise level of roughly 1 W lasers is low. Other aberrations besides wavefront tilt that may be important are variations in wavefront curvature and beam center displacements. The laser power would only be a consideration if the finesse needed is fairly high.

The wavefront aberration noise requirement for AGIS-Sat. 2 is much tighter than for LISA because of the far shorter baseline between satellites. For the statistical limit on sensitivity rom the atom sublevel measurements, the very short de Broglie wavelength of the atoms is the elevant length scale. However, when laser beams between spacecraft are used to provide the eference for gravitational wave sensing, the laser wavelength becomes an important scale for ystematic measurement limitations. Even for possible LISA satellite separations as short as 1×10^6 km, the AGIS-Sat. 2 baseline is a factor 1,000 shorter, and the sensitivity to wavefront iberration noise would be increased by this factor

For the requirement on the atom cloud temperature variations, it seems difficult to see a olution other than reducing the time T substantially or developing methods for extremely precise control of cloud temperatures. In Section IV B 5 of ref. 5, it is suggested that "Spatially resolved detection of the atom cloud can help mitigate the wavefront requirements that result from spatially averaging." However, even with an extra requirement for measurement of the atom spatial distribution, this wouldn't help with determining fluctuations in the atom cloud temperature, since such measurements would be made only at the time of atom sublevel population determination.

In the Introduction to ref. 1, it is stated that the use of atom interferometry "leads to a natural reduction in many systematic backgrounds, allowing such an experiment to reach sensitivities comparable to and perhaps better than LISA's with reduced engineering requirements." But, in fact, nothing in that paper or in ref. 5 supports that claim.

References

1. Dimopoulos, S., *et al., Phys. Rev. D* 78, 122002 (2008).
2. Danzmann, K., & Ruediger, A., *Class. & Quantum Grav.* 20, S1 (2003).
3. Bender, P. L., in: S. A. Klioner, P. K. Seidelmann, & M. H. Soffel, (eds.), *Proc. IAU Symp 261, Relativity in Fundamental Astronomy*, (Cambridge) 240-248 (2010).
4. Comment: Atomic gravitational wave interferometric sensor, *Phys. Rev. D.* (accepted), (2011).
5. Hogan, J. M., *et al.,* An atomic gravitational wave interferometric sensor in low Earth orbit *(AGIS-LEO), arXiv:1009.2702v1*, 14 Sep (2010).
6. Kwee, P., & Willke, B., *Applied Optics* 47, 6022 (2008).

REALISATION OF THE ALIGO FUSED SILICA SUSPENSION

A. S. BELL[1], A. V. CUMMING[1], G. D. HAMMOND[1], A. HEPTONSTALL[2], W. CUNNINGHAM[1], A. A. VAN VEGGEL[1], R. JONES[1], K. A. STRAIN[1], J. HOUGH[1], S. ROWAN[1]
[1]*SUPA, Institute for Gravitational Research, School of Physics and Astronomy, University of Glasgow, Glasgow G12 8QQ. Scotland*
[2]*LIGO Laboratory, California Institute of Technology, Pasadena, California 91125, USA*

The planned upgrade for the LIGO gravitational wave detectors (Advanced LIGO) has been underway for a number of years. One of the most significant aspects of this upgrade is the use of all-fused-silica pendulums to reduce thermal noise. The test mass mirrors, made from fused silica, will each be suspended using four fused silica fibres from a fused silica isolation mass. The fibres are welded in place using a CO_2 laser. We describe the realisation of a working prototype suspension at the LIGO Advanced Systems Test Interferometer (LASTI) facility.

1 Introduction

The suspension design for the Advanced LIGO (aLIGO) interferometers is based on that used in the UK-German GE600 gravitational wave detector [1], but adapted to the requirements of aLIGO [2]. As shown in Figure 1, it consists of four masses, the upper two of which are made from steel and suspended by wires from maraging steel blade springs [3]. The lower two stages of the suspension consist of synthetic fused silica pieces which are 340 mm in diameter, 200 mm thick and each has a mass of 40 kg. The test mass is suspended by 4 fused silica fibres from the penultimate mass. The fibres are welded at both ends to silica attachment points (known as *ears*) that are hydroxide-catalysis bonded to the masses [4]. One can minimise thermoelastic noise caused by temperature fluctuations close to the bending point, by choosing the fibre dimensions in that region such that there is a cancellation between the noise terms originating from the thermal expansion coefficient and the combination of applied stress with the change in Young's modulus with temperature [5].

2 Fibre production

The silica fibres are drawn from 3 mm diameter fused silica stock using a laser heating method [6]. A copy of the original Glasgow designed machine was constructed at the LASTI facility at MIT

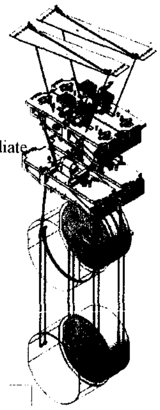

Figure 1: Schematic of the quadruple suspension showing the test mass, three isolation masses and the parallel reaction chain. The reaction chain provides a means to apply low noise control of the main suspension.

to produce fibres for the suspension. The preferred profile is one that has a 400 μm diameter along most of the fibre length but transitions to 800 μm for 20 mm near the ends and then, within a few millimetres, to 3 mm diameter. The 3 mm diameter sections allow the ends to be welded to the attachment point. The 800 μm sections are where most of the bending of the fibre takes place. The 400 μm diameter is determined by a compromise between fibre strength and the suspension vertical and fibre transverse mode frequencies. After the fibre has been pulled, its cross-sectional profile is measured using an optical non-contact method to ensure that it matches the required profile[7].

3 Welding the monolithic suspension

The development of the welding process is described in more detail elsewhere[8] . In this paper we note that before welding the fibres on the prototype suspension at LASTI, we carried out ten successful tests on a mock-up suspension that had fused silica attachment points affixed to 40 kg aluminium masses. These tests were used to determine any issues with the process and verify that the technique was robust. The welding of the fibres took place within a class 100 clean room tent. A CO_2 laser beam with up to 100 W power was used. The beam was directed to the welding head through an enclosed articulated arm as shown in Figure 2. The welding head consists of a two lens telescope, to set the beam size to the 3 mm working diameter, and two mirrors mounted on galvanometer drives, to enable the operator to direct the beam at any position on the weld. An angled mirror is placed behind the stock to allow 360^o access to the weld, as can be seen in Figure 3. Due to the high laser power involved, care must be taken to ensure that specular reflections do not escape from the working area. A number of purpose designed baffles are used to contain the beam within the working area and a thermal imaging camera was used (with the laser set at low power) to search for any beams that were not caught by these baffles. With the laser running at low power, the thermal imager easily detects the few Kelvin increase in temperature caused by the reflections. Before welding, a fibre is selected from storage and *proof-tested*, by applying a force of 150 N (150 % of nominal load) for 10

Figure 2: Welding the fibre to the penultimate mass. The picture shows the articulated arm bringing in the laser beam to the weld head. The suction tube to remove the silica vapour can also be seen.

minutes. Any fibre that has been damaged, by inadvertent touching for example, will break within 1 or 2 minutes at this tension. The tested fibre is then transferred to a *cutter*, which has been set to give the exact fibre length required. In the cutter, the excess lengths of stock are removed and the fibre is held by tweezers with zirconium dioxide tips. The tweezers are mounted on three-axis stages that are in turn mounted on an aluminium section. When released from the cutter, the fibre can then be transported to the structure that is used for holding the suspension during the welding procedure. When the fibre has been pulled, characterised and cut to length it can then be welded in position. When the suspension is complete, the fibres will stretch approximately 6 mm under load. The initial vertical position of the test mass is set with this correction applied. The fibres are welded in place one at a time. An example of a completed weld can be seen on the right-hand attachment point in Figure 3. When all 8 welds are complete, and before the test mass is released, the pitch of the test mass can be set with respect to the penultimate mass. At the same time, the tension in the fibres is set to zero. The test mass is lowered by 0.25 mm, putting a tension of 4 N on each fibre. The 4 welds at the penultimate mass are heated in turn until the silica softens and the fibre aligns itself with the tension and relaxes to reduce the tension to zero. The process is then repeated for the welds at the test mass. This time, after the mass has been lowered, the pitch alignment of the mass is set. The relaxation process is then carried out on all four lower welds. This means that before the test mass is released, the pitch is set to within 1 mrad, and all 4 fibres have nominally zero tension.

4 Post-welding

After the completion of the welds and the annealing and pitch alignment stage, the test mass is lowered until it hangs freely, to ensure that fibres and welds are strong enough. The pitch angle of the freely hanging mass was confirmed to be within 1 mrad of the expected value. After this test the two silica masses were connected to the upper part of the suspension and the full suspension was then transferred to the vacuum system. The suspended mirror formed one end

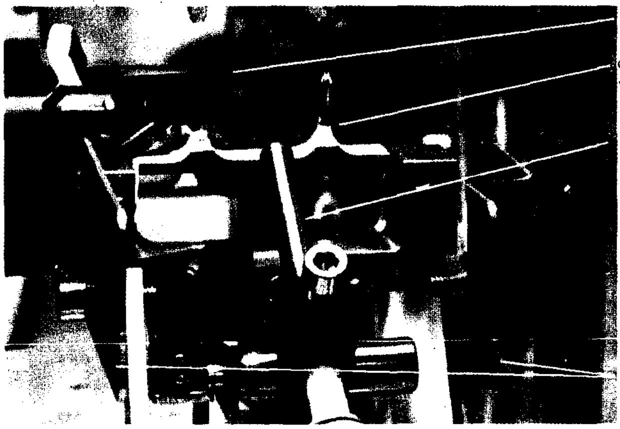

Figure 3: This picture shows two attachment points where the fibres are welded to the mass, the one on the right already has a finished weld. Weld tooling is in place on the one on the left. The long thin steel pipe is the extraction pipe to remove any silica vapour and stop deposition on the fibres or test mass during welding. The angled mirror that allows full access to the weld can be seen, as can the baffles used to catch errant beams.

of an optical cavity and the error signal from a laser that was frequency locked to this cavity, was used to measure the quality factor of test mass acoustic modes and the suspension fibres violin modes, to confirm the low mechanical loss of the monolithic suspension technique.

Acknowledgements

The authors would like to thank their colleagues at MIT, Cambridge, USA for their support and hospitality during this work, particularly Brett Shapiro, Myron McInnis, Gregg Harry and Rich Mittleman. We further acknowledge the aLIGO suspensions team and the technical expertise of Mr Stephen Craig and Mr Colin Craig. We are grateful for financial support from the Science and Technology Facilities Council and the University of Glasgow. SR is a holder of a Royal Society Wolfson Research Merit Award.

References

1. B. Willke *et al*, *Classical and Quantum Gravity* **19**, 1377 (2002).
2. G. M. Harry (for the LIGO Scientific Collaboration), *Classical and Quantum Gravity*, **27**, 084006 (2010).
3. N. A. Robertson *et al*, *Classical and Quantum Gravity* **19**, 4043 (2002).
4. L. Cunningham *et al*, *Physics Letters A* **374**, 3993 (2010).
5. G. Cagnoli and P. A. Willems, *Phys. Rev. B* **65**, 174111 (2002).
6. A. Heptonstall *et al*, *Rev. Sci. Instrum.* **82**, 011301 (2011).
7. A. V. Cumming*et al*, *submitted to Classical and Quantum Gravity*
8. A. V. Cumming*et al*, *Rev. Sci. Instrum.* **82**, 044502 (2011).

SYSTEMATIC STUDY OF NEWTONIAN GRAVITATIONAL CONSTANT MEASUREMENT IN MAGIA EXPERIMENT

Y.-H. LIEN, G. ROSI, F. SORRENTINO, M. PREVEDELLI[a], L. CACCIAPUOTI[b], Q. BODART, and G. M. TINO

Dipartimento di Fisica e Astronomia and LENS, Universita di Firenze, INFN Sezione di Firenze, via Sansone 1, I-50019 Sesto Fiorentino (FI), Italy

The MAGIA experiment using atom interferometry to determine Newtonian gravitational constant G and the relevant study on systematic issues are presented. The G constant was experimentally determined by measuring the additional gravity gradient created by tungsten alloy cylinders with atom interferometer based gradiometer. The gradiometer comprised two laser-cooled rubidium clouds which were launched in a fountain configuration and then simultaneously interrogated by a Raman-pulse interferometry sequence. The system has recently been upgraded to improve the signal-to-noise ratio. Besides, the long-term stability and systematic issues of the gravity gradiometer are evaluated for pushing the G measurement precision toward the 100 ppm level.

1 Introduction

The Newtonian gravitational constant G plays a key role in the fields of gravitation, cosmology, geophysics and astrophysics. Nevertheless, it is still the least precisely known among the fundamental constants. The Committee on Data for Science and Technology (CODATA) acknowledges the value of G with relative uncertainty 100 ppm in 2006 by evaluating eight different measurements obtained in the past few years [1]. These measurements with two more new additions [2,3] are shown in Fig. 1. Although the measurement of G has improved considerably since 1998 [4] and the most precise measurements of G even assigned uncertainties lower than 50 ppm [2,5,6,7,8], most available values are still in poor agreement with the scattering of several standard deviations, especially, the latest JILA measurement [3] shows almost 300 ppm discrepancy to CODATA 2006 recommendation. With a few exceptions [8,9,10], most experiments were performed using conceptually similar schemes based on suspended macroscopic masses as probes and torsion balances or pendulums as detectors. From this point of view, the implementation of conceptually different experiments definitely help to identify hidden systematic effects and hence improve the confidence in the final result.

Quantum sensors based on atom interferometry [11] underwent a rapid development during the last decade, and different schemes were demonstrated and implemented. Many applications can be seen in precise measurements of gravity acceleration [12,13], Earths gravity gradient [14,15] and rotations [16,17]. Currently, experiments based on atom interferometry are in progress to test Einsteins Equivalence Principle [18,19] and to measure the Newtonian gravitational constant

[a]Permeant address: Dipartimento di Fisica dellUniversita di Bologna, Via Irnerio 46, I-40126, Bologna, Italy
[b]Permeant address: Research and Scientific Support Department, European Space Agency, Keplerlaan 1, 2201 AZ Noordwijk, The Netherlands

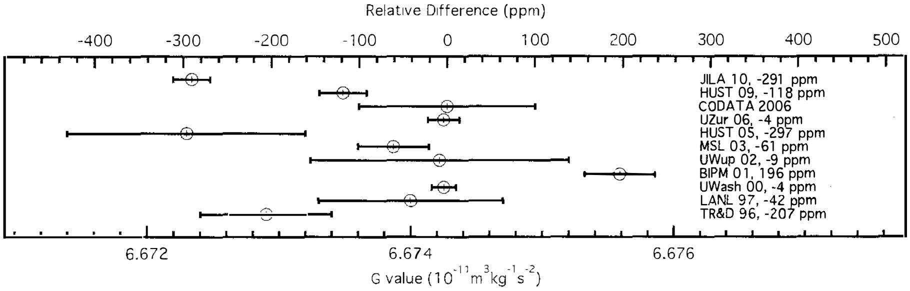

Figure 1: The G values from different experiments and CODATA 2006 recommendation.

G [20,21]. In addition, experiments to test general relativity [19,22] and Newtons inverse square law [23,24,25,26], for a search of quantum gravity effects [27] and for gravitational wave detection [28,29] have been proposed.

Our atom interferometer MAGIA (Misura Accurata di G mediante Interferometria Atomica, Italian acronym for Accurate Measurement of G by Atom Interferometry) was developed for a precise determination of Newtonian gravitational constant G. The basic concepts of the experiment and some preliminary results are presented in [21,31]. In our experiment, freely falling atoms act as probes of the gravitational field and an atom interferometry scheme is used to measure the effect of nearby well-characterized source masses. The projected accuracy for MAGIA shows that the results of the experiment will be important to discriminate between existing inconsistent values.

2 Experiment

The basic concepts of the experiment are illustrated in Fig. 2. A gravity gradiometer based on Mach-Zehnder atom interferometry was built to perform a simultaneous measurement of the differential acceleration experienced by two sub-Doppler-cooled vertically launched ^{87}Rb clouds in the presence of a well-characterized set of source masses. The measurement, performed for two different positions of the source masses, allows us to determine the Newtonian gravitational constant from the precise knowledge of the source masses distribution.

The Mach-Zehnder atom interferometry was implemented by illuminating the atomic clouds with $\pi/2$–π–$\pi/2$ Raman pulse sequence, and the $\pi/2$ and π pulses acted exactly as beam splitter and mirror in interferometry terminology, respectively. The Raman laser beam comprised two laser frequencies, denoted by ω_{ca} and ω_{cb} respectively, and these two frequencies were resonant with the Λ-type transition between two hyperfine levels $|a>$ and $|b>$ of ground state and the excited state $|c>$. The Raman laser beams which counter-propagated along the vertical axis were used to drive two-photon Raman transition between $|a>$ and $|b>$. Assuming atoms were initially prepared in $|a>$, the first $\pi/2$ pulse with pulse duration $\tau = \pi/2 \times \Omega$, where Ω was Rabi frequency of the A-type transition, split the atomic wavefunction into an equal superposition of $|a>$ and $|b>$. Accompanying with the change of the internal state, the atoms acquried an effective recoil momentum $\hbar k_e = \hbar(k_{ca} + k_{cb})$ and the trajectories changed accordingly. After a period T, a π pulse with a duration of 2τ switched the internal state from $|a>$ to $|b>$ and vice versa, and the atomic trajectories were redirected as well. Finally, again after a period T, a $\pi/2$ pulse recombined the atomic packets in the two complementary output ports of the interferometer. At the output of the interferometer, the probability of atoms in the state $|a>$ was given by $P_a = (1 - \cos\Phi)/2$, where Φ represented the phase difference accumulated by the wave packets along the two interferometer arms. In the presence of a gravity field, atoms

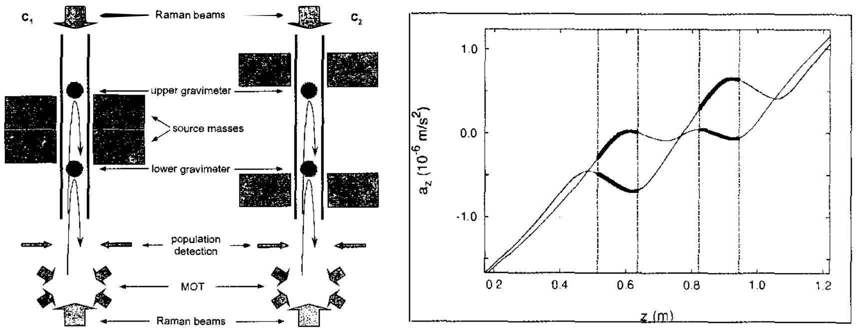

Figure 2: Left: illustration of the apparatus. Right: The gravity gradient caused by different source masses configurations. The red trace is corresponding to C_1 and the blue trace is corresponding to C_2.

experienced a phase shift $\Phi = k_e\, g\, T^2$ depending on the local gravitational acceleration g and on the time interval T between the Raman pulses. The gravity gradiometer consisted of two absolute accelerometers operated in differential mode. Two spatially separated atomic clouds in free fall along the same vertical axis are simultaneously interrogated by the same Raman beams to provide a measurement of the differential acceleration induced by gravity on the two clouds.

The gravity gradiometer setup and the configurations of the source masses (C_1 and C_2) are visible in Fig. 2. At the bottom of the apparatus, a magneto-optical trap (MOT) with beams oriented in 1–1–1 configuration collected ^{87}Rb atoms. Using the moving molasses technique, the atoms were launched vertically along the symmetry axis of the vacuum tube and cooled down to a temperature of about 2.5 μK. The gravity gradient was probed by two atomic clouds moving in free flight along the vertical axis of the apparatus and simultaneously reaching the apogees of their ballistic trajectories at 60 and 90 cm above the MOT. Such a geometry, requiring the preparation and launch of two clouds with a large number of atoms in a time interval of about 100 ms, was achieved by juggling the atoms loaded in the MOT [32]. Shortly after launch, the two atomic clouds were velocity selected and prepared in the ($F = 1$, $m_F = 0$) state using a combination of triple Raman π pulses and resonant blow-away laser pulses. The interferometers took place at the center of the vertical tube shown in Fig. 2. In this region, surrounded by two μ-metal shields (76 dB attenuation factor of the magnetic field in the axial direction), a uniform magnetic field of 25 μT along the vertical direction defined the quantization axis. The field gradient along this axis was below 5 nT $\cdot$ mm^{-1}. After the Raman interferometry sequence, the populations of the hyperfine levels were measured in a chamber above the MOT chamber by selectively exciting the atoms and detecting the resulting fluorescence.

Each atom interferometer in the gravity gradiometer measured the local acceleration with respect to the common reference frame identified by the wave fronts of the Raman lasers. Therefore, even if the phase noise induced by vibrations on the retroreflecting mirror completely washed out the interference fringes, the signals simultaneously detected on the upper and lower accelerometers remained coupled and preserved a fixed phase relation. As a consequence, when the trace of the upper accelerometer was plotted as a function of the lower one, experimental points distributed along an ellipse. The differential phase shift $\Delta\Phi = \Phi_u - \Phi_l$, which was proportional to the gravity gradient, was then obtained from the eccentricity and rotation angle of the ellipse best fitting the experimental data [33].

The source masses comprised 24 tungsten alloy (INERMET IT180) cylinders, for a total mass of about 516 kg. They were positioned on two titanium platforms and distributed in hexagonal symmetry around the vertical axis of the tube. Each cylinder was machined to a

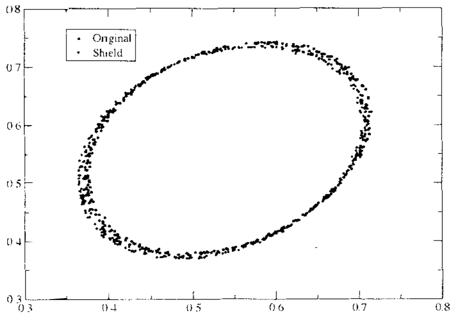

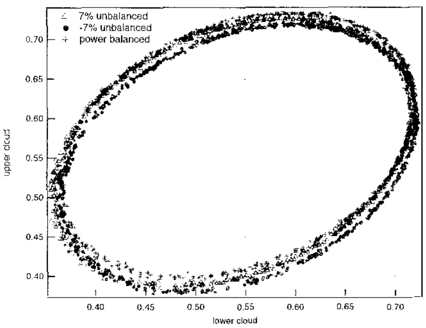

Figure 3: The left on: ellipses with different shielding conditions. The red trace: several layers of shields. The black trace: no soft iron shield.

diameter of 100 mm and a height of 150 mm after a hot isostatic pressing treatment applied to compress the material and reduce density inhomogeneities. The two platforms could be precisely translated along the vertical direction by four step motors, with a resolution of 2 μm provided by an optical encoder; the positioning precision had been tested with a laser tracker [31].

Although the differential measurement can suppress many sources of noises and drifts, this scheme is still prone to the biases synchronized with the movements of source masses, for example, the trajectory variation induced by eddy current in the mass translation platforms. The eddy current is generated by the magnetic field switching for different phases of the experiment, i.e., switching from MOT phase to atomic fountain phase and its magnitude is dependent on the distance between the platforms and MOT coils. Therefore, the transient magnetic field generated by eddy current in MOT chamber is higher when the platforms, especially the lower platform, are approaching to the MOT chamber. The variation of transient magnetic field changes the launching verticality of atomic fountain and turns out an extra phase shift induced by Coriolis effect. To suppress this effect, several layers of soft iron shields were installed and the transient field observed on the bottom surface of the lower platform received more than 10 dB attenuation. The ellipses with different shielding conditions are shown in the left part of Fig. 3. The change of phase angle was more than 10 mrad in C_2 configuration and could not be discriminate in C_1 configuration. Besides the shielding, we also explored the possible phase shift caused by power unbalancing between 1–1–1 MOT cooling laser beams. The results are shown in the right part of Fig. 3. The ellipse shifted its position as power unbalancing ratio changed from -7% to $+7\%$ but the differences between the phase angles of these ellipses were within the fitting errors, i.e., 1.2 mrad or 700 ppm. We even intentionally varied the unbalancing ratio to 20% and no significant change was perceived in that test. The characterization of source masses has been done and the contribution to final uncertainty is given in Table 1.

3 Conclusion

The basic concepts of MAGIA experiment and some of systematic issues are covered in this paper. The experiment received many improvements in these two years, and hence both the signal-to-noise ratio and long term stability have been significantly improved. With the integration time of three weeks, the precision is expected to reach the final goal of 100 ppm. The investigation of various systematic shifts are ongoing at present and the whole experiment would be ready for final measurement in the near future.

		present uncertainty	$\Delta G/G \times 10^{-4}$
Int. Cyl. rad. position	99.90 mm	10 μm	0.22
Ext. Cyl. rad. position	173.00 mm	10 μm	0.05
H_u-H_l (C1)	215.00 mm	10 μm	0.38
H_u-H_l (C2)	449.85 mm	10 μm	0.3
mass of cylinder	21486 g	10 mg	0.01
Density homogeneity	18249 kg·m^{-3}	24 kg·m^{-3}	0.2
mass of platform	24930 g	60 g	0.8
			1.97

Table 1: The characterization of source masses and the contribution to the error budget of G measurement.

References

1. P. J. Mohr, B. N. Taylor, and D. B. Newell, Rev. Mod. Phys. **80**, 633 (2008).
2. J. Luo, Q. Liu, L.-C. Tu, C.-G. Shao, L.-X. Liu, S.-Q. Yang, Q. Li, and Y.-T. Zhang, Phys. Rev. Lett. **102**, 240801 (2009).
3. H. V. Parks and J. E. Faller, Phys. Rev. Lett. **105**, 110801 (2010).
4. P. J. Mohr and B. N. Taylor, Rev. Mod. Phys. **72**, 351 (2000).
5. J. H. Gundlach and S. M. Merkowitz, Phys. Rev. Lett. **85**, 2869 (2000).
6. T. J. Quinn, C. C. Speake, S. J. Richman, R. S. Davis, and A. Picard, Phys. Rev. Lett. **87**, 111101 (2001).
7. T. R. Armstrong and M. P. Fitzgerald, Phys. Rev. Lett. **91**, 201101 (2003).
8. S. Schlamminger, E. Holzschuh, W. Kündig, F. Nolting, R. E. Pixley, J. Schurr, and U. Straumann, Phys. Rev. D **74**, 082001 (2006).
9. J. P. Schwarz, D. S. Robertson, T. M. Niebauer, J. E. Faller, Science **282**, 2230 (1998).
10. U. Kleinevoß, H. Meyer, A. Schumacher, and S. Hartmann, Meas. Sci. Tech. **10**, 492 (1999).
11. A. D. Cronin, J. Schmiedmayer, and D. E. Pritchard, Rev. Mod. Phys. **81**, 1051 (2009).
12. H. Müller, S.-W. Chiow, S. Herrmann, S. Chu, and K.-Y. Chung, Phys. Rev. Lett. **100**, 031101 (2008).
13. J. Le Gouët, T. E. Mehlstäubler, J. Kim, S. Merlet, A. Clairon, A. Landragin, and F. P. Dos Santos, Appl. Phys. B: Lasers Opt. **92**, 133 (2008).
14. J. M. McGuirk, G. T. Foster, J. B. Fixler, M. J. Snadden, and M. A. Kasevich, Phys. Rev. A **65**, 033608 (2002).
15. A. Bertoldi, G. Lamporesi, L. Cacciapuoti, M. de Angelis, M. Fattori, T. Petelski, A. Peters, M. Prevedelli, J. Stuhler, and G. M. Tino, Eur. Phys. J. D **40**, 271 (2006).
16. B. Canuel *et al.*, Phys. Rev. Lett. **97**, 010402 (2006).
17. A. Gauguet, B. Canuel, T. Lévèque, W. Chaibi, and A. Landragin, Phys. Rev. A **80**, 063604 (2009).
18. S. Fray, C. A. Diez, T. W. Hänsch, and M. Weitz, Phys. Rev. Lett. **93**, 240404 (2004).
19. S. Dimopoulos, P. W. Graham, J. M. Hogan, and M. A. Kasevich, Phys. Rev. D **78**, 042003 (2008).
20. J. B. Fixler, G. T. Foster, J. M. McGuirk, and M. A. Kasevich, Science **315**, 74 (2007).
21. G. Lamporesi, A. Bertoldi, L. Cacciapuoti, M. Prevedelli, and G. M. Tino, Phys. Rev. Lett. **100**, 050801 (2008).
22. H. Müller, A. Peters, and S. Chu, Nature **463**, 926 (2010).
23. G. M. Tino, Nucl. Phys. B: Proc. Suppl. **113**, 289 (2002).
24. G. Ferrari, N. Poli, F. Sorrentino, and G. M. Tino, Phys. Rev. Lett. **97**, 060402 (2006).
25. P. Wolf, P. Lemonde, A. Lambrecht, S. Bize, A. Landragin, and A. Clairon, Phys. Rev.

A **75**, 063608 (2007).
26. A. Alberti, G. Ferrari, V. V. Ivanov, M. L. Chiofalo, and G. M. Tino, New J. Phys. **12**, 065037 (2010).
27. G. Amelino-Camelia, C. Lämmerzahl, F. Mercati, and G. M. Tino, Phys. Rev. Lett. **103**, 171302 (2009).
28. G. M. Tino and F. Vetrano, Class. Quantum Grav. **24**, 2167 (2007).
29. S. Dimopoulos, P. W. Graham, J. M. Hogan, M. A. Kasevich, and S. Rajendran, Phys. Lett. B **678**, 37 (2009).
30. M. Fattori, G. Lamporesi, T. Petelski, J. Stuhler, and G. M. Tino, Phys. Lett. A **318**, 184 (2003).
31. G. Lamporesi, A. Bertoldi, A. Cecchetti, B. Duhlach, M. Fattori, A. Malengo, S. Pettorruso, M. Prevedelli, and G. M. Tino, Rev. Sci. Instrum. **78**, 075109 (2007).
32. R. Legere and K. Gibble, Phys. Rev. Lett. **81**, 5780 (1998).
33. G. T. Foster, J. B. Fixler, J. M. McGuirk, and M. A. Kasevich, Opt. Lett. **27**, 951 (2002).

ULTRA-STABLE, HIGH-POWER LASER SYSTEMS

P. KWEE
Max-Planck-Institut für Gravitationsphysik (Albert-Einstein-Institut), Callinstr. 38, 30167 Hannover, Germany

Laser systems with a high output power and a comprehensive stabilization of most laser beam parameters are required for ground-based interferometric gravitational wave detectors. The laser system of the second generation gravitational wave detector Advanced LIGO is reviewed and a brief overview about laser development for the third generation is given.

1 Introduction

Interferometric, ground-based gravitational wave detectors (GWDs) are expected to measure the tiny differential length variations caused by gravitational waves emitted by astrophysical sources. The second generation of these kilometer-long baseline Michelson interferometers are currently installed and have a design strain sensitivity of $10^{-23} \ldots 10^{-24}\,\mathrm{Hz}^{-1/2}$. They require laser systems with high output power and at the same time with very good stability concerning all laser beam parameters.

A high output power is required to reach a high signal-to-quantum-noise ratio, since quantum noise in the gravitational wave readout is reduced at high frequencies with increasing circulating laser power in the interferometer. In addition to quantum noise technical laser noise couples to the gravitational wave channel. Thus on the one hand the coupling needs to be reduced e.g. by optical design or by exploiting symmetries; and on the other hand laser noise has to be reduced by different active and passive stabilization schemes.

This article reviews the laser output power scaling and laser stabilization techniques used in the laser system of the second generation detector Advanced LIGO[1] (aLIGO). Furthermore a brief overview about current laser development for third generation detectors is given.

2 Advanced LIGO pre-stabilized laser system

Advanced LIGO requires a reliable, continuous-wave, single-frequency laser system with an output power of 165 W in a TEM_{00} mode at a wavelength of 1064 nm. Laser beam parameters such as power, frequency, or pointing have to be ultra-stable requiring an elaborate stabilization scheme[2]. Furthermore modulation inputs for controlling the beam power and frequency have to be provided.

The laser was developed by *Laser Zentrum Hannover e. V.* (LZH) and consists of three stages (see Fig. 1). The first stage, the master laser, is a commercial non-planar ring-oscillator[3] (NPRO) from *Innolight.* This solid-state laser uses a Nd:YAG crystal as laser medium and resonator at the same time. The laser is pumped by laser diodes at 808 nm and delivers an output power of 2 W. Due to its monolithic resonator the laser has an exceptional intrinsic frequency stability.

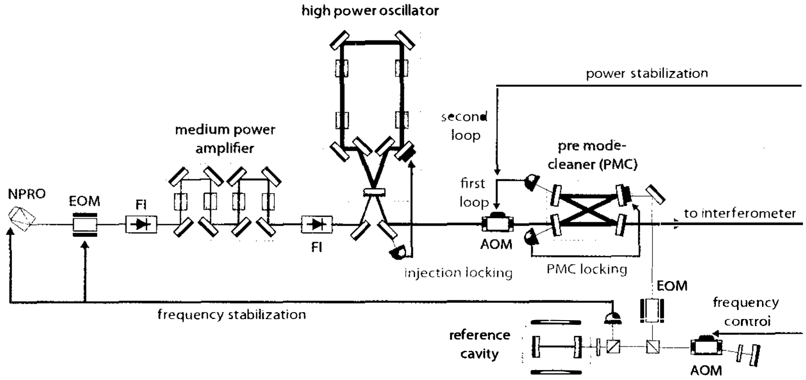

Figure 1: Pre-stabilized laser system of aLIGO. The three-staged laser and the stabilization scheme is shown. EOM, electro-optic modulator; FI, Faraday isolator; AOM, acousto-optic modulator.

The two subsequent laser stages, used for power scaling, adopt the frequency stability of the master laser.

The second stage (medium power amplifier) is a single-pass amplifier[4] with an output power of 35 W. The seed laser beam from the first stage passes four $Nd:YVO_4$ crystals which are longitudinally pumped by fiber-coupled laser diodes at 808 nm.

The third stage is a ring oscillator[5] with an output power of about 220 W. Four Nd:YAG crystals are used as active media. Each is longitudinally pumped by seven fiber-coupled laser diodes at 808 nm. The oscillator is injection locked[6] to the previous laser stage using a feedback control loop. Thus the high output power and good beam quality of this last stage is combined with the good frequency stability of the previous stages.

2.1 Stabilization

The maximum acceptable technical laser noise can be deduced from the anticipated design sensitivity of the GWD and the expected coupling between laser noise and the gravitational wave channel. This yields noise requirements which are several orders of magnitude below the free running laser noise and requires several stabilization stages[7].

A passive bow-tie ring resonator, called pre-mode-cleaner (PMC), is a key component in the stabilization scheme. This resonator consists of four low-loss mirrors glued to an aluminum spacer. A piezo-electric element between one mirror and the spacer is used to stabilize one TEM_{00} resonance frequency to the laser frequency. The beam transmitted through this resonator is the output beam of the overall laser system and is delivered to the subsequent subsystems of the GWD.

The PMC filters the laser beam and has different functions: On one side it improves the beam quality of the laser by suppressing higher order transversal modes[8]. The round-trip Gouy phase of the PMC was chosen in such a way that the resonance frequencies of higher order TEM modes are clearly separated from the TEM_{00} resonance frequency. Thus these modes are not resonant and are mainly reflected by the PMC whereas the TEM_{00} mode is transmitted. This mode-cleaning effect increases the TEM_{00} fraction from about 95% to > 99%.

In particular the TEM_{10} and TEM_{01} modes are suppressed by the PMC and thus beam pointing fluctuations are reduced. Pointing fluctuations can be expressed in first order as power fluctuations of the TEM_{10} and TEM_{01} modes. The PMC reduces the field amplitude of these modes and thus the pointing fluctuations by a factor of about 60.

Finally the PMC reduces technical power fluctuations at radio frequencies. A good power stability between 9 MHz and 100 MHz is important since phase modulated light injected into the interferometer is used to sense several degrees of freedom of the interferometer which need to be controlled. The PMC has a bandwidth of about 600 kHz and acts in first order as a low-pass filter for power fluctuations with a -3 dB corner frequency at this frequency.

Beside these passive stabilization effects of the PMC active stabilizations are necessary to reduce power and frequency noise in the detection band of the GWD from about 10 Hz to 10 kHz. The PMC reduces power fluctuations significantly only above 600 kHz. In the detection band a good power stability is required since fluctuations couple via radiation pressure imbalance and the dark-fringe offset to the gravitational wave channel. The beam power at a pick-off port of the PMC is measured with a low-noise photodetector. An electronic feedback controller and an acousto-optical modulator (AOM) as power actuator upstream of the PMC are used to stabilize the laser power. This first power stabilization loop reduces the relative power fluctuations by about three orders of magnitude to the $10^{-8}\,\mathrm{Hz}^{-1/2}$ level.

A second power stabilization loop with a photodetector directly upstream of the interferometer is used to reach the required power stability in the interferometer. This stabilization is developed at the moment and a precursor experiment[9] demonstrated already the necessary high-sensitivity photodetector.

Finally a good frequency stability is required for the lock acquisition of the interferometer and to reduce frequency noise coupling into the gravitational wave channel via asymmetries in the interferometer arms. The interferometer has to be operated at a specific operation point to reach its design sensitivity requiring an elaborate lock acquisition. A linear rigid-spacer reference resonator is used in the laser system for a frequency pre-stabilization. The Pound-Drever-Hall sensing scheme and a compound frequency actuator is used to stabilize the frequency up to a Fourier frequency of about 500 kHz[10]. The compound actuator consists of the NPRO crystal temperature control, the piezo-electric element attached to the NPRO crystal, and the broad-band electro-optic modulator (EOM) between NPRO and amplifier as phase corrector.

To be able to control the laser frequency while it is stabilized to the reference resonator a frequency shifting AOM in a double-pass configuration is used in front of the reference resonator. By controlling the AOM driving frequency the laser system frequency can be shifted by about 1 MHz with a bandwidth of about 100 kHz.

3 Third generation laser systems

The laser systems for the second generation GWDs are installed at the moment. Meanwhile the development for the third generation has started already. Since only rough third generation conceptual designs[11] exist at the moment different development directions are conceivable: High-frequency GWDs or all-reflective GWDs might require high-power laser systems at the kW level. Cryogenic interferometers with silicon test masses might require a different laser wavelength at 1550 nm since silicon has a low absorption coefficient at this wavelength. Laser systems with a different beam profile, such as Lag_{33} mode or flat-top profiles, might be required to reduce the influence of thermal noise of the test masses due to a more homogenous intensity distribution.

The LZH, e.g., develops a 1 kW 1064 nm TEM_{00} laser at the moment[12]. For this the power of an NPRO master laser is scaled to the kW level by a combination of photonic crystal fiber amplifier, coherent beam combining and/or subsequent Nd:YAG amplifier. Furthermore a 100 W 1550 nm TEM_{00} laser is currently developed. The concept is to amplify a distributed feedback (DFB) fiber master laser with an erbium fiber amplifier[13,14,15]. In general fiber lasers and amplifiers made a substantial progress in recent years. They stand out due to their efficiency, compactness, and high intrinsic beam quality compared to the solid-state lasers and amplifiers which are used at the moment in GWDs. Though long-term tests need to be performed to demonstrate if they are as reliable as solid-state lasers are today.

During the development of the laser stabilization for aLIGO the power and pointing stabilization turned out to be the most critical ones. The achieved power stability in the detection band is limited by the sensitivity of the power sensor. The precursor experiment[9] demonstrated just the sensitivity required for aLIGO. In case third generation detectors require an even better power stability completely different stabilization schemes such as the optical ac coupling technique[16] might be necessary. Until now beam pointing fluctuations were reduced only by the passive filtering effect of the PMC fulfilling just the requirements of aLIGO. If a better pointing stability will be required in the future additional active stabilization schemes or cascaded PMCs might be necessary.

4 Conclusion

Multi-stage laser systems combined with active and passive stabilizations deliver ultra-stable, high-power laser beams for second generation GWDs. The development, in particular of the laser system for aLIGO, has almost finished and these laser systems are currently installed at the observatory sites. One aLIGO laser system is comprehensively characterized at the moment to verify the required performance.

Meanwhile the development of lasers for third generation GWDs has started following different strategies. Probably most stabilization techniques applied in second generation laser systems can be adapted for the third generation, whereas the power and pointing stabilization will be the most challenging aspects.

Acknowledgments

The author thanks Benno Willke, Peter Weßels, and Albrecht Rüdiger for their helpful comments during the preparation of this article.

References

1. P. Fritschel, Proc. SPIE **4856**, 282 (2003).
2. B. Willke, Laser & Photonics Reviews **4**, 780–794 (2010).
3. I. Freitag *et al*, SPIE **2379**, 335–342 (1995).
4. M. Frede *et al*, Opt. Express **15**, 459–465 (2007).
5. L. Winkelmann *et al*, App. Phys. B **102**, 529–538 (2011).
6. A.D. Farinas *et al*, J. Opt. Soc. Am. B **12**, 328–334 (1995).
7. P. Kwee, *Laser Characterization and Stabilization for Precision Interferometry*, Ph.D. thesis, Universität Hannover (2010).
8. A. Rüdiger *et al*, Opt. Acta **28**, 641–658 (1981).
9. P. Kwee *et al*, Opt. Lett. **34**, 2912–2914 (2009).
10. F. Bondu *et al*, Opt. Lett. **21**, 582–584 (1996).
11. Einstein Telescope design study, http://www.et-gw.eu/.
12. M. Karow *et al*, CLEO Europe , CJ7.4 (2011).
13. V. Kuhn *et al*, Opt. Express **17**, 18304–18311 (2009).
14. V. Kuhn *et al*, IEEE Phot. Tech. Lett. **23**, 432–434 (2011).
15. V. Kuhn *et al*, CLEO Europe , CJ7.5 (2011).
16. P. Kwee *et al*, App. Phys. B **102**, 515–522 (2011).

HIGH POWER INPUT OPTICS FOR ADVANCED VIRGO

B. CANUEL, R. DAY, E. GENIN, J. MARQUE, F. NOCERA, F. PAOLETTI
European Gravitational Observatory (EGO), Cascina (Pi), Italy

The laser input power for the current Virgo project is 15W. This will be increased to 125W for the Advanced Virgo (AdV) project. It is therefore required to make the input optics system for AdV compliant for such a power, in particular in terms of thermal and scattering effects. In order to reach these specifications, a 3 year R&D project was carried out at EGO. Optical components (polarizers, wave-plates, Electro-Optical Modulator crystals. materials for beam dumps) have been selected according to their scattering and thermal properties. Measurements have been made of absorption, thermal lensing, polarization and scattering. The following optical systems were then developed, prototyped and characterized: a Faraday isolator (which isolates the input optics from the interferometer), the Electro-Optical Modulation system (which phase modulates the beam at the input of AdV for control purposes) and beam dumps (which can withstand high power under vacuum with low back-scattering).

1 The Advanced Virgo (AdV) Injection System

The Injection System of AdV takes care of the optics after the high power laser, and of the interface between these optics and the laser itself. The whole system must deliver a beam with the required power, geometrical shape, frequency and angular stability. In order to reach the required performances, the system has been designed into 2 parts (Fig. 1).
The "In air optics" mainly consists of the Electro Optical Modulation (EOM) system for Input

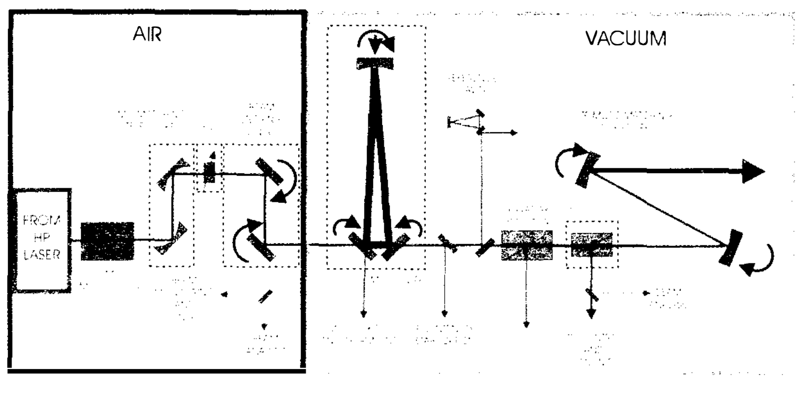

Figure 1: Schematic of the AdV Injection System.

Mode Cleaner (IMC) and Interferometer control, the IMC mode matching telescope, the Input

Power Control system (IPC), the beam pointing control system and the Beam analysis system (wavefront sensor, phase camera). The "In vacuum optics" mainly consists of a 150m long triangular IMC cavity, a Faraday Isolator, an interferometer mode matching telescope, a 32cm long triangular Reference Cavity (RFC), and an Input Power Control system (IPC). The following sections describe the studies and developments done in the last years for some of the previous items in order to withstand about 10 times more power in AdV with respect to Virgo.

2 The Faraday Isolator

The Faraday Isolator requirements for AdV are the following: Ultra High Vacuum compatible, 20mm aperture, 40dB isolation with 200W passing through the Faraday crystal, a residual focal thermal lensing larger than 100m, and a throughput larger than 95%.
The most suitable magneto optic medium for such an application is a Terbium Gallium Garnet (TGG) crystal because of its large Verdet constant, low absorption, and high thermal conductivity at 1064nm. However, there are some relevant thermal issues: the TGG crystal absorbs typically 2000ppm.cm^{-1}, which generates a change of mean temperature and a radial temperature gradient. As a consequence, 3 effects can limit the performances:

- The refractive index of TGG is temperature dependent (2.10^{-5} K^{-1}), and the thermal expansion is not negligible (1.10^{-5} K^{-1}): those induce thermal lensing,

- The Verdet constant is temperature dependent: this induces a variation of the mean rotation angle (Eq. 1),

$$\frac{1}{V}\frac{dV}{dT} = 3.5 \times 10^{-3} K^{-1}. \tag{1}$$

- The thermal expansion results in mechanical stress: radial birefringence leads to depolarization.

To cope with the first issue, that is to say with the induced thermal lensing (measured 10m focal length for 100W), the proposed solution was to add an element on the optical path with a negative thermo-optic coefficient: the selected material is a DKDP crystal (Deuterated Potassium Phosphate) whose thermo-optic coefficient is -4.10^{-5} K^{-1}. By accurately measuring the absorption of each material, and cutting the DKDP at the right length, it was possible to fine compensate the thermal lensing over large dynamics: the lensing remains negligible up to 100W traveling through the Faraday.
The second issue is a decrease of the isolation due to the fact that the mean rotation angle of the TGG crystal is temperature dependent (Eq. 2):

$$\frac{\Delta\theta}{\theta} = \frac{1}{V}\frac{dV}{dT}\Delta T. \tag{2}$$

Indeed, the temperature increase with 250W in vacuum (residual pressure of 2.5 10^{-6} mbar) is approximatively 6 degrees (copper holders are used to optimize heat extract). And this leads to a 7dB drop of the optical isolation. We have verified that by adding a remotely tunable half wave-plate in the optical path to turn the polarization by 1 degree [1] enables to recover the nominal isolation. However, this solution presents as a drawback the decrease of the total throughput of the system by 2%.
The third issue is probably the most critical problem. It has been observed [2] that the depolarization increases as the square of the power at high power, limiting the isolation to 30dB at 200W. Indeed, the gradients of temperature inside the TGG introduce some mechanical stress which creates radial birefringence. Heated TGG acts like complicated wave-plate: the direction of birefringence axis depends on the polar angle while the phase retardation depends on radial coordinate. This problem has been fully treated using Jones matrix formalism, and verified with

optical measurements of the amplitude and phase of the field[3]. The "depolarization" effect can be briefly summarized as follows: there is a self conversion of Spin to Orbital Angular Momentum which explains the non common orbital phase dependence of the beam. A solution has been proposed to this issue using a specific optical configuration for the Faraday [4]: the design consists of 2 TGG crystals, each rotating the polarization by 22.5 degrees and separated by a 67.5 degrees reciprocal polarization rotator. In this way, the second TGG converts back into the gaussian mode the light that was "depolarized" by the first TGG. The complete design including the DKDP, the remote controlled half wave-plate and the 2 TGG crystals configuration is shown in Fig. 2. We have measured in this configuration the isolation for different powers (Fig. 2). The isolation is 50 dB at low power and 38dB for 240W.

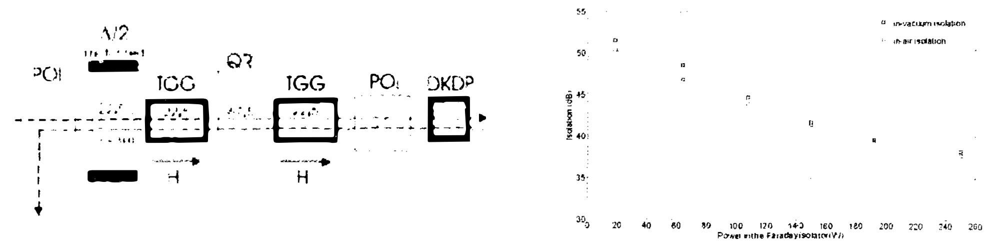

Figure 2: Optical setup of the Faraday isolator for Advanced Virgo and Faraday isolation performance with respect to power traveling through it.

3 The Electro Optical Modulation System

The Electro Optical Modulation System of AdV is required to phase modulate the input beam at 2 frequencies: typically 10 and 65 MHz. First, we have selected the best material in term of thermal effects: an RTP crystal from Raicol (absorption of 45 ppm.cm^{-1}). The system has been designed with a unique crystal with 2 sections of modulation to get the highest modulation index with the lowest possible RF power. Using a Scanning Fabry Perot, we have measured the following modulation depth for 0.5W RF power: 0.16 at 10MHz and 0.12 at 65MHz.

4 Beam Dumps

By experience, it is crucial to design better beam dumps for AdV, in term of damage threshold and back-scattering. The first step has been to make a comparative study of 3 materials: black absorbing glass (KG5), Silicon (Si) and Silicon Carbide (SiC). All these materials are well absorbing at 1064nm but have different thermal conduction: 1W.m^{-1}.K^{-1} for KG5, 150 W.m^{-1}.K^{-1} for Si, and 490 W.m^{-1}.K^{-1} for SiC. As a consequence, they have different damage threshold that have been measured in air: 25 W.cm^{-2} for KG5, 6 kW.cm^{-2} for Si, and 30 kW.cm^{-2} for SiC. The SiC material has been selected then. Super-polished plates of SiC (with Total Integrated Scattering of the order of 10ppm) are under development.
Another related issue has been studied: how to extract the heat from beam dumps into vacuum? A possible solution is to radiate the heat towards the vacuum tank wall. We have developed 2 kinds of mounts having a high emissivity for the beam dumps: sanded copper and pre-baked stainless steel. The emissivity of these mounts has been optimized up to 70%.

5 Thermally Deformable Mirror

The coupling of the input beam into the interferometer can be affected by various factors. In particular, slow thermally induced beam wavefront distortions can be compensated using deformable mirrors driven by thermal actuators. We have designed and prototyped such a system: the set of heating actuators is placed in direct contact with the reflecting surface of the mirror, enabling an efficient control of its refractive index and shape (Fig. 3).

This design has the advantage of being vacuum compatible and noise free. The efficiency of

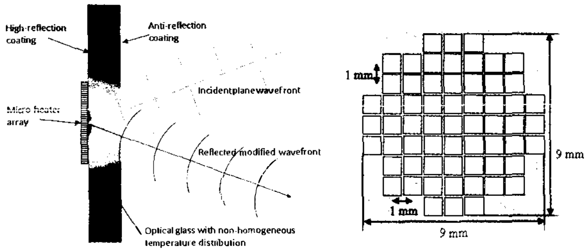

Figure 3: Design of the Thermally Deformable Mirror.

the system relies on the refractive index dependence over the temperature, and on the thermal elasticity. The Optical Path Length (OPL, Eq. 3) efficiency is best for SF57 (88nm.K^{-1}), with compared to BK7 (47nm.K^{-1}):

$$OPL = \int (\Delta T(s)[\frac{dn}{dT} + \alpha_T(1+\nu)n] + n)ds. \tag{3}$$

6 Conclusion

Along the last years, an important effort has been focused on the limitation of the various subsystems of the AdV Injection system at high power, as the understanding of depolarization effects in the Faraday. A careful process of material selection and design optimization has been achieved in order to develop the high power compatible optical components: Faraday Isolator, beam dumps, EOMs and Thermally Deformable Mirrors.

References

1. The Virgo Collaboration, *In-vacuum Faraday isolation remote tuning*, Appl. Opt **49**, 4780 (2010).
2. E. Khazanov et al., Appl. Opt **41-3**, 483-492 (2002).
3. S. Mosca, B. Canuel, E. Karimi, B. Piccirillo, L. Marrucci, R. De Rosa, E. Genin, L. Milano and E. Santamato, *Photon self-induced-spin-to-orbital conversion in a terbium-gallium-garnet crystal at high laser power*, Phys. Rev. A **82**, 043806 (2010).
4. E. Khazanov et al., *Compensation of Thermally Induced Modal Distortions in Faraday Isolators*, IEEE Journ. Quant. Electr. **40**, 10 (2004).

Thermal effects and their compensation in the interferometric gravitational wave detector Advanced Virgo

A. Rocchi[1], E. Coccia[1,2], M. Di Paolo Emilio[1], V. Fafone[1,2], V. Malvezzi[1], Y. Minenkov[1], L. Sperandio[1,2]
[1] *INFN Sezione di Roma Tor Vergata, I-00133 Rome, Italy*
[2] *University of Rome Tor Vergata and INFN, I-00133 Rome, Italy*

Thermal lensing due to the absorption of the laser beam in core optics of gravitational wave interferometers can represent a strong limitation to their operation and sensitivity. This effect has already been observed in the present detectors. Thermal compensation systems, based on CO_2 laser projectors, have been installed in Virgo and LIGO, to heat the peripheral of the input test masses to reduce the lensing effect. In second generation detectors, thermal lensing will become more relevant, due to the much higher circulating power. In this paper, the concept of the compensation system for Advanced Virgo is described.

1 Introduction

The largest currently operating interferometric Gravitational Wave (GW) detectors Virgo [1] and LIGO [2] are power-recycled Michelson interferometers with Fabry-Perot cavities in the arms. They have operated at the initial design sensitivity, completing several observational runs. Upgrades of these detectors are planned on short term time-scale: the second generation detectors Advanced Virgo[3] and Advanced LIGO[4] are now in the construction phase and will see a significant improvement of their sensitivity of about a factor of ten over the whole detection bandwidth, increasing by a factor of a thousand the volume of the observable Universe.

The second generation instruments will be characterized by a very high circulating power (from 20 kW in the initial interferometers to 700 kW in the advanced detectors), necessary to keep the shot noise at the level required by their high sensitivity. In an interferometric GW detector, the amount of allowable circulating power is limited by the non-zero optical absorption in the substrate and coatings of the test masses and the beam splitter, which will affect both the controllability and the sensitivity of the instrument [5 6].

In the test mass, the optical power is predominantly absorbed by the high reflectivity coating and converted into heat, producing a gradient of temperature inside the substrate. Two different effects originate from the heating of the test mass:

- non-uniform optical path length distortions (thermo-optic effect, also termed thermal lensing) mainly due to the temperature dependency of the index of refraction;
- change of the profile of the high reflective surface, due to thermal expansion (thermo-elastic deformation) in both input and end test masses.

In presence of thermal lensing, which changes the power recycling cavity (PRC) mode, the input laser no longer matches the PRC cavity and the coupling coefficient between the

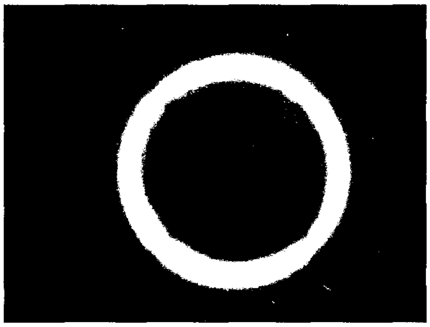

Figure 1: Infrared image of the heating pattern used by the Virgo TCS.

laser TEM_{00} and the cavity TEM_{00} becomes less than one. This leads to a decrease of the recycling cavity gain and thus of the sidebands power. Since sidebands are used to control the interferometer, thermal lensing prevents the detector to operate at high input powers. The consequence is a loss of signal-to-noise ratio at high frequencies due to the increase of shot noise.

In second generation detectors, the thermo-elastic deformation will also be relevant due to the much higher circulating power in the Fabry-Perot cavities. Thermal expansion will change the profile of the high reflectivity surface. A bump will raise in the center of the test mass faces, making their surface profile non-spherical. The cavity will become less concentric, and the spot sizes at the mirrors will shrink. To maintain the arm cavity mode structure, it will be then necessary to control the radii of curvature of all test masses.

Advanced thermal compensation system (TCS) will be required to compensate for both effects, by acting on input and end test masses.

2 Thermal lensing compensation

At present, in LIGO and Virgo, the wavefront distortions in the recycling cavities are corrected by shining an annular heating pattern generated by a CO_2 laser, directly on the input test masses [9]. An axicon lens (special optics with a conical surface) is used to convert the laser Gaussian beam into an annular beam. Figure 1 shows a thermal camera image of the heating pattern currently used in Virgo.

The improved sensitivity of next generation detectors will not allow to shine the test mass directly with the corrective CO_2 beam: the noise introduced by the intensity fluctuations of the laser would not be compatible with the sensitivity requirements, even if a power stabilization system is implemented. This implies the need of an additional transmissive optics, named Compensation Plate (CP), placed in the recycling cavity, where the noise requirements are more relaxed with respect to those in the Fabry-Perot cavity, to act on with the compensating beam. The conceptual scheme of the compensation system foreseen for advanced detectors is shown in figure 2.

An often useful way to picture the effect of a thermal distortions is the fractional power scattered out from the TEM_{00} mode [10], termed "coupling losses" L:

$$L = 1 - A^* A, \tag{1}$$

where

$$A = \frac{\langle E_0 | E \rangle}{\langle E_0 | E_0 \rangle} = \frac{\langle E_0 | e^{i\phi(x,y)} | E_0 \rangle}{\langle E_0 | E_0 \rangle} = 2\pi \int_0^{r_{ITM}} e^{i\phi(r)} |E_0(r)|^2 r dr. \tag{2}$$

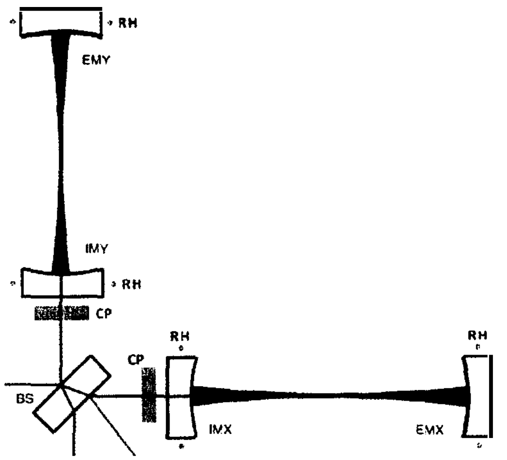

Figure 2: Scheme of the Advanced Virgo TCS: blue rectangles represent the CPs while the green dots around the test masses are the RHs.

E_0 represents the undisturbed cavity field before being subjected to the phase distortion $\phi(x, y)$ and E is the distorted field. A phase distortion in a cavity, in effect, acts to scatter power out of the fundamental mode, and thus out of the cavity, and so can be viewed as a simple coupling loss term.

With no thermal compensation, in Advanced Virgo, the coupling losses would amount to approximately $5 \cdot 10^5$ ppm. For a comparison, in Virgo, the losses due to thermal lensing are of the order of 10^4 ppm. The Advanced Virgo TCS needs to reduce to coupling losses at least by a factor of 10^3 to allow the correct operation of the detector at design sensitivity.

The results of optical simulations have shown that the heating pattern used in the current interferometers (an example is given in figure 1) is not sufficiently precise for the advanced detectors. The study of the optimization of the heating pattern, made with Finite Element Model (FEM), has shown that it is possible to reduce the residual coupling losses to about 6 ppm, thus leading to a reduction factor of about 10^5.

Different solutions are at present being investigated to generate heating profiles that approximate as much as possible the optimal one: diffractive optical elements, scanning systems (galvos or crossed Acousto-Optic-Modulators) or Micro Electro-Mechanical Systems (MEMS) deformable mirrors.

3 Control of the Radius of Curvature of the test masses

The need to control the radius of curvature of the test mass in GW interferometric detectors has already been faced in the past: the GEO detector [7] used a ring heater (RH) to change the ROC of one of the two test masses [8]. The ring was placed on the back of the mirror, radiatively coupled with the face of the optic.

Compensation and control of the test mass high reflectivity (HR) surfaces will be accomplished in Advanced Virgo with the same technique. The TCS baseline design considers four ring heaters, one around each test mass. The input mirror RH also provide limited compensation of thermo-optic effect in the recycling cavities.

In order to study the RH dynamics, an ANSYS coupled thermal-structural FEM has been developed, modeling a simple radiating ring placed around the barrel of the TM at different

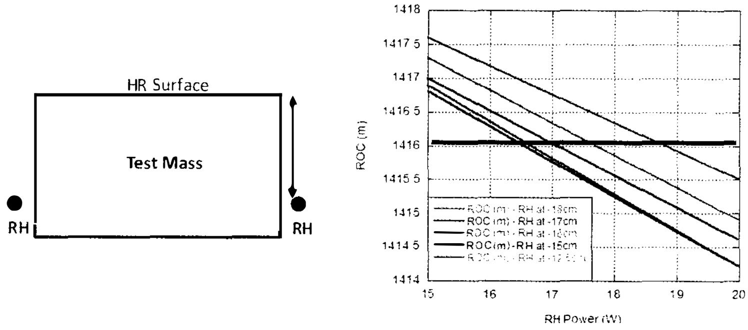

Figure 3: Left: scheme of the positioning of the RH along the barrel of the TM. Right: plot of the TM ROC as a function of the RH power for different positions, the black horizontal line represents the cold state ROC.

distances from the HR surface. At each position, the model calculates the ROC of the TM as a function of the RH power. The result is reported in figure 3.

It is found that if the position of the RH is at about 15 cm from the TM HR surface, the power required to recover the cold state ROC (1416 m) is minimized. It must be underlined that the simple ring heater is a very inefficient solution, since only a small fraction of the emitted power reaches the TM. By adding a reflecting shield around the ring heater, the amount of emitted power reaching the TM will increase, thus decreasing the required total emitted power, with a consequent increase of the RH dynamics with respect to what shown in figure 3.

The engineered design of the ring heater for Advanced Virgo is in progress, taking into account two important constraints: high temperature operation and UHV compatibility. Moreover, since the last stage of the suspension system will use coil-magnet actuators for the control of the mirrors, it is necessary to avoid any stray magnetic field generated by the ring heater. In fact, the coupling of the RH magnetic field to the actuators would introduce displacement noise in the detector, limiting its sensitivity.

4 TCS sensors

In Advanced Virgo, each optic with a significant thermal load will be independently monitored. The HR face of each test mass will be monitored in reflection for deformation. The input test mass/compensation plate phase profile will be monitored on reflection (either on-axis or off-axis) from the recycling cavity side.

The thermal aberrations will be sensed by several complementary techniques. To lowest order, the degree of aberration will be manifest in ITF channels, as it is in Virgo. These are scalar quantities that reflect only the overall conversion of light from the fundamental cavity mode. To sense the spatial structure of the cavity mode, phase cameras will sample the interferometer beam. However, the use of spatial sensors to actively control thermal aberrations has not yet been demonstrated, and the coupled cavity nature of the ITF could make extracting the aberrations of individual mirrors very problematic. Therefore, wavefront sensors will probe the input test masses and beam splitter individually.

The ITM-CP phase profile dedicated sensors consist of a Hartmann Wavefront Sensor (HWS), and a probe beam whose wavefront contains the thermal aberration information to be sensed. The working principle of the device is shown in figure 4.

The Hartmann sensor selected for Advanced Virgo is that already developed and charac-

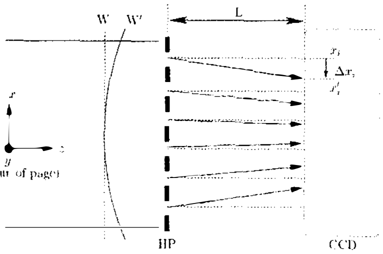

Figure 4: Working principle of the Hartmann Wavefront Sensor: an aberrated wavefront W' is incident on a Hartmann plate (HP). The resulting rays propagate a distance L, normal to the wavefront. and are incident on a CCD. The spot position, x_i', is determined by the centroid of that spot's intensity profile. The reference spot positions, x_i, (either measured using a non-aberrated wavefront, W or calculated using the hole positions in the HP) are indicated by the intersection of the dotted lines and the CCD. The gradient of the wavefront at the i^{th} aperture is given by $\frac{\partial \Delta W}{\partial x} = \frac{\Delta x_i}{L}$.

terized on test bench experiments and in the Gingin High Optical Power Test Facility for the measurement of wavefront distortion [11].

This sensor [12] has been demonstrated to have a shot-to-shot reproducibility of $\lambda/1450$ at 820 nm, which can be improved to $\lambda/15500$ with averaging, and with an overall accuracy of $\lambda/6800$.

The results indicate that the selected Hartmann sensor is both sufficiently sensitive for the measurements of absorption-induced wavefront distortions in advanced GW interferometers and is accurate. A prototype of the sensor is in the Tor Vergata Laboratories for further characterization and integration into the test facility for the development of the Advanced Virgo Thermal Compensation System.

Acknowledgments

This work has been performed with the support of the European Gravitational Observatory, of the European Commission (Framework Programme 7, project Einstein Telescope (ET) design study, grant agreement 211743) and of the Italian Ministero dell'Istruzione, dell'Universitá e della Ricerca (PRIN2007NXMBHP).

References

1. F. Acernese et al., *Class. Quantum Grav.* **25**, 114045 (2009).
2. B. P. Abbott et al., *Rep. Prog. Phys.* **72**, 076901 (2009).
3. T. Accadia et al., *Proceedings of the 12th Marcell Grossmann Meeting*, Paris, July 2009, in press.
4. G.M. Harry (LIGO Scientific Collaboration), *Class. Quantum Grav.* **27**, 084006 (2010).
5. P. Hello and J.-Y. Vinet, *J. Phys. I France* **3**, 717-732 (1993).
6. P. Hello and J.-Y. Vinet, *Phys. Lett. A* **178**, 351-356 (1993).
7. H. Grote (LIGO Scientific Collaboration), *Class. Quantum Grav.* **27**, 084003 (2010).
8. H. Luek et al., *Class. Quantum Grav.* **21**, S985-S989 (2004).
9. T. Accadia et al., *Class. Quantum Grav.* **27**, 084002 (2010).
10. R.C. Lawrence, Ph.D. thesis, MIT, 2003, LIGO-P030001-00-R.
11. Y. Fan et al., *Rev. Sci. Instrum.* **79**, 104501 (2008).
12. A.F. Brooks et al., *Opt. Express* **15**(16), 10370-10375 (2007).

Measuring the Virgo area tilt noise with a laser gyroscope

Jacopo Belfi[1], Nicolò Beverini[1], Filippo Bosi[2], Giorgio Carelli[1], Angela Di Virgilio[2], Enrico Maccioni[1] and Fabio Stefani[1]

[1] *Department of Physics "Enrico Fermi", Università di Pisa and CNISM unità di Pisa, Italy,*
[2] *INFN Sezione di Pisa, Pisa, Italy.*

We report on the measurements of tilt noise performed at the Virgo site with a ring laser gyroscope. The apparatus is a He-Ne laser operating in a square cavity mounted on a vertical plane perpendicular to the north-south arm of the inteferometer. We discuss the possibility of using the ring laser signal to improve the performances of the control system of the Virgo seismic suspensions. The comparison between the ring laser signal and the control signals for the longitudinal traslations of the inverted pendulum (IP) shows remarkable coherence in the frequency range 20 – 200 mHz.

1 Introduction

Over the last 40 years ring laser gyroscopes became one of the most important instruments in the field of inertial navigation and precise rotation measurements. They have high resolution, excellent stability and a wide dynamic range. Furthermore no spinning mechanical parts are required, so these sensors can be manufactured in a very robust way and with a very high rejection of linear cinematic and gravitational accelerations from the rotational signal. More recently, over the last 10 years, mainly thanks to the strong improvement in the mirror manufacture technology, very large perimeter ring laser gyroscopes have found application in Geodesy and General Relativity tests seem feasible in the near future [1].

In the last years "G" [2], a monolithic structure of zerodur (a glass-ceramic with ultra-low thermal expansion coefficient) supporting a squared cavity 4 m in side, operating by the Geodetic Observatory of Wettzel (Germany), was able to detect very small rotation signals like the twice-daily variations of the earth rotation axis due to solid earth tides [3], and the nearly diurnal retrograde polar motion of the instantaneous rotation pole caused by the lunisolar torques [4]. Comparable results have also been obtained by the New Zealand ring-laser research group. Inside the underground laboratory located in Cashmere, Christchurch, New Zealand, operated, the world largest gyrolaser: the UG2, a rectangle 21 m x 40 m [5].

In this paper we present the experimental results concerning the use of a meter size gyrolaser as a very sensitive tilt sensor. The system has been installed inside the Virgo central area with the aim of performing seismic monitoring and improving the control of the inertial suspensions of the Virgo interferometer. The control system for the IP works only in four degrees of freedom; three translational and yaw. Due to the equivalence principle, the linear accelerometers providing the feedback signals are fundamentally unable to distinguish between linear accelerations and tilts. The generic response $a_x(t)$ of an accelerometer, sensitive to the linear acceleration along the longitudinal direction $\hat{x}$, is given by: $a_x(t) = \frac{d^2x}{dt^2} + g\theta(t)$ where g is the modulus of the local gravity vector, and $\theta(t)$ is the angle between the direction $\hat{x}$ and the horizontal plane.

The consequences of the coupling between accelerations and tilts are particularly dramatic for the active control of the IP[6]. In closed loop conditions a rotation introduces a positive feedback in the the system and thus extra noise. A direct measurement of the tilt is expected to provide the correction to the measurement of acceleration and then reduce the overall RMS displacements of the IP. This would in turn improve the sensitivity performances for the gravitational antenna. The Advanced Virgo project foreseen the development of tilt sensors having a sensitivity at the level of 10^{-8} rad/$\sqrt{\text{Hz}}$ in the range $5 - 500$ mHz in order to decouple the pure rotational motion from the linear acceleration measurements (see: Virgo note VIR-027A-09 (26 May 2009)).

In the following we will briefly explain the working principles of laser gyroscope, describe the experimental apparatus and present some measurements of rotational noise detected during severe weather conditions, characterized by strong wind.

2 Measurement principle

The principle of ring-laser gyroscopes operation is based on the Sagnac effect. Two optical beams counter propagating inside the same ring resonator require different times to complete a round-trip. This time difference is proportional to the angular velocity of the local reference frame measured with respect to an inertial reference frame. In the case of a rotating active laser interferometer (gyrolaser) the required resonance condition for sustaining the laser action implies a different optical frequency for the two beams. This difference in frequency is proportional to the rotation rate and it is easily measured combining the beams outside the ring and by measuring their beat frequency. The expression for the optical frequency difference (Sagnac frequency) f_S for a ring laser of perimeter P and an area A takes the following form:

$$f_S = \frac{4A}{\lambda P}\vec{n} \cdot \vec{\Omega}, \tag{1}$$

where A is the area enclosed by the optical path inside the cavity, P the perimeter, λ the optical wavelength, and $\vec{n}$ the area versor. The larger is the ring size, the easier the detection of the Sagnac frequency. Large size also mitigates the effects of lock-in, a major problem with the small size active ring lasers. Lock-in is the tendency (typical of coupled oscillators with similar frequency) of the counter-propagating laser beams to lock to one or the other frequency, practically blinding the ring laser as rotation sensor. The coupling arises in ring laser usually because of backscattering: part of radiation of both beams scattered in the counter-rotating direction. Unlike the small ring lasers used for navigation systems, large gyros easily detect the Earth rotation, which provides a nearly constant background rotation rate. The Earth contribution is enough to bias the Sagnac frequency of the gyrolaser described in this paper. Measuring the local rotations with a resolution at the level of some nrad/s implies to resolve the Earth rotation rate at the level of 1 part in 10^5.

3 Experimental apparatus

The photograph of the experimental apparatus is shown in fig. 1. A 180 mm thick and 1.50 m in side square granite slab supports the whole mechanical ring and defines the laser cavity reference frame. A reinforced concrete monument supports the granite table vertically, in order to measure the rotations around the horizontal direction. The laser resonator is a square optical cavity, 5.40 m in perimeter and 1.82 m^2 in area, enclosed in a vacuum chamber entirely filled with the active medium gas. A fine movement of two opposite placed boxes along the diagonal of the square is also possible. This is provided by two piezoelectric transducers that allow the servo control of the laser cavity perimeter length[7].

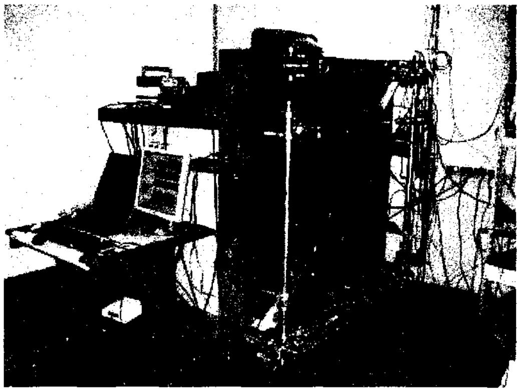

Figure 1: The gyrolaser experimental apparatus installed inside the central area of the Virgo interferometer.

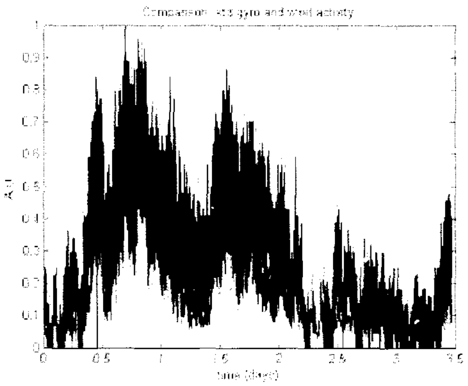

Figure 2: Comparison between the normalized RMS fluctuation of the gyroscope rotation signal and the RMS value of the wind intensity as measured by an anemometer located outside the Virgo central building.

4 Experimental resµlts

The performances of the laser gyroscope as a tilt sensor have been tested in during a measurement run in strong wind weather conditions. In fig 2 is sketched the comparison between the RMS rotational noise and the RMS of the wind intensity. The action of the wind on the building is expected to induce a local tilt on the basement of the Virgo towers containing the super attenuators, so to introduce an excess noise in the inertial damping system.

Fig. 3 shows the coherence calculated for the the rotational signal and the position sensor mounted on top the IP of the north-input and west input towers. A period of 2 hours of strong wind was selected from the data and the coherence function was calculated using the Welch periodogram/FFT method, with a time window of 10^8 s and an overlapping of 50%.

5 Discussion and conclusions

A laser gyroscope operating in a four mirrors ring cavity, 1.35m in side, has been employed to monitor the local ground tilt of the Virgo central area. The detected rotation, superimposed on

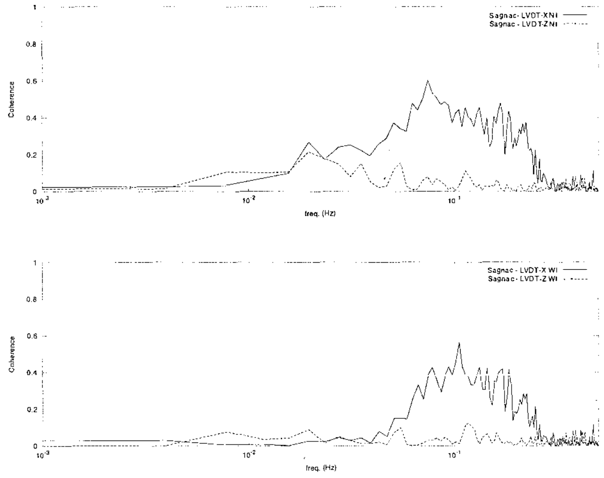

Figure 3: Coherences between the rotation signal measured by the gyrolaser and the longitudinal displacement signals measured by LVDTs of the top of the inverted pendulums of the north-input tower (upper graph) and west-input tower (lower graph). The component of the longitudinal displacement parallel to the plane of the laser gyroscope is labeled as LVDT X for both the graphs.

the Earth-rate constant bias, resulted to be correlated with the excess noise observed in control signals for the longitudinal traslations of the inverted pendulum (IP) control signals for the longitudinal traslations of the (IP) The coherence with the translational degrees of freedom in the plane of propagation of the gyrolaser beams is at the level of 50% in the frequency range 20 – 200 mHz. This result supports the possibility of employing the gyroscope rotation signal to increase the stability of the active position control of the Virgo suspensions during severe weather conditions characterized by strong wind.

References

1. G. E. Stedman, Rep. Prog. Phys. **60-6**, 615 (1997).
2. K.U. Schreiber, T. Klügel, A. Velikoseltsev, W. Schlter, G.E. Stedman, J.-P.R. Wells, Pure Appl. Geophys. **166**, 1485 (2009).
3. K. U. Schreiber, T. Klügel, G. E. Stedman, J. Geophys. Res. **108**, 2003 (.)
4. K. U. Schreiber, A. Velikoseltsev, M. Rothacher. T. Klügel, G. E. Stedman, D. Wiltshire, J. Geophys. Res. **109**, (2004).
5. R. B. Hurst, G. E. Stedman, K. U. Schreiber, R. J. Thirkettle, R. D. Graham, N. Rabeendran, J.-P. R. Wells: J. Appl. Phys. **105**, 113115 (2009).
6. G. Losurdo, D. Passuello and P. Ruggi, VIR-NOT-FIR-1390-318 **1**, April 10 (2006).
7. J. Belfi, N. Beverini, F. Bosi, G. Carelli, A. di Virgilio, E. Maccioni, M. Pizzocaro, F. Sorrentino, F. Stefani, Nuovo Cimento B **125**, 557 (2010).

GRAVITATIONAL WAVE DETECTORS ARE DRIVEN AWAY FROM THERMODYNAMIC EQUILIBRIUM, WHY SHOULD WE CARE

P. DE GREGORIO, L. RONDONI, P ADAMO
Dip. di Matematica, Politecnico di Torino, Corso Duca degli Abruzzi 24, 10129 Torino, Italy and INFN, Sezione di Torino, Via P. Giura 1, 10125 Torino, Italy

M. BONALDI, A. BORRIELLI
Institute of Materials for Electronics and Magnetism, Nanoscience-Trento-FBK Division, 38123 Povo, Trento, Italy and INFN, Gruppo Collegato di Trento, Sezione di Padova, 38123 Povo, Trento, Italy

E. SERRA
Interdisciplinary Laboratory for Computational Science (LISC), FBK-University of Trento, 38123 Povo (Trento), Italy

L. CONTI, R. HAJJ, G. KARAPETYAN, R.K. THAKUR, C. POLI
INFN, Sezione di Padova, Via Marzolo 8, 35131 Padova, Italy

Ground based gravitational wave detectors show extremely high displacement sensitivity which approaches the level set by the quantum limit. However a detection will likely be achieved at a low signal-to-noise ratio, making it mandatory to know the noise budget and statistics. The RareNoise project has pointed out a few mechanisms that cause the instruments to operate at non-equilibrium states. We argue that this aspect has not been given appropriate consideration and that it could alter the overall predicted performance of the detector. The large fluctuations of a nonequilibrium object often differ statistically from those studied at thermodynamic equilibrium. We present experimental and theoretical activity devised to further investigate this question.

1 Introduction

Ground-based Gravitational Wave (GW) detectors are so sensitive low-loss macroscopic objects that managing their thermal fluctuations is a challenging necessity for experimentalists. In fact the intensity of a typical GW of astrophysical origin does not excite the apparatus well above its intrinsic noise threshold. Concurrently, the fact that the intrinsic thermal fluctuations of such low-loss macroscopic objects can be measured is, in and of itself, an impressive achievement, needing further reflection.

One problem that has so far attracted very little attention is the question as to whether the detectors' performance can be hampered by non-equilibrium thermodynamic effects, due to their peculiar architecture [1]. One example is that of interferometers. Test masses are prone to heating due to the absorbed laser power, which in turn causes mechanical deformation of the mirrors, further requiring feedback heating to restore the design optimal geometry [2,3]. By this point, a typical mirror develops a thermal gradient of several degrees, possibly altering its elastic or thermodynamic features. Furthermore, the power must be dissipated through the other parts of the apparatus. This situation is very neatly illustrated in the case of a cryogenic interferometer, in which mirror suspension fibers will mediate a gradient of 10 to 20 K between the mirror and the cryogenic thermal bath [4,5]. Another example, which we shall discuss, concerns extra power exchanged with some electronic feedback mechanism [6,7,8].

Situations in which thermal equilibrium is not attained are very peculiar and hotly debated in statistical mechanics. It is almost a general principle that the fluctuations of observables, far away from the mean, can be very different from those of equilibrium, one example being the rate of energy dissipation. If GW detectors are not in equilibrium, then it is crucial that we distinguish an 'event' from a mere rare nonequilibrium fluctuation.

One of the few results demonstrated to be applicable with some generality deals with the probability that the time-average of an observable $\mathcal{O}$ of positive mean, say $\mathcal{O}_\tau$, assumes values around $+x$, over the probability that it assumes values around $-x$, with τ the duration of the observation. Loosely speaking, relations have been shown to hold [9], of the kind,

$$\frac{P(\mathcal{O}_\tau \approx x)}{P(\mathcal{O}_\tau \approx -x)} \propto e^{\tau x} \tag{1}$$

provided that $\mathcal{O}$ satisfies certain criteria. One instance is the case of a harmonic oscillator, i.e. a precision torsion pendulum [10], which is excited by an electrical field and dissipates energy through the fluid it is immersed into, the rate of energy dissipation playing the role of $\mathcal{O}$. As GW detectors are monitored for long enough time scales, the rare events characterized by Eq. 1 may become observable.

2 The electro-mechanical feedback in AURIGA

A first striking conclusion has been drawn by studying the feedback cooling system that has been developed recently, in the AURIGA detector [6]. One useful and intuitive mathematical scheme is to consider the fundamental mode of vibration of the electro-mechanical oscillator modeled by an instantaneous current $I(T)$ satisfying a Langevin equation [11], which in the absence of feedback would read,

$$L\dot{I}(t) + RI(t) + \frac{1}{C}q(t) = V_T(t) \tag{2}$$

where L, R and C are circuital parameters explicitly related to the mechanical and circuital features of the apparatus, while $V_T(t)$ is the exciting force due to the thermal cryogenic bath. It satisfies $\langle V_T(t)V_T(t')\rangle = 2Rk_BT\delta(t-t')$, T being the temperature and k_B Boltzmann's constant. Via a feedback apparatus that recycles the current with an appropriate phase shift, to a 'quasi-harmonic' approximation Eq. (2) turns into [11],

$$L\dot{I}(t) + \tilde{R}I(t) + \frac{1}{C}q(t) = V_T(t) \tag{3}$$

Here, $\tilde{R}$ is an effective resistance which can be expressed in terms of the feedback parameters The ratio $\tilde{R}/R > 1$ quantifies the extra damping, and therefore the effective 'cooling'. The current around the resonance preserves its approximate Lorentzian shape, with a modified quality factor decreased precisely by the mentioned ratio.

While this paradigm which describes the feedback to have the effect of 'cooling' the system is suggestive and useful for some purposes, it may be misleading if taken too literally. The thermodynamic balance [11] is completely different from that at a mere lowered T. Take for instance the heat absorbed by the oscillator averaged over a time interval of duration τ, Q_τ, or the power injected by the (stochastic) thermal force, P_τ, which would both have zero mean without the feedback. Now we have,

$$Q_\tau = \Delta U_\tau + W_\tau; \qquad P_\tau = Q_\tau + Q_\tau^{(\to\text{bath})} \quad (\simeq Q_\tau \text{ if } \tilde{R} \gg R) \tag{4}$$

ΔU_τ is the stored energy, $Q_\tau^{(\to\text{bath})}$ the heat dissipated toward the bath. The key is W_τ, the work done on the feedback by the oscillator, which is an entirely new factor in the thermodynamic balance. It is strictly positive in the quasi harmonic approximation of Eq. 3. More surprisingly, P_τ satisfies relations other than Eq. 1. Indeed, writing $\mathcal{O}_\tau = P_\tau L/(k_B T R)$, we now have,

$$\frac{P(\mathcal{O} \approx x)}{P(\mathcal{O} = -x)} \propto e^{a\tau x} \quad (\text{small } x); \qquad \frac{P(\mathcal{O} \approx x)}{P(\mathcal{O} = -x)} \propto e^{b\tau x} \quad (\text{large } x) \tag{5}$$

with $a/b = 16/7$ [12], a and b dependent on $\tilde{R}$.

A step further in the characterization of the feedback effect can be obtained by abandoning the quasi harmonic approximation and writing a Langevin equation with explicit memory terms, a more correct expression for the dynamical evolution of the current. The formalism is far from trivial and is treated elsewhere[13]. One obtains an improved prediction for the power spectrum of the current $I(t)$, $S_I(\omega)$, which reveals the possibility that the resonance frequency be fine tuned, by adjusting the cut-off frequency of the low-pass filter, Ω. Figure 1 illustrates one example.

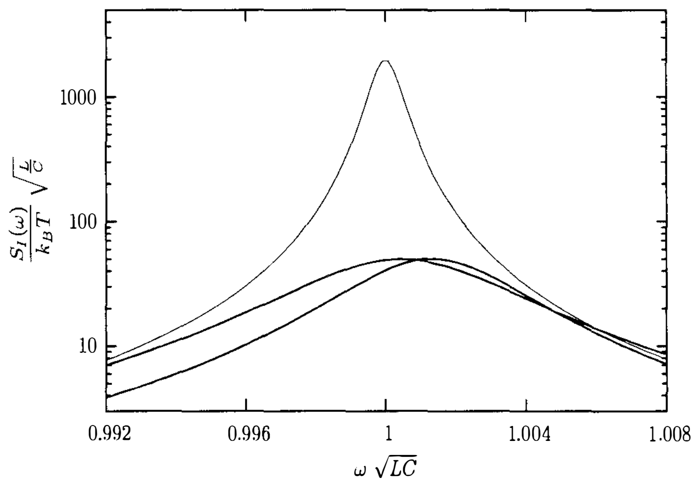

Figure 1: Thin solid line is a Lorenzian curve representing the power spectrum of the current in the absence of feedback. The two thick solid lines approximate Lorenzians and represent two instances in which the control frequency Ω (the low-pass cut-off) is varied, to illustrate the shift of the resonance frequency. The effective resistance $\tilde{R}$ is kept fixed. The damping effect is visible in both cases.

3 Oscillators with gradients - the RareNoise project

The RareNoise project [1] deals with the systematic study of fluctuations of oscillators of high quality factors, which are subject to thermal gradients. As mentioned, this is a situation more reminiscent of interferometric detectors. Other than the implementation of a thermal gradient, crucial aspects are the possibility to control the effect of the bath temperature and of the quality factor of the material. One dimensional models of molecular dynamics have also been devised to mimic the thermo-elastic properties of solids. These models are very simple, hence their length vibrations and thermal fluctuations are more easily controllable and measurable than in more realistic, but more complicated, models. Indeed, they provide qualitative agreement with rea solids, for example the behavior of their elastic constant E with temperature, see Figure 2 More advanced, 3 dimensional models of molecular dynamics are also being developed. Together witl the ongoing experiment, they will provide the groundwork for advancing our knowledge in botl GW detectors, and general nonequilibrium problems.

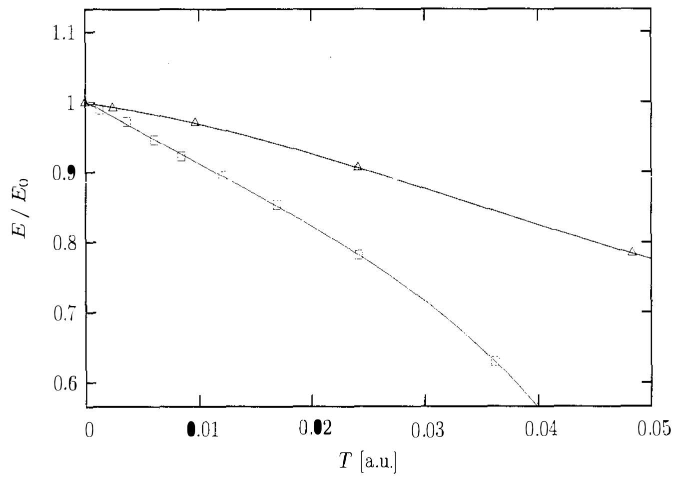

Figure 2: Elastic constants E for classical MD simulations of one-dimensional models with two different interatomic potentials, referred to the extrapolated constant at zero temperature (harmonic oscillators).

Acknowledgments

The research leading to these results has received funding from the European Research Council under the European Community's Seventh Framework Programme (FP7/2007-2013) / ERC grant agreement n 202680. The EC is not liable for any use that can be made on the information contained herein.

References

1. L. Conti, M. Bonaldi and L. Rondoni, *Class. Quantum Grav.* **27**, 084032 (2010)
2. P. Hello, *Eur. Phys. J. D* **15**, 373 (2001)
3. T. Accadia, F. Acernese, F. Antonucci *et al*, *Class. Quantum Grav.* **28**, 114002 (2011)
4. T. Tomaru, T. Suzuki, T. Uchiyama *et al*, *Phys. Lett.* A **301**, 215 (2002)
5. F. Basti, F. Frasconi, M. Granata *et al*, *Journal of Physics: Conference Series* **228**, 012030 (2010)
6. A. Vinante, M. Bignotto, M. Bonaldi *et al*, *Phys. Rev. Lett.* **101**, 033601 (2008)
7. B.Abbott, *New J. Phys.* **11**, 073032 (2009)
8. T. Corbitt, C. Wipf, T. Bodiya *et al*, *Phys. Rev. Lett.* **99**, 160801 (2007)
9. L. Rondoni and C. Mejia-Monasterio, Nonlinearity **20**, R1 (2007), and references therein.
10. S. Ciliberto, S. Joubaud and A. Petrosyan, *J. Stat. Mech.* **12**, P12003 (2010)
11. M. Bonaldi, L. Conti, P. De Gregorio *et al*, *Phys. Rev. Lett.* **103**, 010601 (2009)
12. J. Farago, *J. Stat. Phys.* **107**, 781 (2002)
13. P. De Gregorio, L. Rondoni, M. Bonaldi and L. Conti, *J. Stat. Mech.* , P10016 (2009)

II.
Experimental Gravity

6.
Short Range Gravity

GRAVITATION AT SHORT DISTANCES : THEORY

I. ANTONIADIS

Department of Physics, CERN - Theory Division, 1211 Geneva 23, Switzerland[a]

Lowering the string scale in the TeV region provides a theoretical framework for solving the mass hierarchy problem and unifying all interactions. The apparent weakness of gravity can then be accounted by the existence of large internal dimensions, in the submillimeter region, and transverse to a braneworld where our universe must be confined. I review the main properties of this scenario, as well as the warped case, and its implications for observations at non-accelerator gravity experiments.

1 Strings and extra dimensions

In all physical theories, the number of dimensions is a free parameter fixed to three by observation, with one exception: string theory, which predicts the existence of six new spatial dimensions (seven in the case of M-theory). For a long time, string physicists thought that strings were extremely thin, having the smallest possible size of physics, associated to the Planck length $\sim 10^{-35}$ meters. However, the situation changed drastically over the recent years. It has been realized that the "hidden" dimensions of string theory may be much larger than what we thought in the past and they become within experimental reach in the near future, together with the strings themselves [1,2,3]. These ideas lead in particular to experimental tests of string theory that can be performed in particle colliders, such as LHC.

The main motivation came from considerations of the so-called mass hierarchy problem: why the gravitational force remains much weaker than the other fundamental forces (electromagnetic, nuclear strong and weak), at least up to present energies? In a quantum theory, the masses of elementary particles receive important quantum corrections which are of the order of the higher energy scale present in the theory. Thus, in the presence of gravity, the Planck mass $M_P \sim 10^{19}$ GeV attracts all Standard Model particles to become 10^{16} times heavier than what they are. To avoid this catastrophy, one has to adjust the parameters of the theory up to 32 decimal places, resulting in a very ugly fine tuning.

A possible solution is provided by the introduction of supersymmetry, which may be a new fundamental symmetry of matter. One of its main predictions is that every known elementary particle has a partner, called superparticle. Since none of these superparticles have ever been produced in accelerators, they should be heavier than the observed particles. Supersymmetry should therefore be broken. However, protection of the mass hierarchy requires that its breaking scale, i.e. the mass splitting between the masses of ordinary particles and their partners, cannot be larger than a few TeV. They can therefore be produced at LHC, which will test the idea of supersymmetry [4].

[a] On leave from CPHT (UMR CNRS 7644) Ecole Polytechnique, F-91128 Palaiseau.

On the other hand, a new idea was proposed that solves the problem if the fundamental string length is fixed to $10^{-18} - 10^{-19}$ meters[3]. In this case, quantum corrections are controlled by the string scale, which is in the TeV region, and do not destabilize the masses of elementary particles. Moreover, it offers the remarkable possibility that string physics may be testable soon in particle colliders.

2 The string scale at the TeV

An attractive and calculable framework allowing the dissociation of the string and Planck scales without contradicting observations is provided by the so-called type I string theory. In this theory, gravity is described by closed strings which propagate in all nine dimensions of space, while matter and all other Standard Model interactions are described by open strings ending on the so-called D-branes (where D stands for Dirichlet)[5]. This leads to a braneworld description of our universe, localized on a hypersurface, i.e. a membrane extended in p spatial dimensions, called p-brane (see Figure 1). Closed strings propagate in all nine dimensions of string theory: in those extended along the p-brane, called parallel, as well as in the transverse ones. On the contrary, open strings are attached on the p-brane. Obviously, our p-brane world must have

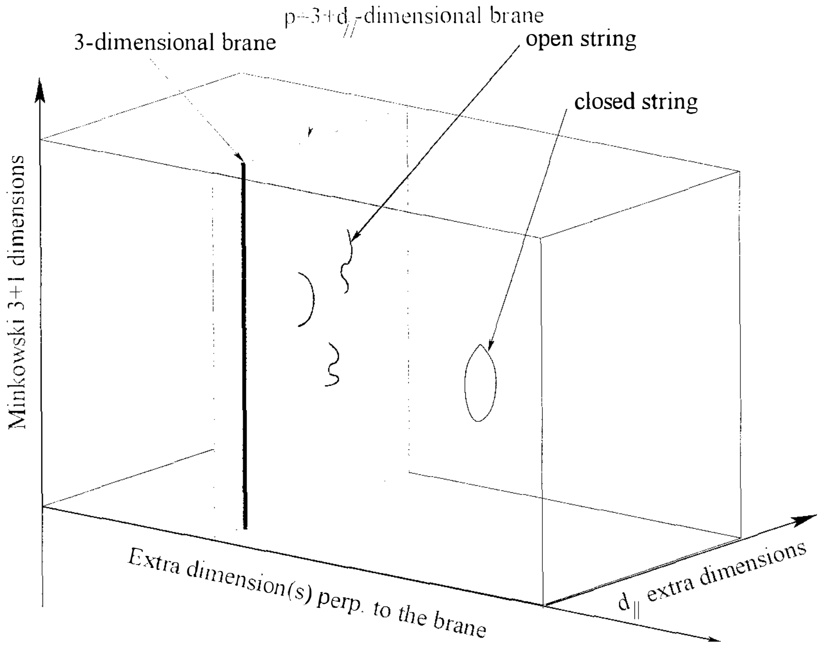

Figure 1: *In the type I string framework, our Universe contains, besides the three known spatial dimensions (denoted by a single blue line), some extra dimensions ($d_{\|} = p - 3$) parallel to our world p-brane (green plane) where endpoints of open strings are confined, as well as some transverse dimensions (yellow space) where only gravity described by closed strings can propagate.*

at least the three known dimensions of space. But it may contain more: the extra $d_{\|} = p - 3$ parallel dimensions must have a finite size, in order to be unobservable at present energies, and can be as large as $\mathrm{TeV}^{-1} \sim 10^{-18}$ m[1]. On the other hand, transverse dimensions interact with us only gravitationally and experimental bounds are much weaker: their size could reach 0.1

mm [6].

In the framework of type I string theory, the string scale M_s can be lowered in the TeV region at the expense of introducing large transverse dimensions of size much bigger than the string length. Actually, the string scale fixes the energy at which gravity becomes strongly coupled with a strength comparable to the other three interactions, realizing the unification of all fundamental forces at energies lower by a factor 10^{16} from what we thought in past. On the other hand, gravity appears to us very weak at macroscopic distances because its intensity is spread in the large extra dimensions [2]. The basic relation between the fundamental (string) scale and the observed gravitational strength is:

$$\text{total force} = \text{observed force} \times \text{transverse volume}\,,$$

expressing the Gauss law for higher-dimensional gravity. In order to increase the gravitational force at the desired magnitude without contradicting present observations, one has to introduce at least two extra dimensions of size that can be as large as a fraction of a millimeter. At distances smaller than the size of extra dimensions, gravity should start deviate from Newton's law, which may be possible to explore in laboratory tabletop experiments [6,7,8] (see Figure 2).

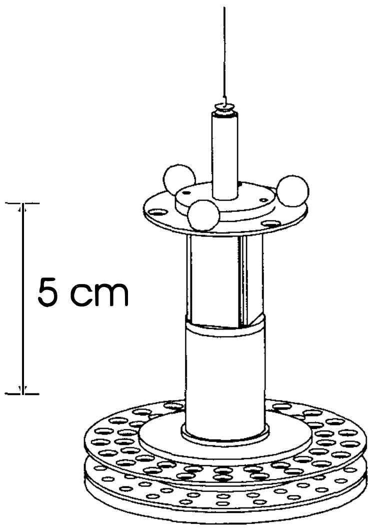

Figure 2: *Torsion pendulum that tested the validity of Newton's law at 55 μm.*

Type I string theory provides a realization of this idea in a coherent theoretical framework. Calculability of the theory implies that parallel dimensions should not be much bigger than the string length, while the size of transverse dimensions is fixed from the observed value of Newton's constant; it should thus vary from the fermi scale (10^{-14} meters) to a fraction of a millimeter, depending on their number (varying from six to two, respectively). It is remarkable that this possibility is consistent with present observations and presents a viable and theoretically well motivated alternative to low energy supersymmetry, offering simultaneously a plethora of spectacular new phenomena that can be tested in laboratory experiments and be a surprise in LHC and other particle accelerators. The main experimental signal is gravitational radiation in the bulk from any physical process on the world-brane, that gives rise to missing-energy. Explicit computation of these effects leads to the collider bounds given in Table 1.

Table 1: Collider bounds on the size of gravitational extra dimensions $R_\perp$ in mm.

Experiment	$n=2$	$n=4$	$n=6$
LEP 2	5×10^{-1}	2×10^{-8}	7×10^{-11}
Tevatron	5×10^{-1}	10^{-8}	4×10^{-11}
LHC	4×10^{-3}	6×10^{-10}	3×10^{-12}

3 Short range forces

There are three categories of predictions in "table-top" experiments that measure gravity at short distances:

(i) Deviations from the Newton's law $1/r^2$ behavior to $1/r^{2+n}$, which can be observable for $n=2$ large transverse dimensions of sub-millimeter size. This case is particularly attractive on theoretical grounds because of the logarithmic sensitivity of Standard Model couplings on the size of transverse space [9], that allows to determine the hierarchy [10].

(ii) New scalar forces in the sub-millimeter range, related to the mechanism of supersymmetry breaking, and mediated by light scalar fields φ with masses:

$$m_\varphi \simeq \frac{m_{susy}^2}{M_P} \simeq 10^{-4} - 10^{-6}\ \mathrm{eV}\,, \tag{1}$$

for a supersymmetry breaking scale $m_{susy} \simeq 1 - 10$ TeV. They correspond to Compton wavelengths of 1 mm to 10 μm. m_{susy} can be either the compactification scale of parallel dimensions $1/R_\parallel$ if supersymmetry is broken by compactification [11], or the string scale if it is broken "maximally" on our world-brane [2,3]. A universal attractive scalar force is mediated by the radion modulus $\varphi \equiv M_P \ln R$, with R the radius of the longitudinal ($R_\parallel$) or transverse ($R_\perp$) dimension(s). In the former case, the result (1) follows from the behavior of the vacuum energy density $\Lambda \sim 1/R_\parallel^4$ for large $R_\parallel$ (up to logarithmic corrections). In the latter, supersymmetry is broken primarily on the brane, and thus its transmission to the bulk is gravitationally suppressed, leading to (1). For $n=2$, there may be an enhancement factor of the radion mass by $\ln R_\perp M_s \simeq 30$ decreasing its wavelength by an order of magnitude [10].

The coupling of the radius modulus to matter relative to gravity can be easily computed and is given by:

$$\sqrt{\alpha_\varphi} = \frac{1}{M}\frac{\partial M}{\partial\varphi}\ ;\quad \alpha_\varphi = \begin{cases} \frac{\partial \ln \Lambda_{QCD}}{\partial \ln R} \simeq \frac{1}{3} & \text{for } R_\parallel \\ \frac{2n}{n+2} = 1 - 1.5 & \text{for } R_\perp \end{cases} \tag{2}$$

where M denotes a generic physical mass. In the longitudinal case, the coupling arises dominantly through the radius dependence of the QCD gauge coupling [11], while in the case of transverse dimension, it can be deduced from the rescaling of the metric which changes the string to the Einstein frame and depends slightly on the bulk dimensionality ($\alpha = 1 - 1.5$ for $n = 2 - 6$) [10]. Such a force can be tested in microgravity experiments and should be contrasted with the change of Newton's law due the presence of extra dimensions that is observable only for $n=2$[6,7]. The resulting bounds for the higher dimensional gravity scale M_*, from an analysis of the radion effects, are [12]:

$$M_* \gtrsim 6\,\mathrm{TeV} \quad (\text{for } R_\perp)\,. \tag{3}$$

In principle there can be other light moduli which couple with even larger strengths. For example the dilaton, whose vacuum expectation value determines the string coupling, if it does not acquire large mass from some dynamical mechanism, can lead to a force of strength 2000 times bigger than gravity [13].

(iii) Non universal repulsive forces much stronger than gravity, mediated by possible abelian gauge fields in the bulk [2,14]. Such fields acquire tiny masses of order M_s^2/M_P, as in (1), due to brane localized anomalies [14]. Although their gauge coupling is infinitesimally small, $g_A \sim M_s/M_P \simeq 10^{-16}$, it is still bigger that the gravitational coupling E/M_P for typical energies $E \sim 1$ GeV, and the strength of the new force would be $10^6 - 10^8$ stronger than gravity.

In Figure 3 we depict thc actual information from previous, present and upcoming experiments [6,7,8]. The solid lines indicate the present limits from the experiments indicated. The

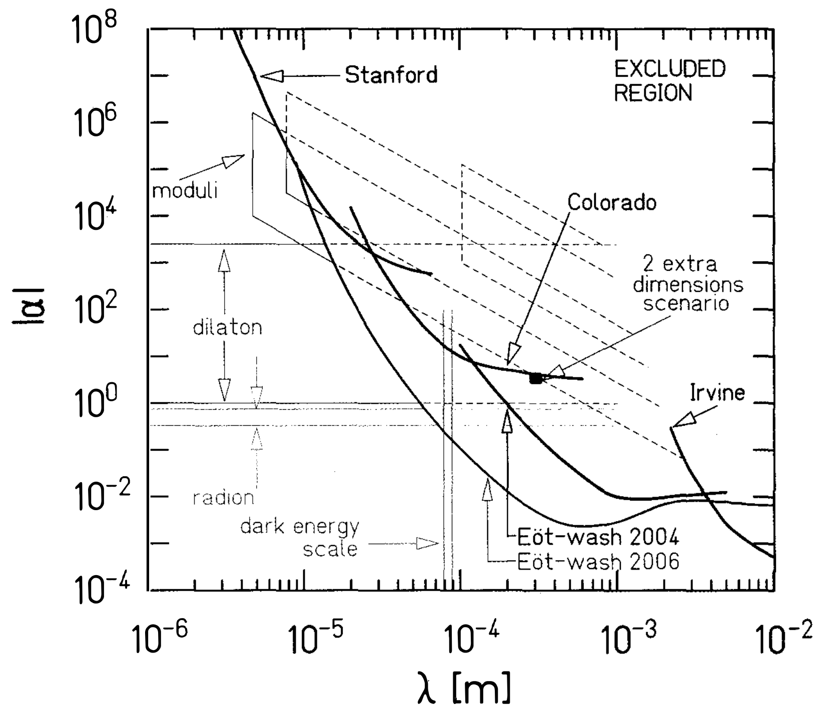

Figure 3: Present limits on new short-range forces (yellow regions), as a function of their range λ and their strength relative to gravity α. The limits are compared to new forces mediated by the graviton in the case of two large extra dimensions, and by the radion.

excluded regions lie above these solid lines. Measuring gravitational strength forces at short distances is challenging. The horizontal lines correspond to theoretical predictions, in particular for the graviton in the case $n = 2$ and for the radion in the transverse case. Finally, in Figures. 4, 5 and 6, recent improved bounds for new forces at very short distances are displayed by focusing on the left hand side of Figure 3, near the origin [7,8].

4 Warped spaces

Braneworld models in curved space (warped metric) with non-compact extra dimensions may lead also to gravity modification at short distances. In particular in RS2, space-time is a slice of anti de Sitter space (AdS) in $d = 5$ dimensions while our universe forms a four-dimensional

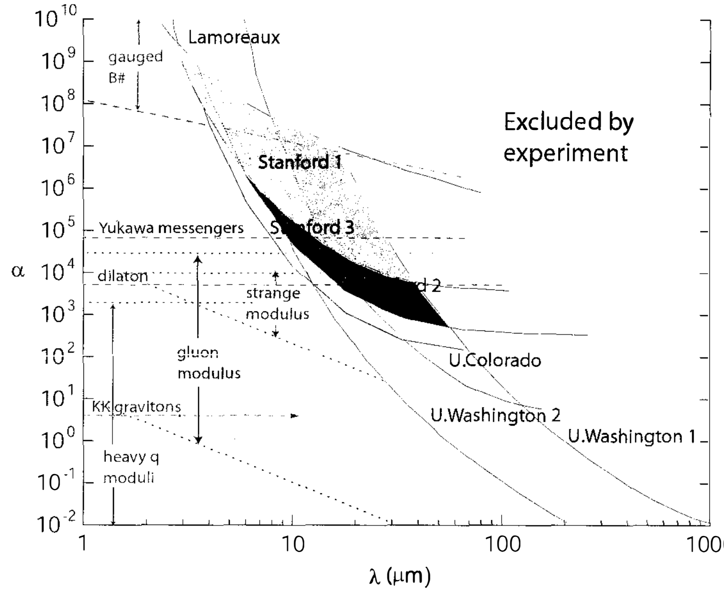

Figure 4: Bounds on non-Newtonian forces in the range 6-20 μm (see S. J. Smullin et al.[7]).

(4d) flat boundary[15]. The 4d Planck mass is given by: $M_P^2 = M_*^3/k$, with $k^2 = -\Lambda/24M_*^3$ in terms of the 5d cosmological constant Λ. Note that M_P is finite, despite the non-compact extra dimension in the 5d AdS space, because of the finite internal volume. As a result, gravity is kept localized on the brane, while the Newtonian potential gets corrections, $1/r + 1/k^2r^3$, which are identical with those arising in the compact case of two flat extra dimensions. Using the experimental limit $k^{-1} \lesssim 0.1$ mm, one finds a bound for the 5d gravity scale $M_* \gtrsim 10^8$ GeV, corresponding to a brane tension $T \gtrsim 1$ TeV. Notice that this bound is not valid in the compact case of six extra dimensions, because their size is in the fermi range and thus the $1/r^3$ deviations of Newton's law are cutoff at shorter distances.

In the presence of the string dilaton, the RS setup has a different solution, which is a linear dilaton background with flat metric in the string frame[16]. An exponential hierarchy is then obtained via the string coupling $g_s^2 = e^{-\alpha r_c}$ with α a mass parameter and r_c the distance of the Planck from the Standard Model brane in the 5th dimension. The 4d Planck mass is now given by: $M_P^2 \sim \frac{M_*^3}{\alpha} e^{\alpha r_c}$. This case extrapolates between flat extra dimension and RS warping with a graviton Kaluza-Klein spectrum $m_n^2 = (n\pi/r_c)^2 + \alpha^2/4$. Because of the mass gap given by α, one extra dimension is possible, for $\alpha^{-1} \lesssim 0.1$ mm with possible deviations of Newton's law in microgravity experiments.

Acknowledgments

Work supported in part by the European Commission under the ERC Advanced Grant 226371 and the contract PITN-GA-2009-237920.

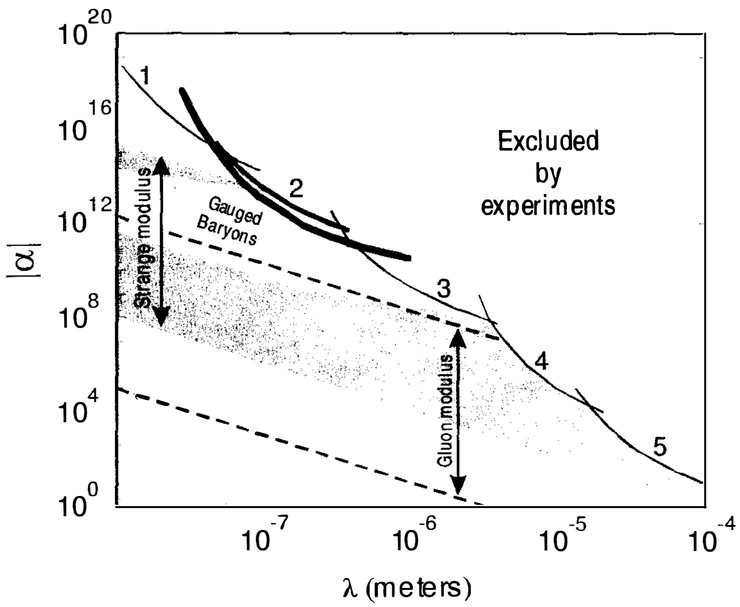

Figure 5: Bounds on non-Newtonian forces in the range of 10-200 nm (see R. S. Decca et al. in Ref. [7]). Curves 4 and 5 correspond to Stanford and Colorado experiments, respectively, of Figure 4 (see also J C. Long and J. C. Price of Ref. [7]).

References

1. I. Antoniadis, Phys. Lett. **B246** (1990) 377; J.D. Lykken, Phys. Rev. **D54** (1996) 3693, [hep-th/9603133].
2. N. Arkani-Hamed, S. Dimopoulos and G. Dvali, Phys. Lett. **B429** (1998) 263, [hep-ph/9803315]; Phys. Rev. **D59** (1999) 086004.
3. I. Antoniadis, N. Arkani-Hamed, S. Dimopoulos and G. Dvali, Phys. Lett. **B436** (1998) 263, [hep-ph/9804398].
4. For a recent review, see *e.g.* M.E. Peskin, "Supersymmetry in Elementary Particle Physics", arXiv:0801.1928 [hep-ph] and references therein.
5. J. Polchinski, Phys. Rev. Lett. **75** (1995) 4724, [hep-th/9510017].
6. D. J. Kapner, T. S. Cook, E. G. Adelberger, J. H. Gundlach, B. R. Heckel, C. D. Hoyle and H. E. Swanson, Phys. Rev. Lett. **98** (2007) 021101.
7. J. C. Long and J. C. Price, *Comptes Rendus Physique* 4 (2003) 337; R. S. Decca, D. Lopez, H. B. Chan, E. Fischbach, D. E. Krause and C. R. Jamell, *Phys. Rev. Lett.* **94** (2005) 240401; R. S. Decca et al., arXiv:0706.3283 [hep-ph]; S. J. Smullin, A. A. Geraci, D. M. Weld, J. Chiaverini, S. Holmes and A. Kapitulnik, arXiv:hep-ph/0508204; H. Abele, S. Haeßler and A. Westphal, in 271th WE-Heraeus-Seminar, Bad Honnef (2002).
8. V. V. Nesvizhevsky, G. Pignol and K. V. Protasov, Phys. Rev. D **77** (2008) 034020 [arXiv:0711.2298 [hep-ph]].
9. I. Antoniadis, C. Bachas, Phys. Lett. **B450** (1999) 83; N. Arkani-Hamed, S. Dimopoulos and J. March-Russell, hep-th/9908146.
10. I. Antoniadis, K. Benakli, A. Laugier and T. Maillard, Nucl. Phys. **B662** (2003) 40 [arXiv:hep-ph/0211409].

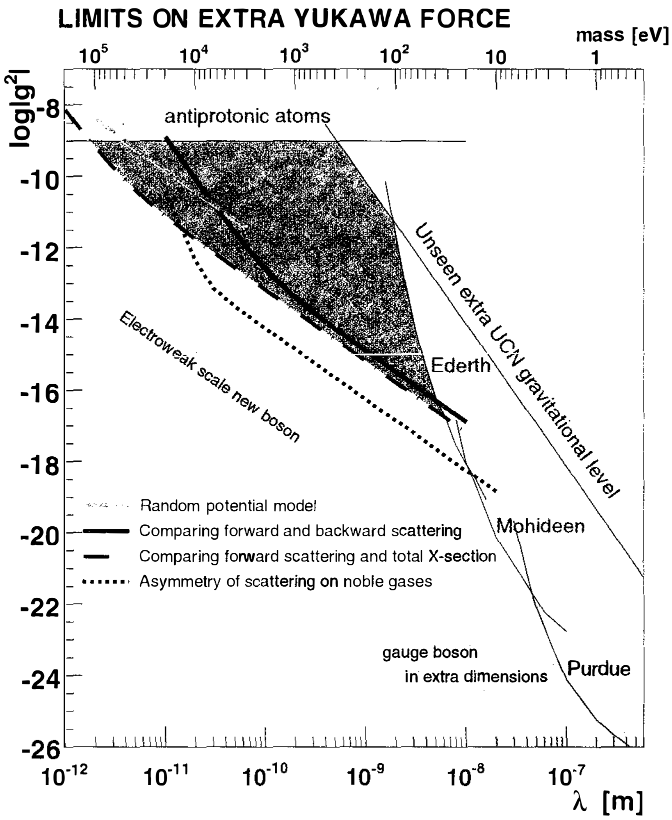

Figure 6: Bounds on non-Newtonian forces in the range of 1 pm-1 nm[8].

11. I. Antoniadis, S. Dimopoulos and G. Dvali, Nucl. Phys. **B516** (1998) 70; S. Ferrara, C. Kounnas and F. Zwirner, Nucl. Phys. **B429** (1994) 589.
12. E. G. Adelberger, B. R. Heckel, S. Hoedl, C. D. Hoyle, D. J. Kapner and A. Upadhye, Phys. Rev. Lett. **98** (2007) 131104.
13. T. R. Taylor and G. Veneziano, Phys. Lett. **B213** (1988) 450.
14. I. Antoniadis, E. Kiritsis and J. Rizos, Nucl. Phys. **B637** (2002) 92.
15. L. Randall and R. Sundrum, Phys. Rev. Lett. **83** (1999) 3370.
16. I. Antoniadis, A. Arvanitaki, S. Dimopoulos and A. Giveon, arXiv:1102.4043 [hep-ph].

CASIMIR AND SHORT-RANGE GRAVITY TESTS

A. LAMBRECHT and S. REYNAUD
Laboratoire Kastler Brossel, ENS, UPMC, CNRS, Jussieu, 75252 Paris, France
serge.reynaud@upmc.fr , www.lkb.ens.fr

Comparison with theory of Casimir force measurements are used to test the gravity force law at ranges from 0.1 to 10 micrometers. The interest of such tests depends crucially on the theoretical evaluation of the Casimir force in realistic experimental configurations. We present the scattering approach which is nowadays the best tool for such an evaluation. We then describe the current status of the comparisons between theory and experiments.

1 Introduction

The Casimir effect is an observable effect of quantum vacuum fluctuations which deserves careful attention as a crucial prediction of quantum field theory [1,2,3,4,5,6].

Casimir physics also plays an important role in the tests of gravity at sub-millimeter ranges [7,8]. Strong constraints have been obtained in short range Cavendish-like experiments [9,10]. For scales of the order of the micrometer, similar tests are performed by comparing with theory the results of Casimir force measurements [11,12]. At even shorter scales, the same can be done with atomic [13,14,15] or nuclear [16,17] force measurements. A recent overview of these short-range tests can be found in [18].

In the following, we focus our attention on Casimir tests of the gravity force law. They are performed at distances from 0.1 to 10 micrometers for which the Casimir force dominates the standard gravity force. It follows that the hypothetical new force would be seen as a difference between the experimental result F_{exp} and theoretical prediction F_{th}. This implies that these two quantities have to be assessed independently from each other. This situation should clearly forbid anyone to use theory-experiment comparison to prove (or disprove) a specific experimental result or theoretical model.

2 The problem of vacuum energy

Before entering this discussion, we want to emphasize that the Casimir effect has a fascinating interface with the puzzles of gravitational physics through the problem of vacuum energy [19,20,21].

Nernst was the first physicist to notice as soon as in 1916 that zero-point fluctuations of the electromagnetic field constituted a challenge for gravitation theory [22,23]. The very existence of these fluctuations dismisses the classical idea of an empty space. When the vacuum energy density is calculated by adding the zero-point energies over all field modes, an infinite value is obtained. When a high frequency cutoff is introduced, the sum is finite but still much larger than the mean energy observed through gravitational phenomena [24,25].

This problem has led famous physicists to deny the reality of vacuum fluctuations. In particular, Pauli crudely stated in his textbook on Wave Mechanics [26] :

> *At this point it should be noted that it is more consistent here, in contrast to the material oscillator, not to introduce a zero-point energy of $\frac{1}{2}\hbar\omega$ per degree of freedom. For, on the one hand, the latter would give rise to an infinitely large energy per unit volume due to the infinite number of degrees of freedom, on the other hand, it would be principally unobservable since nor can it be emitted, absorbed or scattered and hence, cannot be contained within walls and, as is evident from experience, neither does it produce any gravitational field.*

A part of these statements is simply unescapable : the mean value of vacuum energy does not contribute to gravitation as an ordinary energy. This is just a matter of evidence since the universe would look very differently otherwise. But it is certainly no longer possible to uphold today that vacuum fluctuations have no observable effects. Certainly, vacuum fluctuations can *be emitted, absorbed, scattered...* as shown by their numerous effects in atomic [27] and subatomic [28] physics. And the Casimir effect [29] is nothing but the physical effect produced by vacuum fluctuations when they are *contained within walls.*

3 The Casimir force in the ideal and real cases

Casimir calculated the force between a pair of perfectly smooth, flat and parallel plates in the limit of zero temperature and perfect reflection. He found universal expressions for the force F_{Cas} and energy E_{Cas}

$$F_{\text{Cas}} = -\frac{\mathrm{d}E_{\text{Cas}}}{\mathrm{d}L} \quad , \quad E_{\text{Cas}} = -\frac{\hbar c \pi^2 A}{720 L^3} \tag{1}$$

with L the distance, A the area, c the speed of light and $\hbar$ the Planck constant. This universality is explained by the saturation of the optical response of perfect mirrors which reflect 100% (no less, no more) of the incoming fields. In particular the expressions F_{Cas} and E_{Cas} do not depend on the atomic structure constants. Of course, this idealization is no longer tenable for the real mirrors used in the experiments.

The effect of imperfect reflection is large in most experiments, and a precise knowledge of its frequency dependence is essential for obtaining a reliable theoretical prediction [30]. Meanwhile, experiments are performed at room temperature so that the effect of thermal fluctuations has to be added to that of vacuum [31,32]. Then, precise experiments are performed between a plane and a sphere whereas calculations are often devoted to the geometry of two parallel planes. The estimation of the force in the plane-sphere geometry involves the so-called *Proximity Force Approximation* (PFA) [33] which amounts to averaging over the distribution of local inter-plate distances the force calculated in the two-planes geometry. But the PFA can only be valid when the radius R is much larger than the separation L and even in this case its accuracy has to be assessed.

4 The calculation of the force in the scattering approach

The best tool available for addressing these questions is the scattering approach. This approach has been used for years for evaluating the Casimir force between non perfectly reflecting mirrors [34,35]. It is today the best solution for calculating the force in arbitrary geometries [36,37].

The basic idea is that mirrors are described by their scattering amplitudes. When studying first the geometry of two plane and parallel mirrors aligned along the axis x and y, these amplitudes are specular reflection and transmission amplitudes (r and t) which depend on frequency ω, the transverse vector $\mathbf{k} \equiv (k_x, k_y)$ and the polarization p = TE, TM (all these quantities being preserved by scattering). Two mirrors form a Fabry-Perot cavity described by a global $S-$matrix which can be evaluated from the elementary $S-$matrices associated with the two mirrors. Thermal equilibrium is here assumed for the whole system *cavity + fields*. Care has to be taken to account for the contribution of evanescent waves besides that of ordinary modes freely propagating outside and inside the cavity. The properties of the evanescent waves are described through an analytical continuation of those of ordinary ones, using the well defined analytic behavior of the scattering amplitudes. At the end of this derivation, this analytic properties are also used to perform a Wick rotation from real to imaginary frequencies.

The sum of the phaseshifts associated with all field modes leads to the expression of the Casimir free energy $\mathcal{F}$

$$\mathcal{F} = \sum_{\mathbf{k}} \sum_{p} k_{\mathrm{B}} T {\sum_m}' \ln d(i\xi_m, \mathbf{k}, p) \quad , \quad d(i\xi, \mathbf{k}, p) = 1 - r(i\xi, \mathbf{k}, p) e^{-2\kappa L} \tag{2}$$

$$r \equiv r_1 r_2 \quad , \quad \xi_m \equiv \frac{2\pi m k_{\mathrm{B}} T}{\hbar} \quad , \quad \kappa \equiv \sqrt{\mathbf{k}^2 + \frac{\xi^2}{c^2}}$$

$\sum_{\mathbf{k}} \equiv A \int \frac{\mathrm{d}^2\mathbf{k}}{4\pi^2}$ is the sum over transverse wavevectors with A the area of the plates, $\sum_p$ the sum over polarizations and $\sum_m'$ the Matsubara sum (sum over positive integers m with $m = 0$ counted with a weight $\frac{1}{2}$); r is the product of the reflection amplitudes of the mirrors as seen by the intracavity field; ξ and κ are the counterparts of frequency ω and longitudinal wavevector k_z after the Wick rotation.

This expression reproduces the Casimir ideal formula in the limits of perfect reflection $r \to 1$ and null temperature $T \to 0$. But it is valid and regular at thermal equilibrium at any temperature and for any optical model of mirrors obeying causality and high frequency transparency properties. It has been demonstrated with an increasing range of validity in [34], [35] and [36]. The expression is valid not only for lossless mirrors but also for lossy ones. In the latter case, it accounts for the additional fluctuations accompanying losses inside the mirrors.

It can thus be used for calculating the Casimir force between arbitrary mirrors, as soon as the reflection amplitudes are specified. These amplitudes are commonly deduced from models of mirrors, the simplest of which is the well known Lifshitz model [38,39] which corresponds to semi-infinite bulk mirrors characterized by a local dielectric response function $\varepsilon(\omega)$ and reflection amplitudes deduced from the Fresnel law.

In the most general case, the optical response of the mirrors cannot be described by a local dielectric response function. The expression (2) of the free energy is still valid in this case with reflection amplitudes to be determined from microscopic models of mirrors. Attempts in this direction can be found for example in [40,41,42].

5 The case of metallic mirrors

The most precise experiments have been performed with metallic mirrors which are good reflectors only at frequencies smaller than their plasma frequency ω_{P}. Their optical response is described by a reduced dielectric function usually written at imaginary frequencies $\omega = i\xi$ as

$$\varepsilon[i\xi] = \hat{\varepsilon}[i\xi] + \frac{\sigma[i\xi]}{\xi} \quad , \quad \sigma[i\xi] = \frac{\omega_{\mathrm{P}}^2}{\xi + \gamma} \tag{3}$$

The function $\hat{\varepsilon}[i\xi]$ represents the contribution of interband transitions and is regular at the limit $\xi \to 0$. Meanwhile $\sigma[i\xi]$ is the reduced conductivity (σ is measured as a frequency and the SI conductivity is $\epsilon_0\sigma$) which describes the contribution of the conduction electrons.

A simplified description corresponds to the lossless limit $\gamma \to 0$ often called the plasma model. As γ is much smaller than ω_P for a metal such as Gold, this simple model captures the main effect of imperfect reflection. However it cannot be considered as an accurate description since a much better fit of tabulated optical data is obtained [38] with a non null value of γ. Furthermore, the Drude model $\gamma \neq 0$ meets the important property of ordinary metals which have a finite static conductivity

$$\sigma_0 = \frac{\omega_P^2}{\gamma} \tag{4}$$

This has to be contrasted to the lossless limit which corresponds to an infinite value for σ_0.

When taking into account the imperfect reflection of the metallic mirrors, one finds that the Casimir force is reduced with respect to the ideal Casimir expression at all distances for a null temperature [36]. This reduction is conveniently represented as a factor

$$\eta_F = \frac{F}{F_{\text{Cas}}} \quad , \quad F = -\frac{\partial \mathcal{F}}{\partial L} \tag{5}$$

where F is the real force and F_{Cas} the ideal expression. For the plasma model, there is only one length scale, tha plasma wavelength $\lambda_P = 2\pi c/\omega_P$ in the problem (136nm for Gold). The ideal Casimir formula is recovered ($\eta_F \to 1$) at large distances $L \gg \lambda_P$, as expected from the fact that metallic mirrors tend to be perfect reflectors at low frequencies $\omega \ll \omega_P$. At short distances in contrast, a significant reduction of the force is obtained ($\eta_F \ll 1$), which scales as L/λ_P, as a consequence of the fact that metallic mirrors are poor reflectors at high frequencies $\omega \gg \omega_P$. In other words, there is a change in the power law for the variation of the force with distance. This change can be understood as the result of the Coulomb interaction of surface plasmons living at the two matter-vacuum interfaces [43,44].

As experiments are performed at room temperature, the effect of thermal fluctuations has to be added to that of vacuum fields [45]. Significant thermal corrections appear at distances L larger than a critical distance determined by the thermal wavelength λ_T (a few micrometers at room temperature). Boström and Sernelius were the first to remark that the small non zero value of γ had a significant effect on the force at non null temperatures [46]. In particular, there is a large difference at large distances between the expectations calculated for $\gamma = 0$ and $\gamma \neq 0$, their ratio reaching a factor 2 when $L \gg \lambda_T$. It is also worth emphasizing that the contribution of thermal fluctuations to the force is opposite to that of vacuum fluctuations for intermediate ranges $L \sim \lambda_T$.

This situation has led to a blossoming of contradictory papers (see references in [47,48,49]). As we will see below, the contradiction is also deeply connected to the comparison between theory and experiments.

6 The non-specular scattering formula

We now present a more general scattering formula allowing one to calculate the Casimir force between stationary objects with arbitrary geometries. The main generalization with respect to the already discussed cases is that the scattering matrix $\mathcal{S}$ is now a larger matrix accounting for non-specular reflection and mixing different wavevectors and polarizations while preserving frequency. Of course, the non-specular scattering formula is the generic one while specular reflection can only be an idealization.

The Casimir free energy can be written as a generalization of equation (2)

$$\mathcal{F} = k_B T \sum_m {}' \operatorname{Tr} \ln \mathcal{D}(i\xi_m) \tag{6}$$
$$\mathcal{D} = 1 - \mathcal{R}_1 \exp^{-\mathcal{K}L} \mathcal{R}_2 \exp^{-\mathcal{K}L}$$

The symbol Tr refers to a trace over the modes at a given frequency. The matrix $\mathcal{D}$ is the denominator containing all the resonance properties of the cavity formed by the two objects 1 and 2 here written for imaginary frequencies. It is expressed in terms of the matrices $\mathcal{R}_1$ and $\mathcal{R}_2$ which represent reflection on the two objects 1 and 2 and of propagation factors $\exp^{-\mathcal{K}L}$. Note that the matrices $\mathcal{D}$, $\mathcal{R}_1$ and $\mathcal{R}_2$, which were diagonal on the basis of plane waves when they described specular scattering, are no longer diagonal in the general case of non specular scattering. The propagation factors remain diagonal in this basis with their diagonal values written as in (2). Clearly the expression (6) does not depend on the choice of a specific basis. But it may be written in specific basis fitting the geometry under study.

The multiple scattering formalism has been used in the past years by different groups using different notations (see as examples [50,51,52]) and numerous applications have been considered. In particular, the case of corrugated plates or gratings has been extensively studied [53,54,55,56] and it has given rise to interesting comparisons with experiments [57,58,59]. Note also that calculations have been devoted to the study of atoms in the vicinity of corrugated plates [60,61,62].

7 The plane-sphere geometry beyond PFA

Recently, it has also become possible to use the general scattering formula to obtain explicit evaluations of the Casimir force in the plane-sphere geometry. Such calculations have first been performed for perfectly reflecting mirrors [63]. They have then been done for the more realistic case of metallic mirrors described by a plasma model dielectric function [64]. Even more recently, calculations were made which treat simultaneously plane-sphere geometry and non zero temperature, with dissipation taken into account [65].

In these calculations, the reflection matrices are written in terms of Fresnel amplitudes for plane waves on the plane mirror and of Mie amplitudes for spherical waves on the spherical mirror. The scattering formula is then obtained by writing also transformation formulas from the plane waves basis to the spherical waves basis and conversely. The energy takes the form of an exact multipolar formula labeled by a multipolar index ℓ. When doing the numerics, the expansion is truncated at some maximum value $\ell_{\max}$, which degrades the accuracy of the resulting estimation for very large spheres $x \equiv L/R < x_{\min}$ with $x_{\min}$ proportional to $\ell_{\max}^{-1}$.

The results of these calculations may be compared to the experimental study of PFA in the plane-sphere geometry [66]. In this experiment, the force gradient is measured for various radii of the sphere and the results are used to obtain a constraint $|\beta_G| < 0.4$ on the slope at origin β_G of the function $\rho_G(x)$

$$\rho_G = \frac{G}{G^{\mathrm{PFA}}} = 1 + \beta_G x + O(x^2) \quad , \quad x \equiv \frac{L}{R} \tag{7}$$

The slope obtained by interpolating at low values of x our theoretical evaluation of ρ_G reveals a striking difference between the cases of perfect and plasma mirrors. The slope β_G^{perf} obtained for perfect mirrors is larger than that β_G^{Gold} obtained for gold mirrors by a factor larger than 2

$$\beta_G^{\mathrm{perf}} \sim -0.48 \quad , \quad \beta_G^{\mathrm{Gold}} \sim -0.21 \tag{8}$$

As a result, β_G^{Gold} is compatible with the experimental bound whereas β_G^{perf} is not [64].

The effect of temperature is also correlated with the plane-sphere geometry. The first calculations accounting simultaneously for plane-sphere geometry, temperature and dissipation have been published very recently [65] and they show several striking features. The factor of 2 between the long distance forces in Drude and plasma models is reduced to a factor below 3/2 in the plane-sphere geometry. Then, PFA underestimates the Casimir force within the Drude model at short distances, while it overestimates it at all distances for the perfect reflector and plasma model. If the latter feature were conserved for the experimental parameter region R/L ($> 10^2$), the actual values of the Casimir force calculated within plasma and Drude model could turn out to be closer than what PFA suggests. This would affect the discussion of the next section, which is still based on calculations using PFA.

8 Discussion of experiments

We end up this review by discussing the status of comparisons between Casimir experiments and theory. We emphasize that, after years of improvement in experiments and theory, we have to face a lasting discrepancies in their comparison.

On one side, the Purdue and Riverside experiments [67,68,69] appear to favor predictions obtained with $\gamma = 0$ rather than those corresponding to the expected $\gamma \neq 0$ (see Fig.1 in [68]). This result stands in contradiction to the fact that Gold has a finite conductivity. Note that these experiments are done at distances smaller than 0.75μm where the thermal contribution is small, so that accuracy is a critical issue here.

On the other side, a new experiment at Yale [70] has been able to measure the force at larger distances (0.7μm-7μm) where the thermal contribution is larger and the difference between the predictions at $\gamma = 0$ and $\gamma \neq 0$ significant. The results favor the expected Drude model ($\gamma \neq 0$), but only after subtraction of a large contribution of the patch effect.

It is worth emphasizing that the results of the new experiment see a significant thermal contribution and fit the expected model. Of course, they have to be confirmed by further studies [71]. In particular, the electrostatic patch effect remains a source of concern in Casimir experiments [72,73]. It is not measured independently in any of the experiments discussed above. This means that the Casimir effect, which is now verified in several experiments, is however not tested at the 1% level, as has been sometimes claimed. This also entails that the tests of gravity at the micrometer range have still room available for improvement.

Acknowledgments

The authors thank A. Canaguier-Durand, A. Gérardin, R. Guérout, J. Lussange, R.O. Behunin, I. Cavero-Pelaez, D. Dalvit, C. Genet, G.L. Ingold, F. Intravaia, M.-T. Jaekel, P.A. Maia Neto, V.V. Nesvizhevsky for contributions to the work reviewed in this paper, and the ESF Research Networking Programme CASIMIR (www.casimirnetwork. com) for providing excellent opportunities for discussions on the Casimir effect and related topics.

References

1. P.W. Milonni, *The quantum vacuum* (Academic, 1994).
2. S.K. Lamoreaux, Resource Letter in *Am. J. Phys.* **67** 850 (1999).
3. M. Bordag, U. Mohideen and V.M. Mostepanenko, *Phys. Rep.* **353** 1 (2001).
4. K.A. Milton, *J. Phys. A* **20** 4628 (2005).
5. R.G. Barrera and S. Reynaud eds., *Focus on Casimir Forces*, *New J. Phys.* **8** (2006).
6. D. Dalvit *et al* eds., *Casimir physics*, Lecture Notes in Physics **834** (Springer, 2011)
7. E. Fischbach and C. Talmadge, *The Search for Non Newtonian Gravity* (AIP Press/Springer Verlag, 1998).
8. E.G. Adelberger, B.R. Heckel and A.E. Nelson, *Ann. Rev. Nucl. Part. Sci.* **53** 77 (2003).
9. D.J. Kapner, T.S. Cook, E.G. Adelberger *et al*, *Phys. Rev. Lett.* **98** 021101 (2007).
10. E.G. Adelberger *et al*, in this book.
11. A. Lambrecht and S. Reynaud, *Poincaré Seminar on Vacuum Energy and Renormalization* **1** 107 (2002) [arXiv:quant-ph/0302073] and references therein.

12. R. Onofrio, *New J. Phys.* **8** 237 (2006).
13. P. Wolf, P. Lemonde, A. Lambrecht *et al*, *Phys. Rev. A* **75** 063608 (2007).
14. S. Lepoutre *et al*, *EPL* **88** 20002 (2009).
15. B. Pelle *et al*, in this book.
16. V.V. Nesvizhevsky *et al*, *Phys. Rev. D* **77** 034020 (2008).
17. V.V. Nesvizhevsky *et al*, in this book.
18. I. Antoniadis, S. Baessler, M. Buchner, V.V. Fedorov, S. Hoedl. V.V. Nesvizhevsky, G. Pignol, K.V. Protasov, S. Reyñaud and Yu. Sobolev, *Compt. Rend. Acad. Sci.* (2011).
19. C. Genet, A. Lambrecht and S. Reynaud, in *On the Nature of Dark Energy* eds. U. Brax, J. Martin, J.P. Uzan, 121 (Frontier Group, 2002) [arXiv:quant-ph/0210173].
20. M.-T. Jaekel and S. Reynaud, in *Mass and Motion in General Relativity*, eds L. Blanchet, A. Spallicci and B. Whiting 491 (2011) [arXiv:0812.3936] and references therein.
21. M.-T. Jaekel *et al*, in this book.
22. W. Nernst, *Verh. Deutsch. Phys. Ges.* **18** 83 (1916).
23. P.F. Browne, *Apeiron* **2** 72 (1995).
24. S. Weinberg, *Rev. Mod. Phys.* **61** 1 (1989).
25. R.J. Adler, B. Casey and O.C. Jacob, *Am. J. Phys.* **63** 620 (1995).
26. W. Pauli, Die Allgemeinen Prinzipien der Wellenmechanik, in *Handbuch der Physik* **24** 1 (1933); translation reproduced from Enz C.P., in Enz C.P. andMehra J. eds, Physical Reality andMathcmatical Description (Reidel, 1974) p.124.
27. C. Cohen-Tannoudji, J. Dupont-Roc and G. Grynberg, *Atom-Photon Interactions* (Wiley, 1992).
28. C. Itzykson and J.-B. Zuber, *Quantum Field Theory* (McGraw Hill, 1985).
29. H.B.G. Casimir, *Proc. K. Ned. Akad. Wet.* **51** 793 (1948).
30. A. Lambrecht and S. Reynaud, *Euro. Phys. J. D* **8** 309 (2000).
31. J. Mehra, *Physica* **37** 145 (1967).
32. J. Schwinger, L.L. de Raad and K.A. Milton, *Ann. Phys.* **115** 1 (1978).
33. B.V. Deriagin, I.I. Abrikosova and E.M. Lifshitz, *Quart. Rev.* **10** 295 (1968).
34. M.T. Jaekel and S. Reynaud, *J. Physique I* **1** 1395 (1991) [arXiv:quant-ph/0101067].
35. C. Genet, A. Lambrecht and S. Reynaud, *Phys. Rev. A* **67** 043811 (2003).
36. A. Lambrecht, P.A. Maia Neto and S. Reynaud, *New J. Phys.* **8** 243 (2006).
37. A. Lambrecht, A. Canaguier-Durand, R. Guérout, and S. Reynaud, in[6] [arXiv:1006.2959].
38. E.M Lifshitz, *Sov. Phys. JETP* **2** 73 (1956).
39. I.E. Dzyaloshinskii, E.M. Lifshitz and L.P. Pitaevskii, *Sov. Phys. Uspekhi* **4** 153 (1961).
40. L.P. Pitaevskii, *Phys. Rev. Lett.* **101** 163202 (2008); *Phys. Rev. Lett.* **102** 189302 (2009); B. Geyer *et al*, *Phys. Rev. Lett.* **102** 189301 (2009).
41. D.A.R. Dalvit and S.K. Lamoreaux, *Phys. Rev. Lett.* **101** 163203 (2008); *Phys. Rev. Lett.* **102** 189304 (2009); R.S. Decca *et al*, *Phys. Rev. Lett.* **102** 189303 (2009).
42. V.B. Svetovoy, *Phys. Rev. Lett.* **101** 163603 (2008); *Phys. Rev. Lett.* **102** 219903 (E) (2009).
43. C. Genet, F. Intravaia, A. Lambrecht, and S. Reynaud, *Ann. Found. L. de Broglie* **29** 311 (2004).
44. F. Intravaia and A. Lambrecht, *Phys. Rev. Lett.* **94** 110404 (2005).
45. C. Genet, A. Lambrecht and S. Reynaud, *Phys. Rev. A* **62** 012110 (2000) and references therein.
46. M. Boström and Bo E. Sernelius, *Phys. Rev. Lett.* **84** 4757 (2000).
47. S. Reynaud, A. Lambrecht and C. Genet, in *Quantum Field Theory Under the Influence of External Conditions*, ed. K.A.Milton (Rinton Press, 2004) p.36 [arXiv:quant-ph/0312224].
48. I. Brevik, S.A. Ellingsen and K. Milton, *New J. Phys.* **8** 236 (2006).
49. G.-L. Ingold, A. Lambrecht and S. Reynaud, *Phys. Rev. E* **80** 041113 (2009).

50. T. Emig, *J. Stat. Mech.: Theory Exp.* P04007 (2008).
51. O. Kenneth and I. Klich, *Phys. Rev. B* **78** 014103 (2008).
52. K.A. Milton and J. Wagner, *J. Phys. A* **41** 155402 (2008).
53. R.B. Rodrigues, P.A. Maia Neto, A. Lambrecht and S. Reynaud, *Phys. Rev. Lett.* **96** 100402 (2006); *Phys. Rev. Lett.* **98** 068902 (2007).
54. R.B. Rodrigues, P.A. Maia Neto, A. Lambrecht and S. Reynaud, *Phys. Rev. A* **75** 062108 (2007).
55. R.B. Rodrigues, P.A. Maia Neto, A. Lambrecht and S. Reynaud, *EPL* **76** 822 (2006).
56. A. Lambrecht and V.N. Marachevsky, *Phys. Rev. Lett.* **101** 160403 (2008); A. Lambrecht, *Nature* **454** 836 (2008).
57. H.B. Chan, Y. Bao, J. Zou *et al*, *Phys. Rev. Lett.* **101** 030401 (2008).
58. H.C. Chiu, G.L. Klimchitskaya, V.N. Marachevsky *et al*, *Phys. Rev. B* **80** 121402 (2009).
59. Y. Bao, R. Gurout, J. Lussange *et al*, *Phys. Rev. Lett.* **105** 250402 (2010).
60. D.A.R. Dalvit, P.A. Maia Neto, A. Lambrecht and S. Reynaud, *Phys. Rev. Lett.* **100** 040405 (2008).
61. R. Messina, D.A.R. Dalvit, P.A. Maia Neto, A. Lambrecht and S. Reynaud, *Phys. Rev. A* **80** 022119 (2009).
62. A.M. Contreras-Reyes, R. Gurout, P.A. Maia Neto, D.A.R. Dalvit, A. Lambrecht and S. Reynaud, *Phys. Rev. A* **82** 052517 (2010).
63. P.A. Maia Neto, A. Lambrecht and S. Reynaud, *Phys. Rev. A* **78** 012115 (2008).
64. A. Canaguier-Durand, P.A. Maia Neto, I. Cavero-Pelaez, A. Lambrecht and S. Reynaud, *Phys. Rev. Lett.* **102** 230404 (2009).
65. A. Canaguier-Durand, P.A. Maia Neto, A. Lambrecht and S. Reynaud, *Phys. Rev. Lett.* **104** 040403 (2010).
66. D.E. Krause, R.S. Decca, D. Lopez and E. Fischbach, *Phys. Rev. Lett.* **98** 050403 (2007).
67. R.S. Decca, D. López, E. Fischbach *et al*, *Annals Phys.* **318** 37 (2005).
68. R.S. Decca, D. López, E. Fischbach *et al*, *Phys. Rev. D* **75** 077101 (2007).
69. G.L. Klimchitskaya, U. Mohideen and V.M. Mostepanenko, *Rev. Mod. Phys.* **81** 1827 (2009).
70. A.O. Sushkov, W.J. Kim, D.A.R. Dalvit and S.K. Lamoreaux, *Nature Physics* **7** 230 (2011).
71. K. Milton, *Nature Physics* **7** 190 (2011).
72. C.C. Speake and C. Trenkel, *Phys. Rev. Lett.* **90** 160403 (2003).
73. W.J. Kim, A.O. Sushkov, D.A.R. Dalvit and S.K. Lamoreaux, *Phys. Rev. A* **81** 022505 (2010).

TESTING THE INVERSE SQUARE LAW OF GRAVITATION AT SHORT RANGE WITH A SUPERCONDUCTING TORSION BALANCE

E.C. Chalkley, S. N. Aston, C. J. Collins, M. J. Nelson, C. C. Speake

Department of Physics & Astronomy, University of Birmingham, Edgbaston, Birmingham, B15 2TT

We discuss a search for violations of the inverse square law of gravitation at $14\mu m$. A superconducting torsion balance instrument is described and some sources of systematic error are discussed.

1 Motivation for Short-range Measurements of Gravitation

A postulated solution to the conflict between the density of Dark Energy and the observed magnitude of the Cosmological Constant is to modify spacetime to include compactified additional dimensions [1]. The presence of these large extra dimensions (LED) would increase the strength of the gravitational attraction at the range of the radii of the dimensions. The density of Dark Energy can be used to estimate a scale for these LED; in the case of two extra dimensions this scale is about 14 μm [2] .

More generally, theorised deviations from the gravitational inverse square law are often characterised as Yukawa potentials. The Yukawa potential energy for a pair of point masses has the form,

$$V = -\frac{GM_1M_2}{r}\left(1 + \alpha e^{-r/\lambda}\right) \tag{1}$$

where λ is the characteristic range of the potential, α parameterises the strength of the potential and M and r represent the masses and separations of objects. This form is also applicable for LED potentials when r is much larger than the radius of the extra dimensions. In Section 3, the full extra-dimensional gravitational potential which is required to calculate the extra-dimensional gravitational potential is discussed.

2 The Superconducting Torsion Balance Instrument

Torsion balances have historically been used to set limits on possible deviations from the gravitational inverse square law [3]. Previously we have developed a spherical superconducting torsion balance, which employed magnetic levitation [4]. The current instrument follows on from this work, using multiple coils to control all the degrees of freedom of the test mass and to provide simultaneously high sensitivity to applied torques.

2.1 A Magnetically Levitated Bearing

A novel element in the instrument is the use of a superconducting levitating bearing to replace the fibre supporting the test mass. The levitation system consists of a bearing structure (see Figure 1) which supports twelve coils which produce lift and transverse stiffness. The levitation system is currently being tested using coils handwound from lead wire into milled aluminium substrates. The final coils used in the experiment are to be manufactured photolithographically by our collaborators at Heriot-Watt University.

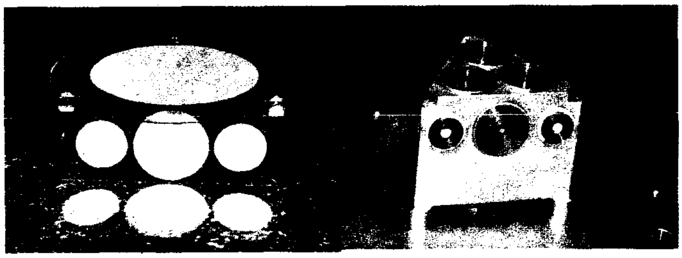

Figure 1: Left: A silica prototype of the float structure that will be levitated, bearing one test mass on the top circular face Right: The levitating bearing, showing hand-wound lead servo and levitation coils.

The levitated structure or 'float' which forms the free element in the torsion balance fits over the top of the bearing with a test mass forming the upper surface of the disc. A silica prototype float has been constructed for testing (Figure 1) but the final version used in the experiment will be an all-copper assembly.

2.2 Experimental Test Masses

The gravitational sources and test masses in the instrument are two identical discs, one placed on the levitated float structure (the test disc) and one controlled by the micropositioning system (the source disc). The discs bear identical patterns of 2048 radial stripes, alternating between Au and Cu organised into 16 sectors of alternating pattern phase. These materials were chosen because of their large density contrast and their well-matched thermal contraction at 4 K. The technology for depositing these metals is also very well known, and good results for producing the experimental surfaces to a high level of flatness can be expected.

3 Torques from Newtonian Gravity and the LED Signal

The gravitational potential of an object of mass M in a spacetime with 2 extra dimensions is given by,

$$V_{4+2} = -\frac{G_{4+2}M}{(r^2 + \sum_{n=1}^{\infty}(\xi_1 - 2\pi Rn)^2 + \sum_{m=1}^{\infty}(\xi_2 - 2\pi Rm)^2)^{3/2}}, \tag{2}$$

where r is the Euclidean distance given by $\sqrt{x^2+y^2+z^2}$ and the components of the higher dimensional distance are (x, y, z, ξ_1, ξ_2), G_{4+2} is the higher-dimensional gravitational constant and n and m are integers representing the number of revolutions around the extra dimensions [5]. By numerically integrating this potential for the case of $4+2$ dimensions it was calculated that with a 15 μm spacing, the LED extra torque would be 3.49×10^{-17} Nm. The pitch of the alternating Au/Cu pattern was set at 90 μm after examining the trade-off between sensitivity to the LED torque at a spacing of 15 μm and sensitivity to torques due to a Yukawa potential with $\lambda = 14$ μm, as shown in Figure 2.

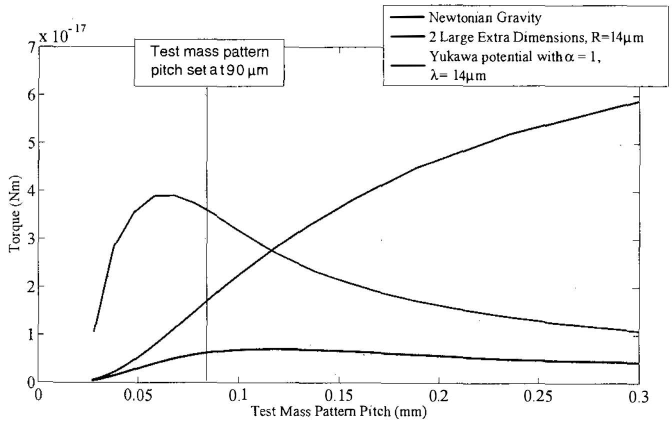

Figure 2: The calculated strength of the forces on the superconducting torsion balance at a separation of 15 μm due to LED gravity, a Yukawa potential with $\alpha = 1$ and $\lambda = 14$ μm and 4D Newtonian gravity as a function of pattern pitch.

4 Analysis of Spurious Forces

The torque on the superconducting torsion balance may contain non-gravitational components that are ideally eliminated from the readout. These excess torques are caused by the coupling of electrostatic, magnetic, Casimir and other forces to aspects of the test masses.

The experimental surfaces of the test mass are to be constructed to be optically flat at room temperature, with no correlation between the surface roughness and the underlying pattern. At 4 K, the slightly different thermal contractions mean that the Au stripes will stand 0.2 nm higher than the Cu stripes. This modulation of the gap between the experimental surfaces couples to the forces which vary with the local gap size so that a torque may exist to align the Au stripes on both surfaces. This interaction of the modulation of the gap results in a transverse Casimir force per unit length per stripe pair, which is given by,

$$F_{Cas} = -\frac{\pi^3 \hbar c A_C^2}{60 g_{v0}^5} \sin\left(\frac{2\pi\delta}{p}\right) Nm^{-1}, \tag{3}$$

where A_C is the amplitude of the thermal corrugations, p is the pitch of the spoke pattern, δ represents the shift parameter of the test mass patterns with respect to one another, and g_{v0} is the vacuum distance between the surfaces of the test masses, which is the separation . Using the values $g_{v0} = 13$ μm, $A_C = 0.2$ nm and $p = 90$ μm , the value of F_{Cas} is 1.76×10^{-21} Nm^{-1}. At this spacing size, and assuming that the corrugations of the test mass at 4 K are no larger than would be expected from thermal contraction mismatches, the transverse Casimir force is negligible.

Electrostatic forces are likely to contribute significantly and in the same manner as the Casimir force, by producing a torque that seeks to align the raised corrugations on both experimental surfaces. The electrostatic force per unit length per spoke pair is given by,

$$F_{Elec} = -\frac{\epsilon_0}{2}\frac{\Delta V^2 A_C^2}{g_{v0}^3} 2\pi \sin\left(\frac{2\pi\delta}{p}\right) Nm^{-1}, \tag{4}$$

where all symbols retain their earlier definitions and ΔV is the potential difference between the two masses. With ΔV set at a value of 0.01 V and the same gap and corrugation parameters as used above, the force $F_M = -4.12 \times 10^{-18}$ Nm^{-1} - an order of magnitude smaller than the LED signal torque.

The torque on the test masses per unit length per stripe pair caused by the contact potential between the Au and Cu stripes is,

$$F_{cpd} = -p\frac{\epsilon_0}{2}\frac{\Delta V_{cpd}^2}{\sinh\left(\frac{2\pi g_{v0}}{p}\right)}\left(\frac{2\pi}{p}\right)^2 \sin\left(\frac{2\pi\delta}{p}\right) Nm^{-1}, \tag{5}$$

where ΔV_{cpd} is the voltage difference due to contact potentials. Without mitigation, V_{cpd} between Au and Cu can be of the order of 0.5 V. In this experiment, the experimental surfaces are to be covered in a micron-thick layer of Au, effectively masking the difference in contact potentials. The maximum allowed value of the residual contact potential is 5 μV.

The force per unit length per spoke pair due to the differences in diamagnetic polarisation of the Au and Cu stripes in test masses in a constant magnetic field is given by,

$$F_M = \frac{p}{\mu_0}(\Delta\chi B)^2 e^{-2\pi(g_{v0}/p} \sinh^2\left(\frac{2\pi t}{p}\right) \sin\left(\frac{2\pi\delta}{p}\right) Nm^{-1}, \tag{6}$$

where $\Delta\chi$ is the difference between the magnetic susceptibilities of the test mass materials, and t is the thickness of the test mass stripes. For Au-Cu, $\Delta\chi$ is -1×10^{-5} and the maximum allowed residual magnetic field is around 1 Gauss. The experimental chamber contains μ-metal and niobium shielding to ensure the residual field remains significantly lower than 1 Gauss.

5 Conclusions

This experiment is currently in the construction and commissioning stages. If the instrument performs to design sensitivity at a spacing of 15 μm, it will be possible to provide a limit on the size of Large Extra Dimensions for the case of 2 extra dimensions at the length scale suggested by the known density of Dark Energy. Sources of torque noise from spurious forces acting on the test masses are quantifiable and aspects of experimental design have been designed to mitigate them.

Acknowledgments

This project is funded by STFC. We would also like to acknowledge the support of the University of Birmingham and our technical staff, and our collaborators at EUminafab, Heriot-Watt University and the National Physical Laboratory UK.

References

1. N. Arkani-Hamed *et al Phys. Lett.* B42926 31998
2. P. Callin, C. P. Burgess, *Nucl. Phys.* B75260 2006
3. D. J. Kapner *et alPhys. Rev. Lett.*98021 1012007
4. G. H. Hammond *et al Phys. Rev. Lett.*98 0811012007
5. A. Kehagias, K. Sfetsos, *Phys. Lett.* B47239 2000

SHORT RANGE TESTS WITH NEUTRONS AT ILL

V. V. NESVIZHEVSKY, on behalf of the GRANIT collaboration

Institut Laue-Langevin, 6 rue Jules Horowitz, Grenoble, France, F-38042

The present report is based on a talk given at the Recontres de Moriond and GPhyS lloquium "Gravitational Waves and Experimental Gravity" in La Thuile in 2011, and on the alysis of neutron constraints for short range forces to be published soon in ref. (1). It overviews vances in neutron experiments constraining short-range interactions. All measurements have been rformed at the high-flux reactor of the Institut Laue-Langevin in Grenoble. We compare the best utron constraints with those following from all most precise alternative methods and discus ospects for their further improvements.

The existence of other fundamental interactions in nature, mediated by new bosons, has be extensively discussed, given their possibility in many extensions of the standard model of parti physics (2), (3), (4), (5), (6), (7), (8). Theories with large extra spatial dimensions provide stro motivation to search for such forces. If a boson is allowed to travel in large extra compactifi dimensions, with a strong coupling constant in the bulk, it behaves in our 4D world as a ve weakly coupled new boson, the coupling being diluted in the extra dimensions. The light da matter hypothesis also argues in favor of the existence of new short range interactions. New boso for example, are predicted by most of the grand unified theories embedding the standard mod with the coupling constant of ~0.1. These strongly coupled bosons have to be heavier than ~1 Te if they were not to conflict with present observations; heavier bosons will be searched for at t LHC. Lighter bosons could mediate a finite range interaction between two fermions: $V(r)$ $Q_1 Q_2 \frac{g^2}{4\pi}\frac{\hbar c}{r} e^{-\frac{r}{\lambda}}$, where $V(r)$ is the interaction potential, g is the coupling constant, Q_1 and Q_2 a the charges of the fermions under the new interaction, and the range of this Yukawa-like potent $\lambda = \hbar/Mc$ is inversely proportional to the boson mass M. We consider the interactions of neutro with nuclei of atomic number A, thus the charge of the atom under the new interaction is equ $Q_1 = A$, and the neutron charge is equal to unity $Q_2 = 1$. The presence of light bosons would shown by deviations from the gravitational inverse square law.

The characteristic range of extra interactions as well as their strength varies largely various theories. Therefore a phenomenological approach is chosen: searches for extra Yukaw type forces are pursued over a very broad range λ. Nevertheless, in many cases one could point o promising distances. In theories with two large extra spatial dimensions, the characteristic range $\sim 10^{-5}\ m$; in theories with three large extra dimensions it is $\sim 10^{-8}\ m$. Other numbers of ext spatial dimensions are ruled out by experiments or correspond to too small effects to be observ with known methods. In all mentioned interesting cases the ranges are accessible for neutro experiments: $10^{-10} - 10^{-5}\ m$; the optimum condition is usually met if $\lambda \sim \lambda_n$, where λ_n is t neutron wavelength. Concerning the strength of extra interactions, one should compare t constraints resulting from precision neutron experiments with those using all alternative metho Searches for short-range modifications of gravity are most sensitive at distances $> 10^{-5}\ m$ (9 (10). Searches for extra forces on top of the van der Waals or Casimir-Polder or (vdW/CP) forc give the best constraints in the nanometer range λ: $10^{-7(8)} - 10^{-5}\ m$ (11), (12). Exotic ato constrain the sub-picometer domain: $< 10^{-12}\ m$ (13). Even shorter distances are probed in hig energy accelerator experiments. Neutron constraints are most sensitive in the intermediate range

$10^{-12} - 10^{-8}$ m. In the range of λ: $10^{-8(7)} - 10^{-5}$ m neutron experiments could provide mplementary information as well, and higher sensitivity in limited cases.

An attractive feature of neutrons is smallness of false effects due to their electric neutrality. ı the other hand, neutron experiments are strongly limited by the available statistics; this awback might be overcome with new low-energy neutron sources. The current constraints for in-independent short-range interactions as well as perspectives for their improvement using utron experiments are shown in Fig. 1. The range of distances in this figure covers the range of terest for neutron experiments plus that for the best alternative methods on its lower and upper undaries. In this plot, we give the limits for g^2 as defined above, and for α in another ırameterization of spin-independent short-range interactions, where α is normalized to the strength gravity: $V(r) = \alpha G \frac{m_1 m_2}{r} e^{-\frac{r}{\lambda}}$. Here m_1 and m_2 are masses of the fermions that interact. eglecting the small difference between the neutron mass m_n and the proton mass m_p we can anslate: $g^2 = \frac{4\pi G m_n^2}{\hbar c} \alpha$.

The neutron constraints are derived:

1) From studies of neutron gravitational quantum states (14), (15), (16), (17), (18), based on ıta published in refs. (19), (20), (21)) (line 5 in Fig. 1). This first experiment has proven existence the phenomenon itself. Much more precise measurements seem to be feasible concerning both ventual systematic effects and statistical sensitivity (22), (23). First improvements might be xpected in near future in flow-through-type experiments (24), (25), (26); thus the sensitivity of 25) to new short-range interactions is discussed in (27), and is shown as line 9 in Fig. 1. In a econd step we aim at large increase in sensitivity profiting from long storage of UCN in avitational quantum states in the closed trap in the GRANIT spectrometer (line 10 in Fig. 1);

2) From the data on neutron whispering gallery effect (28), (29), (30) (line 6 in Fig. 1). This ery first measurement provided already the absolute accuracy of measuring energy differences of uantum states significantly better than 10^{-3}, however, proper analysis of eventual systematic effects as not yet been done. We present therefore a conservative estimation for the short-range-forces onstraints based on the given accuracy that could be guaranteed on the present stage of our ıalysis, and will continue working on further improvements (line 11 in Fig. 1, (31));

3) From neutron scattering on nuclei (13)) (line 7 in Fig. 1). The idea of this method was roposed in ref. (32). Preliminary estimation of an even stronger constraint from neutron scattering

on nuclei at shortest distances is available (33); as the calculation procedure used there is based o possibly incomplete information, as stated by the author, on resonances in the nuclei used, as we as on complex multi-parametric mathematical analysis, without any study of global and loc minima in the fit, it would be of interest to finalize the analysis and provide a reliable constrair Concerning neutron scattering on nuclei, further improvements in sensitivity (line 11 in Fig. 1) a expected to follow from measurements of quasi-elastic scattering of UCN on atoms in diluted nob gases using gravitational spectrometers of total energy (31), and from measurements of asymmet of scattering of slow neutrons on atoms in diluted noble gases (13). A possibility of improvir constraints using neutron-optical experiments is discussed in ref. (34). High-energy neutron-proto scattering on small angles was analyzed in view of getting constraints at even shorter distances tha

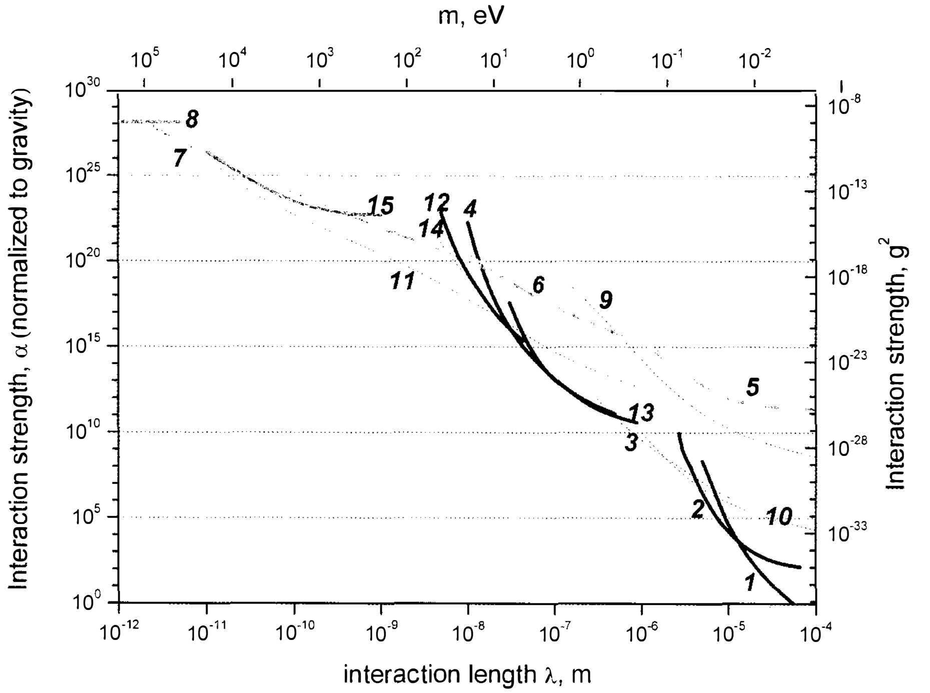

those presented in Fig. 1 in ref. (35).

Fig. 1. The exclusion plot for new spin-independent interactions: the interaction strength α normalized to the gravitational interaction (on left), and the interaction strength g^2 (on right) given as a function of the characteristic distance. The best currently constraints are shown in thic solid lines; preliminary results are indicated in thick dash-dotted lines; the best neutron constraint but not the best currently available, are given in thick dashed lines; thin dotted lines in purple col

espond to projected sensitivity in various neutron experiments. Red color is reserved for surements of gravity at short distances; blue-color constrains result from precision surements of Casimir interactions; all constraints originated from neutron experiments are wn in green; constraint from measurements of exotic atoms is indicated in orange. Constraints and "2" are obtained from measurements of short-range gravity in the torsion-balance (9) and cantilever (10) experiment respectively. Constraints "4", "12" and "13" follow from surements of extra forces on top of Casimir and van der Waals interactions in refs. (12), (36), eanalysis presented in ref. (11) of the experiment (37), and in ref. (38) respectively. We do not w the limit "3" from ref. (11), based on an experiment by Lamoreaux (39), as well as the limit " from ref. (40), based on an experiment by Ederth (41), as solid constraints; ref. (42) shows correlations between fitted parameters deteriorate the sensitivity; furthermore a new ematical uncertainty was found (43) in the original experiment (39). Constrain "5" follows n measurements of neutron gravitational quantum states (14). Constrain "6" is derived from the a on neutron whispering gallery effect (these proceedings). Constrain "7" follows from neutron ttering on nuclei (13)). Constrain "8" is obtained from analysis of precision measurements of tic atoms (13). Constrain "15" is obtained using searches for low-mass bosons from the Sun in igh-purity germanium detector (44). Lines "9", "10", "11" correspond to our estimations of ntual improvements in neutron constraints following from measurements of gravitational ntum states in a flow-through mode, in storage mode using the GRANIT spectrometer, from si-elastic scattering of UCN at diluted noble gases and from neutron whispering gallery effect pectively.

Many experiments look for spin-dependent short-range forces. Additional spin-dependent raction could be caused by new, light, pseudoscalar bosons such as the Axion. The Axion was ginally proposed in refs. (45), (46), (47), (48) as a solution to the strong CP problem, caused by smallness of the neutron electric dipole moment. The Axion would have profound consequences cosmology and astrophysics (49), and the non-observation of these effects limits the Axion to e a mass in between 10 μeV and 10 meV. The general form of the potential caused by the hange of a pseudoscalar, axion-like, boson between a polarized spin-1/2 particle and another polarized particle of the same kind is (50): $V(r) = g_S^1 g_P^2 \frac{(\hbar c)^2}{8\pi m_2 c^2} (\sigma_2 \cdot \hat{r}) \left[\frac{1}{r\lambda} + \frac{1}{r^2}\right] exp(-r/\lambda)$. re, $g_S^1 g_P^2$ is the product of the relevant coupling coefficient between particle 1 (unpolarized) and polarized), and gives the strength of the potential. m_2 and σ_2 are the mass and the spin of the arized particle, r is the distance between the particles, and $\lambda = \hbar/mc$ is the Yukawa range of new interaction. The Yukawa range is used as a free parameter in the analysis, as the mass m of new exchange boson is not known a priori.

Most experiments look for new forces between electrons. More recently, much progress was de in searches for new forces between nucleons. Comparisons between the coupling strengths for ctrons and nucleons require a particular model of the new interaction. Fig. 2 shows the exclusion new interactions between nucleons. The range for the λ values shown here is given by optimum sitivity of neutron and polarized ^{3}He experiments.

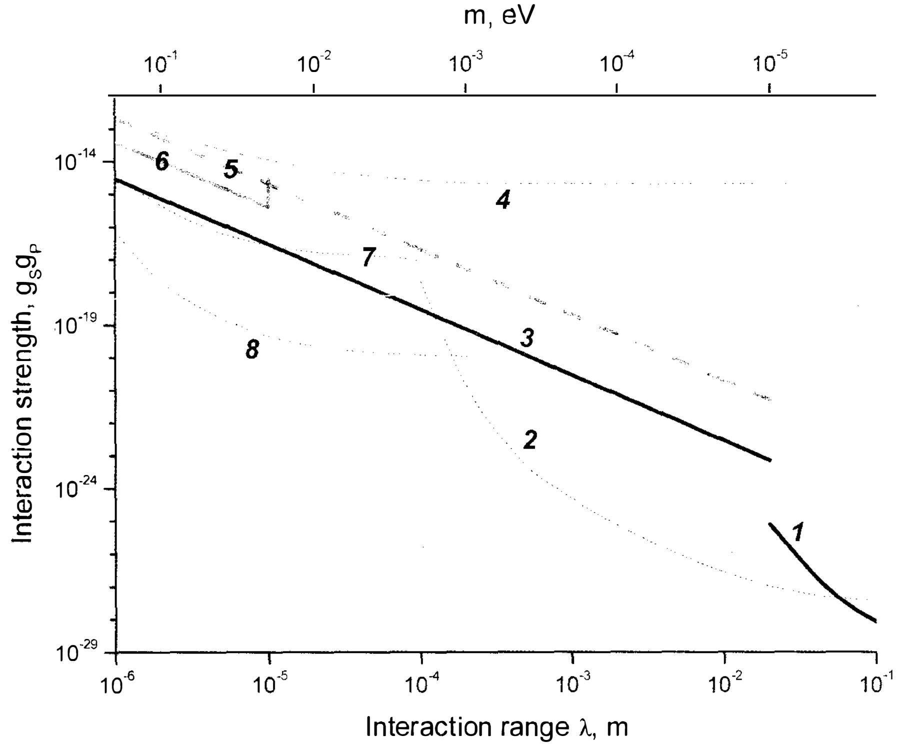

Fig. 2. Searches for short-range nucleon spin-dependent interactions. Each line is excludi the region to the top. The limit from (55) *(1, black solid line) was achieved by comparing t precession frequencies of atomic magnetometers made from either* ^{199}*Hg or Cs atoms in presence a 475 kg source mass made from lead. The sensitivity of the experiment with polarized* ^{3}*H described in these proceedings by Yuri Sobolev, is indicated in (2, thin dotted blue line). The lin from ref.* (56) *(3, blue solid line) was derived from the spin relaxation rate in polarized* ^{3}*He cel after subtraction of known causes of relaxation, the new interaction would constitute an ext relaxation channel. An even more constraining limit from experiments on storage of polarized* ^{3} *has been proposed* (57) *but the validity of the method used is being questioned* (58). *The limit ref.* (59) *(4, thin green dash-dotted line) was derived from the study of gravitationally bound sta of ultracold neutrons; the publication* (59) *triggered in significant extend the whole experimen program on spin-dependent short-range nucleon-nucleon interaction presented in the prese proceedings. The limit from ref.* (60) *(5, thick green dashed line, proposed in* (61)*) was deriv from comparison of the precession frequencies of ultracold neutrons in chambers in a vertic magnetic field, where the chamber bottom plate is made from a more dense material than top pl and vice versa. A force as in eq. (2) changes the precession frequency with a sign which depends the position of the denser plate. The limit from ref.* (62) *(6, thick green solid line, criticized in r* (63)*) was derived from the fact that a new short-range spin-dependent force would cause sp relaxation of ultracold neutrons in vicinity of a reflecting surface; limits on the depolarizati probability were turned into limits on new forces of that kind. The transmission of an unpolari sample through a horizontal slit with an absorber at the top would look differently from t*

asurement if a sufficiently strong new interaction given by eq. (2) would modify the wave ıctions of the gravitational bound states in dependence of their spin, as in a Stern-Gerlach ɔeriment. We add projected sensitivities of different stages of the study of gravitationally bound antum states: Assuming that an accuracy of 10^{-3} can be reached in the determination of the ergy difference between ground state and second excited state in the flow-through experiment, we uld be exploring some new territory in the exclusion plot at the range of a few micrometers (7, n purple dotted line). The ultimate goal of GRANIT is to measure energy difference between antum states of stored ultracold neutrons. Assuming an accuracy of 10^{-6}, which is achieved if the ecision is just the natural line-width of the transition, and assuming this line width is limited only the neutron beta decay lifetime, we get the second project limit (8, thin purple dotted line). In ref. 4), *a more optimistic scenario where a precision better than the size of the natural line width with e help of a Ramsey technique is discussed. An analogous method based on spin precession in a tup measuring neutron EDM and not requiring gravitational quantum states of neutrons is oposed in ref.* (65).

Conclusion

The neutron methods considered in this report include asymmetric and quasi-elastic neutron attering on atoms of diluted noble gases, as well as centrifugal and gravitational quantum states of utrons near surface. Neutron constraints are competitive in the distance range of 10^{-11}-10^{-7} m, gnificant further improvements could be expected here in near future. Intense efforts are ntinuing to improve constraints for short-range forces at larger distances up to 10^{-5} m, with the al to approach the currently best methods.

We appreciate financial support of Agence National de Recherche.

Antoniadis, I. et al. *Compt. Rend. Acad. sciences.* 2011 (accepted).

Antoniadis, I. *Phys. Lett. B.* 246 (1990) 377.

Lykken, J.D. *Phys. Rev. D.* 54 (1996) R3693.

Arkani-Hamed, N. et al. *Phys. Lett. B.* 429 (1998) 263.

Antoniadis, I. et al. *Phys. Lett. B.* 436 (1998) 257.

Rubakov, V.A. et al. *Phys. Lett. B.* 125 (1983) 136, 139.

Visser, M. *Phys. Lett. B.* 159 (1985) 22.

Frank, A. et al. *Phys. Lett. B.* 582 (2004) 15.

Kapner, D.L., et al. *Phys. Rev. Lett.* 98 (2007) 021101.

). **Geraci, A.A., et al.** *Phys. Rev. D.* 78 (2008) 022002.

11. **Bordag, M., et al.** *Phys. Rep.* 353 (2001) 1.

12. **Decca, R.S., et al.** *Phys. Rev. Lett.* 94 (2005) 240401.

13. **Nesvizhevsky, V.V., et al.** *Phys. Rev. D.* 77 (2008) 034020.

14. **Abele, H., et al.** *Lect. Notes Phys.* 631 (2003) 355.

15. **Nesvizhevsky, V.V., Protasov, K.V.** *Class. Quant. Grav.* 21 (2004) 4557.

16. **Zimmer, O., Kaiser, N.** *Class. Quant. Grav.* 23 (2006) 6077.

17. **Nesvizhevsky, V.V., Protasov, K.V.** *Class. Quant. Grav.* 23 (2006) 6081.

18. **Westphal, A. et al.** *arXiv:hep-ph/0703108.*

19. **Nesvizhevsky, V.V. et al.** *Nature.* 415 (2002) 297.

20. **Nesvizhevsky, V.V. et al.** *Phys. Rev. D.* 67 (2003) 102002.

21. **Nesvizhevsky, V.V. et al.** *Europ. Phys. J. C* . 40 (2005) 479.

22. **Baessler, S., Beau, M. et al.** *Compt. Rend. Acad. Sciences.* 2011 (accepted).

23. **Baessler, S., Gagarski, A.M. et al.** *Compt. Rend. Acad. Sciences.* 2011 (accepted).

24. **Sanuki, T., et al.** *NIM A.* 600 (2009) 657.

25. **Kreuz, M. et al.** *NIM A.* 611 (2009) 326.

26. **Jenke, T. et al.** *NIM A.* 611 (2009) 318.

27. **Pignol, G.** *PhD Thesis.* Grenoble : University Joseph Fourier, 2009.

28. **Nesvizhevsky, V.V. et al.** *Phys. Rev. A.* 78 (2008) 033616.

29. **Nesvizhevsky, V.V., et al.** *Nature Phys.* 6 (2010) 114.

30. **Nesvizhevsky, V.V. et al.** *New J. Phys.* 12 (2010) 113050.

31. **Nesvizhevsky, V.V. et al.** *Compt. Rend. Acad. Sciences.* 2011 (accepted).

32. **Leeb, H. et al.** *Phys. Rev. Let.* 68 (1992) 1472.

33. **Pokotilovsky, Yu.N.** *Phys. At. Nucl.* 69 (2006) 924.

34. **Gudkov, V. et al.** *Phys. Rev. C.* 83 (2011) 025501.

35. **Kamyshkov, Y. et al.** *Phys. Rev. D.* 78 (2008) 114029.

36. **Decca, R.S. et al.** *Europ. Phys. J. C.* 51 (2007) 963.

37. **Mohideen, U. et al.** *Phys. Lett. A.* 132 (1988) 313.

38. **Fischbach, E. et al.** *Phys. Rev. Lett.* 94 (2005) 240401.

39. **Lamoreaux, S.K. et al.** *Phys. Rev. Lett.* 78 (1997) 5.

40. **Mostepanenko, V.M., and Novello, M.** *Phys. Rev. D.* 63 (2001) 115003.

41. **Ederth, T.** *Phys. Rev. A.* 62 (2000) 062104.

42. **Long, J. et al.** *Nucl. Phys. B.* 539 (1999) 23.

43. **Lamoreaux, S.K.** *Phys. Rev. A.* 82 (2010) 024102.

44. **Horvat, R. et al.** *Phys. Lett. B.* 699 (2011) 21.

45. **Peccei, R.D. et al.** *Phys. Rev. Lett.* 38 (1977) 1440.

46. **Peccei, R.D. et al.** *Phys. Rev. D.* 16 (1977) 1791.

47. **Weinberg, S.** *Phys. Rev. Lett.* 40 (1978) 223.

48. **Wilczek, F.** *Phys. Rev. Lett.* 40 (1978) 279.

49. **Kuster, M. et al.** *Lect. Not. Phys.* 741 (2008) 1.

50. **Moody, J.E., Wilczek, F.** *Phys. Rev. D.* 30 (1984) 130.

51. **Adelberger, E. et al.** *Prog. Part. Nucl. Phys.* 62 (2009) 102.

52. **Hoedl, S.A. et al.** *Phys. Rev. Lett.* 106 (2011) 041801.

53. **Hammond, G.D. et al.** *Phys. Rev. Lett.* 98 (2007) 081101.

54. **Ni, W.-T. et al.** *Phys. Rev. Lett.* 82 (1999) 2440.

55. **Youdin, A.N. et al.** *Phys. Rev. Lett.* 77 (1996) 2171.

56. **Petukhov, A.K. et al.** *Phys. Rev. Lett.* 105 (2010) 170401.

57. **Fu, C.B. et al.** *Phys. Rev. D.* 83 (2011) 031504.

58. **Petoukhov, A.K. et al.** *arXiv:1103.1770.*

59. **Baessler, S. et al.** *Phys. Rev. D.* 75 (2007) 075006.

60. **Serebrov, A.P. et al.** *JETP Lett.* 91 (2010) 6.

61. **Zimmer, O. et al.** *Phys. Lett. B.* 685 (2010) 38.

62. **Serebrov, A.P. et al.** *Phys. Lett. B.* 680 (2009) 423.

63. **Ignatovich, V.K. et al.** *Europ. Phys. J. C.* 64 (2009) 19.

64. **Abele, H. et al.** *Phys. Rev. D.* 81 (2010) 065019.

65. **Zimmer, O.** *Phys. Lett. B.* 685 (2010) 38.

Gravity Spectroscopy

Tobias Jenke[1], Peter Geltenbort[2], Hartmut Lemmel[1,2], Hartmut Abele[1,3,4a]

[1]*Atominstitut, Technische Universität Wien, Stadionallee 2, 1020 Vienna, Austria*

[2]*Institut Laue-Langevin, 6 Rue Horowitz, 38042 Grenoble Cedex 9, France*

[3]*E18, Physikdepartment, Technische Universität München, 85748 Garching, Germany*

[4]*Physikalisches Institut, Universität Heidelberg, Philosophenweg 12, 69120 Heidelberg, Germany*

We demonstrate that - for the first time - the method of Rabi spectroscopy usually used in atom optics can now be applied to quantum states in the gravity potential of the Earth together with a mechanical or magnetic coupling[1]. This technique allows a precise measurement of quantum mechanical phase shifts of a Schrödinger wave packet bouncing off a hard surface in the Earth's gravitational field. The idea behind this method is that phase shifts in gravity potentials can now be related to frequency measurements with unprecedented accuracy.
The experiment addresses some of the unresolved questions of modern science: the nature of the fundamental forces and underlying symmetries, the nature of gravitation at very small distances, and the nature of cosmological mass and the energy density of the universe.

1 Introduction

Gravity experiments at short distances might provide an answer for the "big questions" about space, time, and a unification of all forces, where space-time may not be restricted to four dimensions. Hypothetical extra-dimensions, curled up to cylinders or tori with a small compactification radius would lead to deviations from Newton's gravitational law at very small distances[2]. These ideas triggered gravity experiments of different kinds, which in the past ten years have validated Newton's gravitational law down to about 50 μm[3–7]. The basic problem in searching for new physics at small distances is that the size of the objects under study needs to be reduced, too, which is accompanied by a reduction in signal intensity.
Our test of the law of gravity at small distances is based on quantum objects[8] using a new resonance spectroscopy technique. This method allows precise measurement[9] of quantum states with neutrons in the gravity potential of the earth with a Schrödinger wave packet bouncing off a hard horizontal surface. The concept is related to Rabi's magnetic resonance technique for measurements of nuclear magnetic moments[10]. The sensitivity is extremely high, because a quantum mechanical phase shift is converted into a frequency measurement. The sensitivity of resonance methods reached so far[11] is 6.8×10^{-22} eV, or one Bohr rotation every six days.

[a]Correspondence should be addressed to: abele@ati.ac.at

2 The Gravity Resonance Spectroscopy Method

In a two-level spin-1/2-system coupled to a resonator, magnetic transitions occur, when the oscillator frequency ω equals the Bohr frequency of the system. Rabi[10] resonance spectroscopy measures the energy difference between these levels $|p\rangle$ and $|q\rangle$ and damping γ. The wave function of the two level system is

$$\Psi(\bar{r},t) = \langle \bar{r}|\Psi(t)\rangle = C_p(t)\, e^{-i\omega_p t} u_p(\bar{r}) + C_q(t)\, e^{-i\omega_q t} u_q(\bar{r}) \tag{1}$$

with the time varying coefficients $C_p(t)$ and $C_q(t)$.
With the frequency difference ω_{pq} between the two states, the frequency ω of the driving field, the detuning $\delta\omega = \omega_{pq} - \omega$, the Rabi frequency Ω_R and the time t, the coupling between the time varying coefficients is given by

$$\frac{d}{dt}\begin{pmatrix}\tilde{C}_p(t)\\ \tilde{C}_q(t)\end{pmatrix} = \frac{i}{2}\begin{pmatrix}\delta\omega & \Omega_R\\ \Omega_R^* & -\delta\omega\end{pmatrix}\begin{pmatrix}\tilde{C}_p(t)\\ \tilde{C}_q(t)\end{pmatrix} \tag{2}$$

with a transformation into the rotating frame of reference:

$$\begin{aligned} C_p(t) &= \tilde{C}_p(t)\cdot e^{-\frac{1}{2}\delta\omega t}\\ C_q(t) &= \tilde{C}_q(t)\cdot e^{-\frac{1}{2}\delta\omega t}. \end{aligned} \tag{3}$$

Ω_R is a measure of the strength of the coupling between the two levels and is related to the vibration strength. Such oscillations are damped out and the damping rate depends on how strongly the system is coupled to the environment.

We succeeded in generalizing this system and describe quantum states in the gravity field of the Earth in analogy to a spin-1/2-system, where the time development is described by the Bloch equations. The linear gravity potential leads to measured[12–14] discrete non-equidistant energy eigenstates $|n\rangle$ of a bouncing quantum particle above a horizontal mirror. Neutron matter waves are excited by an oscillator coupled to these states and we drive transitions between state $|p\rangle$ and state $|q\rangle$. The energy scale is the pico-eV-scale.

In our case, the damping is caused by the scatterer[14] at height h above a mirror. A key point for the demonstration of this method is that it allows for the detection of resonant transitions $|p\rangle \to |q\rangle$ at a frequency, which is tuned by this scatterer height. The additional mirror potential[14] shifts the energy of state $|3\rangle$ as a function of height, see Fig. 2. The absorption is described phenomenologically by adding decay terms γ_p and γ_q to the equations of motion:

$$\frac{d}{dt}\begin{pmatrix}\tilde{C}_p(t)\\ \tilde{C}_q(t)\end{pmatrix} = \frac{i}{2}\begin{pmatrix}(\delta\omega + i\gamma_p) & \Omega_R\\ \Omega_R^* & (-\delta\omega + i\gamma_p)\end{pmatrix}\begin{pmatrix}\tilde{C}_p(t)\\ \tilde{C}_q(t)\end{pmatrix}. \tag{4}$$

The oscillator is realized by a vibrating mirror i.e. a modulation of the hard surface potential in vertical position. It is also proposed to use oscillating magnetic gradient fields[15] for that purpose. Neutron mirrors are made of polished optical glass. Interactions limit the lifetime of a state of a two-level system. Lifetime limiting interactions are described phenomenologically by adding decay terms to the equations of motion termed as damped oscillation.

A typical Rabi resonance spectroscopy experiment consists of three regions, where particles pass through. One firstly has to install a state selector in region 1, secondly a so called π-pulse creating the superposition of the two states, whose energy difference is to be measured in region 2, and a state detector in region 3, see Fig. 2. In our experiments with neutrons, regions 1 to 3 are realized with only one bottom mirror coupled to a mechanical oscillator, a scatterer on top and a neutron detector behind, see Fig. 2. The scatterer only allows the ground state to pass and prepares the state $|p\rangle$. It removes and absorbs higher, unwanted states[14]. The vibration, i.e.

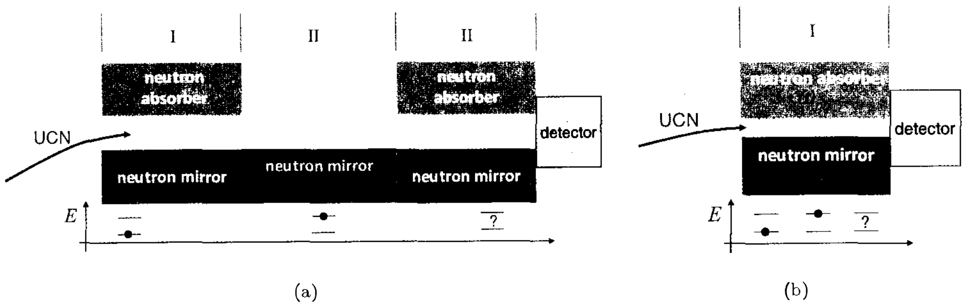

Abbildung 1: Comparison of different Resonance Spectroscopy Techniques

a modulation of the mirror's vertical position, induces transitions to $|q\rangle$, which are again filtered out by the scatterer. The neutrons are taken from the ultra-cold neutron installation PF2 at Institute Laue-Langevin (ILL). We restrict the horizontal velocity to $5.7\text{m/s} < v < 7\text{m/s}$. The experiment itself is mounted on a polished plane granite stone with an active and a passive anti-vibration table underneath. This stone is leveled with a precision better than 1 μrad. A mu-metal shield suppresses the coupling of residual fluctuations of the magnetic field to the magnetic moment of the neutron is sufficiently.

3 Experimental Results

Within the qBounce[2] experiment, we performed several resonance spectroscopy measurements with different geometric parameters, resulting in different resonance frequencies and widths. In general, the oscillator frequency at resonance for a transition between states with energies E_p and E_q is

$$\omega_{pq} = \frac{E_q - E_p}{\hbar} = \omega_q - \omega_p. \tag{5}$$

The transfer is referred to as Rabi transition. We have measured transitions $|1\rangle \leftrightarrow |2\rangle$, $|1\rangle \leftrightarrow |3\rangle$, $|2\rangle \leftrightarrow |3\rangle$, and $|2\rangle \leftrightarrow |4\rangle$. In detail, we describe the $|1\rangle \leftrightarrow |3\rangle$ transition with $\omega_{13} = \omega_3 - \omega_1$, see Table 1. On resonance ($\omega = \omega_{13}$), this oscillator drives the system into a coherent superposition of state $|1\rangle$ and $|3\rangle$ and we can chose amplitude a in such a way that we have complete reversal of the state occupation between $|1\rangle$ and $|3\rangle$. It is - as we have done - convenient to place the scatterer at a certain height h on top of the bottom mirror. This allows us to tune the resonance frequency between $|1\rangle$ and $|3\rangle$ due to the additional potential of the scatterer, which shifts the energy[14] of state $|2\rangle$ and $|3\rangle$, but leaves state $|1\rangle$ unchanged, see Fig. 2. The energy levels and the probability density distributions for these states are also given in Fig. 2. The scatterer removes neutrons from the system and the Rabi spectroscopy contains a well defined damping.

The observable is the measured transmission $|1\rangle$ to $|3\rangle$ as a function of the modulation frequency and amplitude, see Fig. 3-3. For this purpose, we attached piezo-elements underneath. They induce a rapid modulation of the surface height with acceleration a. We measure a with a noise and vibration analyzer attached to the neutron mirror system. In addition to this, the position-dependent mirror vibrations were measured using a laser-based vibration analysis system. The piezo-system by itself does not possess small resonance curves, which might influence

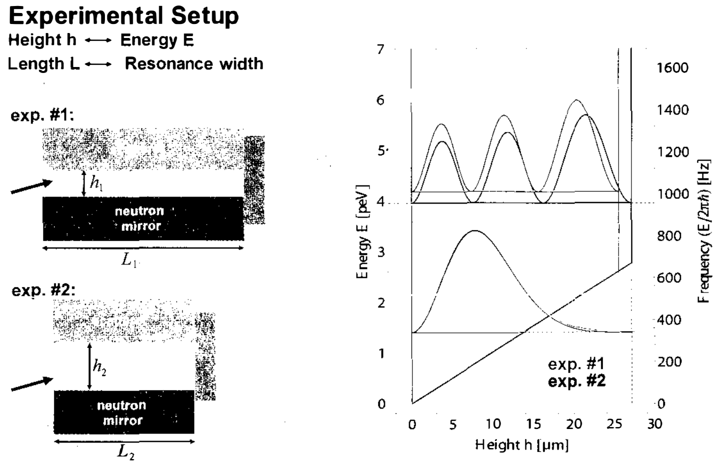

Setup Parametres and Experimental Results

	Length of the neutron mirror Length L[cm]x Width W[cm]x Height H[cm]	Height of scatterer h [m]	Mean time of flight τ [ms]	Energy difference E_{13} [peV]	Resonance frequency (prediction) ω_{13} [s^{-1}]	Resonance frequency (measurement) ω_{13} [s^{-1}]	Resonance width (FWHM) $\Delta\omega$[s^{-1}]
Experiment 1	15 x 3 x 3	25.5	23	2.78	$2\pi \times 671$	$2\pi \times (705 \pm 6)$	$2\pi \times 41.2$
Experiment 2	10 x 3 x 3	27.1	15	2.55	$2\pi \times 615$	$2\pi \times (592 \pm 11)$	$2\pi \times 61.6$

Abbildung 2: Experimental Parameters (Figure taken from [1])

the neutron transmission in the frequency range considered.

For the first experiment, Fig. 3 shows the measured count rate as a function of ω. Blue (brown) data points correspond to measurements with moderate (high) vibration strength $1.5 \leq a \leq 4.0$ m/s^2 ($4.9 \leq a \leq 7.7$ m/s^2). The corresponding Rabi resonance curve was calculated using their mean vibration strength of 2.95m/s^2(5.87m/s^2). The black data point sums up all of the measurements at zero vibration. The gray band represents the one sigma uncertainty of all off-resonant data points. The brown line is the quantum expectation as a function of oscillator frequency ω for Rabi transitions between state $|1\rangle$ and state $|3\rangle$ within an average time of flight $\tau = L/v = 23$ ms. The normalization for transmission T, frequency at resonance ω_{13} and global parameter f are the only fit parameters. It was found that the vibration amplitude is constant to the flight path of the neutrons but depends in a linear way on their transversal direction. f is a weighting parameter to be multiplied with the measured vibration strength to correct for these linear effects. A sharp resonance was found at frequency $\omega_{13} = 2\pi \times (705 \pm 6)$ Hz, which is close to the frequency prediction of $\omega_{13} = 2\pi \times 671$ Hz, if we remember that the height measurement has an uncertainty due to the roughness of the scatterer[14]. The weighting factor is found $f = 0.56 \pm 0.16$. The full width at half maximum is the prediction made from the time the neutrons spend in the modulator. The significance for $|1\rangle \rightarrow |3\rangle$ excitations is 3.5 standard

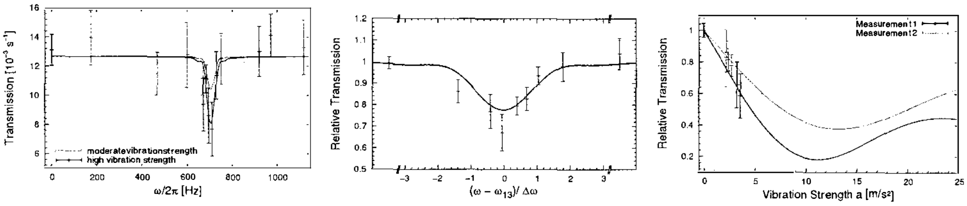

(a) (b) (c)

Abbildung 3: Gravity resonance spectroscopy and excitation[1]: **a** The transmission as a function of modulation frequency shows a sharp resonance at $\omega_{13} = 2\pi \times (705 \pm 6)\mathrm{s}^{-1}$. The grey band represents the statistical 1σ uncertainty of all off-resonant data points. Blue (brown) data points correspond to measurements with moderate (high) vibration strength $1.5 \leq a \leq 4.0\mathrm{m/s}^2 (4.9 \leq a \leq 7.7\mathrm{m/s}^2)$. The corresponding Rabi resonance curve is calculated using their mean vibration strength of $2.95\mathrm{m/s}^2 (5.87\mathrm{m/s}^2)$. The black data point sums up all measurements at zero vibration. **b** Combined result for both measurements with mirror length $L = 10$ cm and $L = 15$ cm. The transmission in units of the unperturbed system is displayed as a function of detuning. The significance for gravity spectroscopy between state $|1\rangle$ and $|3\rangle$ at ω_{13} is 4.9 standard deviations. The left and right data points combine all off-resonant measurements with $|(\omega - \omega_{13})/\Delta\omega| \geq 3$. **c** Measured damped Rabi oscillation as a function of Ω_R converted in vibration strength in units of $[\mathrm{m/s}^2]$ and extrapolation to higher vibration strengths according to Eq. 9. In resonance, the neutron transmission decreases as expected theoretically in the same frequency band $|(\omega - \omega_{13})/\Delta\omega| \leq 0.6$. This effect is visible for both experiments (black, red). The shorter mirror length in the second measurement results in a reduced sensitivity to $|1\rangle \leftrightarrow |3\rangle$ transitions, and the Rabi oscillation reaches its minimum at higher vibration amplitudes.

deviations.

The fit used in Fig. 3 contains three parameters, the resonant frequency ω_{pq}, the transmission normalization N, and vibration strength parameter f to be multiplied with the measured acceleration. The damping as a function of Ω_R was measured separately, see Fig. 3, as well as the width of the Rabi oscillation and background $(0.005 \pm 0.0002\ \mathrm{s}^{-1})$.

In a second measurement, the length $L = 10$ cm reduces the average flight time to $\tau = 15$ ms. The scatterer height differs by 1.6 μm from the first measurement, thus changing the resonant frequency prediction to $\omega_{13} = 615$ Hz. We observe the resonance frequency $\omega_{13} = 2\pi \times (592 \pm 11)$ Hz close to the prediction and $f = 0.99 \pm 0.29$. Fig. 3 shows the combined result for both measurements with mirror length $L = 10$ cm and $L = 15$ cm. The transmission in units of the unperturbed system is displayed as a function of detuning. In total, the significance for gravity resonance spectroscopy between state $|1\rangle$ and $|3\rangle$ at ω_{13} is 4.9 standard deviations. The left and right data points combine all off-resonant measurements with $|(\omega - \omega_{13})/\Delta\omega| \geq 3$, where $\Delta\nu$ is the half width at half maximum.

4 Summary and Outlook

For the experiments discussed, the sensitivity of the measured energy difference between the gravity levels is 7.6×10^{-3}. This corresponds to $\Delta E = 2 \times 10^{-14}$ eV, which allows a test of Newton's law at short distances.
This is interesting, because it addresses some of the unsolved questions of modern science: the nature of the fundamental forces and underlying symmetries and the nature of gravitation at small distances[3]. Another example is suggested by the magnitude of the vacuum energy in the universe[16,17], which again is linked to the modification of gravity at small distances.
The long term plan is to apply Ramsey's method of separated oscillating fields to the spectroscopy of the quantum states in the gravity potential above a horizontal mirror[9]. Such measurements

with ultra-cold neutrons will offer a sensitivity to Newton's law or hypothetical short-ranged interactions that is about 21 orders of magnitude below the energy scale of electromagnetism.

Acknowledgments

We gratefully acknowledge support from the Austrian Science Fund (FWF) under Contract No. I529-N20 and the German Research Foundation (DFG) within the Priority Programme (SPP) 1491 „Precision experiments in particle and astrophysics with cold and ultracold neutrons", the DFG Excellence Initiative „Origin of the Universe", and DFG support under Contract No. Ab128/2-1.

References

[1] Jenke et al., *Nature Physics* **7**, 468 (2011).
[2] Arkani-Hamed, N., Dimopolos, S. & Dvali. G., *Phys. Rev.* **D59**, 086004 (1999).
[3] Fischbach E. & Talmadge C. L. The search for non-Newtonian gravity. Springer-Verlag New York (1999).
[4] Adelberger, E. G., Heckel B. R. & Nelson, A. E., *Ann. Rev. Part. Sci.* **53** 77 (2003).
[5] Long J. C. et al., *Nature* **421**, 922 (2003).
[6] Geraci, A. A. et al., *Phys. Rev.* **D72**, 022002 (2008).
[7] Abele, H., *Prog. Part. Nucl. Phys.*, **60**, 1 (2008).
[8] Abele, H. et al., *Nucl. Phys.* **A827**, 593c (2009).
[9] Abele, H. et al., *Phys. Rev.* **D81**. 065019 (2010).
[10] Rabi I. I. et al., *Phys. Rev.* **55**. 526 (1939).
[11] Baker, C. A. et al., *Phys. Rev. Lett.* **97**. 131801 (2006).
[12] Nesvizhevsky, V. V. et al., *Nature* **415**, 299 (2002).
[13] Nesvizhevsky, V. V. et al., **C40**, 479 (2005).
[14] Westphal, A. et al.. Eur. Phys. J **C51**, 367 (2007).
[15] Kreuz, M. et al., arXiv:physics.ins-det 0902.0156.
[16] Callin. P. & Burgess, C. P., *Nucl.Phys.* **B752** 60-79 (2006).
[17] Sundrum, R., *J. High Energy Phys.* **07**, 001 (1999).

Forca-G: A trapped atom interferometer for the measurement of short range forces

B. PELLE, G. TACKMANN, Q. BEAUFILS, X. WANG, A. HILICO and F. PEREIRA DOS SANTOS
S. PELISSON, R. MESSINA, M.-C. ANGONIN and P. WOLF
LNE-SYRTE, Observatoire de Paris, LNE, CNRS, UPMC, 61 avenue de l'Observatoire, 75014 Paris, France

The aim of the Forca-G project [1] lies into the study of short range atom-surface interactions. Using cold ^{87}Rb atoms trapped into a 1D-optical lattice close to the reflecting surface, an atomic interferometer involving a coherent superposition between atomic states at different distances from the mirror can be realized. This would allow a precise measurement of the potential experienced by the atoms. In the range of 1-20 μm, the atom-surface interaction is dominated by QED potential (Casimir-Polder or Van der Waals). Besides, a precise measurement of this interaction would also allow a test of Newton's law at short distance. In a first step, we have demonstrated the efficienty of our atomic interferometer in a regime far from the surface with a measurement of the Bloch frequency.

Introduction

Measurement of short range (< 1 mm) forces is one of the challenge of modern experimental physics. The use of cold atoms for the measurement of atom-surface forces [2] can be a promising alternative to microelectromechanical systems and torsion balance which probe surface-surface forces. [3] In particular, good control of the experimental parameters and coherence properties make the use of trapped cold atoms an interesting candidate to compete in precision with mechanical systems.

1 Principle of the experiment

In this first step, our system is composed of ^{87}Rb atoms trapped in a vertical 1D-optical lattice far from the reflecting mirror.

The internal atomic structure is approximated by a two-level system, with two long lived states, $|g\rangle = \left|5^2S_{1/2}, F=1, m_F=0\right\rangle$ and $|e\rangle = \left|5^2S_{1/2}, F=2, m_F=0\right\rangle$, the ground and excited hyperfine levels separated in energy by $h\nu_{HFS}$ (see Fig. 1).

In a vertical geometry, the atoms confined in the periodic potential experience a linear acceleration due to Earth's gravity, which is described by the following external Hamiltonian: [4]

$$H_{ext} = \frac{\hbar^2\hat{k}^2}{2m_a} + \frac{U_l}{2}\left(1 - cos\left(2k_l\hat{z}\right)\right) + m_a g\hat{z} \tag{1}$$

where $\hbar$ is the Planck's constant, $\hat{k}$ the atomic momentum, m_a the atomic mass, U_l the lattice depth, k_l the optical lattice wavevector, $\hat{z}$ the vertical position and g the gravity.

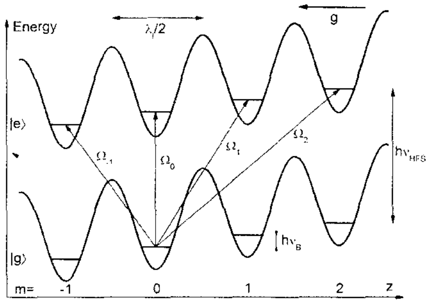

Figure 1: Wannier-Stark ladder where ν_B is the Bloch frequency, ν_{HFS} the hyperfine transition between the states $|g\rangle = |5^2S_{1/2}, F = 1, m_F = 0\rangle$ and $|e\rangle = |5^2S_{1/2}, F = 2, m_F = 0\rangle$ of ^{87}Rb. m the quantum number corresponding to the lattice sites and $\Omega_{\Delta m}$ the coupling between the wells m and $m \pm \Delta m$.

For this system, the solution of the time independant Schrödinger's equation is the so-called Wannier-Stark ladder where the Eigenstates $|W_m\rangle$ are separated in energy by the Bloch frequency ν_B (see Eq. 2) and spatially localised in the lattice site corresponding to the quantum number m (see Fig. 1). Indeed, in the presence of gravity acceleration, the energy levels of each lattice site are shifted out of resonance and provided the trap depth is sufficiently high, Landau-Zener tunneling can be neglected.[4]

$$h\nu_B = m_a g \lambda_l / 2 \tag{2}$$

Transitions between $|g\rangle$ and $|e\rangle$ can be induced by a probe laser, with wavevector k_{eff}, which couples $|W_m, g\rangle$ to $|W_{m'}, e\rangle$ either in the same well or in neighboring wells. This coupling between these two states (see Fig. 1) leads to Rabi oscillations with a Rabi frequency given by:[4]

$$\Omega_{\Delta m} = \Omega_{U_l=0} \langle W_m | e^{-ik_{eff}\hat{z}} | W_{m\pm\Delta m} \rangle \tag{3}$$

where $\Omega_{U_l=0}$ is the Rabi frequency in the absence of the lattice potential. $\Omega_{\Delta m}$ does not depend on the initial site m but only on the absolute value of Δm. Such transitions are realized with a two photon transition connecting the ground and excited hyperfine levels, $|g\rangle$ and $|e\rangle$, using counterpropagating vertical Raman beams which implies a momentum transfer of $k_{eff} = k1 + k2 \approx \frac{4\pi}{\lambda_{Raman}}$, where $\lambda_{Raman} = 780$ nm.

2 Experimental setup

Before being transferred into the mixed dipole trap, about 10^7 ^{87}Rb atoms are cooled down to $2\mu K$ by a far detuned molasse after a magneto-optical trap (MOT) in 3-dimensions, fed in 500 ms by a 2D-MOT delocalised in a second vacuum chamber limiting the residual pressure inside the main chamber.

Our vertical optical lattice loading is made with a far blue detuned laser ($\lambda_l = 532$ nm, beam waist 600μm). A red detuned ($\lambda = 1064$ nm, beam waist 200μm) dipole trap is superimposed on it in order to provide a transverse confinement (see Fig. 2).

To prepare our atoms in the states $|g\rangle$ and $|e\rangle$ and to be sensitive to stray magnetic fields only to second order, we apply a depumping pulse to obtain atoms in $|F = 1\rangle$, followed by an optical pumping with 95% efficiency, transferring the Zeeman sublevels from $|m_F = \pm 1\rangle$ to $|m_F = 0\rangle$.

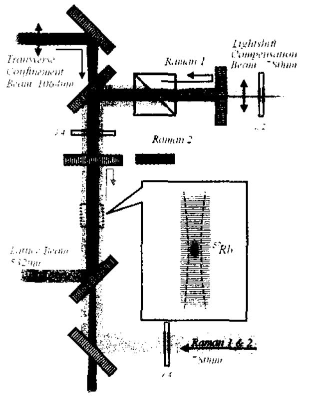

Figure 2: Experimental setup for the optical trapping and Raman intersite transitions. The different beams are superimposed using dichroic mirrors. The Raman beams are also superimposed and one of them is retro-reflected to allow counterpropagating transitions.

At this stage, the atoms are ready to be interrogated by stimulated Raman transitions where we coherently transfer atoms from one lattice site to another. These transitions are driven by two circularly polarized counterpropagating beams (λ = 780 nm, collimated beam radius 1 cm) far detuned from atomic resonance which are aligned along the mixed dipole trap beams (see Fig. 2).

At the end of the sequence, the confining lasers are shut down and a time of flight detection is made by state selective fluorescence giving the information about the population, N_g and N_e, in the two states $|g\rangle$ and $|e\rangle$ and the transition probability, $P_e = \frac{N_e}{N_g+N_e}$.

3 Results

During the interrogation phase of our measurement sequence, we realise an atomic Ramsey-Raman interferometer by the use of Raman transition with two Raman $\pi/2$-pulses separated by a time T. This leads to a quantum superposition of two different states at different positions, $|W_m, g\rangle$ and $|W_{m'}, e\rangle$, leaving the possibility to extract from their phase difference their difference of potential energy experienced during the time T.

This interference pattern is displayed on Fig. 3 where we plot the measured transition probability P_e as a function of the Raman frequency ν_{Raman}. We observe multiple sets of Ramsey fringes when $\nu_{Raman} = \nu_{HFS} + \Delta m \times \nu_B$ (see Fig. 1), which is the signature that the atoms actually tunneled across Δm lattice sites. The strength of the coupling of these resonances, given by Eq. 3, varies from one transition to the other, but goes to zero for far lattice sites.

To go further in our difference of potential energy measurement, we investigate the sensitivity and the stability of our Bloch frequency measurement. This is done by locking with a controlled servo computer integrator the frequency difference of the counterpropagating Raman lasers on the center interference fringe of the intersite transition $\Delta m = \pm 3$. Measuring alternatively on the right or left transition and calculating the half-difference allow us to be sensitive to $6\nu_B$ and cancel some of the systematics on frequency shifts as quadratic Zeeman effect or differential lightshifts. Then for an interrogation time T = 400 ms and a cycle time of T_c = 1.4 s, the Allan standard deviation of the frequency difference decreases as $0.1 Hz.\tau^{-1/2}$ until τ = 7,000 s,

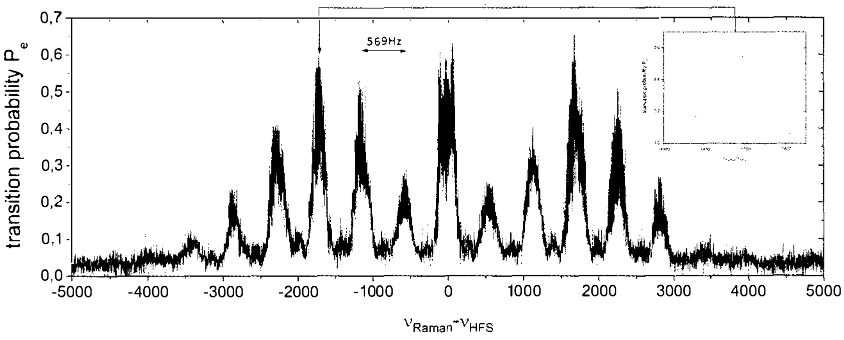

Figure 3: Ramsey-Raman interferometer showing evidence of transitions between up to 6 neighboring lattice sites, each having a different Rabi frequency (see Eq. 3) and all separated by the Bloch frequency $\nu_B = 569$ Hz, modulated by interference fringes which are separated by $\nu = 1/T$, with T the time in between the two Raman $\pi/2$-pulses. Inset: zoom on the transition $\Delta m = -3$ to let appear the interference fringes.

with τ the integration time in seconds. This corresponds to a statistical uncertainty on the measurement of the Bloch frequency of 6×10^{-5} in relative value after 1 s integration.

Conclusion

Providing some technical issues as the necessity to initially select atoms in one well or to reach the same level of accuracy near the reflecting mirror of the lattice, this result would lead to a statistical uncertainty in the measurement of the Casimir-Polder potential of 1% for a distance of 5 μm and an integrating time of 1000 s.

On the long view, by comparison with numerical calculations made by R. Messina *et al.*[5] in order to cancel down to the 1% level the shift in difference of potential energy due to Casimir-Polder, tests of gravity in the range of 1-20 μm could be improved with such a Wannier-Stark interferometer as discussed in P. Wolf *et al.*.[6]

Acknowledgments

This research is carried on within the project iSense, which acknowledges the financial support of the Future and Emerging Technologies (FET) programme within the Seventh Framework Programme for Research of the European Commission, under FET-Open grant number: 250072. We also gratefully acknowledge support by Ville de Paris ("Emergence(s)" program) and IFRAF. G. Tackmann thanks the Intercan network and the UFA-DFH for financial support.

References

1. F. Pereira dos Santos et al., *Proceedings of the 7th symposium Frequency Standards and Metrology*, (World scientific printers, Singapore, 2009), p. 44.
2. J. M. M. D. M. Harber, J. M. Obrecht and E. A. Cornell, *Phys. Rev.* A **72**, 033610 (2005).
3. V. M. M. E. Fischbach, D. E. Krause and M. Novello, *Phys. Rev.* D **64**, 075010 (2001).
4. P. Lemonde and P.Wolf, *Phys. Rev.* A **72**, 033409 (2005).
5. R. Messina, S. Pelisson, M.-C. Angonin, and P. Wolf, *Phys. Rev.* A **83**, 052111 (2011).
6. P. Wolf, P. Lemonde, A. Lambrecht, S. Bize, A. Landragin and A. Clairon, *Phys. Rev.* A **75**, 063608 (2007).

7.
Tests of relativity in the solar system

Planetary ephemerides and gravity tests in the solar system

A. Fienga
Institut UTINAM, 41 bis avenue de l'observatoire
Besançon, France

We review here the tests of fundamental physics based on the dynamics of solar system objects.

1 Introduction

The solar system has the most well known dynamics with a very ancient history of observations. GR (GR) was first tested at the astronomical scale since the dynamical impact of GR has then astronomical effects. The Eddington first observations of the light bending during the 1919 solar eclipse and the explanation by GR of the perihelia advance of Mercury in 1915 are the first stones of regular checks obtained at the astronomical scale with the Moon, the planets and the asteroids of the solar system. Since the nineties, planetary dynamics was drastically improved thanks to the numerous space missions orbiting planets and very accurately tracked by radio and VLBI observations. Since the Apollo missions, the Moon is also intensively observed with even greater accuracy. The figure 1 pictures the situation. For the Moon, the accuracy is at the centimeter level on a period of 35 years. For the planets, the geocentric distances are estimated at the meter level for Mars on a period of about 10 years due to MGS, MO and MEX tracking data. For Venus the improvement is also important but over a more limited period (2006-2010) thanks to the VEX mission. The improvement of the accuracy of Jupiter orbit stops with the latest available flyby data obtained with the Cassini mission in 2000. This latest gives very good constraints on the Saturn orbit which is now known with an accuracy of 20 meters over 3 years. GR is then confronted with very accurate observed positions of the Moon and the planets. The solar system is then an ideal laboratory for testing gravity.

In the same time, theoretical developments ask to be tested in the solar system or forecast GR violations at the solar system scales. One can cite for example the violation of the equivalence principal by the standard models for unification of quantum physics and GR, the supplementary advances of planet perihelia and nodes expected by the MOND theories, the variation with distance of the PPN parameters β and γ induced by dark energy ([1]) or string theory ([2, 3]), variation of the gravitational constant G induced by dark energy ([4]) or scalar field theories ([5]) as well as supplementary accelerations due to dark matter ([6,7]), MOND theories ([8]) or modified gravitational potentials ([9, 10]).

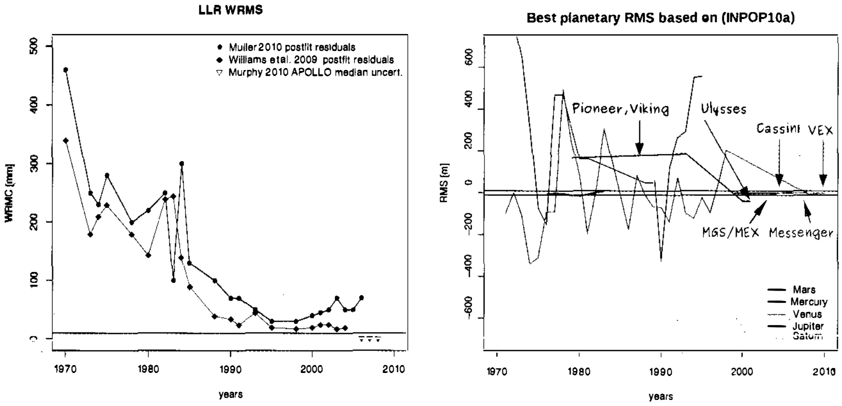

Figure 1: Best fitted residuals for Moon and planets. The planetary residuals have been estimated with INPOP10a ([11]) when the Moon residuals labelled (Muller 2010) have been estimated by [12] and those labelled (Williams et al. 2009) have been presented by [13] as well as the APOLLO median uncertainties.

2 General overview

2.1 Tests based on direct spacecraft dynamics

The accuracy of the spacecraft tracking data orbiting a planet, in interplanetary phase or during a flyby can reach up to few centimeters over several months. Such tracking is done using doppler shift observations or VLBI differential measurements which are very sensitive to the deflection of light. With such accuracy, the tracking data of space missions seem to be a good tool to test gravity. However, some factors as navigation unknowns (AMDs, solar panel calibrations), planet unknowns (potential, rotation...), effect of the solar plasma, or the correlation with planetary ephemerides limit such gravity tests. Dedicated missions have then to be planed in order to overcome such difficulties. For example, the PPN γ determination obtained by [14] was done during very specific periods of the Cassini mission, especially dedicated to such tests.

The dynamics of the solar system planets and moons is less affected by non gravitational or unexpected accelerations and by technical unknowns and is constrained with also high accuracy.

2.2 LLR tests

With LLR observations, positions and velocities of the Moon are known with an accuracy from 10 to 1 centimeter over 35 years. With the APOLLO project ([19]), new developments in observational techniques improve this accuracy with an observational error of about 1 millimeter. With such accuracy, [20] plans improvements of at least one order of magnitude in the test of the equivalence principle, the determination of the PPN parameter β and of the test of inverse square law. The table 1 gathers the main tests of gravity done using LLR observations as well as planetary ephemerides and spacecraft tracking. The LLR analysis is clearly one of the main source of information for gravity. It produces tests with the best available accuracy for the equivalence principal, the prefered-frame tests and the detection of possible supplementary accelerations induced by dark matter. Present limitations in the modeling of the lunar interior, the Earth rotation as well as the planetary ephemerides induce differences between the teams analyzing the LLR observations ([16], [15]) of several centimeters where the supposed accuracy of the APOLLO observations is about 1 millimeter. These discrepancies are obvious on figure 1. An intensive

Table 1: Results of gravity tests realized in the solar system. Columns 1 and 2 give the label of the tests and the studied objects. The Column 3 gives the obtained results with the mean value and 1 σ least square standard deviations of the estimated parameter, except for the β, γ, $\dot{\varpi}_{\mathrm{sup}}$, and $\dot{\Omega}_{\mathrm{sup}}$ obtained with the planets. see the text for more details. The last column gives the alternative theories of gravity which can be constrained by these results. The values of β given here were all obtained with a value of γ given by [14]. The ISL α obtained with LLR is for $\lambda = 4 \times 10^8$ km when the ISL α based on Mars data analysis is for $\lambda = 10^{10}$ km.

Tests	Objects	Results	References	Theoretical impact
EP $\eta \times 10^4$	Moon-LLR	4.4 ± 4.5	[15]	Standard model,
		6 ± 7	[16]	string theory
$[\Delta M/M]_{SEP} \times 10^{13}$	Moon-LLR	-2 ± 2	[15]	
PPN $\gamma \times 10^4$	Spacecraft	0.21 ± 0.23	[14]	Dark Energy,
with $\beta = 1$	Planets	0.45 ± 0.75	this paper	string theory
	Moon-LLR	40 ± 50	[16]	
PPN $\beta \times 10^4$	Moon-LLR	1.2 ± 1.1	[15]	Dark Energy,
	Moon-LLR	1.5 ± 1.8	[16]	string theory
	Planets	-0.41 ± 0.78	this paper	
	Planets	0.4 ± 2.4	[17]	
$\dot{G}/G \times 10^{13}$	Moon-LLR	2 ± 7	[16]	scalar-field theory
$[\mathrm{y}^{-1}]$	Planets	0.1 ± 1.6	[17]	
	Planets	-0.6 ± 0.4	[18]	
$\alpha_1 \times 10^5$	Moon-LLR	-7 ± 9	[16]	scalar-field theory
$\alpha_2 \times 10^5$	Moon-LLR	2 ± 2	[16]	
ISL α	Moon-LLR	10^{-10}	[16]	Standard model
	Planets	10^{-10}	[17]	
$\Omega_{\mathrm{deSitter}}$ $[\mathrm{mas.cy}^{-1}]$	Moon-LLR	6 ± 10	[16]	MOND, Dark matter
$\dot{\varpi}_{\mathrm{sup}}, \dot{\Omega}_{\mathrm{sup}}$ $[\mathrm{mas.cy}^{-1}]$	Planets	$40 \rightarrow 0.1$	this paper	
a_{supp}	Moon-LLR	10^{-16}	[16]	Dark Matter density
$[\mathrm{m.s}^{-2}]$	Planets	10^{-14}	this paper,	Pioneer anomaly

work of comparisons and improvement of the Moon dynamics is now in progress.

2.3 *Tests based on planetary ephemerides*

As already discussed in section 1, the tracking observations of spacecrafts orbiting or flying by planets became very accurate in the nineties. The Mars data are crucial for the adjustment of the planetary ephemerides due to their high accuracy (about few meters on the Earth-Mars distances), their number (about 30 % of the complete data set) and their long time span (from 1998 to 2010). This makes the planetary ephemerides very depend on this type of data and also very sensitive to the Mars orbit modeling and to the perturbations of the asteroids. On table 1 are found the tests done with planetary ephemerides. The dynamics of the planets give very competitive estimations of β and γ PPN parameters as well as variations with time of the gravitational constant. Supplementary acceptable advances in the nodes and perihelia of planets are also constrained with the observations used in the adjustment of the planetary ephemerides. Tests of possible Pioneer-like accelerations on outer planet orbits have also been tested with high accuracy. The limitations of the gravity tests obtained with planetary ephemerides are mainly linked with the overweight of the Mars datasets and with the perturbations of the asteroids. As demonstrated in [16], there is a strong correlation on the geocentric Mars distances between the sun oblatness, the PPN parameter β and the mass of the asteroid ring used to average the perturbations of small asteroids on planet orbits. The decorrelation between the PPN parameters, the sun oblateness and the asteroid perturbations is then better obtained when the global adjustement of all the planet orbits is done simultaneously. Furthermore, the decorrelation between the β and γ parameters are only possible if the two following equations are solved together in the fitting procedure.

$$\Delta\dot{\varpi} = \frac{2\pi(2\gamma - \beta + 2)GM_{\odot}}{a(1-e^2)c^2} + \frac{3\pi J_2 R_{\odot}^2}{a^2(1-e^2)^2} \text{ and } \Delta \mathrm{t} = (1+\gamma)\mathrm{GM}_{\odot}\ln\frac{\mathrm{l}_0 + \mathrm{l}_1 + \mathrm{t}}{\mathrm{l}_0 + \mathrm{l}_1 - \mathrm{t}},$$

where $\Delta\dot{\varpi}$ is the advance of perihelia of the perturbed planet induced by GR (first term) and the oblateness of the sun J_2 (second term with $R_{\odot}^2$, the sun radius). In the first equation, a,e are the semi-major axis and the eccentricity of the perturded planet and $GM_{\odot}$ is the mass of the sun. In the second equation, Δt is the Shapiro delay, the supplementary delay induced by the deflection of the light path by the sun.

3 Results and discussions

3.1 *Equivalence principal*

A detailed description of the method used to test the equivalence principal in using LLR observations is given in [15]. The test is an estimation of the gravitational mass to inertial mass ratio of the Moon and of the Earth. In GR, this ratio is equal to 1. However in PPN formalism, it can be formulated as

$$M_G/M_I = 1 + \eta[(\frac{U}{Mc^2})]$$

where U is the body's gravitational self-energy, M is the mass of the body, c the speed of light and η a PPN parameter equal to 0 in GR. In the equation of the geocentric motion of the Moon, [15] have introduced the differences in accelerations induced by $M_G/M_I \neq 1$ for the Moon and of the Earth. By comparisons to the LLR observations, it becomes possible to estimate the acceptable M_G/M_I ratio by direct least square fit of the numerically integrated acceleration or of the analytical estimations based on [21]. The results presented in table 1 are the one obtained by [15] combined with the laboratory estimations of the weak equivalence principal obtained by [22]

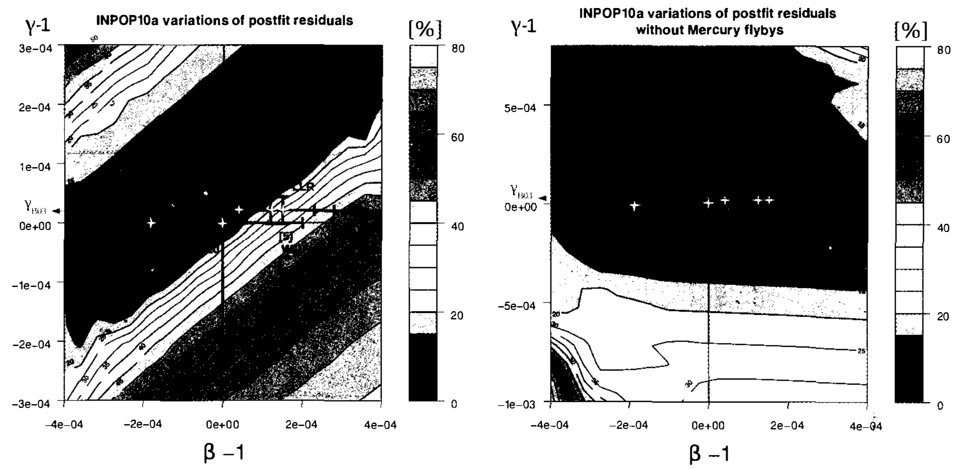

Figure 2: Variations of postfit residuals obtained for different values of PPN β (x-axis) and γ (y-axis). [1] stands for a PPN β value obtained by ([25]) using LLR observations with $\gamma = 0$, [2] stands for [26] by a global fit of EPM planetary ephemerides. K11 stands for [17] determinations based mainly on Mars data analysis. M08 for [16] and W09 for [15] give values deduced from LLR for a fixed value of γ, B03 stands for [14] determination of γ by solar conjunction during the Cassini mission.

As the PPN parameter η is linked to the β and the γ by $\eta = 4\beta - \gamma - 3$, for a given value of γ, values for the β parameters can be deduced. Same methods have been applied by [16] with about the same results. Values obtained by [15] and [16] are given in table 1.

3.2 *PPN parameter β and γ*

Since[23] and[24], estimations of the PPN parameters are done with INPOP on a regular basis as well as estimations of acceptable supplementary advances of perihelia and nodes. A specific method presented in [24] is used for these estimations. In order to overcome the correlation problems, we built up several planetary ephemerides for different values of the PPN parameters (β, γ) with a simultaneous fit of initial conditions of planets, mass of the Sun and asteroid densities. On figure 2 are plotted the variations of postfit residuals induced by the modification of the corresponding β and γ parameters. The left hand side plot gives the variations of postfit residuals including Mercury flyby normal point when the right hand side plot gives the variations of residuals without the Mercury observations. The different levels of colors indicate the percentage of variations of the postfit residuals compared to those obtained with INPOP10a. By projecting the 5% area on the β-axis (or the γ-axis), one can deduced the corresponding β (or γ) interval given in table 1 in which the residuals are modified by less than 5%. In looking at the two figures, one can see that the use of the Mercury flyby data give smallest intervals of possible β,γ. This is consistent with the fact that the Mercury observations are far more sensitive to gravity modifications than other data (see table 1 in [24]).

3.3 *Frame-dragging and prefered frame tests*

Based on LLR observations, [16] estimate a supplementary advance in the node of the Moon induced in GR by the motion of the Moon in the gravitational field of the Earth. The effect is called the de Sitter effect and the results are presented in table 1. Prefered-frame coefficients

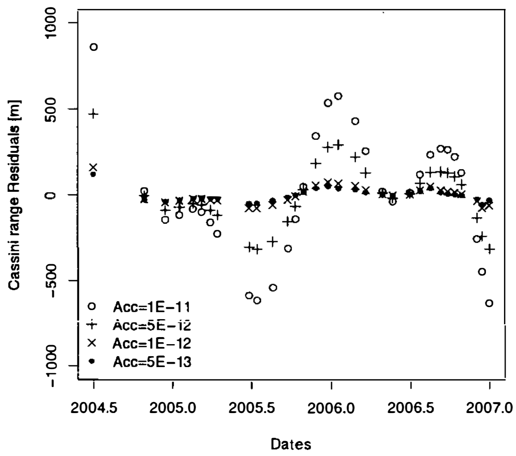

Figure 3: Postfit residuals in meters obtained by comparison between Cassini tracking data and several ephemerides with added Pioneer-like accelerations. The characteristics of the accelerations are given in $m.s^{-2}$

α_1 and α_2 have also been estimated by the same authors. Results are presented in table 1.

3.4 Supplementary accelerations

Supplementary accelerations can be induced by dark matter and dark energy surrounding the solar system or inside the solar system. Alternative descriptions of gravity can also induced modifications in the gravitational potential and then supplementary acceleration in the motion of solar system bodies and spacecraft. Possible tests have been made in introducing either constant accelerations in one specific direction (Pioneer-like anomaly with outer planets, dark matter with the Earth-Moon orbit) either accelerations induced by f(r) gravity or exponential potentials (ISL).[16] and[17] have constrained the ISL potential for the geocentric Moon ($\lambda = 4 \times 10^8$ km) and Mars ($\lambda = 10^{10}$ km). Some other estimations should be investigate for $\lambda > 10^{12}$ km. Results are given in table 1. For the Pioneer-like accelerations, the figure 3.4 gives the postfit residuals obtained by comparisons between the observed Earth-Saturn distances deduced from the Cassini tracking data and planetary ephemerides integrated with supplementary constant accelerations and fitted over the INPOP10a data sample. These accelerations are similar in direction to the Pioneer accelerations but their modules vary from 10^{-11} to 5.10^{-13} $m.s^{-2}$. As one can see on figure 3.4 only accelerations smaller than 5.10^{-13} $m.s^{-2}$ are acceptable compared to the present accuracy of the Cassini observations. This result was confirmed by[27].

3.5 Supplementary advances of perihelia and nodes

New theoretical models ([8], [28]) forecast supplementary advances in the orbits of the solar system objects. Supplementary advances in the perihelia and nodes of the planets (from Mercury to Saturn) have also been tested in INPOP and are presented on table 2. All these results are based on the method presented in[24]. With INPOP10a[11] no supplementary advances in node or perihelia is detected when with INPOP08[24] supplementary advance in the Saturn perihelia

Table 2: Values of parameters obtained in the fit of INPOP08 [24] and INPOP10a [11] to observations. The supplementary advances of perihelia and nodes are estimated in INPOP10a and INPOP08 as the interval in which the differences of postfit residuals from INPOP10a are below 5%. P09 stands for ([26]) and P10 for ([18]).

	INPOP08	INPOP10a	P09	P10
$\dot{\varpi}_{\text{sup}}$ mas.cy^{-1}				
Mercury	-10 ± 30	0.4 ± 0.6	-3.6 ± 5	-4 ± 5
Venus	-4 ± 6	0.2 ± 1.5	-0.4 ± 0.5	
EMB	0.0 ± 0.2	-0.2 ± 0.9	-0.2 ± 0.4	
Mars	0.4 ± 0.6	-0.04 ± 0.15	0.1 ± 0.5	
Jupiter	142 ± 156	-41 ± 42		
Saturn	-10 ± 8	0.15± 0.65	-6 ± 2	-10 ± 15
$\dot{\Omega}_{\text{sup}}$ mas.cy^{-1}				
Mercury		1.4 ± 1.8		
Venus	200 ± 100	0.2 ± 1.5		
EMB	0.0 ± 10.0	0.0 ± 0.9		
Mars	0.0 ± 2	-0.05 ± 0.13		
Jupiter	-200 ± 100	-40 ± 42		
Saturn	-200 ± 100	-0.1 ± 0.4		

was possible. Such variations can be explained by the improvement of INPOP10a outer planet orbits compared to INPOP08.

4 Conclusions

With the present gravity tests done in the solar system, GR is confirmed at the 10^{-4} accuracy for PPN parameter β and the equivalence principal and at 10^{-5} for PPN γ. No supplementary advances of perihelia and nodes are detected at the present accuracy of the planetary ephemerides. Variations of the gravitational constant are not expected above 10^{-13} yr^{-1} and stringent limits for the ISL tests are given for the inner solar system. Messenger tracking data would bring important informations for PPN parameter determinations and ISL tests should be done in the outer solar system.

5 REFERENCES

1. J.-M. Alimi and A. Füzfa. The Abnormally Weighting Energy Hypothesis: The origin of the cosmic acceleration. In J.-M. Alimi & A. Fuözfa, editor, *American Institute of Physics Conference Series*, volume 1241 of *American Institute of Physics Conference Series*, pages 690–699, June 2010.
2. T. Damour. Testing the equivalence principle: why and how? *Classical and Quantum Gravity*, 13:A33–A41, November 1996.
3. S. Kalyana Rama. Some cosmological consequences of non-trivial ppn parameters beta and gamma. *Phys. Rev.*, 373(B):282–288, Apr 1996.
4. P. J. Steinhardt and D. Wesley. Dark energy, inflation, and extra dimensions. , 79(10):104026–+, May 2009.
5. J.-P. Uzan. Tests of Gravity on Astrophysical Scales and Variation of the Constants. *Annales Henri Poincaré*, 4:347–369, December 2003.
6. H. Arakida. Influence of dark matter on light propagation in solar system. *Advances in Space Research*, 45:1007–1014, April 2010.
7. K. L. Nordtvedt. Cosmic acceleration of Earth and the Moon by dark matter. , 437:529–531, December 1994.

8. L. Blanchet and J. Novak. External field effect of modified Newtonian dynamics in the Solar system. , 412:2530–2542, April 2011.
9. A. de Felice and S. Tsujikawa. f(R) Theories. *Living Reviews in Relativity*, 13:3–+, June 2010.
10. S. G. Turyshev and V. T. Toth. The Pioneer Anomaly. *Living Reviews in Relativity*, 13:4–+, September 2010.
11. A. Fienga, J. Laskar, H. Manche, P. Kuchynka, G. Desvignes, . Gastineau, M, and andThereau G. Cognard, I. The planetary ephemerides inpop10a and its applications in fundamental physics. *Celestial Mechanics and Dynamical Astronomy*, 2011.
12. J Müller. LLR by Hannover team. In *ISSI meeting*, 2010.
13. T Murphy. APOLLO news. In *MIT LLR workshop*, 2010.
14. B. Bertotti, L. Iess, and P. Tortora. A test of general relativity using radio links with the Cassini spacecraft. , 425:374–376, September 2003.
15. J.G. Williams, S.G. Turychev, and D.H. Boggs. LLR tests of the equivalence principle with the Earth and Moon. *ArXiv e-prints*, January 2009.
16. J. Müller, M. Soffel, and S. A. Klioner. Geodesy and relativity. *Journal of Geodesy*, 82:133–145, March 2008.
17. A. S. Konopliv, S. W. Asmar, W. M. Folkner, Ö. Karatekin, D. C. Nunes, S. E. Smrekar, C. F. Yoder, and M. T. Zuber. Mars high resolution gravity fields from MRO, Mars seasonal gravity, and other dynamical parameters. , 211:401–428, January 2011.
18. E. V. Pitjeva. EPM Ephemerides. In *Journées Systèmes de Référence Spatio-temporels 2010*, Journees Systemes de references, November 2010.
19. T. W. Murphy, E. G. Adelberger, J. B. R. Battat, L. N. Carey, C. D. Hoyle, P. Leblanc, E. L. Michelsen, K. Nordtvedt, A. E. Orin, J. D. Strasburg, C. W. Stubbs, H. E. Swanson, and E. Williams. The Apache Point Observatory Lunar Laser-ranging Operation: Instrument Description and First Detections. , 120:20–37, January 2008.
20. S. M. Merkowitz. Tests of Gravity Using Lunar Laser Ranging. *Living Reviews in Relativity*, 13:7–+, November 2010.
21. K. Nordtvedt. Testing Relativity with Laser Ranging to the Moon. *Physical Review*, 170:1186–1187, June 1968.
22. E. G. Adelberger. New tests of Einstein's equivalence principle and Newton's inverse-square law. *Classical and Quantum Gravity*, 18:2397–2405, July 2001.
23. A. Fienga, and Laskar J. Manche, H., and M. Gastineau. Inpop06: a new numerical planetary ephemeris. , 477:315–327, 2008.
24. A. Fienga, J. Laskar, P. Kuchynka, C. Le Poncin-Lafitte, H. Manche, and M. Gastineau. Gravity tests with INPOP planetary ephemerides. *American Astronomical Society, IAU Symposium #261. Relativity in Fundamental Astronomy: Dynamics, Reference Frames, and Data Analysis 27 April - 1 May 2009 Virginia Beach, VA, USA, #6.02; Bulletin of the American Astronomical Society, Vol. 41, p.881*, 261:602–+, May 2010.
25. H. Manche, A. Fienga, J. Laskar, M. Gastineau, S. Bouquillon, G. Francou, and P. Kuchynka. LLR residuals of the latest INPOP solution and constraints on post-Newtonian parameters. In *Journées Systèmes de Référence Spatio-temporels 2010*, Journees Systemes de references, November 2010.
26. E. V. Pitjeva. EPM Ephemerides and Relativity. *American Astronomical Society, IAU Symposium #261. Relativity in Fundamental Astronomy: Dynamics, Reference Frames, and Data Analysis 27 April - 1 May 2009 Virginia Beach, VA, USA, #6.03; Bulletin of the American Astronomical Society, Vol. 41, p.881*, 261:603–+, May 2009.
27. W. M. Folkner. Relativistic aspects of the JPL planetary ephemeris. In S. A. Klioner, P. K. Seidelmann, & M. H. Soffel, editor, *IAU Symposium*, volume 261 of *IAU Symposium*, pages 155–158, January 2010.
28. J.-M. Frère, F.-S. Ling, and G. Vertongen. Bound on the dark matter density in the Solar System from planetary motions. , 77(8):083005–+, April 2008.

TESTS OF GRAVITY AT THE SOLAR SYSTEM SCALE

M.-T. JAEKEL
Laboratoire de Physique Théorique de l'Ecole Normale Supérieure, CNRS, UPMC, 24 rue Lhomond, F75231 Paris Cedex 05

S. REYNAUD
Laboratoire Kastler Brossel, Université Pierre et Marie Curie, case 74, CNRS, ENS, Campus Jussieu, F75252 Paris Cedex 05

As confirmed by tests performed in the solar system, General Relativity (GR) presently represents the best description of gravitation. It is however challenged by observations at very large length scales, and already at the solar system scale, tracking of the Pioneer 10/11 probes has failed to confirm their expected behavior according to GR. Metric extensions of GR, which are presented here, have the quality of preserving the fundamental properties of GR while introducing scale dependent modifications. We show that they moreover represent an appropriate family of gravitation theories to be compared with observations when analysing gravity tests. We also discuss different tests which could allow one to determine the metric extension of GR prevailing in the solar system.

1 Introduction

General Relativity (GR) is unique among fundamental theories as it has first been introduced on the basis of general principles [1], before being confirmed by observations [2]. However, while GR agrees with the most precise observations made in the solar system, recent observations performed at larger length scales show inconsistencies between the visible content of larger parts of the Universe and the gravitation laws according to GR. The anomalous rotation curves of galaxies [3] and the anomalous acceleration of type Ia supernovae [4] can point at the existence of important amounts of dark matter in galactic halos [5,6] and of dark matter and energy at the cosmological scale [7,8]. But, should these dark constituents remain unobserved, this could mean that the gravitation laws have to be changed at these scales. The necessity to modify GR may even come earlier, already at the solar system scale, if the anomaly observed on the navigation data of the Pioneer 10/11 probes [9] did not find a conventional explanation.

Beside observational data, theoretical arguments also plead for considering the possibility of scale dependent gravitation laws. The coupling constants of the other three fundamental interactions are known to develop a scale dependence as a consequence of radiative corrections, a property which justifies the idea of a possible unification of all fundamental interactions. Gravitation, being also both geometry and a field theory, should share this property. Assuming "asymptotic safety" [10], renormalization group techniques allow one to derive the general features of the scale dependence of gravitation. When combined with observational constraints, they lead to favour a family of metric extensions of GR for describing gravitation [11].

We briefly review here the properties of such metric extensions of GR and obtain a parametrization of these theories suiting phenomenological purposes. We discuss how they can be used when analysing gravity tests performed in the solar system and when searching anomalous gravitation properties with respect to GR.

2 General Relativity and its metric extensions

GR plays an exemplary role among fundamental theories because of two essential properties: it describes gravitation both as geometry and as a field theory. The first property deeply affects modern spacetime metrology, which relies on a strong relation between gravitation and geometry: definitions of reference systems depend on an underlying metric $g_{\mu\nu}$ which refers to solutions of gravitational equations of motion [12]. This assumption is made possible by the identification of gravitation with the geometry of spacetime. According to GR, all bodies, massive and massless ones as well, follow geodesics in absence of non gravitational forces. Geodesics are obtained from a universal geometric distance, defined by the metric $g_{\mu\nu}$ and which also coincides with the proper time delivered by clocks along their motions. This results in particular in the universality of free fall, a principle which has been verified to hold at very different length scales, ranging from millimeter [13,14] to astronomic scales [15], and at a very high precision level (10^{-13}).

On the other hand, as one of the four fundamental interactions, gravitation is also described by means of a field, characterized by the way it couples to its sources. In GR, the metric field couples to energy-momentum tensors $T_{\mu\nu}$ through its Einstein curvature $E_{\mu\nu}$, a particular combination of Ricci ($R_{\mu\nu}$) and scalar (R) curvatures. As both tensors are divergenceless, $T_{\mu\nu}$ as a consequence of conservation laws and $E_{\mu\nu}$ of Bianchi identities, coupling can be realized by a unique proportionality constant, Newton gravitation constant G_N [16,17] (c is light velocity)

$$E_{\mu\nu} \equiv R_{\mu\nu} - \frac{1}{2} g_{\mu\nu} R = \frac{8\pi G_N}{c^4} T_{\mu\nu} \tag{1}$$

But gravitation is a very weak interaction, so that the particular form of the gravitational equations of motion (1) is extremely difficult to bring to experimental test. Usually, tests of gravity are only performed in an indirect way, by comparing observations with predictions which can be obtained on the basis of metrics satisfying equations (1). As a consequence, the particular field theory characterizing gravitation, and G_N, appear to be tested with much less precision than the geometric nature of gravitation.

Moreover, theoretical arguments suggest that the gravitational equations of motion (1) cannot remain valid over arbitrary energy or length scales. Indeed, as a universal mechanism occuring in field theories, higher order processes modify couplings and propagators. This is the case for electro-weak and strong interactions, whose coupling constants become scale dependent and follow renormalization group trajectories. In a similar way, radiative corrections should lead to a scale dependence of the gravitational coupling, making the gravitational equations specified by GR (1) only approximately valid [10]. Remarkably, these theoretical arguments appear to be met by anomalous observations performed at very large length scales [3,4], which can also be interpreted as questioning the validity of GR at such scales [5,6,7,8].

Although the case of gravitation shows to be theoretically involved, the main features of the expected scale dependences can nonetheless be obtained from general properties. The symmetries, or gauge invariance, underlying gravitation constrain observables to take the form of geometric quantities [18,19]. Hence, the further couplings induced by radiative corrections involve squares of curvatures so that GR can indeed be seen to be embedded in a family of renormalizable field theories. This implies that, when radiative corrections are taken into account, gravitation can still be described by a metric theory, but that the single gravitation constant G_N must be replaced by several running coupling constants [20] characterizing additional terms in the Lagrangian. There results that GR, defined by Einstein-Hilbert Lagrangian (1), is extended to a theory which is both non local, as a result of radiative corrections, and non linear, due to their geometric nature. It leads to gravitational equations of motion which can be put under a general form, with a susceptibility replacing Newton gravitation constant [21]

$$E_{\mu\nu} = \chi_{\mu\nu}(T) = \frac{8\pi G_N}{c^4} T_{\mu\nu} + \delta\chi_{\mu\nu}(T) \tag{2}$$

The resulting equations appear to be difficult to solve due to a particular mixing realized between non linearity and non locality.

As another general property, radiative corrections can be seen to essentially differ in two sectors corresponding to couplings to massless or massive fields [20,21]: in the former case, traceless energy-momentum tensors couple to Weyl curvature only, while in the latter case couplings between energy-momentum traces and the scalar curvature also occur. GR should then be extended to metric theories which are characterized by two sectors, of different conformal weights, with corresponding running coupling constants $G^{(0)}$ and $G^{(1)}$ which generalize Newton gravitation constant G_N. The relations between coupling constants can be given simple expressions in a linearized approximation (using a representation of fields in terms of momentum k and introducing the corresponding projectors π on trace and traceless parts) [22,23]

$$\begin{aligned}
&E_{\mu\nu} = E_{\mu\nu}^{(0)} + E_{\mu\nu}^{(1)}, \qquad \pi_{\mu\nu} \equiv \eta_{\mu\nu} - \frac{k_\mu k_\nu}{k^2} \\
&E_{\mu\nu}^{(0)} = \{\pi_\mu^0 \pi_\nu^0 - \frac{\pi_{\mu\nu}\pi^{00}}{3}\} \frac{8\pi G^{(0)}}{c^4} T_{00}, \qquad E_{\mu\nu}^{(1)} = \frac{\pi_{\mu\nu}\pi^{00}}{3} \frac{8\pi G^{(1)}}{c^4} T_{00} \\
&G^{(0)} = G_N + \delta G^{(0)}, \qquad G^{(1)} = G_N + \delta G^{(1)}
\end{aligned} \tag{3}$$

Although the two running coupling constants remain close to G_N, non locality and non linearity combine in an intricate way and do not allow a decomposition as simple as (3) to hold beyond the linearized approximation. Alternatively, one can look for non linear but local theories which approximate the previous metric extensions of GR. It is remarkable that, due to the presence of two sectors, such approximations can be obtained which involve higher order field derivatives and nonetheless correspond to theories with stable ground states [24].

To the theoretical difficulties implied by non locality combined with non linearity, some compensation can be found in direct observations. Indeed, the latter show that gravitation should remain very close to GR over a large range of scales. They moreover show that departures from GR can happen not only at large energy scales, as expected if gravitation should unify with other fundamental interactions, but also at large length scales [3,4]. Gravitation tests performed up to now make it legitimate to consider the effective gravitation theory at ordinary macroscopic length scales to be a perturbation of GR [2]. Solutions of the generalized equations (2) should then correspond to perturbations of the solutions of GR equations of motion (1). Equivalently, equations (2) may be seen as providing metrics which remain close to those determined by GR and just differ from the latter by curvature anomalies [25]

$$\begin{aligned}
&E = [E]_{\text{GR}} + \delta E, \qquad [E]_{\text{GR}} = 0 \qquad \text{where} \qquad T \equiv 0 \\
&\delta E = \delta E^{(0)} + \delta E^{(1)}
\end{aligned} \tag{4}$$

Metric extensions of GR are thus characterized by two independent components of Einstein curvature tensor $\delta E^{(0)}$ and $\delta E^{(1)}$, reflecting the two different running coupling constants $G^{(0)}$ and $G^{(1)}$ modifying G_N (as seen in the linear approximation (3)). When solving the gravitation equations of motion (2), the two independent Einstein curvature components are replaced by two gauge-invariant potentials Φ_N and Φ_P (for a point-like source, using Schwarzschild coordinates)

$$\delta E_0^0 \equiv 2u^4(\Phi_N - \delta\Phi_P)'', \quad \delta E_r^r \equiv 2u^3 \Phi_P' \qquad u \equiv \frac{1}{r}, \quad ()' \equiv \partial_u \tag{5}$$

In the case of GR, Einstein curvature vanishes and the solution depends on a single potential Φ_N taking a Newtonian form (Φ_P vanishing in this case). In the general case, the potential Φ_N extends Newton potential while Φ_P describes a second gravitational sector. These potentials can be seen as a parametrization of admissible metrics in the vicinity of GR solutions, which thus represent good candidates for extending GR beyong ordinary macroscopic scales. This parametrization appears to be appropriate for analysing existing gravity tests and confronting GR with plausible alternative theories of gravitation.

3 Phenomenology in the solar system and gravity tests

The solution of the gravitation equations of motion (2) takes a simple form in the case of a stationary point-like gravitational source, as it corresponds to a static isotropic metric which reduces to two independent components (written here in spherical isotropic coordinates)

$$\begin{aligned} ds^2 &= g_{00}c^2dt^2 + g_{rr}\left(dr^2 + r^2(d\theta^2 + \sin^2\theta d\varphi^2)\right) \\ g_{00} &= [g_{00}]_{\mathrm{GR}} + \delta g_{00}, \qquad g_{rr} = [g_{rr}]_{\mathrm{GR}} + \delta g_{rr} \end{aligned} \tag{6}$$

$[g]_{\mathrm{GR}}$ denotes the approximate metric satisfying GR equations of motion (1), which can be written in terms of Newton potential. In this case, the two independent components of the metric δg_{00} and δg_{rr} are in one to one correspondence with the two independent components of Eintein curvature $\delta E^{(0)}$ and $\delta E^{(1)}$. Quite generally, the explicit expressions of the metric components in terms of the two gravitational potentials Φ_N and Φ_P (5) are obtained by inverting the usual relation between metrics and curvatures [25].

The most precise tests of GR have been realized in the solar system. Phenomenology in the solar system is usually performed with parametrized post-Newtonian (PPN) metrics [26,27]. Neglecting the Sun's motions, the corresponding PPN metrics reduce to the form (6), with g_{00} and g_{rr} being determined by Newton potential ϕ and two Eddington parameters β and γ

$$\begin{aligned} g_{00} &= 1 + 2\phi + 2\beta\phi^2 + \ldots \quad , \quad g_{rr} = -1 + 2\gamma\phi + \ldots \\ \phi &\equiv -\frac{G_N M}{c^2 r}, \qquad |\phi| \ll 1 \end{aligned} \tag{7}$$

The parameters β and γ describe deviations from GR (obtained for $\beta = \gamma = 1$) in the two sectors, corresponding respectively to effects on the motion of massive probes and on light deflection. PPN metrics are a particular case of metric extensions of GR, corresponding to a two-dimensional family which describes non vanishing but short range Einstein curvatures

$$\begin{aligned} &\Phi_N = \phi + (\beta - 1)\phi^2 + O(\phi^3), \qquad \Phi_P = -(\gamma - 1)\phi + O(\phi^2) \\ &\delta E_0^0 = \frac{1}{r^2}O(\phi^2), \qquad \delta E_r^r = \frac{1}{r^2}\left(2(\gamma - 1)\phi + O(\phi^2)\right) \qquad \text{[PPN]} \end{aligned} \tag{8}$$

In contrast, general metric extensions of GR are parametrized by two gravitational potentials Φ_N and Φ_P (5) describing arbitrary Einstein curvatures. These two functions may be seen as promoting the constant parameters β and γ to scale dependent functions. The latter manifest themselves as an additional dependence of gravitational effects on a geometric distance. The latter can be either a distance between points (as the probe and the gravitational source) or a distance between a point and a geodesic (as the impact parameter of a light ray).

Existing gravity tests put constraints on possible deviations from GR, hence on allowed metric extensions of GR (6) at the scale of the solar system. Direct scale dependence tests have up to now been performed in the first sector only. They were designed to look for possible modifications of Newton potential taking the form of a Yukawa potential ($\delta\phi(r) = \alpha e^{-\frac{r}{\lambda}}\phi(r)$), characterized by a stength parameter α and a range λ. These tests, performed for λ ranging from the submillimeter range, using dedicated experiments [28,29], to the range of planetary orbits, using probe navigation data and planetray ephemerides [28,30], show that the strength α of a Yukawa-like perturbation must remain rather small at all these scales, so that the form of the gravitational potential in the first sector is rather strongly constrained to remain Newtonian. However, constraints become much less stringent below the submillimeter range, where Casimir forces become important [29], and at scales of the order of the outer solar system, where observations used to determine ephemerides become less precise. They moreover only concern the first sector.

The increasing set of observations performed in the solar system has progressively reduced the allowed deviations from GR for the two PPN parameters β and γ. Presently, the best constraint on the value of γ is given by the measurement of the Shapiro time delay, induced by the gravitational field of the Sun on the radio link which was used to follow the Cassini probe during its travel to Saturn [31]. GR prediction for the variation of the deflection angle, near occultation by the Sun, has been confirmed, constraining γ to be close to 1 with a precision of 2.5×10^{-5}. A similar bound is provided by VLBI measurements of light deflection [2]. One may remark that such a precision is obtained when assuming that the parameter γ remains constant. As the deflection angle decreases with the impact parameter of the ray, the precision on the measurement of the deflection angle is mainly due to small impact parameters. As a result, the corresponding constraints should be sensitively less stringent when confronted to general metric extensions of GR, which allow γ to depend on the impact parameter of the ray.

The value of γ being assumed, the parameter β can be obained either by means of a direct measurement, such as Lunar Laser Ranging [15], measuring the Sun polarization effect on the Moon orbit around the Earth, or by means of big fits, using all data made available by probe navigation and astrometry measurements, to determine planet ephemerides [32,33,34]. Both methods lead to similar constraints on β, fixing the latter to remain close to 1, up to deviations less than 10^{-4}. Let us remark that these determinations are performed at the scale of the Moon orbit in one case, and at a scale of several astronomic units (AU) in the other case. They can also be considered as independent estimations of β being performed at different length scales.

Available data for gravitation at large length scales in the solar system are rather few. Hence, the navigation data of the Pioneer 10/11 probes, during their travel in the outer part of the solar system, provide an important consistency check for models of gravitation in the solar system. Remarkably, the analysis of Doppler data has failed to confirm the predictions made according to GR. Comparison of observed with predicted values resulted in residuals which did not vanish but could be interpreted as exhibiting the presence of an anomalous acceleration $a_P = (0.87 \pm 0.13)$ nm s^{-2}, directed towards the Sun or the Earth, and approximately constant over distances ranging from 20AU to 70AU [9]. Many attempts have been made to find a conventional explanation to the Pioneer anomaly as a systematic effect either related to the probe itself, allowed by a loss of energy from power generators on board, or to the environment of the probe, due to the presence of dust or gravitating matter in the outer solar system [35]. These have been followed by sustained efforts for recovering further data and performing new analyses covering the whole Pioner 10/11 missions [36]. Up to now, these attempts have remained unsuccessful in explaining the totality of the Pioneer anomaly.

Furthermore, a recent study, confirming the secular part of the Pioneer anomaly, has also analysed the modulations apparent in the Doppler data, showing that their frequencies correspond to the Earth's motions, and that the Doppler residuals can be further reduced by introducing simple modulations of the radio links [37]. Modulated anomalies cannot be produced by a conventional explanation of the secular part but require a further mechanism (trajectory mismodeling, solar plasma effects, ...) to be accounted for. On the other hand, simple models modifying the metric are able to reproduce both types of anomalies. These features leave the possibility of a common gravitational origin of the Pioneer anomalies, pointing at a deficiency of GR occuring at length scales of the order of the solar system size.

4 Tests of metric extensions of GR

Besides being favoured by theoretical arguments, metric extensions of GR also provide an appropriate tool for analysing gravity tests performed in the solar system. Most precise tests realized at or beyond the AU scale strongly rely on Doppler ranging, hence on an appropriate modeling of electromagnetic links and the trajectories of massive bodies. Metric extensions of GR provide a general and simple expression for the time delay function $\mathcal{T}(\mathbf{x}_1, \mathbf{x}_2)$ which describes the links used to follow a massive probe ($\mathbf{x}_a \equiv r_a(\sin\theta_a \cos\varphi_a, \sin\theta_a \sin\varphi_a, \cos\theta_a)$ with $a = 2, 1$ respectively denoting the coordinates of the probe and a station on Earth, $\mathcal{T}(\mathbf{x}_1, \mathbf{x}_2)$ is written here for a static istropic metric (6))[38]

$$c\mathcal{T}(r_1, r_2, \phi) \equiv \int_{r_1}^{r_2} \frac{-\frac{g_{rr}}{g_{00}}(r)dr}{\sqrt{-\frac{g_{rr}}{g_{00}}(r) - \frac{\rho^2}{r^2}}} \quad , \quad \phi = \int_{r_1}^{r_2} \frac{\rho dr/r^2}{\sqrt{-\frac{g_{rr}}{g_{00}}(r) - \frac{\rho^2}{r^2}}}$$
$$\cos\phi \equiv \cos\theta_1 \cos\theta_2 + \sin\theta_1 \sin\theta_2 \cos(\varphi_2 - \varphi_1) \tag{9}$$

ϕ is the relative angle, when seen from the gravitational source, of the two points $\mathbf{x}_1$ and $\mathbf{x}_2$ and ρ the impact parameter of the light ray joining these points. The two-point function $\mathcal{T}(\mathbf{x}_1, \mathbf{x}_2)$ describes the time taken by a light-like signal to propagate from position $\mathbf{x}_1$ to position $\mathbf{x}_2$ (thus giving a parametrization of lightcones). The time delay function can be seen to be parametrized by metric components (9), hence by the two gravitation potentials (Φ_N, Φ_P). Doppler signals are obtained by taking the time derivative of $\mathcal{T}(\mathbf{x}_1, \mathbf{x}_2)$, and evaluating the latter on the trajectories of the probe and the Earth station. As geodesics must be determined according to the same metric extension of GR, the two potentials also enter the expressions of the trajectories[25].

Comparison between metric extensions and GR predictions can be performed explicitly and analysing the former within the framework of GR leads to deviations which take the form of Pioneer-like anomalies ($\delta a = \delta a_{\mathrm{sec}} + \delta a_{\mathrm{ann}}$ denotes the time derivative of Doppler signals[9])

$$\delta a_{\mathrm{sec}} \simeq -\frac{c^2}{2}\partial_r(\delta g_{00}) + [\ddot{r}_2]_{\mathrm{GR}} \left\{\frac{\delta(g_{00}g_{rr})}{2} - \delta g_{00}\right\} - \frac{c^2}{2}\partial_r^2 [g_{00}]_{\mathrm{GR}}\, \delta r_2$$
$$\delta a_{\mathrm{ann}} \simeq \frac{d}{dt}\left\{\left[\frac{d\phi}{dt}\right]_{\mathrm{GR}} \delta\rho\right\} \tag{10}$$

The gravitational potentials in the two sectors contribute to both the secular part δa_{sec} and the modulated part δa_{ann} of the anomaly. These furthermore depend on the probe and Earth motions, which are obtained from the equations for geodesics and initial conditions. Hence, Pioneer-like anomalies appear as a prediction of metric extensions of GR. These moreover predict strong correlations between secular and modulated anomalies, which can be considered as signatures to be looked for in observations[23,38].

Besides directly, through a precise analysis of probe navigation data, the two gravitational potentials may also be expected to be determined as part of a big fit of all navigation and astrometric data, such as those used to obtain the ephemerides of planets and some of their characteristic constants. In such an approach, the two potentials play the same role as Eddington parameters β and γ[32,33,34], with the additional feature of allowing significant dependences on length scales of the order of the solar system size[25]. The results of Doppler and ranging observations should then be taken into account by using the time delay function (9) and the geodesics, depending on the two gravitational potentials (Φ_N, Φ_P) which define a general metric extension of GR. Clearly, the need to recall to numerical methods entails that the neighborhood defined by the two potentials, in their general form, is too large to be totally scanned by a fit. Hence, it appears crucial to design simplified models which depend on a small number of real parameters but still preserve the scale dependences which are most likely to be observed[39].

Metric extensions of GR also predict effects which can be expected to be exhibited by future experiments benefiting from a high increase in precision measurement. The time delay function (9) results in a particular scale dependence of the gravitational deflection of light which can be equivalently represented as an additional dependence of the deflection angle ω, or else of Eddington parameter γ, on the impact parameter of the light ray (M denotes the mass of the gravitational source, r its distance to the observer, χ the apparent relative angle between the light source and the gravitational source) [23]

$$\omega(\chi) \simeq \frac{G_N M}{c^2 r} \frac{1+\gamma(\chi)}{tan\frac{\chi}{2}}$$

The two gravitational potentials characterizing metric extensions combine to induce a modification of the deflection angle which, in contrast to GR, contains a part which increases with the impact parameter. Such deviations should then become more noticeable for measurements performed with a high precision and at small deflection angles. In a near future, GAIA will perform a survey of our neighborhood in our galaxy and will follow with a very good accuracy an extremely large number of astrometric objects[40,6]. This will include in particular a very large number of light deflection observations performed at small deflection angles, or at large angular distances from the Sun

$$\delta\omega < 40\mu\text{as}, \qquad \omega \sim 4\text{mas}, \qquad \chi \in [45°, 135°]$$

As a consequence, GAIA data will improve the accuracy for the observed mean value of γ (better than 2×10^{-6}) and will make it possibe to map the dependence of γ on χ over its whole range of variation. Such a mapping could put into evidence small deviations from GR and moreover allow to determine and fit their particular dependence.

A definite answer to the question of modifying the gravitation theory at the solar system scale would be provided by missions embarking dedicated means for directly measuring the effects of gravity. A first example is OSS mission [41] which, beside ranging facilities, will also possess a high precision accelerometer, thus allowing to distinguish the effects of gravitation from other forces affecting the probe and hence to determine unambiguously whether the probe follows a geodesic, and whether the latter corresponds to GR. Another mission, SAGAS [42], aims at reaching the outer part of the solar system with, beside an accelerometer, an atomic clock on board. Using the combined information obtained, with a very high precision, from the optical links and the clock on board, one would be able to reconstruct the gravitational potentials in the two sectors, and thus to exactly determine the gravitation theory prevailing at the largest scales which can be reached by artificial probes.

5 Conclusion

When generalized under the form of a metric extension, GR remains a successful theory of gravitation within the whole solar system. Minimal modifications allow one to account for all gravity tests performed up to the solar system scale and to confirm the position of GR as the basis of gravitation theory. They moreover correspond to scale dependences of the gravitational coupling, thus bringing gravitation closer to the other fundamental interactions.

From a phenomenological point of view, metric extensions of GR appear as a convenient tool for testing gravity within the solar system. They may also provide a natural answer to the presence of anomalies when observations are analysed by confrontation with GR. The actual theory of gravitation can be approached by looking for such anomalies occuring in residuals of direct ranging data or big fits. It may also be determined by future high precision observations (GAIA) or dedicated missions in the solar system (OSS, SAGAS).

References

1. A. Einstein, *Annalen der Physik* **49**, 769 (1916).
2. C.M. Will, *Living Rev. Rel.* **9**, 3 (2005).
3. S.S. McGaugh, *Phys. Rev. Lett.* **106**, 121303 (2011).
4. S. Perlmutter *et al*, *Astrophys. J.* **517**, 565 (1999).
5. G. Gentile *et al.*, *Mon. Not. R. Astron. Soc.* **351**, 903 (2004).
6. see O. Bienaymé in this volume.
7. L.D. Ferramacho, A. Blanchard and Y. Zolnierowski, *Preprint* arXiv:0807.4608.
8. see A. Blanchard in this volume.
9. J.D. Anderson *et al* , *Astrophys. J.* **459**, 365 (1996); *Phys. Rev. Lett.* **81**, 2858 (1998); *Phys. Rev.* D **65**, 082004 (2002).
10. S. Weinberg, "Ultraviolet divergences in quantum theories of gravitation", in S.W. Hawking and W. Israel eds., *General Relativity, An Einstein Centenary Survey*, (Cambridge U.P., Cambridge, U.K., 1979).
11. M.-T. Jaekel and S. Reynaud, *Proc. Gravitational waves and experimental gravity XLIIèmes Rencontres de Moriond*, J. Dumarchez, J. Trân Thanh Vân eds., (Thé Gioi, Hanoi, 2007) 271.
12. M. Soffel *et al.*, *Astron. J.* **126**, 2687 (2003).
13. E.G. Adelberger *et al.*, *Part. Nucl. Phys.* **62**, 102 (2009).
14. see E.G. Adelberger in this volume.
15. J.G. Williams, S.G. Turyshev and D.H. Boggs, *Phys. Rev. Lett.* **93**, 261101 (2004).
16. A. Einstein, *Sitz. Preuss. Akad. Wiss. Berlin* **844**, (1915).
17. D. Hilbert, *Nach. Ges. Wiss. Göttingen* **395**, (1915).
18. A.D. Sakharov, Doklady Akad. Nauk SSSR **177**, 70 (1967) [*Sov. Phys. Doklady* **12**, 1040].
19. G. t'Hooft and M. Veltman, *Ann. Inst. H. Poincaré* A **20**, 69 (1974).
20. E.S. Fradkin and A.A. Tseytlin, *Nucl. Phys.* B **201**, 469 (1982).
21. M.-T. Jaekel and S. Reynaud, *Annalen der Physik* **4**, 68 (1995).
22. M.-T. Jaekel and S. Reynaud, *Mod. Phys. Lett.* A **20**, 1047 (2005).
23. M.-T. Jaekel and S. Reynaud, *Class. Quantum Grav.* **22**, 2135 (2005).
24. J.P. Bruneton and G. Esposito-Farese, *Phys. Rev.* D **76**, 124012 (2007).
25. M.-T. Jaekel and S. Reynaud, *Class. Quantum Grav.* **23**, 777 (2006).
26. C.M. Will and K. Nordtvedt, *Astrophys. J.* **177**, 757 (1972).
27. K. Nordtvedt and C.M. Will, *Astrophys. J.* **177**, 775 (1972).
28. E. Fischbach and C. Talmadge, *The Search for Non Newtonian Gravity* (Springer Verlag, Berlin, 1998); see E. Fischbach in this volume.
29. see S. Reynaud in this volume.
30. S. Reynaud and M.-T. Jaekel, *Int. J. Mod. Phys.* A **20**, 2294 (2005).
31. B. Bertotti, L. Iess and P. Tortora, *Nature* **425**, 374 (2003).
32. W.M. Folkner, *Proc. IAU Symposium* **261**, 155 (2010).
33. E.V. Pitjeva, *Proc. IAU Symposium* **261**, 170 (2010).
34. A. Fienga *et al.*, *Proc. IAU Symposium* **261**, 159 (2010); see A. Fienga in this volume.
35. M.M. Nieto and J.D. Anderson, *Contemp. Phys.* **48**, 41 (2007).
36. S.G. Turyshev and Toth, *Living Rev. Rel.* **13**, 4 (2010).
37. A. Levy *et al.*, *Adv. Space Res.* **43**, 1538 (2009).
38. M.-T. Jaekel and S. Reynaud, *Class. Quantum Grav.* **23**, 7561 (2006).
39. see A. Hees in this volume.
40. M.A.C. Perryman *et al.*, *Astron. Astrophys.* **369**, 339 (2001).
41. B. Christophe *et al.*, *Exp. Astron.* **23**, 529 (2009); see B. Christophe in this volume.
42. P. Wolf *et al.*, *Exp. Astron.* **23**, 651 (2009).

OSS (Outer Solar System) Mission

B. Christophe and OSS Team
ONERA - The French Aerospace Lab, F-92322 Chatillon, France

OSS is an M-class mission to explore the Neptune system almost half a century after flyby of the Voyager 2 spacecraft with a unique opportunity to visit a selected Kuiper Belt object subsequent to the passage of the Neptunian system. The probe will also embark instruments allowing precise tracking of the probe during cruise. It allows to perform the best controlled experiment for testing, in deep space, General Relativity, on which is based all the models of Solar system formation. The design of the probe is mainly constrained by the deep space gravity test in order to minimise the perturbation of the accelerometer measurement.

1 Introduction

Outer Solar System (OSS) Mission, proposed in the frame of the ESA Cosmic Vision call for a M mission, continues a long and bright tradition by associating the communities of fundamental physics and planetary sciences in a mission with ambitious goals in both domains. OSS will visit Neptune and its moon Triton, nearly half a century after Voyager 2 and then a Kuiper Belt object.
During its cruise to the Outer Solar System, the precise tracking of the probe will be used for testing the predictions of General Relativity (deep space gravity and measurement of Eddington's parameter γ).
This paper focuses on the fundamental physics aspect of the mission, with a brief description of the scientific objectives, the instrumentation suite, the mission trajectory and the spacecraft.

2 Fundamental Physic Scientific Objectives

2.1 Deep space gravity

General Relativity, the current theoretical formulation of gravitation, is in good agreement with most experimental tests of gravitation [1]. But General Relativity is a classical theory and all attempts to merge it with the quantum description of the other fundamental interactions suggest that it cannot be the final theory of gravitation. Meanwhile, the experimental tests leave open windows for deviations from General Relativity at short [2] or long distance [3] scales.

General Relativity is also challenged by observations at galactic and cosmic scales. The rotation curves of galaxies and the relation between redshifts and luminosities of supernovae deviate from the predictions of the theory. These anomalies are interpreted as revealing the presence of new components of the Universe, the so-called "dark matter" and "dark energy" which are thought to constitute respectively 25% and 70% of the energy content of the Universe [4 5]. Their nature remains unknown and, despite their prevalence, they have not been detected by any other means than gravitational measurements. Given the immense challenge posed by

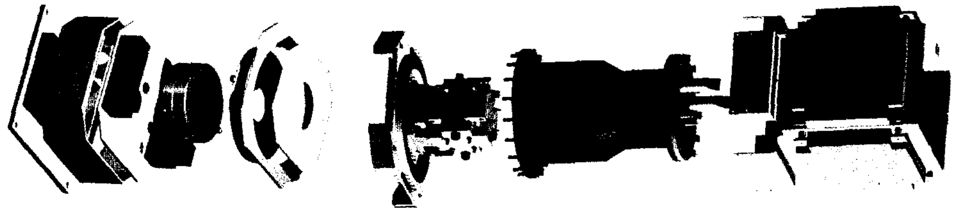

Figure 1: GAP exploded view: Bias Rejection System (left) and MicroSTAR accelerometer (right)

these large scale behaviors, it is important to explore every possible explanation including the hypothesis that General Relativity is not a correct description of gravitation at large scales[6,7].

Testing gravitation at the largest scales reachable by man-made instruments is therefore essential to bridge the gap between experiments in the Solar System and astrophysical or cosmological observations. A key idea of OSS mission (as previously proposed[8,9,10,11]) is to measure non-gravitational forces acting on the spacecraft, with a target accuracy of 10 pm.s^{-2}. Combining these measurements with radio tracking data, it becomes possible to improve by orders of magnitude the precision of the comparison with theory of the spacecraft gravitational acceleration.

2.2 Measurement of the Eddington's parameter γ

The Eddington parameter γ, whose value in General Relativity is unity, is a fundamental parameter in most tests of relativistic gravitation. In fact, $(1-\gamma)$ yields one measurement of the deviation from General Relativity from competing theories: it gauges for example, the fractional strength of scalar interaction in scalar-tensor theories of gravitation. This deviation $(1-\gamma)$ has been shown to be smaller than 2×10^{-5} by the Cassini relativity experiment performed at solar conjunctions in June 2002[12].

The orbit of the spacecraft will be tracked during the whole cruise phase, in order to test General Relativity to an unprecedented level of accuracy (see previous section). A particularly interesting test will take benefit of solar conjunctions to repeat the Cassini relativity experiment but with a largely improved accuracy (at the 10^{-7} level) thanks to the laser ranging equipment onboard.

3 Fundamental Physic Payload

3.1 Accelerometer: GAP

The DC accelerometer GAP is used in complement of the navigation instruments to measure the non gravitational acceleration applied to the spacecraft. GAP is composed of an electrostatic accelerometer MicroSTAR, based on ONERA expertise in the field of accelerometry and gravimetry (CHAMP, GRACE, GOCE missions, [13]), and a Bias Rejection System (see Figure 1).

The three axes accelerometer is based on the electrostatic levitation of the inertial mass with no mechanical contact with the instrument frame. The mechanical core of the accelerometer is fixed on a sole plate and enclosed in a hermetic housing in order to maintain a good vacuum around the proof-mass. The bias calibration system consists in a flip mechanism which allows a 180° rotation of the accelerometer to be carried out at regularly spaced times[14]. It is equipped with a piezo-electric rotating actuator and a high-resolution angle encoder working in closed loop operation.

The resolution of the instrument is 1 pm/s^2 in DC, with a global performance of 10 pm/s^2 aking into account the effect of integration in the S/C (alignment, centrifugal acceleration, S/C elf-gravity ...).

?.2 Laser Science Instrument

For the laser Doppler measurement, two different concepts are proposed and briefly described pelow.

One way Laser - TIPO

The TIPO experiment (Télémétrie Inter Planétaire Optique) proposed by the OCA team is a one-way laser ranging project derived from satellite and lunar laser ranging (SLR/LLR) and optical time transfer T2L2. The TIPO principle is based on the emission of laser pulses from an Earth based station towards the spacecraft. These pulses are timed in the respective timescales at departure on Earth and upon arrival on the spacecraft. The propagation time and the respective distance between Earth and spacecraft are derived from the difference of the dates of departure and arrival. This one-way laser ranging permits distance measurements on a Solar System scale (up to 30 AU) as the one-way link budget varies only with the square of the distance, contrary to the power of four for usual laser telemetry.

Two way coherent laser - DOLL

The DOLL optical link concept for OSS is the optical equivalent of the radio link, with an onboard laser transponder and ground terminals at already operating satellite/lunar laser ranging stations. In its baseline version OSS-DOLL features in particular:

- continuous wave laser operation in both directions (two-way system) at λ=1064.5 nm;
- heterodyne onboard laser transponder (minor modification of the present homodyne LCT transponder);
- high precision optical Doppler (range-rate) measurement;
- data transfer and range measurement;
- large stray light rejection from heterodyne detection and thanks to a controlled frequency offset (100 MHz) between incoming and outgoing laser signals, using a space qualified USO (ACES/PHARAO Quartz oscillator).

3.3 Radio-Science and Very Large Baseline Interferometer

The probe navigation is based on precision Doppler tracking, which are optimized at two wavelengths, X- and Ka-bands, in a two-way coherent mode. The dual link enables the calibration of the dispersive effects of the charged particles in the interplanetary plasma. X- and Ka-bands have been flown reliably in a coherent mode on at least two deep space missions (Cassini and Juno) and are planned for several more upcoming missions (Bepi-Colombo). The two-way coherent mode enables the transponder(s) to take advantage of the superior stability of H-maser based clocks at the ground stations. The performance can be expressed in Doppler noise in units of velocity or in terms of the dimensionless Allan deviation and should be at least 10^{-14} at an integration time of 1000 s.

Observations of the spacecraft using global Very Large Baseline Interferometer arrays with 10 or more radio telescopes and maximum baselines of ~10 000 km at X-band in a phase referencing mode using the natural extragalactic radio sources for phase calibration can provide positioning accuracy at a level of 0.1 nrad, or 150 m at a distance of 10 AU.

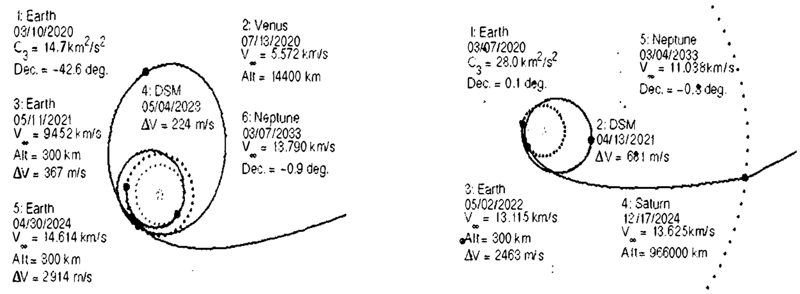

Figure 2: OSS orbit for a launch in 2020, with Venus and Earth flybys (left) or Earth and Saturn flybys (right)

4 Mission and Spacecraft

A direct trajectory would enable almost annual launch windows at the expense of a relatively heavy launcher due to the high initial velocity which is required. Transfers using inner solar system gravity assists would require less heavy launchers. Two optimized trajectories are compared in Figure 2. A preliminary analysis of the mission profile shows the capability to deliver a 500 kg class probe.

The spacecraft architecture, illustrated in Figure 3, is organized so as to:

- provide a planet-pointing side with the observation instruments;

- accommodate the laser instrument for the measurement of the Eddington parameter with a pointing towards the Earth;

- provide the lowest and most axisymmetrical self-gravity as viewed from GAP;

- make coincide as much as possible the dry mass centre of gravity, the propellant centre of gravity, the radiation pressure force line and the GAP;

- ensure a stable and reliable alignment between the GAP and the High Gain Antenna (HGA) to ensure consistency between radio science and accelerometry;

- accommodate the two Advanced Stirling Radioisotope Generators (ASRG) required for the mission by minimising their impact on the rest of the spacecraft (including radiation).

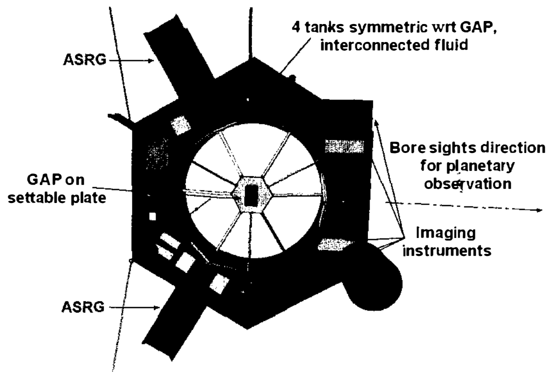

Figure 3: Spacecraft viewed from top, with HGA and closure panels removed:

ıcknowledgments

)SS Team is composed by: B. Christophe, B. Foulon, B. Lenoir, A. Levy, C. Robert, P. Touboul ONERA - The French Aerospace Lab, France), L.J. Spilker, J.D. Anderson, S.W. Asmar, G. Oron, K.R. Reh, T.R. Spilker (JPL/NASA, USA), N. André (CESR, France), D. Banfield (Cornell Jniversity, USA), J. Helbert, H. Hussmann, N. Schmitz, F. Sohl, K. Stephan (DLR/Institute of Planetary Research, Germany), H. Dittus (DLR/Institute of Space System, Germany), P. Brown Imperial College London, UK), R. Srama (IRS, University of Stuttgart and MPIK, Heidelberg, Germany), F. Francisco, P.J.S. Gil, J. Pàramos (Instituto Superior Técnico, Portugal), S.V. Pro- ;rebenko (JIVE, Joint Institute for VLBI in Europe, The Netherlands), A. Barucci, B. Cecconi, ,. Lamy (LESIA, Observatoire de Paris, CNRS, Meudon, France), J.-M. Courty, B. Lamine, 5. Reynaud (LKB, CNRS, Paris, France), W. Grundy (Lowel Observatory, USA), E. Samain Observatoire de la Côte d'Azur, GeoAzur, France), C. Hansen (PSI, USA), R. Bingham (RAL, JK), P. Wolf (SYRTE, Observatoire de Paris-Meudon, France), J. Poncy (Thales Alenia Space, Cannes, France), K.H. Glassmeier (Technical University of Braunschweig, Germany), O. Bertoami (Universidade do Porto, Portugal), J. Saur (Universität zu Köln, Germany), J. Aurnou, R. Helled, K.M. Sayanagi (University of California, USA), F. Postberg (University of Heidelberg, Germany), L.N. Fletcher (University of Oxford, UK), C. Lämmerzahl, H. Selig (ZARM, University of Bremen, Germany).

This proposal was supported by CNES (France) through a phase 0 study managed by E. Hinglais and S. Léon-Hirtz.

References

1. Will C.M., Living Reviews in Relativity **9**, 3 (2006)
2. Adelberger E., et al, Annual Review of Nuclear and Particle Science **53**, 77 (2003)
3. Reynaud, S. and Jaekel, M.-T., International Journal of Modern Physics A **20**, 2294 (2005)
4. Copeland E., Sami M., Tsujikawas S., Int J Mod Phys D **15**, 1753 (2006)
5. Frieman J.A., et al, Annual Review of Astronomy and Astrophysics **46**, 385 (2008)
6. Aguirre A., Burgess C., Friedland A., Nolte D., Class Quantum Grav **18**, R223 (2001)
7. Nojiri S., Odintsov S., Int. J. of Geometric Methods in Modern Physics **4**, 115 (2007)
8. Dittus H., Turyshev S., Lämmerzahl C. *et al*, ESA Special Publications **588**, 3 (2005)
9. Johann U., Dittus H., Lämmerzahl C. in *Lasers, Clocks and Drag-Free Control: Exploration of Relativistic Gravity in Space*, ed. H. Dittus, C. Lämmerzahl, and S.G. Turyshev (Astrophysics and Space Science Library, vol 349, pp 577, 2008)
10. Christophe B., Andersen P.H., Anderson J.D. *et al*, Exp. Astronomy **23**, 529 (2009)
11. Wolf P., Bordé C.J., Clairon A. *et al*, Exp Astronomy **23**, 651 (2009)
12. Bertotti B., Iess L., Tortora P., Nature **425**, 374 (2003)
13. Touboul P., Willemenot E., Foulon B., Josselin V. Joint Meeting of the International Gravity Commission and the International Geoid Commission No2, Bollettino di Geofisica Teorica ed Applicata **40**, 321 (1999)
14. Lenoir B., Levy A., Foulon B., Christophe B., Lamine B., Reynaud S., ArXiv e-prints arXiv:1011.6263 [physics.ins-det], Submitted to Advances in Space Resarch, (2010)

ON THE ANOMALOUS INCREASE OF THE LUNAR ECCENTRICITY

L. IORIO
Ministero dell'Istruzione, dell'Università e della Ricerca (M.I.U.R.)
Viale Unità di Italia 68, 70125, Bari (BA), Italy.

Possible explanations of the recently reported anomalous increase of the eccentricity of the lunar orbit are sought in terms of classical Newtonian mechanics, general relativity, and long-range modifications of gravity.

Anderson and Nieto, in a recent review[1] of some astrometric anomalies detected in the olar system by some independent groups, mentioned also an anomalous secular increase of the ccentricity e of the orbit of the Moon

$$\dot{e}_{\rm meas} = (9 \pm 3) \times 10^{-12}\ {\rm yr}^{-1} \tag{1}$$

ased on an analysis of a long LLR data record spanning 38.7 yr performed by Williams and loggs[2] with the dynamical force models of the DE421 ephemerides[3,4] including all the known elevant Newtonian and Einsteinian effects. Notice that Eq. 1 is statistically significant at a σ−level. The first account[5] of this effect appeared in 2001 by Williams *et al.*, who gave an xtensive discussion of the state-of-the-art in modeling the tidal dissipation in both the Earth nd the Moon. Later, Williams and Dickey[6], relying upon the 2001 study[5], released an anomalous ccentricity rate as large as $\dot{e}_{\rm meas} = (1.6 \pm 0.5) \times 10^{-11}\ {\rm yr}^{-1}$. Anderson and Nieto[1] commented hat Eq. 1 is not compatible with present, standard knowledge of the dissipative processes in the nteriors of both the Earth and Moon, which were, actually, modeled by Williams and Boggs[2].

Naive, dimensional evaluations of the effect caused on e by an additional anomalous accelration A can be made by noticing that

$$\dot{e} \simeq \frac{A}{na}, \tag{2}$$

vith

$$na = 1.0 \times 10^{3}\ {\rm m\ s}^{-1} = 3.2 \times 10^{10}\ {\rm m\ yr}^{-1} \tag{3}$$

or the geocentric orbit of the Moon, whose mass is denoted as m. In it, a is the orbital emimajor axis, while $n \doteq \sqrt{\mu/a^3}$ is the Keplerian mean motion in which $\mu \doteq GM(1 + m/M)$ the gravitational parameter of the Earth-Moon system: G is the Newtonian constant of ravitation and M is the mass of the Earth. It turns out that an extra-acceleration as large as

$$A \simeq 3 \times 10^{-16}\ {\rm m\ s}^{-2} = 0.3\ {\rm m\ yr}^{-2} \tag{4}$$

ould satisfy Eq. 1. In fact, a mere order-of-magnitude analysis based on Eq. 2 would be nadequate to infer meaningful conclusions: finding simply that this or that dynamical effect induces an extra-acceleration of the right order of magnitude may be highly misleading. Indeed, exact calculations of the secular variation of e caused by such putative promising candidate extra-accelerations A must be performed with standard perturbative techniques in order to check if they, actually, cause an averaged non-zero change of the eccentricity. Moreover, it may well happen, in principle, that the resulting analytical expression for $\langle \dot{e} \rangle$ retains multiplicative factors $1/e^j, j = 1,2,3,...$ or $e^j, j = 1,2,3...$ which would notably alter the size of the found non-zero secular change of the eccentricity with respect to the expected values according to Eq. 2.

It is well known that a variety of theoretical paradigms[7,8] allow for Yukawa-like deviations[9] from the usual Newtonian inverse-square law of gravitation. The Yukawa-type correction to the Newtonian gravitational potential $U_{\rm N} = -\mu/r$, where $\mu \doteq GM$ is the gravitational parameter of the central body which acts as source of the supposedly modified gravitational field, is

$$U_{\rm Y} = -\frac{\alpha\mu_\infty}{r}\exp\left(-\frac{r}{\lambda}\right), \tag{5}$$

in which μ_∞ is the gravitational parameter evaluated at distances r much larger than the scale length λ. In order to compute the long-term effects of Eq. 5 on the eccentricity of a test particle it is convenient to adopt the Lagrange perturbative scheme[10]. In such a framework, the equation for the long-term variation of e is[10]

$$\left\langle \frac{de}{dt} \right\rangle = \frac{1}{na^2}\left(\frac{1-e^2}{e}\right)\left(\frac{1}{\sqrt{1-e^2}}\frac{\partial \mathcal{R}}{\partial \omega} - \frac{\partial \mathcal{R}}{\partial \mathcal{M}}\right), \tag{6}$$

where ω is the argument of pericenter, $\mathcal{M}$ is the mean anomaly of the test particle, and $\mathcal{R}$ denotes the average of the perturbing potential over one orbital revolution. In the case of a Yukawa-type perturbation, Eq. 5 yields

$$\langle U_{\rm Y} \rangle = -\frac{\alpha\mu_\infty \exp\left(-\frac{a}{\lambda}\right)}{a} I_0\left(\frac{ae}{\lambda}\right), \tag{7}$$

where $I_0(x)$ is the modified Bessel function of the first kind $I_q(x)$ for $q = 0$. An inspection of Eq. 6 and Eq. 7 immediately tells us that there is no secular variation of e caused by an anomalous Yukawa-type perturbation.

The size of the general relativistic Lense-Thirring[11] acceleration experienced by the Moon because of the Earth's angular momentum[12] $S = 5.86 \times 10^{33}$ kg m^2 s^{-1} is just

$$A_{\rm LT} \simeq \frac{2vGS}{c^2a^3} = 1.6 \times 10^{-16}\ {\rm m\ s^{-2}} = 0.16\ {\rm m\ yr^{-2}}, \tag{8}$$

i.e. close to Eq. 4. On the other hand, it is well known that the Lense-Thirring effect does not cause long-term variations of the eccentricity. Indeed, the integrated shift of e from an initial epoch corresponding to f_0 to a generic time corresponding to f is[13]

$$\Delta e = -\frac{2GS\cos I' \left(\cos f - \cos f_0\right)}{c^2 na^3\sqrt{1-e^2}}, \tag{9}$$

in which I' is the inclination of the Moon's orbit with respect to the Earth's equator and f is the true anomaly. From Eq. 9 it straightforwardly follows that after one orbital revolution, i.e. for $f \rightarrow f_0 + 2\pi$, the long-term gravitomagnetic shift of e vanishes.

A promising candidate for explaining the anomalous increase of the lunar eccentricity is, at least in principle, a trans-Plutonian massive body X of planetary size located in the remote peripheries of the solar system. Indeed, the perturbation induced by it would, actually, cause a ıon-vanishing long-term variation of e. Moreover, since it depends on the spatial position of X n the sky and on its tidal parameter

$$\mathcal{K}_{\rm X} \doteq \frac{Gm_{\rm X}}{d_{\rm X}^3}, \tag{10}$$

vhere $m_{\rm X}$ and $d_{\rm X}$ are the mass and the distance of X, respectively, it may happen that a suitable ombination of them is able to reproduce Eq. 1. Let us recall that, in general, the perturbing otential felt by a test particle orbiting a central body due to a very distant, pointlike mass can e cast into the following quadrupolar form

$$U_{\rm X} = \frac{\mathcal{K}_{\rm X}}{2}\left[r^2 - 3\left(\vec{r}\cdot\hat{l}\right)^2\right], \tag{11}$$

vhere $\hat{l} = \{l_x, l_y, l_z\}$ is a unit vector directed towards X determining its position in the sky. In Eq. 11 $\vec{r} = \{x, y, z\}$ is the geocentric position vector of the perturbed particle, which, in the resent case, is the Moon. Iorio[14] has recently shown that the average of Eq. 11 over one orbital evolution of the particle is

$$\langle U_{\rm X}\rangle = \frac{\mathcal{K}_{\rm X}a^2}{32}\mathcal{U}\left(e, I, \Omega, \omega; \hat{l}\right), \tag{12}$$

vhere $\mathcal{U}\left(e, I, \Omega, \omega; \hat{l}\right)$ is a complicated function of its arguments[14]: Ω is the longitude of the scending node and I is the inclination of the lunar orbit to the ecliptic. In the integration ielding Eq. 12 $\hat{l}$ was kept fixed over one orbital revolution of the Moon, as it is reasonable given he assumed large distance of X with respect to it. Eq. 6, applied to Eq. 12, straightforwardly ields

$$\langle\dot{e}\rangle = \frac{15\mathcal{K}_{\rm X}e\sqrt{1-e^2}}{16n}\mathcal{E}\left(I, \Omega, \omega; \hat{l}\right). \tag{13}$$

Also $\mathcal{E}\left(I, \Omega, \omega; \hat{l}\right)$ is an involved function of the orientation of the lunar orbit in space and of the osition of X in the sky[14]. Actually, the expectations concerning X are doomed to fade away. ndeed, apart from the modulation introduced by the presence of the time-varying I, ω and Ω in Eq. 13, the values for the tidal parameter which would allow to obtain Eq. 1 are too large for all he conceivable positions $\{\beta_{\rm X}, \lambda_{\rm X}\}$ of X in the sky. This can easily be checked by keeping ω and Ω fixed at their J2000.0 values as a first approximation. Indeed, Iorio[14] showed that the physical ınd orbital features of X postulated by two recent plausible theoretical scenarios[15,16] for X would nduce long-term variations of the lunar eccentricity much smaller than Eq. 1. Conversely, it urns out that a tidal parameter as large as

$$\mathcal{K}_{\rm X} = 4.46 \times 10^{-24}\ {\rm s}^{-2} \tag{14}$$

vould yield the result of Eq. 1. Actually, Eq. 14 is totally unacceptable since it corresponds to listances of X as absurdly small as $d_{\rm X} = 30$ au for a terrestrial body, and $d_{\rm X} = 200$ au for a ovian mass.

An empirical explanation of Eq. 1 can be found by assuming that, in addition to the usual Newtonian inverse-square law for the gravitational acceleration imparted to a test particle by a entral body orbited by it, there is also a small radial extra-acceleration of the form

$$A = kH_0v_r. \tag{15}$$

n it k is a positive numerical parameter of the order of unity to be determined from the bservations, $H_0 = (73.8 \pm 2.4)$ km s^{-1} Mpc^{-1} $= (7.47 \pm 0.24) \times 10^{-11}$ yr^{-1} is the Hubble arameter at the present epoch[17], defined in terms of the time-varying cosmological scaling factor

$S(t)$ as $H_0 \doteq \dot{S}/S\Big|_0$, and v_r is the component of the velocity vector $\vec{v}$ of the test particle's proper motion about the central body along the common radial direction. Indeed, a straightforward application of the Gauss perturbative equation for e to Eq. 15 yields

$$\langle \dot{e} \rangle = kH_0 \frac{\left(1-e^2\right)\left(1-\sqrt{1-e^2}\right)}{e}. \tag{16}$$

Since $e_{\rm Moon} = 0.0647$, Eq. 16 can reproduce Eq. 1 for $2.5 \lesssim k \lesssim 5$. Here we do not intend to speculate too much about possible viable physical mechanisms yielding the extra-acceleration of Eq. 15. It might be argued that, reasoning within a cosmological framework, the Hubble law may give Eq. 15 for $k = 1$ if the proper motion of the particle about the central mass is taken into account in addition to its purely cosmological recession which, instead, yields the well-known local extra-acceleration of tidal type $A_{\rm cosmol} = -q_0 H_0^2 r$, where q_0 is the deceleration parameter at the present epoch.

Acknowledgments

I gratefully acknowledge the financial support by the MORIOND scientific committee

References

1. J. D. Anderson and M. M. Nieto in *Relativity in Fundamental Astronomy: Dynamics, Reference Frames, and Data Analysis, Proceedings IAU Symposium No. 261*, ed. S. A. Klioner, P. K. Seidelmann and M. H. Soffel (Cambridge University Press, Cambridge, 2010), pp. 189-197.
2. J. G. Williams and D. H. Boggs in *Proceedings of the 16th International Workshop on Laser Ranging*, ed. S Schilliak, pp. 101-120.
3. W. M. Folkner, J. G. Williams and D. H. Boggs JPL IOM 343R-08-003 (2008).
4. J. G. Williams, D. H. Boggs and W. M. Folkner JPL IOM 335-JW,DB,WF-20080314-001 (2008).
5. J. G. Williams, D. H. Boggs, C. F. Yoder, J. T. Ratcliff and J. O. Dickey , *J. Geophys. Res.* **106**, 27933 (2001).
6. J. G. Williams and J. O. Dickey in *Proceedings of the 13th International Workshop on Laser Ranging, NASA/CP-2003-212248*, ed. R. Noomen, S. Klosko, C. Noll, M. Pearlman, pp. 75-86.
7. E. G. Adelberger, B. R. Heckel and A. E. Nelson, *Ann. Rev. Nucl. Part. Sci.* **53**, 77 (2003).
8. O. Bertolami and J. Páramos, *Phys. Rev.* D **71**, 023521 (2005).
9. C. P. Burgess and J. Cloutier, *Phys. Rev.* D **38**, 2944 (1988).
10. B. Bertotti, P. Farinella and D. Vokrouhlický *Physics of the Solar System*, (Kluwer Academic Press, Dordrecht, 2003).
11. J. Lense and H. Thirring, *Phys. Z.* **19**, 156 (1918)
12. D. D. McCarthy and G. Petit, *IERS Technical Note No. 32. IERS Conventions (2003). 12.* (Verlag des Bundesamtes für Kartographie und Geodäsie, Frankfurt am Main, 2003).
13. M. H. Soffel, *Relativity in Astrometry, Celestial Mechanics and Geodesy*, (Springer, Berlin, 1989).
14. L. Iorio, *Mon. Not. Roy. Astron. Soc.* doi:10.1111/j.1365-2966.2011.18777.x (2011).
15. P. S. Lykawka and T. Mukai, *Astron. J.* **135**, 1161 (2008).
16. J. J. Matese and D. P. Whitmire, *Icarus* **211**, 926 (2011).
17. A. G. Riess, L. Macri, S. Casertano, H. Lampeit, H. C. Ferguson, A. V. Filippenko, S. W. Jha, W. Li, R. Chornock and J. M. Silverman, *Astrophys. J.* **730**, 119 (2011).

Radioscience simulations in General Relativity and in alternative theories of gravity

A. Hees[1,2], P. Wolf[2], B. Lamine[3], S. Reynaud[3], M.T. Jaekel[4], C. Le Poncin-Lafitte[2], V. Lainey[5], A. Füzfa[6], V. Dehant[1]

[1] *Royal Observatory of Belgium, Avenue Circulaire 3, 1180 Bruxelles, Belgium, ahees@oma.be*

[2] *LNE-SYRTE, Observatoire de Paris, CNRS, UPMC, France*

[3] *Laboratoire Kastler Brossel, UPMC, Campus Jussieu, France*

[4] *Laboratoire de Physique Théorique de l'ENS, Paris, France*

[5] *IMCCE, Observatoire de Paris, France*

[6] *naXys, University of Namur (FUNDP), Belgium*

In this communication, we focus on the possibility to test GR with radioscience experiments. We present a new software that in a first step simulates the Range/Doppler signals directly from the space time metric (thus in GR and in alternative theories of gravity). In a second step, a least-squares fit of the involved parameters is performed in GR. This software allows one to get the order of magnitude and the signature of the modifications induced by an alternative theory of gravity on radioscience signals. As examples, we present some simulations for the Cassini mission in Post-Einsteinian gravity and with the MOND External Field Effect.

1 Introduction

There is still a great interest in testing General Relativity (theoretical motivations such as quantification of gravity, unification with other interactions...). Within the solar system, the gravitational observations are always related with radioscience measurements (Range and Doppler) or with angular measurements (position of body in the sky, VLBI). In this communication, we present a new tool that performs simulations of radioscience experiments in General Relativity and in alternative metric theories of gravitation. The developed software simulates Range and Doppler signals directly from the space time metric (and from the initial conditions of the bodies considered). The aim of this tool is to provide orders of magnitude and signatures for the variations of the Range/Doppler induced by alternative theories of gravity. In order to compare signals in different theories, a least-squares fit of the different parameters involved in the problem (mainly the initial conditions) is performed. In this communication, we present the principles of the software and results of simulations of the Cassini probe mission during its cruise from Jupiter to Saturn with Post-Einsteinian modifications of gravity (PEG) [1,2] or with an external field effect due to a MONDian modification of gravity [3].

2 Description of the software

Our software directly generates Doppler/Range signal from the metric considered in a fully-relativistic way. This includes the integration of the equations of motion in a given coordinate time, the computation of the time transfer of light and the clock behavior.

The equations of motion are derived from the metric and the geodesic equations integrated with respect to coordinate time [4].

The connection between the coordinate and proper time of clocks is obtained by integrating the equation of proper time [4]

$$\frac{d\tau}{dt} = \sqrt{g_{00} - 2g_{0i}v_i - g_{ij}v_iv_j} \tag{1}$$

where $g_{\mu\nu}$ is the space-time metric, v_i is the velocity of the clock and τ its proper time.

Finally, the time transfer is also determined directly from the metric using Synge World's function formalism [5]. Within this formalism, one does not need to integrate the photon trajectory in order to get the time transfer or the frequency shift (in the linear approximation). Instead, those quantities are expressed as integrals of functions defined from the metric (and their derivatives) along the photon Minkowski path. For example the coordinate propagation time can be expressed as [5]

$$T(x_e^i(t_e), x_r^i(t_r), t_r) = \frac{R_{er}}{c} + \frac{R_{er}}{c}\int_0^1 f(z^\alpha(\mu))d\mu \tag{2}$$

with

$$f = -h_{00} - 2N_{er}^i h_{0i} - N_{er}^i N_{er}^j h_{ij}, \qquad h_{\mu\nu} = g_{\mu\nu} - \eta_{\mu\nu}, \qquad N_{er}^i = \frac{x_r^i - x_e^i}{R_{er}}, \tag{3}$$

x_e^i, t_e are the position and time of the emitter (computed iteratively assuming flat space time), x_r^i, t_r are the position and time of the receptor and $R_{er} = \|x_e^i(t_e) - x_r^i(t_r)\|$. The integral in (2) is performed over a Minkowski path between emitter and receptor ($z^\alpha(\mu)$ is a straight line). A similar expression is used for the frequency shift.

In order to investigate the observable signatures of an alternative theory of gravity in the Range and Doppler data we perform a least-squares fit in GR on the different parameters (initial conditions and masses of the bodies) and search for identifiable signatures in the residuals. The fit of initial conditions is necessary in order to avoid effects due to the choice of coordinates. As a matter of fact, this fit is always done in practice, which means that a reasonable analysis of the signal produced by an alternative theory has to be done after the fit.

3 Simulations of Cassini mission

As an example, we simulate the two-way range and Doppler signals to the Cassini spacecraft from June 2002 during 3 years (when the probe was between Jupiter and Saturn). To simplify the situation we only consider the Sun, the Earth and Cassini spacecraft.

3.1 Post-Einsteinian Gravity (PEG)

The first alternative metric theory considered is Post-Einsteinian Gravity (PEG) [1,2]. From a phenomenological point of view this theory consists in including two potentials $\Phi_N(r)$ and $\Phi_P(r)$ to the metric. Here we concentrate on the sector $\Phi_P(r)$. We consider a series expansion. That is to say we suppose the spatial part of the metric to be modified as follows

$$g_{ij} = [g_{ij}]_{GR} - 2\delta_{ij}\left(\chi_1 r + \chi_2 r^2 + \delta\gamma\frac{GM}{c^2 r}\right) \tag{4}$$

where r is a radial isotropic coordinate, M is the sun mass, c the velocity of light and G the gravitational constant. The parameter $\delta\gamma$ is related to the post-newtonian parameter $\delta\gamma = \gamma - 1$.

Different simulations were performed with different values of the three PEG parameters. For example, Figure 1 represents the Range and Doppler differences between a simulation in a theory with $\delta\gamma = \gamma - 1 = 10^{-5}$ and in GR. The three peaks occur during solar conjunctions. The signal due to the conjunction is not absorbed at all by the fit of the initial conditions which nevertheless absorbs a large modulations in the range signal.

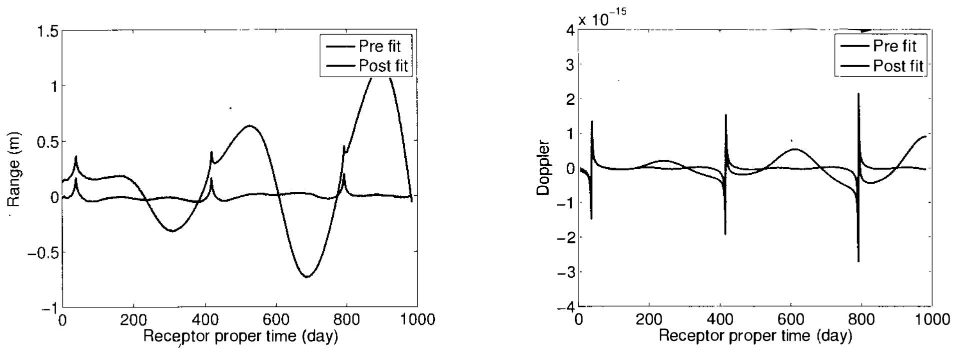

Figure 1: Representation of the Range (on the left) and Doppler (on the right) signals due to an alternative theory with $\gamma - 1 = 10^{-5}$. The blue line is the difference between a simulation in the alternative theory and a simulation in GR (with the same parameters). The green line is the residuals obtained after analyzing the simulated data in GR (which means after the fit of the different parameters).

To summarize, Figure 2 represents the maximal difference between the Doppler generated in PEG theory and the Doppler generated in GR for different PEG theories (characterized by their values of χ_1, χ_2 and $\delta\gamma$). If we request the residuals to be smaller than Cassini Doppler accuracy (roughly 10^{-14}), we get boundary values for the three parameters: $\chi_1 < 5\ 10^{-22} m^{-1}$, $\chi_2 < 2\ 10^{-33} m^{-2}$ and $\gamma - 1 < 3\ 10^{-5}$ (which is very similar to the real estimation[6]).

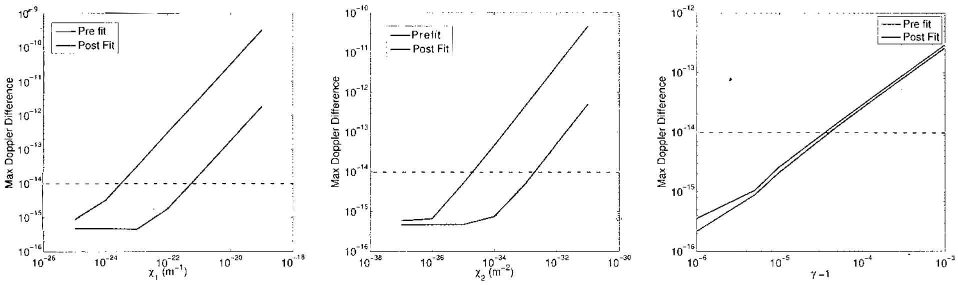

Figure 2: Representation of the maximal Doppler signal due to PEG theory (parametrized by three parameters $\chi_1, \chi_2, \gamma - 1$) for the Cassini mission between Jupiter and Saturn. The blue lines represent the maximal Doppler difference between a simulation in the alternative theory and a simulation in GR (with the same parameters). The green lines represent the maximal residuals obtained after analyzing the simulated data's in GR (i.e. after the fit of the parameters). The read lines represent the assumed Cassini accuracy.

3.2 MOND External Field Effect (EFE)

Another alternative theory considered is the External Field Effect produced by a MOND theory[3]. In this framework, the dominant effect is modeled by a quadrupolar contribution to the Newtonian potential $U = \frac{GM}{r} + \frac{Q_2}{2} x^i x^j \left(e_i e_j - \frac{1}{3}\delta_{ij} \right)$ where e_i is a unitary vector pointing towards the galactic center and $2.1\ 10^{-27} s^{-2} \leq Q_2 \leq 4.1\ 10^{-26} s^{-2}$ is the value of the quadrupole moment whose value depends on the MOND function.

Figure 3 represents the effect of the EFE on the Range and Doppler signals from Cassini. It can be seen that the signal are just below the Cassini accuracy (10^{-14} in Doppler). Therefore, the Cassini arc considered here is not sufficient to provide a good test of MOND External Field Effect.

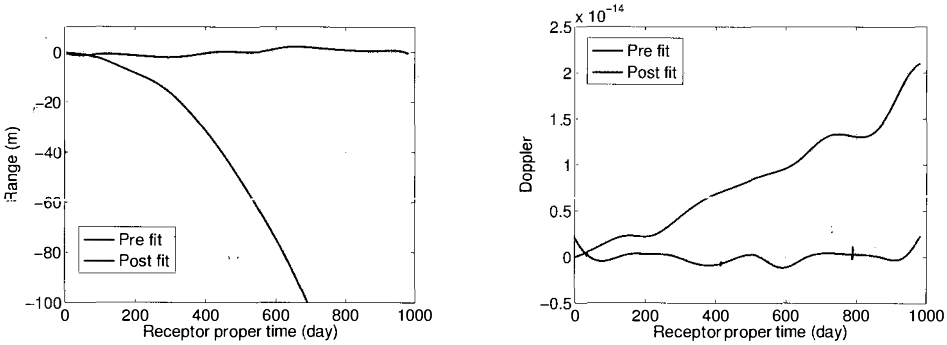

Figure 3: Representation of the Range (on the left) and Doppler (on the right) signals due to the MOND EFE ($Q_2 = 4.1\ 10^{-26}s^{-2}$). The blue line is the difference between a simulation with the EFE and a simulation in GR (with the same parameters). The green line shows the residuals obtained after analyzing the simulated data in GR (which means after the fit of the different parameters).

4 Conclusion

In this communication, we have presented a new tool that performs Range/Doppler simulations in metric theories of gravity. With this software, it is easy to get the order of magnitude and the signature of the modifications induced by alternative theories of gravity on radioscience signals. As an example, we have presented some simulations for the Cassini mission in Post-Einsteinian Gravity and we have derived boundary values for some PEG parameters. We have also presented simulations including the MOND External Field Effect and we have shown that this effect is too small to be detected during the Cassini cruise between Jupiter and Saturn.

In the future, further simulations can be done for other theories and other (future and past) space missions.

Acknowledgments

A. Hees is research fellow from FRS-FNRS (Belgian Fund for Scientific Research). Numerical simulations were made on the local computing ressources (Cluster URBM-SYSDYN) at the University of Namur (FUNDP, Belgium).

References

1. M.T. Jaekel, S. Reynaud *Class. and Quantum Grav.* **22**, 2135 (2005).
2. M.T. Jaekel, S. Reynaud *Class. and Quantum Grav.* **23**, 777 (2006).
3. L. Blanchet, J. Novak *MNRAS* **412**, 2530 (2011).
4. C. Misner, K. Thorne, J. Wheeler *Gravitation*, San Francisco: W. H. Freeman, 1973.
5. P. Teyssandier, C. Le Poncin-Lafitte, *Class. and Quantum Grav.* **25**, 145020 (2008).
6. B. Bertotti, L. Iess, P. Tortora, *Nature* **425**, 374 (2003).

GAME - Gravitation Astrometric Measurement Experiment

M. GAI
INAF - Astronomical Observatory of Torino, 20 V. Osservatorio
10025 Pino Torinese (TO), Italy

The Gravitation Astrometric Measurement Experiment (GAME) is a mission concept based on astronomical techniques (astrometry and coronagraphy) for Fundamental Physics measurements, namely the γ and β parameters of the Parameterized Post-Newtonian formulation of gravitation theories extending the General Relativity. The mission concept, measurement approach and instrument design are briefly described.

1 Introduction

The experiment of Dyson, Eddington and Davidson, whose concept is sketched in the left panel of Fig. 1, gave the first confirmation of Einstein's General Relativity theory by observation of known stellar fields during the May 29th, 1919 eclipse. It measured the apparent positions of a few stars, within a few degrees from the solar limb during the eclipse, compared to their unperturbed relative positions. The arc variation is interpreted in terms of light deflection, providing an estimate of the γ parameter with precision $\sim 10\%$, i.e. to a 10^{-1} accuracy estimation of the PPN γ parameter. Measurements of light deflection from the ground are affected by several shortcomings, as short eclipse duration, high background flux from the solar corona, atmospheric disturbances and the limited number of bright sources in the field, thus limiting the achievable performance independently from foreseeable technological improvements. The current best estimate of γ, from the Cassini experiment, is in the 10^{-5} range[1]. The β parameter was estimated through accurate orbit determination of Solar System bodies [2] which put to evidence the effect of perihelion shift excess, extending the historical case of Mercury.

The main scientific goal of GAME is the estimation of key parameters of the Parametrized Post-Newtonian formalism, commonly used to test the metric theories of gravity in the weak-field regime of the Solar System. The focus is on Eddington's parameters, γ, to a few 10^{-8}, and β, to a few 10^{-6}. The possibility of testing gravity theories to this accuracy has significant implications for our understanding of several physical and astrophysical issues at a very fundamental level. GAME can also provide crucial information on several other issues of Solar system (in particular Near Earth Object orbit determination), extra-solar planetary systems, stellar astrophysics and high angular resolution monitoring of the Corona and circumsolar environment.

2 Science goal: estimation of the PPN γ parameter

The Parametrised Post-Newtonian (PPN) formalism [3] was introduced to classify the metric theories of gravity at their Post-Newtonian level through a set of parameters. The γ parameter

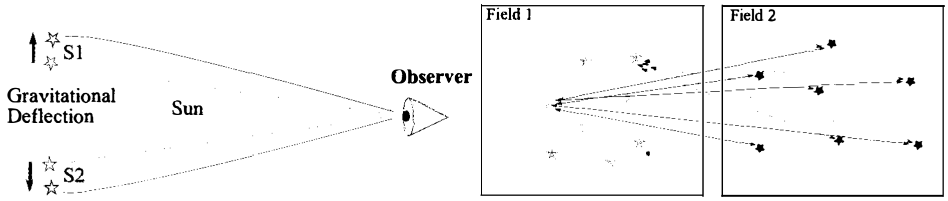

Figure 1: Deflection by the Solar gravitational field of the light rays from stars. The apparent star position is displaced away from the Sun because of the photon path bending (left). On the right, the observable: arcs between stars from each field, whose length is modulated with time, depending on pointing position vs. the Sun.

quantifies the effect of mass on space-time curvature, while β is related to the superposition non-linearity for the gravity fields of different bodies, and in General Relativity (GR) $\gamma = \beta = 1$. However, GR acts as a cosmological attractor for scalar-tensor theories of gravity, with expected deviations on γ in the $10^{-5} - 10^{-7}$ range. Also, observational evidence has been achieved for an accelerated expansion of the Universe at the present time. This was interpreted in the concordance ΛCDM scenario as the effect of a long range perturbation to the gravity of the visible matter, generated by the so-called Dark Energy. Other observations at different scale (e.g. galaxy rotation curves) are explained with non-barionic Dark Matter or some kind of GR modification (e.g. Pioneer anomalies [4]). However, these data might also be explained with a modified version of GR, in which the curvature invariant R in Einstein's equations is no longer constant ($f(R)$ gravity theories). Present experimental data are not accurate enough to discriminate among the options, but this could be done with a $< 10^{-7}$-level measurement of γ [5].

From a phenomenological standpoint, the γ parameter is associated to the light deflection, and it can be shown[6] *that the accuracy on γ is proportional to that on the light deflection, directly related to the measurement precision of the angular separation.*

Light deflection has peak value of $1''\!.74$ at the solar limb, and decreases rapidly at increasing angular distance. Thus, in order to estimate the γ parameter at the 10^{-6} level and beyond, microarcsec (μas) level measurements of relative star positions (Fig. 1, right) are required, at a few degrees from the Sun (Fig. 2, left). Previous simulations showed that the 10^{-7} level of accuracy could be reached within the baseline of this measurement concept, scaled to fit a *small mission* framework [6]. The 10^{-8} accuracy goal of the *medium mission* GAME version [7] comes from improvement factors as the *longer mission duration*, use of *four larger fields of view* labelled North, South, East and West (Fig. 2, right), and an optical configuration which also allows for a *better control of systematic errors*. In addition to the four Sun-ward fields, GAME also observes at the same time four ("outward") fields in the direction opposite to the Sun.

Adoption of a highly symmetrical instrument design mitigates the calibration requirements, as the instrument response is the same, at first order, for all fields. Using the same optical paths and detector, perturbations are expected to act mainly in common mode, reducing their influence on the differential measurement. Observation of selected fields at different epochs modulates the deflection ON (Sun between fields) and OFF (Sun at large distance). The benefits to systematic error control of simultaneous observation of 2 + 2 or 4 + 4 fields are not only related to *increased efficiency*, but above all to *real time compensation of systematic errors* [8].

The superposition can be achieved with techniques similar to those adopted in Hipparcos and Gaia, i.e. a *beam combiner* (BC) folding onto the same detector the images of the two fields. The separation between observing directions, materialised by the BC, is the *base angle* (BA).

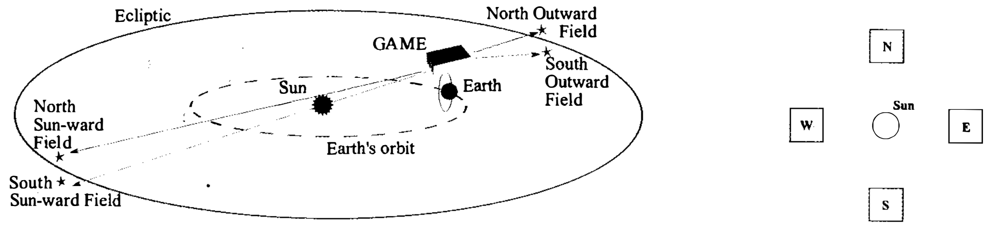

Figure 2: The GAME satellite observing stellar fields close to the Sun and in the opposite direction (left). Nominal position of the four Sun-ward fields (right).

3 The measurement technique and performance

GAME is based on a 1.5 m diameter telescope, with coronagraphic and multiple field beam combination sub-systems. The satellite is oriented with a side always set within 35° to the Sun, thus simplifying the design of payload thermal control and solar panel allocation; the detector radiator is naturally set on the dark side. The telescope is endowed with a pupil mask and a folding mirror for injection of the out-ward field beams. Each sub-aperture acts as a coronagraph for rejection of the Sun disk at the $R \leq 10^{-8}$ level, and of the inner Corona, whereas, with respect to the stellar fields, the set of sub-pupils works as a Fizeau interferometer, feeding the underlying monolithic telescope. The background is limited by the Corona at 2° from the Sun centre, to ~ 9 mag per square arcsec. Suppression of the Sun disk light requires coronagraphic techniques.

GAME observes in step-and-stare mode four fields around the Sun, at radial distance 2° (deflection: $\sim 0''.233$) from the Sun centre, and set at 90° from each other. In addition to the four "Sun-ward" fields, GAME also observes at the same time, and using as much as possible the same parts of the instrument, four "outward" fields with the same relative placement in the direction opposite to the Sun. Subsequent exposures of the superposed fields are taken, to compute the photo-centre location of each star image in deflection ON and OFF epochs. The photo-centre displacement provides an estimate of the angular value of light deflection, which can then be averaged over the star sample. Relaxed requirements are imposed on a priori knowledge of star parameters and on pointing accuracy; accurate reconstruction of attitude and sample astrometry is expected from the data processing.

3.1 Instrument conceptual design and key characteristics

The GAME optical concept is based on Fizeau interferometry, to achieve a convenient trade-off between the angular resolution needed for precision astrometry, and coronagraphic requirements, applied to small apertures achieved by pupil masking on the underlying telescope.

A schematic view of the Sun-ward beam path is shown in the left side of Fig. 3. The Sun beams from PM (dashed lines) are sent out to space through the M1 holes, whereas the stellar beams from two Sun-ward fields (e.g., N and S), shown as dotted and dash-dot lines, are separated by geometric optics. The apertures on M1 also allow photons from star in the outward fields to get into the system, as shown in the right side of Fig. 3. The folding mirror FM between PM and Ml is used to inject the out-ward beams back on Ml and into the telescope. Thus, the out-ward field stars are imaged on the focal plane, superposed to the Sun-ward ones, and using mostly the same optical system, with the only addition of the flat mirror FM.

The aperture geometry is replicated several times, thus providing the desired Fizeau mask on PM, generating images with resolution comparable with the full underlying telescope (image FWHM < 100 mas) for each of the observed fields. The desired *four field instrument, pair-wise symmetric and using as far as possible the same components in common mode*, is thus achieved.

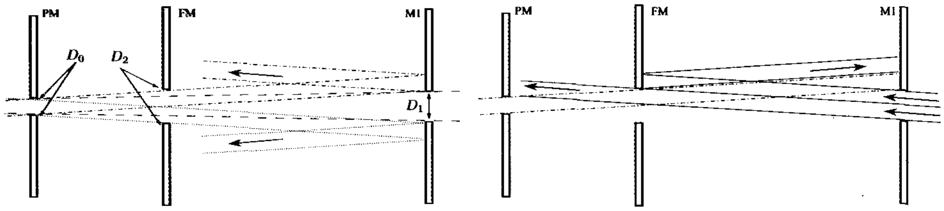

Figure 3: Left panel: Rejection of Sun beam (dashed line) and injection of two Sun-ward field beams (dash-dot and dotted line); right panel: injection of one outward beam (solid line).

3.2 Performance assessment

The measurement scheme of GAME is *fully differential*, since it is based on determination of the variation between epochs of the angular distance between stars in selected fields. The measurement noise performance (random error) depends on the location precision on individual sources, and on the total number of sources. The individual location precision depends on the instrument characteristics, source spectral type and magnitude, and on background level[9].

The expected performance of GAME on γ in terms of noise limit vs. the mission lifetime is $\sigma(\gamma)/\gamma = 2.8 \times 10^{-8}$. The error limit includes a further 30% degradation associated to uncalibrated systematic errors, taking the realistic performance to $\sigma(\gamma)/\gamma = 3.8 \times 10^{-8}$. The performance on β ($\sim 10^{-6}$) and other science topics is estimated in a similar way.

4 Conclusions

The smart combination of modern astrometric and coronagraphic techniques allows the definition of a mission concept able to provide unprecedented results on Fundamental Physics by estimation of the PPN parameters γ and β, respectievly to the 10^{-8} and 10^{-6} range.

1. Bertotti, B., Iess, L., Tortora, P.: A test of general relativity using radio links with the Cassini spacecraft. Nature (London) **425**, 374–376 (2003)
2. Fienga, A., Laskar, J., Morley, T., Manche, H., Kuchynka, P., Le Poncin-Lafitte, C., Budnik, F., Gastineau, M., Somenzi, L.: INPOP08, a 4-D planetary ephemeris: from asteroid and time-scale computations to ESA Mars Express and Venus Express contributions. Astron. Astrophys. **507**, 1675–1686 (2009). DOI 10.1051/0004-6361/200911755
3. Will, C.M.: The confrontation between general relativity and experiment. Living Rev. Relativity **9**(3) (2006). URL http://www.livingreviews.org/lrr-2006-3
4. Leibovitz, J.: Pioneer Anomaly: Artifact or Real Astrophysical Phenomenon of the Solar System. APS Meeting Abstracts pp. 1010–+ (2008)
5. Capozziello, S., Troisi, A.: Parametrized post-Newtonian limit of fourth order gravity inspired by scalar-tensor gravity. Phys. Rev. D **72**(4), 044,022–+ (2005). DOI 10.1103/PhysRevD.72.044022
6. Vecchiato, A., Gai, M., Lattanzi, M.G., Crosta, M., Sozzetti, A.: Gamma astrometric measurement experiment (GAME) – Science case. Adv. Space Res. **44**, 579–587 (2009). DOI 10.1016/j.asr.2009.04.002
7. Gai, M., Vecchiato, A., Ligori, S., Lattanzi, M.G.: Gravitation Astrometric Measurement Experiment. Exp. Astron. [Submitted] (2011).
8. Gai, M.: Sistematic error mitigation in multiple field astrometry. Mon. Not. R. Astron. Soc. [Submitted] (2011).
9. Gai, M., Casertano, S., Carollo, D., Lattanzi, M.G.: Location Estimators for Interferometric Fringes. Pub. Astr. Soc. Pac. **110**, 848–862 (1998). DOI 10.1086/316202

A RELATIVISTIC AND AUTONOMOUS NAVIGATION SATELLITE SYSTEM

P. DELVA
SYRTE, Observatoire de Paris, CNRS and UPMC,
61 avenue de l'Observatoire, F-75014 Paris, France

A. ČADEŽ, U. KOSTIĆ
Department of Physics, University of Ljubljana
Jadranska 19, 1000 Ljubljana, Slovenia

S. CARLONI
ESA Advanced Concepts Team, ESTEC, DG-PI
Keplerlaan 1, 2201 AZ Noordwijk, The Netherlands

A relativistic positioning system has been proposed by Bartolomé Coll in 2002. Since then, several group developed this topic with different approaches. I will present a work done in collaboration with Ljubljana University and the ESA Advanced Concepts Team. We developed a concept, Autonomous Basis of Coordinates, in order to take advantage of the full autonomy of a satellite constellation for navigation and positioning, by means of satellite inter-links. I will present the advantages of this new paradigm and a number of potential application for reference systems, geophysics and relativistic gravitation.

1 Relativistic Positioning Systems (RPS)

The first proposal for a relativistic positioning system is SYPOR ("Système de Positionnement Relativiste"), proposed by Bartolomé Coll in 2002 [1]. It is an alternative to the scheme of usual positioning systems. The idea is to give the constellation of satellites the possibility to constitute by itself a *primary* and *autonomous* positioning system, without any *a priori* realization of a terrestrial reference frame.

The relativistic positioning system is defined with the introduction of *emission coordinates*, which contain dynamical information of the satellite constellation. They have been reintroduced recently by several articles [2,3,4,5]. The definition of these coordinates is rather simple, but they are a very powerful tool in general relativity. Let us define four particles $a = 1, 2, 3, 4$ coupled to general relativity. Along their worldlines C_a, one defines four one-parameter families of future null cones $N_a(\tau^a)$ which are parametrized by proper time. The intersection of four future null cones $N_a(\tau^a)$ from four worldlines $\mathcal{C}_a$ defines an event with emission coordinates $(\tau^1, \tau^2, \tau^3, \tau^4)$. Then, a user receiving four electromagnetic signals broadcasting the proper time of four satellites knows its position in this particular coordinate system.

RPS have been studied with different approaches these last years [6,7,8,9,10,11,12,13,14,15,16,17,18,19,20,21] The purpose of this proceeding is to present an approach developed by a collaboration between the Advanced Concepts Team of the European Space Agency, the department of physics of Ljubljana University and SYRTE/Paris Observatory/UPMC.

2 From emission to global coordinates

A GNSS is a system of satellites emitting precise timing signals for the purpose of providing a local coordinate basis in space-time. In order to determine his space-time position with respect to this basis, an observer must receive four proper times emitted by four different satellites, and be able to calculate the local coordinates of the four satellites as a function of their emission coordinates.

We studied the use of emission coordinates theoretically and in practical scenarii by numerical simulations [16,20,21]. We provided mathematical tools to translate emission coordinates into space-time coordinates of the observer. A local Schwarzschild coordinate system was introduced as an idealized prototype of space-time in the vicinity of the Earth. The problem of connecting the local Schwarzschild frame to the global inertial frame is well understood in the framework of classical non-relativistic gravitational perturbation theory, but remains to be done in a general relativistic framework.

Analytic solutions for light-like and time-like geodesics were obtained in order to implement two algorithms: (i) an algorithm that calculates emission coordinates corresponding to the local Schwarzschild coordinates of a user, and (ii) the "reverse" algorithm that calculates space-time coordinates of a user from its emission coordinates. In a first approach, we assumed that orbital parameters of satellites are known. We have shown that the use of a fully relativistic code in GNSS offers a very promising alternative to the use of post-Newtonian approximations, and presents no technical obstacle.

The effects of non-gravitational perturbations have been studied. We have shown that the only yardstick of a GNSS is the clock, which provides absolute position both in space and time to any accuracy and stability allowed by noise and clock drifts. Clock drifts, adding up after some time, would result in considerable error in absolute position in space if the the clocks were not controlled. In current positioning scheme, correcting the clocks needs a constant monitoring of the satellites via Earth telemetry and the precise realization of a terrestrial reference frame. However, we realized that a GNSS constellation is also a very precise clock of its own, since orbital periods of its satellites are accurate constants of motion. Therefore, we proposed to use the dynamical information given by mutual timing between satellites to improve the long term phase stability of onboard clocks, as well as to improve the precision of constants of motion of the constellation. This proposal led us to define the concept of Autonomous Basis of Coordinates (ABC). Within such a scheme, we have shown that it is possible to correct the clocks to a level considerably surpassing the classical scheme, which is limited in accuracy by stochastic components of Earth dynamics.

3 Autonomous Basis of Coordinates (ABC)

In a GNSS constellation with more than four satellites, more than four emission coordinates are received by an observer: the positioning problem is over-determined. In order for the local basis to be self consistent, all combinations of emission coordinates, received at any event in space-time, must give the same four local coordinates for this event. The main constraint on self-consistency of a GNSS system comes from the precision of constants of motion. In order to adress this problem, the concept of Autonomous Basis of Coordinates (ABC) is introduced in Čadež *et al.* [20]. We propose that the constants of motion be determined and checked internally by the GNSS system in such a way that each satellite checks its own position as any other observer with respect to all the other satellites: in addition to emitting its proper time, each satellite also receives other satellite's emission coordinates and makes its information available to the central GNSS control [22,23].

The ABC concept aims to describe in a coherent frame both the dynamics of non-interacting test bodies transmitting emission coordinates and the propagation of electromagnetic waves providing those coordinates. It uses the fact that both light and test bodies trajectories are geodesics that can be derived from the same Hamiltonian. It provides a means to translate dynamical information into the conventional representation based on local frames. Dynamical information, expressed in terms of emission coordinates, gives direct information about the Riemannian structure of space-time, and thus allows the construction of a local frame with coordinates and metric that provides a precise definition of equations of motion. We call the reference system and coordinates built via the ABC concept the *ABC reference system* and the *ABC coordinates*.

Let us use the nomenclature introduced by J. Kovalevsky and I. Mueller [24] to describe the ABC reference system:

Concept: the ABC coordinate system is built such that dynamics is consistent; dynamics is given by a Hamiltonian, that both describe space-time geometry and non-gravitational forces.

Physical structure: the reference system is physically materialized by a constellation of satellites in Earth orbit and inter-satellite links. Light and satellite geodesics create a physical space-time web that probe the space-time geometry.

Modelling: the model characterizes a particular choice of the Hamiltonian. We have studied three particular Hamiltonians [20]: Minkowski, Kepler and Schwarzschild. The ultimate goal is to obtain a Hamiltionian containing a complete description of all known gravitational and non-gravitational perturbations. This is the purpose of the Slovenian PECS/ESA project: "Relativistic global navigation system" [a].

Realization: A realization of the reference system needs the implementation on future GNSS constellation of inter-satellite links, which is now under study [22,23]. We have done a simulation [16,20,21] for some specific idealized space-time geometries and have discovered some generic properties of ABC systems, as robustness of recovering constants of motion with respect to noise in the data, consistency of description with redundant number of satellites, the possibility to use the constellation as a clock with long term stability and the possibility to use perturbation theory to refine the Hamiltonian toward a better long term dynamical prediction. For example, we have shown an internal consistency of Galileo satellites positions at the millimetre level after only four orbits ($\sim$ 36 hours) with 200 data points (one point every 10 mn). The accuracy of constants of motion is expected to increase with time, when more data will become available to evaluate smaller and smaller discrepancies between dynamic prediction and dynamic observations provided by exchange of emission coordinates between satellites.

4 Applications in geophysics and relativistic gravimetry

Dynamics of bodies and light in a given space-time is unique to the geometry of this space-time. Therefore, geometry can in principle be determined on the basis of dynamical information and vice versa, dynamics can be predicted with an accuracy limited, in principle, only by the accuracy of geometric information. Thus the GNSS with inter-satellite links is a new type of gravimeter, we call it *Riemannian gravimeter*, that creates a space-time web with light and satellite geodesics that "scan" the space-time geometry around Earth.

The accuracy of an ABC reference system, realized with Galileo satellites, would increase with the accuracy of geometric information derived from dynamics. However, the relation of such an ABC reference system to a celestial reference system is not trivial, since the ABC reference system is gauged with the local geometry of the part of space-time where satellites move, while signals from distant quasars travel long distances accross the universe and are affected by the intervening curvature of spacetime. Thus, the relation between the ABC reference frame and a

[a] `http://www.esa.int/SPECIALS/PECS/index.html`

celestial reference frame could, in principle, reveal important new information about the way in which the local geometry is integrated into the global arena of space-time. A discrepancy between the two frames could also reveal a violation of the equivalence principle, if non-gravitational perturbations as solar pressure can be modelled or measured accurately.

The possibility to define an extremely precise ABC reference frame is also very interesting for geophysics. A sub-millimetre level of accuracy of satellite positions would eventualy allow comparable position accuracy on Earth surface, at least statistically, by properly averaging positions obtained by ground based GNSS receivers. Below millimetre level of accuracy, the shape of Earth and absolute positions of markers on the ground would certainly elucidate many important phenomena about our planet Earth. For example, a much deeper understanding of interior structure of the Earth could be reached by studying Earth and ocean tides. Continental drift would be measured with a precision, that could possibly be sufficient to model changing strain and stress in the Earth crust and eventually lead to earthquake prediction. Gravitational potential differences and driving ocean currents could also be detected, allowing us to study ocean dynamics at the same level of precision as todays meteorology understands dynamics of atmosphere.

References

1. B. Coll, in N. Capitaine and M. Stavinschi, eds., *Journées 2002 - systèmes de référence spatio-temporels. Astrometry from ground and from space, Bucharest, 25 - 28 September 2002* **14**, 34 (2003).
2. B. Coll and J. A. Morales, *Journal of Mathematical Physics* **32**, 9 2450 (1991).
3. C. Rovelli, *Phys. Rev. D* **65**, 4 044017 (2002).
4. M. Blagojević *et al.*, *Phys. Rev. D* **65**, 4 044018 (2002).
5. M. Lachièze-Rey, *Class. Quantum Grav.* **23**, 10 3531 (2006).
6. T. B. Bahder, *Am. J. Phys.* **69** 315 (2001).
7. B. Coll and A. Tarantola, poster at JSR 2003, "Astrometry, Geodynamics and Solar System Dynamics: from milliarcseconds to microarcseconds", St. Petersburg, September 22 - 25, 2003 (2003), URL `http://syrte.obspm.fr/~coll/`.
8. B. Coll *et al.*, *Phys. Rev. D* **73**, 8 084017 (2006).
9. B. Coll *et al.*, *Phys. Rev. D* **74**, 10 104003 (2006).
10. J.-F. Pascual-Sánchez, *Ann. Phys. (Leipzig)* **16** 258 (2007).
11. M. L. Ruggiero and A. Tartaglia, *Int. J. Mod. Phys. D* **17** 311 (2008).
12. D. Bini *et al.*, *Class. Quantum Grav.* **25**, 20 205011 (2008).
13. A. Tarantola *et al.*, *ArXiv e-prints* (2009).
14. B. Coll *et al.*, *Phys. Rev. D* **80**, 6 064038 (2009).
15. A. Tartaglia, *Acta Astronautica* **67** 539 (2010).
16. A. Čadež *et al.*, Mapping the Spacetime Metric with a Global Navigation Satellite System - Final Report, Tech. rep., Advanced Concepts Team, European Space Agency (2010).
17. B. Coll *et al.*, *Classical and Quantum Gravity* **27**, 6 065013 (2010).
18. B. Coll *et al.*, *Phys. Rev. D* **82**, 8 084038 (2010).
19. A. Tartaglia *et al.*, *Advances in Space Research* **47** 645 (2011).
20. A. Čadež *et al.*, Mapping the Spacetime Metric with a Global Navigation Satellite System - Extension of study: Recovering of orbital constants using inter-satellites links, Tech. rep., Advanced Concepts Team, European Space Agency (2011).
21. P. Delva *et al.*, *Advances in Space Research* **47** 370 (2011).
22. I. Rodríguez-Pérez *et al.*, *Advances in Space Research* **47** 197 (2011).
23. L. Arona *et al.*, GNSSPLUS, Final Report. GNSSPLUS-DMS-TEC-FIR01-11-E-R (2006).
24. J. Kovalevsky *et al.*, eds., *Reference frames in astronomy and geophysics*, **154** (1989).

OPTICAL CLOCK AND DRAG-FREE REQUIREMENTS FOR A SHAPIRO TIME-DELAY MISSION

N. ASHBY[1] & P. BENDER[2]
[1] *University of Colorado, Boulder, CO*
[2] *JILA, University of Colorado, Boulder, CO*

In the next decade or two, extremely accurate tests of general relativity under extreme conditions are expected from gravitational wave observations of binary black hole mergers with a wide range of mass ratios. In addition, major improvements are planned in both strong and weak equivalence principle tests; clock measurements based on the ACES program on the ISS; more accurate light-bending measurements; and other new types of tests. However, whether these tests are all consistent with general relativity or not, it still appears desirable to proceed with a much improved measurement of the Shapiro time delay. A suggested approach[1] is based on using a high-quality optical clock in a drag-free spacecraft near the sun-earth L1 point and a smaller drag-free transponder spacecraft in a two-year period solar orbit. Laser phase travel-time measurements would be made between the two spacecraft over a period of 10 or 20 days around the time when the line of sight passes through the Sun. The requirements on the optical clock stability and on the drag-free systems will be discussed. The accuracy achievable for the time-delay appears to be better than 1 part in 100 million.

1 Introduction

The first suggestion to measure the gravitational time delay for electromagnetic waves passing near the sun was made by Irwin I. Shapiro in 1964.[2] The extra gravitational time delay for two-way measurements of light propagating from Earth to a spacecraft passing behind the Sun can be more than 200 microseconds. In the Parametrized Post-Newtonian (PPN) formulation of gravitational theory, the main contribution to the time delay is proportional to $(1+\gamma)$, where γ is a measure of the curvature of space. In General Relativity (GR), $\gamma = 1$.

In view of the well-known lack of a theory that connects GR with quantum theory, improvement of high-accuracy tests of the predictions of GR should be the object of research in the coming decade. Many alternatives to GR involve additional scalar fields. Studies of the evolution of scalar fields in the matter-dominated era of the universe indicate that the universe's expansion tends to drive the scalar fields toward a state in which the scalar-tensor theory is only slightly different from GR. Some scalar-tensor extensions of GR[3,4] predict deviations from the GR value of γ in the range from 10^{-5} to 10^{-8}. Improved information about γ would provide important insight into the evolution of the universe and directly limit the range of applicabilituy of alternative gravitational theories.

Recently, a measurement of γ with accuracy $\pm 2.3 \times 10^{-5}$ was made during the Cassini mission.[5] Further improvements in the accuracy for γ to roughly 10^{-6} are expected from two missions of the European Space Agency (ESA): the GAIA astrometric mission, which will measure the gravitational deflection of light rays by the sun, and the Bepi Colombo mission to

Mercury, which will make improved measurements of the solar time delay. We describe here a mission[1,6,7] that can reach an accuracy of about 1×10^{-8} for determining γ.

2 Mission orbits and predicted time delay

For the proposed mission, one spacecraft (S1) containing a highly stable optical clock would be placed in an orbit near the L1 point, about 1.5 million km from the Earth in the direction of the Sun. The second spacecraft (S2) would have a 2 year period orbit in the ecliptic plane, with an eccentricity of 0.37. S2 would pass through superior solar conjunction about 1, 3, and 5 years after launch and would be near aphelion at those times. Both spacecraft would have drag-free systems to nearly eliminate the effects of spurious non-gravitational forces. A measurement of γ to a level of 1×10^{-8} would be carried out by observing the time delay of laser signals exchanged between the two spacecraft when the line of sight passes near the Sun's limb. Atmospheric effects would be absent and continuous observation would be possible. With S2 near aphelion, the range rate would be low, and the orbit determination problem would be much reduced.

The crucial measurements of time delay occur within a few days of superior conjunction and are primarily characterized by a logarithmic dependence on the distance of closest approach of the light to the mass source. The predicted gravitational time delay due to a non-rotating mass source, expressed in terms of the radii r_A, r_B of the endpoints of the photon path, and the elongation angle Φ between the radius vectors from the source to the endpoints, is[8]

$$c\Delta t_{delay} = \mu(1+\gamma)\log\left(\frac{r_A + r_B + r_{AB}}{r_A + r_B - r_{AB}}\right) - \frac{\mu^2(1+\gamma)^2 r_{AB}}{r_A r_B(1+\cos\Phi)} + \frac{\mu^2 r_{AB}(8 - 4\beta + 8\gamma + 3\epsilon)}{4 r_A r_B \sin\Phi} \tag{1}$$

where $\mu = GM_{\odot}/c^2$, and r_{AB} is the geometric distance between the endpoints in isotropic coordinates and β and ϵ are PPN parameters measuring the nonlinearity of the time-time and space-space components of the metric tensor. In GR, $(8 - 4\beta + 8\gamma + 3\epsilon)/4 = 15/4$. The time delay in Eq. (1) is expressed in terms of observable quantities, and does not involve the unknown impact parameter or distance of closest approach. The non-linear terms are a few nanoseconds so they are significant, but do not have to be estimated with great accuracy. The contributions to time delay due to the solar quadrupole moment are small and can be estimated with sufficient accuracy that they will not contribute significantly to the error budget.

The measurements will be made by transmitting a laser beam with roughly 40 GHz sidebands on it from from S1 to S2, and comparing with a similar beam generated on S2 and sent back to S1. From the phase differences of the sideband beat notes, the round-trip delay time can be obtained. With 20 cm diameter telescopes, and given the one-way travel time of about 1600 s, the received signal would be roughly 1000 counts/s for 1 W of transmitted power. This is a weak signal, but it is strong enough so that the chances of a cycle slip should be very small. If we consider the round-trip delay times Δt_{delay} to be the observable, then the change in delay from 0.75 days to 4 days on either side of conjunction is about 64 microseconds.

3 Signal-to-Noise Analysis

We can estimate the lowest possible uncertainty that could be attained in this experiment on the basis of the optimal Wiener filter, which takes advantage of the known time signature of the signal and includes the expected clock noise.[1,7,9] For this case, uncertainties in the various orbit parameters for the two spacecraft are ignored, and the travel time between the spacecraft is assumed to be constant except for changes in the gravitational time delay. The time signature of $\gamma^* = (1+\gamma)/2$ is taken to be represented by the logarithmic function

$$g(t) = -B(\log|Rt| - M) \tag{2}$$

where M is the mean value of $\log|Rt|$ over the time periods $-t_2$ to $-t_1$ and t_1 to t_2 (a short time interval during occultation is excluded), and for the proposed experiment $B = 0.97 \times 8\mu/c = 3.82 \times 10^{-5}$ s. The rate at which the line of sight to the distant spacecraft passes across the sun is $R = 1.9$ solar radii per day.

Let $g(f)$ be the Fourier transform of $g(t)$ over the time of the measurements. Then the signal-to-noise ratio may be found [1,7,9] in terms of an integral over all frequencies of $|g(f)|^2$. An important consequence of the logarithmic form of the time delay, Eq. (2), is that if the noise has a constant spectral density, only about 2.5% of the signal-to-noise ratio comes from frequencies below 1 microHz, where the acceleration and clock noise are expected to increase. Just integrating down to 1 microHz, we find an uncertainty less than 1×10^{-9} for γ. Almost all of the power in $|g(f)|^2$ is at frequencies between 1 and 8 microHz, so it is clear that the noise at these low frequencies will provide the main limitation on the results.

Actually, all of the in-plane parameters for the orbits of the two spacecraft have to be solved for, as well as γ. Our model for this includes uncorrelated 0.02 picosecond uncertainties for measurements of the round-trip travel time over 3-hr periods. This is in addition to our assumed white clock frequency noise of $5 \times 10^{-15}/\sqrt{\text{Hz}}$ down to at least 1 microHz. Spurious acceleration noise is not included in this model, but its effect has been estimated to be small with our assumptions about its spectrum. The resulting uncertainty in γ is less than 1×10^{-8}.

So far, we have assumed that time-delay measurements are only made over a total period of 8 days around solar conjunction. This was done in order to make sure that spurious acceleration noise at frequencies below 1 microHz would have little effect. However, simulations for longer observing times are desirable, with full allowance for spurious acceleration noise at the lowest frequencies, as well as for the orbit determination part of the problem. The longer observation period may help to improve the determination of orbit parameters as well as γ.

4 Spacecraft S1 clock

The major requirement for the mission is to fly an optical clock on S1 that has very high stability over a period of at least 8 days around superior conjunction. The nominal design goal for the mission is to achieve a fractional frequency noise power spectral density amplitude of $5 \times 10^{-15}/\sqrt{\text{Hz}}$ from 1 Hz down to at least 1 microHz. (This is nearly equivalent to an Allan deviation of $5 \times 10^{-15}/\sqrt{\tau}$ for times from 1 s up to 10^6 s.)

As an example of the desired performance, a spectral amplitude of about $2 \times 10^{-15}/\sqrt{\text{Hz}}$ has been achieved in the laboratory down to 1 mHz for the 267 nm transition in sympathetically-cooled Al^+ ions in a magnetic trap.[10] Other leading candidates for optical clocks in space are cooled Sr^{88} atoms[11,12] and Yb^{171} atoms[13,14] in optical latices. However, substantial development is needed to show that such optical clocks can be designed for use in space and can be space qualified.

5 Drag-free system

The required performance builds on that planned for the LISA mission. For frequencies down to 10^{-4} Hz for LISA, the requirement on the acceleration power spectral density amplitude is less than $3 \times 10^{-15}\text{m/s}^2/\sqrt{\text{Hz}}$. However, the performance is expected to degrade at lower frequencies. The main challenge for achieving good performance at low frequencies is minimizing thermal changes, and particularly thermal gradient changes, near the freely floating test mass in the drag-free system. On LISA this is done almost completely by passive thermal isolation. For a time delay mission, a fairly slow active temperature control system would be used at frequencies below 10^{-4} Hz. Changes in solar heat input over the 8 days around conjunction would be quite small for S2, because conjunction occurs near aphelion. The required drag-free performance is roughly $1 \times 10^{-13} m/s^2/\sqrt{Hz}$ down to 1 microHz.

In fact, much of the desired freedom from spurious accelerations needed for LISA has been demonstrated in the laboratory with torsion pendulum measurements.[15] But, more important, the overall performance of the drag-free system will be demonstrated in the LISA Pathfinder Mission, which is scheduled for launch by ESA in 2014.[16,17]

6 Other scientific benefits from the mission

Additional effects such as those arising from non-linear terms in the 00-component of the metric tensor, parameterized by β, as well as other time delay effects originating in the sun's rotation, can also be measured. The clock at the L1 point will experience frequency shifts from the earth's potential, solar tidal effects, and second-order Doppler shifts. Relative to a reference on earth's surface, the fractional frequency shift is about $+6.9 \times 10^{-10}$, and is almost all gravitational. Comparing the clock at L1 with a similar clock on earth's geoid will give accuracies of a few parts per million in a few hours, which is orders of magnitude more accurate than the Vessot-Levine 1976 Gravity Probe A result. This result is comparable to that expected from the upcoming ACES mission.[18]

7 Postscript

After the Moriond Meeting we learned about proposals[19,20] for a mission called ASTROD I, with improved measurement of the gravitational time delay as one of its main objectives. In the proposed mission, the time delay measurements would be made between a drag-free spacecraft in a solar orbit with a semi-major axis of about 0.6 AU and laser ranging stations on the Earth. The projected accuracy for determining the PPN parameter gamma is 3×10^{-8}.

In these papers the drag-free requirement is given explicitly only over the frequency range from 0.0001 to 0.1 Hz, and is 3×10^{-14} m/s$^2/\sqrt{Hz}$ at 0.0001 Hz. And the only clock frequency stability requirements given are 1×10^{-14} for the clock in the satellite by comparison with ground clocks and 6×10^{-14} stability in the round-trip travel time of roughly 1700 s. However, to reach the accuracy goal given for gamma appears to require low levels of spurious acceleration noise and clock noise down to about 1 microHz or lower. Thus it seems possible that quite low spurious acceleration and clock noise levels at low frequencies actually were implemented in the simulations on which the ASTROD I accuracy goals are based.

References

1. Ashby, N. *et al.*, in: S. A. Klioner, P. K. Seidelmann, & M. H. Soffel, (eds.), *Proc. IAU Symp 261, Relativity in Fundamental Astronomy*, (Cambridge) 414-419 (2010).
2. Shapiro, I. I., *Phys. Rev. Letts.* 13, 789-91 (1964).
3. Damour, T., & Nordtvedt, K., *Phys. Rev.* D48, 3436 (1993).
4. Damour, T., & Esposito-Farese, G., *Phys. Rev.* D54, 5541 (1996).
5. Bertotti, B., Iess, L., & Tortora, P., *Nature*, 425, 374 (2003).
6. Bender, P., *et al.*, in: *Quantum to Cosmos III Workshop*, Warrenton, VA, July 6-10 (2008).
7. Ashby, N., & Bender, P., 2008, in: H. Dittus, C. Laemmerzahl, & S. Turyshev, (eds.), *Lasers, Clocks, and Drag-Free Control*, Bremen, Germany, June 2005 Astrophysics and Space Science Library 349, (Springer) 219-230, (2008).
8. Ashby, N., & Bertotti, B., Accurate light-time correction due to a gravitating mass, *Class. & Quantum Grav.* 26(9), 094001 (2009)

9. Thorne, K. S., Ch. 9 in: S. W. Hawking and W. Israel, (eds.) *300 Years of Gravitation* (Cambridge University Press) 330-459 (1987).
10. Chou, C. W., *et al., Phys. Rev. Letts.* 104,070802 (2010).
11. Swallows, M. D., *et al., Science* 331, 1043-1046 (2011).
12. Ludlow, A. D., *et al., Science* 319, 1805 (2008).
13. Lemke, N. *et al., Phys. Rev. Letts.* 103, 063001 (2009).
14. Jiang, Y.Y., *et al., Nature Photonics* 5, 158 (2011). :L
15. Carbone, L., *et al., Phys. Rev.* D75(4), 042001 (2007).
16. Antonucci, F., *et al., Class. & Quantum Grav.* 28, 094001 (2011).
17. Antonucci, F., *et al., Class. & Quantum Grav.* 28, 094002 (2011).
18. R. Much *et al., Status of the ACES mission* Proc. EFTF Conf. Besançon, 20-24 April, 199-204 (2009).
19. Appourchaux, T., *et al., Exp. Astron.* 23, 491-527 (2009).
20. Braxmaier, C., *et al., arXiv:*1104.0060 (2011).

8.
Long range gravity

Probing the dark energy nature with type Ia supernovae : cosmological constraints from the Supernova Legacy Survey first 3-years

D. Hardin
(on behalf of the SNLS experiment)
LPNHE, Université Pierre et Marie Curie, Université Paris Diderot, CNRS-IN2P3. 4 place Jussieu, 75252 Paris Cedex 05, France

We present the recent cosmology results from the Supernova Legacy Survey (SNLS). Complementing the 242 high redshift type Ia supernovae sample from the first 3 years of the Supernova Legacy Survey with other mostly nearby supernovae samples, we measure a dark energy equation of state parameter w parameter consistent with a cosmological constant. The sytematic uncertainties we fully take into account are approximately equal to the statistical uncertainties. Combining the supernovae data with WMAP7 CMB and SDSS BAO measurements, we obtain a most precise measurement of the dark energy equation of state $w = -1.068$ with a precision of 0.08.

1 Introduction

The first evidence for the universe expansion acceleration was provided at the very end of last century [1,2a]. By using a few dozens of type Ia supernovae as standardized candles, discovered and monitored with CCDs camera on 4-m class telescope, the Supernova Cosmology Project and the High Z Team found that the universe expansion had stop decelerating 5 Gyr ago.

Since then, other cosmological probes — the cosmic microwave background (CMB) temperature fluctuations, the baryon acoustic oscillations (BAO) imprinted in the galaxies spatial distribution, weak gravitational lensing mapping dark matter clustering etc. — have provided new evidence for the presence of a dark energy component opposing gravity and accounting for 75% of the total universe energy density. The physical origin of cosmic acceleration remains though a deep mystery.

In the last decade, new generation supernova surveys have brought improvements in the quantity and the homogeneity of the supernova sample. The supernovae evidence for acceleration has been strengthed. Combining the different cosmological probes, it is now possible to adress the question of the dark energy nature, by measuring its equation of state parameter : $w = p_X/\rho_X$.

With the substantial increase up to $\sim$ 1000 SNeIa distance measurements and the consequent reduction of statistical errors, sytematics errors have become the limiting factor and as such the key issue.

The Supernovae Legacy Survey is a 5 year program which goal is to measure the dark energy equation equation of state w in combination with other measurements to better than 0.10, paying special attention to include and limit thoroughly any systematics effects.

[a] See e.g. (Frieman, 2009)[3] for a review.

2 Expansion history and the universe content

In an expanding isotropic and homogeneous universe, distances between galaxies at rest scale as $d \propto a(t)$. In such an expanding universe, light emitted by one observer at time t and observed by another at later time t_0 is observed to be redshifted, by a factor $1 + z = \lambda(t_0)/\lambda(t) = a(t_0)/a(t)$, directly related to the scale factor $a(t)$. The expansion dynamics is governed through the Einstein equations by the universe energy content. Matter, with a present day reduced density $\Omega_M = \rho_M(t_0)/\rho_{crit}(t_0)$ – the critical density corresponds to a flat geometry for the universe — decelerates the universe expansion. If the expansion is accelerating, one of the simplest explanation is the existence of a second energy component, a perfect fluid X, with a repulsive equation of state $w = p_X/\rho_X < -1/3$ and a corresponding reduced density Ω_X : the dark energy. Mapping the expansion history $a(t)$ thus yields measurements of the cosmological parameters Ω_M, Ω_X, and w.

The nature of the dark energy remains enigmatic. It could be a constant energy component, such as the cosmological constant Λ originally postulated by Einstein, or, formally equivalent, the vacuum energy of particle physics, in these cases $w = -1$. Another possibility is that the dark energy be a dynamical fluid, whith a time variating equation of state $w(z)$ – or $w(a)$. An alternative explanation would require to modify the General Relativity at cosmologically large scales, or invoke inhomogeneities inducing apparent acceleration (the "back-reaction").

3 Type Ia supernovae : standard candles as cosmological probes

For an object of intrinsic luminosity L, the flux f measured by the observer defines the luminosity distance in term of the usual inverse square law : $f = L/(4\pi d_L^2)$. The dependency of d_L on the redshift z (the Hubble diagram) is related to the integrated expansion history, and as such to the energy content of the universe and the aforementionned cosmological parameters :

$$d_L \equiv \sqrt{f/4\pi L} = cz/H_0 \times \mathcal{D}(z; \Omega_M, \Omega_X, w) \tag{1}$$

As one measure fluxes and not luminosities, the use of standard candles is of particular importance. With these objects of fixed luminosity L, one can measure relative distances. and thus be able to constrain the cosmological parameters without having to know the luminosity L, nor the Hubble constant H_0 values.

Type Ia supernovae (SNe) are cosmic explosions that display an impressive homogeneity. These rare (1 per galaxy per millenium) and bright events, observable at cosmological distances, are thought to arise from the explosion of a white dwarf accreting matter from a companion and reaching the stability Chandrasekhar mass limit. The companion could be an evolved main sequence star, a red giant or a white dwarf. They are easily identified using spectroscopy, as they exhibit strong absorption features at the time of their peak luminosity.

With a 40% dispersion of their peak luminosity measured in the Johnson B band, they qualify as standard candles. But they do however exhibit a correlation bewteen their peak luminosity and the time evolution behaviour of their lightcurve and also with their restframe colors. By taking into account these empirical relations — acknowledged as the brighter-slower and the brighter-bluer relations —, the observed dispersion is reduced to ~10%. This results in a dispersion of ~5% for the estimated distance : they are standardized candles.

In order to estimate the cosmological parameters, we will be comparing the restframe peak fluxes (e.g. in the restframe Johnson B band) of SNe Ia exploding at different redshifts (Eq. 1). This requires to observe them in different filters, which intercalibration must then be precisely known. To evaluate the restframe Johnson B band value at peak, one needs to interpolate the fluxes measurement between several different filters and also at different dates : for this we use a time dependent spectrophometric model of the SN Ia emission, $\phi(\lambda, t)$, that we construct empirically using spectrophometric data of nearby and distant SNe Ia.

The relationship between distance d, flux f and luminosity L translates simply in the logarithmic scales of the magnitudes, involving the corresponding quantities of distance modulus μ, apparent magnitude m and absolute magnitude $\mathcal{M}$:

$$\mu = m_B^\star - \mathcal{M}, \quad \mathcal{M} = M_B - \alpha \times \mathit{shape} + \beta \times \mathit{color} \tag{2}$$

For each SN are estimated the three quantities $m_B^\star$, corresponding to the peak B flux, the *shape* of its lightcurve, and its *color* at peak. The absolute magnitude of the SN is parametrized so that M_B (fully degenerated with H_0[b]) corresponds to the luminosity of the (*shape*=0, *color*=0) standard SN Ia, and α and β empirically account for the linear corrections corresponding respectively to the brighter-slower and the brighter-bluer relations. The cosmological parameters are evaluated through a χ^2 fit where μ is compared to its predicted value $\mu_{\mathrm{cosmo}}(z; \vec{\theta})$, $\vec{\theta}$ beeing the parameters describing the cosmological model. M_B, α and β are fitted on the Hubble diagram along with the cosmological parameters.

4 The Supernova Legacy Survey

The Supernova Legacy Survey experimental setup and strategy have been designed so as to obtain sufficient quality data and to meet the necessary requirements to control the systematics.

Using the 1 square degree imager Megacam[4] mounted on the 3.6-m Canadian-France-Hawai Telescope at Mauna Kea (Hawaii), we obtain a survey deep enough to reduce the Malmquist bias that affects all flux limited surveys[6].

Both supernovae discovery and photometry are carried out with one instrument. We can thus devoid all the necessary time to the thorough understanding and the calibration of the instrument[5].

SNLS is a rolling search i.e. we repeat observations of the same 4 fields, enabling the follow-up of the already discovered SN and the detection of newly exploded SN at the same time. It is thus possible to go back in our image data base to recover early, pre-discovery SN photometry. This strategy permits to obtain well sampled lightcurve so as to measure precisely of $m_B^\star$ and the lightcurve *shape*.

The four g r i z filters make it possible to measure the B restframe flux from z=0.1 to z=1., and also estimate precisely the restframe U-B and B-V colors of the SNe.

By observing 40 nights a year during 5 years (the survey ended in August, 2008), we obtained $\sim$ 450 SNe Ia. All were spectroscopically identified on 10-m class telescopes[7,9,10,11], which allows to limit the non Ia contamination of the sample.

Finally, deep SN-free images stacks were built, to estimate the SNe host galaxy colors, enabling to caracterize the SN environment.

5 SNLS-3 years data Analysis

The constraints and systematic uncertainties from the SNLS-3 data are fully detailed in Conley et al.[12]. We present here the SN sample, and some of the different steps involved in the data analysis.

SNLS is mainly a European and Canadian project : all the analysis steps were performed with independent pipelines on each side of the atlantic ocean. Calibration, the spectro-photometric model have been improved since the SNLS-1 year results. We also reckon with the host galaxy nature influence.

[b] We fix $H_0 = 70$ km/s/Mpc.

Finally, when estimating the cosmological parameters, we fully take into account the sytematics uncertainties as well as the statistical ones by incorporating them in the covariance matrix that enter the χ^2 minimization procedure. Publishing this full covariance matrix makes it possible to other authors to exploit the SN data without loss of information.

5.1 *The supernovae sample*

To obtain precise cosmological measurement requires a long enough lever-arm in redshift in the Hubble diagram (Eq. 1). We must then add to the SNLS sample complementary supernovae sample coming from external surveys.

The supernovae sample consists of 472 SNe Ia : 123 nearby supernovae, 93 at intermediate redshift form the Sloan Digitized Sky Survey (SDSS) supernovae search, 242 from SNLS and 14 Hubble Space Telescope (HST) supernovae.

The nearby sample at $z \sim 0$ are gathered from various sources, mainly the Calan/Tololo[13], the CfAI-II-III[14] and the CSP[15] searches. The photometry of one third of this sample is expressed in the Landolt system, to which the Megacam magnitude system must be tied : this cross-calibration requirement induces the main systematic effect in this analysis.

At $z > 1$, ground observations are difficult, and the HST sample of 14 SNe Ia at z=0.7-1.4 complements the high redshift part of the Hubble diagram.

Finally, we add 146 SNe Ia at intermediate redshift $z < 0.4$ from the SDSS Supernova Survey. This component of the SDSS-II survey carried out repeat imaging of a 300 square degree southern equatorial stripe using a dedicated 2.5-meter telescope in drifts scan mode at Apache Point Observatory, New Mexico. They discovered and measured about 500 spectroscopically confirmed SNe Ia. The SDSS filter system has been thouroughly studied and is very similar to the Megacam system : as a consequence the intercalibration is not as problematic as with the nearby sample.

5.2 *Calibration*

The calibration procedure of the SNLS data achieved an accuracy of a 1% precision[5]. It consists in two steps : the observations are first standardized onto some magnitude system, using a catalog of standard stars of known magnitudes. Then the standard system magnitudes are converted into absolute fluxes : for this we rely on a reference star, of known magnitudes and spectral energy density (SED). Both SNLS and SDSS survey selected a red reference star measured by the HST CALSPEC[16] calibration program.

To achieve the required precision, the spatial non-uniformities of the imager were mapped using dithered observation of dense stellar fields. Because part of the external low-z SNe sample is calibrated against the Landolt UBVRI system, the Megacam griz system has to be anchored to the Landolt system. The uncertainties in the Landolt magnitudes of our reference star BD 17° 4708 are the largest single identified sytematic uncertainty in our current analysis.

5.3 *The spectro-photometric model : SALT2 & SIFTO*

To obtain for each SN the peak restframe B band magnitude and its lightcurve *shape* and *color*, we make use of two independent lightcurve fitters, SIFTO[17] and SALT2[18]. The SALT2 model for the rest-frame flux parametrization may be written as :

$$\phi(\lambda, t) = X_0 \times [M_0(\lambda, t) + X_1 \times M_1(\lambda, t)] \exp(C\,CL(\lambda))$$

M_0 is the mean spectrum and the corresponding parameter X_0 is the flux normalisation. M_1 describes the main variability of the SNe Ia and happens to naturally reproduce a brighter-slower relation : X_1 is thus equivallent to a lightcurve shape parameter. C corresponds by construction to a color, and the color law CL encodes the corresponding variation of the model.

M_0, M_1 and CL are computed using a training sample of nearby and SNLS SNe Ia lightcurves and spectra. The SNe distances are not used, which makes it possible to use nearby as well as distant SNe for the training. As the U band data from nearby SNe turned out to be problematic, we used u' measurement of nearby data when available, and we especially rely on distant SNe g optical data, which sample the UV restframe at a redshift of $z \sim 0.4$.

No assumption were made on the color law CL wavelength dependency nor its cause — wether it be due to intrinsic SNe Ia variation or to the reddening by dust somewhere along the line of sight : in the intergalactic medium, the host galaxy or a dust shell around the SN. As there is no a-priori knowledge of the dust properties, or its putative evolution with environment and/or redshift, no prior was set on the distribution of the SNe Ia C (*color*) parameter.

The color law is mathematically equivalent to an extinction law, but it does differ in the UV part from the dust extinction law as measured in the Milky Way Galaxy[19], and also the selective ratio corresponding to $\beta \sim 2.5 - 3$ in Eq. 2 is smaller than the MW value $R_B \sim 4$. This differences can be interpreted either as an unusual extinction occuring in the SN environnement, or an intrinsic color variation dominating the extinction effects.

In a nutshell, we make no assumption and let the SNe Ia data decide : on the range of their *color* value, on the selective ratio β value, and on the color law CL wavelength dependency.

SIFTO model consists of a SED sequence, which is time dilated by a stretch factor depending on the wavelentgh. It does not contain an explicit color variation law but a linear color relation tailing the *color*=B-V to the U-B color, and the lightcurve *shape.*

Comparing the two fitters results permits to evaluate the uncertainties associated with the different choices involved in their design. As they perform equally well, we use the average of the two, and propagate the differences as systematic uncertainties.

5.4 Host galaxy nature influence

To address the question whether M_B, α and β in Eq. 2 are universal parameters, and whether there is any dependence on the SN environnement, we undertook a photometric study of the SN host galaxies. Their ugriz fluxes were measured on deep stacked images free of SN light, and supplementary data from the WIRDS survey[20] in the IR part was added. The photometric data are fitted by templates spectral energy densities, using the redshift information from the SN : this permits to derive the restframe colors of the galaxy, and its intrinsic luminosity. Using SEDs computed with the population synthesis model PEGASE.2[21], one can recover the caracteristics of the synthetic model galaxy, such as its present star formation rate (SFR), and its stellar mass content.

The host galaxies properties are known[22,23] to correlate with the SNe *shape* parameter : SNe Ia in red/high SFR/ low mass/faint galaxies are slower, and as a consequence, brighter. This could result from different evolutionary pathes leading to the explosion of the parent white dwarf[24,25].

Although in massive galaxies the mean SN Ia is fainter, it has been recently brought to evidence[26,27,28] that the standard (*shape*=0, *color*=0) SN Ia is in fact there slightly brighter, at a $4-\sigma$ significance : this is a subtle effect - 0.08 mag, or 8% - smaller than the *shape* or *color* corrections.

We take this dependency into account by splitting the sample at $M = 10^{10} M_\odot$ between low and high mass galaxies, and using two different M_B values for each sub-sample. This leads to a significative improvement in the cosmological fits (at a $\sim 4\sigma$ level) and also to a shift in the measured cosmology : for a flat universe, Ω_M value is shifted by an amount comparable to the statistical precision.

The χ^2 minimization procedure involves the residuals computed for each SN i : $r_i = \mu_i - \mu_{cosmology}(z_i;\vec{\theta})$ and the associated covariance matrix $\mathbf{C}$: $\chi^2 = {}^t r \mathbf{C}^{-1} r$. The covariance matrix $\mathbf{C}$ can be splitted in 3 terms : $\mathbf{C} = \mathbf{D}_{stat} + \mathbf{C}_{stat} + \mathbf{C}_{sys}$.

$\mathbf{D}_{stat}$ is a diagonal part dealing with purely statistical uncertainties, which includes the errors on the light curve parameters of each SN and on its redshift value, plus several additional terms: σ_{int} to account for the intrinsic scatter of SNe Ia — $\sigma_{int} = 0.07$ mag (or equivalently 7%) for the SNLS sample; $\sigma_{lensing} = 0.055 \times z$ to account for the gravitational lensing by foreground galaxies[29] ; σ_{host} to account for the mis-classification of the SN host due to the host colors statistical errors.

As all the SNe shares the same spectro-photometric model used to estimate ($m_B^\star$, *shape,color*), the statistical covariance is not diagonal and $\mathbf{C}_{stat} \neq 0$.

Finally, the $\mathbf{C}_{syst}$ part accounts for the systematic errors affecting the SN measurements i.e. the uncertainties that will not be reduced by increasing the sample size. For example, the uncertainty on one of the calibration zero point will affect for each SN the estimation of ($m_B^\star$, *color*), not only through the value of this SN photometric points, but also through the model, which is trained on many other SNe photometry. The most important term entering $\mathbf{C}_{syst}$, in terms of consequence on the cosmological parameters systematic uncertainties, is by far the calibration, especially the intercalibration of the different SNe sample.

6 SNLS-3 years cosmological results

The SNLS-3 cosmological results are presented in Conley et al.[12] and Sullivan et al.[30]. Including all identified systematic effects in the $\Omega_M - w$ plane assuming a flat universe is shown on Fig.1 as the blue contours. They are consistent with a cosmological constant. Including the systematic nearly double the size of the uncertainty-"ellipse". Excluding the calibration sytematic reduces this increase down to ~10 %.

The degeneracy along the Ω_M axis is lifted when constraints from other cosmological probes are added. The measurements of the CMB temperature fluctuation yields estimation for[31] : the acoustic scale $l_A = \pi(1+z_*)D_A(z_*)/r_s(z_*)$; the shift parameter R ; the redshift at decoupling z_* ; The imprint of the Baryon Acoustic Oscillation (BAO) in the galaxies correlation function at a given redshift z yields a measurement of $r_s(z_d)/D_V(z)$ where $r_s(z_d)$ is the comoving sound horizon at the baryon drag epoch and $D_V(z)$ is the spherical average of the angular-diameter distance and the radial proper distance[32,33].

Combining results from the Wilkinson Microwave Anisotropy Probe 7-years (WMAP7)[34] and from the SDSSS Data Release 7 BAO measurement[35] yield the "green" contours shown on Fig.1. Combining both contours which are almost orthogonal yields $w = -1.068^{+0.080}_{-0.082}$ — this result is nearly equivalent to fix $\Omega_M = 0.27$ for the SNe Ia only contour.

7 Conclusion

Combining the SNLS-3 SNe Ia sample with measurements from observations of the CMB and of large scale structures, we obtain a most precise measurement of the dark energy equation of state consistent whith a cosmological constant.

The statistical uncertainties on the cosmological parameters are now exceeded by the systematics, although the situation could change were the major contribution of the calibration to the systematics to be reduced.

As the SDSS filter system is similar to the Megacam system, and as low redshift sample observed in a very similar way become available, we will in the future take full advantage of the

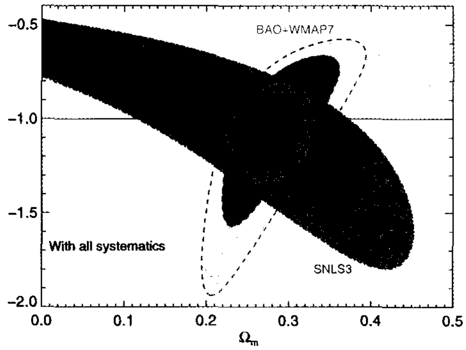

Figure 1: Confidence contours in the plane $\Omega_M - w$ obtained when fitting with the SNe Ia -only fit (in blue). A flat cosmology is assumed. Taking into account the systematics nearly double the size of the contour. The degeneracy along the Ω_M axis is lifted when adding the SDSS BAO and WMAP7 CMB constraints (in green).

inter-calibration improvements possibilities.

In the near future, the SkyMapper[36] project will provide nearby SNe Ia at $z \sim 0.05$ discovered and observed with a similar technique than SNLS. Next generation surveys either ground-based such as the Large Synodic Survey Telescope (LSST) project or space-born such as the Wide Field Infrared Survey Telescope (WFIRST) or the EUCLID mission could bring thousands of distant SNe Ia up to $z \sim 1.5$. Providing an adapted strategy , they could adress the question of a time variating equation of state for the dark energy, $w(a) = w_0 + (1-a)w_a$[37].

References

1. A. G. Riess et al., *Astronomical Journal* **116**, 1009 (1998)
2. S. Perlmutter et al., *Astrophysical Journal* **517**, 565 (1999)
3. J. Frieman, "Lectures on Dark Energy and Cosmic Acceleration", *arXiv:0904.1832*
4. O. Boulade et al., *Instrument Design and Performance for Optical/Infrared Ground-based Telescopes, ed M.Iye & A.F.M. Moorwood, Proc SPIE, 4841, 72*
5. N. Regnault et al., *Astronomy and Astrophysics* **506**, 999 (2009)
6. C. Perrett et al., *Astronomical Journal* **140**, 518 (2010)
7. D.A. Howell, et al., *Astrophysical Journal* **634**, 1190 (2005)
8. T.J. Bronder, et al., *Astronomy and Astrophysics* **477**, 717 (2008)
9. R.S. Ellis, et al., *Astrophysical Journal* **674**, 51 (2008)
10. C. Balland et al., *Astrophysical Journal* **507**, 85 (2009)
11. E. Walker et al., *Monthly Notices of the Royal Atronomical Society* **410**, 1262 (2011)
12. A. Conley et al., *The Astrophysical Journal Supplement* **192**, 1 (2011)
13. M. Hamuy et al., *Astronomical Journal* **112**, 2408 (1996)
14. M. Hicken et al., *Astrophysical Journal* **700**, 331 (2009)
15. C. Contreras et al., *Astronomical Journal* **139**, 519 (2010)
16. Bohlin, R.C. *Astronomical Journal* **111**, 1743 (1996)
17. A. Conley et al., *Astronomical Journal* **681**, 482 (2008)
18. J. Guy et al., *Astronomy and Astrophysics* **466**, 11 (2007)
19. J.A. Cardelli et al., *Astrophysical Journal* **345**, 245 (1989)
20. R. Bielby et al., *in preparation*
21. D. Le Borgne et al., *Astronomy and Astrophysics* **386**, 446 (2002)

22. M. Hamuy et al., *Astronomical Journal* **120**, 1479 (2000)
23. M. Sullivan et al., *Astrophysical Journal* **648**, 868 (2006)
24. E. Scannapieco et al., *Astronomical Journal* **629**, L85 (2005)
25. F. Manucci et al., *Monthly Notices of the Royal Atronomical Society* **370**, 773 (2006)
26. P.L. Kelly et al., *Astrophysical Journal* **715**, 743 (2010)
27. H. Lampeitl et al., *Astrophysical Journal* **722**, 766 (2010)
28. M. Sullivan et al., *Monthly Notices of the Royal Atronomical Society* **406**, 782 (2010)
29. M. Jönsson et al., *Monthly Notices of the Royal Atronomical Society* **405**, 535 (2010)
30. M. Sullivan et al., submitted
31. E. Komatsu et al., *The Astrophysical Journal Supplement* **180**, 330 (2009)
32. D. Eisentein et al., *Astrophysical Journal* **633**, 560 (2005)
33. C. Blake et al., *arXiv:1105.2862*
34. E. Komatsu et al., *The Astrophysical Journal Supplement* **192**, 18 (2011)
35. W.J. Percival et al., *Monthly Notices of the Royal Atronomical Society* **401**, 2148 (2010)
36. S.C. Keller et al., *Publications of the Astronomical Society of Australia* **24**, 1 (2007).
37. P. Astier et al., *Astronomy and Astrophysics* **525**, 7 (2011)

IS DARK ENERGY NEEDED?

A. BLANCHARD
Université de Toulouse; UPS-OMP; IRAP: ; 14, avenue Edouard Belin
F-31400 Toulouse, France

Evidence for an accelerated expansion of the universe as it has been revealed ten years ago by the Hubble diagram of distant type Ia supernovae represents the lattest revolution of modern cosmology with profound impact for fundamental physics. The construction of a scientfic model of the universe is probably one of the most fascinating success of XXth century science. During its construction, there has been regular debates regarding whether the whole construction being scientific. Indeed, existing evidence for the big bang picture, including its modern version the Λ CDM picture, comes from astrophysical observations. It is therefore interesting and essantial to critically examine the present situation of the astrophysical observations and the possible limitation in their interpretation. In this paper, the main various observational probes at the fundation of the standard view are presented as well as the standard framework to interpret them with special attention to the complex astrophysics and theoretical hypotheses that may limit robust interpretation. It is concluded that, even when scrutinized with sceptical eyes, the evidence for a homogenous accelerated universe. governed by standard Friedman-Lemaître equations, is robust. Therefore the standard Λ CDM picture has to be regarded as the most successful scientific representation of the universe by now, possibly being the only one clearly consistent with the whole family of observations relevant to cosmology. The fact that this model could in principle be easily falsified makes it a very good scientific theory. Understanding the origin of acceleration is probably one of the most challenging problem of fundamental physics.

1 Introduction

The determination of cosmological parameters has been one of the most important objectives of cosmologists after the discovery of the expansion of the universe by Hubble. It is importan to provide a precise framework but also in the perspective to test the model. This problematic has become specially important after the theory of inflation which predicted the universe to be flat, something which was first interpret as a prediction for $\Omega_m = 1$. Although Peebles[16] early noticed that the actual prediction of inflation was $\Omega_m + \Omega_\Lambda = 1$, little attention was paid to the cosmological constant until the detection of small scale fluctuation in the microwave sky[13]. Indeed these measurements were in agreement with a flat universe and inconsistent with open cosmological models with $\Omega_m \sim 0.3$. However the evidence for acceleration as obtained from the Hubble diagram of distant supernovae has been the observational evidence that has lead to a rapid change of paradigm. Since that time the improvment in the accuracy on the estimations of cosmological parameters has been dramatic. This paper is a shortened version of a recent review published by the author[5].

2 The Hubble diagram of distant Supernovae

The Hubble diagram was the first geometrical test of relativistic cosmology. Extension of the Hubble diagram to high redshift has been made possible thanks to the use of type Ia Supernovae (SNIa). SNIa at their maximum luminosity ($M \sim -19.5$) reach a luminosity comparable to that of an cntire galaxy. This means tha these bright objects can be detected extremely far away. Their are therefore observed as there were in an epoch substantially younger than the present universe. Furthermore there is a relation between the decline rate and the intrinsic luminosity making them suitable for distance measurements at cosmological scale. Because SNIa are rare, large sky area have to be surveyed on a regular basis to collect samples of SNIa. At the end of last century, two groups have independently investigated the distant SNIa Hubble diagram and concluded that supernovae at redshift ~ 0.5 were dimmer by ~ 0.2 mag compared to what was expected in a unaccelerated universe. This was interpreted as an evidence for an accelerated expansion. Indeed as supernova are observed in the universe when younger they allowed to measure the history of the expansion. The consequence is very dramatic: gravity is repulsive on the scale of the universe accordingly to this observation!

2.1 What if Supernovae evolved?

Given the importance of the consequence not only for cosmology but also for fundamental physics, the above observation should be scrutinized. The use of geometrical tests is based most of time on the assumption of no-evolution of the parent population. This is also the case for type Ia supernovae. Although strong efforts have been done by observers to track for any sign of evolution by close inspection of the spectra [1], the absence of evidence cannot be considered as an evidence of absence. One possible way to deal with this problem is to assume some evolution and see whether the data still provide evidence for the claim. For instance, an evolution term like :

$$\Delta m_e \propto z \tag{1}$$

can not mimic the observed Hubble diagram without a cosmological constant. However an other form of the evolution term has been suggested, being proportional to the look back time [24] :

$$\Delta m_e \propto \Delta t \tag{2}$$

It happens that such term leads to large degeneracy between cosmology and possible evolution [9] that present day data do not allow to disentangle.
Undoubtfully, despite its possible limitation, the determination of the Hubble diagram from SNIa has led to a major and rapid change of paradigm in modern cosmology. However, this change has been possible because the previous situation was problematic. Although some observational indications were favoring a low density universe, the first detections of fluctuations on degree scales were in conflict with open low density universe [14].

3 Fluctuations

Since the discovery of the CMB fluctuations by COBE [21] the idea that early universe physics has left imprints revealed by these fluctuations has gained an enormous attention. In this respect, DMR results have played a fundamental role in modern cosmology comparable to the discovery of the expansion of the universe or the discovery of the microwave background by Penzias and Wilson, and indeed this has motivated the delivering of the Nobel prize to G. Smoot and J. Mather for this discovery. One of the fundamental reasons for this is that fluctuations on scales larger than one degree in the microwave background radiation correspond to scales greater than the horizon at last scatering epoch and cannot therefore been altered by any physical process

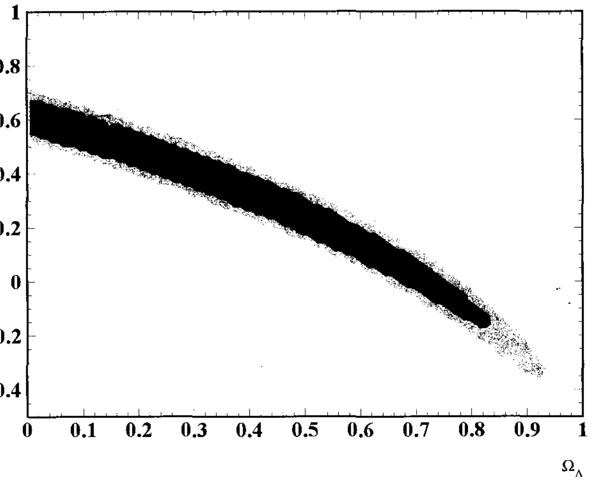

Figure 1: Fitting the SNIa Hubble diagram with two free parameters, one being the cosmological constant in a flat cosmological model and the second being a parameter describing a possible time evolution of the luminosity of distant supernovae ($\Delta m(z) = K(t_0 - t(z))/(t_0 - t(1))$) leads to the following constraints [9]. Contours are 1. 2 and 3 sigma regions on one parameter. This is a strong degeneracy between the two parameters which prevents an unambiguous evidence for a cosmological constant from the sole Hubble diagram of SNIa. From Ferramacho *et al.*[9]

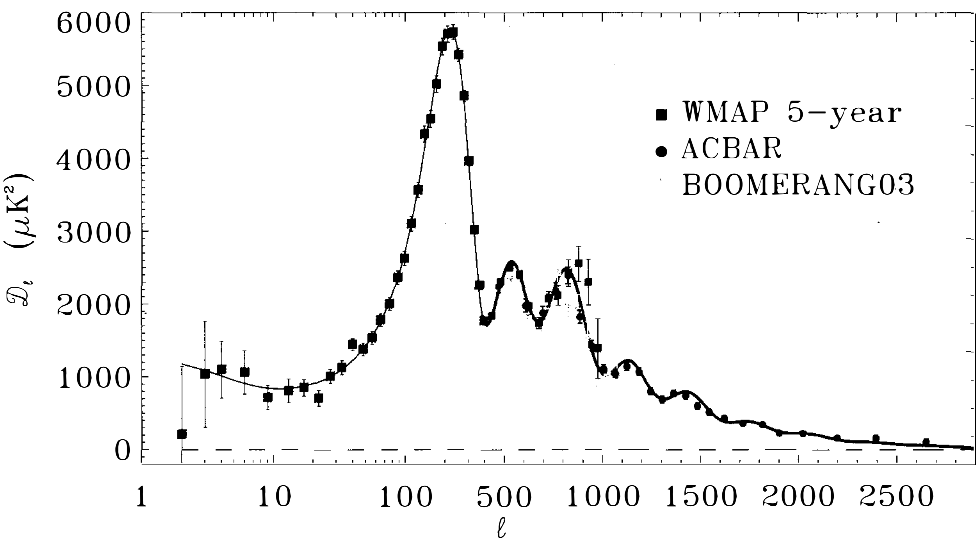

Figure 2: The amplitude of angular fluctuations of the CMB is expressed through their angular power spectrum. Data are WMAP, Boomerang, ACBAR [19]. A simple minimal six parameters model including a cosmological constant provides an excellent fit to the data. This is one of the most important successes of modern cosmology.

and should therefore reflect primordial fluctuations [23]. This also means that the very existence of these fluctuations could be explained only from yet undiscovered physics, probably relevant to the very early universe [10], for which the expansion law is strongly modified compared to the standard picture. The DMR results were providing some constraints on cosmological models [25] but it has been realized that the measure of fluctuations on smaller scales will provide much stringent information. Early detections of fluctuations on degree scales allowed to set interesting constraints and provide the first evidence for a nearly flat geometry of space [13,14]. If estimations of low matter density were to be regarded as robust, this was inevitabily leading to a non-zero cosmological constant. Even before the availability of the WMAP data, considerable progresses have been achieved on the measurement of fluctuations on all angular scales. Archeops [2] and Boomerang [4], as well as many other small scale measurements, already provided data allowing tight constraints on cosmological parameters [3]. It should also be noticed that fast codes to compute the fluctuatiosn spectrum have been made available to the scientific community. The first one was CMBFAST [20] followed by an avatar, CAMB[12]. The authors deserve the warm aknowledgments of the community as these tools have been really critical in the full scientific exploitation of the various CMB experiments.

Although the observed fluctuations were consistent with a Λ dominated universe, a cosmological constant was not explicitly requested by the CMB data alone. Indeed even the WMAP data were consistent with a vanishing cosmological constant, provided the Hubble constant was left as an entirely free parameter. A positive detection of a cosmological constant could be obtained only by using some additional data in conjunction with CMB, like the measurement of the Hubble constant. A further restriction came from the fact that the constraints on cosmological parameters were obtained within the standard CDM picture, and that many ingredients were specified without being necessarily confirmed by observations : for instance initial fluctuations are supposed to be adiabatic and to follow some power law. Therefore the "concordance" [15] cosmology was an appropriate terminology: the model was consistent with most existing data, but the introduction of a cosmological constant was not requested by any single data, and it was far from being clear whether relaxing some of the input hypotheses would not allow for solutions without the introduction of a cosmological constant.

4 What do actually fluctuations tell ?

The first point to notice is that for a random function on the sphere, even with gaussian statistics, each a_l is a random quantity. Therefore fitting the C_l with an acceptable goodness of fit figure means that several thousands of random numbers could be fitted with a 6-parameter theory. A remarkable level of achievement! In addition fitting the C_l curve provide very tight constraints on the six parameters, due to the quality of the measurements. These constraints are generally formulated in term of cosmological parameters and it is often quoted that they provide a direct evidence for an accelerating universe independent of the Hubble diagram of supernovae. It should be realized however, that these constraints are established within a specific model that is the adiabatic cold Dark matter picture with power law initial conditions. Therefore these constraints are model dependent. Modifying the starting hypothesis may change these constraints (and the model may then be rejected, like the standard topological defects scenario has been). An early illustration of this has been obtained soon after the publication of the WMAP data. Relaxing the powerlaw hypothesis, i.e. assuming a non power law power spectrum, it is possible to produce C_l curves within an Einstein de Sitter cosmological model which provided a fit as good as the concordance model. This is illustrated in figure 3 on which 3 models are compared to the WMAP data, two being Einstein de Sitter models. Such models not only reproduce the TT (temperature-temperature) spectrum, but are also extremely close in terms of ET (polarization-temperature) and EE (polarization-polarization) spectra. An un-clustered component of matter like a neutrino

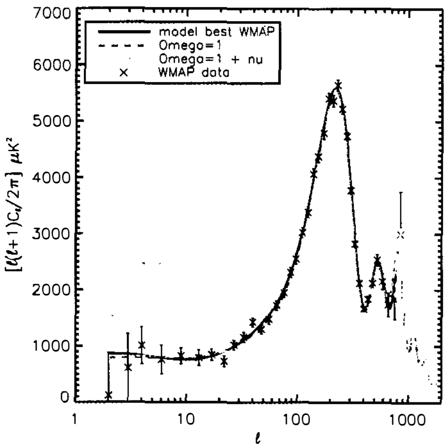

Figure 3: The TT spectrum of the first year WMAP data compared to three different models: one is the concordance, the two others are Einstein de Sitter models, one of which comprises neutrino contribution of $\sim 10\%$ corresponding to three degenerate families with $m_\nu \sim 0.7$eV. From Blanchard *et al.* [6].

contribution or a quintessence field with $w \sim 0$ is necessary to obtain an acceptable amplitude of matter fluctuations on clusters scales [6]. Such models require a low Hubble constant ~ 46 km/s/Mpc at odd with canonical HST key program value (~ 72 km/s/Mpc) but is actually only $\sim 3\sigma$ away from this value, this can certainly not be considered as a fatal problem for an Einstein-de Sitter universe. The introduction of a non-power law power spectrum might appear as unnatural. However, such a feature can be produced by some models of inflation in order to match the C_l curve[11]. Therefore the amplitude and shape of the CMB fluctuations as measured by WMAP is certainly a success for the Λ CDM model but cannot be regarded as a direct indication of the presence of dark energy.

5 Large scale structure

Within a specific model like Cold Dark Matter, not only it is possible to derive the C_l curves, that is the angular power of the fluctuations of the cosmic microwave background, but it is also possible to obtain the power spectrum of the fluctuation in the matter density, or equivalently the correlation function. The galaxy distribution should reflect essentially this matter power spectrum (galaxies may be a "biased" representation and this bias is subject to some modeling, but this represents small corrections that can be neglected at first order). The measure of the power spectrum can therefore be used to disentangle models which produce C_l curves that could not be distinguished. Recently, a critical advance resulted from the availability of very large galaxy surveys, the 2Df redshift survey and the SDSS survey, allowing to measure the amplitude of galaxy fluctuations on scales as large as $100h^{-1}$ Mpc [17,22,8,18]. This has provided a remarkable success to the ΛCDM picture because the shape of the correlation function could be predicted for models that already match the CMB fluctuations measured by WMAP: not only ΛCDM model reproduces the shape of the correlation function, but the specific presence of a bump in the correlation function at scale of the order of $100h^{-1}$Mpc due to the detailled dynamics of fluctuations when the baryons are taken into account, the so called accoustic peak, corresponding to the "peak" in the C_l of the CMB.

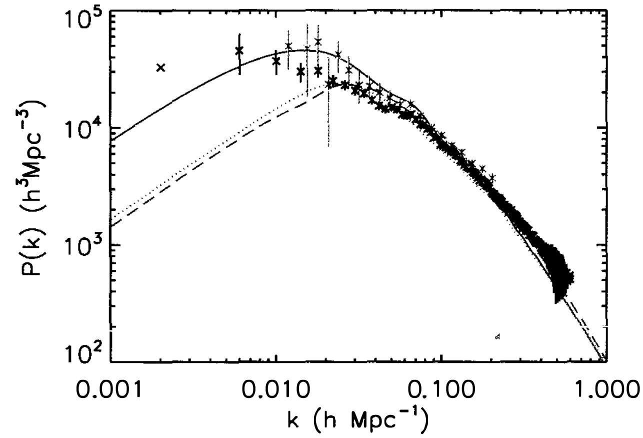

Figure 4: Data from the SDSS have allowed to measure the amplitude of galaxy fluctuations on large scales. In this respect, Luminous Red Galaxies (LRG) provided measurement of the power spectrum on the largest scales. Green crosses correspond to Tegmark et al. [22] and black crosses correspond to the measurements of the power spectrum of LRG from the SDSS Data Release 5 by Percival et al. [18]. The red continuous curve is the predicted spectrum for a typical concordance model, while the dotted and dashed lines correspond to the power spectrum for Einstein de Sitter models consistent with the WMAP fluctuation angular power spectrum C_l [6,11].

Once an Einstein de Sitter model is built in order to reproduce the CMB C_l, the amplitude of the matter fluctuations on large scales is set up and the measurement of the matter fluctuations on large scales in the present day universe is a critical way to distinguish models which are otherwise degenerated in their C_l. The comparison of the power spectrum from the SDSS LRG with the predicted spectra for Einstein de Sitter models is clearly in favor of the concordance model, see Fig. 4. One should add some caution here: it might be possible that the biasing mechanism leads to a power spectrum at small k (large scales) which is not proportional to the actual matter power spectrum [7], in which case the above comparison might not be a fatal failure of the Einstein de Sitter models. However, biasing mechanisms systematically lead to a correlation function on large scales which is still proportional to the matter correlation function on large scales. Comparison of the correlation function on large scales is therefore less ambiguous and its measurement should be unambiguously discriminant. Hunt and Sarkar [11] have provided a comprehensive MCMC investigation of the Einstein de Sitter parameter space, finding models which acceptably fit the correlation function on scales below 70 h^{-1}Mpc, but were nevertheless systematically negative on scales of the BAO peak. This is a strong evidence that there is no way in an Einstein de Sitter universe to fit simultaneously the C_l and the observed distribution of galaxies on large scales. This should be regarded as a remarkable success of the concordance cosmological model: although there were little doubts that this model could fit accurately most of the major existing observational facts in cosmology, the ability to produce predictions that are verified a posteriori is the signature of a satisfying scientific theory.

5.1 Tests based on the growing rate

As we have seen the Cold Dark Matter should be regarded as a successful theory that is able to reproduce most of the data relevant to cosmologyhas and which lead to predictions which were verified a posteriori. The precision on cosmological parameters for the ΛCDM picture is of the

Parameter	Vanilla	Vanilla + Ω_k	Vanilla + w	Vanilla + Ω_k + w
$\Omega_b h^2$	0.0227 ± 0.0005	0.0227 ± 0.0006	0.0228 ± 0.0006	0.0227 ± 0.0005
$\Omega_c h^2$	0.112 ± 0.003	0.109 ± 0.005	0.109 ± 0.005	0.109 ± 0.005
θ	1.042 ± 0.003	1.042 ± 0.003	1.042 ± 0.003	1.042 ± 0.003
τ	0.085 ± 0.017	0.088 ± 0.017	0.087 ± 0.017	0.088 ± 0.017
n_s	0.963 ± 0.012	0.964 ± 0.013	0.967 ± 0.014	0.964 ± 0.014
Ω_k	0	-0.005 ± 0.007	0	-0.005 ± 0.0121
w	-1	-1	-0.965 ± 0.056	-1.003 ± 0.102
Ω_λ	0.738 ± 0.015	0.735 ± 0.016	0.739 ± 0.014	0.733 ± 0.020
Age	13.7 ± 0.1	13.9 ± 0.4	13.7 ± 0.1	13.9 ± 0.6
Ω_M	0.262 ± 0.015	0.270 ± 0.019	0.261 ± 0.020	0.272 ± 0.029
σ_8	0.806 ± 0.023	0.791 ± 0.030	0.816 ± 0.014	0.788 ± 0.042
z_{re}	10.9 ± 1.4	11.0 ± 1.5	11.0 ± 1.5	11.0 ± 1.4
h	0.716 ± 0.014	0.699 ± 0.028	0.713 ± 0.015	0.698 ± 0.037

Table 1: Summary of the mean values and 68% confidence intervals for the cosmological parameters of the ΛCDM model constrained from CMB, SNIa and BAO for different models (θ is the ratio of sound horizon to angular diameter distance). These constraints are quite tight, most of them are below 5%, and are stable when additional degrees of freedom are added to the model (w. Ω_k). adapted from [9].

order of 5% at most, with accuracy close to 1% in some cases. Of course this doesn't mean it is the "right" theory; science does not provide "right" theories but only theories that reproduce all existing data and which are able to lead to predictions that can lead to its *invalidation*. This is the principle that to be scientific a statement has to be falsifiable accordingly to Kark Popper.

It is therefore the only possible path to continue to increase the accuracy of existing measurements and to develop new ways to test the theory. There is a way to test cosmological models which is fundamentally different from geometrical tests: it is based on the growing rate of fluctuations under their own gravity. In principle the abundance of clusters and weak lensing measurements are both sensitive to this growing rate. I do not think that they have by now reach a level of precision that makes them useful, but it is certainly a way on which efforts will concentrated in the future, in particular thanks to space mission like EUCLID or WFIRST. Measurements of this growing rate would allow to test whether predictions of general relativity at the scale of the universe are verified or if we have to turn to alternatives.

6 Conclusions

The Copernician model of the world was the first revolution of a series in the construction of modern cosmology, and the discovery of the accelerated expansion being the latest in date. Theoretical considerations have always been a source of remarkable observational investigations and Cosmology has always benefited from the confrontation of models with observations. Since the thirties, the big bang picture, the modern version of Lemaître's primeval atom has been remarkably successful, based on simple assumptions and physical laws that have been validated by accurate experimental results. Although alternative theories have been developed, these alternative were based on hypothetical unknown physics advocated to interpret cosmological observations. None of these alternative theories has produced significant predictions differing from the standard view that would have been comforted a posteriori. Rather new observations in agreement with predictions of the big bang picture necessitated deep revision of the unorthodox views, at the cost of rather ad hoc assumptions added to fit the new observations. The situation has evolved when the standard picture has necessitated the introduction of new ingredients, first dark matter and more recently dark energy. The very nature of these new ingredients, which are supposed to dominate the mean density of the universe has not been established by direct laboratory experiments, nor by astronomical observations, and this situation may some time lead to the question whether cosmologists have not introduced new aethers. We had the opportunity to see that the situation is not so bad. The introduction of -cold- non-baryonic dark matter has led to specific predictions, the amplitude and shape of the fluctuations of the cosmological background on various angular scales, which were verified with high accuracy. The presence of dark energy has lead to a specific prediction, the shape of the matter power spectrum on large scales, which has been verified a posteriori. Although the inclusion of a cosmological constant was concomitant to general relativity, the actual origin of dark energy remains totally unknown and the presence of dark energy in the present day universe represents probably the most fundamental and unexpected new element in modern physics.

References

1. Balland, C., et al., *A&A*, **507**, 85 (2009)
2. Benoît, A., et al., *A&A*, **399**, L19 (2003).
3. Benoît, A., et al., *A&A*, **399**, L25 (2003).
4. de Bernardis, P., et al., *Nature*, **404**, 955 (2000).
5. Blanchard, A., *A&A Rev.*, **18**, 595 (2010).
6. Blanchard, A., Douspis, M., Rowan-Robinson, M., & Sarkar, S., *A&A*, **412**, 35 (2003).
7. Durrer, R., Gabrielli, A., Joyce, M., & Sylos Labini, F., *ApJL*, **585**, L1 (2003).
8. Eisenstein, D. J., et al., *ApJ*, **633**, 560 (2005).
9. Ferramacho, L. D., Blanchard, A., & Zolnierowski, Y., *A&A*, **499**, 21 (2009).
10. Guth, A. H., *Phys. Rev. D*, **23**, 347 (1981).
11. Hunt, P., & Sarkar, S., *Phys. Rev. D*, **76**, 123504 (2007).
12. Lewis, A., Challinor, A., & Lasenby, A., http://camb.info/, *ApJ*, **538**, 473 (2000).
13. Lineweaver, C. H., Barbosa, D., Blanchard, A., & Bartlett, J. G., *A&A*, **322**, 365 (1997).
14. Lineweaver, C. H., & Barbosa, D., *ApJ*, **496**, 624 (1998).
15. Ostriker, J. P., & Steinhardt, P. J., *Nature*, 377, 600 (1995).
16. Peebles, P. J. E. 1984, *ApJ*, 284, 439
17. Percival, W. J., et al., *MNRAS*, **327**, 1297 (2001).
18. Percival, W. J., et al., *ApJ*, **657**, 645 (2007).
19. Reichardt, C. L., et al., *ApJ*, **694**, 1200 (2009).
20. Seljak, U., & Zaldarriaga, M. *ApJ*, **469**, 437 (1996).
21. Smoot, G. F., et al., *ApJL*, 396, L1 (1992).
22. Tegmark, M., et al., *Phys. Rev. D*, **74**, 123507 (2006).
23. Weinberg, S., Gravitation and Cosmology, ISBN 0-471-92567-5. Wiley-VCH (1972).
24. Wright, E. L., arXiv:astro-ph/0201196 (2002).
25. Wright, E. L., et al., *ApJL*, **396**, L13 (1992).

Testing MOND in the Solar System

Luc BLANCHET
$\mathcal{G}\mathbb{R}\varepsilon\mathbb{C}\mathcal{O}$, Institut d'Astrophysique de Paris, CNRS,
Université Pierre et Marie Curie, 98$^{\rm bis}$ boulevard Arago, 75014 Paris, France

Jérôme NOVAK
Laboratoire Univers et Théories, Observatoire de Paris, CNRS,
Université Denis Diderot, 5 place Jules Janssen, 92190 Meudon, France

The Modified Newtonian Dynamics (MOND) generically predicts a violation of the strong version of the equivalence principle. As a result the gravitational dynamics of a system depends on the external gravitational field in which the system is embedded. This so-called external field effect is shown to imply the existence of an anomalous quadrupolar correction, along the direction of the external galactic field, in the gravitational potential felt by planets in the Solar System. We compute this effect by a numerical integration of the MOND equation in the presence of an external field, and deduce the secular precession of the perihelion of planets induced by this effect. We find that the precession effect is rather large for outer gaseous planets, and in the case of Saturn is comparable to, and in some cases marginally excluded by published residuals of precession permitted by the best planetary ephemerides.

1 The external field effect with MOND

The Modified Newtonian Dynamics (MOND) has been proposed [1] as an alternative to the dark matter paradigm [2]. At the non-relativistic level, the best formulation of MOND is the modified Poisson equation [3],

$$\nabla \cdot \left[\mu\left(\frac{g}{a_0}\right)\nabla U\right] = -4\pi G\rho\,, \tag{1}$$

where ρ is the density of ordinary (baryonic) matter, U is the gravitational potential, $\boldsymbol{g} = \nabla U$ is the gravitational field and $g = |\boldsymbol{g}|$ its ordinary Euclidean norm. The modification of the Poisson equation is encoded in the MOND function $\mu(y)$ of the single argument $y \equiv g/a_0$, where $a_0 = 1.2 \times 10^{-10}\,\mathrm{m/s^2}$ denotes the MOND constant acceleration scale. The MOND function interpolates between the MOND regime corresponding to weak gravitational fields $y = g/a_0 \ll 1$, for which it behaves as $\mu(y) = y + o(y)$, and the Newtonian strong-field regime $y \gg 1$, where μ reduces to 1 so that we recover the usual Newtonian gravity.

An important consequence of the non-linearity of Eq. (1) in the MOND regime, is that the gravitational dynamics of a system is influenced (besides the well-known tidal force) by the external gravitational environment in which the system is embedded. This is known as the external field effect (EFE), which has non-trivial implications for non-isolated gravitating systems. The EFE was conjectured to explain the dynamics of open star clusters in our galaxy [1], since they do not show evidence of dark matter despite the involved weak internal accelerations (i.e. below a_0). The EFE effect shows that the dynamics of these systems should actually be

Newtonian as a result of their immersion in the gravitational field of the Milky Way. The EFE is a rigorous prediction of the equation (1), and is best exemplified by the asymptotic behaviour of the solution of (1) far from a localised matter distribution (say, the Solar System), in the presence of a constant external gravitational field $\boldsymbol{g}_e$ (the field of the Milky Way). At large distances $r = |\mathbf{x}| \to \infty$ we have[3]

$$U = \boldsymbol{g}_e \cdot \mathbf{x} + \frac{GM/\mu_e}{r\sqrt{1+\lambda_e \sin^2\theta}} + \mathcal{O}\left(\frac{1}{r^2}\right), \tag{2}$$

where M is the mass of the localised matter distribution, where θ is the polar angle from the direction of the external field $\boldsymbol{g}_e$, and where we denote $\mu_e \equiv \mu(y_e)$ and $\lambda_e \equiv y_e\mu'_e/\mu_e$, with $y_e = g_e/a_0$ and $\mu'_e = \mathrm{d}\mu(y_e)/\mathrm{d}y_e$. In the presence of the external field, the MOND internal potential $u \equiv U - \boldsymbol{g}_e \cdot \mathbf{x}$ shows a Newtonian-like fall-off $\sim r^{-1}$ at large distances but with an effective gravitational constant G/μ_e.[a] However, contrary to the Newtonian case, it exhibits a non-spherical deformation along the direction of the external field. The fact that the external field $\boldsymbol{g}_e$ does not disappear from the internal dynamics can be interpreted as a violation of the strong version of the equivalence principle.

2 Abnormal influence of the Galaxy in the Solar System

In two recent papers[5,6] it was shown that the imprint of the external galactic field $\boldsymbol{g}_e$ on the Solar System (due to a violation of the strong equivalence principle) shows up not only asymptotically, but also in the inner regions of the system, where it may have implications for the motion of planets. This is somewhat unexpected because gravity is strong there (we have $g \gg a_0$) and the dynamics should be Newtonian. However, because of the properties of the equation (1), the solution will be given by some non-local Poisson integral, and the dynamics in the strong-field region will be affected by the anomalous behaviour in the asymptotic weak-field region.

We assume that the external Galactic field $\boldsymbol{g}_e$ is constant over the entire Solar System.[b] The motion of planets of the Solar System relatively to the Sun obeys the internal gravitational potential u defined by

$$u = U - \boldsymbol{g}_e \cdot \mathbf{x}, \tag{3}$$

which is such that $\lim_{r\to\infty} u = 0$. Contrary to what happens in the Newtonian case, the external field $\boldsymbol{g}_e$ does not disappear from the gravitational field equation (1) and we want to investigate numerically its effect. The anomaly detected by a Newtonian physicist is the difference of internal potentials,

$$\delta u = u - u_N, \tag{4}$$

where u_N denotes the ordinary Newtonian potential generated by the same ordinary matter distribution ρ, and thus solution of the Poisson equation $\Delta u_N = -4\pi G\rho$ with the boundary condition that $\lim_{r\to\infty} u_N = 0$. We neglect here the change in the matter distribution ρ when considering MOND theory instead of Newton's law. This is in general a good approximation because the gravitational field giving the hydrostatic equilibrium (and thus ρ) is strong and MOND effects are very small. Hence u_N is given by the standard Poisson integral.

A short calculation shows that the anomaly obeys the Poisson equation $\Delta\delta u = -4\pi G\rho_{\text{pdm}}$, where ρ_{pdm} is the density of "phantom dark matter" defined by

$$\rho_{\text{pdm}} = \frac{1}{4\pi G}\boldsymbol{\nabla}\cdot(\chi\boldsymbol{\nabla}U), \tag{5}$$

[a] Recall that in the absence of the external field the MOND potential behaves like $U \sim -\sqrt{GMa_0}\ln r$, showing that there is no escape velocity from an isolated system[4]. However since no object is truly isolated the asymptotic behaviour of the potential is always given by (2), in the approximation where the external field is constant.

[b] For the Milky Way field at the level of the Sun we have $g_e \simeq 1.9 \times 10^{-10}$ m/s^2 which happens to be slightly above the MOND scale, i.e. $\eta \equiv g_e/a_0 \simeq 1.6$.

where we denote $\chi \equiv \mu - 1$. The phantom dark matter represents the mass density that a Newtonian physicist would attribute to dark matter. In the model [7,8] the phantom dark matter is interpreted as the density of polarisation of some dipolar dark matter medium and the coefficient χ represents the "gravitational susceptibility" of this dark matter medium.

The Poisson equation $\Delta\delta u = -4\pi G\rho_{\mathrm{pdm}}$ is to be solved with the boundary condition that $\lim_{r\to\infty}\delta u = 0$; hence the solution is given by the Poisson integral

$$\delta u(\mathbf{x}, t) = G \int \frac{\mathrm{d}^3\mathbf{x}'}{|\mathbf{x} - \mathbf{x}'|}\, \rho_{\mathrm{pdm}}(\mathbf{x}', t)\,. \tag{6}$$

We emphasise that, contrary to the Newtonian (linear) case, the knowledge of the matter density distribution does not allow to obtain an analytic solution for the potential, and the solution has to be investigated numerically. We can check that the phantom dark matter behaves like r^{-3} when $r \to \infty$, so the integral (6) is perfectly convergent.

In the inner part of the Solar System the gravitational field is strong ($g \gg a_0$) thus μ tends to one there, and χ tends to zero. Here we adopt the extreme case where χ is *exactly* zero in a neighbourhood of the origin, say for $r \leqslant \varepsilon$, so that there is no phantom dark matter for $r \leqslant \varepsilon$; for the full numerical integration later we shall still make this assumption by posing $\chi = 0$ inside the Sun (in particular we shall always neglect the small MOND effect at the centre of the Sun where gravity is vanishingly small). If $\rho_{\mathrm{pdm}} = 0$ when $r \leqslant \varepsilon$ we can directly obtain the multipolar expansion of the anomalous term (6) about the origin by Taylor expanding the integrand when $r = |\mathbf{x}| \to 0$. In this way we obtain[c]

$$\delta u = \sum_{l=0}^{+\infty} \frac{(-)^l}{l!}\, x^L Q_L\,, \tag{7}$$

where the multipole moments near the origin are given by

$$Q_L = G \int_{r>\varepsilon} \mathrm{d}^3\mathbf{x}\, \rho_{\mathrm{pdm}}\, \partial_L \left(\frac{1}{r}\right)\,. \tag{8}$$

Because the integration in (8) is limited to the domain $r > \varepsilon$ and $\partial_L(1/r)$ is symmetric-trace-free (STF) there [indeed $\Delta(1/r) = 0$], we deduce that the multipole moments Q_L themselves are STF. This can also be immediately inferred from the fact that $\Delta\delta u = 0$ when $r \leqslant \varepsilon$, hence the multipole expansion (7) must be a homogeneous solution of the Laplace equation which is regular at the origin, and is therefore necessarily made solely of STF tensors of type $\hat{x}^L$. Hence we can replace x^L in (7) by its STF projection $\hat{x}^L$. It is now clear from the non-local integral in (8) that the MONDian gravitational field (for $r \geqslant r_0$) can influence the near-zone expansion of the field when $r \to 0$. An alternative expression of the multipole moments can also be proved, either directly or by explicit transformation of the integral (8). We have

$$Q_L = -u_{\mathrm{N}}(\mathbf{0})\,\delta_{l,0} + (-)^l (\hat{\partial}_L u)(\mathbf{0})\,, \tag{9}$$

where the Newtonian potential u_{N} and the STF derivatives of the internal potential u are to be evaluated at the centre $\mathbf{0}$ of the Sun.

The multipole expansion (7) will be valid whenever r is much less than the MOND transition distance for the Solar System, defined by $r_0 = \sqrt{GM/a_0}$ with M the mass of the Sun and a_0 the

[c]Our notation is as follows: $L = i_1 \cdots i_l$ denotes a multi-index composed of l multipolar spatial indices $i_1, \cdots, i_l$ (ranging from 1 to 3): $\partial_L = \partial_{i_1} \cdots \partial_{i_l}$ is the product of l partial derivatives $\partial_i \equiv \partial/\partial x^i$; $x^L = x^{i_1} \cdots x^{i_l}$ is the product of l spatial positions x^i; similarly $n^L = n^{i_1} \cdots n^{i_l} = x^L/r^l$ is the product of l unit vectors $n^i = x^i/r$: the symmetric-trace-free (STF) projection is indicated with a hat, for instance $\hat{x}^L \equiv \mathrm{STF}[x^L]$, and similarly for $\hat{n}^L$ and $\hat{\partial}_L$. In the case of summed-up (dummy) multi-indices L, we do not write the l summations from 1 to 3 over their indices.

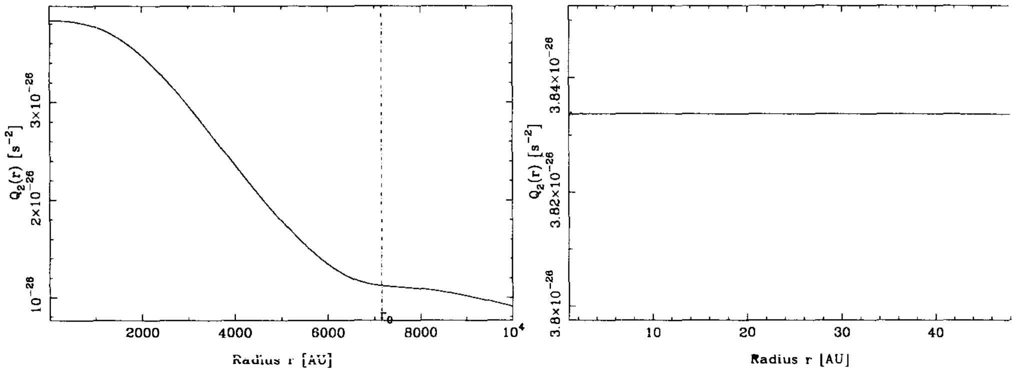

Figure 1: Left panel: profile of $Q_2(r)$ in the Solar System, for a standard choice of function $\mu_1(y)$ [see Eq. (13a)], $a_0 = 1.2 \times 10^{-10}\,\mathrm{m.s}^{-2}$ and $g_e = 1.9 \times 10^{-10}\,\mathrm{m.s}^{-2}$. The MOND transition radius is shown by a dash-dotted line at $r_0 \simeq 7100$ AU. Right panel: zoom of the central region ($r \leqslant 50$ AU), where the quadrupole is almost constant.

MOND acceleration scale. This radius corresponds to the transition region where the Newtonian acceleration becomes of the order of the MOND acceleration a_0 and therefore, MOND effects become dominant. We have $r_0 \simeq 7100\,\mathrm{AU}$ so the results (7)–(9) hold in a large volume around the Sun including all the planets (recall that Neptune's orbit is at 30 AU).

3 Results for the induced quadrupole moment in the Solar System

So far we have elucidated the structure of the multipole expansion of the anomaly $\delta\boldsymbol{u}$ near the origin. Next we resort to a numerical integration of the non-linear MOND equation (1) in order to obtain quantitative values for the multipole moments.[d]

The Sun being assumed to be spherically symmetric, since all the multipole moments are induced by the presence of the external field $\boldsymbol{g}_e$ in the preferred direction $\boldsymbol{e}$, the situation is axisymmetric and all the moments Q_L will have their axis pointing in that direction $\boldsymbol{e}$. Thus we can define some multipole coefficients Q_l by posing $Q_L = Q_l\,\hat{e}^L$, where $\hat{e}^L$ denotes the STF part of the product of l unit vectors $e^L = e^{i_1}\cdots e^{i_l}$. The multipole expansion (7) reads then as

$$\delta\boldsymbol{u}(r,\theta) = \sum_{l=0}^{+\infty} \frac{(-)^l}{(2l-1)!!}\, r^l\, Q_l(r)\, P_l(\cos\theta)\,, \tag{10}$$

where $P_l(z)$ is the usual Legendre polynomial and θ is the angle away from the Galactic direction $\boldsymbol{e}$. Although from the previous considerations the multipole coefficients Q_l should be approximately constant within the MOND transition radius r_0, here we compute them directly from the numerical solution of (1) and shall obtain their dependence on r. With our definition the quadrupolar piece in the internal field is given by

$$\delta u_2 = \frac{1}{2}\, r^2\, Q_2(r) \left(\cos^2\theta - \frac{1}{3}\right)\,. \tag{11}$$

The radial dependence of the anomaly (11) is $\propto r^2$ and can thus be separated from a quadrupolar deformation due to the Sun's oblateness which decreases like $\propto r^{-3}$.

As a first result, we show in Fig. 1 the profile of the quadrupole induced by the MOND theory through the function $Q_2(r)$ defined in Eq. (11). We find that this quadrupole is decreasing from

[d]Our numerical scheme is based on the very efficient integrator of elliptic equations LORENE, available from the website `http://www.lorene.obspm.fr`.

Table 1: Numerical values of the quadrupole Q_2 together with the associated dimensionless quantity q_2 defined by Eq. (12). All values are given near the Sun. We use different choices of the function $\mu(y)$ defined in Eqs. (13).

MOND function	$\mu_1(y)$	$\mu_2(y)$	$\mu_{20}(y)$	$\mu_{\exp}(y)$	$\mu_{\mathrm{TeVeS}}(y)$
Q_2 [s^{-2}]	3.8×10^{-26}	2.2×10^{-26}	2.1×10^{-27}	3.0×10^{-26}	4.1×10^{-26}
q_2	0.33	0.19	1.8×10^{-2}	0.26	0.36

the Sun's neighbourhood to zero, on a typical scale of 10000 astronomical units (AU). However, we check numerically that $Q_2(r)$ is almost constant in a large sphere surrounding the Solar system, as it has a relative variation lower than 10^{-4} within 30 AU (see the zoomed region in Fig. 1). We shall therefore refer to the quadrupole as a simple number, noted $Q_2(0)$ or simply Q_2, when evaluating its influence on the orbits of Solar-system planets.

On dimensional analysis we expect that the quadrupole coefficient Q_2 should scale with the MOND acceleration a_0 like

$$Q_2 = \frac{a_0}{r_0}\, q_2(\eta)\,, \tag{12}$$

where $r_0 = \sqrt{GM/a_0}$ is the MOND transition radius and where the dimensionless coefficient q_2 depends on the ratio $\eta = g_e/a_0$ between the external field and a_0, and on the choice of the interpolating function μ. Our numerical results for the quadrupole are given in Table 1, for different coupling functions $\mu(y)$.[e] Here we consider various cases widely used in the literature:

$$\mu_n(y) = \frac{y}{\sqrt[n]{1+y^n}}\,, \tag{13a}$$

$$\mu_{\exp}(y) = 1 - e^{-y}\,, \tag{13b}$$

$$\mu_{\mathrm{TeVeS}}(y) = \frac{\sqrt{1+4y}-1}{\sqrt{1+4y}+1}\,. \tag{13c}$$

The function μ_1 has been shown to yield good fits of galactic rotation curves[9]; However because of its slow transition to the Newtonian regime it is *a priori* incompatible with Solar System observations. The function μ_2 is generally called the "standard" choice and was used in fits[10]. We include also the function $\mu_{\exp}$ having an exponentially fast transition to the Newtonian regime. The fourth choice μ_{TeVeS} is motivated by the TeVeS theory[11]. One should note that none of these functions derives from a fundamental physical principle.

We have used several functions of type μ_n, as defined in Eq. (13a). One can notice that the value of Q_2 decreases with n, that is with a faster transition from the weak-field regime where $\mu(y) \sim y$, to the strong field regime where $\mu(y) \sim 1$. We have been unable to determine numerically a possible limit for Q_2 as n goes to infinity.

4 Effect on the dynamics of the Solar System planets

We investigate the consequence for the dynamics of inner planets of the Solar System of the presence of an abnormal quadrupole moment Q_2 oriented toward the direction $\boldsymbol{e}$ of the galactic centre. Recall that the domain of validity of this anomaly is expected to enclose all the inner Solar System (for distances $r \lesssim r_0 \approx 7100$ AU), with the quadrupole coefficient being constant up to say 50 AU (see Fig. 1). As we have seen, the anomaly induces a perturbation on the Newtonian gravitational potential, namely $u = u_N + \delta u$, where $u_N = GM/r$ and the perturbation function $R \equiv \delta u$ is given for the quadrupole moment by Eq. (11).

[e] Note that the quadrupole coefficient Q_2 is found to be always positive which corresponds to a prolate elongation along the quadrupolar axis.

We apply the standard linear perturbation equations of celestial mechanics [12]. The unperturbed Keplerian orbit of a planet around the Sun is described by six orbital elements. For these we adopt the semi-major axis a, the eccentricity e, the inclination I of the orbital plane, the mean anomaly ℓ defined by $\ell = n(t - T)$ where $n = 2\pi/P$ (n is the mean motion, P is the orbital period and T is the instant of passage at the perihclion), the argument of the perihelion ω (or angular distance from ascending node to perihelion), and the longitude of the ascending node Ω. We also use the longitude of the perihelion defined by $\tilde{\omega} = \omega + \Omega$.

The perturbation function $R = \delta u_2$ is a function of the orbital elements of the unperturbed Keplerian ellipse, say $\{c_A\} = \{a, e, I, \ell, \omega, \Omega\}$. The perturbation equations are generated by the partial derivatives of the perturbation function with respect to the orbital elements, namely $\partial R/\partial c_A$. We express the planet's absolute coordinates (x, y, z) (in some absolute Galilean frame) in terms of the orbital elements $\{a, e, I, \ell, \omega, \Omega\}$ by performing as usual three successive frame rotations with angles Ω, I and ω, to arrive at the frame (u, v, w) associated with the motion, where (u, v) is in the orbital plane, with u in the direction of the perihelion and v oriented in the sense of motion at perihelion. The unperturbed coordinates of the planet in this frame are

$$\begin{aligned} u &= a\,(\cos U - e)\,, && (14\text{a}) \\ v &= a\sqrt{1-e^2}\,\sin U\,, && (14\text{b}) \\ w &= 0\,, && (14\text{c}) \end{aligned}$$

where U denotes the eccentric anomaly, related to ℓ by the Kepler equation $\ell = U - e\sin U$. The perturbation equations provide the variations of the orbital elements $\mathrm{d}c_A/\mathrm{d}t$ as linear combinations of the partial derivatives $\partial R/\partial c_B$ of the perturbation function. We are interested only in secular effects, so we average in time the perturbation equations over one orbital period P. Denoting the time average by brackets, and transforming it to an average over the eccentric anomaly U, we have

$$\left\langle \frac{\mathrm{d}c_A}{\mathrm{d}t} \right\rangle = \frac{1}{P}\int_0^P \mathrm{d}t\,\frac{\mathrm{d}c_A}{\mathrm{d}t} = \frac{1}{2\pi}\int_0^{2\pi} \mathrm{d}U\,(1 - e\cos U)\,\frac{\mathrm{d}c_A}{\mathrm{d}t}\,. \tag{15}$$

In the following, to simplify the presentation, we shall choose the x-direction of the absolute Galilean frame to be the direction of the galactic centre $\boldsymbol{e} = \boldsymbol{g}_e/g_e$. That is, we assume that the origin of the longitude of the ascending node Ω lies in the direction of the galactic centre. Furthermore, in order to make some estimate of the magnitude of the quadrupole effect, let us approximate the direction of the galactic centre (which is only 5.5 degrees off the plane of the ecliptic) as being located in the plane of the orbit; consequently we choose $I = 0$. In this case $\tilde{\omega} = \omega + \Omega$ is the relevant angle for the argument of the perihelion. We then find the following non-zero evolution equations:

$$\begin{aligned} \left\langle \frac{\mathrm{d}e}{\mathrm{d}t} \right\rangle &= \frac{5Q_2 e\sqrt{1-e^2}}{4n}\sin(2\tilde{\omega})\,, && (16\text{a}) \\ \left\langle \frac{\mathrm{d}\ell}{\mathrm{d}t} \right\rangle &= n - \frac{Q_2}{12n}\Big[7 + 3e^2 + 15(1+e^2)\cos(2\tilde{\omega})\Big]\,, && (16\text{b}) \\ \left\langle \frac{\mathrm{d}\tilde{\omega}}{\mathrm{d}t} \right\rangle &= \frac{Q_2\sqrt{1-e^2}}{4n}\Big[1 + 5\cos(2\tilde{\omega})\Big]\,. && (16\text{c}) \end{aligned}$$

We recall that $\tilde{\omega}$ is the azimuthal angle between the direction of the perihelion and that of the galactic centre (approximated to lie in the orbital plane). Of particular interest is the secular precession of the perihelion $\langle \mathrm{d}\tilde{\omega}/\mathrm{d}t \rangle$ due to the quadrupole effect henceforth denoted by

$$\Delta_2 = \frac{Q_2\sqrt{1-e^2}}{4n}\Big[1 + 5\cos(2\tilde{\omega})\Big]\,. \tag{17}$$

Table 2: Results for the precession rates of planets Δ_2 due to the quadrupole coefficient Q_2. We use the values for Q_2 for various MOND functions as computed in Table 1. Published postfit residuals of orbital precession (after taking into account the relativistic precession). All results are given in milli-arc-seconds per century.

Quadrupolar precession rate Δ_2 in mas/cy								
MOND function	Mercury	Venus	Earth	Mars	Jupiter	Saturn	Uranus	Neptune
$\mu_1(y)$	0.04	0.02	0.16	-0.16	-1.12	5.39	-10.14	7.93
$\mu_2(y)$	0.02	0.01	0.09	-0.09	-0.65	3.12	-5.87	4.59
$\mu_{20}(y)$	2×10^{-3}	10^{-3}	9×10^{-3}	-9×10^{-3}	-0.06	0.3	-0.56	0.44
$\mu_{\exp}(y)$	0.03	0.02	0.13	-0.13	-0.88	4.25	-8.01	6.26
$\mu_{\text{TeVeS}}(y)$	0.05	0.02	0.17	-0.17	-1.21	5.81	-10.94	8.56
Postfit residuals for $\Delta = \langle d\tilde{\omega}/dt \rangle$ in mas/cy								
Origin	Mercury	Venus	Earth	Mars	Jupiter	Saturn	Uranus	Neptune
Pitjeva [13]	-3.6 ± 5	-0.4 ± 0.5	-0.2 ± 0.4	0.1 ± 0.5	-	-6 ± 2	-	-
Fienga *et al.* [14]	-10 ± 30	-4 ± 6	0 ± 0.016	0 ± 0.2	142 ± 156	-10 ± 8	$0 \pm 2 \cdot 10^4$	$0 \pm 2 \cdot 10^4$
Fienga *et al.* [15]	0.4 ± 0.6	0.2 ± 1.5	-0.2 ± 0.9	-0.04 ± 0.15	-41 ± 42	0.15 ± 0.65	-	-

The precession is non-spherical, in the sense that it depends on the orientation of the orbit relative to the galactic centre through its dependence upon the perihelion's longitude $\tilde{\omega}$. The effect scales with the inverse of the orbital frequency $n = 2\pi/P$ and therefore becomes more important for outer planets like Saturn than for inner planets like Mercury. This is in agreement with the fact that the quadrupole effect we are considering increases with the distance to the Sun (but of course will fall down when r becomes appreciably comparable to r_0, see Fig. 1).

Our numerical values for the quadrupole anomalous precession Δ_2 are reported in Table 2. As we see the quadrupolar precession Δ_2 is in the range of the milli-arc-second per century which is not negligible. In particular it becomes interestingly large for the outer gaseous planets of the Solar System, essentially Saturn, Uranus and Neptune. The dependence on the choice of the MOND function μ is noticeable only for functions $\mu_n(y)$ defined by (13a) with large values of n, where the effect decreases by a factor ~ 10 between $n = 2$ and $n = 20$.

We then compare in Table 2 our results to the best published postfit residuals for any possible supplementary precession of planetary orbits (after the relativistic precession has been duly taken into account), which have been obtained from global fits of the Solar System dynamics [13,14,15]. In particular the postfit residuals obtained by the INPOP planetary ephemerides [14,15] use information from the combination of very accurate tracking data of spacecrafts orbiting different planets. We find that the values for Δ_2 are smaller or much smaller than the published residuals except for the planets Mars and Saturn. Very interestingly, our values are smaller or grossly within the range of the postfit residuals for these planets. In the case of Saturn notably, the constraints seem already to exclude most of our obtained values for Δ_2, except for MOND functions of the type μ_n and given by (13a) with rather large values of n.

However let us note that the INPOP ephemerides are used to detect the presence of an eventual abnormal precession, not to adjust precisely the value of that precession [14,15]. On the other hand the postfit residuals are obtained by adding by hands an excess of precession for the planets and looking for the tolerance of the data on this excess [14,15]. But in order to really test the anomalous quadrupolar precession rate Δ_2, one should consistently work in a MOND picture, i.e. consider also the other effects predicted by this theory, like the precession of the nodes, the variation of the eccentricity and the inclination, and so on — see Eqs. (16). Then one should perform a global fit of all these effects to the data; it is likely that in this way the quantitative conclusions would be different.

Finally let us cautiously remark that MOND and more sophisticated theories such as TeVeS[11], which are intended to describe the weak field regime of gravity (below a_0), may not be extrapolated without modification to the strong field of the Solar System. For instance it has been argued[9] that a MOND interpolating function μ which performs well at fitting the rotation curves of galaxies is given by μ_1 defined by (13a). However this function has a rather slow transition to the Newtonian regime, given by $\mu_1 \sim 1 - y^{-1}$ when $y = g/a_0 \to \infty$, which is already excluded by Solar System observations. Indeed such slow fall-off $-y^{-1}$ predicts a constant supplementary acceleration directed toward the Sun $\delta g_{\rm N} = a_0$ (i.e. a "Pioneer" effect), which is ruled out because not seen from the motion of planets. Thus it could be that the transition between MOND and the Newtonian regime is more complicated than what is modelled by Eq. (1). This is also true for the dipolar dark matter model [7,8] which may only give an effective description valid in the weak field limit and cannot be extrapolated as it stands to the Solar System. While looking at MOND-like effects in the Solar System we should keep the previous *proviso* in mind. The potential conflict we find here with the Solar System dynamics (notably with the constraints on the orbital precession of Saturn [14,15]) may not necessarily invalidate those theories if they are not "fundamental" theories but rather "phenomenological" models only pertinent in a certain regime.

In any case, further studies are to be done if one wants to obtain more stringent conclusions about constraints imposed by Solar-system observations onto MOND-like theories. More precise observations could give valuable informations about an eventual EFE due to the MOND theory and restrict the number of possible MOND functions that are compatible with the observations. More generally the influence of the Galactic field on the Solar-system dynamics through a possible violation of the strong version of the equivalence principle (of which the EFE is a by-product in the case of MOND) is worth to be investigated.

1. M. Milgrom. *Astrophys. J.*, 270:365, 1983; *ibid.* 270:371, 1983; *ibid.* 270:384, 1983.
2. R.H. Sanders and S. McGaugh. *Ann. Rev. Astron. Astrophys.*, 40:263, 2002.
3. J.D. Bekenstein and M. Milgrom. *Astrophys. J.*, 286:7, 1984.
4. B. Famaey, J.-P. Bruneton, and H. Zhao. Escaping from modified newtonian dynamics. *Mon. Not. Roy. Astron. Soc.*, 377:L79, 2007.
5. M. Milgrom. Mond effects in the inner solar system. *Mon. Not. Roy. Astron. Soc.*, 399:474, 2009.
6. L. Blanchet and J. Novak. External field effect of modified newtonian dynamics in the solar system. *Mon. Not. Roy. Astron. Soc.*, 412:2530, 2011.
7. L. Blanchet and A. Le Tiec. Model of dark matter and dark energy based on gravitational polarization. *Phys. Rev. D*, 78:024031, 2008.
8. L. Blanchet and A. Le Tiec. Dipolar dark matter and dark energy. *Phys. Rev. D*, 80:023524, 2009.
9. B. Famaey and J. Binney. *Mon. Not. Roy. Astron. Soc.*, 363:603, 2005.
10. K. Begeman, A. Broeils, and R. Sanders. *Mon. Not. Roy. Astron. Soc.*, 249:523, 1991.
11. J.D. Bekenstein. *Phys. Rev. D*, 70:083509, 2004.
12. D. Brouwer and G.M. Clemence. *Methods of celestial mechanics.* Academic Press, New York, 1961.
13. E.V. Pitjeva. *Astron. Lett.*, 31:340, 2005.
14. A. Fienga, J. Laskar, P. Kuchynka, C. Leponcin-Laffite, H. Manche, and M. Gastineau. Gravity tests with inpop planetary ephemerides. 2009. In *Relativity in Fundamental Astronomy: Dynamics, Reference Frames, and Data Analysis*, edited by S. Klioner *et al*, Cambridge University Press, p. 159.
15. A. Fienga, H. Manche, P. Kuchynka, J. Laskar, and M. Gastineau. Planetary and lunar ephemerides, inpop10a. 2010. The documentation of INPOP10A is available at `www.imcce.fr/inpop`.

TESTING DARK MATTER WITH GAIA

O. BIENAYME

Strasbourg Observatory, 11 rue de l'université, 67000 Strasbourg, France

With the advent of Gaia, it will be possible to design tests of gravity on the scale of the Galaxy. Accurate measurements of positions and velocities of few hundred millions stars will allow to detail the stellar kinematics and Galactic dynamics, to draw the gravitational potential and to recover the 3D distribution of dark matter. Gaia data will allow to test modified gravity interpretations on a galactic scale, like MOND that makes very specific predictions allowing to differentiate it from a spheroidal halo of dark matter.

Introduction

:he Gaia satellite will survey the sky with three instruments. It will realize a nearly all sky ›hotometric survey within visible bands, an astrometric survey that will measures positions, ›arallaxes and proper motions, and a radial velocity survey.

The combination of data from these surveys will allow to determine the 3D positions and D velocities of large sample of stars over a significant volume of the Galaxy. This will allow o recover the gravitational potential over this volume of the Galaxy. Gaia will also perform an .ccurate determination of the distribution of visible mass. From these determinations, it will ›e possible for the first time to map precisely the unseen mass within our Galaxy. Hipparcos ıad constrained the amount of dark matter in the solar neigbourhood, Gaia will do it for a ignificant fraction of the volume of our Galaxy.

Tests of the relativity within the solar system will be performed with Gaia. Hestroffer et .l (2009) showed that observations of asteroids with Gaia allow a joint determination of the olar quadrupole J_2 and the PPN parameter β, a possible variation of the gravitational constant dG/dt)/G, and deviation from Newtonian law. A detailed list of tests (Mignard & Klioner 009) includes a measure of γ from light deflection with a precision of 2×10^{-6}, test of the Local ,orentz Invariance, detection of possible gravitational wave flux.

In this presentation, we propose a new test of the gravity on galactic scales: modification of he newtonian dynamics have been proposed to explain flat rotation curve of galaxies without .eed of dark matter. MOND is such a phenomenological 'theory' that implies flat rotation curve .t large radius for galaxies, it also implies predictions on the kinematics of stars and on the 3D hape of the gravitational potential. We may expect that any modifications of the relativity to xplain rotation curves in galaxy should also imply other observable properties identifiable with :aia observations.

2 Dark matter within our Galaxy

2.1 The K_z force perpendicular to the galactic plane

Kapteyn (1922) showed the similarity between the motion of stars perpendicular to the galactic plane and the hydrostatic equilibrium of the terrestrial atmosphere. Thus, Oort (1932) measuring the vertical distribution of stars and their vertical velocity dispersion deduced dynamically the force and potential perpendicular to the galactic plane, and he opened the question of a large amount of unseen mass within the galactic disk. It is only with Hipparcos satellite observations and accurate measure of distances and velocities that it has been clear that no large amount of dark matter was present within the galactic disk in the solar neigbourhood (Crézé et al 1998).

2.2 Flat rotation curve in spiral galaxies

Measuring the rotational velocities of gas, Rubin et al (1978) within Hα regions, Bosma (1981) with HI, found that the rotation curve of spiral galaxies was flat far from the galactic center, implying that the dynamically measured mass of these galaxies was one or more order of magnitudes larger than the visible stellar mass deduced from photometry.

2.3 Our Galaxy

Most of the techniques to estimate the gravitational potential of our Galaxy are described in Binney and Tremaine (2008). With the ongoing RAVE (Siebert et al 2011) and SEGUE (Yanny et al 2009) surveys that are measuring radial velocities of a few hundred thousand stars, it has been possible, using traditional techniques, to revisit more accurately the gravitational potential of our Galaxy, avoiding the limitation of previously tiny samples.

Thus, selecting stars with accurately determined distances at 1 kpc above the galactic plane, radial velocities and proper motions, Siebert et al (2008) determined the exact orientation of the velocity ellipsoid that points towards a direction close to the galactic center. The tilt orientation gives the correlation between galactic radial and vertical motions of stars, it is related to the bending of orbits towards the galactic center when stars move out the galactic plane. Thus Siebert et al (2008) constrained the potential shape within the 1 kpc solar vicinity and showed there is no large amount of dark matter within the galactic disk. Works with larger data samples confirmed this finding (Casetti-Dinesu et al 2011). It may be noted that the coupling between the (u, v, w) velocity components of ~3000 Hipparcos stars, within a 125 pc radius around the Sun, led to the same conclusion (Bienaymé 1999).

The gravitational potential at large distances from the galactic center is obtained by measuring the escape velocity at the solar position. This was achieved by determining the velocity distribution function of high velocity stars by comparison with predicted distribution functions and N-body numerical simulations (Smith et al 2007).

At large distances, a more direct measure of the gravitational potential is obtained from the radial velocity distribution of distant halo stars. Thus, the analysis of BHB stars from SDSS observations showed that the rotation curve remains flat at 60 kpc (Xue et al 2008). A significant uncertainty remains due to present lack of accuracy on proper motions of very distant stars and consequently our partial ignorance of the real 3D motions of these distant stars (Przybilla et al 2010).

2.4 Our Galaxy

Most of the methods used to constrain the potential are applications of the Jeans equations, moments of the Bolzmann equation, but the recent discoveries of streams and tails of accreted galaxy satellites in the galactic halo appeared as a new and efficient opportunity to draw the galactic potential. Moreover, from our current understanding of the formation of galaxies, few hundreds of galaxy satellites must have been accreted by our Galaxy and Gaia should allow to identify a large fraction of the streams, remnants of these accreted galaxies. Most stars within a given stream follow (approximately) the same orbit within the galactic halo: measuring all star positions and velocities we should deduce directly the gravitational forces along each stream.

Such analysis were performed with the tails of the Sagittarius dwarf that cover more than 360 degrees over the sky (Ibata et al 2001). With the help of numerical simulations the galactic potential was deduced from the shape of the tails. Remaining uncertainties results from the modeling of the internal kinematics of the progenitor galaxy that affects the exact trajectories of tails. The velocity dispersion within the tail of the globular cluster Pal 5 is only a few km/s, in concordance with its small thickness. Other sharp and long streams have been discovered from the SDSS survey (Belokourov et al 2007), all these streams are used to obtain new constrains on the galactic potential.

A young stream stays visible in the configuration space, while older streams disappear being diluted within the configuration space. However, even diluted in the halo, stars belonging to the same stream conserve (adiabatically) the three integrals of motion because the gravitational potential of the Galaxy is evolving slowly. These diluted streams could be easily recovered when we know the potential and the integrals of motion associated to this potential. Numerical simulations (Helmi 2008) show it works even with approximate integral of motions.

3 Gaia perfomances

3.1 Gaia performances

Gaia will perform three surveys with three different instruments, an astrometric survey, a photometric survey and a spectroscopic survey. The science-performance pages have been brought in line with the most recent performance predictions made by Astrium (April 2011):
http://www.rssd.esa.int/index.php?project=Gaia&page=Science_Performance

The astrometric survey will perform micro-arcsecond astrometry, parallaxes and proper motions, for all 1,000 million stars down to magnitude G=20 and fainter than G>6. Gaia will observe all objects including asteroids, supernovae, quasars, however in extremely dense areas only the brightest stars will be observed. Photometric observations will be collected for all these objects. Spectroscopic observations will be obtained for objects with G<16 and element abundances for the brightest stars with G<11

For a G2V star (absolute magnitude 0.75) the astrometric accuracy is 24 μas at V=15, corresponding to a 10% accuracy at a distance of 7 kpc, the proper motion accuracy corresponding to 1 km/s (neglecting the error from the parallaxe). This can be compared with the performance of the Hipparcos survey with a 10% accuracy obtained at 200 pc. Thus Gaia will probe a galactic volume 50000 times larger, and the number of stars observed will be increased by a factor $\sim$10000. The error on radial velocity for a G2V star will be 1km/s at G=12 and 13 km/s at G=16.3. Radial velocities will be measured for 150 million stars.

3.2 Selected goals on Milky Way dynamics

The gravitational potential will be measured, with methods as these previously described, using extremely large samples from Gaia catalogues. A very accurate galactic potential should be obtained directly with details within a sphere of 7 kpc radius around the Sun, and resonant orbits should be identified. At larger distances, accurate photometric distances will be available since Gaia will allow accurate photometric calibration from closer stars. For instance all RR Lyrae variable stars will identified with Gaia, and they will be used to probe the dynamics and the potential at very large distances up to 50-80 kpc.

Gaia will also allow an accurate determination of the faint end of the stellar luminosity function and will measure the dominant contribution of low mass stars to the mass budget of the different galactic stellar components. This is a central question since the difference between the galactic mass determined from the dynamics and the stellar one, will give the invisible mass or dark matter distribution.

Other results will be obtained concerning the internal dynamics of the stellar disk and its gravitational potential by the observation and measure of the disk warp and flare as well as their rotation and vertical oscillations.

To measure the gravitational potential, the identification of streams will offer a new and promising perspective. The accretion events remain visible during a very long time in the phase space. While after many billion years, the spatial distribution of an accreted satellites or disrupted globular cluster will be uniform within the inner halo, the distribution of the corresponding stars stays clumpy in the velocity space, and are even easier to identify within the 3D integrals of motion space. If most of the inner halo is formed from such accretion events, a few hundreds streams or clumps will be visible in the phase space.

When a stream is identified, the galactic force is accurately constrained in the surrounding position of every star of that stream. Thus potentially a very fine description of the potential should be achievable at the position of many halo stars, more accurately than any other technique and it will allow an accurate identification of a dark disk, of a dark thick disk, the description of their shape, thickness, triaxiallity... if they exists.

How much clumpy is the dark halo is an open question. Depending on the size of clumps, it will modify and disperse the orbits of streams. This will certainly complicate the analysis and identification of streams, but, as far as we know, not much work has yet explored this question in details.

4 Testing gravity with Gaia

A currently debated question is whether the missing mass problem is due to the existence of dark matter or to a modification of the gravitational law on galaxy scales. Here, following the work of Bienaymé et al (2009), we show how large-scale spectroscopic and astrometric surveys in general, and Gaia in particular, could help answer this question.

4.1 Cold Dark Matter or Modified Newtonian Dynamics?

The concordance cosmological model based on the existence of Cold Dark Matter is successful on large scales. However, the predictions of the model are in contrast with a number of observational facts on galaxy scales. Some well known issues are (i) the predicted overabundance of satellite galaxies; (ii) the prediction of cuspy dark matter halos, whereas observations point toward dark halos with a central constant density core; (iii) the problems to form large enough baryonic disks due to their predicted low angular momentum within simulations. In addition galaxies follow tight scaling relations that involve an acceleration $a_0 = 10^{-10}$ m.s^{-2}, for instance the universality of the dark and baryonic surface densities of galaxies within one scale-length of the dark halo (Gentile et al 2009). Below this gravitational acceleration, the enclosed dark mass starts to dominate over baryons in galaxies, and this acceleration scale also fixes the slope and zero-point of the Tully-Fisher and Faber-Jackson relations.

Milgrom (1983) postulated that for gravitational accelerations below a_0, the true gravitational attraction is modified and MOND, the modified gravity interpretation (Bekenstein & Milgrom 1984), makes very specific predictions allowing to differentiate it from a spherical halo of dark matter. Here, we outline these predictions, that Gaia and other large-scale surveys could help to test.

4.2 How Gaia can help

We build these predictions with the MOND Milky Way model of Wu et al (2008). This model is based on one of the most realistic possible baryonic mass models of the Milky Way, the Besançon model (Robin et al 2003). Once the MOND gravitational potential of the model is known, one can apply the Newtonian Poisson equation to it, in order to find back the density distribution that would have yielded this potential within Newtonian dynamics. In this context, as shown in Bienaymé et al (2009), MOND predicts a disk of phantom dark matter allowing to differentiate it from a Newtonian model with a dark halo. (i) By measuring the force perpendicular to the Galactic plane: at the solar radius, MOND predicts a 60 percent enhancement of the dynamical surface density at 1.1 kpc compared to the baryonic surface density, a value not excluded by current data. The enhancement would become more apparent at large galactic radii where the stellar disk mass density becomes negligible. (ii) By determining dynamically the scale length of the disk mass density distribution. This scale length is a factor 1.25 larger than the scale length of the visible stellar disk if MOND applies. Such test could be applied with existing RAVE data (Zwitter et al 2008), but the accuracy of available proper motions still limits the possibility to explore the gravitational forces too far from the solar neighbourhood. (iii) By measuring the velocity ellipsoid tilt angle within the meridional galactic plane. This tilt is different within the two dynamics in the inner part of the Galactic disk. However the tilt of about 6 degrees at z=1 kpc at the solar radius is in agreement with the recent determination of 7.3 ± 1.8 degrees obtained by Siebert et al (2008). The difference between MOND and a Newtonian model with a spherical halo becomes significant at z=2 kpc.

Such easy and quick tests of gravity could be applied with the first releases of future Gaia data. Let us however note that these predictions are extremely dependent on the baryonic content of the model, so that testing gravity at the scale of the Galaxy heavily relies on star counts, stellar population synthesis, census of the gaseous content (including molecular gas), and inhomogeneities in the baryonic distribution (clusters, gas clouds).

Acknowledgments

We thank Benoît Famaey, HongSheng Zhao, Xufen Wu, and Dominique Aubert for their contribution to Bienaymé et al (2009).

References

1. D. Hestroffer, S. Mouret *et al*, *Proceedings IAU* **261**, 325 (2009).
2. F. Mignard, S.A. Klioner, *Proceedings IAU* **261**, 306 (2009).
3. J.C. Kapteyn, *ApJ* **55**, 302 (1922).
4. J.H. Oort, *BAN* **6**, 249 (1932).
5. M. Crézé, E. Chereul, O. Bienaymé, C. Pichon, *A&A* **329**, 920 (1998).
6. V. C. Rubin, W.K. Ford, N. Thonnard *et al*, *ApJ* **225**, L107 (1978).
7. A. Bosma, *ApJ* **86**, 1825 (1981).
8. J. Binney, S. Tremaine, *Galactic Dynamics* , Princeton University Press (2008).
9. A. Siebert *et al*, *ApJ* , *in press* (2011).
10. B. Yanny *et al*, *AJ* **137**, 4377 (2009).
11. A. Siebert *et al*, *MNRAS* **391**, 793 (2008).
12. D.J. Casetti-Dinescu *et al*, *ApJ* **728**, 7 (2011).
13. O. Bienaymé, *A&A* **341**, 86 (1999).
14. M. Smith *et al*, *MNRAS* **379**, 755 (2007).
15. X.X. Xue *et al*, *ApJ* **684**, 1143 (2008).

16. N. Przybilla *et al*, *ApJ* **718**, 37 (2010).
17. R. Ibata *et al*, *ApJ* **551**, 294 (2001).
18. V. Belokurov *et al*, *ApJ* **658**, 337 (2007).
19. A. Helmi, *ARAA* **15**, 145 (2008).
20. O. Bienaymé *et al*, *A&A* **500**, 801 (2009).
21. L.C. Gentile *et al*, *Nature* **461**, 627 (2009).
22. M. Milgrom *et al*, *ApJ* **270**, 365 (1983).
23. J. Bekenstein, M. Milgrom, *ApJ* **286**, 7 (1984)
24. X. Wu *et al*, *MNRAS* **386**, 2199 (2008).
25. A.C. Robin *et al*, *A&A* **409**, 523 (2003).
26. T. Zwitter *et al*, *AJ* **136**, 421 (2008).

BEYOND EINSTEIN: COSMOLOGICAL TESTS OF MODEL INDEPENDENT MODIFIED GRAVITY

D.B. THOMAS AND C.R. CONTALDI
Theoretical Physics, Blackett Laboratory, Imperial College, London, England SW7 2AZ

Model-independent parametrisations of modified gravity have attracted a lot of attention over the past few years; numerous combinations of experiments and observables have been suggested to constrain these parameterisations, and future surveys look very promising. Galaxy Clusters have been mentioned, but not looked at as extensively in the literature as some other probes. Here we look at adding Galaxy Clusters into the mix of observables and examine whether they could improve the constraints on the modified gravity parameters. In particular, we forecast the constraints from combining the Planck CMB spectrum and SZ cluster catalogue and a DES-like Weak Lensing survey. We've found that adding cluster counts improves the constraints obtained from combining CMB and WL data.

1 Introduction

Einstein's General Relativity (GR) is one of the principal ingredients of modern cosmology. Nonetheless, it is our job as physicists to continue to test even the fundamental pillars of cosmology in order to refine, improve and further justify our model of the universe. Testing GR outside of the solar system can be quite challenging, particularly as the effects of a different theory of gravity could be degenerate with different possible constituents of the universe. This is the case with the current cosmological observations that suggest the presence of dark matter and dark energy. As well as explaining these observations, there are also fundamental physics reasons for considering different theories of gravity: GR is inconsistent with quantum mechanics and the search for "Quantum Gravity" is one of the holy grails of modern physics.

Here, we are interested in testing deviations from GR in a model independent way. There are several advantages to a model independent approach; some alternatives to GR do exist but there is no complete theory of, for example, quantum gravity to draw on. Also, amongst the many options there are no "stand-out" candidates that are universally considered to be strong alternatives. If a model independent approach suggests that the data is inconsistent with concordance cosmology and GR, it will be relatively unambiguous and therefore a strong motivator to develop alternative theories, as well as possibly giving us a clue as to the nature of these theories.

There are studies in the literature on the constraining power of current data [1,2] and the general conclusion is that the concordance cosomology is consistent with all of the current data, although the data isn't strongly constraining. Work has also gone into forecasting future experiments [3,4] and again there is a fair degree of consensus here, namely that future surveys will greatly improve prospects. In this work we will examine the constraints that can be put on model independent modified gravity using the combination of Cosmic Microwave Background anisotropies (CMB) cross-correlated with weak lensing surveys and galaxy cluster counts.

2 Modified Gravity

Our potentials are defined in a flat FRW metric in the Newtonian gauge by $g_{00} = -1 - 2\Psi(\vec{x},t)\,, g_{0i} = 0\,, g_{ij} = a^2\delta_{ij}(1 - 2\Phi(\vec{x},t))$. Ψ is the Newtonian potential and is responsible for the acceleration of massive particles. Φ is the curvature potential, which contributes to the acceleration of relativistic particles only.
Several sets of modified gravity parameters (MGPs) have been proposed, see [5] for one of the first papers and [6] for a partial translation table between the different parameterisations In this work we will use two MGPs, η and μ, following[7] and implemented in the code MGCAMB, to describe departures from GR. The first, η, is the ratio of the two metric potentials, $\eta = \Psi/\Phi$. This will be approximately unity in GR unless any of the particle species has large anisotropic stress. The second, μ, is a modification of the poisson equation, and is essentially a time and space dependent Newton's constant. Fourier expanding the spatial dependence with wavenumbers k and assuming isotropy, the modification of the Possion equation is as follows

$$k^2\Psi(a,k) = -4\pi G a^2 \mu(a,k)\rho(a)\Delta(a,k)\,, \tag{1}$$

where, a is the FRW scale factor, G is Newton's constant, ρ is the background density of cold dark matter and Δ is the gauge invariant density contrast.
We will assume that GR is valid up to a specified redshift $z_{mg} = 30$. Beyond this, we assume that the MGPs transition to a constant value that is different to the GR value. The background expansion history is already constrained to be close to that of a ΛCDM model, we will therefore assume that the modified gravity mimics the expansion history of a standard ΛCDM setup.

3 Observables

3.1 Cluster Counts

Galaxy clusters are some of the largest collapsed structures in the universe. According to the standard ΛCDM cosmology, they typically consist of hot gas bound in a large cold dark matter halo. They are a useful cosmological probe as their size corresponds to scales near the linear to non–linear transition in the underlying dark matter power spectrum. This has several consequences: they probe the tail of the matter perturbation spectrum and are therefore a sensitive probe of growth. In addition, galaxy cluster counts can be predicted accurately from the linear theory matter power spectrum, using semi-analytic formulae or ones calibrated from N-body simulations.
Our theoretical predictions for the number of clusters in redshift bins will be compared to predicted SZ catalogues for a number of future observational stages. The SZ effect [8] is a nearly redshift independent tracer of clusters that is due to the rescattering of CMB photons by hot intracluster gas. The observational limits on SZ observations are, in principle, determined simply by resolution and sky coverage.

3.2 CMB

With the release of Planck satellite [9] results only a few years away we are entering an era where observations of the CMB total intensiy spectrum will have reached the sample variance limit throughout scales where primary effects dominate the signal. The sensitivity to MGPs in the CMB spectrum is restricted to the largest scales and the main signal that will arise on these scales is the ISW effect. This is sourced as the Universe transitions into a dark energy dominated model and the potential starts to decay. The effect can be described by the integral of the time-deritvative of the sum of metric potentials along the line of sight.

3.3 Weak lensing

The third observable we will use is the convergence power spectrum from weak lensing surveys. Weak lensing is a relatively new cosmological tool and is a measure of the small distortions of background galaxies caused by gravitational lensing by large scale structure [10,11]. Distortions of individual bckground galaxies are virtually impossible to measure due to the intrinsic ellipticity of galaxies. However, statistical results averaging over large numbers of galaxies are now routinely reported.

For our initial weak lensing survey, we consider a DES-like survey. DES [12] (Dark Energy Survey) is a ground based survey that is scheduled to begin observations in 2011. It will survey 5000 sq deg over 5 years and aims to constrain dark energy with 4 probes: supernovae, BAO, galaxy clusters and weak lensing, the latter being the probe we are interested in here.

4 Forecasts

In this Section we carry out forecasts for two future observational 'Stages'. For weak lensing and cluster counts we will assume two distinct observational stages corresponding to short and long term development of survey sizes and accuracies. This is unnecessary for the CMB as the data from Planck over the range of interest will be cosmic variance limited and therefore essentially as good as theoretically possible.

Stage 1 corresponds to a Planck-like SZ survey and a DES-like weak lensing survey. DES will be carried out on the Cerro Tololo Inter-American Observatory in the Chilean Andes and should start taking data in late 2011. The stage 2 weak lensing survey is based on the LSST [13], due to begin taking data in 2020. The stage 2 SZ survey corresponds to a Planck-like survey, but with a better flux resolution, allowing smaller mass clusters to be detected.

Our forecasts will be based on Fisher matrix [14,15] estimates of errors in a subset of parameters comprising the MGPs η and μ and two parameters from the standard model that are expected to be most correlated with them, namely, the total matter density Ω_m and the primordial amplitude of scalar curvature perturbations A.

5 Results

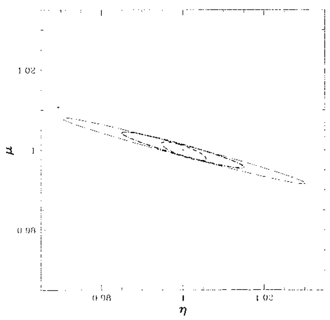

Figure 1: Fisher constraints on η and μ from combined CMB and weak lensing (including cross-correlations), red (dashed). The improvement obtained by adding cluster counts is seen in the blue (short-dashed) ellipse. When self-calibration uncertainties of the cluster data are included the constraints are weakened slightly (black, dash-dotted). All cases are for Stage I.

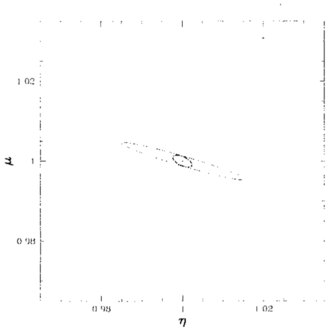

Figure 2: Fisher constraints on η and μ from combined CMB and weak lensing (including cross-correlations). red (dashed). The improvement obtained by adding cluster counts is seen in the black (dash-dotted) ellipse. All cases are for Stage III.

Table 1: 1σ constraints for first stage experiments

Parameter	CMB and WL cross-correlation	Clusters added	Cluster counts self calibrated
Ω_m	0.00104	0.00104	0.00104
Log $(10^{10}$ A)	0.00215	0.00214	0.00214
η	0.0300	0.00548	0.0150
μ	0.00835	0.00234	0.00451

After cross-correlating the CMB with weak lensing, the constraints on the MGPs are quite good. This is due to the complementarity between the data sets; with the CMB providing strong constraints on the standard parameters, any degeneracies between the standard parameters and the MGPs in the weak lensing data are broken. However, since both the CMB and weak lensing rely on the sum of the two potentials, there is still a degeneracy between the MGPs that is affecting the constraints. This is where the galaxy cluster counts are useful, as only Ψ is relevant and hence only μ contributes. Thus, the data from the cluster counts breaks the degeneracy between the MGPs from the CMB and Weak lensing, creating a much tighter constraint as shown in figure 1. There are some uncertainties associated with cluster counts[16], and these are also shown in figure 1. Although marginalising over these uncertainties reduces the impact of clusters, clusters still add to the constraining power of the CMB and Weak lensing. The constraints on the parameters for the first stage of experiments are shown in table 1. In addition, figure 2 shows how galaxy clusters are still a worthwhile addition to cross correlated CMB and weak lensing measurements for the longer term survey.

6 Conclusion

Over the next 5-10 years, deviations from GR should be well constrained, and the concordance cosmology will either be more secure or may even have undergone a paradigm shift. If the latter is the case, then the results from the model independent tests could be crucial in helping to find a new theory of gravity.

References

1. G.B. Zhao *et al*, *Phys. Rev.* D **81**, 103510 (2010)
2. R. Bean *et al*, *Phys. Rev.* D **81**, 083534 (2010)
3. P. Serra *et al*, *Phys. Rev.* D **79**, 101301 (2009)
4. G.B. Zhao *et al*, *Phys. Rev. Lett.* **103**, 241301 (2009)
5. W Hu *et al*, *Phys. Rev.* D **76**, 104043 (2007).
6. S.F. Daniel *et al*, *Phys. Rev.* D **81**, 123508 (2010)
7. G.B. Zhao *et al*, *Phys. Rev.* D **79**, 083513 (2009).
8. R.A. Sunyaev *et al*, Comments on Astrophysics and Space Physics **2**, 66 (1970)
9. The Planck Collaboration, astro-ph/0604069
10. N. Kaiser, Astrophys.J. **388**, 272 (1992)
11. A. Refregier, Ann.Rev.Astron.Astrophys. **41**, 645 (2003)
12. http://www.darkenergysurvey.org
13. http://www.lsst.org/lsst
14. M. Tegmark,*Phys. Rev. Lett.* **79**, 3806 (1997)
15. M. Tegmark *et al*,Astrophys.J **480**, 22 (1997)
16. M. Lima *et al*, *Phys. Rev.* D **72**, 043006 (2005)

9.
Weak equivalence principle

Equivalence Principle Torsion Pendulum Experiments

T. A. Wagner
Center for Experimental Nuclear Physics and Astrophysics, Box 354290,
University of Washington, Seattle, WA, 98195, USA

1 The equivalence principle

The universality of free fall exists as one of the oldest concepts in physics, yet even today measurements of the universality of free fall provide some of the strongest fundamental tests of physics. The universality of free fall is the most precisely tested aspect of the equivalence principle — in Newtonian terms the equality of inertial and gravitational mass. General relativity, which successfully describes all observed gravitational phenomena, incorporates the equivalence principle as a basic assumption. Ideas for unifying of the standard model and general relativity generally predict violations of the equivalence principle at some level[1]. Testing for violations constrains alternative theories of gravity and possible new forces weaker than gravity. Equivalence principle tests also provide a means of searching for non-gravitational interactions between ordinary matter and dark matter. The variety of concepts tested by equivalence principle experiments demonstrates their utility for expanding our understanding of physics. For a more detailed discussion of the physics that equivalence principle tests probe see Adelberger *et al* 2009[2], and for a discussion of ordinary equivalence principle tests and their relation to tests using antimatter see Adelberger *et al* 1991.[3]

The Yukawa potential provides a useful parameterization for equivalence principle tests. For two point particles separated by a distance r the potential is the following:

$$V(r) = -\alpha\frac{G\, m_A m_B}{r}\left(\frac{\tilde{q}}{\mu}\right)_A\left(\frac{\tilde{q}}{\mu}\right)_B e^{-r/\lambda}, \tag{1}$$

where α gives the strength relative to gravity, $\tilde{q}/\mu$ is the hypothetical new charge per atomic mass unit, and λ is the range of the interaction. The charge can be further parameterized in terms of the particles in ordinary, electrically neutral matter (composed of protons, electrons and neutrons) that could carry some hypothetical new charge:

$$\tilde{q}(\psi) = Z\cos(\psi) + N\sin(\psi), \tag{2}$$

where Z is proton number (degenerate with the number of electrons for electrically neutral matter) and N is neutron number. Other interesting charges include baryon number (B = Z + N), lepton number (L = Z), and B - L, which all appear to be conserved or nearly conserved. B - L is conserved in supersymmetric theories, though B and L individually are not.

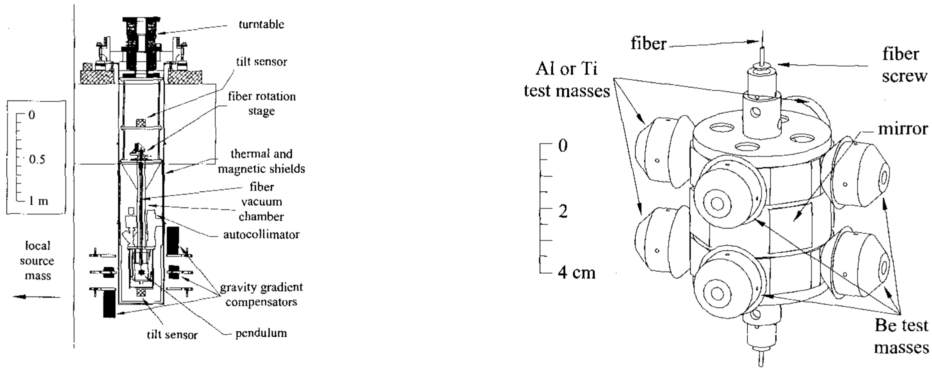

Figure 1: Left frame: The apparatus. A rotating turntable supports the vacuum enclosure for a torsion pendulum. Right frame: The equivalence principle torsion pendulum. Two sets of four test bodies form the composition dipole. The pendulum's symmetry reduces coupling to environmental gravity gradients. The fiber attaches onto the pendulum through a special fiber screw.

2 Rotating torsion balance

A torsion pendulum provides a nearly ideal apparatus for performing tests of the equivalence principle. A conceptual equivalence principle torsion balance experiment is realized by arranging test bodies of different composition at ends of a rod suspended from its center by a thin fiber. The twist of the pendulum about the fiber then depends only on the difference in the vector direction of the forces on the test bodies, inherently providing a differential measurement. An equivalence principle violation would exert different forces on the test bodies of different composition, resulting in a torque about the fiber. To minimize couplings to gravitational gradients the actual pendulum design has up-down reflection symmetry and a four-fold azimuthal symmetry, see the right frame of Figure 1. It has been designed such that the gravitational multipole moments for $\ell < 6$ are small. See Su *et al*[4] for a detailed description of the multipole moment formalism and typical steps taken to minimize the resulting systematic uncertainties.

The left frame of Figure 1 shows the apparatus. The torsion pendulum mounts on a rotating, air-bearing turntable. The air-bearing turntable is smoothly rotated using an eddy-current drive and feedback to a high-resolution angle encoder. An optical system reflecting a laser off a mirror on the pendulum and onto a position sensitive photo-diode produces a signal proportional to the pendulum twist. The laser and photo-diode are mounted in an autocollimator configuration. The vacuum system is initially pumped out using a turbo pump, but is maintained using an ion pump while the apparatus rotates. The vacuum remains below 10^{-6} Torr for several months at a time. Environmental sensors measuring tilt and temperature provide measurements to control for systematic effects. The torsion balance has 3 layers of magnetic shielding and a rotating and a stationary thermal shields, which attenuate temperature gradients using layered insulation and good thermal conductors.

The smooth rotation provided by the turntable shifts an equivalence-principle-violating signal towards the Earth from an offset in the equilibrium angle to the rotation frequency of the apparatus. The centrifugal acceleration due to Earth's rotation must be opposed by a gravitational acceleration, which is oriented toward North in the northern hemisphere because the

Table 1: 1-σ systematic uncertainties and associated corrections for North and West differential acceleration using Be-Ti.

Systematic uncertainty	Δa_N $(10^{-15} m/s^2)$	Δa_W $(10^{-15} m/s^2)$
Gravity gradients	1.6 ± 0.2	0.3 ± 1.7
Tilt	1.2 ± 0.6	-0.2 ± 0.7
Magnetic	0 ± 0.3	0 ± 0.3
Temperature gradients	0 ± 1.7	0 ± 1.7

pendulum swings out to the south. This horizontal gravitational acceleration depends on latitude. In Seattle, Washington, the horizontal gravitational acceleration of the Earth is about 3 times larger than the gravitational acceleration towards the Sun.

3 Systematic Effects

Gravitational gradients, tilt, temperature gradients and magnetic fields are the four systematic effects of primary concern for this experiment. Magnetic fields and temperature gradients are primarily reduced with passive shielding, though the mean room temperature is actively stabilized. Gravitational gradient couplings were minimized in the design of the pendulum and the environmental gradients are reduced using a system of masses, called gravity gradient compensators, positioned close to the apparatus. The rotation axis is actively aligned with local vertical through a feedback system on the tilt sensors. Each systematic was individually exaggerated and the induced effect measured. For a detailed description of gravitational gradient systematics and methods to address them see Su *et al.*[4] For an explanation of the tilt feedback loop see Heckel *et al.*[5] A summary of the systematic uncertainties for the Be-Ti combination is shown in Table 1 and is discussed in more detail in Schlamminger *et al.*[6]

4 Results

Using the Be-Ti and Be-Al test body pairs, we collected 75 days and 96 days of data, respectively. The physical test bodies were interchanged with respect to the pendulum once for each test body pair. The measured differential accelerations in the laboratory frame are the following:

$$\begin{aligned}
&\Delta a_N(Be-Ti) = (+0.6 \pm 3.1) \times 10^{-15} m/s^2 \Rightarrow \eta_{\oplus}(Be-Ti) = (+0.3 \pm 1.8) \times 10^{-13} \\
&\Delta a_W(Be-Ti) = (-2.5 \pm 3.5) \times 10^{-15} m/s^2 \\
&\Delta a_N(Be-Al) = (-2.6 \pm 2.5) \times 10^{-15} m/s^2 \Rightarrow \eta_{\oplus}(Be-Al) = (-1.5 \pm 1.5) \times 10^{-13} \\
&\Delta a_W(Be-Al) = (+0.7 \pm 2.5) \times 10^{-15} m/s^2.
\end{aligned}$$

The N (W) subscript corresponds to results towards north (west). Because the centrifugal acceleration due to the Earth's rotation causes the pendulum to swing out to the south, the horizontal gravitational acceleration due to the Earth is towards north. Taking the ratio of the measured differential acceleration towards north with the horizontal gravitational acceleration gives $\eta_{\oplus}$.

5 Current projects

Currently, a pendulum with test bodies that mimic the composition of the Earth's core and the Moon (similar to Earth's mantle) resides in the apparatus. The data taken with this pendulum can be used in conjunction with lunar laser ranging tests of the strong equivalence principle to set limits on how gravitational binding energy obeys the equivalence principle. Using these results and results stemming from the more precise lunar laser ranging capability of the APOLLO collaboration, an order of magnitude improvement over existing limits of $\eta_{grav} \approx 1 \times 10^{-3}$ should be possible.[7,8]

Seasonal changes in gravitational gradients produce one of the largest systematic uncertainties for this apparatus. The Eöt-Wash group is currently examining different approaches for continual monitoring of these gravitational gradients. Some possible approaches include dedicated gradiometer torsion pendulums and using vertically displaced tilt sensors to monitor the lowest order (Q_{21}) gravitational gradients.

Acknowledgments

This work was funded by a grants from the NSF grant Nos. PHY0355012, PHY0653863, by NASA grant No. NNC04GB03G, and by DOE funding for the CENPA laboratory. I would like to thank Eric Adelberger, Jens Gundlach, Blayne Heckel, Tom Butler, Ki-Young Choi, Stephen Merkowitz, Stephan Schlamminger, Ulrich Schmidt, Hank Simons, Chris Spitzer and Erik Swanson for their contributions.

References

1. Thibault Damour. Testing the equivalence principle: why and how? *Class. Quantum Grav.*, 13:A33–A44, 1996.
2. E. G. Adelberger, J. H. Gundlach, B. R. Heckel, S. Hoedl, and S. Schlamminger. Torsion balance experiments: A low-energy frontier of particle physics. *Prog. Part. Nuc. Phys.*, 62:102–134, 2009.
3. E. G. Adelberger, B. R. Heckel, C. W. Stubbs, and Y. Su. Does antimatter fall with the same acceleration as ordinary matter? *Phys. Rev. Lett.*, 66:850–853, 1991.
4. Y. Su, B. R. Heckel, E. G. Adelberger, J. H. Gundlach, M. Harris, G. L. Smith, and H. E. Swanson. New tests of the universality of free fall. *Phys. Rev.* D, 50:3614–3636, September 1994.
5. B. R. Heckel, E. G. Adelberger, C. E. Cramer, T. S. Cook, S. Schlamminger, and U. Schmidt. Preferred-frame and cp-violation tests with polarized electrons. *Phys. Rev.* D, 78(9):092006, 2008.
6. S. Schlamminger, K.-Y. Choi, T. A. Wagner, J. H. Gundlach, and E. G. Adelberger. Test of the equivalence principle using a rotating torsion balance. *Phys. Rev. Lett.*, 100(4):041101, 2008.
7. J. G. Williams, S. G. Turyshev, and D. H. Boggs. Progress in Lunar Laser Ranging Tests of Relativistic Gravity. *Phys. Rev. Lett.*, 93:261101, 2004.
8. S. Baeßler, B. R. Heckel, E. G. Adelberger, J. H. Gundlach, U. Schmidt, and H. E. Swanson. Improved test of the equivalence principle for gravitational self-energy. *Phys. Rev. Lett.*, 83:3585, 1999.

AMONG SPACE FUNDAMENTAL PHYSICS MISSIONS, MICROSCOPE, A SIMPLE CHALLENGING FREE FALL TEST

P. TOUBOUL[1], R. CHHUN[1], D. BOULANGER[1], M.RODRIGUES[1], G.METRIS[2]

[1]*Onera, The French Aerospace Lab, Chemin de la Hunière, 91761 Palaiseau Cedex, France*

[2]*Observatoire de la Côte d'Azur, GeoAzur, Grasse, France.*

Several space tests of gravity laws have already been performed but the MICROSCOPE mission is the first one to be fully dedicated to the test of the Equivalence Principle. The dedicated payload is now under qualification and the rather large micro satellite will be produced by Cnes for a launch at beginning of 2015. Each of the two differential accelerometers of the experimental device includes a pair of test-masses whose 720 km altitude orbital motions are constrained along the same purely gravitational trajectory. Evidence of an EP violation is provided by the comparison of the electrostatic configurations needed to maintain the two masses composed of different materials motionless relative to each other. Not only the servo-loop electronics must exhibit very weak level of noise but the geometrical and electrical configuration of the instruments must be very well optimised, accurate, cleaned and steady. Although the accelerometers are saturated on ground by normal gravity, they can be tested on board a free fall capsule in drop tower. These tests complete the fine verification of all mechanical and electrical functions. In addition, the present in flight results of the GOCE mission accelerometers are deeply analysed. Because the sensors of the gravity gradiometer exploits the same technologies, they provide confirmation of the MICROSCOPE instrument models used to extrapolate the in orbit performance and then estimate the expected mission accuracy.

1. The MICROSCOPE space mission

One century after Einstein[1]'s paper on special relativity, initiating his elaboration of the new formulation of gravitational interactions, space remains the favorite environment to perform deep experimental investigation on Gravitation. After the Pound and Rebka [2] experiments in 1959, demonstrating frequency red shift with γ rays emission, R. Vessot [3] has performed in 1976 the comparison of two clocks at different gravity potential taking advantage of the parabolic trajectory of a rocket, up to an altitude of ten thousand kilometers. With this Gravity Probe A mission, redshift of 4.10^{-10} was measured with clock frequency stability of 10^{-14}. The ACES (Atomic Clock Ensemble in Space) payload will be accommodated in 2014 on board the International Space Station and will include Hydrogen Maser and the cold atom PHARAO clock with a fine microwave link in order to perform, among other metrological objectives like C isotropy, time dilatation or time distribution, the comparison with ground clocks with an expected accuracy better than 10^{-16} [L. Cacciapuoti [4]].

The three ton Gravity Probe B satellite was launched in April 2004 for 18 month operating mission. The drag free satellite mainly carries four dedicated cryogenic gyros in a very steady configuration, aligned with an inertially pointed telescope, in order to perform the accurate measurement of both the geodetic and the frame dragging effect along the Earth polar circular orbit at an altitude of 642 km. With a specific data processing, developed to correct the limitation of the gyros, induced by unforeseen electrical anisotropic charging of their spherical rotor and cage, the expected -6606.1 milliarcsecond/year N-S geodetic drift was measured with 0.3 % accuracy

(-6601.8+/-18.3 mas/yr) and the -39.2 mas/yr frame dragging drift with 20 % accuracy (-37.2+/-7.2 mas/yr) [C.W.F. Everitt [5]]. These results agree with the previously measured Lense-Thirring effect on satellite orbital plane, previously performed with the LAGEOS 2 satellite. Eleven years of fine laser tracking of the 5620 km altitude orbit have been revisited taking advantage of the more accurate Earth gravity field model obtained from the GRACE space mission data. 10 % uncertainty on the measured effect was then evaluated by I. Ciufolini [6].
The Parameterized Post-Newtonian (PPN) formalism is often considered to interpret the space tests of general relativity and γ and β are presently respectively limited to the following ranges:

- γ-1 = 2.1 +/- 2.3 10^{-5}, as computed by B.Bertotti et al. [7] from the Cassini spacecraft navigation during its cruise from Jupiter to Saturn with the solar conjunction between Earth and Satellite,
- β-1= 1.2 +/- 1.1 10^{-4}, as deduced by J.G. Williams et al. [8] from the accurate measurements by lunar laser ranging, of the relative motions of the Earth and Moon in Solar gravity field.

Other space tests of gravity are now proposed. Among them, the Outer Solar System mission proposed by B. Christophe et al. [9] envisages long range gravity test by finely tracking the gravitational motion of an interplanetary spacecraft carrying an electrostatic ultra-sensitive accelerometer to permanently survey any deviation from geodesic motion. The SAGAS mission, proposed by P. Wolf et al. [10] is much more ambitious considering a large satellite, able to cross the solar system with an optical atomic clock on board, cold atom interferometers as accelerometers and gyrometers, laser links for the satellite motion tracking with many major objectives like the test of universal redshift, the test of Lorentz invariance, PPN test, large scale gravity, variation of cosmologic constantÖ

For what concerns the MICROSCOPE mission, it is fully dedicated to the test of the Equivalence Principle (EP). It has been selected by Cnes in 2004, the instrument is now under qualification and the satellite production should start this year for a launch of the satellite in 2015.
The accurate test of the universality of free fall represents today much more than the verification of this well known property. The violation of the universality of free fall leads to the violation of the Equivalence Principle (EP), fundamental basis of the Einstein General Relativity. Einstein, himself, considered this symmetry as enacted by the experience. Today, most attempts of Grand Unification like String theory and M-theory allow the violation of this principle, introducing in particular scalar fields [11], while the experimental investigation of quantum gravity does appear directly very weakly accessible. The test of the Equivalence Principle is thus not only the test of general relativity but also the search for new experimental results as the necessary support for new theories: as expressed by T. Damour [12], EP test appears much more relevant by about a factor 10^6 than γ accurate determination when comparing presently obtained γ and EP test accuracy. In addition, Super symmetry might be confirmed by the CERN LHC near future results with new particles to be taken into account. The test of the universality of free fall with ultimate accuracy is then an important challenge and has also to be considered regarding dark matter query.
Present laboratory tests, performed by the E^twash group [13] reached a few 10^{-13} accuracy: the dedicated torsion pendulum exploits the 1m long, 20 µm diameter tungsten fibre, exhibiting a Q factor of about 5000. It is surrounded with 800 kg of lead designed to compensate the local gravity gradients. Much care is also taken to reject the vibrating environment and the thermal effects. The data can be integrated over periods as long as 3 months.
MICROSCOPE space experiment has been designed and the payload and the satellite specified to obtain at least two orders of magnitude better, i.e. 10^{-15} accuracy. Other missions are also proposed by A. Nobili [14] or T. Sumner [15] to perform this test with outstanding accuracy of 10^{-17} or 10^{-18}. But not only the instruments demand new long developments but such missions require quite 10 times heavier satellites with much demanding performance for attitude controls and drag free motions as well as for the experiment environment controls.

2. The MICROSCOPE experiment

The MICROSCOPE satellite is rather small, 270 kg in its definitive definition, with its new cold gas propulsion system, leading to major constraints on the dedicated scientific payload available mass, volume and power, respectively, 35 kg, 40 cm^3 and 40 W, leading to a non cryogenic experiment, with a limited couple of tested materials. The test performance relies on available technologies for the instrument and the satellite. Even better performance could be reached in the future but with more complex satellite, instrument and operation.

The MICROSCOPE space experiment consists in a basic free-fall test of two masses around the Earth, with the availability of long duration of measurement, reduced test-mass disturbing accelerations,. very precise instruments optimized for micro-gravity operation and modulation of the Earth gravity signal by rotation of the satellite and the instrument axis along the orbit.

The two test masses made of different composition will be precisely positioned on the same orbit and so submitted to the same Earth gravity field. In absence of Equivalence Principle violation, the two masses will continue on the same common trajectory. The MICROSCOPE satellite, protecting them from Earth and Sun radiation pressures and from residual atmospheric drag, will be controlled to follow the common trajectory of the masses by acting the thrusters of its propulsion system. In fact, the relative motion of both masses with respect to the instrument frame will be accurately measured and servo-controlled thanks to generated electrical field around the conductive masses. The masses are then maintained motionless with respect to the instrument parts to an accuracy better than 10^{-11}m, insuring the stability of the configuration and thus limiting the fluctuations of the eventual disturbing forces acting on them: gravity field gradients, electro-magnetic field, patch effects...Such protocol permits to linearize the position capacitive sensing and the electrostatic actuations, mainly depending on the configuration geometry. The electrostatic acceleration generated commonly on the two masses is nullified by acting the satellite thrusters in such a way that the common instrument reference frame follows the two masses in their orbital motion. The difference of the applied electrostatic acceleration is accurately measured and the projection along the Earth gravity monopole is analysed as an eventual Equivalence Principle violation signal.

The masses are almost perfectly cylindrical and concentric [16]. Each one is surrounded by two gold coated silica rods which carry electrodes for position sensing and electrical field servo-control. Rods and test mass, associated to six electronics channels for the control of the six degrees of freedom of the mass constitute a six-axis ultra-sensitive inertial sensor [P. Touboul et al.[17]]. The two concentric inertial sensors compose the SAGE instrument (Space Accelerometer for Gravitational Experimentation). The MICROSCOPE satellite can operate two SAGE instruments that will be identical except for the mass materials. The two materials used for the test will be Platinum Rhodium alloy, PtRh10 (90% Pt, 10% Rh), and Titanium alloy, TA6V (90% Ti, 6% Al, 4% Va), respectively 402.336 g and 300.939 g. The two other masses are made of same Pt-Rh alloy, respectively 402.336 g and 1361.230 g measured on masses manufactured by PTB in Braunschweig, as qualification parts. This second instrument is only devoted to the in orbit verification of the systematic experiment errors. The experiment then consists in a double differentiation. The Pt-Rh alloy has been selected for its high density, leading to a better rejection of the spurious surface effects: better performance is expected with the two same material test masses insuring the confidence in the obtained EP test result.

The MICROSCOPE satellite is scheduled to be launched in 2015 along a quasi-circular heliosynchronous orbit at an altitude of 720 km. The heliosynchronism allows a fixed satellite Sun side and optimised AsGa rigid solar panels with maximum delivered power and minimum sizes to reduce the radiation pressure and the atmospheric drag. Furthermore, the thermal external conditions are steady and thus very favourable for its thermo-elastic behaviour and its internal fluctuations of temperature. lmK stability at orbital frequency has been demonstrated by Cnes with the thermal representative model of the instrument accommodated inside its satellite cocoon. The electronics units are stabilized at 10 mK and the external anti-Sun radiator is protected against the Earth albedo to exhibit a steady temperature. The propulsion system consists in two symmetric assemblies accommodated on two faces of the cubic satellite, each one comprising 3 Nitrogen tanks (8,25 kg, 345 bars), servo-valves and command electronics to 4 pods of two thrusters. The continuous and proportional actuation of the thrusters allows fine control of the satellite motion. The satellite positioning must be a posteriori known at the EP orbital frequency with 7 m accuracy radially and 14 m along track, and the inertial pointing with 6 μrad in such a way that the Earth gravity gradient can be rejected. When the satellite is rotating, the specification is even more stringent: 1μrad. In addition, the satellite linear and angular acceleration fluctuations are controlled to be respectively less

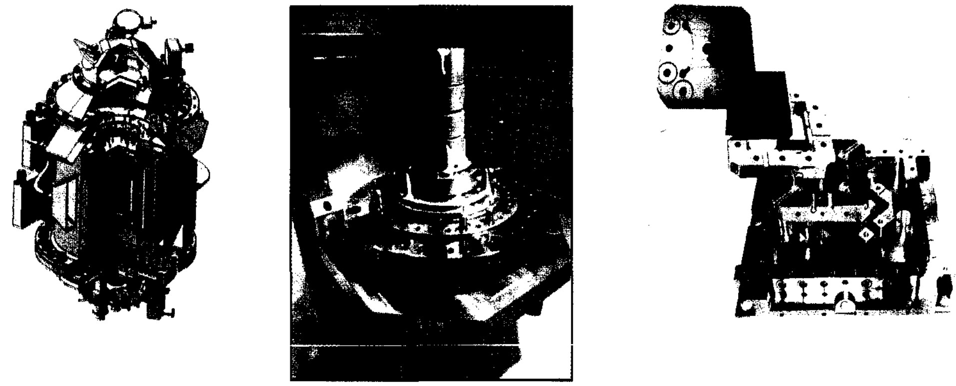

Figure 1: Comparison of MICROSCOPE and GOCE sensor configuration. The parallelepiped GOCE mass is surrounded by three planar gold coated electrode plates *(right)*. The cylindrical configuration of MICROSCOPE includes also 4 quadrant pairs of electrodes for the control of the 2 radial directions, translation and rotation *(left)*.

than 3.10^{-10} $ms^{-2}/Hz^{1/2}$ and $5.10^{-9} rds^{-2}/Hz^{1/2}$ about the EP frequency. This is performed by finely servo-acting the thrusters according to the instrument measurements themselves.
The one year mission includes different instrument calibration and measurement sequences. The symmetry of the electrostatic actuations, the scale factors of the measurement pickup, the alignments of the measurement axes are calibrated in orbit to 10^{-4} relative accuracy in order to reject at same level common motion disturbances [V. Josselin et al. [18]]. The off-centring of the masses, less than 20 µm after instrument integration, is also evaluated to 0.1 µm accuracy in the orbital plane and 0.2 µm normal to the orbit, in order to sufficiently correct the gravity gradient disturbances. Several EP test experiments are performed between calibration sessions with inertial and rotating pointing (at two different frequencies) of the satellite. In case of inertial pointing, the EP test is performed at the orbital frequency, *i.e.* $f_{EPi} = 1.7 \times 10^{-4}$ Hz. In rotating pointing, the test is performed at the sum of the orbital frequency plus the satellite spin rate, *i.e.* f_{EPs} = about 10^{-3} Hz. This is the modulation frequency of the Earth gravity along the axial direction of the instrument. Sessions of 20 orbits are processed to reject the stochastic errors.

3. MICROSCOPE and GOCE instruments

The four MICROSCOPE inertial sensors take advantage of the same concept and technologies already used for the GOCE gradiometer sensors [19]. In the ESA GOCE mission, the gravity gradiometer is composed of six accelerometers mounted in a diamond configuration corresponding to 3 identical orthogonal gradiometer of 50 cm arm [20]. The satellite was launched on March 17th of 2009 and injected in a very low heliosynchronous orbit at altitude of 260 km. Three diagonal components of the Earth gravity gradient can be deduced from the difference of the outputs provided by each pair of aligned sensors.
As in MICROSCOPE, each proof-mass of each sensor is electrostatically levitated at the centre of the instrument silica cage without any mechanical contact except a thin 5µm diameter gold wire to manage the mass global charge against the space high energy proton fluxes bombarding the satellite and creating also secondary electrons (see Figure 1) [21].
Surrounded by electrodes and electrical shield engraved in silica or glass ceramic gold coated parts, the mass is naturally unstable because of the attractivity of the electrostatic forces. So, six channels, including digital controllers, generate, from the data provided by six capacitive position sensors (motion and attitude), opposite electrical voltages. These voltages are applied on related electrodes, used for both capacitive sensing and electrostatic actuation, opposite versus the mass whose electrical potential is biased. Cold damping of all degrees of motion is provided in addition to a very accurate

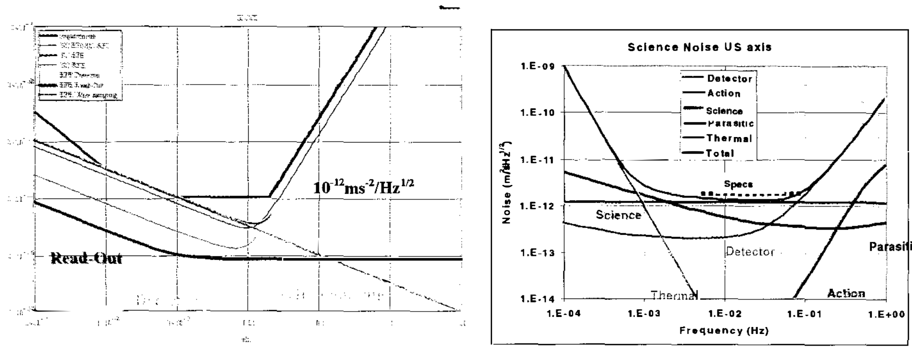

Figure 2: Comparison of MICROSCOPE *(left)* and GOCE *(right)* stochastic errors: √PSD expressed in $ms^{-2}Hz^{1/2}$. Models depend on configuration, electronics performance, thermal stabilities and environment conditions.

mass positioning. The accurate measurements of the applied electrostatic forces and torques provide the data for the satellite pointing and for the drag compensation as well as for the scientific outputs.

Figure 2 compares computed power spectral density of both MICROSCOPE and GOCE stochastic acceleration errors in the instrument frequency bandwidth. Major error sources are the f ollowing from upper frequencies to lower: capacitive sensor noise, analogue to digital data conversion, disturbing mass motion forces and in particular gold wire damping, thermal instabilities of the geometrical and electrical configurations.
The GOCE sensor is optimized for the frequency bandwidth from 5.10^{-3} Hz to 0.1 Hz, corresponding to the fine recovery of the Earth gravity potential harmonics between orders 25 and 500. MICROSCOPE is optimised for lower frequencies, from orbital frequency of 1.7 10^{-4}Hz to calibration frequencies of a few 10^{-3} Hz.
The resolutions presented in Table 1 are obtained along the axial direction of each sensor, with a full measurement range of +/- 2.5 10^{-7} ms^{-2} and the saturation of the electrostatic control larger than 10^{-6} ms^{-2}. GOCE sensor full range is larger, +/- 6.5 10^{-6} ms^{-2}, requiring smaller gaps between the mass and the electrodes, 299 μm instead of 600 μm but increasing the electrical defects due to contact potential differences [22] or thermal sensitivity because of the mass coefficient of thermal expansion versus the quite null silica one.

From the switch on of the GOCE sensors, in April 2009, the operation of the GOCE sensors has been finely verified and tested in orbit through different calibration sequences and by the redundancy of the provided measurements. Each sensor provides six outputs depending on the residual satellite drag, the gravity gradient and the angular and centrifugal acceleration. The drag compensation of the satellite, performed by exploiting the accelerometer outputs, has been verified down to a level of 10^{-9} $ms^{-2}/Hz^{1/2}$, ten times better than required. And the observed sensor noise PSD has confirmed our model of the respective electronics noise contributions, through the servo-loops, of the position sensing and the electrostatic actuation [23].

One invariant in the GOCE mission data is the measured trace of the Earth gravity gradient that should be null in absence mainly of accelerometer noise, in flight calibration inaccuracy and centrifugal acceleration residue. Present analysis leads to flat noise of each gradiometer axis output in the frequency bandwidth from 5.10^{-2} Hz to 0.1Hz: 11 $mE/Hz^{1/2}$ along track (x), 9 $mE/Hz^{1/2}$ normal to the orbit (y) and 19 $mE/Hz^{1/2}$ in the radial direction (z). And the residue in the trace is $24mE/Hz^{1/2}$.
By considering that all residual noises are only due to the six sensors, this leads to 4.9 $10^{-12}ms^{-2}/Hz^{1/2}$ and more precisely for the pairs of each axis: 3.9 $10^{-12}ms^{-2}/Hz^{1/2}$ for both sensors along x, 3.1 $10^{-12}ms^{-2}/Hz^{1/2}$ along y and 6.7 $10^{-12}ms^{-2}/Hz^{1/2}$ along z. Because all six sensors are identical, it is reasonable to consider that their contribution is limited to less than 3.1 $10^{-12}ms^{-2}/Hz^{1/2}$,

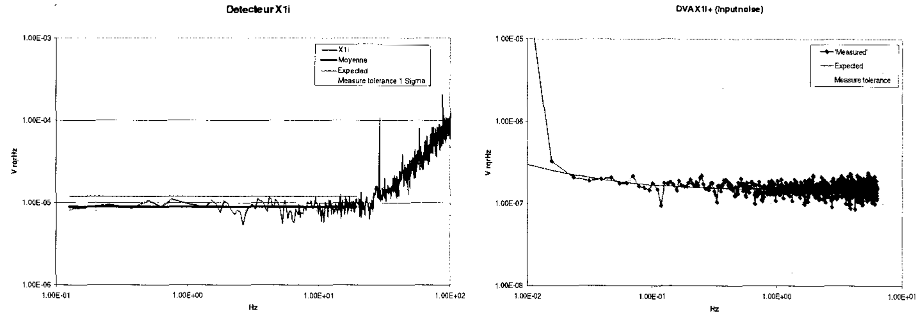

Figure 3: MICROSCOPE capacitive sensor output noise, $10\mu V/Hz^{1/2}$ flat level (left) and actuator input noise (right), $0.15\mu V/Hz^{1/2}$ flat level

to be compared to the MICROSCOPE sensor stochastic error specification including not only the intrinsic noise but also the effect of the thermal environment fluctuations, i.e. $3.3\ 10^{-12}ms^{-12}/Hz^{1/2}$ in inertial pointing and $1.4\ 10^{-12}ms^{-12}/Hz^{1/2}$ in rotating mode.
Dedicated in orbit tests of the GOCE sensors have been also performed by opening the electrostatic loops and observing the electronics outputs while the mass is resting gently on its mechanical stops: this has confirmed the expected electronics contribution of the analogue to digital conversion in particular [24]. By applying in the electrostatic loops biasing position signals, it has also been possible to move the mass in its cage and deduce any unexpected stiffness or non linear behaviour. In addition this has confirmed the operation model assessing the MICROSCOPE sensor error budget derived from the same formulas.
At last, because of the redundancy of two pairs of electrodes to only control the z axis motion of the parallelepiped mass, it is possible to compare two outputs and deduce a $5\mu V/Hz^{1/2}$ residue that is not yet well explained. Nevertheless, such electrical voltage fluctuations applied on the MICROSCOPE sensor electrodes lead to $0.53\ 10^{-13}ms^{-2}/Hz^{1/2}$ for the PtRh inner mass and $0.23\ 10^{-12}ms^{-2}/Hz^{1/2}$ for the TA6V outer mass, which is compatible with MICROSCOPE specifications.

4. Present instrument and tests status, perspectives

In parallel to the satellite and mission definitions, models of the instrument have been developed and tested. The flight models of the analogue functional electronics units have been carefully tested and exhibit very weak noise. The capacitive sensor noise is at lower frequencies than 10 Hz around $10\ \mu V/hz^{1/2}$ (see Figure 3). According to the capacitive sensor sensitivity and the geometry, the position resolution is deduced (see Table 2).
These position resolutions corresponds to less than $6.10^{-17}ms^{-2}$ for the highest EP frequency when integrated over 20 orbits with a back action of the sensor signals limited to less than $3.10^{-17}ms^{-2}$ when expressed in acceleration. In addition the thermal sensitivities of the sensor biases are respectively measured to $71\mu V/°C$ and $12\mu V/°C$, corresponding to $24.10^{-1}m/°C$ and $4.5\ 10^{-1}m/°C$, in agreement to the demonstrated thermal stability of $10^{-2}°C$.

Furthermore, the qualification model of the double inertial sensor instrument, integrating two PtRh masses, has been produced and integrated according to the established procedures for the flight models. This model integrates very accurate test masses and silica parts as well as the blocking mechanism which is used to clamp the masses during launch vibrations. Environmental tests have been performed as well as tests of the instrument operation in micro-gravity. These tests, realized in the ZARM drop tower in Bremen, have allowed optimising the twelve control laws of both masses electrostatic levitation. In spite of the limited duration of the fall, 4.7 s, the convergence of the mass position has been compared to the established models in order to fix the digital recursive filters that will be implemented in the interface and control unit of the experiment.

Table 1: MICROSCOPE inertial sensors computed performances in steady environment deduced from the test of the flight model electronics units and from the characteristics of the qualification models of the sensor; satellite rotation frequency = (π + 1/2) orbital frequency (a) or (π + 3/2) orbital frequency (b)

Pointing	Inner PtRh mass $ms^{-2}/Hz^{1/2}$	Outer TA6V mass $ms^{-2}/Hz^{1/2}$
Inertial $f_{EP} = 1.7\ 10^{-4}$ Hz	$1.92\ 10^{-12}$	$2.55\ 10^{-12}$
Rotating [a] $f_{EP} = 7.8\ 10^{-4}$ Hz	$0.89\ 10^{-12}$	$1.18\ 10^{-12}$
Rotating [b] $f_{EP} = 9.5\ 10^{-4}$ Hz	$0.81\ 10^{-12}$	$1.07\ 10^{-12}$

Table 2: MICROSCOPE test-mass position resolution deduced from capacitive sensor electronic noise and sensitivity as well as from the geometry of the electrical conductors

	Capacitive sensor gain in V/pF	Electronic noise in $pF/Hz^{1/2}$	Capacitive variation vs. mass displacement in pF/μm	Capacitive sensor gain in V/μm	Position sensor resolution in $m/Hz^{1/2}$
PtRh inner mass	80	$1.25\ 10^{-7}$	3.7	0.30	$4.0\ 10^{-11}$
TA6V outer mass	40	$2.5\ 10^{-7}$	6.5	0.26	$3.8\ 10^{-11}$

The qualification of the instrument gives also the latest data to update the instrument and mission error budgets taking into account the expected performance of the satellite sub-systems as defined now. The four major stochastic errors are the following:

- the mass damping induced by the gold wire,
- the radiometer pressure on the mass taking into account the thermal gradient in the instrument tight housing,
- the satellite centrifugal acceleration combined to the mass off-centring,
- the angular acceleration residue combined to the mass off-centring,

leading to a total amount of $1.5\ 10^{-12}\ ms^{-2}/Hz^{1/2}$.

The four major systematic error sources are at the f_{EP} frequency:

- the instability of the star tracker with respect to the instrument measurement axes,
- the drag free residual acceleration when considering the 10^{-4} sensitivity and alignment matching,
- the magnetic field taking into account the rejection by the instrument magnetic shield and the masses susceptibilities,
- and the satellite angular acceleration residue combined to the mass off-centring,

leading to a total amount of $1.1\ 10^{-15}\ ms^{-2}$ tone error at the f_{EP} frequency.

This corresponds, in satellite rotating mode, to the expected EP test accuracy of 6.10^{-16} with 20 orbit signal integration. Tens of 20 orbit measurement sequences are foreseen in the mission scenario. Next step in the mission development will be the satellite production and qualification. The instrument flight models should be delivered in 2012, to be integrated in 2013, for a launch in 2015.

Acknowledgments

The authors would like to thank ONERA and CNES for their financial support and the respective MICROSCOPE and CNES teams for the technical exchanges as well as Bruno Christophe and Bernard Foulon for the fruitful discussions.

References

1. A. Einstein, *Annalen der Physik*, **17** (1905)
2. R.V. Pound and G.A. Rebka *Phys. Rev. Lett.*, **3**, 439ñ441 (1959)
3. R.F.C. Vessot et al., *Phys. Rev. Lett.*, **45**, 2081-2084 (1980)
4. L. Cacciapuoti and C. Salomon, *EPJ*, **172**, 57 (2009)
5. C.W.F. Everitt et al, *Phys. Rev. Lett.*, **106**, 221101, (2011)
6. I. Ciufolini and E.C. Pavlis, *NATURE*, **431**, 7011, 958-960 (2004)
7. B. Bertotti, L. Iess, P. Tortora, *Nature*, **425**, 374-376 (2003)
8. J.G. Williams, S.G. Turyshev, D.H. Boggs, *Phys. Rev. Lett.*, **93**, 261101 (2004)
9. B. Christophe et al, *Exp. Astron.*, **23**, 529-547 (2009)
10. P. Wolf et al, *Exp. Astron.*, **23**, 651-687 (2009)
11. T. Damour and M. Lilley, arXiv:0802.4169vl [hep-th] (2008)
12. T. Damour and J.F. Donoghue, arXiv:1007.2792v2 [gr-qc] (2010)
13. S. Schlamminger et al, *Phys. Rev. Lett.*, **100**, 041101 (2008)
14. A.M. Nobili et al, *Adv. Space Res.*, **25**, 6, 1231-1235 (2000)
15. T. Sumner et al, *Adv. Space Res.*, **39**, 254-258, (2007)
16. R. Chhun et al., *IAU symposium proceedings*, **261**, 402-408 (2009)
17. P. Touboul, *ISSI Space Science Series*, **34**, Springer (2010)
18. V. Josselin et al, *Space Sciences Review*, **151**, 25-38 (2010)
19. P. Touboul et al., *Aerospace Science and Technology*, **8, 5**, 431-441 (2004)
20. J.P. Marque et al, IAC-08-B1.3.7 (2010)
21. P. Touboul et al., *Acta Astronautica*, **45, 10**, 605-617 (1999)
22. C.C. Speake, *Class. Quantum Grav.*, **13**, A291-A297 (1996)
23. P. Touboul et al, *Series Proceedings IAG Symposia*, **136**, Sneeuw Ed. (2011)
24. B. Christophe et al., *SF2A Meeting Proceedings*, 113 (2010)

Atom interferometry and the Einstein equivalence principle

Peter WOLF [1], Luc BLANCHET [2], Christian J. BORDÉ [1,3],
Serge REYNAUD [4], Christophe SALOMON [5], Claude COHEN-TANNOUDJI [5]

[1] *LNE-SYRTE, Observatoire de Paris, CNRS, UPMC, France*
[2] *GRECO, Institut d'Astrophysique de Paris, CNRS, UPMC, France*
[3] *Laboratoire de Physique des Lasers, Université Paris 13, CNRS, France*
[4] *Laboratoire Kastler Brossel, CNRS, ENS, UPMC, France*
[5] *Laboratoire Kastler Brossel et Collège de France, CNRS, ENS, UPMC, France*

The computation of the phase shift in a symmetric atom interferometer in the presence of a gravitational field is reviewed. The difference of action-phase integrals between the two paths of the interferometer is zero for any Lagrangian which is at most quadratic in position and velocity. We emphasize that in a large class of theories of gravity the atom interferometer permits a test of the weak version of the equivalence principle (or universality of free fall) by comparing the acceleration of atoms with that of ordinary bodies, but is insensitive to that aspect of the equivalence principle known as the gravitational redshift or universality of clock rates.

The Einstein equivalence principle is at the basis of our understanding of modern theories of gravity[1]. The weak version of the equivalence principle, also called universality of free fall (UFF), has been verified with high precision using torsion balances[2,3,4] and the Lunar laser ranging[5]. Atom interferometry experiments have also yielded an important test of the UFF at the level 7×10^{-9}, by comparing the acceleration of atoms with that of ordinary bodies[6,12,7].

The gravitational redshift of universality of clock rates (UCR) is the least tested aspect of the equivalence principle. It is currently known with 10^{-4} accuracy[8] and should be tested at the level 10^{-6} in future space experiments with clocks[9]. In this contribution we report arguments[10,11] showing that a recent claim[12] that atom interferometry experiments have actually already tested the UCR at the level 7×10^{-9} (thereby improving the validity of the redshift by several orders of magnitude, even with respect to future space experiments[9]), is fundamentally incorrect. More recently, our arguments have received support from several independent analyses[13,14].

In conventional clock experiments[8,9], the measurement of the gravitational redshift uses two clocks A and B located at different heights in a gravitational field, and operating at the frequency ω of an atomic transition. The two measured frequencies ω_A and ω_B are continuously compared through the exchange of electromagnetic signals. These measurements rely on atomic spectroscopy (Cæsium clocks, hydrogen masers, optical clocks, etc.) or nuclear spectroscopy (like in the Pound-Rebka experiment[15]). The two clocks are put in devices (experimental setups, rockets, satellites, etc.) that are classical and whose trajectories can be measured by radio or laser ranging. The atomic transition of A and B used as a frequency standard is described *quantum mechanically* but the motion of A and B in space can be described *classically*. The motion of the two clocks can thus be precisely measured and the contribution of the special relativistic term (i.e. the Doppler effect) can be evaluated and subtracted from the total frequency shift to get a test of the gravitational redshift.

In the proposal[12] the atoms in an atom interferometer are considered as "clocks" ticking at the Compton frequency $\omega_C = mc^2/\hbar$ associated with their rest mass, and propagating along two "classical" arms of the interferometer. However we dispute this interpretation[10,11]: (i) An atom is not a "Compton clock", since it does not deliver a physical signal at the Compton frequency[11,13]. (ii) In an atom interferometer, we are using an interference between two possible paths followed by the *same* atom, which is described quantum mechanically. Contrary to clock experiments the motion of atoms is not monitored. It is deduced from the theory by using the same evolution equations which allow one to evaluate the phase shift. Thus the two classical paths in the interferometer cannot be determined by a measurement. In an interferometer, where a single atom can propagate along two different paths, trying to measure the path which is followed by the atom destroys the interference signal (wave-particle complementarity). (iii) Using the theory in a consistent manner, the contribution to the phase shift which depends on the mass of the atom (and therefore on its Compton frequency), and includes a contribution from the gravitational redshift, is in fact exactly zero[17,21,18].

The Cæsium (or some alkali) atoms are optically cooled and launched in a vertical fountain geometry. They are prepared in a hyperfine ground state g. A sequence of vertical laser pulses resonant with a $g \to g'$ hyperfine transition is applied to the atoms during their ballistic (i.e. free fall) flight. In the actual experiments the atoms undergo a two-photon Raman transition where the two Raman laser beams are counter-propagating. This results in a recoil velocity of the atoms, with the effective wave vector k transferred to the atoms being the sum of the wave vectors of the counter-propagating lasers[16,17,18]. A first pulse at time $t = 0$ splits the atoms into a coherent superposition of hyperfine states gg' with the photon recoil velocity yielding a spatial separation of the two wave packets. A time interval T later the two wave packets are redirected toward each other by a second laser pulse thereby exchanging the internal states g and g'. Finally a time interval T' later the atomic beams recombine and a third pulse is applied. After this pulse the interference pattern in the ground and excited states is measured.

The calculation of the phase shift $\Delta\varphi$ of the atomic interferometer in the presence of a gravitational field proceeds in several steps[16,22,17]. The first contribution to the phase shift comes from the free propagation of the atoms in the two paths. Since atom interferometers are close to the classical regime, a path integral approach is very appropriate as it reduces to a calculation of integrals along classical paths for a Lagrangian which is at most quadratic in position z and velocity $\dot{z}$, i.e. is of the general type[17]

$$L\left[z, \dot{z}\right] = a(t)\, \dot{z}^2 + b(t)\, \dot{z}z + c(t)\, z^2 + d(t)\, \dot{z} + e(t)\, z + f(t)\,, \tag{1}$$

where $a(t)$, $b(t)$, $c(t)$, $d(t)$, $e(t)$ and $f(t)$ denote some arbitrary functions of time t. The phase shift due to the free propagation of the atoms is given by the *classical* action

$$S_{\rm cl}(z_T, T; z_0, 0) = \int_0^T \mathrm{d}t\, L\left[z_{\rm cl}(t), \dot{z}_{\rm cl}(t)\right]\,, \tag{2}$$

where the integral extends over the classical path $z_{\rm cl}(t)$ obeying the Lagrange equations, with boundary conditions $z_{\rm cl}(0) = z_0$ and $z_{\rm cl}(T) = z_T$. Thus the phase difference due to the free propagation of the atoms in the interferometer is equal to the difference of classical actions in the two paths,

$$\Delta\varphi_S \equiv \frac{\Delta S_{\rm cl}}{\hbar} = \frac{1}{\hbar} \oint \mathrm{d}t\, L\left[z_{\rm cl}, \dot{z}_{\rm cl}\right]\,, \tag{3}$$

where we use the notation $\oint \mathrm{d}\tau$ to mean the difference of integrals between the two paths of the interferometer, assumed to form a close contour.

Theorem[16,22,17,18,19,20,21,11]. *For any quadratic Lagrangian of the form* (1) *the difference of classical actions in the interferometer, and therefore the phase shift due to the free propagation of the atoms, reduces to the contribution of the change of internal states g and g', thus*[a]

$$\Delta S_{\rm cl} = E_{gg'}(T - T')\,, \tag{4}$$

where the internal energy change is denoted by $E_{gg'} \equiv E_{g'} - E_g$. (In particular, when the interferometer is symmetric, which will be the case for a closed Mach-Zehnder geometry, and for $T = T'$, we get exactly $\Delta S_{cl} = 0$.)

One calculates the classical trajectories of the wave packets in the two arms using the equations of motion of massive test bodies deduced from the classical Lagrangian and the known boundary conditions (position and momenta) of the wave packets. In the case of the general quadratic Lagrangian (1) the equations of motion read

$$\frac{\mathrm{d}}{\mathrm{d}t}\Big[2a(t)\dot{z}\Big] = \big[2c(t) - \dot{b}(t)\big]z + e(t) - \dot{d}(t)\,. \tag{5}$$

Then, one calculates the difference in the classical action integrals along the two paths. Denoting by $z_1(t)$ and $z_3(t)$ the classical trajectories between the laser interactions in the upper path, and by $z_2(t)$ and $z_4(t)$ the trajectories in the lower path, we have

$$\Delta S_{\rm cl} = \int_0^T \Big(L[z_1,\dot{z}_1] - L[z_2,\dot{z}_2]\Big)\mathrm{d}t + \int_T^{T+T'} \Big(L[z_3,\dot{z}_3] - L[z_4,\dot{z}_4]\Big)\mathrm{d}t + E_{gg'}(T - T')\,, \tag{6}$$

where the integrals are carried out along the classical paths calculated in the first step. We have taken into account the changes in energy $E_{gg'}$ between the hyperfine ground states g and g' of the atoms in each path. These energies will cancel out from the two paths provided that T' is equal to T, which will be true for a Lagrangian in which we neglect gravity gradients[18].

We now show that the two action integrals in (6) cancel each other in the case of the quadratic Lagrangian (1). This follows from the fact that the difference between the Lagrangians $L[z_1(t),\dot{z}_1(t)]$ and $L[z_2(t),\dot{z}_2(t)]$, which are evaluated at the same time t but on two different trajectories $z_1(t)$ and $z_2(t)$, is a total time-derivative when the Lagrangians are "on-shell", i.e. when the two trajectories $z_1(t)$ and $z_2(t)$ satisfy the equations of motion (5). To prove this we consider the difference of Lagrangians $L_1 - L_2 \equiv L[z_1,\dot{z}_1] - L[z_2,\dot{z}_2]$ on the two paths, namely

$$L_1 - L_2 = a\,(\dot{z}_1^2 - \dot{z}_2^2) + b\,(\dot{z}_1 z_1 - \dot{z}_2 z_2) + c\,(z_1^2 - z_2^2) + d\,(\dot{z}_1 - \dot{z}_2) + e\,(z_1 - z_2)\,. \tag{7}$$

We re-express the first contribution $a(\dot{z}_1^2 - \dot{z}_2^2)$ thanks to an integration by parts as $a(\dot{z}_1^2 - \dot{z}_2^2) = \frac{\mathrm{d}}{\mathrm{d}t}[a(z_1-z_2)(\dot{z}_1+\dot{z}_2)] - (z_1-z_2)\frac{\mathrm{d}}{\mathrm{d}t}[a(\dot{z}_1+\dot{z}_2)]$. The second term is then simplified by means of the sum of the equations of motion (5) written for $z = z_1$ and $z = z_2$. In addition we also integrate by parts the second and fourth contributions in (7) as $b(\dot{z}_1 z_1 - \dot{z}_2 z_2) = \frac{\mathrm{d}}{\mathrm{d}t}[\frac{1}{2}b(z_1^2 - z_2^2)] - \frac{1}{2}\dot{b}(z_1^2 - z_2^2)$ and $d(\dot{z}_1 - \dot{z}_2) = \frac{\mathrm{d}}{\mathrm{d}t}[d(z_1 - z_2)] - \dot{d}(z_1 - z_2)$. Summing up the results we obtain

$$L_1 - L_2 = \frac{\mathrm{d}}{\mathrm{d}t}\left[(z_1 - z_2)\left(a\,(\dot{z}_1 + \dot{z}_2) + \frac{1}{2}b\,(z_1 + z_2) + d\right)\right]. \tag{8}$$

Since the difference of Lagrangians is a total time derivative the difference of action functionals in (6) can be immediately integrated. Using the continuity conditions at the interaction points with the lasers (9), which are

$$z_1(0) = z_2(0)\,, \tag{9a}$$
$$z_1(T) = z_3(T)\,, \tag{9b}$$
$$z_2(T) = z_4(T)\,, \tag{9c}$$
$$z_3(T+T') = z_4(T+T')\,, \tag{9d}$$

[a] Rigorously, in this equation the time interval should be a proper time interval.

and are appropriate to a closed-path interferometer which closes up at time $T + T'$, we obtain

$$\Delta S_{\rm cl} = a(T)\big[z_1(T) - z_2(T)\big]\Big[\dot z_1(T) + \dot z_2(T) - \dot z_3(T) - \dot z_4(T)\Big] + E_{gg'}(T - T')\,. \tag{10}$$

Next we apply the boundary conditions in velocities which are determined by the recoils induced from the interactions with the lasers. We see that once we have imposed the closure of the two paths of the interferometer, only the recoils due to the second pulse at the intermediate time T are needed for this calculation. These are given by

$$\dot z_1(T) - \dot z_3(T) = +\frac{\hbar k}{m}\,, \tag{11a}$$

$$\dot z_2(T) - \dot z_4(T) = -\frac{\hbar k}{m}\,, \tag{11b}$$

where k is the effective wave vector transferred by the lasers to the atoms. This readily shows that the first term in (10) is zero for any quadratic Lagrangian hence $\Delta S_{\rm cl} = E_{gg'}(T - T')$. ■

Finally, one calculates the contribution to the phase shift due to the light phases of the lasers. These are obtained using the paths calculated previously and the equations of light propagation, with the light acting as a "ruler" that measures the motion of the atoms. The phase difference from light interactions $\Delta\varphi_\ell$ is a sum of terms given by the phases ϕ of the laser light as seen by the atom, i.e. $\phi(z,t) = kz - \omega t - \phi_0$ where k, ω and ϕ_0 are the wave vector, frequency and initial phase of the laser in the frame of the laboratory, and evaluated at all the interaction points with the lasers[16,18]. Finally the total phase shift measured in the atom interferometer is

$$\Delta\varphi = \omega_{gg'}(T - T') + \Delta\varphi_\ell\,, \tag{12}$$

and depends only on the internal states g and g' through $\omega_{gg'} = E_{gg'}/\hbar$, and the light phases which measure the free fall trajectories of the atoms. At the Newtonian approximation in a uniform gravitational field g, the interferometer is symmetric, $T' = T$, and one finds[16]

$$\Delta\varphi = \Delta\varphi_\ell = k\,g\,T^2\,. \tag{13}$$

This clearly shows that the atom interferometer is a *gravimeter* (or accelerometer): It measures the acceleration g of atoms with respect to the experimental platform which holds the optical and laser elements. With k and T known from auxiliary measurements, one deduces the component of g along the direction of k. If the whole instrument was put into a freely falling laboratory, the measured signal $\Delta\varphi$ would vanish.

The result for the final phase shift (12) or (13) is valid whenever the result (4) holds, i.e. in all theories of gravity defined by a single (quadratic) Lagrangian and consistent with the principle of least action. In such theories the Feynman path integral formulation of quantum mechanics remains valid, and a coherent analysis of atom interferometry experiments is possible. Most alternative theories commonly considered belong to this class which encompasses a large number of models and frameworks[1]. It includes for example most non-metric theories, some models motivated by string theory[23] and brane scenarios, some general parameterized frameworks such as the energy conservation formalism[24,25], the TH$\varepsilon\mu$ formalism[26], and the Lorentz violating standard model extension (SME)[27,28]. In all such theories the action-phase shift of the atom interferometer is zero (in particular the Compton frequency of the atom is irrelevant). Because there is no way to disentangle the gravitational redshift from the Doppler shift, we conclude that the recent proposal[12] is invalidated.

References

1. C. M. Will, *Theory and experiment in gravitational physics* (Cambridge University Press, 1993).
2. P. Roll, R. Krotkov, and R. Dicke, Ann. Phys. (N.Y.) **26**, 442 (1964).
3. V. Braginsky and V. Panov, Sov. Phys. JETP **34**, 463 (1972).
4. S. Schlamminger, K.-Y. Choi, T. Wagner, J. Gundlach, and E. Adelberger, Phys. Rev. Lett. **100**, 041101 (2008).
5. J. Williams, S. Turyshev, and D. Boggs, Phys. Rev. Lett. **93**, 261101 (2004).
6. A. Peters, K. Chung, and S. Chu, Nature **400**, 849 (1999).
7. S. Merlet, Q. Bodart, N. Malossi, A. Landragin, and F. Pereira Dos Santos. Metrologia **47**, L9 (2010).
8. R. Vessot and M. Levine, Gen. Rel. and Grav. **10**, 181 (1979).
9. L. Cacciapuoti and C. Salomon, Eur. Phys. J. Spec. Top. **127**, 57 (2009).
10. P. Wolf, L. Blanchet, Ch.J. Bordé, S. Reynaud, C. Salomon, and C. Cohen-Tannoudji, Nature **467**, E1 (2010), arXiv:1009.0602 [gr-qc].
11. P. Wolf, L. Blanchet, Ch.J. Bordé, S. Reynaud, C. Salomon, and C. Cohen-Tannoudji, Class. Quant. Grav. **28**, 145017 (2011), arXiv:1009.2485 [gr-qc].
12. H. Müller, A. Peters, and S. Chu, Nature **463**, 926 (2010).
13. S. Sinha and J. Samuel, Class. Quant. Grav. **28**, 145018 (2011), arXiv:1102.2587 [gr-qc].
14. D. Giulini (2011), arXiv:1105.0749 [gr-qc].
15. R. Pound and G. Rebka, Phys. Rev. Lett. **4**, 337 (1960).
16. Ch.J. Bordé, Phys. Lett. A **140**, 10 (1989).
17. P. Storey and C. Cohen-Tannoudji, J. Phys. II France **4**, 1999 (1994).
18. P. Wolf and P. Tourrenc, Phys. Lett. A **251**, 241 (1999).
19. Ch. Antoine and Ch.J. Bordé, Phys. Lett. A **306**, 277 (2003).
20. Ch. Antoine and Ch.J. Bordé, J. Opt. B **5**, S199 (2003).
21. Ch.J. Bordé, Eur. Phys. J. Spec. Top. **163**, 315 (2008).
22. M. Kasevich and S. Chu, Phys. Rev. Lett. **67**, 181 (1991).
23. T. Damour and A. Polyakov, Nucl. Phys. B **423**, 532 (1994).
24. K. Nordtvedt, Phys. Rev. D **11**, 245 (1975).
25. M. Haugan, Ann. Phys. (N.Y.) **118**, 156 (1979).
26. A. Lightman and D. Lee, Phys. Rev. D **8**, 364 (1973).
27. Q. Bailey and V. Kostelecky, Phys. Rev. D **74**, 045001 (2006).
28. V. Kostelecky and J. Tasson (2010), arXiv:1006.4106.

Significance of the Compton frequency in atom interferometry

Michael A. Hohensee and Holger Müller
Department of Physics, University of California, Berkeley, CA 94706, USA

The recent realization that atom interferometers (AIs) can be used to test the gravitational redshift tests has proven to be controversial in some quarters. Here, we address the issues raised against the interpretation of AIs as redshift tests, reaffirming the fact that Müller *et al.* [Nature **463**, 926 (2010)] indeed report a gravitational redshift test.

1 Overview

A variety of arguments have been raised [2-4] against the interpretation of atom interferometers (AIs) as clock comparisons which test the gravitational redshift [1]. To this end, non-relativistic derivations of the AI phase have been offered as evidence that the Compton frequency, $mc^2/\hbar$, is both unphysical and irrelevant to AI tests of the Einstein Equivalence Principle (EEP) [2,3]. As we demonstrate below, non-relativistic treatments of the problem obscure the fact that in the fully relativistic theory, matter-waves do indeed oscillate at the Compton frequency, with relevance to tests of the gravitational redshift.

Other objections focus upon the failings of possible alternative theories of gravity in which critics do consider AIs to be redshift tests [2,3]. AIs are, it is claimed, more properly understood as tests of the weak equivalence principle (WEP) in any consistent theoretical framework [2,3]. We address these objections in more detail elsewhere [5]. For these proceedings, however, we will simply note that in all theories consistent with an action principle and energy conservation, any experiment which constrains violations of WEP also constrains anomalies in the gravitational redshift, and vice versa, as originally hypothesized by Schiff [6], and covered in detail by [7-9], as well as more recent reviews of the subject [2,3]. The inconsistencies arising from the analysis of AIs in the context of a theory that decouples the gravitational redshift from WEP [2] result from that very decoupling, and are not specific to any particular experiment.

Critics have also asserted [2,3] that the precision attained by torsion-balance tests of WEP is such that AI-based redshift tests can only be effectively used to constrain theories that do not conserve energy. This is ironic, given that in 1975 Nordtvedt [7] made the same observation regarding the general utility of any clock experiment in the face of the torsion-balance constraints of the day. The assertion is also incorrect, in light of the subsequent 1977 study by Ni [10].[a]

As noted above, non-relativistic treatments of matter-waves obscure the features of the experiment in the relativistic theory. Specifically, the non-relativistic Hamiltonian describing

[a] In Ni's theory [10], the EEP can be violated without generating signals in experiments in which the test masses are restrained from moving freely, as happens in torsion balance (*i.e.* "WEP 1") experiments. So far as is currently known, however, the EEP cannot be violated without generating signals in experiments involving freely falling masses ("WEP 2" tests), AIs, or other clock tests.

the semiclassical evolution of a particle of mass m in a gravitational potential U takes the form

$$H = mc^2 + mU(\vec{x}) + \frac{p^2}{2m}, \tag{1}$$

where $\vec{x}$ is the particle's position, and $\vec{p}$ is its momentum. As the Compton frequency term is constant, the dynamics and accumulated phase of the particle are equivalently modeled by

$$H = mU(\vec{x}) + \frac{p^2}{2m}, \tag{2}$$

which some have argued demonstrates that the Compton frequency plays no role [2,3]. This analysis hides the fact that in the fully relativistic theory, matter-waves do indeed oscillate at the Compton frequency [11], with important consequences for tests of the EEP. In what follows, we present a discussion of the significance of the Compton frequency in matter-wave tests of the gravitational redshift, prefaced with a general review of how clock frequencies appear in the derivation of experimental observables in any clock comparison test. We find that the Compton frequency of matter-waves appears in the same way as does the oscillation frequency of more conventional clocks, and demonstrate that the direct measurement of the clock frequencies is not required to test the gravitational redshift, just as it was unnecessary for the original Pound-Rebka [12] test. We close with a gedankenexperiment which further illustrates this equivalence.

2 Significance of the Clock Frequency to Gravitational Redshift Rests

All clock comparison tests of the gravitational redshift measure the difference in the phase accumulated by two or more clocks that follow different paths through spacetime. In the simplest case, all paths originate at a point A and end at a point B. The total phase accumulated by clock i between points A and B is given by

$$\varphi_{(i)} = \omega_{(i)} \int_A^B d\tau_{(i)} = \omega_{(i)} \int_A^B \sqrt{-g_{\mu\nu} dx^\mu_{(i)} dx^\nu_{(i)}}, \tag{3}$$

where $\omega_{(i)}$ is the proper oscillation frequency of the ith clock, and $x^\mu_{(i)}$ denotes the path it takes from A to B. To leading order, this reduces to

$$\varphi_{(i)} = \omega_{(i)} \int_A^B \left(1 + \frac{U(\vec{x}_{(i)}(t))}{c^2} - \frac{\dot{x}^2_{(i)}}{2c^2}\right) dt. \tag{4}$$

The calculated value of $\varphi_{(i)}$ its not itself a physical observable under any circumstances, for any kind of clock. All physical phase measurements yield the relative phase between two systems. Thus the physical observable in any clock comparison test is the difference $\Delta\varphi_{ij} = \varphi_{(i)} - \varphi_{(j)}$ between two clocks. If the clocks have the same proper frequency $\omega_{(i)} = \omega_{(j)} = \omega_0$, this becomes

$$\Delta\varphi_{ij} = \omega_0 \int_A^B \left(\frac{U(\vec{x}_{(i)}(t)) - U(\vec{x}_{(j)}(t))}{c^2} - \frac{\dot{x}^2_{(i)} - \dot{x}^2_{(j)}}{2c^2}\right) dt. \tag{5}$$

The first term in the integrand has the form $\Delta U/c^2$, and represents the gravitational redshift, while the second term accounts for the phase shift due to time dilation.

Note that we can also obtain Eq. (5) by replacing $\varphi_{(i)}$ and $\varphi_{(j)}$ with the relative phases $\Delta\varphi_{i\infty}$ and $\Delta\varphi_{j\infty}$ that each clock accumulates relative to a fictional oscillator (∞) lying at rest, far away from sources of the gravitational potential. Our freedom to designate any oscillator, real or notional, as a reference for the purposes of calculation corresponds to our freedom to add total derivatives to our particle Lagrangian, or equivalently, to choose the zero of our energy scale when transforming Eq. (1) to Eq. (2) without changing the physics. Such transformations can save time in carrying out derivations, but serve to obscure the fundamental oscillation frequency of the clock. The quantities $\Delta\varphi_{i\infty}$ are no more physically observable than are the $\varphi_{(i)}$, and such a substitution has no impact on the observable phase $\Delta\varphi_{ij}$ accumulated by clocks of any kind.

3 Significance of the Compton Frequency to Gravitational Redshift Tests

If we compare Eq. (5) with the phase accumulated by matter-waves propagating along the same paths in the semiclassical limit, we obtain the same result; the phase accumulated by the ith matter-wave is simply the integrated action $S_{(i)}/\hbar$. From the form of the standard general relativistic action for a particle of mass m, the phase is given by [13]

$$\varphi_{(i)} = \frac{S_{(i)}}{\hbar} = \frac{mc^2}{\hbar} \int_A^B d\tau_{(i)}, \tag{6}$$

where $mc^2/\hbar$ is the matter-waves' Compton frequency, ω_C. See also [2,14] for a derivation of Eq. (6) using the Feynman path integral formalism, and of the equivalent Schrödinger representation. As has been pointed out [2,3], the phase $\varphi_{(i)}$ is no more physically observable for matter waves than for any other clock. The relative phase $\Delta\varphi_{ij}$, however, is observable. At present, the only practical way to measure the relative phase of two matter-wave oscillators is by interfering coherent superpositions of matter-waves with one another. Thus $\omega_{(i)} = \omega_{(j)} = \omega_C$, and we find that the relative phase is given by Eq. (5) with ω_0 replaced by the Compton frequency.

Although the leading order phase shift $\omega_C \int dt$ is inaccessible to us,[b] this is of no importance for tests of the gravitational redshift, since the Compton frequency also multiplies the redshift and time dilation terms. It is for this reason that AI tests of the gravitational redshift are so competitive with tests involving conventional clocks, despite the fact that they measure the relative phase with far less precision, operate for far shorter periods of time, and involve clocks separated by much smaller potential differences.

We have shown elsewhere that the specific AI configuration reported in [1] is entirely equivalent to an experiment in which conventional clocks follow the same paths, exchanging signals with a stationary reference clock at discrete intervals [15]. That the matter-waves' Compton frequency does not necessarily play a role in the derivation of the redshift signal [2,3] has no bearing on whether the Mach-Zehnder AI constitutes a redshift test. If it did, one could as easily argue that the Pound-Rebka experiment [11] is not a redshift test. There, the redshift of a 14.4 keV Mössbauer transition was determined from the velocity $v = \Delta U/c$ at which an identical oscillator must move to compensate for it via the first order Doppler effect. The actual transition frequency of the 14.4 keV transition drops out of the expression for the velocity, and is not measurable by nor necessary to carry out a test of the redshift.

4 A Concrete Example

The general situation may be clarified by considering a gedankenexperiment [16], Fig. 1: two halves of a matter-wave are held at the extrema of a gravitational potential, where the local acceleration of free fall is zero. Though the net force acting upon the matter-waves is zero, implying a vanishing gravimeter (*i.e.* WEP) signal, they would still accumulate a relative phase φ at a rate of $d\varphi/dt = \omega_C \Delta U/c^2$, as would any pair of similarly positioned clocks ticking with a proper frequency ω_C. This follows from derivations in part 3, or from the Schrödinger equation.

5 Conclusion

Atom interferometers are in every important respect equivalent to other clock tests of general relativity, and their ability to provide competitive limits on violations of EEP stems directly from the fact that the intrinsic oscillation frequency of a matter-wave is the Compton frequency,

[b] In the absence, that is, of a way to coherently convert atoms into microwaves and back again [2], which would allow us to compare the accumulated matter-wave phase directly to that of a conventional clock. Note that $\omega_0 t$ is never observable in direct measurements of the relative phase between separated yet identical clocks.

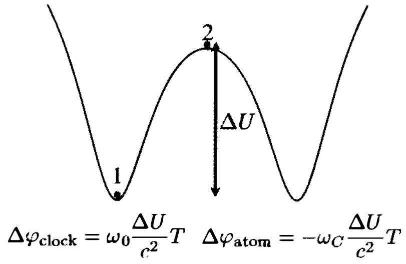

Figure 1: Gravitational redshift experiment at points of vanishing gravitational acceleration.

$mc^2/\hbar$. Matter-wave interferometry enables tests of gravity to be carried out on the tabletop with precision rivaling and in many cases exceeding that of large scale tests with conventional clocks. AIs close the same loopholes for EEP violation that are addressed by other clock comparison experiments. and have the same experimental characteristics as other clock comparison tests. AIs will continue to play an essential role in verifying what may be the most important foundational principle of modern physics, and in future searches for physics beyond general relativity and the standard model.

Acknowledgments

We are grateful to S. Chu, P. Hamilton. and A. Zeilinger for discussions, and the David and Lucile Packard Foundation, the National Institute of Standards and Technology, the National Aeronautics and Space Administration. and the Alfred P. Sloan Foundation for support.

References

1. H. Müller, A. Peters and S. Chu, *Nature* **463**, 926 (2010).
2. P. Wolf, L. Blanchet, C.J. Bordé, S. Reynaud, Ch. Salomon and C. Cohen-Tannoudji, *Class. Quant. Grav.* **28**, 145017 (2011).
3. D. Giulini, arXiv:1105.0749 (2011).
4. S. Sinha and J. Samuel, *Class. Quant. Grav.* **28**, 145018 (2011).
5. M.A. Hohensee, S. Chu, A. Peters. and H. Müller, to be published.
6. L.I. Schiff, *Am. J. Phys.* **28**, 340 (1960).
7. K. Nordtvedt, *Phys. Rev.* D 11, 245 (1975).
8. M.P. Haugan, *Annals of Physics* **118**, 156 (1979).
9. C.M. Will, *Theory and Experiment in Gravitational Physics, Revised Edition*, (Cambridge University Press, Cambridge, 1993) p. 38.
10. W.-T. Ni, *Phys. Rev. Lett.* **38**, 301 (1977).
11. L. de Broglie, *Recherchés sur la théorie des Quanta.* (Ph. D. thesis, Univ. of Paris, 1924). Ch. 1, as translated by J.W. Haslett, *Am. J. Phys.* **40**, 1318 (1972).
12. R.V. Pound and G.A. Rebka Jr., *Phys. Rev. Lett.* **4**, 337 (1960);R.V. Pound and J.L. Snider, *Phys. Rev.* **140**, B788 (1965).
13. C.W. Misner, K.S. Thorne, and J.A. Wheeler, *Gravitation*, (W.H. Freeman and Co., San Francisco, 1973).
14. M.A. Hohensee and H. Müller, *J. Mod. Optics*, in press; arXiv:1106.2241 (2011).
15. M.A. Hohensee, S. Chu, A. Peters and H. Müller, *Phys. Rev. Lett.* **106**, 151102 (2011).
16. A. Zeilinger, private communication (2010).

Observability of short-range gravitation with the experiment FORCA-G

S. Pelisson, R. Messina, M.-C. Angonin, P. Wolf
LNE-SYRTE, Observatoire de Paris, CNRS UMR8630, UPMC
61 avenue de l'Observatoire, 75014 Paris, France

In this work, the states of an atom vertically trapped in front of a macroscopic surface are discussed. This calculation is performed in the context of the recently proposed atomic-interferometry experiment FORCA-G, which aims at measuring the Casimir-Polder atom-surface interaction and, at the same time, setting constraints on hypothetical deviations from Newtonian gravity described by a number of unification theories. The observability of these deviations is here quantitatively investigated.

1 Introduction

Several theories beyond the standard model predict a deviation from Newton's laws of gravity at very short (say micron or submicron) distance. To explore this range of distance, atomic interferometry can be very efficient, the main reason being the high precision frequency measurement that can be obtained with this technique. In this context, the experiment FORCA-G (FORce de CAsimir et Gravitation à courte distance) is being developed at SYRTE-Observatoire de Paris [1,2]. The purpose of this experiment is to study the short-range interaction between a Rubidium atom and a surface, i.e. investigating at the same time the possible deviation from Newton's laws and the Casimir-Polder interaction resulting from the coupling of the atom with the fluctuating electromagnetic field[3]. These goals will be achieved thanks to atomic-interferometry techniques combined with a trapping potential which allows a precise knowledge of the distance between the atom and the surface. The trapping potential is realized by a vertical optical standing wave produced by the reflection of a laser beam on a surface. The vertical configuration induces an additional linear potential due to Earth's gravity: this deviation from a purely periodical potential produces a localization of the atomic wavepacket, corresponding to the transition from Bloch to Wannier-Stark states, well known in solid state physics [4]. The main advantages of FORCA-G are thus the refined control of the atomic position as well as the high precision of interferometric measurements, as demonstrated in the first experimental results[2]. In this paper, we will theoretically discuss the possibility of observing experimentally a possible deviation from Newton's laws at short distance. In the first section, we will present the so-called Wannier-Stark states and their modification in presence of a surface, then we will study the constraints that FORCA-G could impose on a Yukawa-type gravitational deviation. We will not describe here the states in presence of Casimir-Polder effect which are the main subject of another paper (by Messina et al.) in the same volume.

2 Wannier-Stark states

2.1 Physical system

Let us consider a two-level atom trapped in an optical standing wave in proximity of a surface. In our configuration, the standing wave has a vertical orientation so that the Earth's gravitation field acting on the atom must be also taken into account. The complete Hamiltonian of the system is given by

$$
\begin{aligned}
H &= H_0 + H_{\mathrm{int}} = H_{\mathrm{f}} + H_{\mathrm{at}} + H_{\mathrm{WS}} + H_{\mathrm{int}} \\
H_{\mathrm{f}} &= \sum_p \int_0^{+\infty} dk_z \int d^2\mathbf{k}\, \hbar\omega\, a_p^\dagger(\mathbf{k}, k_z) a_p(\mathbf{k}, k_z) \\
H_{\mathrm{at}} &= \hbar\omega_0 |e\rangle\langle e| \\
H_{\mathrm{WS}} &= \frac{p^2}{2m} + mgz + \frac{U}{2}(1 - \cos(2k_l z)) \\
H_{\mathrm{int}} &= -\boldsymbol{\mu} \cdot \mathcal{E}(\mathbf{r}).
\end{aligned}
\tag{1}
$$

This Hamiltonian is written as a sum of a term H_0 describing the atomic and field degrees of freedom and H_{int} which represents the interaction between the atom and the field, written in this case in the multipolar coupling scheme. Here, H_{at} represents the internal hamiltonian of the atom having two levels $|g\rangle$ (ground) and $|e\rangle$ (excited) separated by an energy $E = \hbar\omega_0$. While H_{at} represents the internal degrees of freedom of the system, the term H_{WS} accounts for the external atomic dynamics. As a consequence, it contains the kinetic energy depending on the atomic mass m, the trapping potential due to the optical standing wave of depth U and the linear term due to the Earth's gravity. Finally, H_{f} is the free Hamiltonian of the quantum electromagnetic field, written as usual as a function of a set of creation and annihilation operators. Here, we have treated only the z-dependent terms of the Hamiltonian since the two other degrees of freedom x and y are decoupled from the longitudinal problem.

2.2 States in proximity of the surface

The first step to describe the short-range interaction between the atom and the surface is to calculate the atomic states in the optical trap. In solid states physics, there is a similar class of states known as Wannier-Stark states which are metastable states of an infinite accelerated periodic potential [4]. In our case, the presence of the surface has two effects on the states of the atom. On one hand, it imposes a boundary condition at $z = 0$, breaking in this way the translational symmetry of the system. On the other hand, the quantum electrodynamical interaction between the atom and the surface must be taken into account. This last effect is treated in detail in [5] and will not be described here.

To work out the modified Wannier-Stark states numerically, we have used a finite difference method. The first step of our method is to consider a box $0 < z < z_f$ and to impose that all the wavefunctions vanish at the borders. As for $z = 0$ this is a real physical condition (due to the presence of the surface), whereas the condition at $z = z_f$ is purely numerical. As a consequence, we have to choose a box sufficiently large so that the eigenfunctions of interest decay to zero well before z_f. The next step is the discretization of our interval $[0, z_f]$ using a set of $N+2$ mesh points z_i with $z_0 = 0, z_1, \ldots, z_{N+1} = z_f$ (giving $\delta z = \frac{z_f}{N+1}$ for equally spaced mesh points).

Using this method, the problem is now reduced to an eigenvalues problem of a tridiagonal matrix. To calculate the eigenvalues of such a matrix, an efficient algorithm is described in [6].

3 The search for a new gravitational force

Once the states in the lattice are well described, we can start the search for a new gravitational interaction at short distance. This investigation is based on indications from numerous unification theories and models, that gravity may be modified at short distance. These modifications can be described by an additional Yukawa-type potential to the standard Newtonian potential. The complete gravitational potential between two point-like particles is then written under the form

$$V(z) = \frac{GMm}{z}\left(1 + \alpha_{\rm Y} e^{-\frac{z}{\lambda_{\rm Y}}}\right) \tag{2}$$

where G is the gravitational constant, m and M the masses of the two particles. In this expression $\alpha_{\rm Y}$ and $\lambda_{\rm Y}$ are two parameters introduced to characterize respectively the relative strength of the corrective potential and its typical range. The experiments aimed at testing the existence of such a deviation set constraints on the allowed values of the parameters $\alpha_{\rm Y}$ and $\lambda_{\rm Y}$.

In the experiment FORCA-G, the only relevant contribution of a possible deviation from gravitation is the one due to the interaction between our atom and the surface. At the same time, the Newtonian part of the atom-surface interaction is completely negligible with respect to the Earth-atom term already taken into account in the Wannier-Stark Hamiltonian (1) and with respect to the expected experimental uncertainties. As a consequence, the correction we are looking for is obtained by integrating the Yukawa part of eq. (2) over the volume occupied by the surface. Describing the mirror as a cylinder (the atom being on the direction of its axis) and recalling that we are looking for deviations having length scale $\lambda_{\rm Y}$ in the μm range we obtain, after a straightforward calculation.

$$H_{\rm Y} = 2\pi\alpha_{\rm Y} G\rho_{\rm S} m\lambda_{\rm Y}^2 e^{-\frac{2z}{\lambda_{\rm Y}}} \tag{3}$$

$\rho_{\rm S}$ being the density of the surface. As the Yukawa contribution is due to the surface, we need an experimental configuration where the Casimir-Polder contribution is negligible with respect to the gravitational interaction. In fact, the experiment is planned to have two different configurations. The first one is a measurement at short distance where we compare the results obtained using two different isotopes of Rubidium (^{85}Rb and ^{87}Rb) in order to make the energy differences between wells almost independent on the Casimir-Polder interaction [1]. As a consequence, in this scheme, we need to calculate the energy difference between the ^{87}Rb and ^{85}Rb both in the case of Wannier-Stark states and Yukawa states. The energy difference is noted

$$\mathcal{D}E_n = \left(E_n^{85} - E_n^{87}\right) - \left(E_n^{(Y)85} - E_n^{(Y)87}\right) \tag{4}$$

where E_n is the energy of state n in the absence of a Yukawa term in the total Hamiltonian, and $E_n^{(Y)}$ is the energy of the same state in the presence of a Yukawa term of form 3. A Yukawa-type deviation from gravity's laws will be detectable if this difference is within the experimental sensitivity, i.e. 10^{-4}Hz. The second scheme is a measurement at larger distance, in a region where the Casimir-Polder interaction can be theoretically modelled at a degree of precision comparable to the experimental sensitivity. This region extends approximatively between 10 μm and 20 μm.

In the far regime scheme we have calculated, for an atom of ^{87}Rb, the Yukawa correction on the well $n = 40$ and $n = 70$ (which correspond respectively to a distance of 10 μm and 20 μm) for different values of λ_Y and for each of them we have found our limiting value of α_Y by looking for a correction up to 10^{-4} Hz, coinciding with the experimental sensitivity estimated in [1]. We have performed the same calculation for the near regime discussed above by evaluating the energy difference $\mathcal{D}E_6 - \mathcal{D}E_4$ between the wells $n = 4$ and $n = 6$ and evaluating the minimum $\alpha_{\rm Y}$ allowed that induces a shift of 10^{-4}Hz. The resulting experimental constraints on the Yukawa-type correction is shown on the figure 1, originally taken from [7]. The three superposed curves represent the experimental constraints theoretically calculated for the experiment FORCA-G. They correspond to the near regime, using a superposition between wells $n = 4$ and $n = 6$ (blue solid line, first from the left), the far regime for $n = 40$ (red solid line) and for $n = 70$ (black dashed line).

Figure 1: Regions of the (α_Y, λ_Y) plane (in yellow) already excluded by experiments. See text for the definition

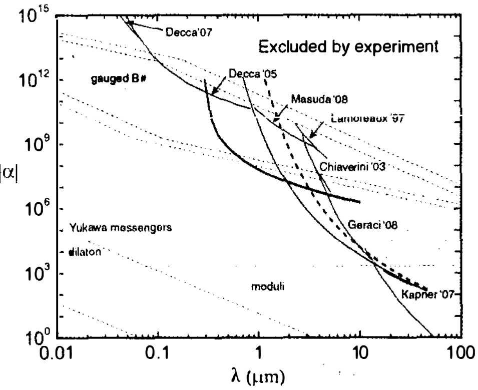

4 Conclusions

In this paper, we have discussed the possibility of observing or setting new constraints on possible deviations to Newton's gravity laws at short distance with the experiment FORCA-G. As a first step, we have calculated the modification of the Wannier-Stark states in presence of a massive surface, described as a boundary condition in $z = 0$. Then we have studied the observability of a deviation from Newton's laws under the hypothesis that the Casimir-Polder effect can be neglected by being sufficiently far from the surface or by a two-isotope measurement.

This work is the first step toward a precise calculation of the states and energy of an atom in a vertical optical trap. The second step will be the description of the dynamic of the system. Indeed, the Wannier-Stark states are metastable states which have a long but finite lifetime in the optical trap. The knowledge of the dynamics for our modified Wannier-Stark states in presence of the Casimir-Polder interaction and of a Yukawa modification of gravitation is the subject of an ongoing work.

References

1. P. Wolf, P. Lemonde, A. Lambrecht, S. Bize, A. Landragin, and A. Clairon, Phys. Rev. A **75**, 063608 (2007).
2. Q. Beaufils, G. Tackmann, B. Pelle, S. Pelisson, P. Wolf, and F. Pereira dos Santos, Phys. Rev. Lett. (2011, in press).
3. S. Scheel and S. Y. Buhmann, Acta Phys. Slov. **58**, 675 (2008).
4. M. Gluck, A. R. Kolovsky, and H. J. Korsch, Phys. Rep. **366**, 103 (2002).
5. R. Messina, S. Pelisson, M.-C. Angonin, and P. Wolf, Phys. Rev. A. **83**, 052111 (2011).
6. G. Peters and J. H. Wilkinson, The Computer Journal **12**, 398 (1969).
7. A. A. Geraci, S. B. Papp, and J. Kitching, Phys. Rev. Lett. **105**, 101101 (2010).

MAJOR CHALLENGES OF A HIGH PRECISION TEST OF THE EQUIVALENCE PRINCIPLE IN SPACE

A.M. NOBILI
Department of Physics "E. Fermi", University of Pisa. Largo B. Pontecorvo 3, 56127 Pisa, Italy

R. PEGNA
INFN-Istituto Nazionale di Fisica Nucleare, Sezione di Pisa, Largo B. Pontecorvo 3, 56127 Pisa, Italy

G. CATASTINI, A. ANSELMI
Thales Alenia Space Italia, Strada Antica di Collegno 253, 10146 Torino, Italy

A. DE MICHELE
Department of Physics "E. Fermi", University of Pisa. Largo B. Pontecorvo 3, 56127 Pisa, Italy

D.M. LUCCHESI
Istituto di Fisica dello Spazio Interplanetario, Istituto Nazionale di Astrofisica. IFSI/INAF, Via del Fosso del Cavaliere 100, 00133 Roma, Italy

A violation of the Equivalence Principle would prove the existence of a new, composition-dependent physical interaction and make for a scientific revolution. Performing the test inside a spacecraft orbiting the Earth at low altitude can potentially improve the best ground results by 4 orders of magnitude. but the experiment faces several major challenges. We discuss them and show how one conceptual experiment and mission design can make the most challenging issues mostly go away.

1 Why testing the Equivalence Principle?

The Equivalence Principle (EP) is the founding pillar of General Relativity and one of the most fundamental principles of Physics. Among all tests of General Relativity, both in weak and strong field, EP tests are the only ones which test the theory for composition dependence. Evidence of an EP violation would not simply call for another metric theory of gravity slightly different from GR; it would prove the existence of a new composition dependent force of Nature. This fact singles out EP tests as of extreme importance and calls for pushing the sensitivity to its limits whenever the experimental possibility for an improvement arises.

2 Why in space?

The Equivalence Principle is tested by measuring the differential acceleration Δa of two proof masses of different composition freely falling in the gravitational field of a source body (like the Earth or the Sun) with an acceleration a (the *driving signal*) and is quantified by the *Eötvös parameter:* $\eta = \Delta a/a$. If EP holds η must be zero. Experimental evidence of $\eta \neq 0$ would show a violation and prove the existence of a new composition-dependent force of Nature: the smaller the measured value of η, the higher the sensitivity of the test. Therefore, for a given experimental capability to detect a differential acceleration Δa, a strong driving signal a is crucial to measure a smaller value of the parameter $\eta = \Delta a/a$ which quantifies the level of testing of the Equivalence Principle. To date the best EP tests have been performed by the Eöt-Wash group with slowly rotating torsion balances finding no violation to $\eta_{E\ddot{o}t-Wash} = 10^{-13}$ (Schlamminger *et al.* [1], Adelberger *et al.* [2]). Torsion balances are sensitive in the horizontal plane, hence they test only the small horizontal component of the free fall acceleration of the proof masses towards the Earth or the Sun. Despite the much smaller driving signal they have won over Galileo-like mass dropping tests by several orders of magnitude. This is due to the very high sensitivity of the torsion balance, to its inherent differential nature and to the possibility to rotate it so as to to modulate the signal at higher frequency.

Flying a space version of the torsion balance, a *differential accelerometer* inside a spacecraft orbiting the Earth at low altitude would provide almost 3 orders of magnitude higher sensitivity just because of the stronger driving acceleration from the Earth. Absence of weight and the fact of running the experiment inside an isolated "lab" (the spacecraft) are additional plus. High sensitivity to very small forces requires the proof masses to be arranged with very small elastic constants; in absence of weight 100 kg mass requires the same suspension spring needed to hold 1 mg on ground, so space is ideal for weak coupling. In an isolated lab local *terrain* noise and disturbances from nearby masses are greatly reduced.

3 Key requirements and major error sources

In order to exploit these advantages and to aim at much a higher precision test than on ground the space experiment must fulfill two key requirements: i) the centers of mass of the test bodies must be well centered on one another, in order to reduce classical tidal differential effects as the bodies orbit around the Earth (the general choice is to have 2 hollow cylinders one inside the other and to find ways of centering their centers of mass on one another); ii) the apparatus should rotate, in order to modulate the signal at a frequency different from (and higher than) the orbital one.

Random error sources -which decrease as the square root of the integration time- are read out noise and thermal noise.

The major challenging systematic errors can be restricted to 4: 1) the radiometer effect; 2) the effect of electric charges patches on the surfaces of the test bodies; 3) the effect of drag due to residual air along the orbit of the satellite; 4) the different coupling of the quadrupole and multipole mass moments of the test bodies with the monopole of the Earth.

Finally it comes the greatest challenge of all: should the mission succeed and achieve its target sensitivity, how to ensure that the effect measured at the expected frequency and phase of an EP violation in the field of the Earth is really the signal of a violation of the Equivalence Principle, hence the proof of the existence of a new force, and not just a very small, unmodeled classical disturbance?

4 A winning idea

One way to fulfill the requirements and reduce the challenging disturbances is by pushing every single mission element to the extreme limits of what is currently feasible. While this may be possible, it is costly and risky. Our experience shows that a much better strategy is to design a mission which —by exploiting the cylindrical symmetry of the experiment (the test masses are two cylinders one inside the other) and the 2 degrees of freedom of the problem (i.e. the 2-body problem of each test body orbiting around the Earth)— can make the challenging issues mostly go away.

"Galileo Galilei" (GG) satellite experiment, which aims at testing the EP to 10^{-17} (Nobili *et al.*[3]), has been designed as a rotating torsion balance modified for flight such that both the key requirements listed above are passively fulfilled: a) The test cylinders, together with the whole spacecraft surrounding them (of cylindrical symmetry too) spin around the *symmetry axis*; b) The test cylinders are weakly coupled to each other *in the plane* perpendicular to it, where they can detect the differential effect of an EP violation signal from the Earth in the orbital plane around it.

Thus, the satellite can be passively stabilized by one axis rotation (e.g. at 1 Hz) while at the same time modulating the signal. In this design the proof masses form a rotating 2-*D harmonic oscillator* characterized by weak coupling and fast rotation (above the natural coupling frequency), which ensures auto-centering of their centers of mass by physics laws, no active centering being required. This is possible only if the test cylinders are weakly coupled in both directions of the plane and spin around the symmetry axis. In one dimension only --e.g. by making the symmetry axis the sensitive one and rotating around an axis perpendicular to it– it is impossible to spin fast and achieve auto-centering.

We can show how from this choice the most relevant error sources listed in Sec. 3 are largely reduced or even eliminated. More importantly, we can also show how very stringent null checks can be performed so as to establish beyond question whether the measured effect is an EP violation or not.

Let us first put things in perspective by comparing the sensitivity to be achieved by an experiment in space aiming at testing EP to 10^{-17} with the sensitivity achieved by rotating torsion balanced in their best EP tests to 10^{-13}. Quite remarkably, they have been able to sense differential accelerations as small as $10^{-16}g$, which yields $\eta_{E\ddot{o}t-Wash} = 10^{-13}$ due to the small driving signal. In space, for GG to meet its target $\eta_{GG} = 10^{-17}$ in the field of the Earth, it must reach a sensitivity to differential accelerations of $10^{-17}g$, i.e. only one order of magnitude better than slowly rotating torsion balances. This is the main advantage of space: a one order of magnitude improvement in sensitivity yields a 4 order of magnitude improvement in testing the Equivalence Principle.

GG originally relied on a capacitance read-out sensor. In collaboration with JPL it has now been replaced by a JPL-developed laser interferometry gauge which is ideal for rejecting common mode effects (laser metrology is linear, hence large common mode motions do not give rise to false signals when two measurements are subtracted), allows a gap several times larger than cap sensors (thus reducing many error sources) and has an extremely low noise (well below $1\mathrm{pm}/\sqrt{\mathrm{Hz}}$). Read-out noise is not a limitation.

Once all systematic errors are reduced below the signal, thermal noise is the ultimate limitation and sets the length of the integration time required for it to become smaller than the signal. It is known that when a low frequency signal is modulated at higher frequency by rotating an oscillator of high mechanical quality surrounded by low pressure residual gas, thermal noise is reduced, as it has been measured by rotating torsion balances which are operated at thermal noise level (Adelberger *et al.*[2]). GG can spin well above the natural frequency without the signal being attenuated, so the modulation frequency is much higher and thermal noise is reduced accordingly (Pegna *et al.*[4]). As a result, the integration time required to reduce thermal noise below the target signal is very short and a few orbits are sufficient to identify its size, frequency and phase. In 1 day the satellite makes about 15 orbits around the Earth and this is the typical timespan for GG to make a measurement at the 10^{-17} target level. This fact has far reaching consequences (see next Section) and it is unique to GG. By comparison, a proposed EP test with cold atoms requires an integration time of 3 months despite a target 1 order of magnitude worse than GG (Ertmer *et al.*[5]).

Consider now the first systematic disturbance of our list, the radiometer effect, a well known *killer* of EP experiments in space. Inside the spacecraft there is a residual gas pressure, and it is exposed to infrared radiation from the Earth, which gives rise to temperature gradients along the symmetry axis of the test cylinder. Since the cylinders have different composition, hence different density, there will be a differential acceleration. This is the radiometer effect. Then, if the cylinders axis is the sensitive axis for detecting an EP violation in the field of the Earth, a radiometer differential acceleration originated by the Earth (through its infrared radiation) would mimic the signal and be undistinguishable from it. The only way out would be to make absolutely sure that the radiometer effect is smaller than the signal by sufficiently reducing the residual pressure and/or the fractional temperature gradients along the axis. In GG the test masses are sensitive in the plane perpendicular to the symmetry axis and rapidly spinning around it; any temperature gradient in this plane driven by the Earth would give rise to a radiometer effect competing with signal, but only in the presence of azimuthal temperature asymmetries, which are greatly reduced by the rotation, making the main radiometer effect not an issue (Nobili *et al.* [6], [7]). An indirect effect from radiometer along the symmetry/spin axis remains to be taken care of, but it is a minor effect.

Were not for this choice, the radiometer effect would make an EP test to 10^{-17} utterly impossible unless one could manage to perform it in cryogenic conditions, at supefluid He temperature at which extremely low pressures ($< 10^{-14}$torr) can be achieved as in GP-B (Everitt *et al.* [8]). Thus, the GG experiment design makes the difference between a room temperature and a cryogenic mission.

The next systematic error in the list of Sec. 3 is due to the so called electric *patch effects.* In spite of being equipotential the surface of a conductor is known to have residual patches of electric charges which have low frequency variations, including a component at the frequency of the signal. This is the case also if the test bodies are electrically grounded as in GG by their mechanical suspensions. The GP-B mission of NASA has in fact been limited by this single effect (Everitt *et al.* [8]). The patch effect decreases as the gap between the surfaces of the test masses squared. in GG a method has been devised to measure the direct effect of electric patches on the test masses and make sure that it is small enough. The method has been successfully demonstrated in the laboratory prototype and can be used also in space as check. However, this is no longer needed because the laser interferometry gauge allows a gap several times larger than originally planned with capacitance sensors, thus getting rid of the patch effect.

The residual atmosphere at the satellite altitude along its orbit around the Earth acts on the external surface of the spacecraft giving rise to an acceleration of its center of mass; any mass weakly suspended inside the spacecraft will feel an inertial acceleration exactly equal and opposite to the acceleration of the spacecraft. Were the test cylinders suspended exactly the same, the effect of this inertial acceleration would also be the same on both of them, and therefore it would not compete with the differential acceleration due to an EP violation. Air drag has a component at the frequency and phase of the signal which –though in common mode– is larger than the signal by several orders of magnitude. Since it is common mode, it is passible to deal with it in 2 ways: by active drag compensation (so as to reduce the inertial common mode acceleration on the test masses) and by common mode rejection, that is by the capability of the test masses and of their read out sensor to *reject* the effects of accelerations which are common mode in nature. By sharing the burden between drag free control and common mode rejection it is possible not to put an extremely tight requirement on either of them

The test cylinders have non zero multipole mass moments, which are also not the same for the two bodies (they are made of different materials, have different mass distribution and size) and therefore couple differently with the monopole mass moment of the Earth. This results in a differential acceleration (the dominant contribution coming from the quadrupole moment) always pointing to the center of mass of the Earth exactly like the differential acceleration due to an EP violation. The effect is deterministic (it is derived unambiguously in celestial mechanics from the orbital parameters) and is proportional to the quadrupole mass moments of the test masses. It is made smaller than the signal by manufacturing them with small enough quadrupole moments so that the differential effect is adequately small.

We show in Sec. 5 how the GG design is crucial in checking competing systematic effects like these in order to establish if the measured effect is due to an EP violation or not.

5 Null checks of the effect measured by a single differential accelerometer

The signature of an EP violation signal for the GG differential accelerometer orbiting around the Earth is perfectly known. We know how it should vary along each orbit and during the mission —as the orbital plane precesses about the North celestial pole at about 1 degree per day due to the quadrupole mass moment of the Earth (a sunsynchronous orbit at about 630 km altitude has finally been selected for GG) while the spin axis of the satellite is fixed in space (due to its very high spin energy, at about 1 Hz spin rate). The geometrical configuration between the sensitive plane of the test cylinders (perpendicular to the spin/symmetry axis) and the plane of the signal (the orbital plane of the satellite) varies in a known way. During 80 days, *in a totally passive deterministic way*, the angle between the two planes varies from $-40°$ to $+40°$, thus making the EP violation signal also vary in a perfectly known way (only the sign and amplitude of it are obviously not known). Since GG can make a full measurement to the required target level of 10^{-17} in 1 day, in a timespan of 80 days it will perform 80 such measurement, allowing us to map the variation of the measured effect with the changing geometry. As shown in Sec. 4, this is possible in GG thanks to the high frequency modulation of the signal and consequently reduced thermal noise and integration time.

It can be easily demonstrated that none of the systematic effects listed in Sec. 3 has the same dependence on such geometry as the signal. In a single 1 day measurement they have the same frequency -and in some cases even the same phase- as the violation signal, but over many days days of data they can all be distinguished from the signal without ambiguity. This is possible also for systematic effects whose frequency is not exactly the same as the frequency of the signa but close to it (e.g. some tidal effects) and are therefore worth a careful check.

These are very powerful null checks which allow us to establish beyond question whether at the orbital frequency there is a non zero signal due to a violation of the Equivalence Principle and the existence of a new, composition dependent force of Nature. Any other research group can independently analyze the mission data by standard methods of celestial mechanics and space geodesy.

GG null checks are carried out by off line data analysis. They do not require any additional accelerometer, such as a "zero check accelerometer" with equal composition test bodies (the EP violation signal should be detected only by the accelerometer with test masses of different composition while classical disturbances would affect both) or even several more accelerometers with an appropriate choice of different material for a cyclic check. In addition to increasing the complexity and cost of the mission, different accelerometers onboard the spacecraft designed to reach the same sensitivity do not ensure the same performance, because the satellite has only one center of mass and that is where disturbances on the test masses are minimized. Moreover, there are subtle systematic errors -such as the radiometer- which do not produce a differential effect on test bodies of the same composition if they have the same density, and could therefore be mistaken for an EP violation (they would affect the accelerometer with test masses of different composition and not the zero check one, just as the violation signal; Nobili *et al.*[7])

Acknowledgments

GG and the lab prototype are supported by the Italian Space Agency (ASI) and by INFN

References

1. S. Schlamminger, K.-Y. Choi, T.A. Wagner, J.H. Gundlach, E.G. Adelberger, Phys. Rev. Lett. 100 (2008) 041101
2. E.G. Adelberger, J.H. Gundlach, B.R. Heckel, S. Hoedl, S. Schlamminger, Progress in Particle and Nuclear Physics 62 (2009) 102
3. A.M. Nobili *et al.*, Phys. Lett. A 318 (2003) 172
4. R. Pegna, A.M. Nobili, M. Shao, S.G. Turyshev, G.L. Comandi, G. Catastini, A. Anselmi, A. De Michele, submitted (2011)
5. W. Ertmer *et al.*, Exp. Atron. 23 (2009) 611
6. A.M. Nobili, D. Bramanti, G. Comandi, R. Toncelli, E. Polacco, G. Catastini, Phys. Rev. D 63 (2001) 101101-1
7. A.M. Nobili, D. Bramanti, G.L. Comandi, R. Toncelli, E. Polacco, New Astronomy 7 (2002) 521
8. C.W.F. Everitt et al., Phys. Rev. Lett. 106 (2011) 21101-1

10.
Lorentz invariance and CPT

LORENTZ SYMMETRY, THE SME, AND GRAVITATIONAL EXPERIMENTS

JAY D. TASSON
Department of Physics, Whitman College
Walla Walla, WA 99362, USA
E-mail: tassonjd@whitman.edu

This proceedings contribution summarizes the implications of recent SME-based investigations of Lorentz violation for gravitational experiments.

1 Introduction

General Relativity along with the Standard Model of particle physics provide a remarkable description of known physics. Lorentz symmetry is a foundational principle of each, and thus should be well tested experimentally. It is also likely that General Relativity and the Standard Model are limits of a more fundamental theory that provides consistent predictions at the Planck scale. Tests of Lorentz symmetry provide a technically feasible means of searching for potential suppressed signals from the Planck scale in existing experiments and observations.[1] The gravitational Standard-Model Extension (SME) provides a comprehensive test framework for searching for such potential signals across all areas of known physics.[2,3]

In spite of both the many high-sensitivity investigations of Lorentz symmetry[4] performed in the context of the SME in Minkowski spacetime,[3] the scope of which continues to deepen and broaden,[4,5,6] and the many investigations of metric theories of gravity performed in the context of the Parametrized Post-Newtonian (PPN) formalism,[7] there remain numerous potential Lorentz-violating deviations from General Relativity that have not yet been sought observationally and experimentally. Some of these violations would lead to qualitatively new types of signals.

Lorentz-violating effects in gravitational experiments can originate from two basic places: the pure-gravity action and gravitational couplings in the other sectors of the theory. While some distinct theoretical issues are associated with each origin, and some of the associated experimental signatures are quite different, the relevant effects can be observed in many of the same classes of experiments. The pure-gravity sector was the subject of Ref. 8, and Sec. 2 summarizes some of the key theoretical issues associated with that work. Section 3 provides a similar summary of theoretical issues associated with matter-gravity couplings, which were the subject of Ref. 9. Experiments relevant for investigations of Lorentz violation originating from both sectors are then considered in Sec. 4.

2 Lorentz violation in pure gravity

Investigations of Lorentz violation performed in the context of the minimal SME in Minkowski spacetime are extended to include the post-Newtonian implications of Lorentz violation in the pure-gravity sector in Ref. 8, and several associated theoretical and phenomenological investigations have expanded aspects of that work.[10,11] The action for the minimal pure gravity sector takes the form [2]

$$S = \frac{1}{2\kappa}\int d^4x e(R - uR + s^{\mu\nu}R^T_{\mu\nu} + t^{\kappa\lambda\mu\nu}C_{\kappa\lambda\mu\nu}), \tag{1}$$

where $C_{\kappa\lambda\mu\nu}$ is the Weyl tensor, $R^T_{\mu\nu}$ is the traceless Ricci tensor, and e is the vierbein determinant. The first term here is the standard Einstein-Hilbert term. The relevant Lorentz-violating signals in the post-Newtonian analysis to follow stem from the third term involving the coefficient field $s^{\mu\nu}$. The second term is not Lorentz violating, and the fourth term provides no contributions in the post-Newtonian analysis.

It has been shown that in the present context of Riemannian spacetime, consistent Lorentz symmetry breaking must be spontaneous,[2] though use of more general geometries may admit explicit breaking.[12] A number of implications stemming directly from spontaneous symmetry breaking can also be considered;[13,14,15] however, a detailed discussion of these issues is beyond the scope of the present discussion.

As a result of the specialization to spontaneous symmetry breaking in the present context, a primary theoretical issue addressed in Ref. 8 is establishing a procedure for correctly accounting for the fluctuations in the coefficient fields, including the massless Nambu-Goldstone modes of Lorentz-symmetry breaking.[13] This challenge is met in a general way, without specializing to a specific model of spontaneous symmetry breaking, under a few mild assumptions. Upon addressing this issue, the leading-order Lorentz-violating contributions to the linearized field equations are obtained and can be expressed in terms of the metric fluctuation $h_{\mu\nu}$ and the vacuum value $\overline{s}^{\mu\nu}$ associated with the coefficient field $s^{\mu\nu}$. The post-Newtonian metric is obtained from these equations. With a suitable gauge choice [8] the metric takes the form

$$\begin{aligned}
g_{00} &= -1 + 2U + 3\overline{s}^{00}U + \overline{s}^{jk}U^{jk} - 4\overline{s}^{0j}V^j + O(4), && (2)\\
g_{0j} &= -\overline{s}^{0j}U - \overline{s}^{0k}U^{jk} - \tfrac{7}{2}(1 + \tfrac{1}{28}\overline{s}^{00})V^j + \tfrac{3}{4}\overline{s}^{jk}V^k - \tfrac{1}{2}(1 + \tfrac{15}{4}\overline{s}^{00})W^j \\
&\quad + \tfrac{5}{4}\overline{s}^{jk}W^k + \tfrac{9}{4}\overline{s}^{kl}X^{klj} - \tfrac{15}{8}\overline{s}^{kl}X^{jkl} - \tfrac{3}{8}\overline{s}^{kl}Y^{klj}, && (3)\\
g_{jk} &= \delta^{jk} + (2 - \overline{s}^{00})\delta^{jk}U + (\overline{s}^{lm}\delta^{jk} - \overline{s}^{jl}\delta^{mk} - \overline{s}^{kl}\delta^{jm} + 2\overline{s}^{00}\delta^{jl}\delta^{km})U^{lm}, && (4)
\end{aligned}$$

where U, U^{jk}, V^j, W^j, X^{klj}, and Y^{klj} are potentials formed from appropriate integrals over the source body. The explicit form of the potentials is provided in Ref. 8.

The above metric is then compared and contrasted with the PPN metric. The basic idea is that the pure-gravity sector of the minimal SME provides an expansion about the action of General Relativity, while the PPN provides an expansion about the metric. Perhaps surprisingly, an overlap of only one parameter is found between the 20 coefficients in the minimal pure-gravity sector of the SME and the 10 parameters of the PPN formalism. This implies that leading corrections to General Relativity at the level of the action do not match those typically studied in an expansion about the metric. Note also that the focus of the SME is on Lorentz violation throughout physics, while the focus of the PPN is on deviations from General Relativity, which may or may not be Lorentz violating. Thus the minimal pure-gravity sector of the SME and the PPN formalism provide complementary approaches to studying deviations from General Relativity.

Finally, Ref. 8 introduces bumblebee models[16] that provide specific examples of complete theories with spontaneous symmetry breaking that fit into the post-Newtonian results established in the general context of the SME.

3 Lorentz violation in matter-gravity couplings

Though many high-sensitivity investigations of Lorentz violation [4] have been performed in the context of the fermion sector of the minimal SME in Minkowski spacetime,[3] there remains a number of coefficients for Lorentz violation in that sector that have not been investigated experimentally. A methodology for obtaining sensitivities to some of these open parameters by considering gravitational couplings in the fermions sector of the SME is provided by Ref. 9. The set of coefficients $\overline{a}_\mu$ for baryons and charged leptons, which are unobservable in principle in Minkowski spacetime, is of particular interest. Due to gravitational countershading,[17] these coefficients could be large relative to existing matter-sector sensitivities.

Prior to developing the necessary results for experimental analysis, the theoretical portion of Ref. 9 addresses a number of useful conceptual points. One such point is consideration of the circumstances under which relevant types of Lorentz violation are observable in principle. Though the $\overline{a}_\mu$ coefficient can be removed from the single fermion theory in Minkowski spacetime via a spinor redefinition, it is highlighted that it cannot typically be removed in the presence of gravity.[2] This results in the gravitational countershading pointed out in Ref. 17.

A coordinate choice that can be used to fix the sector of the theory that defines isotropy is also discussed, and the role of the gravitational sector in this context is established. Ultimately, the photon sector is chosen to have $\eta_{\mu\nu}$ as the background metric, though no generality is lost, and other choices can be recovered.

The treatment of the fluctuations in the coefficient fields established for the gravitational sector is adapted to the context of matter-gravity couplings. Two notions of perturbative order are introduced to treat the fluctuations perturbatively under the assumptions that gravitational and Lorentz-violating corrections are small. One notion of perturbative order, denoted $\mathrm{O}(m,n)$, tracks the orders in Lorentz violation and in gravity. Here the first entry represents the order in the coefficients for Lorentz violation, and the second entry represents the order in the metric fluctuation $h_{\mu\nu}$. A secondary notion of perturbative order, which tracks the post-Newtonian order, is denoted PNO(p). The O(1,1) contributions are of primary interest in Ref. 9, since the goal of that work is to investigate dominant Lorentz-violating implications in matter-gravity couplings.

To proceed toward the analysis of relevant experiments, the results necessary for working at a number of energy levels are developed from the full field-theoretic action of the gravitationally coupled fermion sector of the SME, which takes the form

$$S_\psi = \int d^4x (\tfrac{1}{2} i e e^\mu{}_a \overline{\psi} \Gamma^a \overleftrightarrow{D_\mu} \psi - e\overline{\psi} M \psi). \tag{5}$$

where

$$\begin{aligned} \Gamma^a \quad \equiv \quad & \gamma^a - c_{\mu\nu} e^{\nu a} e^\mu{}_b \gamma^b - d_{\mu\nu} e^{\nu a} e^\mu{}_b \gamma_5 \gamma^b \\ & - e_\mu e^{\mu a} - i f_\mu e^{\mu a} \gamma_5 - \tfrac{1}{2} g_{\lambda\mu\nu} e^{\nu a} e^\lambda{}_b e^\mu{}_c \sigma^{bc} \end{aligned} \tag{6}$$

and

$$M \equiv m + a_\mu e^\mu{}_a \gamma^a + b_\mu e^\mu{}_a \gamma_5 \gamma^a + \tfrac{1}{2} H_{\mu\nu} e^\mu{}_a e^\nu{}_b \sigma^{ab}, \tag{7}$$

where a_μ, b_μ, $c_{\mu\nu}$, $d_{\mu\nu}$, e_μ, f_μ, $g_{\lambda\mu\nu}$, $H_{\mu\nu}$ are coefficient fields for Lorentz violation.

Starting from Eq. 5, the relativistic quantum mechanics in the presence of gravitational fluctuations and Lorentz violation is established after investigating two methods of identifying an appropriate hamiltonian. The explicit form of the relativistic hamiltonian involving all coefficients for Lorentz violation in the minimal fermion sector is provided.

The standard Foldy-Wouthuysen procedure is then employed to obtain the nonrelativistic quantum Hamiltonian. At this stage, attention is specialized to the study of spin-independent Lorentz-violating effects, which are governed by the coefficient fields $(a_{\mathrm{eff}})_\mu$, $c_{\mu\nu}$ and the metric fluctuation $h_{\mu\nu}$. Though interesting effects may exist in couplings involving spin, gravity, and Lorentz violation, the pursuit of spin-independent effects maintains a reasonable scope focused on the least well-constrained coefficients including the countershaded $\overline{a}_\mu$ coefficients.

For many relevant applications, the classical theory[18] associated with the quantum-mechanical dynamics is the most useful description. Thus the classical theory involving nonzero $(a_{\rm eff})_\mu$, $c_{\mu\nu}$, and $h_{\mu\nu}$ is established at leading order in Lorentz violation for the case of the fundamental particles appearing in QED as well as for bodies involving many such particles. The modified Einstein equation and the equation for the trajectory of a classical test particle follow from the classical theory. Obtaining explicit solutions for the trajectories of particles requires knowledge of the coefficient and metric fluctuations. A systematic procedure for calculating this information is established, and general expressions for the coefficient and metric fluctuations are obtained to O(1,1) in terms of gravitational potentials and the vacuum values $(\overline{a}_{\rm eff})_\mu$ and $\overline{c}_{\mu\nu}$ associated with the coefficient fields $(a_{\rm eff})_\mu$ and $c_{\mu\nu}$. With this, we find that the equation of motion for a test particle can be written

$$\begin{aligned}
\ddot{x}^\mu &= -\Gamma_{(0,1)}{}^\mu{}_{\alpha\beta}u^\alpha u^\beta - \Gamma_{(1,1)}{}^\mu{}_{\alpha\beta}u^\alpha u^\beta + 2\eta^{\mu\gamma}(\overline{c}^{\rm T})_{(\gamma\delta)}\Gamma_{(0,1)}{}^\delta{}_{\alpha\beta}u^\alpha u^\beta \\
&\quad +2(\overline{c}^{\rm T})_{(\alpha\beta)}\Gamma_{(0,1)}{}^\alpha{}_{\gamma\delta}u^\beta u^\gamma u^\delta u^\mu - \frac{1}{m^{\rm T}}[\partial^\mu(\tilde{a}^{\rm T}_{\rm eff})_\alpha - \eta^{\mu\beta}\partial_\alpha(\tilde{a}^{\rm T}_{\rm eff})_\beta]u^\alpha, \qquad (8)
\end{aligned}$$

where the metric to be inserted into the Christoffel symbols is

$$\begin{aligned}
g_{00} &= -1 + 2\left[1 + 2\frac{\alpha}{m}(\overline{a}^{\rm S}_{\rm eff})_0 + (c^{\rm S})_{00}\right]U + 2\left[\frac{\alpha}{m}(\overline{a}^{\rm S}_{\rm eff})_j + 2(c^{\rm S})_{(j0)}\right]V^j - 2\frac{\alpha}{m}(\overline{a}^{\rm S}_{\rm eff})_j W^j, \quad (9) \\
g_{0j} &= \frac{\alpha}{m}(\overline{a}^{\rm S}_{\rm eff})_j U + \frac{\alpha}{m}(\overline{a}^{\rm S}_{\rm eff})_k U^{jk} - \left[4 + \frac{\alpha}{m}(\overline{a}^{\rm S}_{\rm eff})_0 + 4(c^{\rm S})_{00}\right]V^j - \alpha(\overline{a}^{\rm S}_{\rm eff})_0 W^j, \quad (10) \\
g_{jk} &= \delta^{jk} + 2\left[1 - \frac{\alpha}{m}(\overline{a}^{\rm S}_{\rm eff})_0 + (c^{\rm S})_{00}\right]U\delta^{jk} + 2\frac{\alpha}{m}(\overline{a}^{\rm S}_{\rm eff})_0 U^{jk}. \quad (11)
\end{aligned}$$

and the fluctuations in the coefficient field $(a_{\rm eff})_\mu$ take the form

$$(\tilde{a}^{\rm T}_{\rm eff})^{(1,1)}_\mu = \tfrac{1}{2}\alpha h_{\mu\nu}(\overline{a}^{\rm T}_{\rm eff})^\nu - \tfrac{1}{4}\alpha(\overline{a}^{\rm T}_{\rm eff})_\mu h^\nu{}_\nu + \partial_\mu\Psi. \qquad (12)$$

Here the superscripts S and T indicate coefficients associated with the source and test bodies respectively, and a dot over a quantity indicates a derivative with respect to the usual proper time. The subscripts on the Christoffel symbols indicate the order in the small quantities that should be included in the given Christoffel symbol. The vacuum values $(\overline{a}_{\rm eff})_\mu$ and $\overline{c}_{\mu\nu}$ can then be identified with the coefficients for Lorentz violation investigated in the Minkowski spacetime SME.

As in the pure-gravity sector, bumblebee models provide specific examples of the general results.

4 Experiments

4.1 Laboratory Tests

The effects of coefficients $(\overline{a}_{\rm eff})_\mu$, $\overline{c}_{\mu\nu}$, and $\overline{s}_{\mu\nu}$ can be measured in a wide variety of experiments performed in Earth-based laboratories. Tests of this type that have been proposed or performed include gravimeter experiments, tests of the universality of free fall, and experiments with devices traditionally used as tests of gravity at short range.

Analysis performed in Ref. 8 for the case of $\overline{s}_{\mu\nu}$, and in Ref. 9 for $(\overline{a}_{\rm eff})_\mu$ and $\overline{c}_{\mu\nu}$, reveals that the gravitational force acquires tiny corrections both along and perpendicular to the usual free-fall trajectory near the surface of the Earth. Coefficients $(\overline{a}_{\rm eff})_\mu$ and $\overline{c}_{\mu\nu}$ also lead to a modified effective inertial mass of a test body that is direction dependent, resulting in a nontrivial relation between force and acceleration. Both the corrections to the gravitational force and to the inertial mass are time dependent with variations at the annual and sidereal frequencies. In addition, corrections due to $(\overline{a}_{\rm eff})_\mu$ and $\overline{c}_{\mu\nu}$ are particle-species dependent.

Based on the above discussion, laboratory tests using Earth as a source fall into 4 classes. Free-fall gravimeter tests monitor the acceleration of free particles over time, while force-comparison gravimeter tests monitor the gravitation force on a body over time. Both types of gravimeter tests are sensitive to $(\overline{a}_{\rm eff})_\mu$, $\overline{c}_{\mu\nu}$, and $\overline{s}_{\mu\nu}$ coefficients. The relative acceleration of, or relative force on a pair of test bodies can also be monitored constituting free-fall and force-comparison Weak Equivalence Principle (WEP) tests respectively. Sensitivities to $(\overline{a}_{\rm eff})_\mu$ and $\overline{c}_{\mu\nu}$ can be achieved in WEP tests. Relevant devices presently used for the above types of tests include experiments with falling corner cubes,[19] atom interferometers,[20,21,22] superconducting levitation,[23] tossed masses,[24] balloon drops,[25] drop towers,[26] sounding rockets,[27] and torsion pendula.[28] Refs. 8 and 9 provide specific predictions and estimated sensitivities for the above tests including a frequency decomposition of the relevant signal to which experimental data could be fit. Note that the effective WEP violation with periodic time dependence considered here is a qualitatively different signal that would likely have been missed in past WEP tests. One experiment of this type has already been performed using an atom-interferometer as a free-fall gravimeter.[21]

Variations of the above laboratory tests involving the gravitational couplings of charged particles, antimatter, and second- and third-generation particles are also studied in Ref. 9. Though they are very challenging experimentally, these tests can yield sensitivities to Lorentz and CPT violation that are otherwise difficult or impossible to achieve. Charged-particle interferometry,[29] ballistic tests with charged particles,[30] gravitational experiments with antihydrogen,[31] and signals in muonium free fall[32] are considered. Some features of antihydrogen tests are illustrated with simple toy-models limits of the SME.

Though less sensitive at present to the range-independent SME effects presently under discussion, systems in which both the source mass and the test mass are contained within the lab, such as those devices traditionally used as tests of gravity at short range, can also be considered. A search for $\overline{s}_{\mu\nu}$ has been performed using a cantilever system[33] and a search for $(\overline{a}_{\rm eff})_\mu$ using a torsion-strip balance[34] have been performed using this approach. A proposal to measure $\overline{s}_{\mu\nu}$ using a torsion pendulum with an asymmetric mass distribution also exists.[8]

4.2 *Satellite-Based Tests*

Space-based experiments can offer unique advantages in testing gravitational physics[35] and in searching for Lorentz violation.[36] The WEP tests considered above are an example of a class of tests for which significant sensitivity improvements might be possible in space, due to the long free-fall times that may be attainable on a drag-free spacecraft. There are several proposals for such missions in the advanced stages of development, including the Micro-Satellite à traînée Compensée pour l'Observation du Principe d'Equivalence (MicroSCOPE),[37] the Satellite Test of the Equivalence Principle (STEP),[38] and the Galileo Galilei (GG) mission.[39] A WEP experiment with reach similar to that of STEP has also been suggested for the Grand Unification and Gravity Explorer (GaUGE) mission.[40]

Monitoring the relative motion of test bodies of different composition as they obit the Earth inside of the spacecraft is the basic idea underlying these missions. Nonzero coefficients for Lorentz violation $(\overline{a}^w_{\rm eff})_\mu$ and $(\overline{c}^w)_{\mu\nu}$, would result in material dependent orbits. Ref. 9 provides the differential acceleration of the test masses, decomposed by frequency, that are relevant for fitting data for each of the above proposed tests, and achievable sensitivities are estimated. As in the lab-based tests, the SME signals would be distinguised from other sources of WEP violation by the characteristic time dependences of the signals. A ground-based version of the GG experiment, Galileo Galilei on the Ground (GGG),[39] which is presently taking data, could also obtain sensitivities to Lorentz violation.

Another test with sensitivity to Lorentz violation that was made possible using a space-based platform is the gyroscope experiment, Gravity Probe B (GPB).[41] The geodetic or de Sitter precession about an axis perpendicular to the orbit and the gravitomagnetic frame-dragging or Lens-Thirring precession about the spin axis of the Earth are the primary conventional relativistic effects for a gyroscope in orbit around the Earth. An analysis of such a system in the presence of $\bar{s}_{\mu\nu}$ was performed in Ref. 8. It was found that additional Lorentz-violating precessions result, including a precession about an axis perpendicular to both the angular-momentum axis of the orbit and Earth's spin axis. A similar investigation considering the effects of $(\bar{a}_{\rm eff})_\mu$ and $\bar{c}_{\mu\nu}$ is possible based on the theoretical work in Ref. 9, but it remains an open problem at present.

4.3 Orbital Tests

The search for anomalous effects on orbits provides a natural way of testing gravitational physics. References 8 and 9 consider tests which search for such effects via laser ranging to the Moon and other bodies, perihelion precession measurements, and binary-pulsar observations.

Lunar laser ranging provides extraordinarily sensitive orbital measurements.[42] Based on the detained proposal to search for the effects of pure-gravity sector coefficient $\bar{s}_{\mu\nu}$ provided by Ref. 8, some of the best existing constrains on several components of that coefficient have been placed using lunar laser ranging data.[43] A similar proposal to search of $(\bar{a}_{\rm eff})_\mu$ and $\bar{c}_{\mu\nu}$ effects on the lunar orbit is made in Ref. 9. Ranging to other satellites in different orientations or of different composition could yield additional independent sensitivities.

Measurements of the precession of the perihelion of orbiting bodies [44] are also considered for the case of $(\bar{a}_{\rm eff})_\mu$ and $\bar{c}_{\mu\nu}$ coefficients [9] as well as $\bar{s}_{\mu\nu}$ coefficients.[8] Based on the established advance of the perihelion for Mercury and for the Earth, constraints on combinations of $(\bar{a}_{\rm eff})_\mu$, $\bar{c}_{\mu\nu}$, and $\bar{s}_{\mu\nu}$ are placed. These constrains provide the best current sensitivity to $(\bar{a}_{\rm eff})_J$, though it comes as a part of a complicated combination of coefficients.

Binary-pulsar observations complement the above solar-system tests by providing orbits of significantly different orientations.[45] Reference 8 contains detailed predictions for the effects of $\bar{s}_{\mu\nu}$ on binary-pulsar systems. The effects of $(\bar{a}_{\rm eff})_\mu$ and $\bar{c}_{\mu\nu}$ on such systems could also be investigated, but detailed observational predictions remain to be made.

4.4 Photon and Clock Tests

A final class of tests involves the interaction of photons with gravity as well as effects on the clocks typically associated with such tests. References 11 and 9 consider signals arising in measurements of the time delay, gravitational Doppler shift, and gravitational redshift, along with comparisons of the behaviors of photons and massive bodies for Lorentz violation in the pure gravity sector and matter sector respectively. Null redshift tests are also considered in Ref. 9 resulting in expected sensitivity to $(\bar{a}_{\rm eff})_\mu$ and $\bar{c}_{\mu\nu}$ coefficients. Implications for a variety of existing and proposed experiments and space missions are considered.[46] An analysis of a variety of clocks has been performed and sensitivities to $(\bar{a}_{\rm eff})_\mu$ and $\bar{c}_{\mu\nu}$ coefficients have been achieved.[22] Note that these results and proposals are in addition to the Minkowski spacetime clock experiments which have been performed on the ground [4] and could be improved in space.[36]

5 Summary

Existing sensitivities from the experiments and observations summarized above can be found in *Data Tables for Lorentz and CPT Violation*.[4] Expected sensitivities based on the proposals summarized above are collected in Table 6 of Ref. 8 and Tables XIV and XV of Ref. 9. These sensitivities reveal excellent prospects for using gravitational experiments to seek Lorentz violation. Of particular interest are the opportunities to measure the countershaded coefficients

$(\bar{a}_{\text{eff}})_\mu$ since these coefficients typically cannot be detected in nongravitational searches.[17] Thus the tests of Lorentz symmetry proposed in Refs. 8 and 9 offer promising opportunities to search for signals of new physics, potentially originating at the Planck scale. The effects can be sought in existing, planned, or feasible experiments and in some cases provide experimental signatures that are qualitatively different from those sought to date.

References

1. V.A. Kostelecký and S. Samuel, Phys. Rev. D **39**, 683 (1989); V.A. Kostelecký and R. Potting, Nucl. Phys. B **359**, 545 (1991).
2. V.A. Kostelecký, Phys. Rev. D **69**, 105009 (2004).
3. D. Colladay and V.A. Kostelecký, Phys. Rev. D **55**, 6760 (1997); Phys. Rev. D **58**, 116002 (1998).
4. *Data Tables for Lorentz and CPT Violation,* 2010 edition, V.A. Kostelecký and N. Russell, Rev. Mod. Phys. **83**, 11 (2011), arXiv:0801.0287v4.
5. V.A. Kostelecký and M. Mewes, Phys. Rev. D **80**, 015020 (2009).
6. A. Peters, these proceedings; W. Terrano, these proceedings; M. Romalis, these proceedings; M. Tobar, these proceedings; M. Nagel, these proceedings.
7. C.M. Will, *Theory and Experiment in Gravitational Physics*, Cambridge University Press, Cambridge, 1993.
8. Q.G. Bailey and V.A. Kostelecký, Phys. Rev. D **74**, 045001 (2006).
9. V.A. Kostelecký and J.D. Tasson, Phys. Rev. D **83**, 016013 (2011).
10. Q.G. Bailey, Phys. Rev. D **82**, 065012 (2010); B. Altschul, Q.G. Bailey, and V.A. Kostelecký, Phys. Rev. D **81**, 065028 (2010); M.D. Seifert, Phys. Rev. D **79**, 124012 (2009).
11. Q.G. Bailey, Phys. Rev. D **80**, 044004 (2009).
12. V.A. Kostelecký, arXiv:1104.5488.
13. R. Bluhm and V.A. Kostelecký, Phys. Rev. D **71** 065008 (2005); R. Bluhm *et al.*, Phys. Rev. D **77**, 065020 (2008).
14. V.A. Kostelecký and R. Potting, Gen. Rel. Grav. **37**, 1675 (2005); Phys. Rev. D **79**, 065018 (2009).
15. Y. Bonder, these proceedings.
16. V.A. Kostelecký and S. Samuel, Phys. Rev. Lett. **63**, 224 (1989); Phys. Rev. D **40**, 1886 (1989).
17. V.A. Kostelecký and J.D. Tasson, Phys. Rev. Lett. **102**, 010402 (2009).
18. V.A. Kostelecký and N. Russell, Phys. Lett. B **693**, 443 (2010).
19. I. Marson and J.E. Faller, J. Phys. E **19**, 22 (1986); K. Kuroda and N. Mio, Phys. Rev. D **42**, 3903 (1990); T.M. Niebauer, M.P. McHugh, and J.E. Faller, Phys. Rev. Lett. **59**, 609 (1987).
20. A. Peters, K.Y. Chung, and S. Chu, Nature **400**, 849 (1999): J.M. McGuirk *et al.*, Phys. Rev. A **65**, 033608 (2002); N. Yu *et al.*, Appl. Phys. B **84**, 647 (2006); B. Canuel *et al.*, Phys. Rev. Lett. **97**, 010402 (2006); H. Kaiser *et al.*, Physica B **385-386**, 1384 (2006); S. Fray *et al.*, Phys. Rev. Lett. **93**, 240404 (2004). S. Dimopoulos *et al.*, Phys. Rev. D **78**, 042003 (2008); M. Kasevich, these proceedings; E. Rasel, these proceedings; Y.-H. Lien, these proceedings.
21. K.-Y. Chung *et al.*, Phys. Rev. D **80**, 016002 (2009); H. Müller *et al.*, Phys. Rev. Lett. **100**, 031101 (2008).
22. M. Hohensee *et al.*, Phys. Rev. Lett. **106** 151102 (2011); M. Hohensee, these proceedings.
23. R.J. Warburton and J.M. Goodkind, Astrophys. J. **208**, 881 (1976); S. Shiomi, arXiv:0902.4081; L. Carbone *et al.*, in T. Damour, R.T. Jantzen, and R. Ruffini, eds., *Proceedings of the Twelfth Marcel Grossmann Meeting on General Relativity*, World Sci-

entific, Singapore, 2010.

24. R.D. Reasenberg, in V.A. Kostelecký, ed., *CPT and Lorentz Symmetry II*, World Scientific, Singapore, 2005.
25. V. Iafolla *et al.*, Class. Quantum Grav. **17**, 2327 (2000).
26. H. Dittus and C. Mehls, Class. Quantum Grav. **18**, 2417 (2001).
27. R.D. Reasenberg and J.D. Phillips, Class. Q. Grav. **27**, 095005 (2010).
28. Y. Su *et al.*, Phys. Rev. D **50**, 3614 (1994); S. Schlamminger *et al.*, Phys. Rev. Lett. **100**, 041101 (2008); T. Wagner, these proceedings.
29. F. Hasselbach and M. Nicklaus, Phys. Rev. A **48**, 143 (1993); B. Neyenhuis, D. Christensen, and D.S. Durfee, Phys. Rev. Lett. **99**, 200401 (2007).
30. F.S. Witteborn and W.M. Fairbank, Phys. Rev. Lett. **19**, 1049 (1967).
31. G. Gabrielse, Hyperfine Int. **44**, 349 (1988); N. Beverini *et al.*, Hyperfine Int. **44**, 357 (1988); R. Poggiani, Hyperfine Int. **76**, 371 (1993); T.J. Phillips, Hyperfine Int. **109**, 357 (1997); AGE Collaboration, A.D. Cronin *et al.*, *Letter of Intent: Antimatter Gravity Experiment (AGE) at Fermilab*, February 2009; D. Kaplan, arXiv:1007.4956; J. Walz and T.W. Hänsch, Gen. Rel. Grav. **36**, 561 (2004); P. Pérez *et al.*, *Letter of Intent to the CERN-SPSC,* November 2007; F.M. Huber, E.W. Messerschmid, and G.A. Smith, Class. Quantum Grav. **18**, 2457 (2001); AEGIS Collaboration, A. Kellerbauer *et al.*, Nucl. Instr. Meth. B **266**, 351 (2008); C. Canali, these proceedings; P. Dupré, these proceedings.
32. K. Kirch, arXiv:physics/0702143; B. Lesche, Gen. Rel. Grav. **21**, 623 (1989).
33. J. Long, these proceedings.
34. C. Speake, these proceedings.
35. For reviews of space-based tests of relativity see, for example C. Lämmerzahl, C.W.F. Everitt, and F.W. Hehl, eds., *Gyros, Clocks, Interferometers ...: Testing Relativistic Gravity in Space*, Springer, Berlin, 2001.
36. R. Bluhm *et al.*, Phys. Rev. Lett. **88**, 090801 (2002); Phys. Rev. D **68**, 125008 (2003).
37. P. Touboul, M. Rodrigues, G. Métris, and B. Tatry, Comptes Rendus de l'Académie des Sciences, Series IV, **2**, 1271 (2001); P. Touboul, these proceedings; A. Levy, these proceedings.
38. T.J. Sumner *et al.*, Adv. Space Res. **39**, 254 (2007).
39. A.M. Nobili *et al.*, Exp. Astron. **23**, 689 (2009); A.M. Nobili, these proceedings.
40. G. Amelino-Camelia *et al.*, Exp. Astron. **23**, 549 (2009).
41. C.W.F. Everitt *et al.*, arXiv:1105.3456.
42. J.G. Williams, S.G. Turyshev, and H.D. Boggs, Phys. Rev. Lett. **93**, 261101 (2004); T.W. Murphy *et al.*, Pub. Astron. Soc. Pac. **120**, 20 (2008).
43. J.B.R. Battat, J.F. Chandler, and C.W. Stubbs, Phys. Rev. Lett. **99**, 241103 (2007).
44. C.M. Will, Living Rev. Rel. **4**, 4 (2001).
45. I.H. Stairs, Living Rev. Rel. **6**, 5 (2003); these proceedings.
46. B. Bertotti, L. Iess, and P. Tortora, Nature **425**, 374 (2003); T. Appourchaux *et al.*, Exp. Astron. **23**, 491 (2009); L. Iess and S. Asmar, Int. J. Mod. Phys. D **16**, 2117 (2007); P. Wolf *et al.*, Exp. Astron. **23**, 651 (2009); B. Christophe *et al.*, Exper. Astron. **23**, 529 (2009); S.G. Turyshev *et al.*, Int. J. Mod. Phys. D **18**, 1025 (2009); S.B. Lambert and C. Le Poncin-Lafitte, Astron. Astrophys. **499**, 331 (2009); R. Byer, *Space-Time Asymmetry Research*, Stanford University proposal, January 2008; L. Cacciapuoti and C. Salomon, Eur. Phys. J. Spec. Top. **172**, 57 (2009); S.G. Turyshev and M. Shao, Int. J. Mod. Phys. D **16**, 2191 (2007); S.C. Unwin *et al.*, Pub. Astron. Soc. Pacific **120**, 38 (2008); M. Gai, these proceedings; P.L. Bender, these proceedings; S. Bize, these proceedings; P. Lemonde, these proceedings; L. Cacciapuoti, these proceedings; T. Schuldt these proceedings.

ELECTROMAGNETIC CAVITY TESTS OF LORENTZ INVARIANCE ON EARTH AND IN SPACE

M. NAGEL, K. MÖHLE, K. DÖRINGSHOFF, E.V. KOVALCHUCK, and A. PETERS
Humboldt-Universität zu Berlin, Institut für Physik, Newtonstr. 15, 12489 Berlin, Germany

We present a Michelson-Morley type experiment for testing the isotropy of the speed of light in vacuum and matter. The experiment compares the resonance frequency of an actively rotated monolithic optical cryogenic sapphire resonator against the resonance frequency of a stationary evacuated optical cavity made of ultra-low-expansion glass. The results yield an upper limit for the anisotropy of the speed of light in matter (sapphire) of $\Delta c/c < 1 \times 10^{-16}$, limited by the frequency stability of the sapphire resonator.

1 Introduction

Testing the isotropy of the speed of light serves as a sensitive test of special relativity and Lorentz invariance. The classic experiment to test the isotropy of the speed of light uses a Michelson interferometer and was first performed by A.A. Michelson more than hundred years ago. He was later joined by E.W. Morley and they published a 10^{-9} null-result in 1887,[1] which surprised the scientific community at that time. Modern such type of experiments use electromagnetic resonators to probe for Lorentz invariance violations and are generally based on comparing the resonance frequencies of two similar orthogonal resonators while either actively rotating the setup or relying solely on Earth's rotation.[2,3,4,6,5,7,8,9] The basic principle of a modern Michelson-Morley type experiment is to search for orientation dependent relative changes of the eigenfrequencies $\delta\nu/\nu_0$ of the employed electromagnetic resonators which might be caused by Lorentz invariance violation.

In case of a linear resonator a relative frequency change is most generally described by $\delta\nu/\nu_0 = \delta c/c_0 - \delta L/L_0 - \delta n/n_0$, where $\delta c/c_0$ denotes a relative change in the speed of light in vacuum along the optical path, $\delta L/L_0$ denotes a relative change in the length of the optical path, and $\delta n/n_0$ denotes a relative change in the index of refraction along the optical path. All three effects can occur in the case of spontaneous Lorentz symmetry breaking.[10,11,12] The magnitude of the different types of Lorentz violations depend on the composition of the material the resonator is made of. Comparing the eigenfrequencies of two similar resonators made of the same material – as has been done in almost all previous reported modern Michelson-Morley experiments – makes it impossible to distinguish between the different types of Lorentz violation and due to the substraction of the different types an overall Lorentz violating signal could be even suppressed or canceled. However, the material dependency makes it possible to distinguish between the different types of Lorentz violations by using dissimilar electromagnetic resonators.

In the past, we have combined results of an experiment performed in our laboratory in Berlin, Germany, consisting of linear optical resonators made of fused-silica with mirrors made of BK7

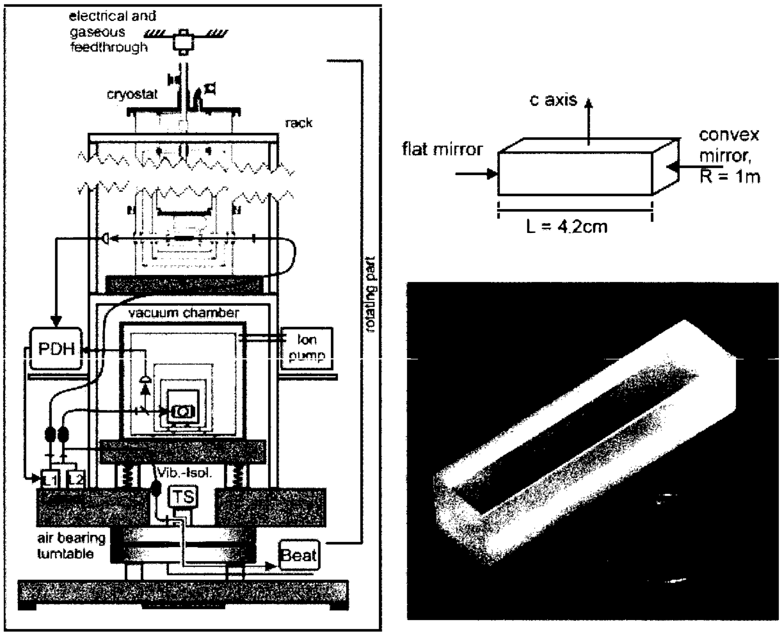

Figure 1: Right: schematic (top) and picture (bottom) of the monolithic sapphire resonator. Left: schematic of the new setup. The monolithic sapphire resonator is located in the cryostat at the upper level. The fused-silica resonators are located in the vacuum chamber at the lower level. PDH = Pound-Drever-Hall locking electronics. TS = tilt sensor.

with the results of an experiment performed by Stanwix *et al.* in Perth, Australia, consisting of whispering gallery microwave resonators made of sapphire in order to give separate bounds on the different types of Lorentz violations.[13] It is worth mentioning that since the experiments have not been optimized for this kind of comparison and have not been synchronized timewise, not all in principle obtainable information of such a combined experiment could be utilized.

2 A slightly different modern Michelson-Morley experiment

We have realized a combined experiment in our laboratory in which we could compare the resonance frequency of a monolithic linear optical sapphire resonator[14] with the resonance frequency of a stationary evacuated linear optical cavity made of ultra-low-expansion glass as well as with two evacuated optical resonators made of fused silica (used in our previous experiment).[9] The monolithic resonator and the fused silica resonators were actively rotated in a Michelson-Morley configuration on an air bearing turntable once every 45 s.

The monolithic sapphire resonator (see Figure 1) features a finesse of about 10 000, corresponding to a linewidth of 200 kHz. The round trip loss inside the resonator is on the order of 600 ppm, although the loss due to absorption should only be on the order of $\sim$ 10 ppm/cm as measured by calorimetry. This leads to the conclusion that most of the losses are caused by flawed coatings. The incoupling efficiency of the monolithic sapphire resonator is less than 0.3% resulting in a transmission of only 1.2×10^{-7}.

We placed the monolithic resonator inside a cryostat and cooled it down to liquid helium temperatures (4.2K) to reduce previously observed strong thermal noise effects within the monolithic crystal. At cryogenic temperatures an improvement of more than one order of magnitude

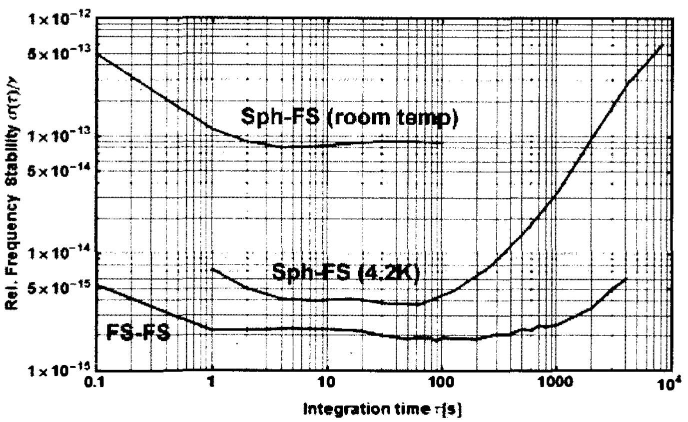

Figure 2: Relative frequency stability derived from the beat between the stabilized lasers (Sph = laser stabilized to the monolithic sapphire resonator, FS = laser stabilized to one of the fused-silica cavities).

in frequency stability for the eigenfrequencies of the monolithic sapphire resonator can be seen in the Allan deviation of the beat note (see Figure 2). The cryostat containing the monolithic sapphire resonator offered optical free beam access through windows. For the Michelson-Morley experiment it was placed on a breadboard containing all necessary optics. The breadboard itself was mounted on the rotating part of the previously existing setup above the vacuum chamber containing the crossed fused-silica resonators (see Figure 1) and thus represented a second new level within this setup. The sapphire resonator axis was orientated parallel to one of the fused silica's resonator axis and thus orthogonal to the resonator axis of the other fused-silica cavity. Except for these modifications there were no further changes of the previously existing setup and all measures implemented to reduce systematics connected with active rotation [9] also applied for the monolithic sapphire resonator.

Ten days of comparison of the resonance frequency of the actively rotated monolithic sapphire resonator with the stationary ULE cavity were performed in August 2010 (see Figure 3). This corresponds to more than 19 000 turntable rotations. The advantage of comparing the rotating monolithic resonator with the stationary ULE cavity is that the prime modulation signal at twice the turntable rotation period can only originate from the monolithic resonator. Thus, less assumptions are needed in the analysis to extract any possible Lorentz invariance violating effects that are connected to light propagation in matter. As an additional check, we also recorded the beat-note between one of the fused silica cavities with the monolithic sapphire resonator as well as with the stationary ULE cavity.

The analysis of the beat note with respect to anisotropy signals characterizing Lorentz invariance violations follows the same procedure as in our previous experiment.[9] No significant anisotropy signal was found fixed to a sidereal frame (see Figure 4). Using the obtained sidereal modulation amplitudes we can conclude an upper limit for the anisotropy of the relative difference of the speed of light in vacuum and matter (sapphire) of $\Delta c/c = (0.8 \pm 0.7) \times 10^{-16}$ (one standard deviation). A detailed analysis within the framework of the Lorentz invariance and CPT violating extension of the standard model of particle physics (SME)[15] has not been done, since the dependence of the index of refraction of sapphire in the optical region on Lorentz violating coefficients of the photonic and fermionic sector has not been completely worked out yet. However, Müller [12] has already outlined a recipe for deriving this dependency.

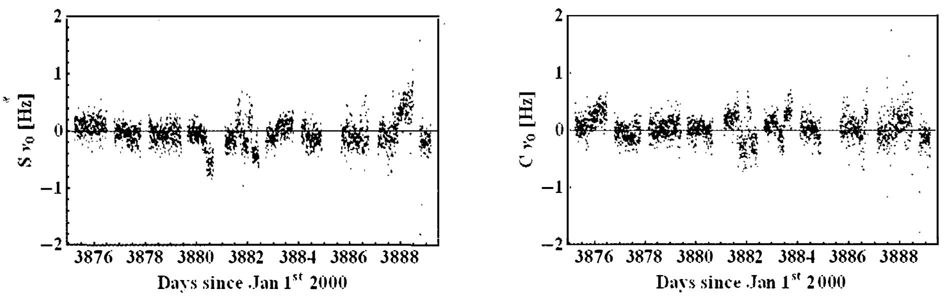

Figure 3: Quadrature amplitudes C and S at twice the rotation frequency of recorded beat note. Nomenclature as in our previous experiment.[9]

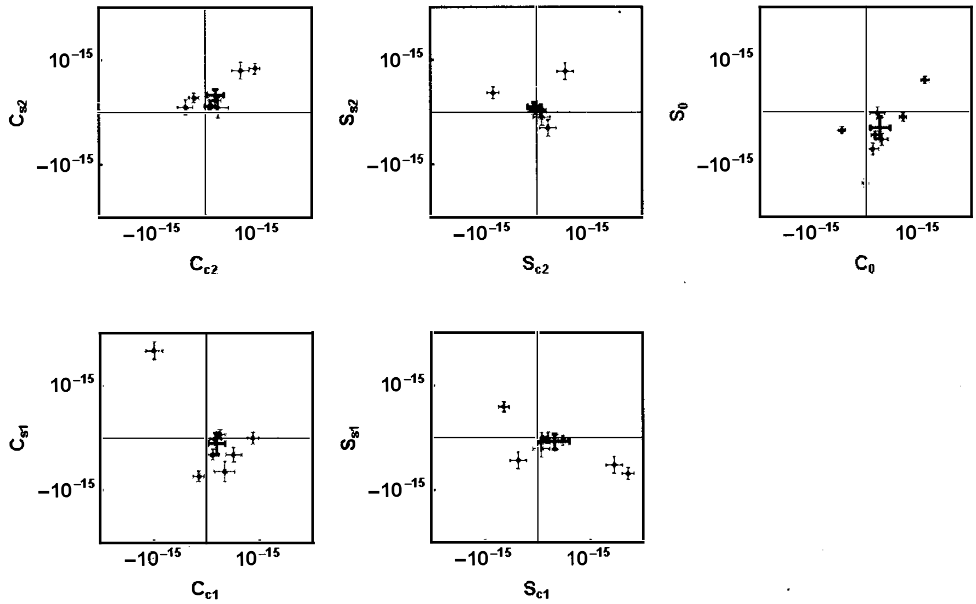

Figure 4: Modulation amplitudes (gray) and their mean values (black) as expected for an anisotropy of the speed of light fixed within a sidereal frame. Nomenclature as in our previous experiment.[9] Amplitudes C_0 and S_0 are most prone to constant systematic effects. The mean values and standard errors (one sigma) are $S_0 = -3. \pm 2.1$, $C_0 = 2.6 \pm 1.8$, $C_{s1} = -1.1 \pm 2.1$, $S_{s1} = -0.8 \pm 1.5$, $C_{c1} = 1.8 \pm 1.6$, $S_{c1} = 3.3 \pm 2.8$, $C_{s2} = 3.4 \pm 1.1$, $S_{s2} = 1.1 \pm 0.9$, $C_{c2} = 1.8 \pm 1.5$, $S_{c2} = -0.4 \pm 1.3$ (all values $\times 10^{-16}$).

3 Next generation experiment

We plan to use ultra-stable cryogenic optical cavities made of sapphire to set up a next generation of a modern Michelson-Morley experiment with light propagation in vacuum. The new cavities should feature a relative frequency stability of better than 1×10^{-16} up to long integration times.[16] The cavities will be arranged in a Michelson-Morley configuration and continuously rotated with a rotation period between 10s and 100s for more than one year using a custom-made high-precision low noise turntable system made of granite. The sensitivity of this setup to violations of Lorentz invariance should be in the 10^{-19} to 10^{-20} regime. This corresponds to more than a 100-fold improvement in precision of modern Michelson-Morley type experiments.[9]

Furthermore, ultra-stable cryogenic microwave whispering gallery resonators will be added to the experiment in collaboration with the University of Western Australia.[17] With this co-rotating microwave and optical resonator setup we will be able to search for additional types of Lorentz violating signals.

Additionally, we are involved in the planning of a space borne mission called STAR[a] to test different aspects of the theory of relativity using optical resonators and an atomic reference.[18]

References

1. A.A. Michelson and E.W. Morley, Am. J. Sci. **34**, 333 (1887).
2. A. Brillet and J. Hall, Phys. Rev. Lett. **42**, 549 (1979).
3. H. Müller *et al.*, Phys. Rev. Lett. **91**, 020401 (2003).
4. P. Wolf *et al.*, Phys. Rev. D **70**, 051902 (2004).
5. S. Herrmann *et al.*, Phys. Rev. Lett. **95**, 150401 (2005).
6. P. Antonini *et al.*, Phys. Rev. A **71**, 050101 (2005).
7. P. Stanwix *et al.*, Phys. Rev. D **74**, 081101 (2006).
8. Ch. Eisele *et al.*, Phys. Rev. Lett. **103**, 090401 (2009).
9. S. Herrmann *et al.*, Phys. Rev. D **80**, 105011 (2009).
10. H. Müller *et al.*, Phys. Rev. D **68**, 116006 (2003).
11. H. Müller *et al.*, Phys. Rev. D **67**, 056006 (2003).
12. H. Müller, Phys. Rev. D **71**, 045004 (2005).
13. H. Müller *et al.*, Phys. Rev. Lett. **99**, 050401 (2007).
14. M. Nagel *et al.*, *Proceedings of the Fifth Meeting on CPT and Lorentz Symmetry*, ed. V.A. Kostelecký, (World Scientific, Singapore, 2010), pp. 94-102.
15. D. Colladay and V.A. Kostelecký, Phys. Rev. D **58**, 116002 (1998).
16. M. Nagel *et al.*, "Towards an ultra-stable optical sapphire cavity system for testing Lorentz invariance", this Proceedings.
17. S. Parker *et al.*, "Testing Lorentz invariance and fundamental constants using precision microwave techniques", this Proceedings.
18. T. Schuldt *et al.*, "The STAR Mission: Space-Based Tests of Special and General Relativity", this Proceedings.

[a]STAR (Space-Time Asymmetry Research) is a collaboration between NASA Ames, JILA, Standford, Saudi-Arabian KACST, DLR, ZARM at University of Bremen, HTWG Konstanz, and Humboldt-University Berlin.

11.
Clocks

THE ACES MISSION: FUNDAMENTAL PHYSICS TESTS WITH COLD ATOM CLOCKS IN SPACE

LUIGI CACCIAPUOTI
European Space Agency, Research and Scientific Support Department,
Keplerlaan 1, P.O.Box 299, 2200 AG Noordwijk ZH The Netherlands
Luigi.Cacciapuoti@esa.int

CHRISTOPHE SALOMON
Laboratoire Kastler Brossel, CNRS, UPMC, ENS
24, rue Lhomond, 75005 Paris, France

High-performance clocks and links in space are key instruments to probe space-time properties. As such, they can be used to test Einstein's theory of general relativity to high accuracy. Operated on-board the International Space Station, ACES will distribute a clock signal with fractional frequency instability and inaccuracy of $1 \cdot 10^{-16}$. Space-to-ground and ground-to-ground comparisons of atomic frequency standards will be used to test Einstein's theory of general relativity including a precision measurement of the gravitational red-shift, a search for time variations of fundamental constants, and tests of the Standard Model Extension. This paper presents the ACES mission concept and discussed its development status.

1 Introduction

Atomic Clock Ensemble in Space (ACES) is a fundamental physics mission of the European Space Agency based on a new generation of clocks to be operated in the microgravity environment of the International Space Station (ISS). ACES is a distributed system designed to disseminate a high stability and accuracy clock signal [1,2]. It consists of a payload generating an atomic frequency reference in space and a network of ground terminals connected to high-performance clocks on ground. Transported on the ISS by the Japanese transfer vehicle HTV, the ACES payload will be installed at the external payload facility of the Columbus module (see Fig. 1). The ACES payload accommodates two atomic clocks: PHARAO (acronym of "Projet d'Horloge Atomique par Refroidissement d'Atomes en Orbit"), a primary frequency standard based on samples of laser cooled cesium atoms and SHM (acronym of "Space H-Maser"), an active hydrogen maser for space applications. The performances of the two clocks are combined to generate an on-board timescale with the short-term stability of SHM and the long-term stability and accuracy of the PHARAO clock. The on-board comparison of PHARAO and SHM and the distribution of the ACES clock signal are ensured by the Frequency Comparison and Distribution Package (FCDP), while all data handling processes are controlled by the eXternal PayLoad Computer (XPLC). The ACES clocks are compared to clocks on the ground using both a microwave link (MWL) and an optical link (ELT). A GNSS receiver connected to the on-board time scale provides orbit determination of the ACES clocks.
ACES will be ready for launch in 2014, for a planned mission duration of 18 months. During the

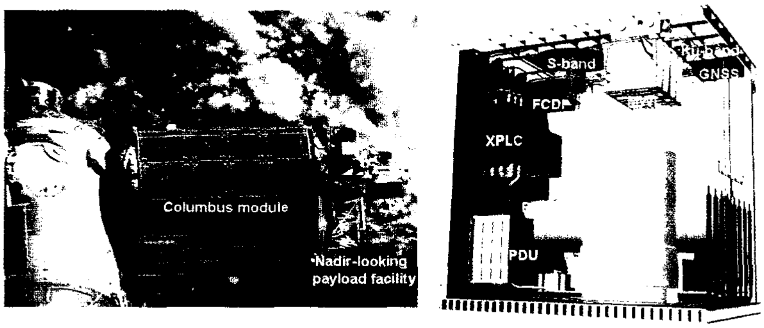

Figure 1: Left: The external payload facility of the Columbus module. Right: Detail of the ACES payload; the ACES payload has a volume of $1.340 \times 1.117 \times 1.320$ m^3, a mass of 240 kg, for a total power consumption of 450 W.

first two weeks, the functionality of the ACES clocks and links will be tested. Then, a period of 6 months will be devoted to the characterization and performance evaluation of the clocks. During this phase, a clock signal with frequency inaccuracy in the 10^{-15} range will be available to ground users. Under microgravity conditions, it will be possible to tune the linewidth of the atomic resonance of PHARAO by two orders of magnitude, down to sub-Hz values (from 11 Hz to 110 mHz). After the clocks are optimized, performances in the 10^{-16} range both for frequency instability and inaccuracy are expected. In the second part of the mission (12 months, possibly extended to 30 months), the on-board clocks will be compared to a number of atomic clocks on ground operating both in the microwave and optical domain. ACES will perform worldwide comparisons of advanced clocks operating on different atoms or molecules reaching a frequency resolution in the 10^{-17} regime. These measurements will test general relativity and seek for new interactions beyond the Standard Model.

2 ACES Science Objectives

ACES will conduct experiments with cold atoms in a freely falling laboratory, it will perform fundamental physics tests to high resolution, and develop applications in different areas of research.

2.1 High-performance Microwave Clocks for Space

A new generation of space clocks reaching frequency instability and inaccuracy of few parts in 10^{16} will be validated by ACES. PHARAO will combine laser cooling techniques and microgravity conditions to significantly increase the interaction time and consequently reduce the linewidth of the clock transition. Improved stability and better control of systematic effects will be demonstrated in the space environment. PHARAO will reach a fractional frequency instability of $1 \cdot 10^{-13}/\sqrt{\tau}$, where τ is the integration time expressed in seconds, and an inaccuracy of a few parts in 10^{16}.

The reliability offered by active H-masers will be made available for space applications by SHM. SHM will demonstrate a fractional frequency instability of $1.5 \cdot 10^{-15}$ after 10000 seconds of integration time. Two servo-loops will lock together the clock signals of PHARAO and SHM generating an on-board time scale combining the short-term stability of the H-maser with the long-term stability and accuracy of the cesium clock (Fig. 2).

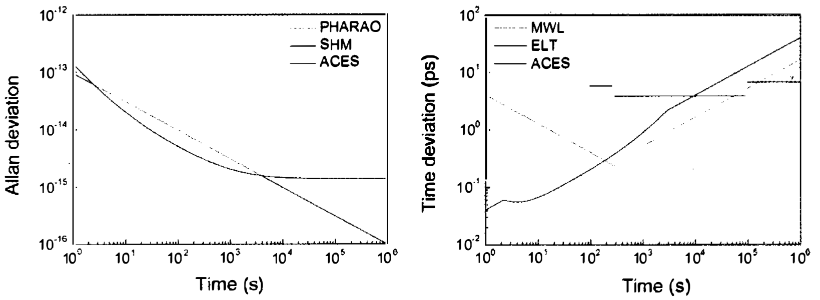

Figure 2: Left: Specified Allan deviation of PHARAO, SHM, and of the ACES clock signal. Right: Specified time deviation of MWL and ELT, compared with the time stability of the ACES clock signal.

2.2 ACES Time and Frequency Transfer Systems

ACES is developing high-performance links for the comparison of distant clocks.
The ACES MWL will allow space-to-ground comparisons with time deviation better than 0.4 ps at 300 s, 8 ps at 1 day, and 25 ps at 10 days of integration time (see Fig. 2). This performance, surpassing existing techniques (TWSTFT and GPS) by one to two orders of magnitude, will enable common view and non-common view comparisons of ground clocks with 10^{-17} frequency resolution after a few days of integration time. MWL will also deliver a global atomic time scale with 10^{-16} accuracy, it will allow clock synchronization at the 100 ps uncertainty level, and it will contribute to international atomic time scales (TAI, UTC...).
ELT, acronym of "European Laser Timing", will provide ACES with an alternative time and frequency transfer system reaching a time stability of 6 ps after 100 s of integration time, down to 4 ps between 300 s and 10000 s, and with a long-term stability of 7 ps (see Fig. 2). The system can be calibrated to deliver the ACES time reference with an accuracy better than 50 ps, finding important applications in the dissemination of time scale and in the synchronization of geodetic observatories.
The ACES clocks and links will allow to establish a global network for the comparison and the synchronization of distant clocks.

2.3 Fundamental Physics Tests with ACES

According to Einstein's theory of general relativity, identical clocks placed in different gravitational fields experience a frequency shift that depends on the difference between the Newtonian potentials at the clocks positions. The comparison between the ACES on-board clocks and ground-based atomic clocks will measure the frequency variation due to the gravitational redshift with a 35-fold improvement on the GP-A experiment [3], testing Einstein's prediction at the 2 ppm uncertainty level.
Time variations of fundamental constants can be measured by comparing clocks based on different transitions or different atomic species [4]. Indeed, the energy of an atomic transition can be expressed in terms of the fine structure constant α and the two dimensionless constants m_q/Λ_{QCD} and m_e/Λ_{QCD}, which depend on the quark mass m_q, the electron mass m_e, and the QCD mass scale Λ_{QCD} [5,6]. ACES will perform crossed comparisons of ground clocks both in the microwave and in the optical domain with a frequency resolution of $1 \cdot 10^{-17}$ in a few days of integration time. These comparisons will impose strong and unambiguous constraints on time variations of the three fundamental constants reaching an uncertainty as low as $1 \cdot 10^{-17}$/year in case of a 1-year mission duration, down to $3 \cdot 10^{-18}$/year after three years.

The foundations of special relativity lie on the hypothesis of Local Lorentz Invariance (LLI). According to this principle, the outcome of any local test experiment is independent of the velocity of the freely falling apparatus. In 1997, LLI tests based on the measurement of the round-trip speed of light have been performed by comparing clocks on-board GPS satellites to ground hydrogen masers[7]. In such experiments, LLI violations would appear as variations of the speed of light c with the direction and the relative velocity of the clocks. ACES will perform a similar experiment by measuring relative variations of the speed of light at the 10^{-10} uncertainty level.

2.4 Applications

ACES will also demonstrate a new geodesy technique to map the Earth gravitational potential. This technique uses a precision measurement of the Einstein's gravitational red-shift between two clocks to determine the corresponding difference in the local gravitational potentials. The possibility of performing comparisons of ground clocks at the 10^{-17} frequency uncertainty level will allow ACES to resolve geopotential differences down to 10 cm on the geoid height.
A dedicated GNSS receiver on-board the ACES payload will ensure orbit determination, important for comparing clocks and for performing fundamental physics tests. In addition, the receiver will be connected to the ACES clock signal, opening the possibility to use the GNSS network for clock comparisons and remote sensing applications (radio-occultation and reflectometry experiments).
The simultaneous operation of the optical (ELT) and microwave (MWL) links will provide a test bench for their mutual characterization. Optical versus dual-frequency microwave measurements will also provide useful data for the study of atmospheric propagation delays and for the construction of atmosphere mapping functions at the three different wavelengths. In addition, the ACES links will provide absolute range measurements, both in the microwave and in the optical domain.

3 ACES Status

All ACES instruments and subsystems have now reached a high technology maturity, demonstrated by the engineering models, now delivered or in final assembly, and by the ongoing activities on the flight hardware. The system tests on the ACES Engineering Model (EM) workbench (see Sec. 3.3) have represented a major milestone in the ACES development cycle. Their successful completion has indeed closed the EM phase with the performance verification of the ACES clock signal and it has confirmed the adequacy of the ACES design, releasing the manufacturing for the flight hardware. ACES Flight Model (FM) activities are expected to be completed in 2013.

3.1 The PHARAO Clock

PHARAO is a cesium clock based on laser cooled atoms developed by LNE-SYRTE, LKB, and CNES. Its concept is very similar to ground based atomic fountains, but with a major difference: PHARAO will be operated under microgravity conditions. Atoms, launched in free flight along the PHARAO tube, cross a resonant cavity where they interact twice with a microwave field tuned on the transition between the two hyperfine levels of the cesium ground state (9.192631770 GHz, from the SI definition of the second). In a microgravity environment, the velocity of the atoms along the ballistic trajectories is constant and can be continuously changed over almost two orders of magnitude (5 to 500 cm/s), allowing the detection of atomic signals with sub-Hz linewidth.
The engineering model of the PHARAO clock has been completed and tested. Cesium atoms

have been loaded in the optical molasses, cooled down to a few μK, interrogated on the clock transition by the resonant microwave field, and detected by laser-induced fluorescence emission. Microwave resonance signals (Ramsey fringes) with a signal-to-noise ratio of $\sim$ 700 have been recorded. For a typical launch velocity of about 3.56 m/s, the duration of the free flight between the two Ramsey interaction regions is about 100 ms, corresponding to a width of the central fringe of about 5 Hz. Once operated in microgravity, the longer interaction times will allow PHARAO to measure linewidths 10 to 50 times narrower.
The tuning and optimization of the instrument on ground has been performed with the atomic clouds launched vertically against gravity at a speed of 3.56 m/s. In these conditions, an Allan deviation of $3.5 \cdot 10^{-13}/\sqrt{\tau}$ has been measured, where τ is the integration time expressed in seconds. PHARAO performance on ground is mainly set by the phase noise of the local oscillator, which is sampled by the atoms in the microwave cavity (Dick effect). In space, this effect will be reduced by one order of magnitude because of the longer interrogation time and the narrower resonance width.
PHARAO accuracy evaluation has been completed. The contribution of the second order Zeeman effect to the clock accuracy budget is at the level of $6.6 \cdot 10^{-16}$ for a bias field along the PHARAO tube of 35 nT. The cold collisions shift has been evaluated to an accuracy of $9.5 \cdot 10^{-16}$. Second order Zeeman effect and collisional shift are indeed the two major contributors to the clock accuracy, presently evaluated to $1.3 \cdot 10^{-15}$. PHARAO accuracy evaluation has been verified by measuring the clock frequency output with respect to the SYRTE mobile fountain clock FOM. The result is in agreement with a zero frequency difference within 1 part in 10^{15}.
Figure 3 shows the flight model of the PHARAO tube, recently completed and successfully tested against vibrations.

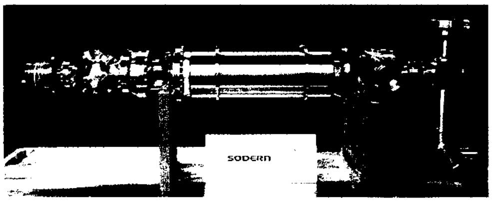

Figure 3: Flight model of the PHARAO tube. Fully assembled (including thermal shields, μ-metal shields, fiber-coupled collimators, and harness), the tube has a volume of 990 × 336 × 444 mm^3 and a mass of 44 kg.

3.2 The SHM Clock

SHM operates on the hyperfine transition of atomic hydrogen at 1.420405751 GHz. H_2 molecules are dissociated in a plasma discharge and the resulting beam of H atoms is state-selected and sent to a storage bulb. The bulb is surrounded by a microwave cavity that, tuned on the atomic resonance, induces the maser action. Developed by SpectraTime under ESA contract, SHM provides ACES with a stable fly-wheel oscillator. The main challenge of SHM is represented by the low mass and volume figures (42 kg, 390 × 390 × 590 mm^3) required by the space clock with respect to ground H-masers. For this purpose, the number of thermal shields of the clock has been reduced and a dedicated Automatic Cavity Tuning (ACT) system has been implemented to steer the resonance frequency of the maser cavity against thermal drifts. SHM ACT injects two tones, symmetrically placed around the H-maser signal. The two tones are coherently detected and the unbalance between their power levels is used to close a feedback loop acting on the cavity varactor and stabilizing the resonance frequency of the microwave cavity against temperature variations. This method allows SHM to reach fractional frequency instabilities down to $1.5 \cdot 10^{-15}$ at 10^4 s of integration time. Figure 4 shows the H-maser physics package in the different assembly phases.

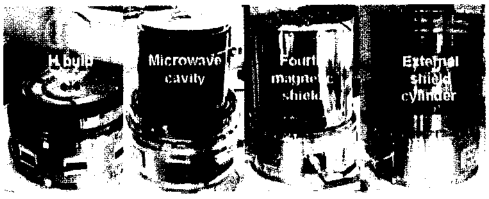

Figure 4: Physics package of the SHM engineering model during the different assembly phases.

The active oscillation signal on the clock transition has a power of -101 dBm. The cavity quality factor is about 44000 and the atomic quality factor is $1 \cdot 10^9$. The H-maser electronics, including the receiver and the ACT system, have been completed and tested showing an Allan deviation in agreement with SHM performance requirements. SHM EM is presently under test. This verification campaign will close the EM phase and release the manufacturing of the SHM flight model.

3.3 Ground Tests of the ACES Clock Signal

At completion of the ACES engineering model phase, the ACES EM workbench has been integrated at CNES premises in Toulouse with the objective of testing interfaces, functions, and performance. The ACES EM workbench includes: PHARAO EM, FCDP EM, SHM ground model (EM0), an XPLC test crate, and a PDU (Power Distribution Unit) simulator. Both PHARAO EM and FCDP EM were mounted in the CNES vacuum chamber and operated under vacuum.

As first test step, the ACES clocks and subsystems have been switched on to test their mutual compatibility. The frequency stability of the clocks (Allan deviation) and the power spectrum of their phase noise have been continuously monitored showing no degradation with respect to stand alone measurements.

Then, both the short-term and the long-term servo-loops have been closed to generate the ACES clock signal, now reproducing SHM EM0 for short-to-medium integration times and PHARAO on the long-term. The stability of the ACES clock signal has been measured against FOM, the mobile fountain clock of LNE-SYRTE. A long duration measurement has been performed both to characterize the Allan deviation of the ACES signal and to measure PHARAO frequency with respect to FOM.

Figure 5 shows the stability of the ACES clock signal measured with respect to FOM. For integration times shorter than the long-term servo-loop time constant (1000 s), the ACES clock signal closely follows SHM EM0 and the Allan deviation measurement is limited by the FOM performance. For longer integration times, the long-term servo loop forces ACES on the PHARAO clock signal providing it with the long-term stability and accuracy of the Cs clock.

3.4 The Microwave Link

The ACES microwave link is developed by ASTRIUM, TIMETECH, TZR, and EREMS under ESA contract. The proposed MWL concept is an upgraded version of the Vessot two-way technique used for the GP-A experiment in 1976[3] and the PRARE geodesy instrument. The system operates continuously with a carrier frequency in the Ku-band. The high carrier frequencies of the up and down links (13.5 GHz and 14.7 GHz respectively) allow for a noticeable reduction of the ionospheric delay. A third frequency in the S-band (2.2 GHz) is used to determine the Total

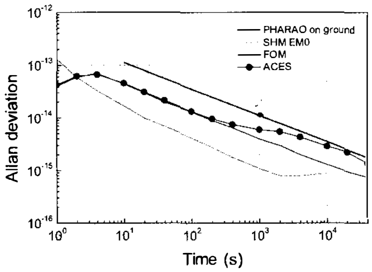

Figure 5: Performance of the ACES clock signal measured on ground with respect to FOM (red) and compared to the performance of FOM (blue), SHM EM0 (green), and PHARAO on ground (black).

Electron Content (TEC) and correct for the ionosphere time delay. A PN-code modulation (100 Mchip/s) on the carrier removes the phase ambiguity between successive comparison sessions separated by large dead times. The system is designed for multiple access capability, allowing up to 4 simultaneous ground users distinguished by the different PN-codes and Doppler shifts.

MWL Flight Segment

The engineering model of the flight segment electronic unit has been completed and tested (see Fig. 6). MWL long-term stability is ensured by the continuous calibration of the receiver channels provided by a built-in test-loop translator. For shorter durations (<300 s), time stability is driven by the noise performance of the Ku transmitter and receiver and of the DLL (Delay-Locked Loop) boards. The 100 MHz chip rate allows to reach a time stability better than 0.2 ps already with code measurements. However, the ultimate performance is achieved with the carrier phase measurements, whose time stability is as low as 70 fs at about 100 s of integration time (see Fig. 6). For longer durations, the time stability remains well below the 1 ps level even in the worst conditions of signal-to-noise density ratio, corresponding to very low elevation angles of the ISS over a ground terminal. The thermal sensitivity of the system has been evaluated and used to calibrate MWL phase comparison measurements against temperature variations. The sensitivity to a series of key parameters such as clock input power, received signal-to-noise density ratios, supply voltage, Doppler, Doppler rate, etc. has been measured. The susceptibility of the system to narrowband and broadband interference, as well as to multipath effects has been characterized.

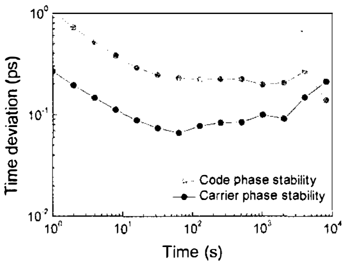

Figure 6: Left: Time stability of the code (green) and carrier (red) phase measurement performed by the MWL flight segment electronics. Right: MWL ground terminal in its assembly phase.

MWL Ground Terminal

The MWL ground terminal electronics is similar to the MWL flight hardware, symmetry being important in a two-way system to reduce instrumental errors. The ACES MWL Ground Terminal (GT) is a microwave station interfacing the local clock on ground to the ACES payload (see Fig. 6). To reduce phase instabilities due to the tracking motion, the electronic unit of the MWL GT has been rigidly attached to the antenna unit. The Ku-band signal is delivered to the antenna feeder via a waveguide; a high stability RF cable is used for the S-band. The antenna is a 60 cm offset reflector with a dual-band feed system automatically pointed in azimuth and elevation by a steering mechanism. A computer controls the steering unit based on ISS orbit prediction files, collects telemetry and science data both from the local clock and the MWL GT electronics, and interfaces directly with the ACES Users Support and Operation Center (USOC). The system is housed below a protective radome cover, which also allows to stabilize the temperature of the enclosed volume by an air conditioning system, part of a separate service pallet. The total weight of the MWL GT is 650 kg: 270 kg for the radome pallet and 380 kg for the service pallet. About 10 kW are needed to power the MWL GT electronics, the steering unit, and the air conditioning system. The thermal design allows to operate the MWL GT for an external temperature between −30°C and +45°C.

The ACES microwave link will be validated in an end-to-end test campaign. MWL FS and GT electronic units will be connected by cables through a signal simulator. The signal simulator will mimic frequency and amplitude variations of the Ku and S-band signals according to the orbit dynamics. The link delays will also be measured, preparing for the link calibration campaign which will take place on the flight hardware and on the ground terminals after on-site installation.

3.5 The ELT Optical Link

ELT is an optical link exchanging laser pulses between Satellite Laser Ranging (SLR) stations on ground and the ACES payload for the space-to-ground comparison of clocks. The on-board hardware consists of a Corner Cube Reflector (CCR), a Single-Photon Avalanche Diode (SPAD), and an event timer board connected to the ACES time scale. Laser pulses fired towards ACES by a SLR station are detected by the SPAD diode. The fire and the detection events are tagged in the local clock time scales both in space and on ground. At the same time, the ELT CCR re-directs the laser pulses towards the ground station where they are detected and stamped in the time scale maintained at the SLR station. The measurement of the start and return times on ground and of the detection times in space provide the desynchronization between space and ground clocks, together with precise ranging information.

The SPAD diode has been tested at the SLR stations of Wettzell and Graz . A time deviation of 5 ps after 500 s of integration time has been measured with the SPAD diode integrated in the Wettzell detection channel. This measurement was limited by the timing resolution of the Wettzell time tagging system. Time deviations down to about 1 ps after already 10 s of integration time have been measured at the Graz station [8,9] thanks to the higher firing rate and the better timing resolution available there.

The SPAD diode is presently being characterized in terms of optical-to-electrical detection delay. Recent measurements have shown that the absolute delay in the detector can be calibrated at the 10 ps level [10].

Acknowledgments

The authors express their warm thanks for their valuable contribution to the ACES science team, to the ACES project team at ESA, ASTRIUM, and TimeTech, to the PHARAO team at LNE-SYRTE and CNES, to the SHM team at SpectraTime. This paper has been written on behalf of the many scientists and engineers contributing to the mission development.

References

1. C. Salomon *et al*, *C. R. Acad. Sci. Paris* **t.2 Séries IV**, 1313 (2002).
2. L. Cacciapuoti and C. Salomon, *Eur. Phys. J. Special Topics* **172**, 57 (2009).
3. R.F.C. Vessot *et al*, *Phys. Rev. Lett.* **45**, 2081 (1980).
4. T. Fortier *et al*, *Phys. Rev. Lett.* **98**, 070801 (2007).
5. V.V. Flambaum *et al*, *Phys. Rev.* D **69**, 115006 (2004).
6. V.V. Flambaum *et al*, *Phys. Rev. C* **73**, 055501 (2006).
7. P. Wolf and G. Petit, *Phys. Rev. A* **56**, 4405 (1997).
8. U. Schreiber *et al*, *IEEE Trans* **57**, 728 (2009).
9. I. Prochazka *et al*, in *Proc of 2010 European Time and Frequency Forum* (2010).
10. I. Prochazka *et al*, *Metrologia* **48**, L13 (2011).

12.
Pulsars

GRAVITATIONAL WAVE DETECTION THROUGH PULSAR TIMING ARRAYS

DAVID J. CHAMPION
Max-Planck-Institut für Radioastronomie, Auf dem Hügel 69, 53121 Bonn, Germany

Pulsar timing arrays are the only means to detect very low frequency nanohertz gravitational waves (GWs). GWs in this part of the spectrum are expected to be generated by binary super-massive black-hole (SMBH) systems which are a consequence of the merger of galaxies. Individual nearby strong emitters can be detected, allowing the GW and parameters of the SMBH system to be determined. A stochastic background of GWs from weaker, more distant but more numerous sources, is also expected. This will provide a measure of the galactic merger rate which is important for our understanding of galaxy evolution. GW detection via pulsar timing provides science complementary to the space- and ground- based detectors, observing similar sources at different mass ranges and stages of evolution.

1 Introduction to Pulsar Timing

Pulsars are extraordinary tools for astronomy, condensed matter physics, electromagnetism and, in particular, testing general relativity. They are rapidly rotating neutron star remnants of massive stars. Their strong magnetic fields focus streams of electromagnetic radiation from the poles which sweep like the beam of a lighthouse as the neutron star rotates. If these beams intersect the line-of-sight of an observer, a pulse of emission is detected.

1.1 Pulsars

Pulsars are born in the explosive death of a high-mass star, a supernova. As the outer layers of the star are blown off, the core collapses and extreme pressure forms a neutron star with a mass of $\sim$1.4 $M_\odot$ within a diameter of only $\sim$20 km. During the collapse the angular momentum is conserved causing the star to spin up to rotation periods of tens of milliseconds. The magnetic flux is also conserved, meaning that the neutron star inherits a surface magnetic field of typically 10^{12} G.

As the pulsar ages it slows down due to energy lost in magnetic dipole radiation. Eventually the neutron star rotates so slowly that emission from the poles becomes unstable and ceases. However if the pulsar is in a binary system (not disrupted by the supernova that created the neutron star) then the pulsar may undergo 'recycling'. As the companion star evolves it swells, eventually overfilling its Roche lobe. At this point the outer layers of the star feel a stronger gravitational pull from the neutron star than from the companion and material streams onto the neutron star. The conservation of angular momentum spins the pulsar up to periods of only a few milliseconds. The accretion of matter also suppresses the magnetic field, reducing the spin-down of the pulsar. These millisecond pulsars (MSPs) are the most stable branch of the pulsar family.

1.2 *Pulsar Timing*

The technique of pulsar timing is the origin of the incredible accuracy of pulsar measurements. Each observation of a pulsar creates a time series which is then folded at the period of the pulsar resulting in a single, high signal-to-noise ratio (S/N) pulse. For the majority of the pulsars this averaged pulse profile is extremely stable. The precise time of arrival (ToA) of the pulse is determined by convolving the averaged pulse profile with a template (often created by fitting Gaussian components to a sum of the average profiles) and adding the offset to the start time of the observation.

The ToAs from the observations are used to fit a model of the pulsar. The timing model contains the pulsar period, period derivative, sky position and any binary parameters of the pulsar system. The timing model is used to determine the number of integer rotations of the pulsar between ToAs, the difference between the predicted and actual ToA is the residual. The residuals are the minimised by performing a least-squares fit over the model. The pulsar timing model allows the data to be analysed coherently, accounting for every rotation of the pulsar over the extent of the model, often tens of years.

The precision to which the parameters of the model can be determined depends on the length of the data set, the number and distribution of ToAs, the type of parameter, but most importantly on the uncertainties on the ToAs themselves. The precision of a ToA relates directly to the shape (pulse of width W) and S/N of the profile[1]:

$$\sigma_{ToA} \simeq \frac{W}{S/N} \propto \frac{T_{sys}}{A_{eff}} \times \frac{1}{\sqrt{t_{obs}\Delta\nu}} \times \frac{P\delta^{3/2}}{S_{PSR}} \tag{1}$$

Strong sharp peaks provide the most precise ToAs. We cannot control the shape of the profile (pulsar period P and duty cycle δ) or the luminosity (S_{PSR}) of the pulsar but the signal-to-noise ratio can be improved by increasing the aperture (A_{eff}) and decreasing the system temperature (T_{sys}) of the telescope. We can also increase the bandwidth ($\Delta\nu$) and length (t_{obs}) of the observation. The optimisation of the observations for a PTA to make best use of available telescope time is an ongoing effort[2].

While pulsars are excellent clocks they are not totally free of noise and the reduced χ^2 of the model fit is significantly larger than unity in most pulsar data sets which indicates that the model does not fully describe the data. The unmodelled residual is frequently referred to as timing noise. Timing noise can be caused by intrinsic variations of the rotation period, subtle changes of the integrated pulse profile, clock or instrumental artifacts, variations of the propagation of the pulse through the interstellar medium or gravitational waves.

For PTAs these noise sources have to be minimised. The noise intrinsic to the pulsar is reduced by timing the MSPs which are observed to be the most stable rotators. Interstellar medium effects are reduced through multi-frequency observations. Finally the instrumental effects are determined and removed through the concurrent timing of multiple pulsars.

2 Pulsars as Gravitational Wave Detectors

Gravitational waves (GWs) are a prediction of general relativity in which the acceleration of masses releases energy in the form of gravitational radiation propagating as ripples in spacetime. While they have never been directly detected the binary pulsar system B1913+16 exhibits orbital decay that agrees precisely with the prediction and is seen as the first strong evidence for the existence of GWs[3 4].

In a very simplified view a GW will cause a subtle change in the distance between the observatory and the pulsar. Pulsar timing cannot be used to directly measure the distance to the majority of pulsars, and even those with measured parallaxes cannot be determined to sufficient accuracy to allow a detection of such a minute change. However the period of the pulsar is known to great accuracy, better than one part in 10^{14} for the most precise timers, and the Doppler shift caused by the rate of change of distance to the pulsar is a measurable quantity[5]:

$$\frac{\delta v}{v} = H^{ij}(h^e_{ij} - h^p_{ij}), \tag{2}$$

where h^e_{ij} and h^p_{ij} are the GW strains at the Earth and pulsar respectively. H^{ij} is a geometrical term dependent on the angular separation of the Earth, pulsar and GW source.

A simple application of this period shift suggests that pulsar timing should already be very sensitive to GWs. However the effect of the pulsar fit itself must be taken into account. None of the pulsar parameters are known a-priori and must be fit for in the timing model. Of particular importance is the period of the pulsar and its period derivative. Due to the low frequencies of the GWs these parameters can fit out the majority of the Doppler shift. Only over timescales of the wave length of the GW does the residual caused by the GW separate from the period and period derivative.

The sensitivity of pulsars to different frequencies of GWs is limited by the time span and cadence of the observations. The lower frequency limit is approximately twice the time span of the observations as this is the time required for the GW residual to become differentiated from the period and period derivative of the pulsar. The upper limit is the cadence of the observations, usually two to four weeks, and is limited by the available telescope time combined with the spectrum of the expected sources.

2.1 Single Source Detection

The GWs generated by a binary system have twice the frequency of the orbital period. If the binary system is near and strong enough this can be measured directly. The expected size of the residuals induced by a binary system can be calculated using[6]:

$$t = 10 \text{ ns} \left(\frac{1 \text{ Gpc}}{d_L}\right) \left(\frac{M}{10^9 \text{ M}_\odot}\right)^{5/3} \left(\frac{10^{-7} \text{ Hz}}{f}\right)^{1/3}, \tag{3}$$

where d_L is the luminosity distance to the binary, the system has a total mass of $M/(1-z)$ and the GWs have a frequency of f. Lee et al. [7] have calculated the precision to which GW and the orbital parameters of the SMBH system can be determined given the amplitude of the measured signal. They also showed that a GW detection from a single source could be used to determine the distances from the Earth to the pulsars in the array to a sub-light year level.

In 2003 Sudou et al. [8] published evidence for a SMBH binary system in the galaxy 3C 66B. Jenet et al. (2004) [9] demonstrated that the proposed orbital parameters could be ruled out by showing that such a binary would be detectable in the current pulsar timing data, see Fig. 1 from Yardley et al. (2010) [10]. Beyond 3C 66B the nearest candidate for a single source is in OJ287 however sensitivity to this system is unlikely to be reached with current telescopes.

2.2 Detection of the Stochastic Background

The stochastic background of GWs is generated by binary SMBH systems which are in the early phase of coalescence. As galaxies merge the SMBHs at their centre enter orbit around each other, eventually coalescing. It is not the final merger but the long period of inspiral that is expected to be the strongest source of background GWs. However cosmic strings, and relic GWs from the big bang are other potential sources.

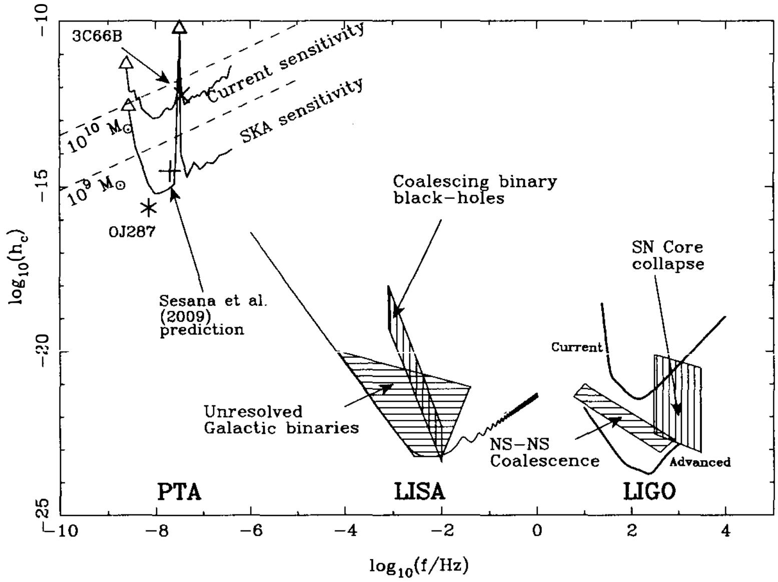

Figure 1: The sky-averaged sensitivity of pulsar timing arrays using current telescopes and the SKA to single sources as a function of the source GW frequency. Figure from Yardley et al. 2009.

To detect the stochastic background a different technique is used. The residuals of each pair of pulsars are correlated and plotted against the angular separation of the pair. Due to the quadrupolar nature of the GWs, pulsars close to each other on the sky would be expected to be highly correlated while those separated by 90° would be anti-correlated. As the separation increases to 180° the degree of correlation also increases. The resulting curve is usually referred to as the Hellings and Downs curve. An example of a such a correlation is shown in Fig. 2 from Hobbs et al 2009[11].

3 Comparison with other Detection Efforts

The frequency range in which PTAs are sensitive and the expected sources are complementary to the up-coming ground- and space- based detectors. The SMBHs seen in PTA data will be at an earlier evolutionary phase to those observed with the space-based Laser Interferometer Space Antenna (LISA): as the SMBHs in the binary coalesce, the frequency of the orbit increases moving into the LISA band. Observations of a coalescence in the LISA band could trigger a deep search of the archival PTA data (now that the position of the system is known) for the pre-ring-down system[12]. Indeed any simultaneous observations would provide a full description of the system including the elusive distance measurement[13]. Finally all three types of detectors are looking at black hole systems from stellar masses through to super-massive.

4 Current Pulsar Timing Array Projects

There are three large PTAs currently in operation. The Parkes Pulsar Timing Array[14] is the longest running with more than 5 years of development and is based on data from the Parkes 64-m telescope in Australia. The European Pulsar Timing Array[15] uses the 100-m Effelsberg, 100-m (equivalent) Nançay, 76-m Lovell, and (when completed) the 64-m Sardinia telescopes in addition

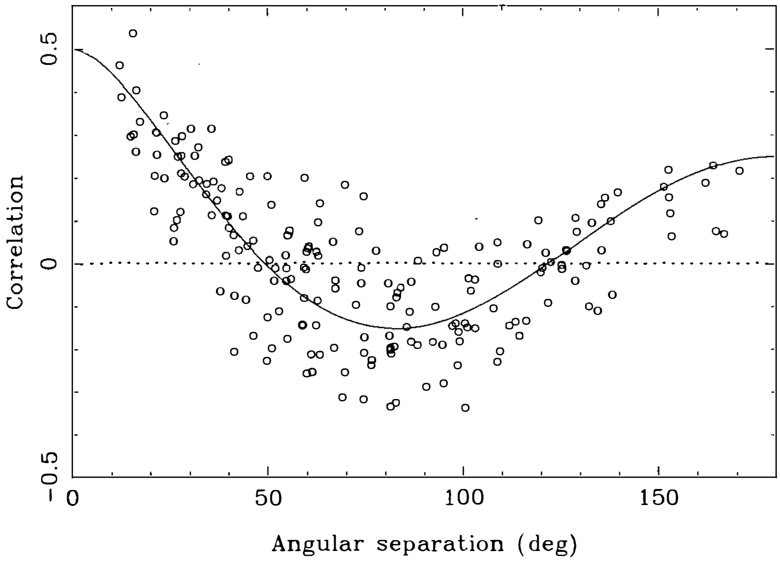

Figure 2: An example Hellings and Downs plot. The degree of correlation of pairs of pulsar residuals against the angular separation of the pulsar pair. The solid line is the fitted Hellings and Downs curve. Figure from Hobbs et al. 2009.

to the Westerbork Sythesis Radio Telescope array. The North American Nanohertz Observatory for Gravitational Waves[6] uses the 100-m Green Bank and 305-m Arecibo telescopes, the largest single dish telescopes in the world. The three arrays work together as the International Pulsar Timing Array to facilitate the sharing of data, techniques and personnel[16].

4.1 Large European Array for Pulsars

To make best use of the five large telescopes in use by the European Pulsar Timing Array a project is underway to coherently combine baseband data to form the Large European Array for Pulsar (LEAP)[15,17], a telescope with an equivalent collecting to a dish 200 m in diameter (approximately the same as the illuminated area of Arecibo). LEAP will be able to reach a wide range of declinations and should provide up to an order of magnitude improvement in timing for pulsars outside the Arecibo range.

4.2 Pulsar Surveys

The global PTA effort would be greatly aided by the discovery of more precisely timed pulsars. This is important for providing more pulsar pairs for correlation and for the overall sensitivity of the arrays. There are several large scale ongoing surveys which are partially motivated by PTA science. The High Time Resolution Universe survey is a full sky survey covering both hemispheres. The southern sky is covered by the Parkes telescope using a 13 beam receiver while the northern sky is covered by the Effelsberg telescope using a 7 beam receiver. The high time and frequency resolution of the survey means that over eight times more galactic volume is being searched than by previous surveys. The Arecibo sky is being search using a 7 beam receiver and, thanks to the incomparable gain, this will be the deepest blind search for pulsars. The LOw Frequency ARray (LOFAR) will perform a search for pulsars at very low frequency. While this will not probe deep in the Galaxy it should provide an excellent census of the local

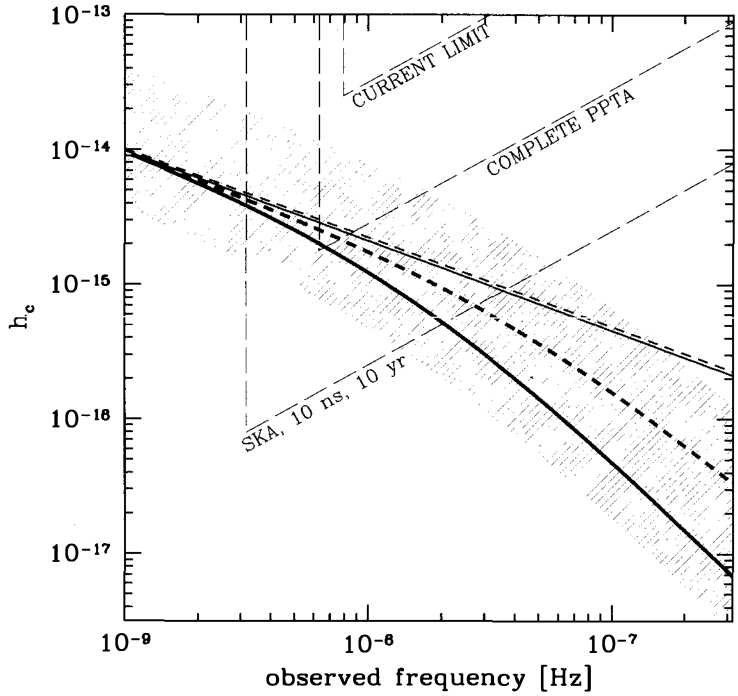

Figure 3: The shaded area is the expected range of amplitudes of the stochastic GW background from SMBH binaries. The sensitivity of the current limit, 10 years of the PPTA and 10 years of the SKA-PTA is also plotted. Figure from Sessana et al. 2009.

population. It seems unlikely that these surveys will be bettered before the arrival of the Square Kilometre Array.

5 Pulsar Timing Arrays with the Square Kilometre Array

The Square Kilometre Array (SKA) is a proposed telescope which will provide a total collecting area of a square kilometre. It will be sited in a rural location the southern hemisphere providing and excellent view of the Galaxy and a low radio interference environment. The SKA will be a major improvement for PTAs in two main areas. Firstly it will be sensitive enough to detect all pulsars in the Galaxy that are beamed toward Earth. This increase in the population of pulsars will provide a substantial number of excellent timers. Secondly the unrivaled gain of the telescope will provide one or two orders of magnitude in the timing precision. This combined with increased numbers of observations and a potentially increased frequency range will provide a dramatic increase in sensitivity see Fig. 3 from Sessana et al. 2009[18].

6 Conclusions

PTAs offer the only means to detect the very low frequency nHz range of GWs. This is particularly important to measure SMBH coalescence rates and understand galaxy evolution in the early universe. In combination with other space- and ground- based GW detectors a comprehensive view of black holes in different mass ranges and evolutionary stages can be achieved. With the sensitivity of the SKA and the newly found pulsars it will provide, will allow for GW astronomy. Additionally the properties of the GWs wiill can be compared with predictions of general relativity and of alternate theories of gravity. With current PTAs a detection is possible and vital research required for the SKA will be done. A future with the SKA-PTA, LISA and ground-based detectors observing concurrently would certainly usher in a new era for astronomy.

References

1. Lorimer, D. R., & Kramer, M. 2005, Handbook of pulsar astronomy, by D.R. Lorimer and M. Kramer. Cambridge observing handbooks for research astronomers, Vol. 4. Cambridge, UK: Cambridge University Press, 2004
2. K.J. Lee et al., In prep.
3. Hulse, R. A., & Taylor, J. H. 1975, ApJL, 195, L51
4. Taylor, J. H., & Weisberg, J. M. 1982, ApJ, 253, 908
5. Hellings, R. W., & Downs, G. S. 1983, ApJL, 265, L39
6. Jenet, F., et al. 2009, arXiv:0909.1058
7. Lee, K. J., Wex, N., Kramer, M., Stappers, B. W., Bassa, C. G., Janssen, G. H., Karuppusamy, R., & Smits, R. 2011, MNRAS, 628
8. Sudou, H., Iguchi, S., Murata, Y., & Taniguchi, Y. 2003, Science, 300, 1263
9. Jenet, F. A., Lommen, A., Larson, S. L., & Wen, L. 2004, ApJ, 606, 799
10. Yardley, D. R. B., et al. 2010, MNRAS, 407, 669
11. Hobbs, G., et al. 2009, MNRAS, 394, 1945
12. Pitkin, M., Clark, J., Hendry, M. A., Heng, I. S., Messenger, C., Toher, J., & Woan, G. 2008, Journal of Physics Conference Series, 122, 012004
13. Gopukumar et al. In prep.
14. Verbiest, J. P. W., et al. 2010, Classical and Quantum Gravity, 27, 084015
15. Ferdman, R. D., et al. 2010, Classical and Quantum Gravity, 27, 08401
16. Hobbs, G., et al. 2010, Classical and Quantum Gravity, 27, 084013
17. http://www.leap.eu.org
18. Sesana, A., Vecchio, A., & Volonteri, M. 2009, MNRAS, 394, 2255

13.
Other Topics

Measuring g with a beam of antihydrogen (AEgIS)

C.CANALI [a]

Istituto Nazionale di Fisica Nucleare and Department of Physics, University of Genoa, via Dodecaneso 33, 16146 Genova, Italy

The gravitational interaction between matter and antimatter has never been tested experimentally. According to some attempts to unify gravity with the other forces, the possibility that $g(p) \neq g(\overline{p})$ cannot be excluded [1]. The AEGIS experiment [2] intends to measure for the first time the gravitational acceleration of antimatter using cold antihydrogen atoms. Antihydrogen atoms will be obtained trough a charge exchange process between Rydberg positronium atoms and antiprotons. Once $\overline{H}$ are accelerated to form a horizontal beam, they travel through a Moiré deflectometer, able to measure the vertical displacement of atoms due to gravity. Knowing the velocity of the antiatoms from the time of flight measurement and the length of the flight path allows to estimate the gravity acceleration g for antihydrogen. With this setup an initial precision on the measure of g of 1% is expected.

1 Introduction

In recent years few experiments at CERN have demonstrated the feasibility of producing large amounts of antiatoms at low temperature [4],[5],[6]. This result opens a very interesting scenario of studies on fundamental symmetries between matter and antimatter such as the CPT invariance (through high precision spectroscopy) and direct measurements of the validity of the equivalence principle for antimatter (through ballistic experiments).

A precise test of CPT could arise from measurements on gross structure, fine structure, Lamb shifts and hyperfine structures in antihydrogen to be compared with analougue measurements done on hydrogen. The CPT theory predicts that all these properties are identical for matter and antimatter systems. This kind of measurements, in principle, could reach a very high precision: a comparison of the 1S-2S frequency for hydrogen [7] and antihydrogen with a precision of 10^{-15} or higher will be the most accurate CPT tests for baryons regardless of any theoretical model.

While CPT test based on antihydrogen spectroscopy could give very precise results, at the same time antihydrogen can be used to perform for the first time a direct measurement of gravity on an antimatter system.

Such a kind of measurement could be in principle performed using charged particles (for example positrons), but a huge experimental trouble arises because the gravitational force is much weaker than the Coulomb force, and is virtually impossible to reduce electric fields to a negligible level (an electric field of only $6 \cdot 10^{-11} V/m$ gives to a positron an acceleration equal to that of gravity). This make $\overline{H}$ a simple (and neutral) system with which WEP can be directly tested.

The primary scientific goal of the AEGIS experiment is the direct measurement of the Earth

[a] on behalf of AEGIS collaboration

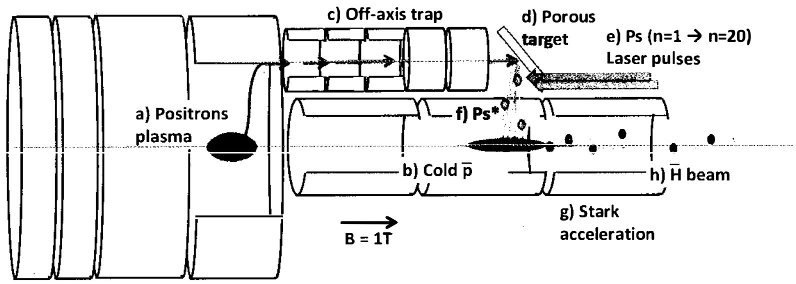

Figure 1: Formation of an horizzontal travelling beam of antihydrogen in AEgIS. Particles (e^+ and *overlinep* are stored in cylindrical penning traps. The $\overline{H}$ production occur in few steps: positrons are sent with several keV energy on a porous target here they form positronium that is excited to Rydberg state with a double laser pulse. Rydberg positronium atoms (Ps^*) cross the cold $\overline{p}$ cloud producing $\overline{H}$ via charge exchange reaction: $Ps^* + \overline{p} \rightarrow \overline{H}^* + e^-$ (see text for detailed explanation of each step). A proper electric field accelerate horizzontally $\overline{H}^*$ atoms to form the beam.

's gravitational acceleration g on antihydrogen. CPT spectroscopy is included in the long term scientific goal of the experiment.

2 The AEgIS experiment (Antimatter Experiment: Gravity, Interferometry, Spectro

2.1 $\overline{H}$ beam formation

The AEgIS experiment is under construction at CERN, in the AD (Antiproton Decelerator) hall.

In Fig.1 a scheme of the core of the AEgIS apparatus, with a sketch of the operations leading to the antihydrogen beam formation, is shown. Particles (e^+ and $\overline{p}$) are manipulated inside several cylindrical Penning traps: here an uniform axial magnetic field (B=1-5 T) ensure the radial confinement of charged particles while proper configuration of potentials applyed to the various segments of the trap provides to axial trapping of particles.

The Antiproton Decelerator delivers antiprotons with a kinetic energy of $5MeV$ in bunches of $2.5 \cdot 10^7$ particles within $100ns$. In typical operations a bunch of $\overline{p}$ is delivered every $\simeq 200s$. Antiprotons will be captured in a dedicated trap inside a $5T$ superconducting magnet: the use of fast high voltage pulses applyed to the entrance electrode of the trap will allow to capture more than 10^4 $\overline{p}$ at each cycle of AD. Once captured, antiprotons will be transferred in a second trap with a lower magnetic field ($1T$) where antihydrogen is produced and the beam is formed, as it will be discussed in the following.

A positron plasma ($N_{e^+} \simeq 10^8$, density $N_{e^+} \simeq 10^8 cm^{-3}$) is stored in the first penning trap (**a**, in Fig.1) after being transfereed in this region from a Surko-type accumulator [3].

At the same time in a second trap the antiprotons cloud (**b**) is cooled to $100mK$ using electron cooling tecniques and a resistive tuned circuit. The cooling of antiprotons is a key-point of the whole experiment since this temperature determines the quality of the antihydrogen

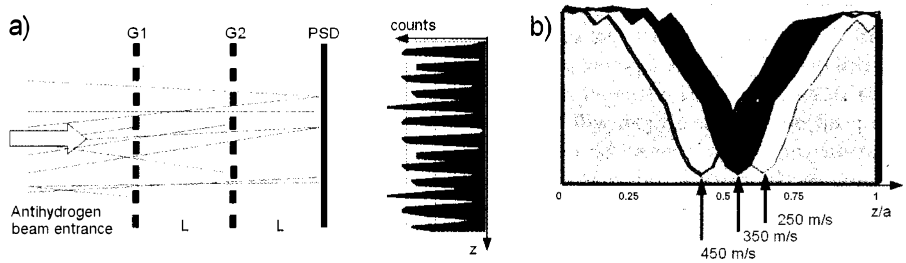

Figure 2: a) The antihydrogen beam travel trought two gratings (G1 and G2) and reach a position sensitive detector (PSD) where the annihilation point is detected. An interference pattern is shaped on the detector on the right. b) The interference pattern can be binned (modulo the grating period). Lowering the beam velocity causes the pattern to shift down along the z-axis. Realistic values for the gratings system are $L = 40cm$, grating period $a = 80\mu$, grating size $20cm$.

beam: obtaining cold $\overline{p}$ means having antihydrogen atoms with a velocity low enough to allow the gravity measurement: once $\overline{p}$ will be cooled at the same temperature of the ambient ($100mK$), they will have a velocity of few tens of m/s.

At this point positrons are moved off axis with a diocotron excitation[11], they travel trought an off-axis trap (**c**) where they are accelerated to several keV, bunched and sent in direction of a target of porous material (**d**) . When the positrons hits this target with keV energy they penetrate inside the nanometric-size channels of the target, it cools by collisions with the pore walls and form positronium (Ps): the long-life ortopositronium drifts outside the target and is excited by a double laser pulse (**e**) from ground state to Rydberg state ($n_{Ps} > 20$) just before it start crossing the cold antiprotons cloud. Cold antiprotons and Rydberg positronium react via charge exchange[13]:

$$Ps^* + \overline{p} \to \overline{H}^* + e^- \tag{1}$$

the cross section of this reaction scales with $\propto n_{Ps}^4$ and the produced $\overline{H}^*$ is in its turn produced in excited Rydberg level. It's important to underline again that the temperature of produced antihydrogen is basically the same of antiprotons stored in the trap just before the interaction with Ps^*. Immediatelly after their formation, Rydberg antihydrogen atoms will be accelerated via Stark effect (**g**) up to a velocity of several hundreds m/s to form an horizontally travelling beam. This tecqnique has been already demonstrated to work with hydrogen[14].

2.2 Measure of the gravity acceleration g of $\overline{H}$ atoms

The antihydrogen beam will travel horizzontally along a path about $1m$ long with a velocity of several hundreds m/s.

During its flight $\overline{H}$ fall in the gravitational field produced by the Earth. Assuming $g = 9.8m/s$ and a horizzontal velocity of $500m/s$, the vertical deflection is too small ($\simeq 10\mu m$) to be measured directly since a poor beam collimation must be taken into account. Nevertheless a moiré deflectometer will make still possible to perform this measurement[12].

The device (Fig.2.a), sligtly modified respect to standard moiré deflectometers, consists of two gratings (G1 and G2) and a position sensitive detector (PSD) separated by a distance $L \simeq 40cm$. Both gratings have a size of $20x20cm^2$ and a period of $\simeq 80\mu m$. The PSD is a silicon microstrip detector with an active area of about $20x20cm^2$, and a resolution of about $10\mu m$ working at cryogenic temperatures.

Since the width of the slits is much larger than the De Broglie wavelength of the antihydrogen, diffraction can be neglected and all effects will be purely classically, so the PSD just records a shadow pattern corresponding to the positions of antiatom annihilations. The velocity of the beam can be tuned changing the parameters of the Stark acceleration, so it is possible to measure the vertical deflection of the shadow path for several values of velocities. The precise velocity of $\overline{H}$ can be desumed from the time of flight measurement.

The position of anthydrogen will be detected reconstructing the annihilation point of each antiatom on the position sensitive detector. The detected positions of annihilations can be binned modulo the grating period as plotted in Fig.2.b. Here it's shown from Montecarlo results how the verical shift of the shadow pattern increase with lower horizzontal velocity of the beam, assuming $g = 9.8m/s$.

The use of this method allow to measure the gravity acceleration g of antihydrogen with a precision of 1% detecting 10^5 antihydrogen atoms: it will be the first direct measurement of gravity acceleration on an antimatter system.

3 Conclusion

Antihydrogen will be used in next years to investigate CPT validity and equivalence principle. Related to this latter topic, AEgIS will use antiprotons delivered from AD (the antiproton decelerator at CERN) to produce an horizzontal beam of antihydrogen to measure the gravity acceleration g of antiatoms. The initial precision on the measured g is expected to be 1%, and long and medium terms goals intends to improve noticeably this precision.

1. E. Fischbach, C.L. Talmadge *The search for non Newtonian Gravity* Springer (1999)
2. AEgIS proposal http://doc.cern.ch/archive/electronic/cern/preprints/spsc/public/spsc-2007-017.pdf
3. T. J. Murphy and C. M. Surko, Phys. Lett. B **46**, 5696 (1992).
4. ATHENA Coll. Nature **419**, 2002 (456)
5. http://hussle.harvard.edu/ atrap/
6. http://alpha.web.cern.ch/alpha/
7. M. Niering et al., Phys. Rev. Lett. **84**, 2000 (5496)
8. C Jarlskog in *CP Violation*, ed. C Jarlskog (World Scientific, Singapore, 1988).
9. J.D. Bjorken and I. Dunietz, *Phys. Rev.* D **36**, 2109 (1987).
10. C.D. Buchanan *et al*, *Phys. Rev.* D **45**, 4088 (1992).
11. J. R. Danielson, T. R. Weber, and C. M. Surko Physics Of Plasmas **13**, 123502 (2006)
12. M. K. Oberthaler et al., Physical Review A **54**, 3165 (1996).
13. M. L. Wall, C. S. Norton, and F. Robicheaux Physical Review A **72**, 052702 (2005)
14. E. Vliegen and F. Merkt, J. Phys. B: At. Mol. Opt. Phys. **39**, L241 (2006)

GBAR
Gravitational Behavior of Antihydrogen at Rest

P. Dupré
CEA Saclay, service de physique des particules
Gif-sur-Yvette, France

The GBAR experiment aims to test the Equivalence Principle with antimatter by measuring the time of flight of ultra-cold antihydrogen atoms $\bar{H}$ in free fall. Antihydrogen atoms at ~20 μK are provided by sympathetic cooling of antihydrogen ions $\bar{H}^+$ with laser cooled Be^+ ions. $\bar{H}^+$ ions are produced via two successive reactions using antiprotons and positroniums. The synthesis of $\bar{H}^+$ is obtained by the injection of a pulse of 10^7 slow antiprotons from the AD at CERN in a dense cloud of positronium. This target of positronium is created with a positron-to-positronium converter and requires an intense source of slow positrons, a few 10^8 per second. Such a source based on a small electron accelerator is under construction at Saclay. A few 10^{10} positrons are accumulated in a Penning-Malmberg trap from which they are ejected towards the e^+/Ps converter to produce the target. The overall scheme of the experiment is described along with the estimated efficiency of each step.

1 Introduction

The aim of the GBAR project is to perform the first test of the Weak Equivalence Principle (WEP) with antimatter. The Einstein Equivalence Principle is at the heart of general relativity. It has been tested with a very high precision with matter, but no conclusive direct test with antimatter is available. This is a basic scientific question, the interest of which is enhanced by the unknown origin of the acceleration of the expansion of the universe and by the hypothetical presence of dominant quantities of dark matter: these observations suggest that our understanding of gravitation may be incomplete. Extensions of gravitation theory can lead to differences in behavior between matter and antimatter [1].

Direct tests have been attempted with positrons [2] and antiprotons [3], but they turned out to be too difficult to reduce electromagnetic effects sufficiently. It seems also out of present reach to perform gravity experiments with antineutrons [4] or positronium [5]. The antihydrogen atom is the next simplest candidate system. Indirect tests of the Equivalence Principle for antimatter have been obtained by comparing the properties of particles and their antiparticles (such as p-$\bar{p}$ [6] and K_0-$\bar{K}_0$ [7]) or by arguing about the virtual content of the nuclei of ordinary matter. However, all these tests rely upon disputable theoretical hypotheses - refer for example to the review [8] on experimental and theoretical arguments.

2 Principle of the GBAR experiment

The GBAR experiment will measure the time of flight of ultra-cold antihydrogen atoms in free fall. The principle of GBAR has been described in a Letter of Intent to CERN [9]. The original way to produce ultra-cold $\bar{\mathrm{H}}$ atoms at $\sim$20 μK consists to cool down $\bar{\mathrm{H}}^+$ ions via sympathetic cooling with laser cooled beryllium ions Be^+. Then $\bar{\mathrm{H}}^+$ ions are neutralized by photodetachment of their extra positron and the $\bar{\mathrm{H}}$ atoms produced fall freely in the gravitational potential of the Earth. The height h of the free fall is of the order of ten centimeters. The gravity acceleration, called $\bar{\mathrm{g}}$, is determined by measuring the time Δt between the photodetachment and the annihilation of $\bar{\mathrm{H}}$ in the walls of the experiment, $\bar{\mathrm{g}} = 2h/(\Delta t)^2$ (figure 1).

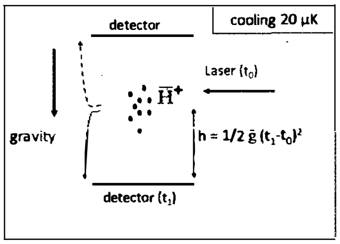

Figure 1: Scheme of the $\bar{\mathrm{g}}$ measurement.

The main source of uncertainty comes from the initial velocity of the anti-atom. The precision on $\bar{\mathrm{g}}$ is mainly statistical. About 10^4 measures are needed to reach a precision below 1%. This method has been proposed by J. Walz and T. W. Hänsch [10], but they did not describe the way to produce the $\bar{\mathrm{H}}^+$ ions. These ions are produced via two successive reactions (1) and (2) using antiprotons $\bar{\mathrm{p}}$ and positroniums Ps:

$$\bar{\mathrm{p}} + \mathrm{Ps} \rightarrow \bar{\mathrm{H}} + \mathrm{e}^- \quad (1)$$
$$\bar{\mathrm{H}} + \mathrm{Ps} \rightarrow \bar{\mathrm{H}}^+ + \mathrm{e}^- \quad (2)$$

The cross section of the first reaction has been measured for its matter counterpart [11]. The one of the second reaction has been estimated [12]. These cross sections are very low and require the production of large quantities of low energy (in the keV range) antiprotons, and a very high flux of positrons, well above the capacity of β^+ sources, in order to produce enough Ps. The overall scheme of the measurement is thus as follows:

1. 5-10 MeV electrons from a small linear accelerator are dumped onto a tungsten target and produce fast positrons
2. These positrons are moderated to the electrovolt and accumulated in a Penning-Malmberg trap.
3. Once the required amount of positrons is stored, they are ejected and dumped onto the positron-to-positronium converter.
4. The antiprotons pulse is synchronously injected in the newly formed positronium cloud.
5. The few $\bar{\mathrm{H}}^+$ ions produced are decelerated and trapped in a segmented Paul trap, where they are sympathetically cooled with beryllium ions.
6. The extra positron is photodetached and the free fall time of the produced $\bar{\mathrm{H}}$ is measured.

Steps 1 to 4 are tested at CEA Saclay before the experiment, if accepted, is installed at CERN. The following sections describe each step in more detail.

3 Slow positrons production

Our intense source of slow positrons is based on a small linear accelerator. It delivers 4 μs bunches of 5.5 MeV electrons at a rate of 200 Hz with a mean current of 0.14 mA. Electrons are dumped onto a tungsten target in order to produce electron/positron pairs via the Bremsstrahlung radiation of the injected electrons. The efficiency of production of positrons downstream the target has been simulated with GEANT4. It is expected to be about 10^{-4} corresponding to a flux of about 10^{11} fast e^+s^{-1}. In a first stage, fast positrons are moderated from MeV to eV energies with a tungsten foil close to the target, with an efficiency expected to be about 10^{-4}. In a second stage, a solid Neon moderator will be set after an e^+/e^- selector, with a moderation efficiency of a few 10^{-3}. This cryogenic system[a] cannot be placed directly after the tungsten target because of the energy deposit of the escaped electrons. The expected flux of slow positrons is 10^7 to 10^8 e^+s^{-1} depending on the moderator.

Slow positrons will be stored in the RIKEN Multi Ring Trap (MRT). The positron accumulation technique with this kind of electromagnetic trap has been developed by N. Oshima *et al* with a continuous positron beam from a ^{22}Na source [13]. They succeeded to store 10^6 positrons with 1% trapping efficiency. This trap consists of a 5T superconducting solenoid and a set of 23 ring electrodes. The uniform magnetic field confines radially the antiparticles. An electrostatic potential well confines them along the direction of the field. Positrons are cooled down in the trap by Coulomb-collisional damping in an electron plasma. This accumulation technique will be adapted to the pulsed beam in order to store a few 10^{10} e^+ in a few minutes. Slow positrons have to be bunched and reaccelerated to about 1 keV to go through the magnetic mirror and be trapped before they make a round trip in 85 ns (see figure 2). They are cooled down in less than 5 ms in a previously injected electron plasma of 10^{17} m^{-3} density, the expected overall trapping efficiency is in excess of 20 %.

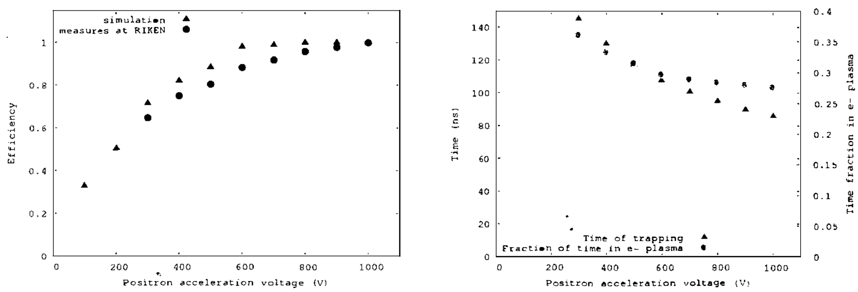

Figure 2: As a function of the acceleration potential. Left: efficiency for slow positrons to go through the magnetic mirror of the RIKEN MRT. Right: round trip time of positrons in the MRT and fraction of time spent by positrons in the electron plasma.

The linear accelerator, the e^+/e^- selector and the RIKEN MRT have been installed at Saclay and the slow positrons beam line is under construction (figure 3).

4 Production of the dense positronium target

The positronium target is produced with a e^+/Ps converter. It is a nanoporous SiO_2 material. Positrons are injected onto the converter and catch an electron into the pores. A part of the Ps thus formed diffuses in the porous network until the surface and is ejected in the vacuum.

[a]the melting point of Neon is about 13 K

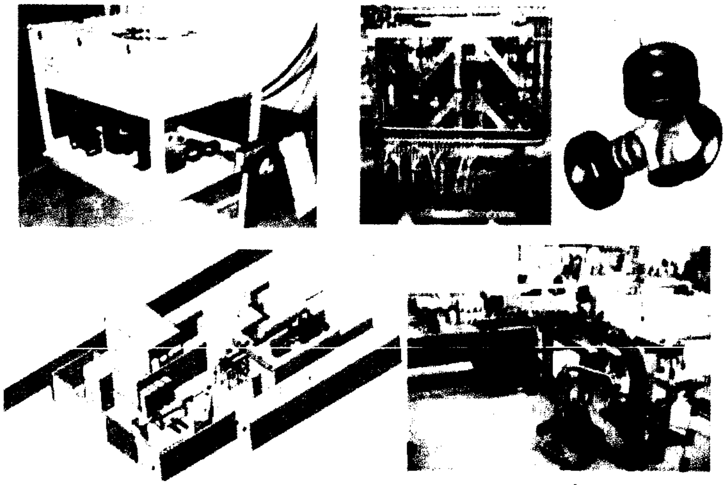

Figure 3: Top left : prototype linac. Top right : positron magnetic separator. Bottom left: design of the experiment at Saclay. The linac and the magnetic separator are in a bunker. They are connected to the cylindrical trap with the slow positron beam line.. Bottom right : slow positron beam line under installation and tests.

This converter has been tested at CERN with the ETHZ positron beam [14,15] and at UCR [16]. The conversion efficiency is above 30% with positron fluxes as different as 3.5×10^5 $e^+cm^{-2}s^{-1}$ from a radioactive source at CERN and 5.6×10^{16} $e^+cm^{-2}s^{-1}$ dumped from a trap at UCR. The emitted positronium kinetic energy can be as low as 40 meV at a few keV implantation energy. The cylindrical geometry of the converter with an inner diameter of 1mm and the low energy of positroniums keep a high Ps density of order 10^{12} cm^{-2} (figure 4,a).

a) b)

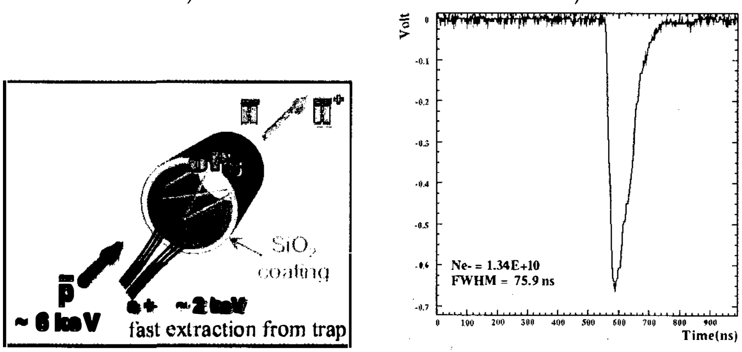

Figure 4: a) Artists view of the geometry of the positron-positronium converter. b) Pulse of 1.3×10^{10} e^- ejected from the RIKEN trap in 76 ns.

To produce this dense cloud of Ps, positrons stored in the trap are dumped in the converter in less than 142 ns, the oPs lifetime in vacuum. This fast ejection has been tested with 10^{10} electrons in less than 80 ns with the RIKEN trap (figure 4,b).

5 Production of ultra-cold $\bar{H}$

A bunch of 10^7 antiprotons is injected into the Ps cloud newly formed in order to synthesize $\bar{H}^+$ ions via the two successives reactions 1 et 2. This amount of $\bar{p}$ can be delivered in about 20 minutes by the Antiproton Decelerator at CERN (in 85 s by ELENA upgrade) and will be previously accumulated in a dedicated trap.

The cross section of thc matter counterpart of the first reaction has been measured [11] above 10 keV for the $\bar{p}$ energy and estimated over a lower energy range at an order of 10^{-15} cm^2. The second reaction has been estimated [12] for its matter counterpart. Its cross section is about 10^{-16} cm^2. This cross section is expected to be strongly enhanced with n = 3 excited Ps because the binding energy of this positronium state, 0.75 eV, is very close to that of $\bar{H}^+$. Such kind of effect has been calculated with n = 2 Ps states [17]. The cross section increase is strongly dependent on the incident energy. The optimization of the whole process formation is under way, this involves the theoretical calculation of the cross section, the optimization of the fraction of Ps to be excited, and the choice of the antiproton kinetic energy. First estimates show that it is reasonable to expect a factor 10 enhancement on the $\bar{H}^+$ production above the previous numbers. This would lead to about 10 $\bar{H}^+$ ions produced with 2.5×10^{10} positrons and 10^7 antiprotons.

The produced $\bar{H}^+$ ions have almost the same energy as the incident antiprotons. First, they have to be slowed down to enter in a segmented Paul trap where they will be cooled down by sympathetic cooling with Be^+ ions. These ions can be cooled to temperatures below 10 μK [18]. The sympathetic cooling to less than 20 μK of $\bar{H}^+$ ions has to be demonstrated.

Once the $\bar{H}^+$ ions are cooled at $\sim$20 μK, the extra positron is photodetached with a laser. This photodetachment has to be close to the threshold to avoid a too large recoil which would prevent making the measurement.

6 Perspectives

The GBAR collaboration has recently been formed. Based on the initial Letter of Intent [9], the technical design of the experiment is in progress, and a proposal is being prepared. In the next two years, the main objectivcs will be to test the accumulation of several 10^{10} positrons in the RIKEN MRT at Saclay, and to optimize the positronium cloud formation and excitation. If the project is approved, the installation at CERN and tests with antiprotons will follow. On a longer term, a much higher precision on the measurement of $\bar{g}$ could bc reached with the spectroscopy of gravitational levels of $\bar{H}$ [19]. This idea looks promising because the $\bar{H}$ atoms are prepared at a very low temperature and in a very compact system.

Acknowledgments

In addition to the involved institutes and laboratories, part of this work has been funded by the Conseil Général de l´ Essonne and by the Agence Nationale de la Recherche in France.

References

1. J. Scherk, Antigravity: a crazy idea?, Phys. Lett. B 88, 265-267 (1979).
2. F. Witteborn and W. Fairbank, Experimental Comparison of the Gravitational Force on Freely Falling Electrons and Metallic Electrons, Phys. Rev. Lett. 19 1049-1052 (1967).
3. N. Beverini, J.H. Billen, B.E. Bonner, L. Bracci, R.E. Brown, L.J. Campbell el al., PS200 proposal, Los Alamos National Laboratory report, LAUR-86-260 (1986).
4. T. Brando, Observations of low-energy antineutrons in a time-separated neutral beam, Nucl. Instr. Methods 180, 461-467 (1981).

5. A.P. Mills, Positronium molecule formation, Bose - Einstein condensation and stimulated annihilation, Nucl. Instr. Methods in Physics Research B 192, 107116 (2002).
6. G. Gabrielse et al., Precision Mass Spectroscopy of the Antiproton and Proton Using Simultaneously Trapped Particles, Phys. Rev. Lett. 82, 3198-3201 (1999).
7. CP LEAR collaboration, Tests of the Equivalence Principle with neutral kaons, Phys. Lett. B 452, 425-433 (1999).
8. M.M. Nieto and T. Goldman, The Arguments Against Antigravity and the Gravitational Acceleration of Antimatter, Phys. Rep. 205, 221-281 (1991).
9. P. Pérez et al. A new path to measure antimatter free fall., CERN-SPSC-2007-038. December 2007.
10. J. Walz and T. Hänsch, A Proposal to Measure Antimatter Gravity Using Ultracold Antihydrogen Atoms, General Relativity and Gravitation 36, 561-570 (2004).
11. J.P. Merrison et al., Hydrogen Formation by Proton Impact on Positronium, Phys. Rev. Lett. 78, 2728-2731 (1997).
12. H.R.J.Walters and C. Starrett, Positron and positronium scattering, Phys. Stat. Sol. C, 3429-3436 (2007).
13. N. Oshima et al., New Scheme for Positron Accumulation in Ultrahigh Vacuum, Phys. Rev. Lett. 93, 195001 (2004).
14. L. Liszkay et al., Positronium reemission yield from mesostructured silica films, Appl. Phys. Lett. 92, 063114 (2008).
15. P. Crivelli et al., Measurement of the ortho-positronium confinement energy in mesoporous thin films, Phys. Rev. A 81, 052703 (2010).
16. D. B. Cassidy et al., Positronium cooling in porous silica measured via Doppler spectroscopy, Phys. Rev. A 81, 012715 (2010).
17. S. Roy and C. Sinha, Formation of negative hydrogen ion in positronium-hydrogen collisions, Eur. Phys. J. D 47, 327-334 (2008).
18. M.D. Barrett et al., Sympathetic cooling of $^9B^+$ and $^{24}Mg^+$ for quantum logic, Phys. Rev. A 68, 042302 (2003).
19. A.Yu. Voronin, P. Froelich, and V.V. Nesvizhevsky, Gravitational quantum states of Antihydrogen, Phys. Rev. A 83, 032903 (2011).

EVIDENCE FOR TIME-VARYING NUCLEAR DECAY DATES: EXPERIMENTAL RESULTS AND THEIR IMPLICATIONS FOR NEW PHYSICS

E. FISCHBACH
Department of Physics, Purdue University, 525 Northwestern Ave, West Lafayette, Indiana, 47907 USA
ephraim@purdue.edu

J.H. JENKINS
School of Nuclear Engineering, Purdue University, West Lafayette, Indiana 47907 USA

P.A. STURROCK
Center for Space Science and Astrophysics, Stanford University, Stanford, California 94305 USA

Unexplained annual variations in nuclear decay rates have been reported in recent years by a number of groups. We show that data from these experiments exhibit not only variations in time related to Earth-Sun distance, but also periodicities attributable to solar rotation. Additionally, anomalous decay rates coincident in time with a series of solar flares in December 2006 also point to a solar influence on nuclear decay rates. This influence could arise from some flavor of solar neutrinos, or through some other objects we call "neutrellos" which behave in some ways like neutrinos. The indication that neutrinos or neutrellos must interact weakly in the Sun implies that we may be able to use data on time-varying nuclear decay rates to probe the interior of the Sun, a technique which we may call "helioradiology".

1 Introduction

The widely held view that nuclear decay rates, along with nuclear masses, are fundamental constants of nature has been challenged recently by reports from various groups of periodic variations in nuclear decay rates.[1,2,3,4,5,6,7,8] Following the discovery of natural radioactivity by Becquerel in 1896 an intense effort was mounted to determine whether nuclear decay rates were in fact constant. By 1930 Rutherford, Chadwick, and Ellis concluded that "the rate of transformation of an element has been found to be a constant under all conditions.[9] Subsequent work by many groups has supported this conclusion, except for decays proceeding by electron capture. In such decays the decay rate depends on the overlap of the electron wavefunction and the nucleus, and this can be slightly modified by subjecting the decaying nucleus to extreme pressure, or by modifying its chemical environment.[10,11,12,13,14,15,16]

Notwithstanding the impressive body of evidence supporting the conventional view that the decay rate $\lambda = ln2/T_{1/2}$ of an unstable isotope is an intrinsic property of that isotope, there are growing indications of small $(\mathcal{O}(10^{-3}))$ time-dependent variations in the decay rates of some nuclei. In Sec. 2 we summarize the existing experimental evidence for these variations, along with the arguments against some claims that the variations are simply the results of local environmental influences on the detector systems. What emerges from these considerations is a picture in which the observed time-dependent variations are in fact occurring in the decay process itself, in response to time-dependent solar perturbations. Although a detailed mechanism is not yet available to explain how the Sun influences radioactive decays, previous work[3] along with the discussion in Sec. 3 below, provide a general framework for a future theory.

2 Experimental Results

In this section we summarize the experimental evidence for a solar influence on nuclear decay processes. A more detailed discussion of the various experiments can be found in the accompanying paper by Jenkins *et al.*[17] The interest of our group in time-dependent nuclear decay rates began with our attempt to understand an annually-varying periodic signal in the decay rate of ^{32}Si reported by Alburger, et al.[18] in a 4-year experiment at the Brookhaven National Laboratory (BNL). A subsequent examination of the literature revealed a ~15-year experiment at the Physikalisch-Technische Bundesanstalt (PTB) in Germany in which data from ^{226}Ra exhibited a similar annual variation.[19] Coincidentally, these two experiments overlapped in time for approximately two years, and the data from these experiments during this period were quite similar in both amplitude and phase.[2,3] Further exploration of the literature has uncovered other experiments in which periodic effects in various decays were reported. These include the results of Falkenberg[20], Parkhomov[21,22], Baurov et al.[23], Ellis[24], and Shnoll et al.[25,26].

The observation of periodic effects in what had been previously been thought of as random decay data motivated a series of experiments by our group at Purdue, chiefly focused on the electron capture process: $e^- + ^{54}\text{Mn} \to \nu_e + ^{54}\text{Cr} + \gamma\,(834.8\text{ keV})$. Our apparatus was operating during a series of solar flares in November and December of 2006. On 13 December 2006 a major solar flare erupted at 02:37 UT (21:37 EST 12 December) which coincided with a $\sim 7\sigma$ drop in the measured ^{54}Mn counting rate.[1] A smaller flare with a large coronal mass ejection on 17 December 2006 also coincided with a decrease in the ^{54}Mn counting rate. Subsequently, an examination of data acquired during December 2008 revealed a correlation between a change in the measured ^{54}Mn count rate and a solar storm on the far side of the Sun.

The correlations between observed changes in measured ^{54}Mn count rates and solar flares are significant for several reasons:

1. They now reinforce the inference, drawn from the annual periodicities in the BNL and PTB data, that these periodicities arise from the annual variation of the Earth-Sun distance R due to the ellipticity of the Earth's orbit.

2. Since the flares erupt and subside over fairly short time-scales (typically minutes to hours), any apparent correlation between decay data and solar activity cannot plausibly be attributed to environmental effects on the detector systems in question due to a local change in temperature, pressure, humidity, etc.[27]

3. Finally, in all the cases we have observed, there is a precursor signal in which the ^{54}Mn count rate begins to change ~1 day before the solar event. This observation raises the possibility of establishing an "early-warning" system for potentially dangerous impending solar storms, whose damaging effects on astronauts; communications, navigation, defense and other satellites; and power grids and other electronic infrastructure could thus be prevented.[1]

The observation in decay data of time-dependent influences attributable to the Sun (either from a change in $1/R^2$ or via a solar flare), raises the question of whether other time-dependent signals could be present in decay data associated, for instance, with solar rotation. This could happen if the sources of whatever influences were affecting decay rates were not distributed homogeneously throughout the Sun, for which there were earlier indications.[28] Further analysis of the BNL, PTB, and Parkhomov data sets has indeed revealed evidence of a ~32 d periodicity, which can be interpreted as evidence for an East-West asymmetry in the Sun, perhaps associated with a slowly rotating solar core.[29] Additionally, the BNL and PTB data sets also revealed evidence of a ~173 d periodicity, similar to the Rieger periodicity, which arises from retrograde waves in a rotating fluid.[7] Finally, recent work by our group has shown that the apparent phase-shift of the maximum count rate noted in BNL, PTB, and other data sets from what would be expected from the variation in $1/R^2$ alone could be attributed to a North-South asymmetry in the Sun.[8] While this observation does not directly deal with solar rotation, it does support the assumption that there are asymmetries in the Sun whose presence can be detected via periodicities in decay data. In this way decay data may allow us to probe the interior of the Sun via a new technique which we may refer to as "helioradiology".

3 Towards a Mechanism: Neutrinos and Neutrellos

Although the evidence for a solar influence on nuclear decay rates is quite compelling, what is lacking is a mechanism through which this influence can be transmitted. Elsewhere[3] we explore in detail a mechanism based on an interaction between solar neutrinos and decaying nuclei. Here we broaden that discussion to address the question of whether nuclear decay rates are affected by the Sun through some generic particles which we call "neutrellos", which may or may not be the same as neutrinos. In what follows we describe some of the properties that we would like neutrellos to possess in order to account for existing data.

1. The solar flare of 13 December 2006 at 02:37UT was coincident in time with a local minimum (dip) in the ^{54}Mn counting rate.[1] Since this dip occurred at 21:37 EST in our laboratory, this suggests that neutrellos must be capable of passing unimpeded through the Earth at essentially the speed of light.

2. Although the solar flare was of short duration and occurred without warning, the decay rate of ^{54}Mn began to decrease much earlier, approximately 40 hours before the flare. This "precursor signal" suggests that neutrellos originated from a region below the surface of the Sun and reached us before the actual flare because the Sun is effectively transparent to neutrellos, but not to photons.

3. As the Sun rotated, the region on the surface of the Sun from which the 13 December 2006 flare originated, region 930, dropped over the West Limb of the Sun on 17 December and hence was no longer visible via X-rays. Nevertheless, a significant drop in the ^{54}Mn count rate was detected on 22 December, suggesting that neutrellos were reaching the Earth from the far side of the Sun by passing through the Sun. This again implies that the Sun is transparent to neutrellos, at least to some degree.

4. Our ^{54}Mn experiment also detected a solar event on 16 December 2008 which coincided with a storm on the far side of the Sun. This reinforces the assumption that the Sun is relatively transparent to neutrellos.

5. The phase of the annual variation in decay rates seen in a number of experiments is shifted from what would be expected from the annual variation of $1/R^2$, where R is the Earth-Sun distance.[2,3] However, we have shown recently[8] that if there is a North-South asymmetry in the emission of neutrellos from the Sun, then the resulting contribution to the annual phase could explain the observed data. Interestingly, evidence for a North-South asymmetry was observed in data from the Homestake solar neutrino experiment.[7]

6. As noted previously, there is evidence that nuclear decay data are modulated not only by the variation of $1/R^2$ and the presence of a North-South asymmetry in the Sun, but also by the rotational motion of the Sun. Evidence for rotational modulation is based on the presence in the decay data of periodicities of ~ 32 d and ~ 173 d, the latter being analogous to the well-known Rieger periodicity. Since similar evidence for rotational modulation has been noted previously in data from the Homestake and GALLEX neutrino experiments[28], this suggests that our hypothetical neutrellos may actually be neutrinos.

7. The ~ 32 d rotational modulation mentioned above points to a source where the rotation rate is slower than that of the radiative and convection zones in the Sun. The fact that we observe a solar influence from a source below the radiative zone indicates that the putative neutrellos experience only slight (or no) scattering or absorption in travelling the outer layers of the Sun.

8. The very existence of a signal in nuclear decay data for rotational modulation by the Sun implies that neutrello production by the Sun is anisotropic. If neutrellos were in fact neutrinos, then the rotational modulation could arise from the resonant spin flavor precession (RSFP)[30] effect induced by a strong magnetic field deep in the solar interior. This mechanism, which assumes that neutrinos have a non-zero transition magnetic moment, is supported by existing neutrino data from Super-Kamiokande.[28]

Although the preceding considerations are compatible with the inference that neutrellos are in fact neutrinos, there is at least one major difference: to account quantitatively for existing experimental data the interaction strength of neutrellos with decaying nuclei must be significantly greater than the strength of the known interactions of neutrinos with protons, neutrons, electrons, or with other neutrinos as described by the standard electroweak model. As an example, to produce a fractional peak-to-trough variation in tritium of order 10^{-3} (which is the nominal value suggested by the BNL, PTB, and Falkenberg data) requires an input of energy $\Delta E \approx 5eV$. Although this is small on the scale of the $\mathcal{O}(1MeV)$ energies carried by incoming solar neutrinos, a value of ΔE this large is more characteristic of an electromagnetic interaction than a weak interaction. This can be seen in another way by picturing solar neutrinos or neutrellos affecting nuclear decays by transferring a momentum $\Delta p \approx \Delta E/c$ via a scattering process with an effective cross section σ,

$$\sigma \equiv \frac{1}{\phi}\frac{(\Delta N/N)}{\Delta t}. \tag{1}$$

Here ϕ is the presumed flux (or change in flux) of solar neutrinos or neutrellos responsible for inducing a fractional change $\Delta N/N$ in the number of decays over a time interval Δt. Evidently the smallest estimate of σ will result from the largest assumed value for ϕ for which we adopt the known solar flux $\phi = 6\times10^{10}cm^{-2}s^{-1}$. Using the flare data of Jenkins and Fischbach[1] we estimate $(\Delta N/N)/\Delta t \approx 2.6\times10^{-11}s^{-1}$ per atom, and hence $\sigma \approx 4.3\times10^{-22}cm^2$. By way of comparison, the Thomson cross section for photon scattering of electrons is $\sigma_T = (8\pi r_o^2/3) = 6.6\times10^{-25}cm^2$, where $r_o = 2.82\times10^{-13}cm$ is the classical electron radius.

The implication of the above calculations, that neutrinos could influence decaying nuclei through an interaction of electromagnetic strength, is likely incompatible with existing data on $\nu_s - e$, $\nu_s - p$, and $\nu_s - n$ interactions (ν_s = solar neutrino), but could be compatible with a possible $\nu_s - \nu_e$ interaction coupling a generic solar neutrino to an emitted ν_e from beta decay or electron capture. On the other hand, a much broader range of possibilities is available for nutrello couplings, and these may be accessible experimentally through appropriate "fifth force" experiments.[31] Additional constraints on a possible influence of $\bar{\nu}_e$ on radioactive decay follow from an elegant reactor experiment by de Meijer *et al.*[32]

4 Discussion and Outlook

From the discussion in the previous sections several conclusions emerge: There is by now overwhelming evidence of anomalous and unexpected time-dependent features present in the count rates of various nuclei. Although some early criticism claimed that these features were merely experimental artifacts arising form the response of the detection systems to local seasonal changes in temperature, pressure, humidity, etc.,[33] it now appears that the observed effects are intrinsic to the decay process itself. This follows from the detailed analysis of Jenkins, Mundy and Fischbach[27] of the detector systems used in the BNL, PTB and Purdue experiments, and also from observation in multiple data sets of time-dependent features for which there is no known "environmental" cause.[17]

Although the preceding discussion, along with the analysis in Section 2, suggests that the decay process is being influenced in some way by the Sun, there is at yet no detailed mechanism to explain how this influence comes about. Our discussion of neutrinos and neutrellos is an attempt to frame a future theory by outlining some of the specific characteristics that it should possess, given the limited experimental data currently available.

Evidently, more experimental data on a variety of different isotopes are needed before we can realistically expect to understand how the Sun influences radioactive decays. To start with, it is clear that there should be no expectation that time-dependent effects will show up in all decays, or that they should be detected at the same level when they are present. This follows by noting that the same details of nuclear structure that are responsible for the wide range of half-lives, from fractions of a second to tens of billions of years, will likely produce a range of responses to any solar influence. Moreover, if the Sun is in fact the source of the time-dependent effects observed in nuclear decays, its influence cannot be assumed to be constant in time. The well known $\sim$ 11 year solar cycle is but one example of a time-dependent solar feature whose affects would not be constant, or even periodic, over the duration of a typical laboratory experiment. For this reason, experiments on the same isotopes carried out at different times may not exhibit the same features. It is thus likely that "helioradiology" will be an important tool in studying the Sun, while at the same time creating new methods for studying neutrino (or neutrello) physics.

Acknowledgments

The work of PAS was supported in part by the NSF through Grant AST-06072572, and that of EF was supported in part by U.S. DOE contract No. DE-AC02-76ER071428.

References

1. J.H. Jenkins and E. Fischbach, *Astropart. Phys.* **31**, 407 (2009)
2. J.H. Jenkins *et al*, *Astropart. Phys.* **32**, 42 (2009)
3. E. Fischbach *et al*, *Space Sci. Rev.* **145**, 285 (2009)
4. P.A. Sturrock *et al*, *Astropart. Phys.* **34**, 121 (2010)
5. Javorsek II *et al*, *Astropart. Phys.* **34**, 173 (2010)
6. P.A. Sturrock *et al*, *Sol. Phys.* **267**, 251 (2010)
7. P.A. Sturrock, E. Fischbach and J.H. Jenkins, *Sol. Phys.* **In Press**, (2011)
8. P.A. Sturrock *et al*, *ApJ* **In Press**, (2011)
9. E. Rutherford, J. Chadwick and C.D. Ellis, Radiations from radioactive substances, (Cambridge University Press, Cambridge, 1930).
10. G.T. Emery, *Annual Rev. of Nucl. Sci.* **22**, 165 (1972)
11. P.K. Hopke, *Jour. Chem. Ed.* **51**, 517 (1974)

12. H.P. Hahn, *Radiochimica Acta* **23**, 15 (1976)
13. K.P. Dostal, M. Nagel and D. Pabst, *Zeitschrift fur Naturforschung A* **23A**, 345 (1977)
14. E.B. Norman *et al*, *Phys. Lett.* B **519**, 15 (2001)
15. T.H. Ohtsuki, Phys. Rev. Lett. **93**, 11 (2004)
16. B.F. Limata *et al*, *Eur. Phys. J.* A **28**, 251 (2006)
17. J.H. Jenkins, E. Fischbach, P.A. Sturrock and D.W. Mundy, *Moriond 2011 Proceedings* , (2011)
18. D.E. Alburger, G. Harbottle and E. Norton, *Ear. and Planet. Sci. Lett.* **78**, 168 (1986)
19. H. Siegert, H. Schrader and U. Schötzig, *Appl. Rad. and Isot.* **49**, 1397 (1998)
20. E.D. Falkenberg, *Aperion* **8**, 14 (2001)
21. A.G. Parkhomov, *Intl. J. Pure Appl. Phys.* **1**, 119 (2005)
22. A.G. Parkhomov, *arXiv:1004.1761v1 [physics.gen-ph]* , (2010)
23. Y.A. Baurov *et al*, *Phys. Atomic Nuclei* **70**, 1825 (2007)
24. K.J. Ellis, *Phys. Med. Biol.* **35**, 1079 (1990)
25. S.E. Shnoll *et al*, *Physics-Uspekhi* **41**, 1025 (1998)
26. S.E. Shnoll *et al*, *Biophysics* **43**, 864 (1998)
27. J.H. Jenkins, D.W. Mundy, and E. Fischbach, *Nucl. Instrum. Methods* A **620**, 332 (2010)
28. P.A. Sturrock, *ApJ Lett.* **688**, L53 (2008)
29. P.A. Sturrock, *Solar Physics* **254**, 227 (2009)
30. E.K. Akhmedov, *Phys. Lett.* B **257**, 163 (1991)
31. E. Fischbach and C.L. Talmadge, The Search for Non-Newtonian Gravity, (Springer, Ney York, 1999).
32. R.J. de Meijer, M. Blaauw and F.D. Smit, **69**, 320 (2011)
33. T.M. Semkow *et al*, *Phys. Lett.* B **675**, 415 (2009)

ANALYSIS OF EXPERIMENTS EXHIBITING TIME-VARYING NUCLEAR DECAY RATES: SYSTEMATIC EFFECTS OR NEW PHYSICS?

J.H. JENKINS
School of Nuclear Engineering, Purdue University,
400 Central Dr., West Lafayette, Indiana 47907 USA
jere@purdue.edu

E. FISCHBACH
Department of Physics, Purdue University, West Lafayette, Indiana, 47907 USA

P.A. STURROCK
Center for Space Science and Astrophysics, Stanford University, Stanford, California 94305 USA

D.W. MUNDY
Department of Radiation Oncology Physics, Mayo Clinic, Rochester, Minnesota 55905 USA

Since the 1930s, and with very few exceptions, it has been assumed that the process of radioactive decay is a random process. unaffected by the environment in which the decaying nucleus resides. There have been instances within the past few decades, however, where changes in the chemical environment or physical environment brought about small changes in the decay rates. But even in light of these instances, decaying nuclei that were undisturbed or un-"pressured" were thought to behave in the expected random way. subject to the normal decay probabilities which are specific to each nuclide. Moreover, any "non-random" behavior was assumed automatically to be the fault of the detection systems, the environment surrounding the detectors, or changes in the background radiation to which the detector was exposed. Recently, however, evidence has emerged from a variety of sources, including measurements taken by independent groups at Brookhaven National Laboratory, Physikalisch-Technische Bundesanstalt, and Purdue University, that indicate there may in fact be an influence that is altering nuclear decay rates, albeit at levels on the order of 10^{-3}. In this paper, we will discuss some of these results, and examine the evidence pointing to the conclusion that the intrinsic decay process is being affected by a solar influence.

Introduction

has long been a universal belief that radioactive decay is a random process. one that is almost ompletely insensitive to external influences. There have been a few special cases in recent times here minor changes in decay rates have been measured due to artificially produced changes in e physical environment of the decaying nuclides[1,2,3,4,5,6,7], but on the whole the assumption has en that radioactive decays follow the standard exponential decay law which is based on these cays being a random process. In recent years, however, a few independent groups have identid some interesting behaviors in measured nuclear decay rates that did not arise from a change the physical or chemical environment of the decaying nuclei.[8,9,10,11,12,13,14,15] In these results, ere appears to be some structure in what should be randomly distributed data points. More cently, however, Recent work by our group[16,17,18,19,20,21,22,23] has gone further and detailed the existence of periodicities and other non-random behaviors in measured nuclear decay data fro Purdue University[16], Brookhaven National Laboratory (BNL)[24], and the Physikalisch-Technisc Bundesanstalt (PTB)[25]. The suggestion of this recent work is that there is a solar influence on t these measured decay rates, via some particle or field of solar origin such as solar neutrinos.

Such a proposal is, without question, going to generate criticism from the physics communit based on the belief that the observed effects were the result of changes in the environment of t detector systems (i.e., temperature, background, etc.) or systematic effects.[27,28,29,30] However, thorough analysis by our group of the Purdue, BNL and PTB detector systems has effective refuted essentially all of this criticism.[31] In this report we will further strengthen this view providing additional perspective and results that support the conjecture that whatever is influenci the measured decay rates is external to the terrestrial environment, and could in fact have a sol origin.

2 Review of Experimental Evidence

To begin this discussion, it is helpful to collect together the information related to the observ decay rate changes from multiple independent experiments. Table 1 lists several experiments whi utilize different isotopes as well as different different detector technologies, all of which show anom lous behaviors, either in the form of periodicities, or a localized departure from the expected dec trend over a short duration.

Table 1: Experiments exhibiting time-dependent decay rates.

Isotope &, Decay Type	Detector Type	Radiation Type Measured	Experiment Duration	Effect Observed
^{3}H, β^-	Photodiodes	β^-	1.5 years	*freq*(1/yr)[9]
^{3}H, β^-	Sol. St. (Si)	β^-	4 years	*freq*(~2/yr)[26]
^{36}Cl, β^-	Proportional	β^-	8 years	*freq*(1/yr, 11.7/yr, 2.1/yr)[17,19,22]
^{54}Mn, κ	Scintillation	γ	2.5 months	Short term decay rate decrease[16]
^{54}Mn, κ	Scintillation	γ	2.5 years	*freq*(1/yr)
^{56}Mn, β^-	Scintillation	γ	9 years	*freq*(1/yr)[8]
^{60}Co, β^-	Geiger-Müller	β^-, γ	4.5 years	*freq*(1/yr)[12,13]
^{60}Co, β^-	Scintillation	γ	4 months	*freq*(1/d, 12.1/yr)[11]
$^{90}Sr/^{90}Y$, β^-	Geiger-Müller	β^-	10 years	*freq*(1/yr, 11.7/yr)[12,13]
^{137}Cs, β^-	Scintillation	γ	4 months	*freq*(1/d, 12.1/yr)[11]
^{152}Eu, κ	Sol. St. (Ge)	γ	>16 years	*freq*(1/yr)[25]
^{226}Ra, α, β^-	Ion Chamber	γ	>16 years	*freq*(1/yr, 11.7/yr, 2.1/yr)[17,19,22]

What should be evident from the information presented in Table 1 is that the "problem" apparent non-random behavior in nuclear decay measurements is apparent in a number of d ferent experiments. What will probably also become evident as time passes is that the effect more widespread than even this list indicates. A simple search of the literature reveals multi instances of articles discussing the discrepancies in nuclear decay measurements, particularly ha life determinations.[32,33,34,35] It is interesting, given recent advances in detector technology, and t precision with which we can make measurements in the present day, that there would be discre ancies as large as are observed to be present in nuclear decay data. However, if some of the measurements are of β^- decays that are affected by an influence external to the Earth, and t influence has a variable output, then the picture becomes a little clearer. It is imperative, thoug to rule out the possible terrestrial influences such as the detector systems themselves, or changes the local environment (temperature, barometric pressure, relative humidity, or background rad tion) that could play a role in producing these effects in the measured decay rates. Therefore, n experiments should record local conditions carefully if they are not able to be controlled complete

Returning to Table 1, we can draw some conclusions about the possible influence of envir mental and systematic effects from the list presented there. To begin, all of the isotopes present n Table 1 are β-decays, or β-decay related, even the ^{226}Ra measured on the ionization chamber at he PTB.[25] Clearly, while ^{226}Ra is not a β-decay itself, there are several β-decaying daughters in s decay chain, nearly all of which are in equilibrium with the ^{226}Ra parent.[a] Since the ionization hamber system utilized in the PTB experiment was not designed to differentiate between the spe- ific photons emitted by the ^{226}Ra or or any of its daughters, it is impossible to determine whether he decay rate changes were occurring in the α- or β-decays of the chain. No effects have been seen n α-decays to this point,[12,27,28] which is not surprising. Since the mechanisms of α- and β-decays re so different, the fact that the effect has not been observed in α-decays should not exclude the ossibility of the effect existing in β-decays.[27]

Upon further examination of the experiments described in Table 1, we see that there is rep- esentation of all three major classes of detector types, solid state (2), scintillation (5), and gas etectors (4). There is also a mix of the types of radiation detected, about equally split between harged particles (β^-) and photons (γ). There is one experiment (the one presented by Falkenberg[9]) n Table 1 that is unique in that the detection method did not fit into any of the standard classes. he experiment utilized photodiodes to measure the radioluminescence of tritium tubes.

When examining the possible environmental influences on the radiation transport (from source o detector, which is in general over a very short distance on the order of a few millimeters in ost cases), the primary consideration is the air density of the source-detector gap, which will be function of temperature (T), barometric pressure (P), and relative humidity (RH). A thorough iscussion of this is presented in Jenkins, Mundy and Fischbach,[31] who note that cool, dry air is uch more dense than warm, moist air. Interestingly, the effect seen in *all* of the experiments listed Table 1 exhibit higher counts in the winter, when the air is ostensibly denser. If air density (as function of T, P, and RH) is higher in the winter due to the air being cooler and drier, then the ount rates of the charged particles should be lower in the winter due to the greater energy loss s the β-particles interact with more gas atoms in the denser air, not higher. The transport of hotons across the small source-detector gaps will not be affected by air density at a level worth onsidering. Furthermore, a detailed analysis utilizing MCNPX performed by our group[31] supports he above qualitative arguments, and thus refutes claims to the contrary by Semkow *et al.*[29] that he observed effects were strictly due to environmental influences on the detector systems.

The variety of detector systems helps to offset other possible environmental or systematic nfluences as well, since there are no known systematic effects that would affect each of the different ystems in the same way. For instance, with the Geiger-Müller detectors, a single ionization can ause an avalanche and ionize all of the gas that can be ionized within the entire tube, thus there is o pre-amplifier or amplifier required. This eliminates the opportunity for shifting in the electronics hat would affect peak shape, or other similar properties of the system. One may reasonably draw he conclusion that there are no systematic effects which would be likely to have caused these eriodicities. However, we can pursue that in yet another way.

Looking at the "Observed Effect" column in Table 1, we note there exists more than just an nnual frequency in seven of the twelve experiments. We note here that the "Observed Effects" olumn list the frequencies discussed in the respective articles describing the experimental results n one case, the ^{54}Mn data that show an annual oscillation, the full frequency analysis has not et been performed, these are new data presented for the first time here, see Section 3). While here may be other frequencies present in these experimental data sets, those analyses are not vailable. What is important to remember, however, is that these frequencies are exhibited in ata that should not have any frequency structure at all. While it may be easier to discard an nnual frequency by attributing it to the change of the seasons, it is impossible to say the same bout an approximate monthly frequency (which appears in five of the experiments) or a roughly emi-annual frequency (which appears in three, and two of those three also contained the monthly equencies). It is also not likely that one could offer a systematic explanation for the existence

[a] Good descriptions of the ^{226}Ra decay chain and the equilibrium activities of a ^{226}Ra source are presented by hristmas[37] and Chiste *et al.*[38]

of those periodicities. Therefore, it is reasonable to look outside the local laboratory conditio making the solar influence certainly plausible.

3 New Results

In November 2008, our group began measuring ^{54}Mn again, taking continuous, 3600 s live-ti counts. The results of the measurement series are still preliminary, but we present an overvi here. Each of the counts in a 24-hour period were aggregated into one data point which represe counts/day, then a 21-day sliding average centered on each point was calculated to smooth t data set in order to show long-period oscillations more clearly. The results are shown in Fig 1. The presence of a frequency with a period of one year is obvious, as is the indication of so shorter period frequencies. A detailed analysis will be presented in a forthcoming paper. T annual frequency is also listed in the data presented in Table 1.

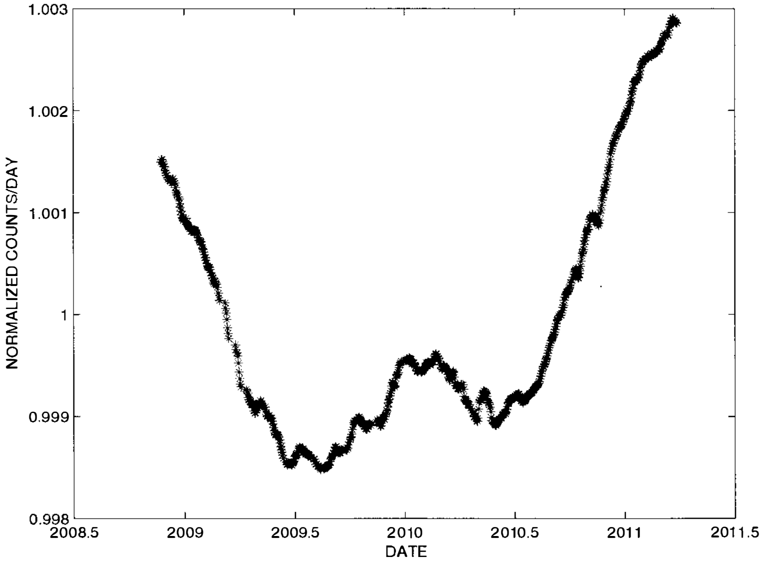

Figure 1: ^{54}Mn decays measured at Purdue University. The 834.8 keV photon was measured with a 2-inch detector, and were taken continuously for 3600 seconds live time, then aggregated into counts/day. These integra counts were then undecayed (detrended), and normalized to the average of the series.

The presently accepted half-life of ^{54}Mn is 312.12(6) days;[39] and from our data we have det mined the half-life to be 310.881(2) days. Our data set contains 19,191 separate 3600 s live-ti counts over 877 days (2.81 half-lives) totalling 1.01×10^{11} measured decay events. What is curi is that the χ^2/d.o.f of the weighted least-squares fit is 7.99, which is fairly large. However, af examining the plot in 1, the fact that the data are not distributed randomly around the value 1. and stray from that normalized value of 1, raises an interesting question: How does the half- vary in shorter segments of the entire set, which is a question similar to the one examined Siegert, Schrader and Shötzig[25] for ^{152}Eu. We have calculated the half-life for each month of d by performing a weighted least squares fit to an average of 664 data points per month, with $\sqrt{N}$ fractional uncertainty of each point varying from $\sim 0.03\%$ at the beginning of the experim to $\sim 0.07\%$ near the end. These monthly half-lives are shown in 2. The average $\chi^2/d.o.f$

ach month's fit was ~ 1.3, which is a great improvement over the fit to the whole line. It is asy to see that there is a fairly significant variability in the measured count rates. We measured he environmental conditions in the laboratory (T, P *and* RH) and these were found not to vary ignificantly, and also did not correlate with the variability in the measured count rates. A more igorous analysis is under way, the results of which will be available soon.

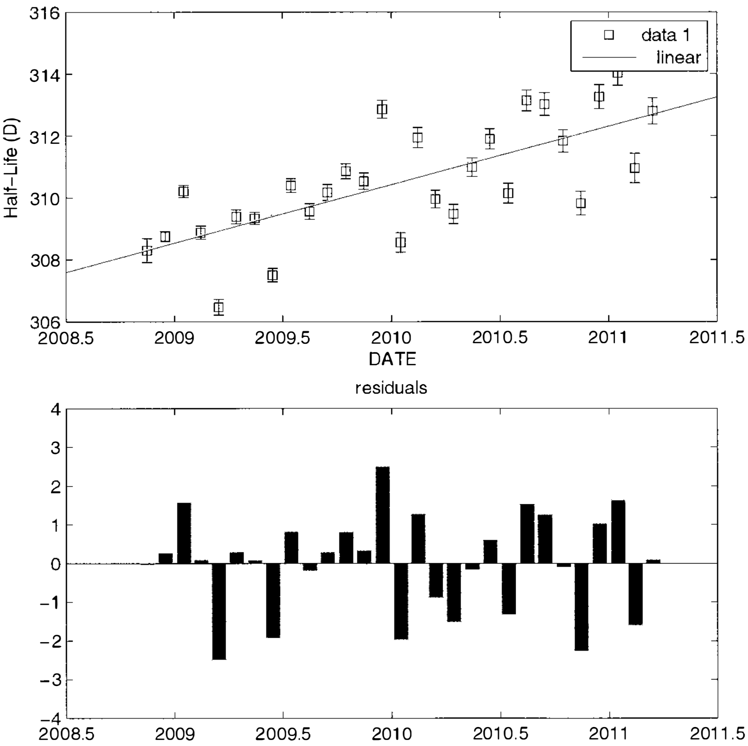

igure 2: Variation in the measured ^{54}Mn half-life, looking at one-month segments of the decay measurement series. he half-life value for each month was calculated by performing a weighted least squares fit to an average of 664 data oints, with the $\sqrt{N}$ fractional uncertainty of each point varying from $\sim 0.03\%$ at the beginning of the experiment to $\sim 0.07\%$ near the end. The average $\chi^2/d.o.f$ for each fit was ~ 1.3.

In light of all of this evidence, it seems clear that all of the possible, known systematic effects or nvironmental effects are too small to have caused the oscillatory or other "non-random" characeristics in the data from the experiments listed in Table 1. Without question, more work needs to e done in determining what the cause is, but based on all of the evidence presented by our group, t appears that the most likely external influence at this time is the Sun. It is, therefore, our hope hat many new experiments will be undertaken by groups around the world to continue this work. ven if the cause turns out to not be solar-related, identifying and understanding this effect will ave a broad impact across the world of science and technology related to nuclear decays.

Acknowledgments

The work of PAS was supported in part by the NSF through Grant AST-06072572, and that of E
was supported in part by U.S. DOE contract No. DE-AC02-76ER071428.

References

1. G.T. Emery, *Annual Rev. of Nucl. Sci.* **22**, 165 (1972)
2. P.K. Hopke, *Jour. Chem. Ed.* **51**, 517 (1974)
3. H.P. Hahn, *Radiochimica Acta* **23**, 15 (1976)
4. K.P. Dostal, M. Nagel and D. Pabst, *Zeitschrift fur Naturforschung A* **23A**, 345 (1977)
5. E.B. Norman *et al*, *Phys. Lett.* B **519**, 15 (2001)
6. T.H. Ohtsuki, Phys. Rev. Lett. **93**, 11 (2004)
7. B.F. Limata *et al*, *Eur. Phys. J.*A **28**, 251 (2006)
8. K.J. Ellis, *Phys. Med. Biol.* **35**, 1079 (1990)
9. E.D. Falkenberg, *Aperion* **8**, 14 (2001)
10. A.G. Parkhomov, *Intl. J. Pure Appl. Phys.* **1**, 119 (2005)
11. Y.A. Baurov *et al*, *Phys. Atomic Nuclei* **70**, 1825 (2007)
12. A.G. Parkhomov, *arXiv:1004.1761v1 [physics.gen-ph]* , (2010)
13. A.G. Parkhomov, *arXiv:1012.4174v1 [physics.gen-ph]* , (2010)
14. S.E. Shnoll *et al*, *Physics-Uspekhi* **41**, 1025 (1998)
15. S.E. Shnoll *et al*, *Biophysics* **43**, 864 (1998)
16. J.H. Jenkins and E. Fischbach, *Astropart. Phys.* **31**, 407 (2009)
17. J.H. Jenkins *et al*, *Astropart. Phys.* **32**, 42 (2009)
18. E. Fischbach *et al*, *Space Sci. Rev.* **145**, 285 (2009)
19. P.A. Sturrock *et al*, *Astropart. Phys.* **34**, 121 (2010)
20. Javorsek II *et al*, *Astropart. Phys.* **34**, 173 (2010)
21. P.A. Sturrock *et al*, *Sol. Phys.* **267**, 251 (2010)
22. P.A. Sturrock *et al*, *Sol. Phys.* **In Press**, (2011)
23. P.A. Sturrock *et al*, *ApJ* **In Press**, (2011)
24. D.E. Alburger, G. Harbottle and E. Norton, *Ear. and Planet. Sci. Lett.* **78**, 168 (1986)
25. H. Siegert, H. Schrader and U. Schötzig, *Appl. Rad. and Isot.* **49**, 1397 (1998)
26. V.M. Lobashev *et al*, *Phys. Lett.* B **460**, 227 (1999)
27. P.S. Cooper, *Astropart. Phys.* **31**, 267 (2009)
28. E.B. Norman *et al*, *Astropart. Phys.* **31**, 135 (2009)
29. T.M. Semkow *et al*, *Phys. Lett.* B **675**, 415 (2009)
30. M.P. Silverman and W. Strange, *Europhys. Lett.* **87**, 32001 (2009)
31. J.H. Jenkins, E. Fischbach and D.W. Mundy, *Nucl. Instrum. Methods* A **620**, 332 (2010)
32. F. Begemann *et al*, *Geochim. Cosmochim. Acta* **65**, 111 (2001)
33. T.-C. Chiu *et al*, *Quaternary Sci. Rev.* **26**, 18 (2007)
34. M.J. Woods, Nucl. Instrum. Methods *A* **286**, 576 (1990)
35. M.J. Woods and S.E.M. Lucas, Nucl. Instrum. Methods *A* **369**, 534 (1996)
36. R.J. de Meijer, M. Blaauw and F.D. Smit, **69**, 320 (2011)
37. P. Christmas *et al*, *J. Appl. Radiat. Isot.* **34**, 1555 (1983)
38. **V**. Chiste, M.M. Be, and C. Dulieu, in *Int'l Conf. on Nucl. Data for Sci. and Tech. 200*
ed. O. Bersillon *et al*EDP Sciences, Nice, France, 2007
39. H. Junde and H. Su, *Nucl. Data Sheets* **107**, 1393 (2006)

14.
Posters

Einstein Equivalence Principle and Bose–Einstein condensates

J. I. Rivas
Departamento de Física, Universidad Autónoma Metropolitana-Iztapalapa
Apartado Postal 55-534, C.P. 09340, México, D.F., México.

A. Camacho
Departamento de Física, Universidad Autónoma Metropolitana-Iztapalapa
Apartado Postal 55-534, C.P. 09340, México, D.F., México.

The behavior of a Bose–Einstein condensate in a homogeneous gravitational field is analyzed. The trapping potential is an isotropic harmonic oscillator and the effects of the gravitational field and of the zero–point energy on the condensation temperature are also considered. These results are employed in order to put forward an experiment which could test the so called Einstein Equivalence Principle.

1 Introduction

Gravity can be understood at the classical level as a purely geometric effect, i.e., the motion of a free classical particle moving in a curved manifold is given by the Weak Equivalence Principle (WEP) [1]. The introduction of additional interactions is done resorting to the so–called Einstein Equivalence Principle (EEP) [1]. The present work addresses the behavior of a Bose–Einstein condensate under the influence of a homogeneous gravitational field. The idea here is to consider the possibility of testing the Einstein Equivalence Principle resorting to the temperature as the parameter to be monitored. We will deduce the changes in the condensation temperature as a consequence of the presence of a homogeneous gravitational field.

2 Condensation in a homogeneous gravitational field

2.1 Gas in a harmonic trap

In the experimental realm the condensation process does not resort to a gas within a container, the trapping potential has a more sophisticated structure. Indeed, there are several kind of traps, for instance magneto-optical traps (MOT), Optical traps (OT), etc. [2]. The mathematical description of the available magnetic traps, at least for alkali atoms, is that the corresponding confining potential can be approximated by a three–dimensional harmonic oscillator

$$U(x, y, z) = \frac{m}{2}\Big(w_1^2x^2 + w_2^2y^2 + w_3^2z^2\Big). \tag{1}$$

We now consider the presence of a homogeneous gravitational field along the z–axis, hence, the complete potential becomes

$$U(x, y, z) = \frac{m}{2}\left(w_1^2 x^2 + w_2^2 y^2 + w_3^2\left(z + \frac{g}{w_3^2}\right)^2\right) - \frac{1}{2}\frac{mg^2}{w_3^2}. \tag{2}$$

The energy eigenvalues are given by

$$\varepsilon = \hbar w_1\left(n_x + \frac{1}{2}\right) + \hbar w_2\left(n_y + \frac{1}{2}\right) + \hbar w_3\left(n_z + \frac{1}{2}\right) - \frac{1}{2}\frac{mg^2}{w_3^2}; \quad n_x, n_y, n_z \epsilon \mathbb{N}. \tag{3}$$

The density of states is provided by

$$\Omega(\varepsilon) = \frac{\left(\varepsilon + \frac{mg}{2w_3^2} - \frac{\hbar}{2}(w_1 + w_2 + w_3)\right)^2}{2\hbar^3 w_1 w_2 w_3}. \tag{4}$$

This last expression allows us to calculate the average number of particles N and the change in the condensation temperature T_c due to the presence of a non-vanishing homogeneous gravitational potential

$$N = \int_0^\infty \frac{\Omega(\varepsilon)}{z^{-1}e^{\beta\varepsilon} - 1} d\varepsilon + \frac{1}{z^{-1}e^{\beta\varepsilon_0} - 1}. \tag{5}$$

$$\Delta T_c = -\frac{\zeta(2)}{3\zeta(3)}\frac{\Delta\mu}{\kappa}. \tag{6}$$

For our particular case the change in the chemical potential, $\Delta\mu = -(0.456)\frac{mg^2}{2\omega_z^2}$, namely, the condensation temperature under the presence of a homogeneous gravitational field reads

$$T_c^{(g)} = T_c^{(0)} - (0.456)\frac{mg^2}{2\kappa\omega_z^2}. \tag{7}$$

In this last expression $T_c^{(g)}$ is the condensation temperature if there is a non-vanishing gravitational field , whereas $T_c^{(0)}$ denotes the condensation temperature without gravitational field.

2.2 Conclusions

According to EEP, the temperature of a freely falling condensate, trapped by a harmonic oscillator, should be higher than the corresponding temperature if the condensate lies at rest with respect to the surface of the Earth.

Acknowledgments

JIRS acknowledges CONACyT grant No. 160453.

References

1. C. M. Will, *Theory and Experiment in Gravitational Physics*, Cambridge University Press, Cambridge (1993).
2. C. J. Pethick and H. Smith, *Bose-Einstein Condensation in Diluted Gases*, Cambrige University Press,Cambrige (2006).

MICROSCOPE INSTRUMENT SERVO-LOOPS AND DIGITIZATION

A. LEVY, P. TOUBOUL, M. RODRIGUES
ONERA. BP72-29 Av. de la Division Leclerc,
Châtillon FR-92322, France

A. ROBERT
CNES, 18 Av. Edouard Belin,
Toulouse 31401 Cédex 9, France

G. MÉTRIS
Observatoire de la Côte d'Azur, Av. Nicolas Copernic,
Grasse 06130, France

MICROSCOPE is a fundamental physics space mission which aims at testing the Equivalence Principle (EP) with an accuracy of 10^{-15}. The gravitational signal is measured precisely on-board a drag-free microsatellite by a differential electrostatic accelerometer which includes two cylindrical test masses made of different materials. The masses are servo-controlled along their six degrees of freedom and the MICROSCOPE experiment takes advantage of this specific configuration with 12 data channels. A major point concerns the digitization and computation noise throughout the loop, which should be maintained negligible with respect to the physical noise. This requires dedicated converters, filters and high frequency operations even if the EP test is performed at frequency about 10^{-3} Hz.

1 The MICROSCOPE space mission

The MICROSCOPE space mission aims at testing the The Equivalence Principle (EP) expressed by Einstein as a basis of its theory of General Relativity with the best accuracy ever reached of 10^{-15}. This high accuracy can be achieved by taking profit of the minimized noise and the non limited duration of the free fall in space. A 200 kg dedicated satellite is developed by CNES within its MYRIAD program of micro-satellite. The Earth is the gravitational source of the EP test and the satellite will be injected on a quasi circular (eccentricity $< 5 \times 10^{-3}$) and heliosynchronous orbit, at an altitude around 720 km. The characteristics of the orbit ensure thermal stability and a reduced correlation between the EP signal and the gravity gradient. The duration of the mission is planned to be one year while the orbit period is about 6000 s.

The payload of the satellite is composed of two independent electrostatic differential accelerometers developed in our laboratory at Onera. Each differential accelerometer includes two cylindrical test masses and measures the difference between the inertial accelerations of the two masses. One accelerometer is composed of two different masses (platinum/titanium) to perform the EP test and one is composed of two identical masses (platinum/platinum) to be used as a reference. The mass and power budgets of the payload lead to 35 kg and 40 W.

The mass motions of the accelerometer are servo-controlled to follow the same orbit with a precision better than 10^{-11} m. Each test mass is surrounded by a cylindrical electrode part enabling the electrostatic actuation which forces the masses to remain concentric. Thus, the two masses undergo the same gravity field and a difference between the electrostatic accelerations applied to the masses will indicate an EP violation. The environment is maintained very steady limiting any perturbation and the System of Control of Attitude and Acceleration (SCAA) exploits the measurement of the accelerometer in order to make the satellite drag free along the three degrees of freedom: the surface forces and torques applied on the satellite are countered continuously by the thrust of the propulsion system.

2 The measurement process

The operation of the accelerometer is similar along the six axes and hereafter detailed along the measurement axis which is the cylinder axis (X axis): when the mass moves along this axis, a variation of the recovering surface appears leading to a difference of capacitance between the mass and each electrode corresponding to an analog signal provided by the position detector. This signal is numerized with a sampling frequency equal to 1027.96 Hz and processed by the control loop laws in order to generate a voltage proportional to the acceleration of the sensor. This voltage is amplified and applied to the electrodes in order to keep the mass at the center. The output of the control laws, after being filtered and down-sampled to 4 Hz, is used by the drag free system. The scientific measurement must have a better accuracy so it is picked up, after filtering and down-sampling to 4 Hz, on the electrodes at the end of the loop in order to get advantage of the loop gain on all electronics noise sources. The control laws, anti-aliasing filters and down-sampling processes are implemented in an Interface Control Unit (ICU) far away from the sensor core while the analogue electronics and the analogue to digital converters must be close to the instrument sensor core to reduce electro-magnetic disturbances.

The anti-aliasing filters are at the order 5 and have cutoff frequency of 1 Hz for the scientific measurement and either 2 Hz or 3.3 Hz for the drag-free channels, depending on the axes; they are implemented as combinations of biquad filters which are defined as second-order recursive linear filters with transfer function $H(z) = \frac{b_0+b_1z^{-1}+b_2z^{-2}}{1+a_1z^{-1}+a_2z^{-2}}$ in the Z-domain. The usual implementation of the biquad filter with x as input and y as output corresponds to the differential equation:

$$y(n) = b_0x(n) + b_1x(n-1) + b_2x(n-2) - a_1y(n-1) - a_2y(n-2) \tag{1}$$

All the computations in the ICU are performed with 40 bits. In spite of this large number, this leads to a computation error which is not negligible, especially because some intermediate variable of the computation are only memorized with 32 bits instead of 40 bits in order to be compatible with the hardware components. This latter error is amplified through the recursive filter and becomes the dominant error. Considering the expected accuracy of the MICROSCOPE EP test, we have demonstrated that the scientific X channel configuration with 40 bits for computation and memorization is required. For the drag free channels, fortunately the requirements are less stringent. Therefore, in order to reduce the computation load by saving the variables with 32 bits, an alternative algorithm which nullifies the amplification of the error through the biquad has been developed. The corresponding difference equations are:

$$\begin{aligned} u(n) &= (b_0-1)u(n) + (b_1-a_1)u(n-1) + (b_2-a_2)u(n-2) - a_1u(n-1) - a_2u(n-2) \\ y(n) &= x(n) + u(n) \end{aligned} \tag{2}$$

The advantage of this implementation is that the recursive filter is applied on an intermediate variable and therefore the amplification of the saving error through the filter does not concern the output y any more. With this method, the computation noise in the SCAA channel is also compatible with the specifications. Much care has been paid to verify the limitation of the aliasing of the high frequency noise of the loops at the EP frequency because of the heterodyne type detection of any violation signal in the experiment.

ELECTROSTATIC ACCELEROMETER WITH BIAS REJECTION FOR DEEP SPACE GRAVITATION TESTS

B. LENOIR*, B. CHRISTOPHE*, S. REYNAUD†
*Onera - The French Aerospace Lab
29 avenue de la Division Leclerc, F-92322 Châtillon, France
†Laboratoire Kastler Brossel (LKB), ENS, UPMC, CNRS
Campus Jussieu, F-75252 Paris Cedex 05, France

The trajectory of an interplanetary spacecraft can be used to test gravitation in the Solar System. Its determination relies on radio tracking and is limited by the uncertainty on the spacecraft non-gravitational acceleration. But the addition of an accelerometer on board provides another observable which measures the departure of the probe from geodesic motion.

Such a concept has been proposed for the OSS mission[3] which embarks the Gravity Advanced Package[6]. This instrument, which is the focus of this article, is designed to make unbiased acceleration measurements[7]. This proposal is in line with the Roadmap for Fundamental Physics in Space issued by ESA in 2010[4]. Indeed, there exist theoretical as well as experimental motivations to test gravitation in the Solar System. The fact that General Relativity is a classical theory while the three other fundamental interactions have a quantum description suggests that it is not the final theory for gravitation. From the experimental point of view, the existence of "dark matter" and "dark energy" may be interpreted as the inability of General Relativity to describe gravitation at cosmic scales[1]. And in the Solar System, the anomalous Pioneer signal[2,8] may be an experimental artifact as well as a hint of considerable importance for fundamental physics[5].

1 Presentation of the instrument

The Gravity Advanced Package is made of two subsystems: MicroSTAR, an electrostatic accelerometer which inherits mature technology developed at Onera, and the Bias Rejection System used to rotate MicroSTAR with respect to the spacecraft around one axis. MicroSTAR measures the non-gravitational acceleration of the satellite and the measurement noise is characterized by the following power spectrum density[6] (for a measurement range of 1.8×10^{-4} m.s^{-2}):

$$\sqrt{S_n(f)} = K = 5.7 \times 10^{-11} \text{ m.s}^{-2}.\text{Hz}^{-1/2} \times \sqrt{1 + \left(\frac{f}{4.2 \text{ mHz}}\right)^{-1} + \left(\frac{f}{0.27 \text{ Hz}}\right)^{4}}. \quad (1)$$

Thanks to the Bias Rejection System, which rotates the accelerometer of a monitored angle called θ, the quantities measured along the orthogonal axis y and z of the accelerometer are (assuming that there is no quadratic terms and the gain of the instrument is perfectly known)

$$\begin{cases} m_y = [\cos(\theta)a_Y + \sin(\theta)a_Z] + b_y + n_y & (2a) \\ m_z = [-\sin(\theta)a_Y + \cos(\theta)a_Z] + b_z + n_z & (2b) \end{cases}$$

with a_ν ($\nu \in \{Y; Z\}$) the components of the acceleration in the reference frame of the spacecraft, b_y and b_z the bias of MicroSTAR on each axis, and n_y and n_z the measurement noise.

2 Signal processing

Assuming that N measurements are made with a time step δt, there are $4N$ unknowns in equations (2) and only $2N$ measurements. Calling $\mathbf{x}$ the column vectors whose components are the values of x at each sampling time and using the linearity of the equations, it is however possible to retrieve from the measurements the values of the projection of $\mathbf{a_Y}$ and $\mathbf{a_Z}$ on a vector subspace defined by the columns of the matrix $V_a \in \mathcal{M}_{N,p_a}$ ($p_a < N$). If

$$V_a{}'\Lambda_\nu \mathbf{b}_\kappa = 0, \text{ with } \nu \in \{c; s\} \text{ and } \kappa \in \{\mathbf{y}; \mathbf{z}\}. \tag{3}$$

where $\Lambda_c = \mathrm{diag}[\cos(\theta_k)]$ and $\Lambda_s = \mathrm{diag}[\sin(\theta_k)]$ ($k \in ||1; N||$), then

$$\begin{cases} V_a'\mathbf{a_Y} = V_a'\Lambda_c\mathbf{m_y} - V_a'\Lambda_s\mathbf{m_z} & \text{(4a)} \\ V_a'\mathbf{a_Z} = V_a'\Lambda_s\mathbf{m_y} + V_a'\Lambda_c\mathbf{m_z} & \text{(4b)} \end{cases}$$

Assuming that the bias on each axis also belongs to a subspace defined by the matrix V_b, is is possible to design pattern for the rejection angle θ which fulfills conditions (3). This signal has a period called τ.

In addition to retrieving the unbiased non-gravitational acceleration of the spacecraft, this method allows characterizing the uncertainty on the demodulated quantities $V_a'\mathbf{a_Y}$ and $V_a'\mathbf{a_Z}$, given MicroSTAR noise power spectrum density (cf. eq. (1)). Assuming that $V_a \in \mathcal{M}_{N,1}(\mathbb{R})$ and $|V_a| = 1$, the precision on the quantities $V_a'\mathbf{a_Y}$ and $V_a'\mathbf{a_Z}$ is given by[7]

$$\int_{-\frac{1}{2\delta t}}^{\frac{1}{2\delta t}} S_n(f)\frac{|\mathcal{F}_{\delta t}\{\Lambda_c V_a\}(f)|^2 + |\mathcal{F}_{\delta t}\{\Lambda_s V_a\}(f)|^2}{\delta t^2}df \approx \frac{1}{\tau}S_n\left(\frac{1}{\tau}\right) \tag{5}$$

where $\mathcal{F}_{\delta t}$ is the Discrete Time Fourier Transform. One has to notice that the noise is selected, as expected, at the modulation frequency $1/\tau$.

3 Experimental validation

This demodulation scheme will be validated experimentally at Onera using a pendulum. A control loop allows controlling its inclination to the 10^{-9} rad level. It is possible to incline it at a known angle in order to simulate an external acceleration. On this pendulum, an accelerometer is mounted on a rotating stage. There are two goals for this experiment :

– Validate the demodulation scheme by showing that it properly separates the bias from the signal of interest allowing to make unbiased acceleration measurements.

– Verify the value of the uncertainty on $V_a'\mathbf{a_Y}$ and $V_a'\mathbf{a_Z}$ predicted by equation (5).

References

1. A. Aguirre *et al.*, *Class. Quantum Grav.* **18**, R223 (2001).
2. J.D. Anderson *et al.*, *Phys. Rev.* D **65**, 082004 (2002).
3. B. Christophe *et al.*, arXiv:1106.0132 (2011).
4. ESA, "Fundamental Physics Roadmap", available at http://sci.esa.int/fprat (08/23/2010).
5. M.T. Jaekel and S. Reynaud, *Mod. Phys. Lett.* A **20**, 14 (2005).
6. B. Lenoir *et al.*, arXiv:1011.6263 (2011).
7. B. Lenoir, B. Christophe and S. Reynaud, arXiv:1105.4979 (2011).
8. A. Lévy *et al.*, *Adv. Space Res.* **43**, 10 (2009).

Lorentz invariant phenomenology of quantum gravity: Main ideas behind the model

Yuri Bonder[a]
Instituto de Ciencias Nucleares, Universidad Nacional Autónoma de México
A. Postal 70-543, México D.F. 04510, México

In the past decade the phenomenology of quantum gravity has been dominated by the search of violations of Lorentz invariance. However, there are very serious arguments that led us to assume that this invariance is a symmetry in Nature. This motivated us to construct a phenomenological model describing how a Lorentz invariant granular structure of spacetime could become manifest. The proposal is fully covariant, it involves non-trivial couplings of curvature to matter fields and leads to a well defined phenomenology.

General relativity is currently the accepted theory of spacetime and gravity and its quantum version, which is still unknown, could involve a discrete structure of spacetime at microscopic (Planckian) scales. This non-trivial microstructure is generically known as spacetime granularity and the idea of studying its consequences empirically through Lorentz invariance violations (*i.e.*, by looking for a preferential reference frame) has received a great deal of attention. This is essentially because a naive granularity would take its most symmetric form in a particular reference frame. However, there are very serious experimental bounds on Lorentz invariance violations[1] and, moreover, the radiative corrections of a quantum field theory on a granular background that induces a preferential frame would magnify the effects of this granularity to a point where they would have been already detected[2].

This motivates us to assume that, if a spacetime granularity exists, it respects Lorentz invariance and we investigate if there is a phenomenological way to study its consequences. Since there is no intuitive way to imagine a discrete structure of spacetime which is Lorentz invariant, the proposal[3] is to use an analogy: Imagine a building made of cubic bricks and having, say, a pyramidal shape. Then it is possible to detect the incompatibility between the bricks and the building symmetry, for example, by looking the mismatch at the building's surface. Given that we assume that the symmetry of spacetime's building blocks is Lorentz invariance, according to the analogy, in regions where spacetime is not Lorentz invariant, namely, where the Riemann curvature tensor (R_{abcd}) does not vanish, it would be possible to detect the presence of this granularity. In other words, this analogy led us to assume that a Lorentz invariant spacetime granularity could manifest through couplings of matter and R_{abcd}.

For simplicity we only focus on fermionic matter fields (ψ) and since the Ricci tensor at x is determined by the matter energy-momentum tensor at x, to study a coupling of Ricci and the matter fields, at a phenomenological level, looks like a self-interaction. Thus we consider the Weyl tensor (W_{abcd}) which, loosely speaking, is R_{abcd} without Ricci. In addition, in order

[a]email: yuri.bonder@nucleares.unam.mx. In collaboration with A. Corichi and D. Sudarsky

to produce an effect that it is observable in principle, the Lagrangian coupling term involving W_{abcd} and fermionic matter fields should have mass dimensions five (we set $c = \hbar = 1$) so there is no need to divide it by more than one power of a mass which is taken to be proportional to Planck mass M_{Pl}. Since the only coupling term of these objects with dimension five vanishes[3], an alternative is sought. The idea is to use $\lambda^{(s)}$ and the (dimensionless) 2-forms $X^{(s)}_{ab}$ such that

$$W_{ab}{}^{cd} X^{(s)}_{cd} = \lambda^{(s)} X^{(s)}_{ab}. \tag{1}$$

Observe that s labels the different eigenvalues and eigen-forms of the Weyl tensor and it runs from 1 to 6. The first interaction Lagrangian (for one fermionic field) to be proposed[3] is

$$\mathcal{L}_f = \bar{\psi}\gamma^a\gamma^b\psi \sum_s \frac{\xi^{(s)}}{M_{Pl}} \lambda^{(s)} X^{(s)}_{ab}, \tag{2}$$

where $\xi^{(s)}$ are free dimensionless parameters and γ^a are Dirac matrices. Note that this interaction is fully covariant, however, it suffers from some ambiguities which have been cured[3,4] and that are briefly described:

- **Normalization**: The norm of the Weyl tensor's eigen-forms is not set by equation (1), thus, an additional condition to fix it must be given. The proposal is to use a pseudo-Riemannian metric on the space of 2-forms that can be constructed from spacetime metric[3]. The null eigen-forms are discarded since there is no way to normalize them, the rest are normalized to ± 1.

- **Degeneration**: The symmetries of the Weyl tensor imply that there is an unavoidable degeneration on all its eigen-forms. In fact, if we denote the spacetime volume element by ϵ_{abcd}, a generic eigen-form of the Weyl tensor, X_{ab}, has the same eigenvalue as $\epsilon_{ab}{}^{cd} X_{cd}$. Thus, one needs a criteria to discriminate between all the linear combinations of the degenerated 2-forms. The suggested alternative is to use the linear combinations Y_{ab} satisfying $\epsilon^{abcd} Y_{ab} Y_{cd} = 0$.

- **Sign**: Equation (1) and all the conditions listed above are insensible to the substitution of any Weyl eigen-form, X_{ab}, by $-X_{ab}$. Essentially, we have solved this ambiguity by introducing a new coupling term which is quadratic in the eigen-forms.

Finally, let us remark that, using the formalism of the Standard Model Extension[5] and other approximations, we have been able to obtain the non-relativistic Hamiltonian coming from this model which can be compared with experiments. Since only polarized matter is sensible to the effects predicted by the model, it is difficult to test it empirically, however, using data of Canè et al.[6] we have put bounds on some of the model's free parameters[4].

Acknowledgments This work and its presentation at the *Rencontres de Moriond and GPhyS Colloquium: Gravitational Waves and Experimental Gravity* was supported by CONACYT 101712 project.

References

1. S. Liberati and L. Maccione *Ann. Rev. Nucl. Part. Sci.* **59**, 245 (2009).
2. J. Collins, *et al.*, *Phys. Rev. Lett.* **93**, 191301 (2004).
3. A. Corichi and D. Sudarsky, *Int. J. Mod. Phys.* **D 14**, 1685 (2005).
4. Y. Bonder and D. Sudarsky, *Class. Quantum Grav.* **25**, 105017 (2008); *Rep. Math. Phys.* **64**, 169 (2009); *AIP Conf. Proc.* **1256**, 157 (2010).
5. V.A. Kostelecky and C. Lane, *J. Math. Phys.* **40**, 6245 (1999).
6. F. Canè, *et al.*, *Phys. Rev. Lett.* **93**, 230801 (2004).

TOWARDS AN ULTRA-STABLE OPTICAL SAPPHIRE CAVITY SYSTEM FOR TESTING LORENTZ INVARIANCE

M. NAGEL and A. PETERS

Humboldt-Universität zu Berlin, Institut für Physik, Newtonstr. 15, 12489 Berlin, Germany

We present a design for an ultra-stable cryogenically cooled sapphire optical cavity system, with fractional frequency stability better than 1×10^{-16} at one second integration time. We plan to use such ultra-stable cavities to perform a test of the isotropy of light propagation at the 10^{-20} level.

1 Motivation

Many experimental and technical applications, e.g. optical atomic clocks, demand ultra-stable cavity systems for laser frequency stabilization. Nowadays, the main limiting factor in frequency stability for room temperature resonators has been identified to be the displacement noise within the resonator substrates and mirror coatings due to thermal noise. Different approaches are being proposed right now to lower the influence of thermal noise, such as using higher order modes, longer cavities, or new types of coating materials. A straightforward method is to cool down the resonators to cryogenic temperatures. Following this approach, we will set up an advanced cryogenic optical resonator system using specially designed sapphire cavities with the goal to reach a relative frequency stability of better than 1×10^{-16} up to long integration times.

2 Next Generation Cryogenic Optical Cavity System

Two normally opposing requirements need to be matched in designing a cryogenic resonator and its mounting structure: high thermal conductivity towards the liquid helium bath and low mechanical coupling of the optical path length to vibrations. We used FEM computations to optimize the design of a resonator made of sapphire which reduces the influence of vertical and horizontal vibrations and at the same time features large thermal contact areas for the mounting structure (see Figure 1).

Calculations on the shot noise and thermal noise level show that the theoretical frequency stability at a temperature of 4.2K is in total an order of magnitude better than the best ever value obtained with an optical resonator system (see Figure 1). We will also implement novel measures to enhance the long term performance of the optical cavity system in order to maintain the potential relative frequency stability below 1×10^{-16} up to long integration times.

As a future perspective, we plan to exchange the Ta_2O_5/SiO_2 mirror coatings, which are the thermal noise limiting source for these cryogenic optical sapphire resonators, with monocrystalline coatings composed of $Al_xGa_{1-x}As$.[1] Those crystalline coatings will further reduce the stability limiting effects of thermal noise by more than an additional order of magnitude.

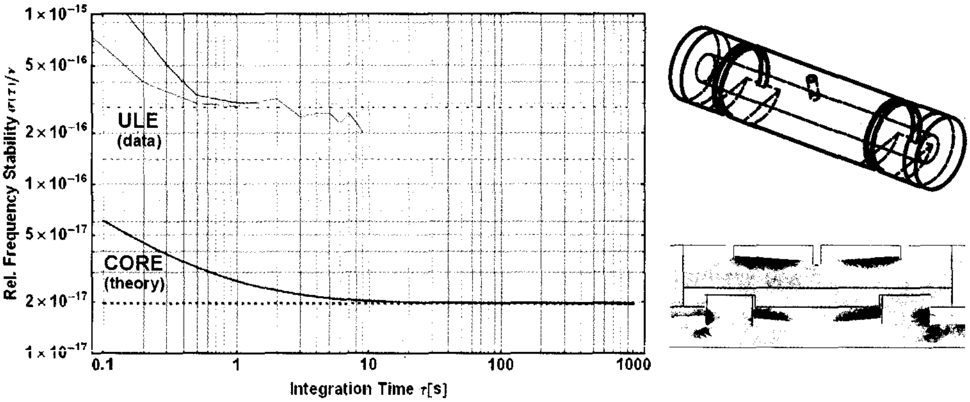

Figure 1: Left: Comparison of measured and predicted rel. freq. stability of the best room temperature (ULE, Young et. al [NIST 1999] green line and Jiang et. al [NIST 2010] orange line) and proposed cryogenic optical resonators (CORE, black line). The dashed lines show the theoretical thermal noise limit. Upper Right: Sketch of an optimized design for a CORE. Lower Right: FEM simulation of vertical vibration (gravitational) induced bending (deformation scaled up by a factor of 10^{10}).

3 Testing Lorentz Invariance

We plan to use the ultra-stable cavities to perform a laboratory-based test of Lorentz invariance - a basic principle of the theories of special and general relativity. While both theories developed by Einstein play an integral part in modern physics and in today's ordinary life, there have been claims that a violation of Lorentz invariance might arise within a yet to be formulated theory of quantum gravity.

The cavities will be arranged in a Michelson-Morley configuration and continuously rotated with a rotation period between 10s and 100s for more than one year using a custom-made high-precision low noise turntable system made of granite. The sensitivity of this setup to violations of Lorentz invariance should be in the 10^{-19} to 10^{-20} regime. This corresponds to more than a 100-fold improvement in precision of modern Michelson-Morley type experiments.[2]

Furthermore, ultra-stable cryogenic microwave whispering gallery resonators will be added to the experiment in collaboration with the University of Western Australia. With this co-rotating microwave and optical resonator setup we will be able to search for additional types of Lorentz violating signals.

References

1. G. D. Cole, I. Wilson-Rae, M. R. Vanner, S. Gröblacher, J. Pohl, M. Zorn. M. Weyers, A. Peters, and M. Aspelmeyer, "Megahertz monocrystalline optomechnaical resonators with minimal dissipation," *23rd IEEE International Conference on Microelectromechanical Systems*, (Hong Kong SAR, China, 24-28 January 2010), TP133.
2. S. Herrmann, A. Senger, K. Möhle, M. Nagel, E. V. Kovalchuk, and A. Peters, "Rotating optical cavity experiment testing Lorentz invariance at the 10^{-17} level," Phys. Rev. D 80, 105011 (2009).

THE SEARCH FOR PRIMORDIAL GRAVITATIONAL WAVES WITH SPIDER: A BALLOON-BORNE CMB POLARIMETER

CAROLINE CLARK FOR THE SPIDER COLLABORATION
Theoretical Physics, Blackett Laboratory,
Imperial College London, SW7 2AZ, England

SPIDER is a balloon-borne experiment designed to measure the polarisation of the cosmic microwave background (CMB) with high sensitivity in order to probe the energy scale of inflation. The flight is planned for the Austral summer of 2012-2013. The main aim of the experiment is to measure large-scale polarisation of the CMB in an attempt to detect the amplitude of primordial gravitational waves. SPIDER should detect their imprint in the CMB if the tensor-to-scalar ratio, r, is greater than 0.03. This requires minimisation of a variety of systematic effects and the development of powerful analysis techniques.

1 Polarisation

Both E-mode and B-mode polarisation is produced by gravitational waves from inflation, while density perturbations only produce E-mode polarisation. Thus the search for B-modes is important in determining whether inflation occurred. Measurement of the ratio of the tensor-to-scalar power spectra, r, would tell us the energy scale of inflation and restrict allowed inflationary models. SPIDER will be able to detect primordial gravitational waves if $r > 0.03$. Noise thresholds for WMAP, Planck and SPIDER overplotted on the theoretical BB power spectra can be seen in Figure 1.

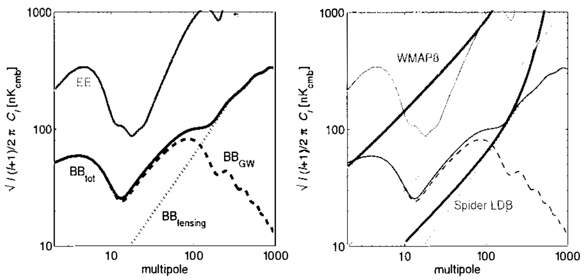

Figure 1: Left: Theoretical EE power spectrum and BB power spectra from both gravitational lensing and inflationary gravitational waves for r=0.1 Right: Noise thresholds derived from a Fisher analysis overlayed on the theoretical spectra for the WMAP, Planck and SPIDER experiments.

2 The Experiment

SPIDER will map approximately 10% of the sky with degree-scale resolution in three frequency bands: 90, 150 and 280GHz. This complements Planck by measuring at slightly smaller scales where polarised foregrounds are expected to present less of a problem.

The primary goals of SPIDER are the search for the primordial gravitational wave background through measurement of CMB polarisation and the characterisation of polarised Galactic foregrounds. The combination of Planck and SPIDER data will break degeneracies between various cosmological parameters, as shown in Figure 2.

The flight plan for SPIDER is a Long Duration Balloon (LDB) flight of about 30 days, from McMurdo, Antarctica during the Austral summer 2012-2013.

The size of datasets for current CMB experiments has outpaced the scaling of computational power predicted by Moore's law. SPIDER's Time Ordered Data (TOD) will be about 5 times larger than that of Planck HFI due to a combination of fast scanning, large arrays of detectors and a long duration flight.

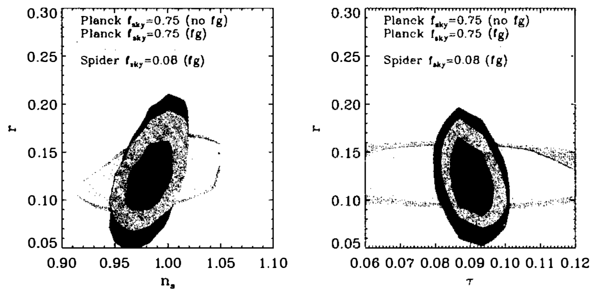

Figure 2: Contour plots showing 1 and 2 σ levels for (r, n_s) (left) and (r, τ) (right). The combination of Planck and SPIDER data breaks the (r, n_s) degeneracy and improves measurements of τ.

3 Conclusion

SPIDER has the sensitivity required to attempt to detect the signature of primordial gravitational waves in the CMB. It's frequency coverage will complement Planck and allow us to place stronger constraints on cosmological parameters. It will also allow characterisation of polarised Galactic foregrounds.

References

1. Spider Optimization II: Optical, Magnetic and Foreground Effects, D. T. O'Dea *et al*, arxiv:1102.0559v1
2. Spider Optimization: Probing the Systematics of a Large Scale B-Mode Experiment, C. J. MacTavish *et al*, arxiv:0710.0375
3. Spider: A Balloon-borne Large-scale CMB Polarimeter, B. P. Crill *et al*, arxiv:0807.1548

STRONG LENSING SYSTEM AND DARK ENERGY MODELS

B. MALEC
Copernicus Center for Interdisciplinary Studies, Gronostajowa 3,
30-387 Kraków, Poland

M. BIESIADA
Department of Astrophysics and Cosmology, Institute of Physics, University of Silesia, Uniwersytecka 4,
40-007 Katowice, Poland

Presently accelerating phase of cosmic expansion is a fundamental challenge to physics and cosmology. Cosmological concordance model (ΛCDM) although in agreement with a variety of data is not a fully satisfactory solution. There is very little theoretical guidance in which direction beyond ΛCDM should one go. One approach is to use very general phenomenology and look at the data for the evidence of evolving cosmic equation of state or the support for the contrary claim. Therefore every alternative cosmological test becomes valuable on its own. Strong gravitationally lensed systems create opportunity to test cosmological models of dark energy in a way alternative to Hubble diagrams (from SNIa or GRBs), CMBR or LSS.

1 Standard rulers versus standard candles

In this paper we would like to present our latest result concerning joint analysis involving data coming from standard rulers and standard candles, done on five contemporary cosmological scenarios. First part of our diagnostic tools makes use of the angular diameter distance, the rest use the luminosity distance. These are two distance concepts which, although theoretically related to each other, have clearly different systematic uncertainties and different parameter degeneracies. Hence their joint analysis is more restrictive in the parameter space.

As standard rulers we used in first place strong lensing systems, namely a combined sample of $n = 20$ constituents with good spectroscopic measurements of central dispersions from the SLACS [1] and LSD [2] surveys. Summary of data is given in Table 1 of paper [3]. In a method used here cosmological models enter through a distance ratio, so results are independent of Hubble constant value. We also used CMBR and Barion Acoustic Oscillation (BAO) data. The so-called shift parameter R, related to the position of the first acoustic peak in the power spectrum of CMBR is adopted from recent results of WMAP7 [4]. Convenient BAO scale measurement, often quoted in the form of distance parameter A, is an observable, well constrained by data at redshift $z = 0.35$. Its current value is taken from [5]. Data from supernovae Ia falls into category of standard candles. We use here the set of $n = 556$ supernovae [6], known as Union2 compilation.

We considered five cosmological scenarios of dark energy, widely discussed in current literature. These are ΛCDM, Quintessence, Chevalier-Polarski-Linder model, Chaplygin gas and Braneworld scenario. Models are parameterized by present density of matter Ω_m and coefficients in the effective equation of state of dark energy. Values are estimated by minimizing appropriate Chi-square function (for details see [3,7]).

Table 1: Fits to different cosmological models from combined standard rulers data (R+BAO+Lenses).

ΛCDM	$\Omega_m = 0.273 \pm 0.018$	$\chi^2 = 63.961$
Quintessence	$\Omega_m = 0.262 \pm 0.035$ $w = -1.066 \pm 0.188$	$\chi^2 = 63.829$
Chevalier-Polarski-Linder	$\Omega_m = 0.276 \pm 0.055$ $w_0 = -0.824 \pm 0.704$ $w_a = -0.757 \pm 2.148$	$\chi^2 = 63.961$
Chaplygin Gas	$\Omega_m = 0.273 \pm 0.018$ $A = 1.000 \pm 0.001$ $\alpha = -0.040 \pm 2.260$	$\chi^2 = 63.961$
Braneworld	$\Omega_m = 0.345 \pm 0.021$	$\chi^2 = 72.697$

Table 2: Joint fits from combined standard rulers data and standard candles (Union2 sample).

ΛCDM	$\Omega_m = 0.274 \pm 0.014$	$\chi^2 = 727.610$
Quintessence	$\Omega_m = 0.274 \pm 0.014$ $w = -1.004 \pm 0.048$	$\chi^2 = 727.603$
Chevalier-Polarski-Linder	$\Omega_m = 0.274 \pm 0.014$ $w_0 = -0.989 \pm 0.124$ $w_a = -0.082 \pm 0.621$	$\chi^2 = 727.584$
Chaplygin Gas	$\Omega_m = 0.274 \pm 0.014$ $A = 1.000 \pm 0.004$ $\alpha = -0.112 \pm 1.282$	$\chi^2 = 727.610$
Braneworld	$\Omega_m = 0.267 \pm 0.013$	$\chi^2 = 777.676$

2 Results

Results are presented in tables. The best fits we obtained for the model parameters in joint analysis turned out to be in agreement with corresponding joint analysis performed by other authors on different sets of diagnostic probes. However, this approach cannot tell us which model is the best. These sort of questions can be answered, in the simplest form, with the aid of information-theoretic criteria like the Akaike Criterion (AIC) and Bayesian Information Criterion (BIC). Effects of such consideration are presented in our paper [7].

Acknowledgments

This work was supported by the Polish Ministry of Science Grant no. N N203 390034.

References

1. T. Treu *et al*, Astrophys.J. **650**, 1219 (2006).
2. T. Treu, L. V. E. Koopmans, Astrophys.J. **611**, 739 (2004).
3. M. Biesiada, A. Piórkowska and B. Malec, M.N.R.A.S. **406**, 1055 (2010).
4. E. Komatsu *et al*, Astrophys.J.Sup. **192**, 18 (2011).
5. B. Reid *et al*, M.N.R.A.S. **404**, 60 (2010).
6. R. Amanullah *et al*, Astrophys.J. **716**, 712 (2010).
7. M. Biesiada, B. Malec and A. Piórkowska, R.A.A. **11**, 641 (2011).

CONSTRAINTS ON A MODEL WITH EXTRA DIMENSIONS FOR THE BLACK HOLE AT THE GALACTIC CENTER

A.F. ZAKHAROV

Institute of Theoretical and Experimental Physics, 117259 Moscow, Russia
Bogoliubov Laboratory of Theoretical Physics, Joint Institute for Nuclear Research, 141980 Dubna, Russia

Different ways to find signatures of extra dimensions are discussing in the literature. If the Randall–Sundrum II braneworld scenario is adopted then a metric of black holes may be different from a standard one and the Schwarzschild metric has to be changed with the Reissner – Nordström metric with a tidal charge. The model may be applied for the black hole at the Galactic Center. Since the Schwarzschild and Reissner – Nordström metrics are different for a significant charge one can expect that geodesics of bright stars near the black hole and their observed fluxes may be different for these metrics due to a difference in gravitational lensing. Therefore, a deviation from the Schwarzschild case flux may be measured for a significant charge and the signature of extra dimensions may found. However, as a theoretical analysis shows that a tidal charge has to be very close to zero and a suggested charge value which may lead to measurable flux deviations for S2 like stars (or their essential displacements or astrometrical lensing) is not consistent with observational constraints on a shadow size.

Theories with extra dimensions admit astrophysical objects (supermassive black holes in particular) which are rather different from standard ones. There were proposed tests which may help to discover signatures of extra dimensions in supermassive black holes since the gravitational field may be different from the standard one in the GR approach. So, gravitational lensing features are different for alternative gravity theories with extra dimensions and general relativity. Recently, Bin-Nun [1, 2, 3] discussed an opportunity that the black hole at the Galactic Center is described by the tidal Reissner– Nordström metric [4] which may be admitted by the Randall–Sundrum II braneworld scenario. Bin-Nun suggested an opportunity of evaluating the black hole metric analyzing (retro-)lensing of bright stars around the black hole in the Galactic Center. Doeleman et al. evaluated a minimal size of a spot for the black hole at the Galactic Center [5]. According to a theoretical consideration and simulations a minimal size of spot practically has to coincide with the shadow size [6, 7, 8].

Measurements of the shadow size around the black hole may help to evaluate parameters of black hole metric [9, 10]. Another opportunity to evaluate parameters of the black hole is an analysis of trajectories bright stars near the Galactic Center [11]. We derive an analytic expression for the black hole shadow size as a function of charge for the tidal Reissner– Nordström metric. We conclude that observational data concerning shadow size measurements are not consistent with significant negative charges, in particular, the significant negative charge $Q/(4M^2) = -1.6$ (discussed in [1, 2, 3]) is practically ruled out with a very probability (the charge is roughly speaking is beyond 9σ confidence level, but a negative charge is beyond 3σ confidence level).

It is known that a Reissner–Nordström metric cross-section for photons is described by the following relation [10, 12]

$$l = \frac{(8q^2 - 36q + 27) + \sqrt{(8q^2 - 36q + 27)^2 + 64q^3(1-q)}}{2(1-q)}, \tag{1}$$

where $\xi^2 = l, Q^2 = q$ (ξ and Q are impact parameter and the black hole charge in M units, M is the black hole mass). If $q = 0$, we obtain the well-known result for the Schwarzschild metric, namely $l = 27$. If we consider the extreme Reissner–Nordström metric ($q = 1$) then $l = 16$. A tidal charge corresponds generally to a negative q or to imaginary Q values.

We could apply these relations for the black hole at the Galactic Center assuming that the black hole mass is about $4 * 10^6 M_\odot$ and a distance toward the Galactic Center is about $8kpc$. In this case a diameter of shadow is about 52 μas for the Schwarzschild metric and about 40 μas for the extreme Reissner–Nordström metric.

Doeleman et al. evaluated a size of the smallest spot near the black hole at the Galactic Center such as 37^{+16}_{-10} microarcseconds at a wavelength of 1.3 mm with 3σ confidence level [5]. Theoretical analysis and observations show that the size of shadow can not be smaller than a minimal spot size at the wavelength [6, 7, 8, 9, 10]. Roughly speaking, it means that a small positive q is consistent with observations but a significant negative q is not. For $q = -6.4$ (as it was suggested by Bin-Nun [1, 2, 3]) we have a shadow size 84.38 μas. It means that the shadow size is beyond of shadow size with a probability corresponding to a deviation about 9σ from an expected shadow size. Therefore, a probability to have so significant tidal charge for the black hole at the Galactic Center is negligible. So, we could claim that the tidal charge is ruled out with observations and corresponding theoretical analysis.

Acknowledgments

AFZ thanks J. Dumarchez for his kind attention to this contribution.

References

[1] A. Y. Bin-Nun, *Phys. Rev.* D **81**, 123011 (2010).

[2] A. Y. Bin-Nun, *Phys. Rev.* D **82**, 064009 (2010).

[3] A. Y. Bin-Nun, arXiv:1011.5848 (2010).

[4] N. Dadhich, R. Maartens, Ph. Papadopoulos, V. Rezania, *Phys. Lett.* B **487**, 1 (2001).

[5] S. S. Doeleman et al., *Nature*, **455**, 78 (2008).

[6] H. Falcke, F. Melia, E. Agol, *Astrophys. J.*, **528**, L13 (2000).

[7] H. Falcke, F. Melia, E. Agol, in *Cosmic Exposions: Tenth Astrophysics Conference*, eds. W. W. Zhang & S. S. Holt, AIP Conference Proceedings, **522**, 317 (2000).

[8] F. Melia, H. Falcke, *Ann. Rev. Astron. Astrophys.*, **39**, 309 (2001).

[9] A. F. Zakharov, A. A. Nucita, F. De Paolis, G. Ingrosso, *New Astronomy*, **10**, 479 (2005).

[10] A. F. Zakharov, A. A. Nucita, F. De Paolis, G. Ingrosso, *Astron. & Astrophys.*, **442**, 795 (2005).

[11] A. F. Zakharov, A. A. Nucita, F. De Paolis, G. Ingrosso, *Phys. Rev.* D **76**, 062001 (2007).

[12] A. F. Zakharov, *Class. Quantum Grav.*, **11**, 1027 (1994).

Cosmological and solar-system constraints on tensor-scalar theory with chameleon effect

A. Hees[1,2], A. Füzfa[3]
[1] *Royal Observatory of Belgium, Avenue Circulaire 3, 1180 Bruxelles, Belgium, ahees@oma.be*
[2] *LNE-SYRTE, Observatoire de Paris*
[3] *naXys, University of Namur (FUNDP), Belgium*

General Relativity (GR) passed all solar system tests until now. However, cosmological observations are not directly compatible with GR and the standard model of elementary particles. A way of modifying gravity at large scale without doing any modification at solar system scale is achieved by the so-called Chameleon mechanism [1,2]. This mechanism appears in tensor-scalar theories of gravity with massive scalars. In this communication, we explore the sensitivity of chameleon mechanism by constraining its parameters by cosmic acceleration on cosmological scales and solar system constraints on small scales. This combined analysis will shed new light on the question whether modified gravity can be safely invoked to solve cosmological problems without any contradiction on Solar System scales.

Model

The model considered here is the one proposed by Khoury and Weltman [1,2] i.e. a tensor-scalar theory of gravitation with a runaway potential $V(\phi)$ (with $c = 1$):

$$S = \int d^4x\sqrt{-g}\left[\frac{m_p^2}{16\pi}R - \frac{m_p^2}{2}\partial_\mu\phi\partial^\mu\phi - V(\phi)\right] + S_M(\Psi_m, A^2(\phi)g_{\mu\nu}) \tag{1}$$

where R is the scalar curvature, m_p is the Planck mass ($m_p^2 = 1/G$) and $A(\phi)$ is a coupling function here given by $A(\phi) = e^{k\phi}$.

The action (1) is expressed in the so-called **Einstein frame**. This frame is useful for doing calculations but all the physical interpretations are easily done in the **Jordan frame** where matter is universally coupled to the metric $\tilde{g}_{\mu\nu} = A^2(\phi)g_{\mu\nu}$ [3,4]. Quantities expressed in Jordan frame are noted with a tilde and are directly observable.

The chosen potential is a Ratra-Peebles potential [5] parametrized by 2 constants α and Λ $V(\phi) = \frac{\Lambda^{4+\alpha}}{m_p^\alpha\phi^\alpha}$.

Cosmological evolution and constraints

Fields equations have been derived by introducing a Friemann-Lemaitre-Robertson-Walker Einstein-frame metric ($ds^2 = -dt^2 + a^2(t)dl^2$) and by replacing the Einstein frame matter density/pressure by the observable one (expressed in Jordan frame [3,4]: $\rho = A^4(\phi)\tilde{\rho}$, $p = A^4(\phi)\tilde{p}$).

By integrating the field equations, it can be seen on Fig. 1 that the universe acceleration is mainly explained by the potential (in green), although a significant contribution from non minimal coupling is present (in red).

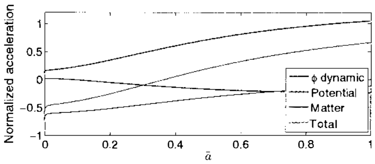

Figure 1: Factor producing universe acceleration

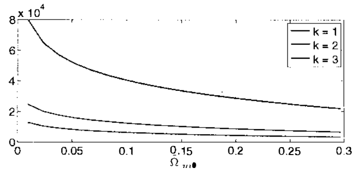

Figure 2: Thin-shell parameter ϵ for $\alpha = 0.5$

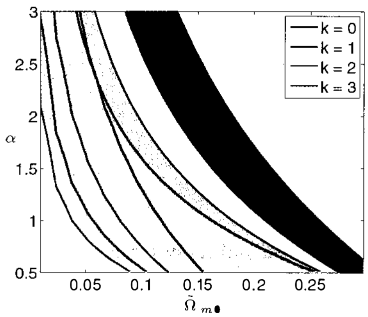

Figure 3: 2σ cosmological confidence region

A likelihood analysis has been performed on SNe Ia measurements (with the UNION dataset[6]) Each model is characterized by 3 parameters: k, α and $\tilde{\Omega}_{m0}$ (the actual matter density). The 2σ confidence region has been derived on Fig. 3. The area of the confidence region decreases when k increases and high coupling constants are excluded from the 1σ confidence region but accepted in the 2σ region.

3 Solar-systems constraint

The static spherical solution of equations deriving from action (1) representing the Sun has been derived by Khoury and Weltman [1] and by Tamaki and Tsujikawa [7]. The key parameter is the **thin-shell parameter** ϵ [1,2]. If $\epsilon << 1$, the effective scalar charge is reduced $k_{eff} = 3\epsilon k$. The γ PPN parameter can be in principle close to 1 even if k is not small ($\gamma = \frac{1-kk_{eff}}{1+kk_{eff}}$). If $\epsilon >> 1$, there is no scalar charge reduction and the theory is equivalent to Brans-Dicke with $k_{eff} = k$ and the current boundary [8] on γ implies $k^2 < 10^{-5}$. For model within the 2σ cosmological confidence region, $\epsilon >> 1$ (see Fig. 2) which means that this version of the chameleon effect can not be invoked to explain the gravity difference at small and large scales. More work taking into account higher order non-linearities in the scalar field are needed to go beoyond the present conclusion.

Acknowledgments

A. Hees is a research fellow from FRS-FNRS. Numerical simulations were made on the local computing resources (cluster URBM-SysDyn) at the University of Namur (FUNDP).

References

1. J. Khoury, A. Weltman, *Phys. Rev.* D **69**, 044026 (2004).
2. J. Khoury, A. Weltman, *Phys. Rev. Lett.* **93**, 171104 (2004).
3. T. Damour, K. Nordtvedt, *Phys. Rev.* D **48**, 3436 (1993).
4. T. Damour, G. Esposito-Farèse, *Class. and Quantum Grav.* **9**, 2093 (1992).
5. B. Ratra, P. J. E. Peebles, *Phys. Rev.* D **37**, 3406 (1988).
6. M. Kowalski. D. Rubin *et al*, *ApJ* **686**, 749 (2008).
7. T. Tamaki, S. Tsujikawa,*Phys. Rev.* D **78**, 084028 (2008).
8. B. Bertotti, L. Iess, P. Tortora, *Nature* **425**, 374 (2003).

The STAR Mission: SpaceTime Asymmetry Research

T. SCHULDT, A. KEETMAN, C. BRAXMAIER
University of Applied Sciences Konstanz, Brauneggerstr. 55, 78462 Konstanz, Germany

K. DÖRINGSHOFF, M. NAGEL, A. PETERS
Humboldt-University Berlin, Newtonstr. 15, 12489 Berlin, Germany

S. HERRMANN, C. LÄMMERZAHL
Center for Applied Space Technology and Microgravity, Am Fallturm, 28359 Bremen, Germany

T. V. ZOEST, H. DITTUS
DLR-Institute for Space Systems, Robert-Hooke-Str. 7, 28359 Bremen, Germany

U. JOHANN
Astrium GmbH – Satellites, Claude-Dornier-Straße, 88090 Immenstaad, Germany

S. BUCHMAN, K.-X. SUN, J. LIPA, R. BYER
Stanford University, Stanford, CA 94307, USA

B. JAROUX, P. WORDEN
NASA AMES research center, Moffett Field, California 94035-1000, USA

J. HALL
JILA, University of Colorado, UCB Campus, Boulder, Colorado 80309-0440, USA

M. ALMAJED, H. ALTWAIJIRY, T. AL-SAUD
King Abdulaziz City for Science and Technology, King Abdullah Road, Riyadh, 11442, Saudi Arabia

The proposed space mission STAR (SpaceTime Asymmetry Research) aims for significantly improved tests of fundamental space-time symmetry and the foundations of special and general relativity. A series of missions is planned where the first mission focuses on a Kennedy-Thorndike experiment. Later missions will additionally carry out Michelson-Morley experiments as well as precision measurements of gravitational redshift and Local Position Invariance. STAR targets an improvement of at least two orders of magnitude compared to previous experimental accuracy on ground.

The SpaceTime Asymmetry Research (STAR) program is a planned series of three missions testing special and general relativity. It is an international cooperative effort of teams with very strong background in experimental tests of relativity, their theoretical description and advanced space technology; the mission lead is carried out by Stanford University (USA). The first mission will perform a Kennedy-Thorndike (KT) experiment and measure the constancy (velocity invariance) of the speed of light to one part in 10^{19} and derive the KT coefficient of the Mansouri-Sexl test theory to $7 \cdot 10^{-10}$. The experiment will be carried out by comparing an absolute reference (baseline: a laser frequency stabilized to a transition in molecular iodine) with a highly stable resonator made e.g. from ULE (ultra low expansion) glass ceramics. Due to an orbital velocity of 7 km/s the sensitivity to a boost dependent violation of Lorentz invariance as modelled by the KT term in the Mansouri-Sexl test theory or a Lorentz violating extension of the standard model (SME) will be significantly enhanced as compared to Earth based experiments. Additional enhancement is obtained by low noise space environment. An overall improvement by a factor of approx. 100 – compared to current Earth-based experiments – is the goal.

The STAR mission program addresses three major goals: (i) perform tests of fundamental physics, (ii) develop small satellite and advanced instrumentation technology, and (iii) educate future scientists and engineers. A 180 kg small attitude, vibration and temperature controlled satellite is used as foundation for all three STAR missions. The power consumption of the whole spacecraft will be less than 185 W. The launch of STAR1 is foreseen for january 2018, the follow-on missions will be flown with an overlap with the previous mission by two to three years. The proposed orbit for STAR1 is a 650 km circular sun-synchronous orbit with a 2 year mission lifetime.

STAR1 Payload Concept

STAR1 will utilize an ultrastable molecular Iodine clock and crossed ULE cavities with a finesse > 100.000. Both clocks require a minimum frequency stability of $9 \cdot 10^{-16}$ at the orbit time of 5800 s. The cavities will be placed in an ultra-stable thermal environment with $\sim 1\,\mu$K stability using a six-stage thermal isolation system with active and passive control. Both clocks are realized in redundancy (2 molecular clocks and 4 cavities) mainly using commercially available components with high TRL for reducing risk and keeping costs low. The setup is fiber-coupled and realized in a modular configuration.

The four cavities are made out of one ULE block with a coefficient of thermal expansion of $\sim 10^{-9}\,K^{-1}$ within the operating temperature range 10 to 20°C. The four cavities are realized as two pairs of crossed cavities which are stacked such that the cavity axes of one pair are rotated by 45 degrees with respect to the other pair. This enables the investigation of systematic effects. The molecular clock is based on modulation transfer spectroscopy (MTS) of hyperfine transitions in molecular Iodine near 532 nm. The optical setup will be realized using thermally and mechanically highly stable materials such as Zerodur or ULE in combination with an appropriate assembly-integration technology.

The proposed baseline laser for STAR1 is an NPRO-type Nd:YAG laser at a wavelength of 1064 nm which is commercially available in a space qualified version providing output powers up to 1.5 W in combination with a space qualified fiber amplifier. For the frequency stabilization to Iodine, a frequency doubling of the laser to 532 nm with an output power of $\sim$20 mW is required.

ON THE MAXIMUM MASS OF DIFFERENTIALLY ROTATING NEUTRON STARS

A. Snopek[1], D. Gondek-Rosinska[1], I. Kowalska[2], L. Villain[3], M. Kucaba[1], M. Szkudlarek[1], M. Ansorg[4]
[1] *Institute of Astronomy, University of Zielona Góra, ul. Lubuska 2, 65-265 Zielona Góra, Poland*
[2] *Astronomical Observatory, University of Warsaw, Al Ujazdowskie 4, 00-478 Warsaw, Poland*
[3] *LMPT, Univ. F. Rabelais, 37200 Tours, France*
[4] *Theoretisch-Physikalisches Institut, Friedrich-Schiller-Universität Jena, Germany*

A binary neutron star merger leads to the formation of a massive differentially rotating neutron star (or strange star) or to the prompt collapse to a black hole. The gravitational wave signal should tell us whether a massive neutron star or a black hole is formed and should allow to put constraints on the (hot) neutron star equation of state. We study the effect of the degree of differential rotation and of the stiffness of the equation of state on the maximum mass of neutron stars. We numerically construct stellar models using a highly accurate relativistic code based on a multi-domain spectral method (Ansorg, Gondek-Rosinska, Villain. 2009). We find various types of configurations, which were not considered in previous works. mainly due to numerical limitations. Among other results, we obtain the largest increase of the maximum mass for moderately stiff equation of state and for these new types of solutions.

1 The maximum mass of neutron stars

For a given equation of state (EOS), the maximum mass ($M_{\mathrm{max,stat}}$) of **non-rotating** neutron stars (NSs) is uniquely determined by the Tolman-Oppenheimer-Volkoff equations and is found to be in the range 1.5-2.5 $M_\odot$. It was shown that rotation allows this maximum mass to be 17%-20 % larger for **rigidly** rotating NSs (Cook et al., 1994) and 34% larger for strange stars (Gondek-Rosinska et al., 2000; Gourgoulhon et al., 1999). It was also found that **differential** rotation can be much more efficient in increasing (by more than 60%) the maximum allowed mass, especially for moderately stiff EOSs (Baumgarte et al., 2000: Lyford et al., 2003).

2 Equation of state and rotation law

We construct relativistic models of differentially rotating NSs for broad ranges of the degree of differential rotation and of the maximal mass density (ρ_{max}). We assume a polytropic EOS, $P = K\rho^\gamma$, where P is the pressure, ρ the mass density, $K = 1$ the polytropic constant and γ the polytropic index. We consider EOS with three different indices (and consequently stiffness): soft ($\gamma = 1.5$), moderately soft ($\gamma = 2$) and stiff ($\gamma = 3$), in order to study both the effect of the stiffness of the EOS and of differential rotation on the maximum mass. We adopt the rotation law introduced by Komatsu et al. (1989) which is parametrized by Ω_c, the angular velocity on the rotation axis, and by a parameter R_0, which measures the degree of differential rotation. We rescale R_0 in terms of the equatorial radius R_e and use $A^{-1} = R_e/R_0$ (for rigid rotation $R_0 \to \infty$ and $A^{-1} = 0$). Hence, the higher A^{-1}, the higher the degree of differential rotation.

3 Results and conclusions

Following Baumgarte et al. (2000), for given EOS and A^{-1} we construct sequences of fixed maximal mass density (in the range 0.01 to 0.6) parametrized by the ratio of the polar to the equatorial radius $r = R_p/R_e$. Then for each sequence we look for the maximum mass and finally for the maximum of those maxima. Four types of sequences turn out to be useful to define. From $A^{-1} = 0$ up to a first threshold value $A^{-1} = A_A$, we find only one type of spheroidal stars (so called **type A**). For $A^{-1} > A_A$ but smaller than a critical value A_C (which depends on $\rho_{\max}$ and on the EOS), we find **types A or B** sequences of differentially rotating stars. For $A^{-1} > A_C$ only **types C or D** stars exist. All types of solutions are described below (see Ansorg, Gondek-Rosinska & Villain 2009 for details):

- **type A** start at a static and spherical body and end at the mass-shedding limit. They exist for all considered EOSs:
- **type B** start at the mass-shedding limit and terminate at $r = 0$ if we restrict calculations to configurations with a spheroidal topology. They exist only for $r < 0.3$;
- **type C** start at a static and spherical body and end at $r = 0$ (for spheroidal topology);
- **type D** both start and end at the mass-shedding limit and exist for a very narrow range of A^{-1}. We shall not consider this type in our paper.

In the literature only type A and type C (with some limitations) sequences were considered.

For small polytropic index ($\gamma = 1.5$) we don't find type B or C sequences, up to $A^{-1} = 2$, while for moderate and stiff EOSs ($\gamma = 2$ and 3), all types mentioned above exist.

We find that differential rotation is very effective in increasing the maximum mass. Independently on the stiffness of the EOS the value of $M_{max,rot}/M_{max,stat}$ is a decreasing function of A^{-1} for sequences of type B and C and an increasing one for type A. The largest increase of the maximum mass is for the polytropic EOS with $\gamma = 2$ and for type B and C sequences of stars. The maximum value of the ratio is 4 reached at $A^{-1} \sim 0.4$ for type B and 2.55 at $A^{-1} \sim 0.8$ for type C. For type A, the maximum value of the ratio is obtained for $\gamma = 2$ at $A^{-1} \sim 0.7$, and $\gamma = 3$ at $A^{-1} \sim 0.4$. In both cases the maximal masses are larger than the maximum mass of the corresponding nonrotating star by over 70%. This confirms the results of Baumgarte et al. (2000) and Lyford et al. (2003).

Acknowledgments

This work was supported by the EGO-DIR-102-2007; the FOCUS 4/2007 Program of Foundation for Polish Science, the Polish grants NN 203 511 238 and DPN/N176/VIRGO/2009, by CompStar a Research Networking Programme of the European Science Foundation and by the Associated European Laboratory "Astrophysics Poland-France"

References

1. Ansorg M., Gondek-Rosinska D., Villain L., *MNRAS* **396**, 2359-2366 (2009)
2. Baumgarte T.W., Shapiro S.L., Shibata M., *ApJL* **528**, L29-L32 (2000).
3. Cook G.B., Shapiro S.L, Teukolsky S.A. , *ApJ* **422**, 227-242 (1994).
4. Gondek-Rosinska D., *et al.*, *A&A* **359**, 143-147 (2000).
5. Gourgoulhon *et al.*, *A&A* **349**, 851-862 (1999).
6. Komatsu H., Eriguchi, Y., & Hachisu, I.,*MNRAS* **237**, 355 (1989)
7. Lyford *et al*, *ApJ* **583**, 410-415 (2003).

Measurement of slow gravitational perturbations with gravitational wave interferometers.

A.V.Gusev, V.N.Rudenko. I.S.Yudin
Sternberg Astronomical Institute of Moscow State University, Universitetsky pr., 13,, Moscow, Russia

Measurement of quasistatic gravity field variations using data of laser gravitational wave interferometers is discussed. New method of taking data at the free spectral range frequency is analized besides a direct read out the mirror correction voltage. Calculated values of geophysical signals are compared with observation at the LIGO interferometer.

Geophysical measurements as a by-product of GW interferometers were discussed early in papers[1,2,3] Such possibility arises because there is no a seismic and gravitational isolation of the interferometer test mass-mirrors at very low (quasi static) frequencies $f < 1$ Hz. First practical steps were performed by VIRGO collaboration during the VSR-1, VSR-2 series [4]. It was a direct measurement of arm deformation through the error signal of control circuits keeping the interferometer operational point (mirror coordinate and angular positions). Typical accuracy of the mirror coordinate fixation in Virgo setup $10^{-12}m$ or $\delta L/L \sim 10^{-16}$. Thus the tidal arm displacement amplitude at 3 km $100\mu km$ or $\delta L/L \sim 10^{-8}$ can be measured with enough high precision. So with this accuracy one can dream about the registration of very weak geodynamical perturbation like the "liquid core daily resonance", "inner core oscillation" etc. More over it was seemed reasonable to investigate a direct measurement of the relativistic gravitational effects like a light frequency shift and time travel delay using GW interferometers located at the Earth surface.

A new method of tidal perturbation measurement was demonstrated during LIGO S5 series. For long base interferometers the circulation (or free spectral range) frequency is so low ($10^4 kHz$) that the correspondent component appeares at the main differential (GW-signal) output. The effect of tidal amplitude modulation of this harmonic was discovered during the S5 LIGO scientific run [5,6]. A mechanism of such modulation obviously has to be associated with a shtocastic luminosity of the FP arm optical mode neighbor with the resonance one. However a calculated estimate of modulation index is ocurred to be in disagreement with the observed values.

Under the supposition that mirrors are fixed by control circuits (arm lengths are kept as constant) a direct interaction of the optical pump with tidal gravity variations is considered as a main reason of optical length changes. In the paper [7] the gravitational photon frequency shift was used for this purpose, meanwhile the refractive index equivalent to the gravity field was explored in [8]. Numerically both effects leads to the same relativistic correction of optical arm length. Calculation was carried out following the simplified scheme of GW interferometer presented at the picture (recycling mirror is omitted) including the data readout procedure. FP arms are considered as complex resonant mirrors. Spectrum of one mode resonant pump with the central frequency $\nu_0 \sim 3 \cdot 10^{14}$Hz was presented by narrow line of phase fluctuation in a few Hz width accompanied by a small spectral density pedestal of amplitude fluctuation having the width $\Delta\nu \sim 100$kHz.Thus a neighbour FP cavity mode $\nu_1 = \nu_0 + \nu_{fsr}$ shifted at the free spectral range $\nu_{fsr} = 2c/L$ is also illuminated with a small intensity so as for the 4 km arm $\nu_{fsr} \sim 37$ kHz.

The light waves at frequency close to resonance modes of arms interfere with the following phase difference:

$$\delta\varphi \simeq \frac{1}{1-r}\left(\frac{2\Delta L}{L} + \frac{4L}{\lambda}\frac{\delta n}{n}\right)$$

where $\Delta L/L$ is static shift due to arm lengths difference, $\delta n/n$ is dynamical shift due to refractive index variation equivalent of tidal gravity changes.

Output signal $\sim \delta\varphi$ contains permanent and variable parts. Estimate of the modulation index in term of power (or amplitude) has resulted in $\delta P/P \sim 3 \cdot 10^{-4}$ meanwhile the observable index was much larger $\sim 2 \cdot 10^{-2}$. Thus the relativistic effect can not explain the observable tidal modulation of the harmonic at free spectral range frequency.

More rigorous analysis (performed after critics) required a taking into account the stochastic excitation a second neighbour mode symmetrical in respect of the carrier [9]. The result was unexpected one: an influence of the second (symmetrical) neighbour mode compensated the parametrical excitation produced by the first one. Output residual noise variance now contained only quadratic term of arm optical length variations in contrast with the previous result.

It is possible to reconstruct the "linear response" refusing from the condition of '"dark spot" at the main interferometer output (at practice the "dark spot" can be realized only with finite accuracy). Then introducing a detuning δl, i.e. passing to the condition of "gray spot", one can get the output noise variance in the form:

$$\sigma^2 \simeq \frac{\text{Const}}{1-r}\left[\left(\frac{2L}{\lambda}\right)^2\left((1-r)\frac{2\delta l}{L} + \delta\xi\right)^2 + \left(\frac{\Delta L}{L}\right)^2\right]$$

The time variable value in this formula is $\delta\xi$. Its ratio to the maximal permanent term gives an estimate of the signal modulation index at free spectral range frequency:

$$\mathrm{m} \simeq \frac{L\delta\xi}{(1-r)\delta l}$$

Numerical estimates are the following. For the relativistic effect hypothesis: $\delta\xi \sim 10^{-19}$, even for unrealistic tuning $\delta l \sim 10^{-4}\lambda$; the estimate of modulation index m$\sim$0.04% is two order of value less the observable one. In the case of residual (noncompensated) arm differential displacements $\delta\xi \sim 10^{-15}$ (less the control accuracy) a reasonable detuning $\delta l = 10^{-2}\lambda$ results in m$\sim$4% that is in a good agreement with the observation.

Radical method for the linear parametric response reconstruction would be a using the two mode pump at neighbour frequencies ν_0 and $\nu_1 = \nu_0 + \nu_{fsr}$; the "dark spot" condition has to be kept for the mode ν_0. A residual part of the mode ω_1 interacting at photo diode with radio sideband ν_1 will produce directly at the Pound-Drever mixer output a low frequency signal I(t) proportional to the optical length variations δl. A possibility of application this method for a registering weak global geodynamical effects as well as the detection of very low frequency GW has to be addressed.

Conclusions

It was demonstrated that VIRGO can be used as a two coordinate very long base strain meter. Geophysical signal reads out from drivers controlling the interferometer operation point.

However the quality of the data strongly depends on a number of locking brake during the observational time.

Up to now the idea of relative angular variations of mirror's plumb lines for a sensing pure gravity perturbations was not realized and has to be tested in nearest future.

LIGO team demonstrated the possibility of tidal gravity registration through a specific method of read out the correspondent information in the main interferometer output at the FSR radio frequency.

It is seemed that the parametric mechanism provided such possibility is associated with the residual arm deformations beyond the control accuracy. However details of this phenomenon has to be studied more closely in respect of its application in geodynamical measurements.

1. Kopaev A.V.,Rudenko V.N., *JETP Lett* **59**, 661 (1994)
2. Rudenko V.N.,*Phys. Lett.* A **223**, 421 (1996)
3. Grishchuk L.,Kulagin V.,Rudenko V.et al.*Class&Quantum Gravity.* **22**, 245 (2005)
4. Gusev A.V.,Manukin A.B.,Rudenko V.N. et al.*Measurement Technique* **52**, 3 (2009)
5. Meliessinos A.,(Talk at MG-12 Paris, July 12-18, (2009) http://xxx.lanl.gov/PS, cache/arxiv/pdf/1001/1001.558 v.2.pdf.)
6. Forrest C.V., Tidal Effects on Laser Gravitational Wave Detectors, Thesis Univ. of Rorester,LIGO Document P09 0000 v1 (2009).
7. Forrest C., Meliessinos A. Technical Note LIGO-T0900507-V3-2 (22/03/2010)
8. Gusev A.V., Rudenko V.N. *JETP Letters* **91**, 10 (2010)
9. Gusev A.V., Rudenko V.N., Yudin I.S.,*Measurement Technique* **59**, 4 (2011) (english trans. Springer Science+Business Media)

Spikes in Gravitational Wave Radiation from Quickly Rotating Galactic Centers

Avetis Abel Sadoyan
Astronomical Rechen Institute, Heidelberg, and Yerevan State University, Department of Physics, 1 Alex Manoogian street, Yerevan 375025, Armenia

Rainer Spurzem
Astronomical Rechen Institute, Heidelberg, and National Astronomical Observatory Beijing

Peter Berczik
Astronomical Rechen Institute, Heidelberg, and National Astronomical Observatory Beijing

We report a work in progress: calculation of Gravitational wave radiation parameters for galaxy models based on N-body simulations. Magnetic fields during the simulations are neglected, only evolution of galactic centers depending on self-gravitation is traced. Gravitational wave frequencies are calculated for the whole timescale of evolution changing in the ultralow frequency band from 10^{-13} to 10^{-10} Hz, average amplitudes are around 10^{-22}. We had calculated the total energy flax from the galaxy (Gravitational Luminosity) over all frequency band and had found unexpectadly large energy spikes. We speculate that sources of such spikes could be those stars that are kicked out by the central binary with velocities enough to leave the galaxy, we also underline that largest spikes are observed in the time period near to the end of simulation..

1 Introduction

Sources of gravitational radiation at ultra-low frequencies are galaxies, active Galactic Nuclei, star clusters, i.e. configurations with enormously large quadruple moments and large relaxation times. Method of self-similar oscillation induced gravitational wave radiation [6] is used to calculate main parameters of gravitational radiation. This method is giving maximal possible values , upper limits for gravitational radiation. We had examined possible gravitational wave radiation from galaxies containing central engine [3], initially rotating as a solid body with given rotational velocity. The initial distribution of stars in galaxy was taken according Aarseth [1]. The evolution for galaxies containing 25000(25k), 50k and 100k elements is done on supercomputers with GRAPE [4] at Heidelberg. During the evolution of the galaxy a bar instability in galaxy was formed which gave additional contribution to oblationes to ellipsoidal form of galaxy making overall gravitational wave radiation from galaxy stronger.

Energy of gravitational radiation from Galaxy

We had calculated the total energy flax from the galaxy (Gravitational Luminosity) over all frequency band and found large energy spikes in Gravitational Luminosity of Galaxies. We considered a supermassive black hole in the center of the galaxy. Such Binaries are formed in galaxy mergers, but their long-term evolution is uncertain, in spherical galaxies. N body evolution shows that binary evolution stalls at separations much too large for significant emission of gravitational waves [3]. Unless the binary mass ratio is large, dynamical friction rapidly brings the binary into a separation of an order of 1 pc, when the central engine start to act like a "hard binary", ejecting passing stars with velocities large enough to leave the galaxy [3 5]. In the used simulations of galaxy evolution with super massive black holes a long term evolution of massive binary is followed in more realistic, triaxial and rotating galaxy models, where binary stalls only in initial phases of evolution, while a binary hardening with rates sufficient to allow close coalescence can be observed later, approximately in 10 Gyear. [3] Our simulations were made up to 25010^{13}s or around 1 Gyear.

Overall intensity of gravitational wave radiation from galaxy in all frequency domain is investigated. Unexpected spikes in Gravitational wave radiation with maximum 10^4 over the average are found. Spikes are becoming more intense with hardening of central binary. This spikes in gravitational luminosity may be conditioned by stars that are kicked out by the central binary. Kicked stars may have very large velocities[3] enough to leave the galaxy, and we speculate that when they pass the perihelion of their orbit, a spike in gravitational wave radiation energy is occurring . Largest spikes are observed in the time period near to the end of evolution, because initial conditions in N-body model do not let stars to approach central binary quickly, stars needs some time to come close to central binary to be accelerated. The existence of spikes in gravitational wave luminosity, if confirmed experimentally can be a direct evidence of existence of stars ejected from the galaxies by central binary.

Discussions

The question of changes of inner structure of ejected stars accelerated by central engine to velocities high enough to leave the galaxy, is not considered in the scope of N-body problem, stars are considered point masses. Changes in star structure, possible mass losses or even destruction of the star can put additional limitations on the existence of spikes in GW radiation. N-body simulations of galaxy evolution were done in Newtonian limits, post-Newtonian simulations are also done[2], showing that the picture of development of bar instabilities in galaxies are becoming sharper, so we expect that the appearance of spikes in gravitational radiation energy from galaxies will also be observed in post-Newtonian models, may be spikes would be sharper.

Acknowledgments

One of the authors, SA, acknowledges DAAD grant in scope of which the visit to ARI was organised .

References

1. Aarseth S. J.*Gravitational N body simulations* (Cambridge:Cambridge press) 2003.
2. I.Berentzen, M.Preto, p.Bertzik, D.Mrrit, R.Spurzem *Astrophys.J.* **695**, 455 (2009).
3. Peter Berczik, D.Merritt ,R. Spurzem, Hans-Peter Bischof*Efficient Merger of Binary super-massive black holes in nonaxisymmetric Galaxies*, The Astrophysical Journal **642**, L21-L24 (2006).
4. J.Makino, T.Fukushige and M.Koga *Grape-6:Massivly Parallel Special purpose computer for Astrophysical particle simulations* Publ.Astron.Soc.Japan **55**, , (1163), 2003.
5. Makino J., Funato Y.*ApJ.* **602**, 93 (2004)
6. Sadoyan A.A. *Gravitational Radiation of superdense objects from incompressible matter*, *Astrophysics* **49**, 243 (2006).

Kick Processes in the Merger of Two Black Holes

R. F. Aranha[1,2], I. Damião Soares[1] and E. V. Tonini[3]
[1] *Centro Brasileiro de Pesquisas Físicas, Rio de Janeiro 22290-180, Brazil,*
[2] *Center for Relativistic Astrophysics, Georgia Institute of Technology, Atlanta, GA 30332, USA,*
[3] *Instituto Federal do Espírito Santo, Vitória 29040-780, Brazil.*

We examine the gravitational wave recoil and associated kick processes in the post-merger phase of a head-on collision of two black holes, based on the Bondi-Sachs characteristic formulation. The impulse imparted on the merged system by the momentum flux carried out by gravitational waves generates kicks and antikicks associated, respectively, to an initial acceleration phase and a final dominant deceleration phase. Both kick V_k and antikick V_{ak} velocities satisfy the post-Newtonian Fitchett's law, with the net antikick velocity $(V_{ak} - V_k)$ having a maximum of $\simeq 102$ km/s at a symmetric mass ratio $\eta \simeq 0.205$. In a suitable inertial frame the final center-of-mass motion of the merged system is approximately the net antikick velocity.

This communication reports the results of Aranha et al.[1] where we have examined the production of kicks velocities by gravitational wave recoil in the post-merger phase of two head-on colliding black holes. Our treatment is made in the realm of Robinson-Trautman (RT) spacetimes with initial data given by

$$K(u_0,\theta) = \Big(\frac{1}{\sqrt{\cosh\gamma + \cos\theta\sinh\gamma}} + \frac{\alpha}{\sqrt{\cosh\gamma - \cos\theta\sinh\gamma}}\Big)^2, \tag{1}$$

where α is the ratio of the ADM masses of the two initial colliding black holes with initial infalling velocity $v = \tanh\gamma$ along the z axis. The data (1) is evolved from the characteristic surface initial data u_0 via the RT dynamics; the final configuration is a boosted Schwarzschild black hole along the z axis.[a] The momentum extraction and the associated recoil along the z axis, due to the emission of gravitational waves by the system, is given by the Bondi-Sachs conservation law[3] $dP^z(u)/du = P^z_W(u)$, where

$$P^z_W(u) = \frac{1}{8}\int_{-1}^{1} \frac{s\,(1-s^2)^2}{K}\Big(\frac{K''}{K} - \frac{2K'^2}{K^2}\Big)^2 ds \tag{2}$$

is the net flux of momentum carried out by the gravitational waves emitted at a time u, this net flux being directed along the z-axis. A prime denotes s-derivative where $s = \cos\theta$. We note that $P^x_W(u) = P^y_W(u) = 0$. In Fig. 1 (Left) we plot $P^z_W(u)$ for $\gamma = 0.5$ and several values of the mass ratio α. For all α we have an initial phase, up to $u = u_k$ (where $P^z_W(u_k) = 0$), that corresponds to an acceleration of the merged system. It is followed by a dominant deceleration regime with $P^z_W(u) < 0$, $u_k < u < u_f$, where u_f corresponds to the final configuration when the gravitational wave emission is considered to have ceased. The impulse imparted to the system in a time u is given by $I^z_W(u) = \int_{u_0}^{u} P^z_W(u')du'$. Specifically the total impulse imparted by gravitational waves (i) during the initial acceleration phase is $I^z_W(u_k)$ and (ii) during the following deceleration phase is $-(I^z_W(u_k) - I^z_W(u_f))$. The impulses in each phase corresponds, respectively, to a kick velocity $V_k = c\, I^z_W(u_k)/M_{\rm rem}$ (initial acceleration phase) and an antikick velocity $V_{ak} = c\,(I^z_W(u_k) - I^z_W(u_f))/M_{\rm rem}$ (final dominant deceleration phase), where $M_{\rm rem}$ is the

[a] Our numerical code is based on the Galerkin and collocation methods: for details of its accuracy and longtime stability see Aranha et al.[2] and references therein.

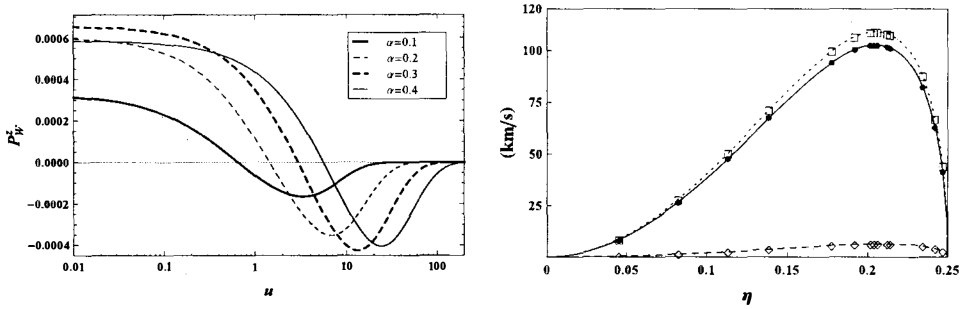

Figure 1: (Left) Linear-log plot of the net momentum flux $P^z_W(u)$ carried out by gravitational waves for several values of mass ratio parameter α. (Right) The distribution of kick velocities associated with the gravitational wave recoils: kicks due to the initial accelerated phase (diamonds), antikicks due to the dominant deceleration phase (squares) and the net antikicks (black dots). The lines are the best fit of Fitchett η-scaling law derived from post-Newtonian estimates (cf. Ref. 1). All the maxima are located approximately at the value $\eta \simeq 0.205$.

rest mass of the remnant black hole. We also define a net antikick velocity $(V_{ak} - V_k)$. In Fig. 1 (Right) we plot the kick velocities V_k, V_{ak} and their difference $(V_{ak} - V_k)$ (net antikick) as a function the symmetric mass parameter $\eta = \alpha/(1+\alpha)^2$. The curves correspond to the best fit of the points to Fitchett's post-Newtonian law[4] $V = A\eta^2(1-4\eta)^{1/2}(1+B\eta) \times 10^3$ km/s, with all maxima at $\eta \simeq 0.205$, consistent with post-Newtonian and full numerical relativity estimates of mergers of inspiral black hole binaries.[5] The maximum of the net antikick $(V_{ak} - V_k)$ is $\simeq 103$ km/s. For a larger initial infalling velocity, say for $\gamma = 0.7$, we obtain substantially larger values $(V_{ak} - V_k) \simeq 527$ km/s also located at $\eta \simeq 0.205$.

Finally from the analysis of the gravitational wave recoil[1] we obtain that the center-of-mass velocity of the merged system is given by $v_{\rm cm}(u) = (M_B(u_0)v_{in} + I^z_W(u))\,(1-v_f^2)^{1/2}/(M_{\rm rem})$, where v_f is the final velocity of the remnant and v_{in} is the ratio of the initial Bondi-Sachs momentum $P^z(u_0)$ to the initial Bondi mass $M_B(u_0)$. By construction $v_{\rm cm}(u_0) \simeq v_{in}$ and $v_{\rm cm}(u_f) = v_f$. For an inertial frame with velocity v_{in} (relative to a rest frame at infinity) we have that $v_{\rm cm}(u_f) \simeq -(V_{ak} - V_k)$.

References

1. R. F. Aranha, I. Damião Soares and E.V. Tonini, *Phys. Rev.* D **82**, 104033 (2010).
2. R. F. Aranha, I. Damião Soares and E.V. Tonini, *Phys. Rev.* D **81**, 104005 (2010).
3. H. Bondi, M.G.J. van der Berg, and A. W. K. Metzner, *Proc. R. Soc. London* **A 269**, 21 (1962); R.K. Sachs, *Proc. R. Soc. London* **A 270**, 103 (1962); R.K. Sachs, *Phys. Rev.* **128**, 2851 (1962).
4. M.J. Fitchett, Mon. Not R. Astron. Soc. **203**, 1049 (1983).
5. A. Le Tiec, L. Blanchet, and C.M. Will, *Class. Q. Grav.* **27**, 012001 (2010); J.A. González, U. Sperhake, Brügmann, M. Hannam, and S. Husa, *Phys. Rev. Lett.* **98**, 091101 (2007).

COSMOLOGY MODELS AND GRAVITON COUNTING IN A DETECTOR

A.W. BECKWITH
Chongquing university department of physics 400044, Chonquing, PRC abeckwith@uh.edu

Initial relic entropy growth is presented We talk of how to count it as gravitons per unit phase space, and use it as an extension of gravitons interacting with a magnetic field of a GW detector. We use it for obtaining values for choosing between cosmology models

1 Introduction

We start off with perturbative electromagnetic power flux, i.e. what was called $\overset{(1)}{T}{}^{uv}$ in terms of a nonzero graviton rest mass, in a detector, in an uniform magnetic field, i.e. what if we have curved space time with say an energy momentum tensor of the electro magnetic fields in GW fields as

$$T^{uv} = \frac{1}{\mu_0} \cdot \left[-F^{\mu}_{\alpha} F^{\nu\alpha} + \frac{1}{4} \cdot g^{\mu\nu} F_{\alpha\beta} F^{\alpha\beta} \right] \tag{1}$$

Li *et al*[1] state that $F_{\mu\nu} = F^{(0)}_{\mu\nu} + \widetilde{F}^{(1)}_{\mu\nu}$, with $\left| \widetilde{F}^{(1)}_{\mu\nu} \right| \ll \left| F^{(0)}_{\mu\nu} \right|$ will lead to

$$T^{uv} = \overset{(0)}{T}{}^{uv} + \overset{(1)}{T}{}^{uv} + \overset{(2)}{T}{}^{uv}. \tag{2}$$

The 1st term to the right hand side of Eq. (2) is the energy–momentum tensor of the back ground electro magnetic field, and the 2nd term to the right hand side of Eq. (1) is the first order perturbation of an electro magnetic field due to gravitational waves. The above Eq. (1) and Eq. (2) lead to Maxwell equations as $\frac{1}{\sqrt{-g}} \cdot \frac{\partial}{\partial x^{\nu}} \cdot \left(\sqrt{-g} \cdot g^{\mu\alpha} g^{\nu\beta} F_{\alpha\beta} \right) = \mu_0 J^{\mu}$ as well as $F_{[\mu v,\alpha} = 0$.

2 Making Sense of the Following Current Term Behavior

Eventually, with GW affecting the above two equations, we have a way to isolate $\overset{(1)}{T}{}^{uv}$. If one looks at if a four-dimensional graviton with a very small rest mass included,[2] we can write

$$\frac{1}{\sqrt{-g}} \cdot \frac{\partial}{\partial x^{\nu}} \cdot \left(\sqrt{-g} \cdot g^{\mu\alpha} g^{\nu\beta} F_{\alpha\beta} \right) = \mu_0 J^{\mu} + J_{\text{effective}}, \tag{3}$$

where for $\varepsilon^{+} \neq 0$ but very small

$$F_{[\mu v,\alpha} \sim \varepsilon^{+}. \tag{4}$$

The claim which A. Beckwith made is that

$$\boldsymbol{J}_{\text{effective}} \simeq \boldsymbol{n}_{\text{count}} \cdot \boldsymbol{m}_{\text{4-D Graviton}}. \tag{5}$$

As stated by Beckwith, in $m_{\text{4-D Graviton}} \sim 10^{-65}$ g, n_{count} is the number of gravitons which are in the detector. What Beckwith, and Li, intend to do is to try to isolate out an appropriate $\overset{(1)}{T}{}^{uv}$ assuming nonzero graviton rest mass. From there, the energy density contributions of $\overset{(1)}{T}{}^{uv}$, i.e. $\overset{(1)}{T}{}^{00}$ can be isolated and reviewed in order to obtain values of Eq. (5), which can be used to interpret Eq. (3) $\overset{(1)}{T}{}^{00}$. We then go to the following metric standard.

3 Taming Incommensurate Metrics, to Make Measurements

$$h_0^2 \Omega_{\text{GW}} \sim 10^{-6} \tag{6}$$

Next, we will commence to note the difference and the variances from using $h_0^2 \Omega_{\text{GW}} \sim 10^{-6}$ as a unified measurement which will be in the different models discussed. We will next give several of our considerations as to early universe geometry which we think are appropriate as to Maggiore's[3] treatment of both wavelength, strain, and Ω_{GW}. To begin with, look at Maggiores Ω_{GW} formulation, strain, which ties in with the 10 to the 14 power increase as to wavelength from pre-Planckian physics to 1–10 GHz inflationary GW frequencies. We proceed to look at how the conclusions factor in with information exchange between different universes. We begin with the following, with h_c a critical sensitivity value.

Table 1: Managing GW generation from pre-Planckian physics.

$h_c \leq 2.82 \times 10^{-33}$	$f_{\text{GW}} \sim 10^{12}$ Hz	$\lambda_{\text{GW}} \sim 10^{-4}$ m
$h_c \leq 2.82 \times 10^{-29}$	$f_{\text{GW}} \sim 10^{8}$ Hz	$\lambda_{\text{GW}} \sim 10^{0}$ m
$h_c \leq 2.82 \times 10^{-25}$	$f_{\text{GW}} \sim 10^{4}$ Hz	$\lambda_{\text{GW}} \sim 10^{1}$ km

4 Conclusion

Table 2 table has rich sources of information we will develop further in relic GW astronomy.

Table 2: Variance of the Ω_{GW} parameters as given by the following models.

Relic pre-Big Bang	QIM	Cosmic String Model	Ekpyrotic
$\Omega_{\text{GW}} \sim 6.9 \times 10^{-6}$	$\Omega_{\text{GW}} \sim 10^{-6}$	$\Omega_{\text{GW}} \sim 4 \times 10^{-6}$	$\Omega_{\text{GW}} \sim 10^{-15}$
when $f \geq 10^{-1}$ Hz	1 GHz $< f <$ 10 GHz	$f \sim 10^{-6}$ Hz	10^7 GHz $< f < 10^8$ GHz
$\Omega_{\text{GW}} \ll 10^{-6}$		$\Omega_{\text{GW}} \sim 0$	$\Omega_{\text{GW}} \sim 0$
when $f < 10^{-1}$ Hz		otherwise	otherwise

References

1. F. Li, *et al*, "Can we observe the high frequency gravitational waves from the big bang and the extra dimensions?" paper in preparation for submission to *Science Magazine.*
2. A.W. Beckwith, "Addressing Strength of GW Radiation Affected by Additional Dimensions", http://vixra.org/abs/1103.0067.
3. M. Maggiore, *Phys. Rep.* **331**, 283 (2000).

Transverse, traceless, plane fronted, monochromatic plane waves in conformal gravity have zero-energy

Luca Fabbri[1,2]
M. B. Paranjape[1]
[1] *Groupe de physique des particules, Département de physique, Université de Montréal, C.P. 6128, succ. Centre-ville, Montréal, Québec, Canada H3C 3J7*

[2] *Theory Group, I.N.F.N. & Department of Physics, University of Bologna, Via Irnerio 46, C.A.P. 40126, Bologna, Italy*

Plane fronted, monochromatic gravitational waves on a Minkowski background are considered in conformal gravity. Assuming the conformal gauge condition Det $[g^{\mu\nu}] = -1$ and the conformal generalization of the harmonic gauge condition $|g|^{-1/4}\partial_\tau(|g|^{1/4}g^{\sigma\tau}) = 0$ implies that the waves are both transverse and traceless. We show, without any perturbative approximation that the metric is reducible to the metric of Minkowski space-time via additional coordinate transformations that preserve the gauge conditions. This implies that the waves are simply coordinate/conformal artifacts. As a consequence, they carry no energy.

1 Conformal gravity plane waves

Conformal gravity with matter is defined by the Lagrange density

$$\mathcal{L} = C_{\alpha\mu\sigma\rho}C^{\alpha\mu\sigma\rho} + k\mathcal{L}^{\text{matter}} \tag{1}$$

where $C_{\alpha\mu\sigma\rho}(x)$ is the Weyl conformal tensor, which gives rise to the field equations

$$W_{\mu\nu} = -\frac{k}{4}T^{\text{matter}}_{\mu\nu} \tag{2}$$

where $W_{\mu\nu}$ is the Bach conformal tensor

$$W_{\mu\nu} = \nabla^2 R_{\mu\nu} - \frac{1}{3}\nabla_\mu\nabla_\nu R - \frac{1}{6}g_{\mu\nu}\nabla^2 R + 2R^{\alpha\beta}(R_{\beta\nu\alpha\mu} - \frac{1}{4}g_{\mu\nu}R_{\alpha\beta}) - \frac{2}{3}R(R_{\mu\nu} - \frac{1}{4}g_{\mu\nu}R) \tag{3}$$

and k is a constant related to the gravitational constant and $T^{\text{matter}}_{\mu\nu}$ is the energy-momentum tensor of the matter fields.

1.1 *Transverse, traceless, plane fronted, monochromatic plane waves*

We consider fluctuations of the form

$$g^{\mu\nu} = \eta^{\mu\nu} + \epsilon^{\mu\nu}F(k\cdot x) \tag{4}$$

where $k\cdot x \equiv k_\mu x^\mu = \omega(t-x)$, ω a constant frequency, and where the propagation vector is to be light-like (see for example [1]).

We must impose two gauge conditions,

$$-\frac{1}{|g|^{1/4}}\partial_\mu(|g|^{1/4}g^{\mu\rho}) = 0. \tag{5}$$

to fix coordinate transformations [2] and

$$g = -1 \tag{6}$$

which fixes the possibility to perform any conformal transformations. We find this requires

$$[g^{\mu\nu}] = [\eta^{\mu\nu}] + [\epsilon^{\mu\nu}]F = [\eta^{\mu\nu}] + \begin{pmatrix} \epsilon & \epsilon & b & c \\ \epsilon & \epsilon & b & c \\ b & b & 0 & 0 \\ c & c & 0 & 0 \end{pmatrix} F. \tag{7}$$

This result is valid exactly, no perturbative assumption was made. The further coordinate transformation, and this is our new contribution,

$$x'^\mu = x^\mu + \epsilon^\mu \Phi(kx) \tag{8}$$

with

$$[\epsilon^\mu] = -\frac{1}{2}\begin{pmatrix} \epsilon \\ \epsilon \\ 2b \\ 2c \end{pmatrix} \tag{9}$$

respects the two gauge conditions and the form of the metric ansatz, if $\Phi(y) = \int^y dzF(z)$, the indefinite integral of F, and brings the metric given in Eq. (4) to $\eta_{\mu\nu}$, the flat Minkowski metric. The energy-momentum tensor for our waves, is identically zero:

$$\begin{aligned} T^{\text{gravity}}_{\mu\nu} &= (\partial^2 R^{\text{linear}}_{\mu\nu} - \nabla^2 R_{\mu\nu}) - \tfrac{1}{3}(\partial_\mu\partial_\nu R^{\text{linear}} - \nabla_\mu\nabla_\nu R) - \tfrac{1}{6}(\eta_{\mu\nu}\partial^2 R^{\text{linear}} - g_{\mu\nu}\nabla^2 R) - \\ &\quad -2R^{\alpha\beta}(R_{\beta\nu\alpha\mu} - \tfrac{1}{4}g_{\mu\nu}R_{\alpha\beta}) + \tfrac{2}{3}R(R_{\mu\nu} - \tfrac{1}{4}g_{\mu\nu}R) = 0 \end{aligned} \tag{10}$$

2 Conclusions

We cannot conclude from the analysis here that the full Weyl gravity does not contain gravitational waves. Waves of the form

$$g^{\mu\nu} = \eta^{\mu\nu} + B^{\mu\nu} n\cdot xF(k\cdot x) \tag{11}$$

do carry energy and momentum. Surprisingly, standard transverse, traceless monochromatic gravitational waves do not exist in conformal gravity. For full details please see the article [4].

Acknowledgments

We thank NSERC of Canada for financial support and the Perimeter Institute for Theoretical Physics, Waterloo, Canada for their hospitality, where this paper was finalized. We thank P. D. Mannheim, R. B. MacKenzie and P. R. Giri for useful discussions. We also thank Jacques Dumarchez and the organizers of Moriond 2011 for a stimulating and interesting meeting.

References

1. S. Weinberg, "Gravitation and cosmology" (John Wiley and Sons, New York, 1972).
2. P. D. Mannheim, *Progress in Particle and Nuclear Physics* **56**, 340 (2006).
3. P. D. Mannheim, *Gen. Rel. Grav.* **43**, 703 (2011).
4. L. Fabbri and M. B. Paranjape, arXiv:0812.2491 [gr-qc], to be published Phys. Rev. D.

Gravitational wave recoil in nonsymmetric Robinson-Trautman spacetimes

Rodrigo P. Macedo
Max-Planck-Institut für Gravitationsphysik, Albert Einstein Institut, Potsdam, Germany, and Theoretical Physics Institute, University of Jena, 07743 Jena, Germany

Alberto Saa
Departamento de Matemática Aplicada, UNICAMP, 13083-859 Campinas, SP, Brazil

We present some preliminary results on the gravitational recoil due to gravitational wave emission in the context of nonsymmetric Robinson-Trautman spacetimes. As in the axisymmetric case, regular initial data evolve generically into a final configuration corresponding to a Schwarzschild black-hole moving with constant speed. If the initial data is symmetric under reflection by a given plan, the remnant black-hole velocity must be parallel to this plan. In particular, for the case of completely reflection-symmetric initial configurations, the remnant black-hole velocity vanishes and the final configuration can be determined exactly from the initial data as in the axisymmetric case.

1 Introduction

We have recently [1] presented an analysis of the recoil due to gravitational wave emission [2] in the context of axisymmetric Robinson-Trautman (RT) spacetimes. Several physically relevant situations can be described by axisymmetric spacetimes. We mention, in particular, the cases corresponding to the evolution of the Brill-Lindquist initial data [3], which can be interpreted as the frontal collision of two black-holes [4,5]. Clearly, however, realistic physical applications demand the analysis of nonsymmetric situations.

We are now extending our previous analysis [1] to nonsymmetric RT spacetimes. We are particulary interested in approximated or "empirical" formulas relating the recoil velocity and the initial data [6], which could have potential application to the problem of the merging process of binary black-holes, where asymmetrical gravitational wave emission is known to make the merger remnant to recoil with velocities up to several thousands of km/s [7]. Our idea is to introduce an efficient full numerical approach based in the Galerkin spectral method to analyze the non-linear regime of the nonsymmetric Robinson-Trautman equations, and we expect to show that the direction and modulus of the recoil velocity can indeed be estimated with good accuracy from the initial data with fairly modest computational resources.

The Robinson-Trautman partial differential equation has been analyzed numerically in the recent literature [8,9,10,11]. The axisymmetric approach presented in [1] includes some improvements on the Galerkin method implementation of Oliveira and Soares [10,11] which has allowed us to get simpler equations and a better overall accuracy. Nevertheless, as we will see, computational complexity issues prevent us of applying the Galerkin method of [1] directly to the nonsymmetric case. A full-numerical approach with some intermediate projections is mandatory for the nonsymmetric case.

2 Nonsymmetric Robinson-Trautman spacetimes

The standard form of the RT metric in the usual spherical radiation coordinates (u, r, θ, ϕ) reads [12]

$$ds^2 = -\left(K - 2\frac{m_0}{r} - r(\ln Q^2)_u\right) du^2 - 2dudr + \frac{r^2}{Q^2}d\Omega^2, \tag{1}$$

where $Q = Q(u, \theta, \phi)$, m_0 is a constant mass parameter, and $d\Omega^2$ and K stand for, respectively, the metric of the unit sphere and the gaussian curvature of the surface corresponding to $r = 1$ and $u = u_0$ constant, which is given by $K = Q^2\left(1 + \frac{1}{2}\nabla^2_\Omega \ln Q^2\right)$, with ∇^2_Ω corresponding to the Laplacian on the unit sphere. Vacuum Einstein's equations for the metric (1) implies the Robinson-Trautman non-linear partial differential equation [12]

$$6m_0\frac{\partial}{\partial u}\left(\frac{1}{Q^2}\right) = \nabla^2_\Omega K. \tag{2}$$

The stationary solution of (2) are such that $\nabla^2_\Omega K = 0$, which implies, since we are restricted to a compact surface spanned by the coordinates (θ, ϕ), that K is constant. In our case, this implies that the surface corresponding to $r = 1$ and $u \to \infty$ is the unity sphere. In particular, we have the following asymptotic solution for $Q = Q(u, \theta, \phi)$

$$Q_\infty(\theta, \phi) = \frac{1 + v_x \sin\theta\cos\phi + v_y \sin\theta\sin\phi + v_z\cos\theta}{\sqrt{1 - v^2}}, \tag{3}$$

with $v^2 = v_x^2 + v_y^2 + v_z^2$ being the speed of the remanent Schwarzschild black hole.

Acknowledgments

This work was supported by FAPESP, CNPq, and DAAD.

References

1. R. P. Macedo and A. Saa, Phys. Rev. D **78**, 104025 (2008).
2. W. B. Bonnor and M. A. Rotenberg, Proc. R. Soc. Lond. A. **265**, 109 (1961); A. Peres, Phys. Rev. **128**, 2471 (1962); J.D. Bekenstein, Astrophys. J. **183**, 657 (1973);
3. D. R. Brill and R. W. Lindquist, Phys. Rev. **131**, 471 (1963).
4. O. M. Moreschi and S. Dain, Phys. Rev. D **53**, R1745 (1996).
5. R.F. Aranha, H.P. de Oliveira, I.D. Soares, and E.V. Tonini, Int. J. Mod. Phys. **D17**, 55 (2008).
6. K. S. Thorne, Rev. Mod. Phys. **52**, 299 (1980); L. E. Kidder, Phys. Rev. D **52**, 821 (1995); M. Campanelli, C. O. Lousto, Y. Zlochower, and D. Merritt, Astrophys. J. **659**, L5 (2007); C. O. Lousto, Y. Zlochower, Phys. Rev. D **77**, 044028 (2008); C. O. Lousto, Y. Zlochower, gr-qc/0805.0159; S. H. Miller, R.A. Matzner, arXiv:0807.3028.
7. J.A. Gonzalez, M. Hannam, U. Sperhake, B. Brugmann, and S. Husa, Phys. Rev. Lett. **98**, 231101 (2007); M. Campanelli, C.O. Lousto, Y. Zlochower, D. Merritt, Phys. Rev. Lett. **98**, 231102 (2007).
8. R. Gomez, L. Lehner, P. Papadopoulos, and J Winicour, Class. Quantum Grav. **14**, 977 (1997); O. Moreschi, A. Perez, and L. Lehner, Phys. Rev. D **66**, 104017 (2002).
9. D. A. Prager and A. W.-C. Lun, J. Austral. Math. Soc. Ser. B **41**, 271 (1999).
10. H.P. de Oliveira and I.D. Soares, Phys. Rev. D **70**, 084041 (2004).
11. H.P. de Oliveira and I.D. Soares, Phys. Rev. D **71**, 124034 (2005).
12. H. Stephani, D. Kramer, M. MacCallum, C. Hoenselaers, E. Herlt, *Exact Solutions of Einstein's Field Equations*, Second Edition, Cambridge University Press, 2002.

Modification of atomic states in a vertical optical trap near a surface

R. Messina, S. Pelisson, M.-C. Angonin, P. Wolf
LNE-SYRTE, Observatoire de Paris, CNRS UMR8630, UPMC
61 avenue de l'Observatoire, 75014 Paris, France

The problem of the modification of the atomic states in a vertical optical trap near a surface is discussed. The surface acts as a boundary condition modifying the shape of the ordinary Wannier-Stark states. Moreover, the Casimir-Polder interaction between atom and surface must be taken into account, resulting in a shift of atomic energy levels. This is done by introducing an effective model describing the finite size of the atom. The experimental observability of Casimir-Polder corrections is finally briefly discussed.

1 Introduction and physical system

Several theories aiming at unifying gravity and quantum mechanics predict the existence of deviations from Newton's law of gravity at different length scales. Two experiments have been recently proposed to study non-Newtonian gravitation in the micron and submicron range [1,2], based on interferometric measurements on atoms trapped in a vertical optical lattice in proximity of a surface. Their main idea is to combine the refined control of position typical of atomic traps with the high precision of interferometric frequency measurements. Before discussing the observability of non-Newtonian gravitation (see the companion paper, S. Pelisson et al., in these proceedings), a precise knowledge of the atomic states in this configuration is mandatory. In particular, it is important to know how the energy levels and states of the trap are influenced by the presence of the surface. This problem is addressed in this paper, where the influence of the surface acting as a boundary condition and of the Casimir-Polder interaction is investigated.

To this aim we consider a two level atom (with $|g\rangle$ and $|e\rangle$ representing its ground and excited states respectively) in presence of earth's linear gravitational potential and of the electromagnetic field. Moreover, the atomic position is controlled by means of an optical trap produced by reflection of a laser on the surface $z = 0$. Our complete Hamiltonian reads

$$H = H_0 + H_{\text{int}} = H_{\text{f}} + H_{\text{at}} + H_{\text{WS}} + H_{\text{int}} \qquad H_{\text{f}} = \sum_p \int_0^{+\infty} dk_z \int d^2\mathbf{k}\, \hbar\omega\, a_p^\dagger(\mathbf{k}, k_z) a_p(\mathbf{k}, k_z)$$
$$H_{\text{at}} = \hbar\omega_0 |e\rangle\langle e| \qquad H_{\text{WS}} = \frac{p^2}{2m} + mgz + \frac{U}{2}(1 - \cos(2k_l z)) \qquad H_{\text{int}} = -\boldsymbol{\mu}\cdot\mathcal{E}(\mathbf{r}). \tag{1}$$

where the *free* term H_0 includes the Hamiltonian of the electromagnetic field in standard second quantization, the atomic two-level term H_{at} as well as the external atomic Hamiltonian, sum of kinetic energy and external gravitational and optical potentials. Finally, the Hamiltonian includes an atom-field interaction term H_{int}, written here in multipolar coupling [3]. The analytic expression of the quantized electric field in presence of a perfectly conducting surface in $z = 0$ can be found in[4]. For an atom in absence of external potentials, the atom-field interaction term is usually treated using time-independent perturbation theory with respect to $H_{\rm at} + H_{\rm f}$ (the atomic position z is only an external parameter). This calculation leads to a position-dependent atom-surface potential usually known as Casimir-Polder (CP) potential[3]: this interaction energy is purely quantum, and it behaves as z^{-3} (z^{-4}) for atom-surface distances much smaller (larger) than the typical atomic transition wavelength (generally of the order of 100 nm). In our case, because of the presence of external potentials, the coordinate z as well must be treated as a quantum operator. As a consequence, before tackling the perturbative calculation, we need a description of the unperturbed eigenstates of the free Hamiltonian H_0.

2 Modified Wannier-Stark states

The eigenstates of a particle in a potential sum of a periodic and a linear term are the so-called Wannier-Stark states [5]. It is well known that the addition of a linear potential breaking the periodicity of the system produces a localization on the Bloch states: in particular the band structure is still defined, but for each band a discrete ladder of states is introduced. Two successive states of the ladder are separated by a constant energy gap (the gravitational-energy difference between the centers of the wells) and their wavefunctions are connected by a translation of the optical period $\lambda_l/2$ (in this sense, each state is said to be *centered* on a given well of the optical trap). A generic eigenstate will be noted with $|n, b\rangle$, b and n being the indices associated to Bloch band and well respectively. Nevertheless, whereas in the standard Wannier-Stark problem the coordinate z is defined over the whole real axis, in our case we must take into account the impenetrability of the surface: this is done here by means of the boundary condition $\psi(z = 0) = 0$. We will define the new class of states obtained in this context as *modified Wannier-Stark states*[6]. We show in figure 1 the shape of the first three modified wavefunctions of the first band. All the numerical applications correspond to the experiment FORCA-G[6], where $U = 3E_r$, being $E_r = \hbar^2 k_l^2/2m$, evaluated for a ^{87}Rb atom and with $\lambda_l = 532\,\text{nm}$. Moreover, the atomic coordinate z is expressed in units of period $\lambda_l/2$. The figure shows that increasing

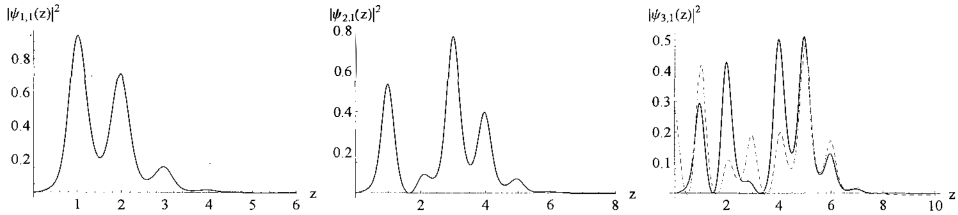

Figure 1: Density probability of modified Wannier-Stark states $\psi_{n,1}(z)$ for $n = 1, 2, 3$ and $U = 3$. The last function (solid line) is compared to the corresponding standard Wannier-Stark state (dashed line).

the well index n makes the modified wavefunctions approach the ordinary one, i.e. far from the surface the quasi-periodicity of the system is reestablished. The gap between successive eigenvalues tends as well to the expected one ($mg\lambda_l/2 \simeq 0.070068E_r$) by increasing the value of n[6]: the energy difference $E_2 - E_1$ is $0.12302E_r$, while we already have $E_9 - E_8 \simeq 0.070070E_r$.

3 Generalized perturbative approach to CP corrections

The presence of the surface also modifies the mode structure of the electromagnetic field, resulting in a force on the atom. This effect can be calculated using static perturbation theory. Our unperturbed state will be the eigenstate $|\psi\rangle = |0_p(\mathbf{k}, k_z)\rangle|g\rangle|n, 1\rangle$ of H_0 appearing in (1), where the field is in its vacuum state. Second-order perturbation theory is needed: H_{int} can connect $|\psi\rangle$ to any intermediate state having one photon in a given mode, while the atom can occupy any well of any band being nevertheless necessarily in its excited internal state. We then obtain

$$\Delta E_{n,1} = -\sum_p \int_0^{+\infty} dk_z \int d^2\mathbf{k} \sum_{s=1}^{+\infty} \sum_{b=1}^{+\infty} \frac{\left|\langle n,1|\langle g|\langle 0_p(\mathbf{k},k_z)|H_{\text{int}}|1_p(\mathbf{k},k_z)\rangle|e\rangle|s,b\rangle\right|^2}{E^{(0)}_{s,b} - E^{(0)}_{n,1} + \hbar(\omega + \omega_0)} \tag{2}$$

where $E^{(0)}_{s,b}$ is the unperturbed external atomic energy associated to the s-th well of the b-th Bloch band. It can be shown [6] that for our physical system the correction (2) approximately equals the average on the state $|n,1\rangle$ of the standard CP potential. This interaction energy is theoretically known for a neutral atom having dynamical polarizability $\alpha(\omega)$, at an arbitrary temperature $T > 0$ and for a surface having arbitrary dielectric properties [3]. Since each wavefunction of interest $\psi_{n,1}(z)$ tends to zero linearly in z for $z \to 0$ and the CP potential behaves as z^{-3} near the origin, each correction $\Delta E_{n,1}$ is indeed divergent. Nevertheless, the z^{-3} behaviour is a consequence of treating the atom as pointlike and can be corrected by replacing it with a probability distribution $\rho(\mathbf{r})$ different from zero over a spherical volume [7]. In this case, for any atomic effective radius R and choice of the probability distribution, the potential energy shows, a z^{-1} behaviour near the origin. This property regularizes our energy correction. The new CP potential (to be averaged on the $|n,1\rangle$ state in order to obtain the energy shift) is itself obtained from the average over $\rho(\mathbf{r})$ of the standard potential $V_{\text{CP}}(z)$. The energy corrections to each well can now be evaluated, after choosing an effective radius and a probability distribution. We present in table 1 the results (in the case of a perfectly conducting surface) for the first twelve wells for a uniform distribution over a sphere having the effective radius $R = 235$ pm [8]. From the

Table 1: Absolute value (in units of Hertz) of the CP energy corrections (they are all changed in sign) to the first 12 modified Wannier-Stark states for $U = 3$. The notation $a[b]$ corresponds to $a \times 10^b$.

n	$\Delta E_{n,1}$	n	$\Delta E_{n,1}$	n	$\Delta E_{n,1}$	n	$\Delta E_{n,1}$	n	$\Delta E_{n,1}$	n	$\Delta E_{n,1}$
1	1.88[5]	3	9.37[4]	5	2.26[4]	7	1.51[3]	9	5.34[1]	11	6.76
2	1.38[5]	4	5.31[4]	6	6.80[3]	8	2.79[2]	10	1.47[1]	12	4.14

table we see that, in virtue of the absolute precision of approximately 10^{-4} Hz in the frequency measurement, the energy shift due to the CP interaction is detectable up to at least the twelfth well. Two measurement schemes can be imagined. A first one is at short distances (say less than 5 μm) where the validity of the model can be tested: this would at the same time allow to give an estimation of the effective radius. A second one is at larger distances, for example between 5 and 10 μm, where the influence of regularization is below the experimental sensitivity: in this case, since the CP correction is still experimentally detectable (at 10 μm we have $V_{\text{CP}} \simeq 0.06$ Hz), we would obtain a measurement of the electrodynamical effect.

References

1. P. Wolf et al., Phys. Rev. A **75**, 063608 (2007).
2. F. Sorrentino et al., Phys. Rev. A **79**, 013409 (2009).
3. S. Scheel and S. Y. Buhmann, Acta Phys. Slov. **58**, 675 (2008) (and references therein).
4. G. Barton, J. Phys. B **7**, 2134 (1974).
5. M. Gluck, A. R. Kolovsky, and H. J. Korsch, Phys. Rep. **366**, 103 (2002).
6. R. Messina, S. Pelisson, M.-C. Angonin, and P. Wolf, Phys. Rev. A **83**, 052111 (2011).
7. G. Compagno, R. Passante, and F. Persico, Europhys. Lett. **7**, 399 (1988).
8. J. C. Slater, J. Chem. Phys. **41**, 3199 (1964).

TORSION PENDULUM WITH 2 DOF FOR THE STUDY OF RESIDUAL COUPLINGS BETWEEN THE TM AND THE GRS: APPROACHING THERMAL NOISE LIMITED SENSITIVITY

L. MARCONI, R. STANGA, C. GRIMANI, M. BASSAN, L. DI FIORE, R. DE ROSA and F. GARUFI

Università degli Studi di Firenze and INFN Firenze, Italy
Università degli Studi di Firenze and INFN Firenze, Italy
Università di Urbino and INFN FIRENZE, Italy
Università di Roma Tor Vergata and INFN Roma 2, Italy
INFN Napoli, Italy
Università Federico II and INFN Napoli, Italy
Università Federico II and INFN Napoli, Italy

The LISA test-mass (TM) is sensitive to weak forces along all 6 Degrees of Freedom (DoFs). Extensive ground testing is required in order to evaluate the influence of cross-talks of read-outs and actuators operating on different DoFs. To best represent the flight conditions, we developed in Firenze a facility with 2 soft DoFs. Using this facility we measure the forces and stiffnesses acting simultaneously along the 2 soft DoFs and, more specifically, we will measure actuation cross talks with closed feedback loop. The facility is now completed with a replica of the GRS (Gravitational Reference Sensor) and the flight model of the electronics boards.

1 Introduction

In Firenze we developed a facility to verify the residual acceleration on 2 DoFs between the TM of LISA [?] and the GRS [?]. Following the previous experience from Trento [?] and Washington [?] in order to have a TM in free fall condition on 2 DoFs (1 translation and 1 rotation) we have built a double torsion pendulum [?]. With our choices (of materials and geometry) we will achieve a sensitivity in acceleration for the 2 DoFs comparable with the sensitivity of LISA PF [?]:

$$S_a^{1/2} = 3 \cdot 10^{-14} ms^{-2}/\sqrt{Hz} \quad @ \quad 1mHz, \tag{1}$$

2 Commissioning

After some tests with a preliminary copy of the TM-GRS [?] we are using now a flight model replica of the TM, GRS and the electronics. We started working with only the rotation DoF of the TM. In Fig. **??** we show the results of the feedback control. In the control loop we have also integrated the movement of the motorized stages, necessary to center the TM in the GRS. In Fig. **??** we show the result of the first measurement of the noise on φ. In (a) panel the square root of the power spectral density of the angular displacement is presented, considering an arm length of $0.02m$, equal to the sensing electrodes separation and a mass for the TM equal to the mass of the TM of LISA PF, we derive the square root of the power spectral density of the linear acceleration, shown in the (b) panel. As it can be seen, in the high frequency band we are

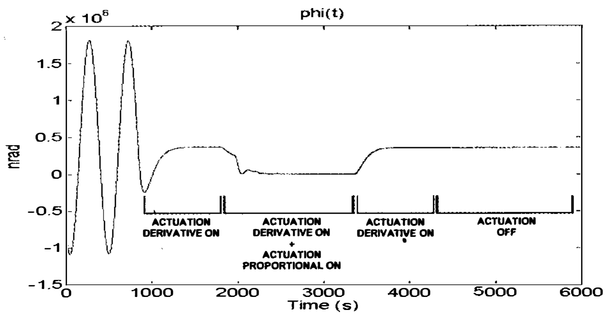

Figure 1: Electrostatics actuation.

limited from the electronics noise and in the low frequency band we are ~ 2 order of magnitude higher than the thermal noise of the suspension fiber. We are presently investigating the origin of the excess noise. After that, we will set free the translational DoF, in order to measure forces and stiffnesses that may act simultaneously on the 2 DoFs.

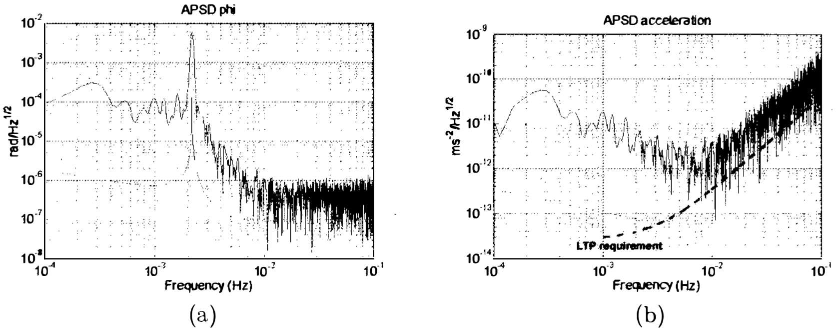

Figure 2: Angular (a) and acceleration (b) noise spectrum (the instrument limit in red). The acceleration has been obtained for an arm length $0.02m$ and for an equivalent TM of $2kg$.

References

1. S. Vitale *et al*, *Phys. Lett.* B **110**, 210 (2002).
2. R. Dolesi *et al*, *Class. and Quant. Grav.* **20**, S99 (2003).
3. M. Hueller *et al*, *Class. and Quant. Grav.* **19**, 1757 (2002).
4. R. C.D. Hoyle *et al*, *Proc. Marcel Grossman Meeting*, Rio de Janeiro 2003.
5. L. Marconi *et al*, *Proc. NSS/MIC IEEE*, Roma 2003.
6. R. Stanga *et al*, *JPCS* **154**, 012032 (2007).

List of Participants

XLVIth Rencontres de Moriond

Gravitational Waves & Experimental Gravity

List of Participants

amily name	First name	Institution	Country	Email address
Abele	Hartmut	Atominstitut - TU Wien	Austria	abele@ati.ac.at
Adelberger	Eric	University of Washington - CENPA	USA	eric@npl.washington.edu
Allen	Bruce	MPI - Gravitational Physics	Germany	bruce.allen@aei.mpg.de
Angonin	Marie-Christine	SYRTE Observatoire de Paris / UPMC	France	m-c.angonin@obspm.fr
Ansari	Reza	LAL	France	ansari@lal.in2p3.fr
Antoniadis	Ignatios	CERN - TH	Switzerland	ignatios.antoniadis@cern.ch
Bambi	Cosimo	IPMU - The University of Tokyo	Japan	cosimo.bambi@ipmu.jp
Bassan	Massimo	Universitá Tor Vergata	Italy	bassan@roma2.infn.it
Beckwith	Andrew	Chongquing University	China	abeckwith@uh.edu
Belczynski	Chris	Warsaw University	Poland	kbelczyn@astrouw.edu.pl
Belfi	Jacopo	Universitá di Pisa	Italy	belfi@df.unipi.it
Bell	Angus	Institute for Gravitational Research	UK	angus.bell@glasgow.ac.uk
Bender	Peter L.	JILA - Univ. of Colorado	USA	pbender@jila.colorado.edu
Bienaymé	Olivier	Astronomiacl Strasbourg Observatory	France	olivier.bienayme@unistra.fr
Bize	Sébastien	SYRTE, Observatoire de Paris	France	sebastien.bize@obspm.fr
Blair	David	University of Western Australia	Australia	dgb@physics.uwa.edu.au
Blanchard	Alain	IRAP	France	alain.blanchard@ast.obs-mip.fr
Blanchet	Luc	IAP	France	blanchet@iap.fr
Blas	Diego	EPFL	Switzerland	diego.blas@epfl.ch
Bodiya	Timothy	LIGO - MIT	USA	bodtim@mit.edu
Bonder	Yuri	Universidad Nacional Autónoma	Mexico	yuri.bonder@nucleares.unam.mx
Bouyer	Philippe	Lab. Photonique, Numériques & Nanosciences	France	philippe.bouyer@institutoptique.fr
Branchesi	Marica	INFN / Universitá di Urbino	Italy	marica.branchesi@uniurb.it
Brueckner	Frank	University of Jena	Germany	frank.brueckner@uni-jena.de
Cacciapuoti	Luigi	European Space Agency / ESTEC	The Netherlands	Luigi.Cacciapuoti@esa.int
Camacho	Abel	Univ.Autonoma Metropolitana-Iztapalapa	Mexico	acq@xanum.uam.mx
Canali	Carlo	Uiversitá degli Studi di Genova - INFN	Italy	canali@ge.infn.it
Cavalier	Fabien	LAL	France	cavalier@lal.in2p3.fr
Chalkley	Eleanor	University of Birmingham	UK	eleanor@star.sr.bham.ac.uk
Champion	David	Max-Planck-Institut für Radioastronomie	Germany	davidjohnchampion@gmail.com
Chen	Yanbei	California Institute of Technology	USA	yanbei@caltech.edu
Christensen	Nelson	Carleton College	USA	nchriste@carleton.edu
Christophe	Bruno	ONERA - DMPH	France	bruno.christophe@onera.fr
Clark	Caroline	Imperial College London	UK	caroline.clark05@imperial.ac.uk
Coward	David	University of Western Australia	Australia	coward@physics.uwa.edu.au
Cruise	Mike	University of Birmingham	UK	a.m.cruise@bham.ac.uk
De Gregorio	Paolo	Politecnico di Torino	Italy	paolo.degregorio@polito.it
Delva	Pacôme	SYRTE - Paris Observatory / UPMC	France	pacome.delva@obspm.fr
Dent	Thomas	Physics & Astronomy, Cardiff University	UK	thomas.dent@astro.cf.ac.uk
Dumarchez	Jacques	LPNHE	France	jacques.dumarchez@cern.ch
Dupré	Pierre	CEA Saclay DSM/IRFU/SPP	France	pierre.dupre@cea.fr
Fafone	Viviana	University of Roma Tor Vergata	Italy	viviana.fafone@roma2.infn.it
nga-Schultheis	Agnes	Observatoire de Besançon / Inst. UTINAM	France	agnes.fienga@obs-besancon.fr
Figueroa	Daniel	University of Helsinki / HIP	Finland	daniel.FIGUEROA@helsinki.fi
Fischbach	Ephraim	Purdue University	USA	ephraim@purdue.edu
Gai	Mario	INAF- Osservatorio Astronomico di Torino	Italy	gai@oato.inaf.it
Geraci	Andrew	University of Nevada	USA	ageraci@unr.edu
Grote	Hartmut	AEI Hannover	Germany	hartmut.grote@aei.mpg.de
Gualtieri	Leonardo	Sapienza Universitá di Roma	Italy	leonardo.gualtieri@roma1.infn.it
Hardin	Delphine	LPNHE - UPMC	France	hardin@in2p3.fr
Hees	Aurelien	Royal Observatory of Belgium	Belgium	ahees@oma.be
Hewitson	Martin	AEI Hannover	Germany	martin.hewitson@aei.mpg.de
Hirtz-Léon	Sylvie	CNES	France	sylvie.leon@cnes.fr

Family name	First name	Institution	Country	Email address
Hohensee	Michael	University of California	USA	hohensee@berkeley.edu
Hough	James	University of Glasgow	UK	j.greig@physics.gla.ac.uk
Huwyler	Cédric	University of Zurich	Switzerland	chuwyler@physik.uzh.ch
Iorio	Lorenzo	MIUR	Italy	lorenzo.iorio@libero.it
Jaekel	Marc-Thierry	LPT - ENS	France	jaekel@lpt.ens.fr
Jenke	Tobias	Atominstitut	Austria	tjenke@ati.ac.at
Jenkins	Jere	Purdue Univ. School of Nuclear Engineering	USA	jere@purdue.edu
Jennrich	Oliver	European Space Agency	The Netherlands	oliver.jennrich@esa.int
Kandhasamy	Shivaraj	University of Minnesota	USA	shivaraj@physics.umn.edu
Kasevich	Mark	Varian Physics	USA	kasevich@stanford.edu
Kluzniak	Wlodek	Copernicus Astronomical Center	Poland	wlodek@camk.edu.pl
Kowalska	Izabela	University of Warsaw	Poland	ikowalska@astrouw.edu.pl
Krolak	Andrzej	Institute of Matheamtics - PAN	Poland	krolak@impan.gov.pl
Kwee	Patrick	AEI	Germany	pakwee@aei.mpg.de
Lamine	Brahim	UPMC - LKB	France	brahim.lamine@upmc.fr
Le Tiec	Alexandre	Maryland Center for Fundamental Physics	USA	letiec@umd.edu
Lemonde	Pierre	CNRS - LNE - SYRTE	France	pierre.lemonde@obspm.fr
Lenoir	Benjamin	ONERA	France	benjamin.lenoir@onera.fr
Levy	Agnès	ONERA	France	agnes.levy@onera.fr
Long	Josh	Indiana University	USA	jcl@indiana.edu
Magneville	Christophe	CEA Saclay	France	cmv@hep.saclay.cea.fr
Magueijo	João	Imperial College	UK	magueijo@ic.ac.uk
Malec	Beata	Copernicus Center For Interdisciplinary Studies	Poland	beata.malec@us.edu.pl
Marconi	Lorenzo	Universitá di Firenze / INFN	Italy	marconi@fi.infn.it
Marque	Julien	European Gravitational Observatory	Italy	julien.marque@ego-gw.it
Mazur	Pawel	University of South Carolina	USA	mazur@physics.sc.edu
McNamara	Paul	ESA- ESTEC	The Netherlands	Paul.McNamara@esa.int
Messina	Riccardo	SYRTE, Observatoire de Paris	France	riccardo.messina@obspm.fr
Meyer	Hinrich	University of Wuppertal	Germany	Hinrich.Meyer@desy.de
Meynadier	Frédéric	SYRTE -- Observatoire de Paris	France	Frederic.Meynadier@obspm.fr
Mezzacappa	Anthony	Oak Ridge National Laboratory	USA	mezzacappaa@ornl.gov
Mozaffari	Ali	Imperial College London	UK	ali.mozaffari@imperial.ac.uk
Nagel	Moritz	Humboldt-Universität / AG QOM	Germany	moritz.nagel@physik.hu-berlin
Nawrodt	Ronny	Friedrich-Schiller-University Jena	Germany	ronny.nawrodt@uni-jena.de
Nedelec	Patrick	IPNL	France	p.nedelec@ipnl.in2p3.fr
Nesvizhevsky	Valery	Institut Laue-Langevin	France	nesvizhevsky@ill.eu
Nobili	Anna M	Universitá di Pisa	Italy	nobili@dm.unipi.it
Normandin	Marc	University of Texas	USA	marc.normandin@utb.edu
Palomba	Cristiano	INFN	Italy	cristiano.palomba@roma1.infn
Paranjape	Manu	Université de Montréal	Canada	paranj@lps.umontreal.ca
Pelisson	Sophie	SYRTE, Observatoire de Paris	France	sophie.pelisson@obspm.fr
Pelle	Bruno	SYRTE - Observatoire de Paris	France	bruno.pelle@obspm.fr
Perrin	Guy	Observatoire de Paris / LESIA	France	guy.perrin@obspm.fr
Peters	Achim	Humboldt-Universitaet zu Berlin	Germany	achim.peters@physik.hu-berlin
Rasel	Ernst Maria	Hannover Institute of Quantum Optics	Germany	office-iq@iqo.uni-hannover.de
Raymond	Vivien	Northwestern University - CIERA	USA	ciera@northwestern.edu
Reynaud	Serge	LKB	France	serge.reynaud@upmc.fr
Rezzolla	Luciano	Albert Einstein Institute	Germany	Ute.Schlichting@aei.mpg.de
Robinet	Florent	LAL	France	robinet@lal.in2p3.fr
Rocchi	Alessio	INFN Roma Tor Vergata	Italy	alessio.rocchi@roma2.infn.it
Romalis	Michael	Princeton University	USA	romalis@princeton.edu
Rosinska-Gondek	Dorota	University of Zielona Góra	Poland	dorota@camk.edu.pl
Rosowsky	André	CEA Saclay	France	andre.rosowsky@cern.ch
Rowan	Sheila	University of Glasgow	UK	j.greig@physics.gla.ac.uk
Rudenko	Valentin	Sternberg Astronomical Institute - MSU	Russia	rvn@sai.msu.ru
Saa-Vazquez	Alberto	University of Campinas	Brazil	asaa@ime.unicamp.br
Sadoyan	Avetis Abel	Astronomical Rechen Institute	Germany	asadoyan@ari.uni-heidelberg.
Sandberg	Vern	LIGO Hanford Observatory	USA	sandberg@ligo-wa.caltech.edu
Sathyaprakash	Bangalore	Cardiff University	UK	B.Sathyaprakash@astro.cf.ac.

ily name	First name	Institution	Country	Email address
Schnabel	Roman	AEI	Germany	roman.schnabel@aei.mpg.de
Schuldt	Thilo	University of Applied Sciences	Germany	tschuldt@htwg-konstanz.de
Snopek	Anna	University of Zielona Góra	Poland	snopek.a.m@gmail.com
Soares	Ivano Damião	Centro Brasileiro de Pesquisas Fisicas / MCT	Brazil	ivano@cbpf.br
Speake	Clive	University of Birmingham	UK	c.c.speake@bham.ac.uk
Stairs	Ingrid	University of British Columbia	Canada	stairs@astro.ubc.ca
Suzuki	Toshikazu	KEK	Japan	toshi.suzuki@kek.jp
Tasson	Jay	Whitman College	USA	tassonjd@whitman.edu
Terrano	William	University of Washington CENPA	USA	william.terrano@gmail.com
Thomas	Daniel	Imperial College	UK	dbt08@ic.ac.uk
Tobar	Michael	The University of Western Australia	Australia	mike@physics.uwa.edu.au
Touboul	Pierre	ONERA	France	pierre.touboul@onera.fr
Veitch	John	Cardiff University	UK	john.veitch@astro.cf.ac.uk
Verma	Ashok Kumar	Observatoire de Besançon / inst. UTINAM	France	ashok@obs-besancon.fr
Vinet	Jean-Yves	ARTEMIS, OCA	France	vinet@oca.eu
Wagner	Todd	University of Washington - CENPA	USA	toddwagn@uw.edu
Ward	Robert	APC	France	robert.ward@apc.univ-paris-diderot.fr
Was	Michal	LAL	France	mwas@lal.in2p3.fr
Weber	William Joseph	Universitá di Trento	Italy	weber@science.unitn.it
Wilkinson	Carol	LIGO Hanford Observatory	USA	wilkinson@ligo-wa.caltech.edu
Wolf	Peter	LNE - SYRTE, Observatoire de Paris	France	peter.wolf@obspm.fr
Yakushin	Igor	LIGO Livingston Observatory	USA	igor@ligo-la.caltech.edu
Yu-Hung	Lien	Universita di Firenze	Italy	yh-hung.lien@fi.infn.it
Zakharov	Alexander	ITEP	Russia	zakharov@itep.ru